BULGARIAN CHEMICAL COMMUNICATIONS

*Journal of the Chemical Institutes
of the Bulgarian Academy of Sciences
and of the Union of Chemists in Bulgaria*

Chemical composition of the essential oil of *Plectranthus mollis* roots

R. K. Joshi[*]

Department of Phytochemistry, Regional Medical Research Centre (Indian Council of Medical Research), Belgaum, Karnataka-590 010, India

The hydro-distilled essential oil of the roots of *Plectranthus mollis* Spreng. (Lamiaceae) was examined for the first time to determine its composition. The oil was analyzed by gas chromatography equipped with a flame ionization detector (GC-FID) and gas chromatography coupled with mass spectrometry (GC/MS). Sixty constituents were identified, representing 98.4% of the total oil. The major constituents were γ-eudesmol (22.5%), bornyl acetate (14.9%), khusinol (11.4%), and *ar*-curcumene (6.8%). Oxygenated sesquiterpenes (46.4%), and oxygenated monoterpenes (25.1%) were the prominent groups of compounds, followed by sesquiterpene hydrocarbons (22.1%), monoterpene hydrocarbons (4.4%), and phenyl derivatives (0.4%) type constituents.

Keywords: *Plectranthus mollis* Spreng., Lamiaceae, essential oil composition, γ-eudesmol, GC-MS.

INTRODUCTION

The genus *Plectranthus* of the family Lamiaceae, containing about 300 species, is found in Tropical Africa, Asia and Australia [1]. *Plectranthus* is a large and widespread genus with a diversity of ethnobotanical uses. The roots of *Plectranthus mollis* (Syn. *Plectranthus incanus* Link.) are used to drive away evil spirits in India, Kenya and Tanzania [2, 3], while the leaves are consumed as a vegetable [4]. In traditional medicine *P. mollis* has been used against snakebites in India, Gabon and Kenya [3]. This plant is also used as a tonic [5], respiratory stimulant and vasoconstrictor, cardiac depressant, cure for haemorrhage [6], treatment of mental retardation [7] and rheumatism [8, 5].

P. mollis is reported to exhibit antimicrobial activity [9], relaxant activity on smooth and skeletal muscles [6]. It has cytotoxic and anti-tumour promoting activities, and can be used in the treatment of cancer [10]. The seeds of *P. mollis* are fried in mustard oil and then massaged all over the body as an insect repellant [3]. The compounds fenchone, α-humulene, piperitenone oxide, *cis*-piperitone oxide, and *E-β*-farnesene have been identified in the essential oil of *P. mollis* from South India [9], while fenchone, piperitone oxide, piperitenone, piperitenone oxide [11], *cis*-piperitone oxide and piperitenone oxide [12] have been reported from Northern India. Extensive review of literature revealed that the root oil of *P. mollis* has not been investigated. To the best of the author's knowledge, this is the first report on the essential oil composition of the roots of *P. mollis*.

EXPERIMENTAL

Plant material

The plant was collected in the month of March 2012 from district Belgaum (15º88'66" N - 74º52'35" E) Karnataka, India, at an elevation of 800 m. The plant was identified at the Regional Medical Research Centre, Belgaum (herbarium specimen No RMRC-535).

Isolation of essential oil

The roots (300 g) were chopped to small pieces and subjected to hydro-distillation (2000 mL distilled water + 300 g plant material, in a 3000 mL round-bottom flask) using a Clevenger type apparatus for 3 h [13]. The oil was trapped by adding n-hexane, dried over anhydrous Na_2SO_4, and kept in a sealed vial at -4°C until analysis. The yield of oil was 0.11%, w/w).

Analysis of essential oil

Analysis of the oil was achieved using Varian 450 gas chromatograph (GC) equipped with a fused silica CP-Sil 8 CB capillary column (30 m × 0.25 mm; 0.25 m film thickness) and flame ionization detector. The carrier gas was nitrogen at a flow rate of 1.0 mL/min. The initial oven temperature was 60°C which was increased to 220°C (ramp 3°C/min) and held for 5 min. The injector and detector temperatures were 230 and 240°C, respectively. The injection volume was 1.0 μL diluted in *n*-hexane. The sample was injected using a split ratio of 1:50. The gas chromatography/mass spectrometry (GC-MS) analysis of the oil was

* To whom all correspondence should be sent:
E-mail: joshirk_natprod@yahoo.com

carried out on a Thermo Scientific Trace Ultra GC interfaced with a Thermo Scientific ITQ 1100 mass spectrometer fitted with TG-5 fused silica capillary column (30 m × 0.25 mm i.d., 0.25 μm film thickness) using the above oven temperature program. The carrier gas was helium at 1.0 mL/min. The injector temperature was 230°C, the injection volume 0.1 μL prepared in *n*-hexane. The sample was injected using a split ratio of 1:50. MS were taken at 70 eV over the mass scan range of 40-450 amu. All parameters of GC and GC/MS applied for analysis of the oil were those literatures reported earlier [14-19].

Identification of the compounds

Identification of constituents was done on the basis of the retention index (RI) determined with reference to homologous series of *n*-alkanes C_8-C_{25}, under identical experimental conditions, MS library search (NIST 08 MS Library (Version 2.0 f; Thermo Fisher Scientific, Austria) and WILEY MS 9th Edition (Thermo Fisher Scientific, Austria), and by comparing with MS literature data [20] and co-injection of authentic samples purchased from Sigma-Aldrich, India. The relative amounts of individual components were calculated based on the GC peak area (FID response) without using a correction factor.

RESULTS AND DISCUSSION

Sixty compounds were characterized and identified according to their mass spectra and their relative retention indices determined on a non-polar stationary phase capillary column, comprising 98.4% of the total oil constituents. The identified compounds are listed in Table 1 in elution order from the TG-5 column, along with the percentage composition of each component and its retention index.

Table 1. Chemical composition of the essential oil of *P. mollis* roots

Compound	RI	%	Identification
Tricyclene	901	0.1	RI, MS
α-Pinene	908	0.4	RI, MS, CI
α-Fenchene	919	0.7	RI, MS
Sabinene	927	0.9	RI, MS
β-Pinene	941	0.9	RI, MS
Myrcene	950	0.1	RI, MS
α-Terpinene	974	0.6	RI, MS
o-Cymene	981	0.3	RI, MS
Limonene	985	0.2	RI, MS
1,8-Cineole	988	0.1	RI, MS,CI
(Z)-β-Ocimene	992	t	RI, MS
(E)-β-Ocimene	1003	t	RI, MS
Bergamal	1009	t	RI, MS
γ-Terpinene	1014	0.1	RI, MS

Compound	RI	%	Identification
Fenchone	1046	1.2	RI, MS
endo-Fenchol	1073	0.2	RI, MS
trans-Sabinol	1102	1.0	RI, MS
Camphor	1108	0.7	RI, MS, CI
Borneol	1132	1.5	RI, MS
Terpin-4-ol	1146	0.2	RI, MS, CI
α-Terpineol	1162	0.2	RI, MS, CI
Myrtenal	1169	t	RI, MS
endo-Fenchyl acetate	1196	5.1	RI, MS
Neo-iso-dihydro carveol	1206	0.1	RI, MS
Bornyl acetate	1277	14.9	RI, MS
α-Longipinene	1352	0.2	RI, MS
Cyclosativene	1373	0.5	RI, MS
α-Copaene	1384	0.7	RI, MS
β-Patchoulene	1391	0.4	RI, MS
β-Cubebene	1401	0.8	RI, MS
Longifolene	1424	0.5	RI, MS
cis-α-Bergamotene	1431	0.9	RI, MS
β-Caryophyllene	1436	0.6	RI, MS, CI
trans-α-Bergamotene	1449	0.4	RI, MS
(E)-β-Farnesene	1479	0.4	RI, MS
β-Acoradiene	1491	0.7	RI, MS
β-Chamigrene	1499	2.9	RI, MS
ar-Curcumene	1510	6.8	RI, MS
α-Zingiberene	1525	0.9	RI, MS
Cuparene	1536	4.7	RI, MS
β-Bisabolene	1540	0.2	RI, MS
γ-Cadinene	1546	0.3	RI, MS
cis-Calamenene	1557	t	RI, MS
Kessane	1528	t	RI, MS
Liguloxide	1565	t	RI, MS
α-Cadinene	1573	0.2	RI, MS
trans-Sesquisabinene hydrate	1620	1.2	RI, MS
β-Copaen-4-α-ol	1629	0.5	RI, MS
Khusimone	1637	1.7	RI, MS
10-*epi*-γ-Eudesmol	1658	2.1	RI, MS
γ-Eudesmol	1688	22.5	RI, MS
α-Eudesmol	1698	3.1	RI, MS
Khusinol	1722	11.4	RI, MS
(Z)-α-Santalol	1729	0.4	RI, MS
α-Bisabolol	1734	1.8	RI, MS
(Z)-α-*trans*-Bergamotol	1748	0.2	RI, MS
Cedroxyde	1758	0.7	RI, MS
(Z)-α-Atlantone	1767	0.3	RI, MS
14-oxy-α-Muurolene	1815	0.5	RI, MS
2-hexyl-(Z)-Cinnamaldehyde	1825	0.4	RI, MS
Monoterpene hydrocarbons		4.4	
Oxygenated monoterpenes		25.1	
Sesquiterpene hydrocarbons		22.1	
Oxygenated sesquiterpenes		46.4	
Phenyl derivatives		0.4	
Total identified		98.4	

RI=Retention index relative to C_8-C_{25} *n*-alkanes on TG-5 column, MS=NIST and Wiley library and the literature, CI=Co-injection of authentic samples, t=trace (<0.1%).

The main constituents were identified as *γ*-eudesmol (22.5%), bornyl acetate (14.9%), khusinol (11.4%), *ar*-curcumene (6.8%). The oil was rich in oxygenated sesquiterpenes (46.4%), followed by oxygenated monoterpenes (25.1%), sesquiterpene hydrocarbons (22.1%), monoterpene hydrocarbons (4.4%), and phenyl derivatives (0.4%). This is the first report on the chemical composition of the essential oil of roots of *P. mollis*. Further studies are required to investigate biological activities of roots essential oil of this plant.

It is interesting that constituents identified in the essential oil of the roots of *P. mollis* were found somehow contrary to those in the aerial parts [9, 11, 12] oil. Myrcene, limonene, fenchone, camphor, borneol, terpin-4-ol, *α*-terpineol, *β*-cubebene, *β*-caryophyllene, trans *α*-bergamotene and (*E*)-*β*-farnesene were detected as common constituents in roots and aerial parts [9] oils. The overall quantitative contribution of these common compounds in roots and aerial parts [9] was found to be 6.3% and 50.3%, respectively. Moreover, the quantity of the compound fenchone was reported to be 32.3% in the aerial parts [9] oil, while 1.2% in the roots oil. Furthermore, the major compounds *α*-humulene, piperitenone oxide, and *cis*-piperitone oxide which were reported in significant quantities in the aerial parts oil of *P. mollis* [9, 11, 12] could not be detected even in trace amounts in the roots oil. In addition, the aerial parts oil was reported to be rich in oxygenated monoterpenes type constituents [9, 11, 12], while in this report the roots oil was found to be affluent oxygenated sesquiterpenes type constituents.

The composition of the essential oil often varies between different plant parts [21]. It is noteworthy that the complex composition of essential oils in the same plant parts can differ. The formation of essential oils depends on the tissue differentiation (secretory cells, excretion cavities, etc.) and on the ontogenetic phase of the respective plant [22]. Individual plants also showed variation in the percentage of chemical components depending on the part of the plant from which the oil was extracted [23]. The secondary volatile metabolites from different parts of the same plant virtually showed quantitative differences of compounds reported in the essential oil composition from aerial parts and flowers [24-26] but derived different chemotypes from the roots of same plant [27-29]. Nevertheless, there is an almost uncountable number of single substances and a tremendous variation is observed in the composition of essential oils of aromatic plants.

REFERENCES

1. C. W. Lukhoba, M. S. J. Simmonds, A. J. Paton, *J. Ethnopharmacol.,* **103**, 1 (2006).
2. C. W. Githinji, J. O. Kokwaro, *J. Ethnopharmacol.,* **39**, 197 (1993).
3. S. P. Jain, S. C. Singh, H. S. Puri, *J. Ethnopharmacol.,* **3**, 44 (1994).
4. R. K. Maikhuri, A. K. Gangwar, *Econ. Bot.,* **47**, 345 (1993).
5. M. K. Sebastian, M. M. Bhandari, *J. Ethnopharmacol.,* **12**, 223 (1984).
6. S. N. Yoganarasimhan, Medicinal Plants of India, Tamil Nadu. In V. Srinivasan and N. K. Ram (Eds.), Cyber Media, Bangalore, 2000.
7. V. K. Singh, Z. A. Ali, *Fitoterapia,* **63**, 136 (1992).
8. K. C. Sharma, U. Sharma, *IndianJ. Pharmacol.,* **131**, 96 (1981).
9. R. K. Joshi, *Rev. Biol. Trop.,***62**, 423 (2014).
10. D. S. Bhakuni, M. L. Dhar, M. M.Dhar, B. N. Dhawan, B. Gupta, R. C. Srimali, *Indian J. Exp. Biol.,* **9**, 91 (1971).
11. M. Pal, A. Kumar, S. K. Tewari, *Facta Universitatis,* **9**, 57 (2011).
12. G. C. Shah, R. Bhandari, C. S. Mathela, *J. Essent. Oil Res.,* **4**, 57 (1992).
13. R. K. Joshi, *J. Ethnopharmacol.,* **145**, 621 (2013).
14. R. K. Joshi, *Pharm. Biol.*, **51**, 888 (2013).
15. R. K. Joshi, *Chem. Nat. Compd.,* **47**, 1010 (2012).
16. R. K. Joshi, *Nat. Prod. Commun.,* **8**, 401 (2013).
17. R. K. Joshi, V. Badakar, *Nat. Prod. Commun.,* **7**, 941 (2012).
18. R. K. Joshi, *Nat. Prod. Commun.,* **8**, 225 (2013).
19. R. K. Joshi, *Nat. Prod. Commun.,* **8**, 401 (2013).
20. R. P. Adams, Identification of essential oil components by gas chromatography/mass spectrometry. Allured Publishing Corporation, Carol Stream, IL, 2007.
21. C. B.Johnson, A. Kazantzis, M. Skoula, U. Mitteregger, J. Novak, *Phytochem. Anal.,* **15**, 286 (2004).
22. C. Franz, J. Novak, Sources of essential oils in: Handbook of Essential Oils Science, Technology, and Applications, K. H. C. Baser and G. Buchbauer (Eds.), CRC Press, New York, NY, USA, 2010, p. 39.
23. L. C. M.Rost, R. Bos, *Planta Med*., **36**, 350 (1979).
24. R. K. Joshi, *Maejo Int. J. Sci. Technol.*, **8**, 161 (2014).
25. R. K. Joshi, *Chem. Nat. Compd.,* **50**, 382 (2014).
26. R. K. Joshi, *J. Essent. Oil Bear. Pl.,* **16**, 71.

27. N. K. Leela, A. Tava, P. M. Shahj, S. P. John, B. Chempakam, *ActaPharm.,* **52**, 137 (2002).
28. B. F. Mirjalili, M. H. H. Meybody, M. M. Ardakani, A. Rustaiyan, N. Ameri, S. Masoudi, A. Bamoniri, *J. Essent. Oil Res.,* **18**, 544 (2006).

29. R. K. Joshi, *J. Chem.,* **2013**, 1 (2013).

ХИМИЧЕН СЪСТАВ НА ЕТЕРИЧНО МАСЛО ОТ КОРЕНИ НА *PLECTRANTHUS MOLLIS*

Р. К. Джоши

Департамент по фитохимия, Регионален център за медицински изследвания (Индийски съвет за медицински изследвания), Белгаум, Карнатака, Ииндия

(Резюме)

Изследвано е етерично масло, получено от корените на *Plectranthus mollis* Spreng. (Lamiaceae), получено чрез дестилация с водна пара. За първи път е установен химичният му състав. Маслото е анализирано чрез газ-хроматография с FID-детектор, съчетана с мас-спектрометрия (GC/MS). Идентифицирани са 60 компоненти, представляващи 98.4% от цялото масло. Главните съставки са *γ*-евдесмол (22.5%), борнил-ацетат (14.9%), хусинол (11.4%) и *ar*-куркумен (6.8%). Окислените сески-терпени (46.4%) и окислените монотерпени (25.1%) са главната група от съединенията, следвани от сески-терпенови въглеводороди (22.1%), монотерпенови въглеводороди (4.4%) и фенилови производни (0.4%).

Experimental arrangements for determining the photocatalytic activity of Au/TiO₂ in air and wastewater purification

A. Eliyas[1*], P. Petrova[1], F. J. López-Tenllado[2], D. Tomova[1], A. Marinas[2]

[1]Institute of Catalysis, Bulgarian Academy of Sciences, 1113 Sofia, Bulgaria
[2]Organic Chemistry Department, University of Cordoba, Campus de Rabanales, Marie Curie Building, E-14014-Córdoba,

Photocatalytic material, representing 0.5wt% Au/TiO₂, has been synthesized using the deposition-precipitation method (DP), on the basis of the commercially available TiO₂ (Degussa P25), modifying it with nanosized gold nanoparticles. The single point BET specific surface area has been found to be 52 m^2/g. The Au/TiO₂ slurry has been deposited on an Al TLC sheet pre-coated with SiO₂ and characterized by SEM revealing uniform thin film coating. The TPR profile proved the presence of oxidic species around the nanosized gold particles and transformation of some Ti^{4+} to Ti^{3+} enhanced by gold in close vicinity. The photocatalytic activity in air purification from ethylene has been measured in a continuous flow flat-plate gas-phase photocatalytic reactor (illumination intensity of 0.14 W/cm^2). The reactor configuration was improved with gas circulation pump and air splitter. The efficiency of the Au/TiO₂ suspension has been tested in model wastewater purification from 4-chlorophenol in a semi-batch slurry reactor (illumination intensity of 0.05 W/cm^2). Both photocatalytic experiments proved that the gold-doped TiO₂ is superior in its performance to the Evonik TiO₂ P25 commercially available photocatalyst due to charge separation and prevention of the electron-hole recombination.

Key words: titania photocatalyst, gold doping, air/water decontamination

INTRODUCTION

4-chlorophenol is a popular model pollutant, selected in photocatalytic studies, as it often appears in industrial wastewaters from the production of diazo dyes or pesticides [1, 2]. Chlorophenols are of special interest due to their high toxicity and low biodegradability [3]. Different semiconducting metal oxides have been studied in the photocatalytic oxidation of organic contaminants [4, 5] and TiO₂ is generally accepted to be the most active photocatalyst among them all [6]. Ethylene (C_2H_4) is the most widely manufactured petrochemical, which causes air pollution in industrial sites, [7, 8] and for this reason C_2H_4 and its chlorinated derivatives (applied as solvents) are often selected as model air pollutants in photocatalytic decontamination studies [9- 16].

There is debate in the current literature about modifying TiO₂ with noble metals, whose clusters possibly separate the charge carriers (capturing the photoexcited electrons) and leaving behind the positively charged holes to act as active sites for oxidation reactions [2, 4, 6, 8, 15]. This supposition is based on the existence of Schottky barriers on the metal/semiconductor oxide inter-phase boundary, preventing the return of the photoexcited electrons to the oxide phase (recombination) [17, 18]. In order to test this hypothesis we chose to deposit gold nanoparticles on commercially available TiO₂ Degussa P25. If it is correct one can expect increase in the photocatalytic activity of the Au/TiO₂ composite in view of the fact that longer life-time of holes will result in generation of larger number of hydroxyl radicals on this type of active sites. It is known, in fact, that these hydroxyl radicals are the active particles in a radical-chain type of oxidation reaction mechanism. Increasing the gold content, however, decreases the adsorption capacity of TiO₂ and reduces the reaction rate, i.e. too high metal content could be an unfavorable factor [17]. There are studies, which claim that metal clusters can cause photon absorption in the visible range, which would considerably increase the utilization of a larger portion of the solar light spectrum and this would make the photocatalysts applicable on an industrial scale [18]. Details about the optimal reactor configurations are to be found in [25, 26].

EXPERIMENTAL

Synthesis of Au/TiO₂ photocatalytic composite material

Photocatalytic material has been synthesized using the deposition-precipitation method (DP), on

* To whom all correspondence should be sent:
E-mail: alel@ic.bas.bg

the basis of commercially available TiO_2 (Degussa P25), modifying it with nanosized gold nanoparticles. The deposition was aimed at achieving an optimal gold loading of 0.5% by weight preserving to a great extent the high adsorption capacity of TiO_2. First, the TiO_2 was suspended in deionized water by sonication (Ultrasonic Processor Hielscher UP200S, Germany) aimed at disintegration of the agglomerates and obtaining a stable slurry. Then an aqueous solution of $HAuCl_4$ and K_2CO_3 was added to the suspension and the interaction process was carried out at constant pH of 6.8 and reaction temperature of 60°C. After ageing for 1 hour the precipitate was carefully washed until complete elimination of chloride traces was achieved. Then it was dried first in vacuum at 80°C and then calcined in air at 400°C for 2h. The entire synthesis procedure was carried out with high degree of reproducibility using computer-controlled laboratory reactor Contalab (Contraves AG, Switzerland) under complete and precise control of all reaction parameters: reaction temperature, pH factor of the medium, stirrer speed, reactant feed flow rate.

Single point BET measurements

The standard reference photocatalyst TiO_2 Degussa P25 (80% anatase, 20% rutile), had a specific surface area of $50m^2/g$, measured using $30\%N_2 +70\%He$ mixture in order to obtain adsorbed N_2 monolayer at the boiling temperature of liquid nitrogen (77 K). The obtained value for the gold modified sample was 52 m^2/g – the difference between the two values is of the order of the experimental error so it can be accepted to be practically the same.

Deposition of thin film coating on TLC sheet

The powdered photocatalytic material, representing $0.5\%Au/TiO_2$ Degussa 25, was tested in regard to its photocatalytic activity in air purification from ethylene. The color of the powder material is grayish-violet. An amount of 56 mg of the material was weighed on an analytical balance Precisa XB 220A (Switzerland) in order to obtain a thin film coating of 1 mg/cm^2 on a flat sheet of geometric area of 56 cm^2. The piece of sheet has dimensions 13.4 cm × 4.2 cm with rounded up corners – it was cut out of TLC foil (thin layer chromatography aluminum sheet 20 cm × 20 cm Merck, Art.5554). It is commercially available pre-coated with silica gel 60 F_{254} having layer thickness of 0.2 mm. TiO_2 suspensions form thin film coatings on silica gel having very good adhesion properties (high sticking coefficient) because of the

similar chemical nature of TiO_2 and SiO_2. The sample amount was transferred into a 5 ml volumetric flask and deionized water was filled up to the mark. Then the suspension was treated in ultrasound bath for 15 min to disintegrate the agglomerates using Hielscher Ultrasonic Processor UP200S (Germany) under the following conditions: 24 kHz ultrasound, impulse regime of cycle 0.5, intensity 70% of the maximal amplitude. After the sonication the suspension was deposited drop-wise on the TLC sheet using a capillary with a directing air stream to obtain uniform coating. The coating was dried using an air-drier and left to stay overnight before the photocatalytic activity testing. Then the TLC sheet with the so obtained thin film coating of $0.5\%Au/TiO_2$ Degussa 25 (1 mg/cm^2) (Figure 1) was mounted in the reactor nest of a POLITEF gas-phase flat-plate continuous flow photocatalytic reactor reported in our previous paper [19].
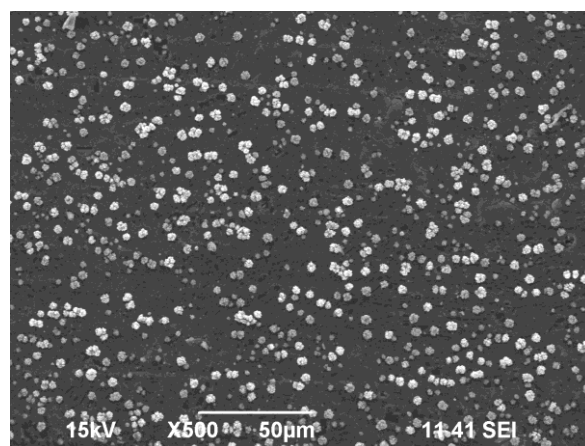
Fig. 1. Secondary electron image of uniform coating of Au/TiO_2 deposited on SiO_2 pre-coated TLC alumina sheet at magnification x 500 and 15 kV acceleration voltage.

RESULTS AND DISCUSSION

TPR Measurements

Titania is among the nonreducible bulk oxides, the standard free energy change (ΔG^o) for reduction has a high positive value of about 200 kJ mol^{-1} [20]. The TPR profile of an Au/TiO_2 sample containing 3 wt% of Au is shown in Figure 2. The detector sensitivity is not enough concerning the samples on TiO_2 with lower Au content. The two registered peaks are with very low intensity. The small LT peak at about 50 °C (HC of only 0.003 mmol/g) can be assigned to the oxidic species around the nanosized gold particles [21]. The peak in the temperature interval 400-500 °C (0.01 mmol/g) could be connected to the transformation of some Ti^{4+} to Ti^{3+} enhanced by gold in close vicinity.

There are literature data for TiO_2 concerning the possibility of Ti^{3+} existing. Since Ti^{3+} ions are not characteristic of anatase, they are assumed to be the places of localization of the hydroxyl groups [22]. Hadjiivanov et al. [23] have reported about anatase reduction with hydrogen at 400 °C (100 Torr of H_2 for 1 h) leading to the formation of some Ti^{3+}ions. Supplementary to the main anatase phase, small quantities of Ti_2O_3 and Ti_4O_7 have been registered by XRD in the case of titania supported on activated carbon. The existence of these Ti^{3+} ion-containing phases were explained by the reducing effect of the carbon [24].
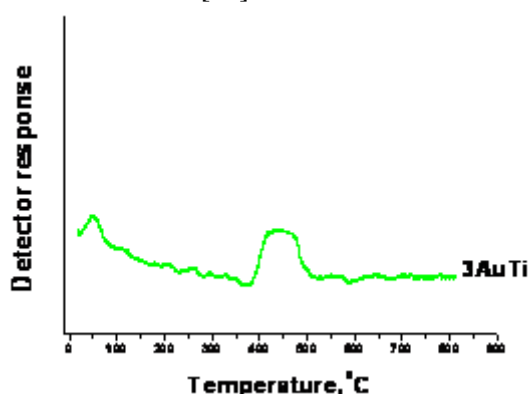
Fig. 2. TPR profile of 3%Au/TiO₂ composite photocatalyst sample.

Continuous flow /flow-circulation photocatalytic reactor

The construction of the POLITEF flat-plate gas-phase continuous-flow photocatalytic reactor (Figure 3), reported previously [19], has been improved by creating a circular contour: reactor-gas pump [20]. Thus the reactor is transformed from plug-flow type PFG reactor [21] into an ideal-mixing type of reactor, when the gas circulation rate inside the circulation contour is more than 50 times greater than the feed flow rate at the reactor inlet [20]. The conversion degree of ethylene, used as a model air contaminant, this time was measured under heavy-duty conditions for the catalyst (in the present study 5% = 50 000 ppm CxHy) – much higher than the concentration used previously (1000 ppm) [19]. The feed concentration of ethylene at the inlet of the reactor is the same as that at the outlet of the reactor when there is no illumination - the reaction is not occurring at room temperature in the dark. In both cases – with illumination and without illumination the LANCOM III gas analyzer (England) is connected to the reactor outlet, measuring feed concentration (the light is off) or converted mixture concentration (the light is on). Multiple flow controller MATHESON model 8249 (Belgium) was used to feed the reactants to the reactor. There are two N₂

flow rates: 30 ml/min dry N₂ (directly into the reactor), while 15 ml/min moist N₂ passes first through a deionized water saturator. The temperature of the saturator was maintained constant using a thermostat set at 25°C. The concentrations of the feed mixture at the inlet of the reactor were 84% N₂, 11% O₂, 5% C₂H₄. All the experimental runs were carried out at one and the same contact time 4.5 min (highest possible contact time) to obtain the highest conversion.
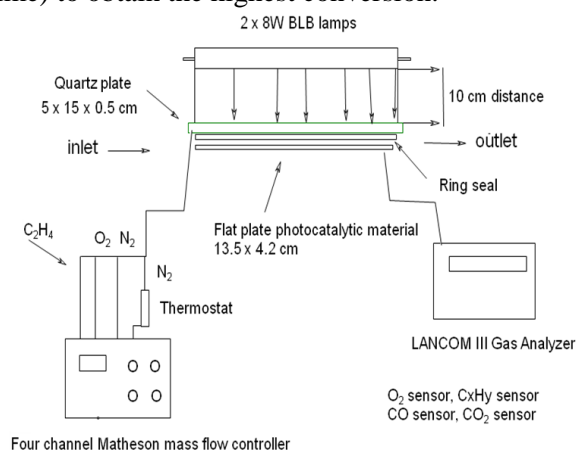
Fig. 3. Gas-phase flat-plate continuous flow photocatalytic reactor, equipped with mass-flow controller and multi-sensor gas analyzer.

The ethylene contact time was calculated as the time interval within which a volume of ethylene equal to the volume of the reactor is passing through the reactor (residence time) – the reactor volume is 11.2 cm³ and ethylene feed flow rate is 2.5 ml/min. All other conditions were preserved the same – oxygen/ethylene feed ratio and optimal relative humidity of 30%. The relative humidity is calculated as the feed flow rate of moist N₂ (15 ml/min) related to the total feed flow rate (53.5 ml/min). As a result of the transition from the diffusion region to the kinetic region of operation and elimination of concentration gradients and the dead zones, existing previously [19], the performance was improved considerably. The performance of this new photocatalytic material is to be compared with the standard reference photocatalyst TiO₂ Degussa P 25 (75% anatase + 25% rutile with average anatase particle size 25 nm). The small nanometer size of both types of photocatalyst particles excludes in advance the pore diffusion retardation effect and so there is no need of grinding the catalyst and collecting specific sieve fraction, as is the case with classical catalysis and industrial catalysts, tested under laboratory conditions. A sheet of desired dimensions (13.4×4.2 cm) is cut out and accommodated in the reactor nest, giving an illuminated surface area of

56 cm^2. The illumination window was a flat plate quartz glass, enabling the use of two UV light lamps Philips TUV 4W/G4 T5 (Holland), achieving illumination intensity of 0.14 W/cm^2 at illumination distance 0 cm. The use of non-gradient external gas circulation catalytic reactor simplifies to a great extent the mathematic task of calculating the reaction rates [19]. In this specific case the reaction rate R (mol/h.g-cat) is calculated simply by dividing the conversion degree of the substrate (in our case – ethylene as a model air pollutant) by the contact time τ (h.g-cat/mol).

The use of a circulation contour: reactor-gas pump and the creation of ideal mixing conditions do not affect, however, the depth of the kinetic region. As in our previous work [19] the optimal thickness of the TiO$_2$ film coating remains about 1 mg of photocatalyst per 1 square centimeter. When this film thickness is increased the lower layers suffer from C$_2$H$_4$ diffusion limitations. The highest conversion degrees were achieved with the gold-doped sample and UV-C light at the highest contact times of ethylene (4 min) and optimal relative humidity of 28% - Table 1. It can be seen from the data in Table 1 that with all the three different types of illumination the performance of the gold-doped sample is superior to the non-doped TiO$_2$ samples. The visible light photocatalytic activity can be attributed to the rutile TiO$_2$ component of Degussa (band gap 3.0 eV and λ$_{max}$ = 413 nm, i.e. activation by visible light) but it is difficult to explain such a huge promoting effect by gold-nanosized particles, which are supposed only to increase the charge carriers separation and promoting the lifetime of the oxidation sites, i.e. the positively charged holes.

Flow-splitter calibration

The second improvement was the application of a flow-splitter at the reactor outlet to improve the precision of the analyses. The LANCOM III gas-analyzer (Land Instruments Co., UK), used for the analyses of the feed mixture and of the converted reaction mixture, creates a problem as it is equipped with a powerful sucking pump creating under-pressure in a small-scale laboratory reactor. In fact this gas-analyzer is designed for use in industrial chimneys at great gas flow velocities to analyze the flue gas. In order to avoid the under-pressure problem in the photocatalytic reactor we had to use a three-way fitting with a loose end – now the analyzer is sucking in the converted mixture together with laboratory air (Figure 4). The ratio between the two split flow rates was calculated for each case based on the gas-analyzer

pump productivity (constant) and the specific outlet mixture flow rate (variable) – the latter is specific for each experimental run. So the ratio is also a variable. This calculation is not sufficiently accurate. We applied precision calibration using a cylinder of standard gas 19.25% CO$_2$, to determine the ratio between the two split flow rates after the reactor outlet and before the LANCOM III gas-analyzer. The analyzer detected 0.36% CO$_2$, which is 53.47 times lower than the actual CO$_2$ concentration. Based on these two values one can calculate that the ratio between the air flow, sucked in by LANCOM and the flow of converted mixture at the outlet of the reactor is:

$$F_{air} : F_{out} = 53.47 : 1$$

Therefore one can calculate the actual CxHy, obtained as a result of the photocatalytic reaction at the reactor outlet by multiplying **C$_{measured}$** by 53.47.
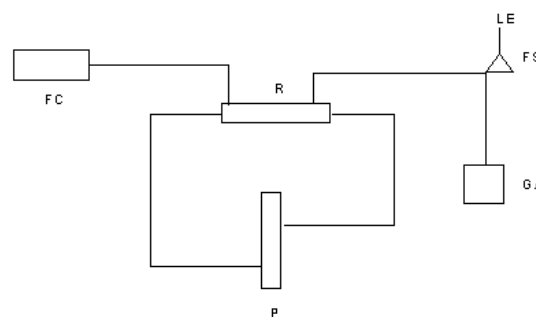
Fig. 4. Block-scheme of a flow-circulation photocatalytic reactor: R-reactor, P –pump, FC – flow controller, FS – flow splitter, LE – loose end, GA – gas analyser

Photocatalytic activity measurements in a semi-batch stirred suspension reactor

The experimental runs for waste water purification were carried out in a semi-batch stirred suspension reactor using 4-chlorophenol as the model contaminant with a concentration of 350 mgC/L. The reactor is "batch type" with respect to the charged amount of photocatalyst (slurry 200 mg in 200 ml 4-chlorophenol solution). At the same time there is continuous air flow through the suspension – it is accepted to denote such combination as "semi-batch reactor". The photocatalytic reactor has a total volume of 300 ml volume (diameter of the reactor 11.2 cm). The reactor is equipped with an electromagnetic stirrer. A sample of the studied photocatalytic powder material is added (200 mg) gradually upon stirring (400 rpm) and bubbling atmospheric air through the suspension, fed by a micro-compressor RESUN AC-2600B at a flow rate of 88 ml/min. The air is fed into the reactor through 2 frits, situated symmetrically on both sides of the UV lamp,

dispersing the air flow in very small bubbles to ensure saturation of the aqueous phase with dissolved oxygen in large stoichiometric excess, compared to the model pollutant 4-chlorophenol. The illumination is achieved by means of a Philips UV-C lamp TUV 4W/G4 T5 (4 Watts), which ensures monochromatic illumination at wavelength λ = 253.7 nm. The lamp is located at a distance of 3 cm from the illuminated suspension. The light intensity is 0.05 W/cm^2. The lamp is covered with an aluminum foil reflector to concentrate the light intensity downwards towards the suspension. In the case of using visible light (Tungsram lamp of 500 Watts) the distance of illumination was 50 cm and the illumination intensity was 8.9 Watts/cm^2.

Table 1. Comparison of C_2H_4 conversion degrees over 0.5%Au/TiO₂ and TiO₂ Degussa P25 photocatalytic materials (film coating 1mg/cm^2) in continuous flow regime. Conditions: 51 010 ppm feed C_2H_4 concentration, UV-C illumination intensity 0.14 W/cm^2, 56 cm^2 illuminated area, ethylene contact time 4.48 min, 28% relative humidity

Photocatalytic material	Type of illumination	Intensity of illumination	C_2H_4 Conversion
0.5%Au/TiO₂	UV-C light	0.14 W/cm^2	88 %
TiO₂ Degussa P25	UV-C light	0.14 W/cm^2	63 %
0.5%Au/TiO₂	UV-A light	0.14 W/cm^2	87 %
TiO₂ Degussa P25	UV-A light	0.14 W/cm^2	40%
0.5%Au/TiO₂	Visible light	8.9 W/cm^2	69%
TiO₂ Degussa P25	Visible light	8.9 W/cm^2	3%

The photocatalytic activity testing was carried out in the course of 5 hours taking 5 ml samples at regular time intervals (1 hour). The photocatalyst powder is filtered through a double-layer Whatman 42 filter paper (ashless, slow filtering, fine crystalline, Cat. No. 1442 110). The concentration of carbon in the chlorophenol measured with a Total Organic Carbon analyser TOC Shimadzu Model VCSH. Then taking the initial concentration and the concentration at a given moment of time (after switching on the lamp and starting the illumination) i.e. at a given time interval of illumination we evaluated the degree of conversion of 4-chlorophenol, which was accepted as a measure of the photocatalytic activity. The dependence of the chlorophenol conversion degree on the time of illumination for the 2 photocatalytic materials is represented in Table 2.

The dependence is initially almost linear tending to a plateau (4th – 5th hour) indicating probable deactivation that could be due either to some impurities in the chlorophenol or to some kind of polymerization of the chlorophenol on the surface in view of its two functional groups and possible interaction with the surface hydroxyl groups on TiO₂.

Table 2. Comparison of the degree of 4-chlorophenol conversion as a function of the time interval of illumination in [mg C/L], measured with total organic carbon analyzer (TOC Shimadzu VCSH) over 0.5%Au/TiO₂, Degussa P25 (Spain) at initial concentration 350 mgC/L and Degussa P25 (Bulgaria Conc 63 mgC/L).

Photocatalyst Sample	Degree of conversion of 4-chlorophenol (%) as a function of the time interval of illumination				
	1 hour	2 hours	3 hours	4 hours	5 hours
Sample 1 Au/TiO₂ Degussa	11.6%	14.1%	17.7%	23.9%	26.1%
Sample 2 - Spain TiO₂ Degussa P25	9.7%	11.3	14.8%	17.1%	20.7%
Sample 3 - BG Degussa P 25	8.9%	10.2%	12.7%	16.3%	19.5%

CONCLUSIONS

The gold-doped photocatalytic material 0.5%Au/TiO₂ exceeds TiO₂ Degussa P25 in its photocatalytic performance in the reaction of air purification from ethylene in heavy duty experiments (5% feed C_2H_4 concentration) in all photocatalytic activity testing experimental runs – under UV-C, UV-A and visible light illumination in continuous flow experiments (Plug Flow Reactor PFG, operation in the diffusion region). The configuration of the reactor was improved by including gas – flow circulation pump and a GC flow splitter to achieve operation in the kinetic region. The role of the gold nano-particles is to serve as electron traps of photoexcited electrons, preventing their recombination with the positively charged holes in the TiO₂. In this way the photonic efficiency (quantum yield) is increased as the holes have longer lifetime - the Schottky barriers at the metal/oxide inter-phase boundary are blocking the return of the photo-excited electrons to the oxide phase. Thus the holes, being the photocatalytically active sites for oxidation reactions, prolong their lifetime and increase their turnover number. It is more difficult to explain the visible light activity – in TiO₂ Degussa it is due to the rutile phase having a band gap of 3.0 eV, activated by visible light and it is not very high (3%). The extension of the light absorption band edge to visible light in the presence of gold nanoparticles is yet to be explained.

REFERENCES

1. G. Ruppert, R. Bauer, G. Heisler, *Chemosphere*, **28,** 1447 (1994).

2. S. Malato, J. Blanco, A. Vidal, D. Alarcon, M.I. Maldonado, J. Caceres, W. Gernjak, *Solar Energy*, **75,** 329 (2003).

3. M. Pera-Titus, V. Garcia-Molina, M.A. Banos, J. Gimenez, S. Esplugas, *Appl. Catal. B: Environ.*, **47,** 219 (2004).

4. K. Tanaka, T. Hisanaga, A. Rivera, in: "Photocatalytic Purification and Treatment of Water and Air", D. F. Ollis, H. Al-Ekabi (eds.) Elsevier, Amsterdam, 1993, p.169.

5. M. R. Hoffman, S.T. Martin, W. Choi, D. W. Bahneman, *Chem. Rev.*, **95,** 69 (1995).

6. K. Hashimoto, H. Irie, A. Fujishima, *Japanese Journal of Applied Physics*, **44,** 8269 (2005).

7. EPA Handbook "Advanced Photochemical Oxidation Processes", United States Environmental Protection Agency, Cincinnati, Ohio 45268, December 1998, p.3.

8. L. Petrov, V. Iliev, A. Eliyas, L. Spassov, L. Prahov, *J. Environ. Prot. & Ecol.*, B.EN.A, **6**, 893 (2005)

9. M. Hussain, R. Ceccarelli, D. Marchisio, D. Fino, N. Russo, F. Geobaldo, *Chem. Eng. J.*, **157**, 45 (2010).

10. X. Fu, L. Clark, W. Zeltner, M. Anderson, *J. Photochem. Photobiol. A: Chem.*, **97,** 181 (1996).

11. T. Tibbitts, K. Cushman, X. Fu, M. Anderson, R. Bula, *Adv. Space Res.*, **22**, 1443 (1998).

12. A. Sirisuk, C. Hill, M. Anderson, *Catal. Today*, **54**, 159 (1999).

13. D. Park, J. Zhang, K. Ikeue, H. Yamashita, M. Anpo, *J. Catal.*, **185**, 114 (1999).

14. S. Kumar, A. Fedorova, J. Golea, *Appl. Catal. B: Environ.*, **57**, 93 (2005).

15. A. J. Maira, K. L. Yeung, C. Y. Lee, P. L. Yue, C. K. Chan, *J. Catal.*, **192**, 185 (2000).

16. Z. Guo-Min, C. Zhen-Xing, Xu Min, Q. Xian-Qing, *J. Photochem. Photobiol. A:Chem.*, **161**, 51 (2003).

17. V. Iliev, D. Tomova, S. Rakovsky, A. Eliyas, G. Li Puma, *J. Mol. Catal. A:Chem.*, **327**, 51 (2010).

18. D. Hufschmidt, D. Bahnemann, J. J. Testa, C. A. Emilio, M. I. Litter, *J. Photochem. Photobiol. A: Chem.*, **148**, 223 (2002).

19. A. Eliyas, K. Kumbilieva, V. Iliev, S. Rakovsky, *Reac. Kinet. Mech. Cat.,* **102**, 251 (2011).

20. N. Hurst, S.J. Gentry, A. Jones, B.D. McNicol, *Catal. Rev. Sci. Eng.*, **24**, 233 (1982).

21. D. Andreeva, T. Tabakova, L. Ilieva, A.Naydenov, D. Mehanjiev, M.V. Abrashev, *Appl. Catal. A: Gen.*, **209**, 291 (2001).

22. K. Hadjiivanov, 0. Saur, J. Lamotte, J -C Lavalley, *Z. Phys Chem.*, **187**, 281(1994).

23. K. Hadjiivanov, J. Lamotte, J.-C. Lavalley, *Langmuir*, **13**, 3374 (1997).

24. A. Eliyas, L. Ljutzkanov, I. Stambolova, V. Blaskov, S. Vassilev, E. Razkazova-Velkova, D. Mehandjiev, *Cent. Eur. J. Chem.*, **11**, 464 (2013).

25. S.L. Kiperman, Fundamentals of chemical kinetics in heterogeneous catalysis, Publ. H. "Khimiya", (In Russian), Moscow, 1979.

26. R.W. Missen, C.A. Mims, B.A. Saville, Introduction to Chemical Reaction Engineering and Kinetics, Chapter 2, John Wiley & Sons, New York, 2008 p. 25.

ОФОРМЛЕНИЕ НА ЕКСПЕРИМЕНТАЛНАТА КОНФИГУРАЦИЯ ЗА ИЗМЕРВАНЕ НА ФОТОКАТАЛИТИЧНАТА АКТИВНОСТ НА Au/TiO₂ ЗА ОЧИСТКА НА ВЪЗДУХ И ОТПАДЪЧНИ ВОДИ

А. Елияс[1*], П. Петрова[1], Ф. Х. Лопес-Тенядо[2], Д. Томова[1], А. Маринас[2]

[1] Институт по катализ, Българска академия на науките, 1113 София, България
[2] Катедра по органична химия, Университет в Кордоба, Кампус Рабаналес, Сграда „Мария Кюри", E-14014-Кордоба

(Резюме)

Синтезиран бе фотокаталитичен материал, представляващ 0.5т% Au/TiO₂, с прилагането на метода отлагане-утаяване (DP), използувайки търговски продукт TiO₂ (Дегуса P25) модифицирайки го с наноразмерни златни частици. Прахообразният материал има специфична площ на повърхността 52 м²/г измерена по едноточковия БЕТ метод. Суспензията на Au/TiO₂ бе отложена като покритие върху Al плака за тънкослойна хроматография, с предварително нанесено покритие от SiO₂. Покритието бе охарактеризирано със сканиращ електронен микроскоп (СЕМ), при което бе наблюдавано равномерно разпределение на TiO₂ върху SiO₂ слой. ТПР профилът показа присъствие на оксидни форми около наноразмерните златни частици и преобразуването на част от Ti^{4+} йони в Ti^{3+} йони, което се подпомага от присъствието на метално злато в непосредствена близост. Фотокаталитичната активност на материала за очистване на въздух, замърсен с етилен, бе измерена в плосък плочест проточен газофазен фотокаталитичен реактор, окомплектован с делител на потока. Ефективността на суспензия от Au/TiO₂ бе тествана за очистване на отпадни води, замърсени с моделен замърсител 4-хлорфенол в полустатичен суспензионен реактор. И двата типа фотокаталитични експеримента показаха, че TiO₂ дотиран със златни частици превъзхожда по своето действие търговския фотокатализатор на фирмата Дегуса (TiO₂ P25) поради разделянето на носителите на заряди, при което се предотвратява рекомбинацията на положително заредени дупки и фотовъзбудени електрони.

Kinetics and mechanism of oil and oil products sorption from water surface onto pyrolyzed waste biomass

S. A. Uzunova[1], I. M. Uzunov[2*], D. R. Mehandjiev[2], V. B. Toteva[1]

[1] *University of Chemical Technology and Metallurgy - Sofia, 8 St.Kl.Ohridski Blvd., 1756 Sofia, Bulgaria*
[2] *Institute of General and Inorganic Chemistry, Bulgarian Academy of Sciences, Acad. G.Bonchev Str., bl.11, 1113 Sofia, Bulgaria*

In the present study an attempt was made to describe the kinetics and mechanism of oil and oil products sorption from aqueous surface on pyrolyzed rice husks. The pseudo-first order and second order kinetic models, Elovich equation and intraparticle diffusion model were applied to describe the kinetics and estimate the rate-limiting stage of the process. The best-fit model was selected based on the linear regression method. The effect of the sorbent granulometry, the density of oil pollutants and the presence of surface functionalities on sorption kinetics was investigated.

Keywords: Rice husks; Pyrolysis; Oil spills; Sorption; Kinetics

INTRODUCTION

The industrial activity, being an integral part of the development of contemporary society, is associated with significant and most often uncontrolled environmental pollution with all the ensuing consequences. The persistent hydrocarbons are some of the dangerous contaminants. They are transferred into the hydrosphere by oil or oil products. Oil mining and processing, as well as transportation and storage of oil products are very often accompanied by oil spillage, due to various reasons. It has been established that large amounts of aromatic, aliphatic and naphthenic acids, alcohols, phenols and aliphatic ketenes are formed as a result of photolytic oxidation of oil in aqueous medium [1,2]. The high toxicity of oil spills is mainly due to the water-soluble compounds of this group. In spite of all the measures taken to reduce pollution, the extent of contamination of water basins with oil products still remains dangerously high. The quantity of oil and oil products spilled in the World Ocean amounts to about 6 millions of tons annually [3].

During the recent years different mechanical, photochemical and physicochemical processes are being applied to solve the problems arising from oil spillages. Among the physicochemical processes the adsorption turns out to be the most effective technology with proven wide-scope potential for the treatment of polluted waters [4-9].

Recently, the application of adsorption methods combines well with the problem to utilize various waste biomasses from the agriculture and foodstuff production industry through converting the by-products into efficient biosorbents – an alternative to the commercial sorbents [8, 10-14]. The advantage is their availability and preparation with relatively low production expenses. An example in this respect is the processing of rice husks waste into efficient adsorbents for purification of water from various contaminants [15-19].

The studies on the options to apply biosorption as an alternative method for the purification of water are focused in three main directions: screening of efficient biosorbents; optimization of the process parameters and elucidation of the kinetics and mechanism of sorption [11, 14, 20-23].

The effectiveness of a specific sorbent in regard to the removal of various oil products from water depends on its structural and surface properties [8, 24]. A real challenge in the field of adsorption would be to study and determine the kinetics of the process. The latter is related to the adsorption capacity of the material and the adsorption mechanism. The knowledge of the kinetics of sorption could permit to evaluate the minimal time interval for complete saturation of the adsorbent; the required height of the sorbent layer, sufficient to eliminate an oil spill with a certain thickness, as well as the theoretical maximum adsorption capacity of the layer.

The influence of the chemical composition, the residual fluid components and the porosity on the adsorption capacity of carbonized rice husks towards heavy oils was examined by Kumagai et al. They also discussed the predominant mechanism of oil

* To whom all correspondence should be sent:
E-mail: uzunov_iv@svr.igic.bas.bg

adsorption by the husks and described a procedure to enhance the sorption capacity [24].

The sorption of accidental spillage of oil products using a sorbent on the basis of waste wood fibers and the corresponding exponential kinetic model were studied by Konseisayo et al. [25].

The kinetic dependences recently published by Kamenshchikov et al. [26] and Dedov [27] for different types of sorbents revealed that the sorption of oil products from water surface follows a two-step mechanism.

Although there are some available publications describing the adsorption of oil and oil products from the water surface, the kinetics of the process, based on utilization of pyrolyzed rice husks has not been studied yet.

The aim of the present investigation was to determine the effect of the granulometry of adsorbent prepared by pyrolysis of rice husks; the density of the oil products and the content of surface functionalities on the kinetics and mechanism of sorption. The present work represents an attempt to apply some known kinetic equations to the sorption of oil and oil products from water surface. The adsorption study was carried out using a method different from the most often applied batch-methods.

MATERIALS AND METHODS

Preparation of the sorbents

The adsorbent was prepared by slow pyrolysis of rice husks at 480°C, under stationary conditions. The experiments were performed in a tubular stainless steel electrically heated reactor, positioned vertically, equipped with temperature controllers, under a residual pressure of 1.33 Pa. The reactor had a heated zone of dimensions 240 mm (L) × 40 mm (ID) × 170 mm. The liquid products were collected in a trap between the reactor and a vacuum pump, maintaining a temperature of 2-3°C. Then the temperature in the reactor was increased linearly from room temperature up to 480° C at a heating rate of 4° min^{-1} and retention time 4 hours. The so obtained solid pyrolysis residue is characterized by 253 $m^2.g^{-1}$ B.E.T. specific surface area, assessed by N_2 adsorption; porosity 56.8 % and average pore diameter of 0.781 μm, determined by Hg-porosimetry [28]. The amount of the fluids, which were extracted with acetone was estimated at 4.2 % w/w, as the oleophilic compounds predominated in the eluent [28].

Six samples with a different fractional composition were obtained from the starting material, as follows: below 0.4; 0.4÷0.8; 0.8÷0.12; 1.2÷1.6; 1.6÷2.0 and greater than 2.0 mm,

designated as: PRH-1; PRH-2; PRH-3; PRH-4; PRH-5; PRH-6, respectively. These samples were used to determine the influence of the bulk density of the composite material on the kinetics of sorption of the oil or oil products.

Methodology for determining the kinetics of sorption

Pre-weighed adsorbent is filled into a glass tube of height 10.0 cm and diameter 1.0 cm, on the bottom of which is mounted a grid with aperture size smaller than the smallest particle size. The glass tube is immersed in a beaker, filled **only** with oil or oil product forming a layer with a depth of 5 mm. The rate of sorption was determined from the data giving the relationship between the time and the height of oil product penetration into the adsorbent layer.

Methodology for determining the sorption capacity with respect to oil or oil products

Blank test: Stainless steel grid, which has about 100–150 apertures per square centimeter and mass M_1 is immersed into crude oil or oil product for 10 min. The grid is drained from excess of the liquid for 10 min and then weighed (M_2). The difference between (M_2 - M_1) is the mass of oil (oil product) retained by the empty grid.

Pre-weighed 1.00 g sorbent is placed on the clean grid. The grid with sorbent (M_3) was: (i) immersed into the oil product for 10 min; (ii) allowed to drain the excess liquid for 10 min; (iii) weighed (M_4). The difference between (M_4 - M_3) gives the mass of oil/oil product which was retained by the grid and the sorbent. The difference (M_4 - M_3) - (M_2 - M_1) is the mass of oil absorbed by the sorbent. The sorption capacity (C_{ads}) of the material was calculated in g g^{-1} (grams of sorbed oil per gram of sorbent) or in percentage by the equation:

$$C_{ads} = \frac{(M_4 - M_3) - (M_2 - M_1)}{M_3 - M_1},\qquad(1)$$

The method is described in details by Angelova et al. [29].

The bulk density of the investigated samples was determined in accordance with BDS EN 13041:2011.

As test-pollutants in the kinetic study were used oil products with different densities, namely: gasoline (BDS 17374-95); diesel (BDS 8884-89); motor oil (BDS 9785-89); light crude oil (Georgia) and heavy crude oil (Bulgaria).

Kinetic studies

The sorption is a real equilibrium process and appears to be a function of the time. This means that the main evidence about the adsorption properties of the material could be derived from the dependence between the amount of adsorbed substance and the time at constant temperature, $q_t = f(t)_T$ where: q_t is the quantity of oil/oil product adsorbed for time t, g;

The amount of the adsorbed oil, corresponding to the level of its penetration into the sorbent layer, using the data for the bulk density of the sorbent and its adsorption capacity was calculated by the equations:

$$V_{t,ads} = \pi R^2 \cdot h_t , \qquad (2)$$

where: $V_{t,ads}$ is the volume of the material which adsorbs oil/oil product for time t, cm^3;

h_t – height of penetration of oil/oil product inside the layer of adsorbent for time t, cm;

R - radius of the layer, cm.

The mass of the sorbent G$_t$, in grams, soaked with sorbate in the glass column for time t is:

$$G_{t,ads} = V_{t,ads} \cdot \rho_{ads} , \qquad (3)$$

and

$$q_t = G_{t,ads.} \cdot C_{ads} , \qquad (4)$$

where: q_t is the mass of adsorbed oil/oil product for time t, g;

ρ_{ads} – bulk density of the sorbent, g.cm^{-3};

C_{ads} – adsorption capacity of the material, g.g^{-1}.

The sorption of oil or oil products from the water surface using a solid-state adsorbent is a heterogeneous process which occurs in the system sorbent/oil/water. This means that its rate will depend on: (i) the interaction between sorbent and sorbate; (ii) the rate of diffusion toward and inside the sorbent; (iii) the phenomena on the interphase boundary; (iv) the interaction of water with the sorbate, etc. The realization of the actual act of adsorption, either physical or chemical, forms the kinetic step of the process. The diffusion step of the process is determined by the external and/or the internal mass transfer. Hereby, the overall process velocity will depend on the speed of the slowest stage. Upon reaching steady state, the rate constants of the two processes remain different and their ratio determined the region in which the process took place - kinetic, diffusion or transition.

The phenomenological mechanism of sorption from solutions is described on the basis of the concepts previously introduced for the sorption from gas phase and these were amended in view of the specific conditions in the case of liquid phase.

The method of linear regression is the one used most often in order to select a suitable kinetic equation, which gives good correlation between experimental data and the theoretically estimated values. The mathematical principles of the method are not too complicated and it can be applied even in cases when the relation between the practically evaluated parameter and its calculated value is not really linear, but it can be approximated to such dependence.

The adsorption of various contaminants from water can be described by different kinetic models [30,31]. In our investigation several of the most often used equations were applied. They describe the occurrence of the process in the kinetic or in the diffusion region, namely:

Pseudo-first order kinetics

Usually the model of Lagergren [32] is used for processes which could be described by kinetic equations of pseudo-first order and occurring in the kinetic region. After integration within limits $q_t = 0$ at $t = 0$ and $q_t = q_e$ for $t = t_e$ the equation can be presented as follows:

$$\lg(q_e - q_t) = \lg q_e - \left(\frac{k_L}{2,303}\right) \cdot t , \qquad (5)$$

where:

q_e is the sorbate amount retained by the material after reaching the equilibrium for time interval t_e, g;

k_L – Lagergren rate constant, min^{-1}.

The rate constant, k_L is determined by the slope of the linear dependence $\lg(q_e - q_t) vs.(t)$.

Second order kinetics

The second order equation is also applicable to the kinetic region [32]. An integrated form of the equation was used:

$$\frac{t}{q_t} = \left(\frac{1}{k_2 \cdot q_e^2}\right) + \left(\frac{t}{q_e}\right), \qquad (6)$$

where: k_2 is the second order rate constant of adsorption, mg.g^{-1}.min^{-1}.

Both, the initial rate of sorption, $(k_2 \cdot q_e^2)$ and the second order rate constant, (k_2) are determined by linear regression of the dependence $t/q = f(t)$, at constant temperature.

Intra-particle diffusion model

The possibility of diffusion to be the only rate-determining step of the adsorption can be verified via the linear equation of Weber-Morris [33]:

$$q_t = k_i \cdot \sqrt{t} + C , \qquad (7)$$

where: C is a coefficient which accounts for the bonding effect between layers; k_i – rate constant of the process, $mg.g^{-1}.min^{-1/2}$.

If the experimental data do not describe a straight but a multi-linear dependence, this means that the sorption is influenced by two or more rate-determining steps, i.e. the process occurs in the transition region.

The diffusion coefficient of the sorbate inside the pores of the adsorbent is calculated (assuming spherical form of the adsorbent particles) by the equation:

$$t_{1/2} = 0,03 \cdot \frac{r_0^2}{D} \qquad , \qquad (8)$$

or

$$D = 0,038 \cdot \frac{r_0^2}{t_{1/2}} \qquad , \qquad (9)$$

where: D is a diffusion constant which depends on the porous structure of the sorbent, $cm^2.s^{-1}$;

r_0 - particle radius, cm;

$t_{1/2}$ – time interval in which half of the sorption process proceeds before reaching equilibrium, s.

Elovich equation

This equation is the most often used model to describe the kinetics of sorption in case when there are valence interactions between the adsorbent and the sorbate, i.e. chemisorption [34]:

$$\frac{dq_t}{dt} = a \cdot \exp(-bq_t), \qquad (10)$$

where: a is initial rate of sorption, $mg.g^{-1}.min^{-1}$;

b – desorption constant, $g.mg^{-1}$.

Chen et al. (1980) accepted $a \cdot b \cdot t >>> t$ and further developed the equation of Elovich [35]. Applying the limits $q_t = 0$ at $t = 0$ and $q_t = q_e$ at $t = t_e$ they obtained the equation:

$$q_t = \left(\frac{1}{b}\right) \cdot \ln(ab) + \left(\frac{1}{b}\right) \cdot \ln t, \qquad (11)$$

The constants a and b in the exponential equation of Elovich are determined on the basis of the intersection and the slope of the plotted dependence $q_t vs. \ln t$. When the correlation between the sorption capacity and the constant b is negative, it is accepted that the adsorbent does not retain the sorbate. The positive value of the constant gives evidence that sorption occurs [36].

RESULTS AND DISCUSSION

Sorption of crude oil

Light crude oil of density 0.833 $g.cm^{-3}$ at 20° C, was used as a sorbate to determine the influence of sorbent granulometry upon the sorption kinetics.

The data for the bulk density of each fraction of the pyrolyzed rice husks, the percentage distribution of the fractions, as well as their sorption capacity, are presented in Table1.

Table 1. Particle size distribution and oil sorption capacity of the fractions of rice husks pyrolyzed at 480°C

Granulo-metry, mm	Distribution, %	Sample	Bulk density, g.cm^{-3}	Oil sorption capacity, g.g^{-1}
> 2,0	15	PRH-6	0.072	6.667
2.0-1.6	21	PRH-5	0.076	8 .771
1.6-1.2	19	PRH-4	0.084	8.247
1.2-0.8	25	PRH-3	0.106	5.909
0.8-0.4	20.8	PRH-2	0.182	4.363
< 0.4	8.1	PRH-1	0.293	4.215

The adsorption kinetic curves obtained at constant temperature depending on the adsorbent granulometry are presented in Fig.1.
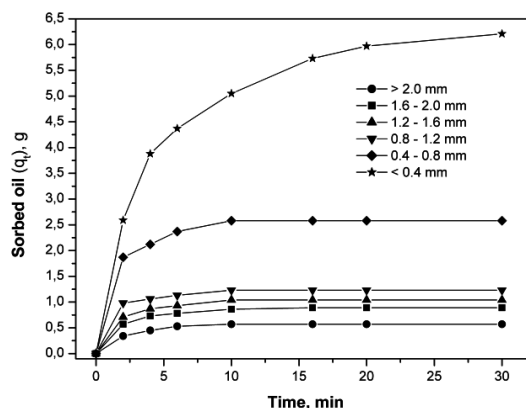
Fig. 1. Dependence between the adsorption and the contact time for pyrolyzed rice husks with different particles size

The shape of the kinetic curves exhibits that the sorption of crude oil by various fractions of the adsorbent is accomplished in two steps. The rate of the first step depends on the ratio between the gravitational and capillary forces, while that of the second step – on the structural characteristics and the oleophilicity of the adsorbent. The time interval for reaching the adsorption-desorption equilibrium is a very important characteristic because it determines the efficiency of the adsorbent [25,27, 37].

The structure of the adsorbent layer can be regarded as a system consisting of capillaries, inside which the process of sorption occurs in two orthogonal directions. In the case of small size fractions, the formed transportation channels possess dimensions, comparable to the pore size of the adsorbent. The impedance, related to the transport of the sorbate inside the layer of the

adsorbent is increasing. Thereupon in capillaries having hydrophobic surface, the capillary effect is in action. As a result, the sorbate rises up to a level higher than the initial one [28]. The horizontal capillary translocation of the oil/oil product also depends on the atmospheric pressure. The condition is: the thickness of the oil layer should exceed that of a monomolecular layer. Hereby, the atmospheric pressure and the pressure of the oil layer are summed up within and beyond the area of the adsorbent. The resultant pressure causes coercive external diffusion, which leads to initial filling of the structural cavities within the adsorbent. The opposite – in case of a fraction with large size, wide transportation channels are formed through which the oil product quickly penetrates inside the sorbent layer and reaches the active surface of the material.

The applicability of the used kinetic equations with respect to the adsorption characteristics, presented in Table 1 and the experimental results was verified by plotting the following functions:

$\lg(q_e - q_t) = f(t)$; $t/q_e = f(t)$; $q_t = f(\sqrt{t})$, Figures 2(a); 2(b) and 2(c).
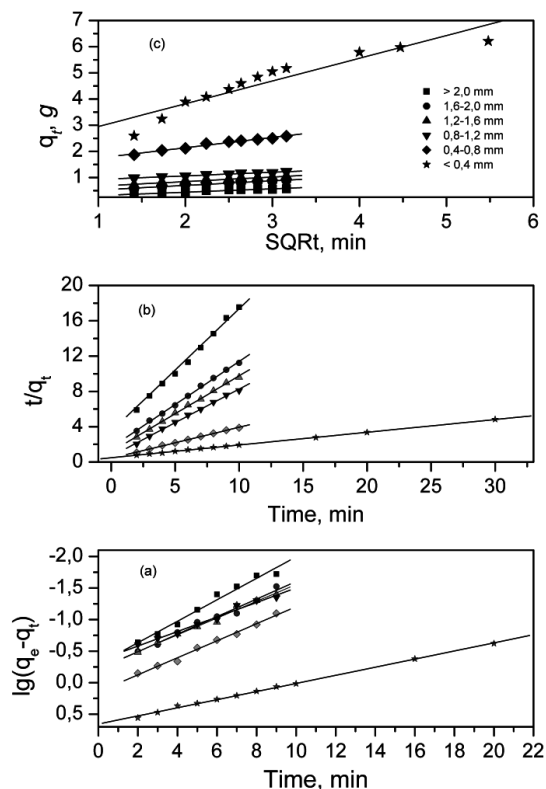
Fig. 2. Test of kinetic equations for the sorption of oil by pyrolyzed rise husks with different granulometry: (a) Lagergren plots; (b) second order kinetics equation; (c) Weber-Morris equation

The statistical data for the linear regression corresponding to the equations are listed in Tables 2, 3 and 4.

Table 2. Parameters of the linear regression for pseudo-first order kinetics, rate constants and theoretical values of the adsorbed amount of oil in equilibrium

Samples	Equilibrium quantities of sorbed oil, g		*SD	**R^2	***k_1
	$q_e^{exp.}$	q_e^{theor}			
PRH-6	0.57	0.51	0.0649	0.9795	0.3919
PRH-5	0.89	0.61	0.0518	0.9806	0.3203
PRH-4	1.04	0.59	0.0401	0.9872	0.3061
PRH-3	1.23	0.45	0.0420	0.9813	0.2648
PRH-2	2.59	1.39	0.0330	0.9916	0.3104
PRH-1	6.12	4.52	0.0167	0.9980	0.1480

*SD-standard deviation; **R^2-correlation coefficient; ***k_1-rate constant

Table 3. Parameters of the linear regression for second order kinetics equation, rate constants and theoretical values of the adsorbed amount of oil in equilibrium state

Samples	Equilibrium quantities of sorbed oil, g		SD	R^2	k_2
	q_e^{exp}	q_e^{theo}			
PRH-6	0.57	0.68	0.2211	0.9973	0.7257
PRH-5	0.89	1.02	0.1176	0.9982	0.5765
PRH-4	1.04	1.16	0.0979	0.9984	0.6358
PRH-3	1.23	1.31	0.0999	0.9980	0.9077
PRH-2	2.58	2.85	0.0396	0.9985	0.2925
PRH-1	6.21	6.94	0.0204	0.9998	0.0427

Table 4. Parameters of the linear regression for the diffusion model

Sample	Parameters					
	coefficients		average square error		SD	R^2
	$a(k_i)$	b	σ_a	σ_b		
PRH-6	0.57	0.51	0.1832	0.1293	0.0213	0.9366
PRH-5	0.89	0.61	0.3535	0.1738	0.0233	0.9571
PRH-4	1.04	0.59	0.5000	0.1739	0.0216	0.9630
PRH-3	1.23	0.45	0.7905	0.1376	0.0108	0.9846
PRH-2	2.59	1.39	1.3513	0.3946	0.0359	0.9797
PRH-1	6.12	4.52	2.0820	0.8690	0.3869	0.8862

As can be seen, the obtained statistical results from the linear regression and the theoretical values of adsorbed amount of oil in the equilibrium state, revealed that the process is most adequately described by a second order kinetic equation. This means that the sorption of oil by pyrolyzed rice husks occurs in the kinetic region, regardless of the bulk density of the sorbent ($R^2 > 0, 99$).

As it was already pointed above, the adsorption is also influenced by some other processes, whereupon the rate-determining step could be single or more than one. The probability the diffusion to be the rate limiting stage of the process could be evaluated with the equation of Weber-Morris. The obtained data of the correlation coefficients for each fraction reveal that in this case

989

the diffusion cannot be assumed as a rate limiting step. In order to evaluate the role of diffusion within the total rate of the process, the coefficient of diffusion D was determined by applying equations (9) and (10) for the fraction of size 0.40 mm. The shape of the granules of the fraction can be approximated to spheres. The calculated diffusion coefficient amounts to 5.3×10^{-5} cm^2.s^{-1}. The value is by two orders of magnitude smaller than the rate of penetration of the oil inside the adsorbent (6.5×10^{-3} cm.s^{-1}, at $t_{1/2}$ and at constant cross section of the layer). This fact confirms the substantial effect of the internal (pore) diffusion on the total rate of the process of sorption [29].

The obtained parameters of linear regression for the applied models, as well as the values of the rate constants showed that whatever be the fractional composition of the pyrolyzed rice husks, the adsorption of crude oil occurs mainly in the kinetic region.

The complex mechanism of oil sorption from the water surface was also confirmed by some authors. They have shown that the applicability of the second order kinetic model is an indication of sorption which proceeds through interaction between the valence forces of the surface functionalities of the adsorbent and those of the sorbate [38-42].

Influence of the dispersed fluids on the kinetics of sorption

The experiment was carried out with the fraction PRH-5 of solid pyrolysis residue and light crude oil ($\rho^{20°} = 0.833$ g.cm^{-3}). It was established that after the quantitative extraction of the finely dispersed fluids by the solid pyrolysis residue, the quantity of oil adsorbed for time interval t decreased considerably, Fig. 3.
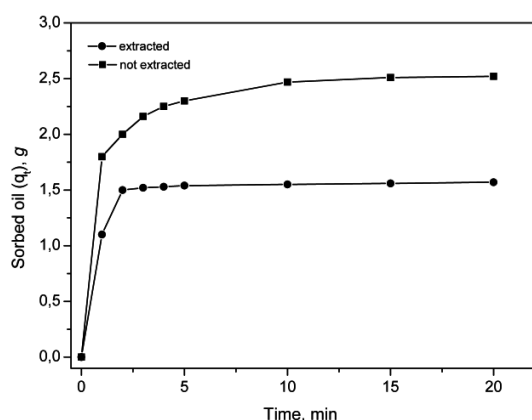
Fig. 3. Effect of the fluids dispersed on the solid pyrolysis residue upon the amount of adsorbed oil depending on the contact time.

The obtained result shows that the kinetics and mechanism of oil sorption are substantially influenced by the chemistry of the sorbent surface.

The possibility the adsorption in the system water/oil/pyrolyzed rice husks to occur with participation of other forces, beside those of Van der Waals was estimated by applying the Elovich equation. The equation was applied to describe the sorption of oil with extracted and with unextracted pyrolyzed rice husks. The results are presented in Fig. 4.
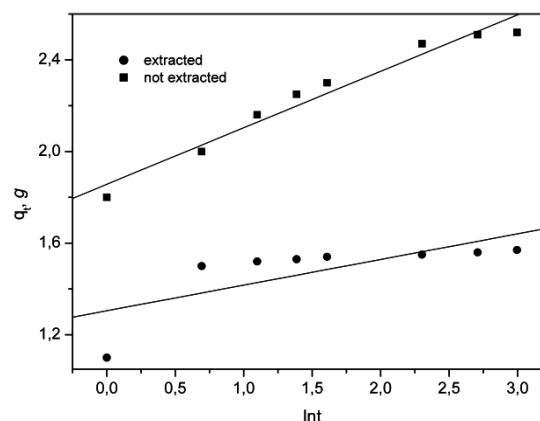
Fig. 4. Plots of the Elovich equation for adsorption of oil with extracted and not extracted pyrolyzed rice husks.

The relevant parameters of the linear regression are listed in Table 5.

The obtained comparative data unambiguously prove the influence of surface functionalities on the oil sorption process. The solid pyrolysis residue by its nature is a natural C/SiO$_2$ hybrid material. It contains carbon atoms in the sp^2-hybridization state and reactive siloxane groups belonging to amorphous silica. Furthermore, the thermal destruction of rice husks is associated with deposition upon the surface of the solid pyrolysis residue of alkanes, cycloalkanes and arenes, as well as compounds possessing functional groups with different reactivity. This promotes the interaction of petroleum hydrocarbons with the sorbent [28,43].

It was established that the extraction of the fluids, deposited on the solid pyrolysis residue, leads to a change in the porosity of the material [29].

Table 5. Parameters of linear regression for the Elovich model, concerning extracted and unextracted rice husks

Sorbent (PRH)	Parameters					
	coefficients		average squared error		SD	R^2
	a	b	σ_a	σ_b		
Unextracted	1.8570	0.2465	0.0375	0.0201	0.0545	0.9624
Extracted	1.3046	0.1120	0.0792	0.0425	0.1152	0.5411

The adsorbent used in the present investigation possesses a high percentage of pores with sizes of 1-50 μm, as well as above 50 μm. After extraction with acetone, the quantity of the pores of dimensions 1-50 μm is increased with 9% at the expense of the pores with size > 50 μm. The effect is due to the fact that a part of the volatile pyrolysis products completely fills up the pores with smaller size. The likelihood for changing the region of occurrence of the adsorption, associated with this fact was checked by using the second order equation.

The obtained results demonstrated a good correlation between the model and the experimental data for both samples, Fig. 5 and Table 6.
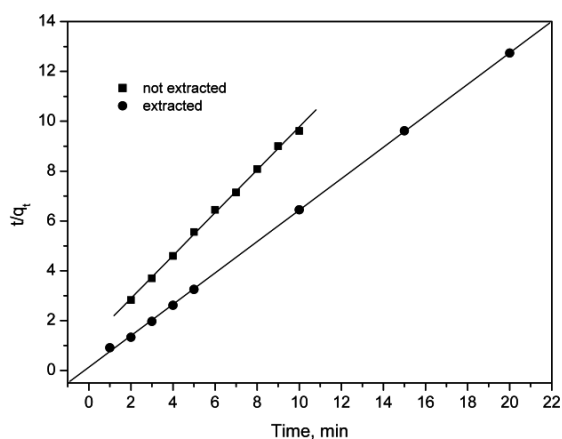
Fig. 5. Test of second order kinetic equation for the sorption of oil on extracted and not extracted pyrolyzed rice husks

Table 6. Parameters of the linear regression for second order kinetic equation, rate constants and theoretical values of the adsorbed amount of oil in equilibrium state for adsorption with extracted and not extracted PRH

Sorbent (pyrolyzed rice husks)	Equilibrium quantities of sorbed oil, g		SD	R^2	k_2
	$q_e^{exp.}$	$q_e^{theor.}$			
Extracted	2.52	1.58	0.0979	0.9984	0.3427
Not extracted	1.57	1.16	0.0736	0.9998	3.1547

The change in the porosity of the material does not lead to any drastic change in the rate of diffusion. In sum, the increase in the quantity of small pores does not hinder the diffusion of the oil into the sorbent structure and the process actually occurs in the kinetic region.

Influence of the density of the oil product on the kinetics of sorption

The investigation was carried out using oil products possessing low ($\rho^{20°} = 0.768$); medium ($\rho^{20°} = 0.886$) and high density ($\rho^{20°} = 0.973$). Data

about the characteristics of the used oil products, including the adsorption capacities of pyrolyzed rice husks were reported by Angelova et al. [44]. Unfractionated pyrolyzed rice husks were used as the adsorbent under investigation. The percentage distribution of the granulometric fractions in the solid pyrolysis residue is presented in Table 1.

The dependences between the adsorbed amount of oil or oil product, q_t and the time are presented in Fig.6.
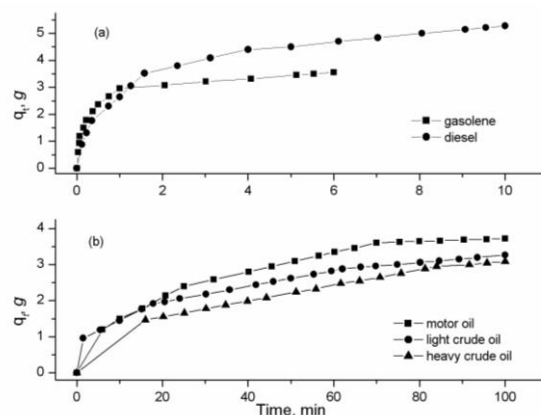
Fig. 6. The effect of oil products density upon the adsorption kinetics

The obtained results prove that the rate of reaching adsorption-desorption equilibrium depends on the density of the hydrocarbon pollutant and the relation is hyperbolical.

Upon increasing the density of the oil product, which is a gravitational characteristic, a partial compensation from the oppositely directed capillary forces appears. As a result, the adsorbed amount of heavy distillate oil products is smaller. In the case of products with low bulk density a high rate of sorption is observed during the first 10 – 15 min after the initial contact between sorbent and sorbate. After this period, the rate decreases until adsorption-desorption equilibrium is reached.

In order to determine the region in which the adsorption process is occurring depending on the density of the oil products, the same equations, already mentioned above were used:

Kinetic equation of pseudo-first order

The plotted dependences $\lg(q_e - q_t) = f(t)$ for the sorption of oil products of different density are illustrated in Figure 7.

In Table 7 are listed the relevant parameters of the linear regression and the theoretical values of the adsorbed amount in the equilibrium state.
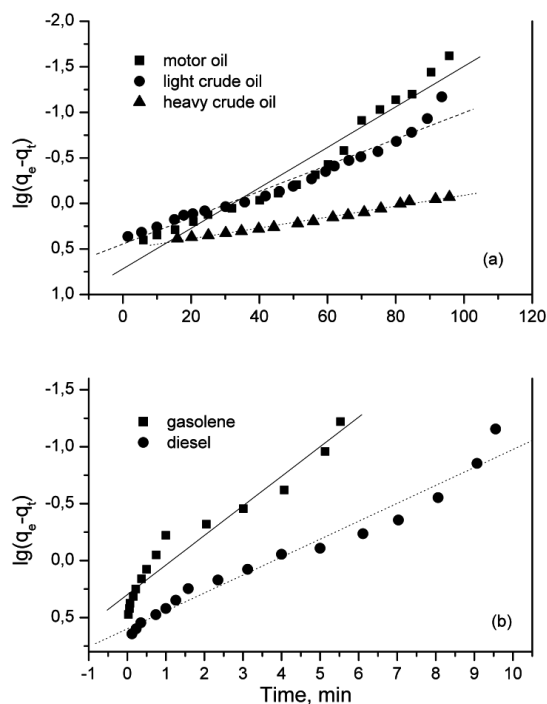
Fig. 7. Lagergren equation for adsorption of oil and oil products by pyrolyzed rice husks

Table 7 Parameters of the linear regression for pseudo-first order kinetics, rate constants and theoretical values of the adsorbed amount when equilibrium is reached, concerning oil products of different density

Petrochemicals	Equilibrium quantities of sorbed pollutant, g		SD	R^2	k_1
	$q_e^{exp.}$	$q_e^{theor.}$			
Gasoline	3.56	1.99	0.1309	0.9438	0.5985
Diesel	5.28	3.97	0.1025	0.9654	0.3627
Motor oil	3.72	5.22	0.1493	0.9505	0.0511
Light crude oil	3.27	2.79	0.0835	0.9626	0.0332
Heavy crude oil	3.09	3.21	0.0164	0.9892	0.0138

Second order kinetic equation

The plotted dependences $t/q_t = f(t)$ for the various oil products are presented in Fig. 8. The parameters of the linear regression are listed in Table 8.

Table 8. Parameters of the linear regression for second order kinetics, rate constants and theoretical values of the adsorbed amount in equilibrium state

Petrochemicals	Equilibrium quantities of sorbed pollutant, g		SD	R^2	k_2
	$q_e^{exp.}$	$q_e^{theor.}$			
Gasoline	3.56	3.60	0.0271	0.9982	1.2365
Diesel	5.28	5.65	0.0365	0.9968	0.1758
Motor oil	3.72	4.60	0.5044	0.9943	0.0096
Light crude oil	3.27	3.64	1.0479	0.9850	0.0172
Heavy crude oil	3.09	4.23	1.0668	0.9740	0.0058
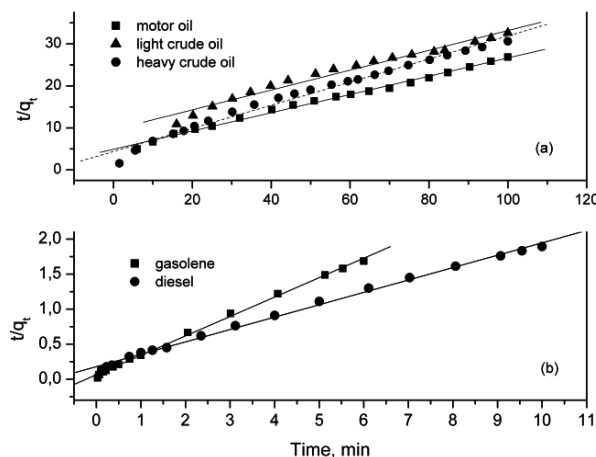
Fig. 8. Test of second order kinetic equation for the adsorption of oil products possessing different densities.

Intra-particle diffusion model

An attempt to apply the model based on diffusion as the only adsorption rate limiting step, in regard to oil products of different densities, has led to the results, presented in Fig.9 (a,b) and Table 9.
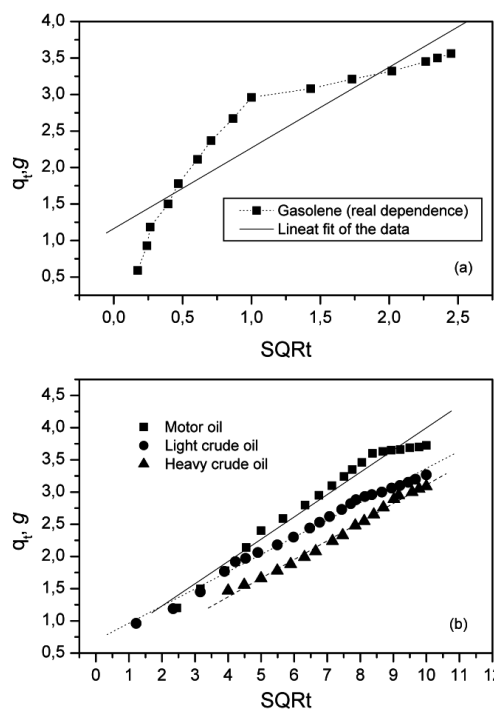
Fig. 9. Test of the Weber-Morris model for the adsorption of: (a) gasoline and (b) motor oil; light and heavy oil with pyrolyzed rice husks.

The results obtained relating to the adsorption of various oil products from water surface by pyrolyzed rice husks, indicated the following:

(i) In spite of the different densities of the oil products the sorption from water surface is occurring in the kinetic region and is described adequately by a second order equation;

(ii) The values of the correlation coefficients for light and heavy crude oils, obtained for the

diffusion equation, converge to unity but the rate constants of diffusion are by one order of magnitude higher than those for physical adsorption. This means that the process actually occurs in the kinetic region.

Table 9. Statistical data originating from the Weber-Morris equation for adsorption of oil products of different densities

Petro-chemicals	Parameters					
	coefficients		average squared error		SD	R^2
	a	b	σ_a	σ_b		
Motor oil	0.5403	0.3557	0.1062	0.0145	0.1416	0.9710
Light crude oil	0.6962	0.2672	0.0398	0.0057	0.0661	0.9906
Heavy crude oil	0.2131	0.2899	0.0475	0.0062	0.0482	0.9926

CONCLUSIONS

The kinetics of sorption of oil and oil products from water surface using fractionated and unfractionated pyrolyzed rice husks was investigated by the method of penetration of the sorbate in the layer sorbent.

The obtained results demonstrated that the fractions of pyrolyzed rice husks can be successfully used for purification of marine oil spills. It was found that the finest fraction has the best adsorption ability.

Some equations which are often applied were used to describe the kinetics and mechanism of the process. Their use in the case of sorption of oil and oil products from water surface was shown. It was found out that the kinetics of sorption of the studied oil and oil products could be adequately described by a second order kinetic equation, irrespective of the grain size of the pyrolyzed rice husks or the bulk density of sorbate.

By applying the Elovich equation the role of the fluids finely dispersed on the solid pyrolysis residue during the sorption of oil and oil products from the water surface was confirmed.

REFERENCES

1. R.A. Larson, L.L. Hunt, S.W. Blankenship, *Environ. Sci. Technol.*, **13**, 296 (1977).
2. J.R. Payne, C.R.Phillips, *Environ. Sci. Technol.*, **19**, 569 (1985).
3. V.Izmaylov, Problems of chemical pollution of the World Ocean: Transformations of oil films in the system ocean-ice-atmosphere, vol.9, Gidrometeoizdat, Leningrad, 1988 (Russ.).
4. V. Broje, A.Keller, *Environ. Sci. Technol.*, **40,** 7914 (2006).
5. I. Mazur, O. Moldovanov, V. Shishov, Engineering Ecology, General Course, Visshaia Shkola, Moscow, vol. **2**, (1996) (Russ.).
6. A. Srinivasan, T.Viraraghavan, *J. Hazard. Mater.*, **175,** 695 (2010).
7. M. Adebajo, R. Frost, J. Kloprogge, O. Carmody, S.Kokot, *J. Porous Mater.*, **10,** 159 (2003).
8. O. Carmody, R. Frost, Y. Xi, S.Kokot, *Surf. Sci.*, **601,** 2066 (2007).
9. D Ceylan, S. Dogu, B. Karacik, S.Yakan, O.S. Okay, O.Okay, *Environ. Sci. Technol.*, **43**, 3846 (2009).
10. I. Sheveleva, A. Kholomeidik, A. Voit, N. Morgun, L.Zemnukhova, *Russ. J. Appl. Chem.*, **82**, 1840 (2009).
11. K. Foo, B. Hamed, *Adv. Colloid Interface Sci.*, **152**, 39 (2009).
12. M. Ahmedna, W. Marshell, R. Rao, *Bioresour. Technol.*, **71**, 113 (2000).
13. Y. Shinogi, Y.Kanri, *Bioresour. Technol.*, **90**, 241 (2003).
14. J. Dias, M. Alvim-Ferraz, M. Almeida, J. Rivera-Utrilla, M.Sanchez-Polo, *J. Environ. Manage.*, **85**, 833 (2007).
15. T. Naiya, A. Bhattacharya, S. Mandal, S.Das, *J. Hazard. Mater.*, **163**, 1254 (2009).
16. M. Akhtar, S. Igbal, A. Kausar, M. Bhanger, M. Shaheen, *Colloid Surface B*, **75**, 149 (2010).
17. T. Chuah, A. Jumasiah, I. Azni, S. Katayon, S. Choong, *Desalination*, **175**, 305 (2005).
18. K. Chou, J. Tsai, C. Lo, *Bioresour. Technol.*, **78**, 217 (2001).
19. I. Dahlan, K. Lee, A. Kamaruddin, A.Mohamed, *J. Hazard. Mater.*, **161**, 570 (2009).
20. V. Srivastava, I. Mall, I. Mishra, *Chem. Eng. J.*, **140**, 136 (2008).
21. K. Krishnani, X. Meng, C. Christodoulatos, V.Boddu, *J. Hazard. Mater.*, **153**, 1222 (2008).
22. D.Mohan, K.Singh, V.Singh, *J. Hazard. Mater.*, **152**, 1045 (2008).
23. V. Srivastava, I. Mall, I.Mishra, *J. Hazard. Mater.*, **B 134**, 257 (2006).
24. S. Kumagai, Y. Noguchi, Y. Kurimoto, K.Takeda, *Waste Manage.*, **27**, 554 (2007).
25. A.Konseisayo, N.Samoilov, R.Hlestkin, *Chem. Technol. Fuel Oils*, **2**, 42 (2007) (Russ.).
26. F.Kamenshchikov, E.Bogomolnii, Removal of oil products from water surfaces and soils, first ed., Moscow, 2006 (Russ.).
27. A.Dedov, *Chem. Technol. Fuel Oils* (Russ.), **1**, 53 (2006).
28. I.Uzunov, S. Uzunova, D. Angelova, A.Gigova, *J. Anal. Appl. Pyrol.* **98**, 166 (2012).
29. D. Angelova, I. Uzunov, S. Uzunova, A. Gigova, L.Minchev, *Chem. Eng. J.*, **172**, 306 (2011).
30. J. Febrianto, A. Kosasih, J. Sunarso, Y. Ju, N. Indraswati, S.Ismadji, *J. Hazard. Mater.*, **162**, 616 (2009).

31. R. Tseng, F. Wu, R. Juang, *Carbon*, **41**, 487 (2003).
32. F. Wu, R. Tseng, R. Juang, *Water Res.*, **35**, 613 (2001).
33. W. Weber, J. Morris, *J. Sanitary Eng. Div. ASCE*, **89**(SA2), 31 (1963).
34. D. Eley, H. Pines, P. Weisz (eds.), Advance in Catalysis and Related Subjects, vol. 21, Academic Press, NY, 1970, p.1.
35. S. Chien, W. Clayton, *Soil Sci. Soc. Am. J.*, **44**, 265 (1980).
36. V. Srihari, A.Das, *Desalination*, **225**, 220 (2008).
37. A.Dedov, *Chem. Technol. Fuel Oils* (Russ.), **6**, 48 (2005).
38. X. Wang, S. Xia, L. Chen, J. Zhao, J. Chovelon, J.Nicole, *J. Environ. Sci.*, **18**, 840 (2006).
39. M. Javed, H. Bhatti, M. Hanif, R.Nadeem, *Sep. Sci. Technol.*, **42**, 3641 (2007).
40. C. Namasivayam, M. Sureshkumar, *Bioresour. Technol.*, **99**, 2218 (2008).
41. J. Yu, M. Tong, X. Sun, B.Li, *Biochem. Eng. J.*, **33**, 126 (2007).
42. X. Guo, A. Zhang, X.Shan, *J. Hazard. Mater.*, **151**, 134 (2008).
43. S. Uzunova, I. Uzunov, S. Vassilev, A. Alexandrova, S. Staykov, D. Angelova, *Bulg. Chem. Comm.*, **42**, 130 (2010).
44. D. Angelova, S. Uzunova, S. Staykov, I. Uzunov, *J. Chem. Technol. Metal.*, **45**, 25 (2010).

КИНЕТИКА И МЕХАНИЗЪМ НА СОРБЦИЯ НА НЕФТ И НЕФТОПРОДУКТИ ОТ ВОДНА ПОВЪРХНОСТ ВЪРХУ ПИРОЛИЗИРАНА ОТПАДНА БИОМАСА

С. А.Узунова[1], И. М.Узунов[2*], Д. Р. Механджиев, В. Б. Тотева[1]

[1] *Химико-технологичен и металургичен университет-София, бул.”Св. Кл.Охридски” 8, 1756 София*
[2] *Институт по обща и неорганична химия-БАН, ул.”Акад. Г.Бончев”, бл.11, 1113 София*

(Резюме)

Настоящето изследване е опит да се изследват кинетиката и механизма на сорбция на нефт и нефтопродукти от водна повърхност с пиролизирани оризови люспи. За определяне на кинетиката и скоростоопределящия етап на процеса бяха използвани кинетични модели от псевдо-първи и втори порядък; уравнение на Елович, както и дифузионен модел. Приложимостта на уравненията бе оценена по статистическите данни на метода на линейна регресия. Бяха изследвани ефектите на: гранулометрията на сорбента, относителната плътност на нефтените замърсители и наличието на повърхностни функционални групи в сорбента върху кинетиката на адсорбция.

Quaternary electrodeposits on nickel-foam for application in a hybrid direct borohydride fuel cell - hydrogen-on-demand system

M. Y. Mitov[1], G. Y . Hristov[1], R. S. Rashkov[2], Y. V. Hubenova[3]

[1]Department of Chemistry, South-West University "Neofit Rilski", Blagoevgrad, Bulgaria,
[2]Insitute of Physical Chemistry "Acad. Rostislav Kaishev", Bulgarian Academy of Sciences, Sofia, Bulgaria
[3]Department of Biochemistry and Microbiology, Plovdiv University "Paisii Hilendarski", Plovdiv, Bulgaria

In this study, CoNiMoW electrodeposits produced under different galvanostatic conditions were investigated as anode materials in a Direct Borohydride Fuel Cell. As a tendency, higher generated power was obtained with electrodeposited anodes produced at lower currents. Maximum power of 250 mW was achieved by using CoNiMoW-anode electrodeposited at the lowest current density (15 mA cm^{-2}) and two air gas-diffusion cathodes. This value exceeds 2.5 times that obtained with the same anode and one gas-diffusion electrode, which indicates that the oxygen reduction on the cathode is the rate-limiting step of the overall process. In addition, the catalytic properties of the CoNiMoW electrodeposits towards the "non-productive" borohydride hydrolysis reaction were also examined. The highest hydrogen generation rate of 15.0 ml min^{-1} was achieved with CoNiMoW electrodeposits produced at the lowest current. Activation energy of the order of 36.5±2.7 kJ mol^{-1} was obtained for all materials studied. Summarizing the results from the fuel cell and catalytic tests, we propose the CoNiMoW electrodeposits as potential candidates for application in a hybrid Direct Borohydride Fuel Cell – Hydrogen-on-demand system.

Keywords: Electrodeposition, CoNiMoW anodes, Direct Borohydride Fuel Cell, catalyst, borohydride hydrolysis.

INTRODUCTION

Fuel cells have attracted increasing attention as alternative power sources as they generate electricity with higher efficiency and lower pollution than the conventional combustion technologies and batteries. Currently, the proton exchange membrane fuel cells (PEMFCs), utilizing hydrogen as a fuel, represent the most advanced fuel cell technology and are promising for transportation, as well as stationary applications [1]. However, the storage and transportation of hydrogen is still a problem as both classical methods with an industrial impact - high pressurized gas and cryogenic liquid, are highly energy-consuming and keep risk for a wide application [2].

Since 1990's, hydrogen-rich compounds such as alkaline hydrides, borohydrides and alanates are intensively studied as safe hydrogen storage materials [3-5]. Sodium borohydride (NaBH$_4$) is one of the most attractive candidates for this purpose. In addition to its high hydrogen content (10.6 wt.%), exceeding that of most hydrogen storage alloys, sodium borohydride is chemically stable, non-combustible, easily stored and distributed.

In the presence of a proper catalyst, sodium borohydride reacts with water to produce hydrogen gas and sodium metaborate according to the following reaction:

$$NaBH_4 + 2H_2O \rightarrow 4H_2 + NaBO_2, \tag{1}$$

The generated H$_2$ is highly pure and humidified, which makes it suitable for direct use in PEMFCs. In addition, the resulting borate may be recycled back to borohydride [6, 7]. Based on catalyzed borohydride hydrolysis, various hydrogen-on-demand (HOD) systems were recently developed as a promising way to overcome disadvantages with existing hydrogen storage and transportation methods [8, 9].

Except as a hydrogen source, alkaline borohydrides can be directly used as a fuel in power sources referred to as direct borohydride fuel cells (DBFCs). In aqueous alkaline medium borohydride ions can undergo electrochemical oxidation on a variety of electrode materials liberating a maximum of eight electrons. The reaction of direct borohydride electrooxidation is as follows:

$$BH_4^- + 8OH^- \rightarrow BO_2^- + 6H_2O + 8e^-$$
$$\left(E_a^0 = -1.24V \, vs. SHE \right), \tag{2}$$
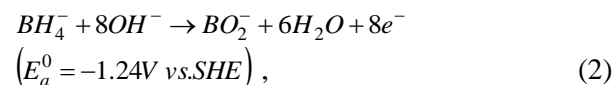
Besides the great number of participating electrons, the direct anodic oxidation of borohydrides provides more negative potential compared to the case when hydrogen is used. In

---

DBFCs, most commonly the anode oxidation of borohydride is coupled to the reduction of oxygen on an air cathode:

$$O_2 + 2H_2O - 4e^- \rightarrow 4OH^-$$
$$\left(E_c^0 = +0.40V \; vs. \, SHE\right), \tag{3}$$
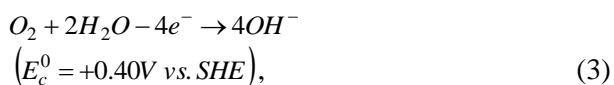
The net cell reaction in this system is represented as:

$$BH_4^- + 2O_2 \rightarrow BO_2^- + 2H_2O$$
$$\left(E_{cell}^0 = 1.64V\right), \tag{4}$$
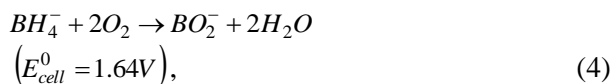
The high electromotive force, exceeding those of hydrogen and direct methanol fuel cells, makes DBFCs attractive energy suppliers, especially for portable applications [10]. The major research on DBFC development is focused on the efficiency of borohydride fuel utilization, which strongly depends on the anode material. Usually, the electrochemical oxidation reaction (2) is accompanied by a parallel hydrolysis reaction (1) due to the high catalytic activity of the electrocatalysts used towards both reactions. Thus, the actual anodic reaction should be described as:

$$BH_4^- + xOH^- \rightarrow BO_2^- + (x-2)H_2O + (4-x/2)H_2 + xe^- \tag{5}$$
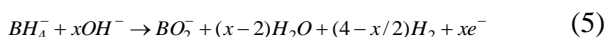
where x is the number of electrons that are generated during electrooxidation of 1 mol BH_4^-.
It has been demonstrated that among the commonly studied metallic catalysts – Pt, Pd, Ni, Au and Ag, gold is the most effective and nickel is the least effective electrocatalyst towards borohydride oxidation [10-12]. High coulombic numbers near the theoretical 8e$^-$ have been obtained by using Au-electrodes [13-15] and associated with its inactivity towards the hydrolysis reaction. The slow kinetics of gold towards borohydride electrooxidation, however, restricts its practical application. Participation of 4 and 6 electrons has been reported for BH_4^- oxidation on Pt- and Pd-electrodes, respectively [15, 16].

Various AB_5 and AB_2-type hydrogen storage alloys have been also explored as anode materials in DBFCs [17-20]. On the metal hydride surface, electrooxidation of borohydrides takes place through a sequence of steps with concomitant atomic hydrogen generation [21]. The released hydrogen (H) is stored in the hydrogen storage alloy anode as a metal hydride (MH_x), which is involved in the discharge reaction as follows:

$$MH_x + xOH^- \rightarrow M + xH_2O + xe^-, \tag{6}$$
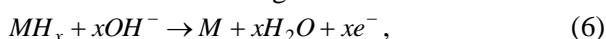
It has been established that the coulombic efficiency of borohydride electrooxidation depends not only on the anode material properties but also on a variety of other experimental factors such as the method of the electrode preparation, the catalyst support, the use of membrane, etc. [10, 22].

Novel multicomponent Co-based electrodeposits containing large amounts of hydrogen (up to 9 at.%), have been recently synthesized by us and investigated as catalysts for different applications [23-25].

In this study, quaternary CoNiMoW alloys, electrodeposited on nickel foam under different galvanostatic conditions, were investigated as anode materials in DBFC. In parallel, the catalytic properties of the obtained CoNiMoW electrodeposits towards the "non-productive" borohydride hydrolysis reaction were also examined.

EXPERIMENTAL

Quaternary CoNiMoW coatings were electrodeposited from alkaline electrolyte (pH 10 adjusted by addition of NH_4OH), containing sodium citrate (72 g L^{-1}), $Na_2WO_4.2H_2O$ (24 g L^{-1}), Na_2MoO_4 (6 g L^{-1}), $Ni(SO_3NH_2)_2$ (16 g L^{-1}), $Co(SO_3NH_2)_2$ (16 g L^{-1}), on nickel foam (RECEMAT, RCM-Ni-2733.03, pore diameter d=0.6 mm, SSA=2500 m^2/m^3) under different galvanostatic regimes for 30 min and electrolyte stirring at 250 min^{-1}. Round shaped samples of Ni-foam with diameter 3 cm were used as electrodes. The applied current density was estimated and presented in respect to the real surface (64 cm^2) of the electrodes.

Scanning electron microscopy (SEM) using Leo 1455VP and Leo Supra 55VP microscopes with energy dispersive X-ray (EDX, Oxford Inca 200 instrument, Software INCA-Version 4) was applied for examination of the surface morphology and elemental analysis of the electrodeposited coatings.

XRD spectra for structure identification of layers was recorded in the angle interval 10–100° (2θ) by using Philips PW 1050 diffractometer, equipped with Cu Kα tube and scintillation detector.

The produced CoNiMoW/Ni-foam samples were applied as anodes in DBFC. Air gas-diffusion electrodes (GDE) developed for metal-air systems [26] were used as cathodes. Stabilized 5% (w/v) $NaBH_4$/6M KOH solution served as borohydride fuel and liquid electrolyte. The investigations were performed in single-chamber DBFCs (10 ml working volume) with one or two air gas-diffusion cathodes and one anode. Polarization measurements at variable load resistances in a borohydride-containing electrolyte were carried out. The power output was calculated from the recorded values of voltage, *U*, and current,

I, by the equation $P=U{\times}I$ and the polarization and corresponding power curves were plotted. Long-term discharge measurements in galvanostatic mode were performed and the discharge capacity was estimated.

In parallel, the catalytic properties of the CoNiMoW electrodeposits towards borohydride hydrolysis were also explored. The examined sample was placed into a reaction vessel, which was then hermetically closed. 10 ml of

5% (w/v) $NaBH_4$/6M KOH solution was injected into the vessel and the volume of the generated hydrogen was measured over time by means of the water-displacement method [23, 24]. The reaction temperature was kept constant by thermostat in the range from 288 to 315 K. The rate constants at different temperatures were estimated from the obtained kinetic curves and the activation energy was calculated from the constructed Arrhenius plots.
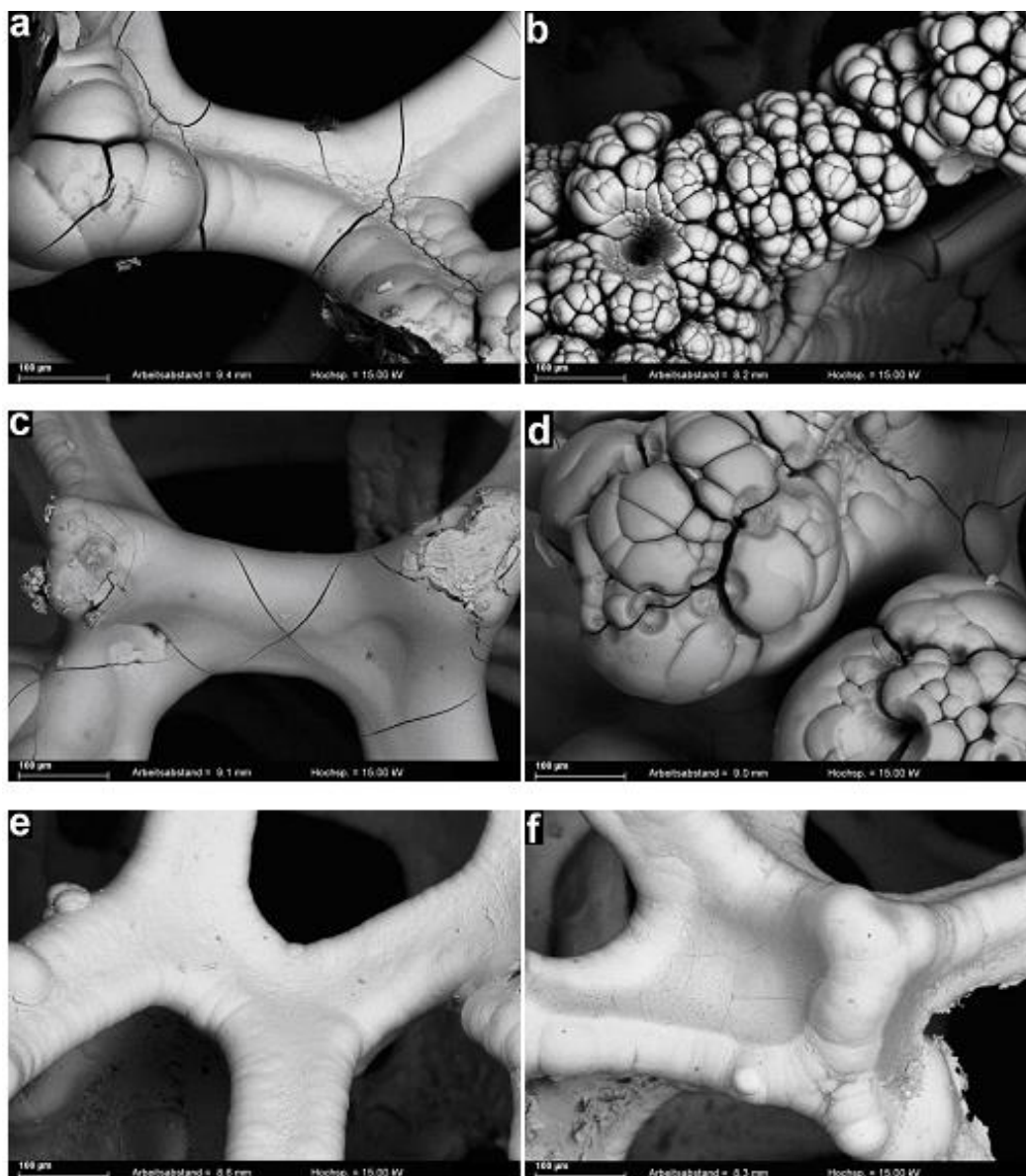
Fig. 1. Morphology of CoNiMoW-coatings on nickel foam at different electrodeposition regimes: (a,b) 75 mA cm^{-2} – center (a), edge (b) of the sample; (c,d) 30 mA cm^{-2} – center (c), edge (d) of the sample; (e,f) 15 mA cm^{-2} – center (e), edge (f) of the sample.

RESULTS AND DISCUSSION

Characterization of CoNiMoW electrodeposits

The SEM images presented in Fig. 1 show that the variation of the current regimes during electrodeposition affects the morphology of the obtained CoNiMoW coatings. The morphology significantly changes from the center to the edge of the samples, especially for those produced at the highest current density applied. The coating turns from nearly smooth with rounded parts on the Ni-support swellings (Fig. 1a) into dendrite-type on the edges (Fig. 1b). More uniform coatings without cracks were obtained at the lowest current density (Fig. 1e).

The results from the elemental analysis, presented in Table 1, show a varying distribution of the elements depending on the applied current, as well as on the different zones of the sample surface. The current increase leads to enrichment of Co, Mo and W and decrease of Ni content in the middle parts of the samples.

Table 1. Elemental content of CoNiMoW-coatings obtained at different current regimes.

Sample zone	$i_{deposit.}$ mA cm^{-2}	Co, wt.%	Ni, wt.%	Mo, wt.%	W, wt.%	O, wt.%
	75	67.4	9.0	7.5	9.9	6.2
Center	30	61.8	4.9	8.8	7.8	16.7
	15	48.4	39.9	3.0	0.6	8.1
	75	56.8	21.1	5.5	9.8	6.8
Edge	30	44.2	9.7	9.6	10.2	26.3
	15	50.9	8.9	11.5	6.4	22.3

Because of the edge effects and complex morphology of the support, the composition of the coatings at the edges significantly differs from that in the central parts of the samples at the same current densities applied.

The XRD study of the electrodeposited CoNiMoW coatings indicates that all of them, except those obtained at 15 mA cm^{-2}, possess amorphous structure - Fig. 2. We suppose that the observed exception is due to deposition of thin layers at the lowest current and appearance of characteristic peaks of Ni from the support.

Fuel cell studies

Polarization and power curves, obtained with DBFC by using the studied CoNiMoW/Ni-foam samples as anodes and one GDE as a cathode are plotted in Fig. 3. Despite the observed variation of anode morphology, composition and structure, the obtained fuel cell outputs do not differ significantly.

The lowest maximum power (81 mW) was obtained with the electrodes deposited at 75 mA cm^{-2} and the highest power (94 mW) was achieved with those obtained at 15 mA cm^{-2}, which shows a slight tendency to increase of the fuel cell power outputs by using CoNiMoW/Ni-foam anodes produced at lower current density of electrodeposition.
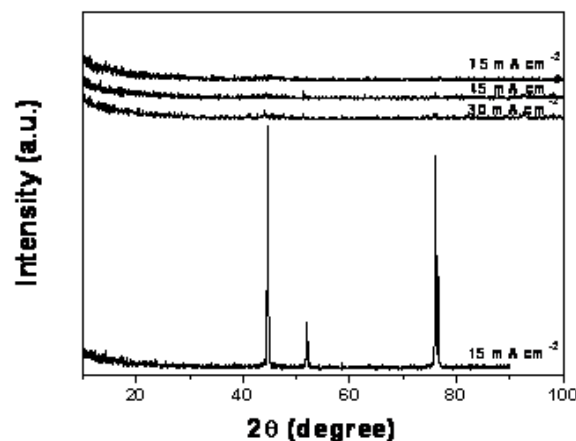
Fig. 2. XRD of CoNiMoW-coatings electrodeposited on nickel foam at different current regimes.

In many cases, when GDEs are used as air cathodes in electrochemical power sources, the kinetics of the overall process is limitted by transportation hindrances connected with the delivery of oxygen to the cathode [27]. To facilitate the oxygen supply and reduce the limitation effect of the cathodic reaction, usually the cathode area is enlarged.

The polarization experiments carried out with a fuel cell using two air cathodes confirmed this suggestion. The obtained polarization curves are characterized by quite smaller slope, resp. internal cell resistance, in comparison with that in the case of DBFC with one air cathode and even at very low load resistances (<1 Ω) no drop of the voltage occurs, while at the same time the power curve does not pass through a maximum. As a result, much higher power of 250 mW compared to that obtained with DBFC using one GDE was achieved – Fig. 4.

The measurements at constant load show that the fuel cell could be used as a power source for over five hours in batch mode – Fig. 5. The estimated discharge capacity of 300 mAh g^{-1} NaBH$_4$, however, is rather below the theoretical one. Based on the observed noticeable hydrogen evolution when the anode was put in contact with the borohydride electrolyte, we supposed that the

obtained low discharge capacity is mainly due to the fuel depletion, connected with "non-productive" catalytic hydrolysis of sodium borohydride.
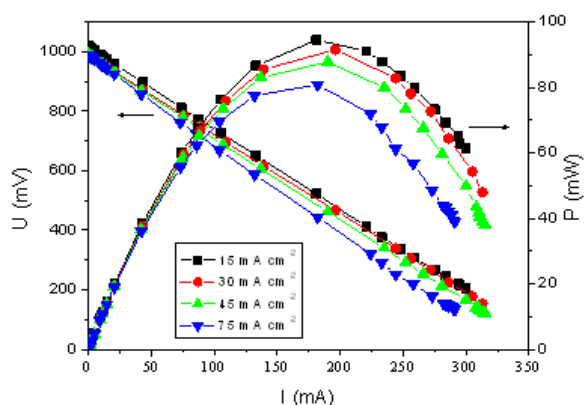
Fig. 3. Polarization and power curves obtained with DBFC by using CoNiMoW/Ni-foam anode and GDE cathode.
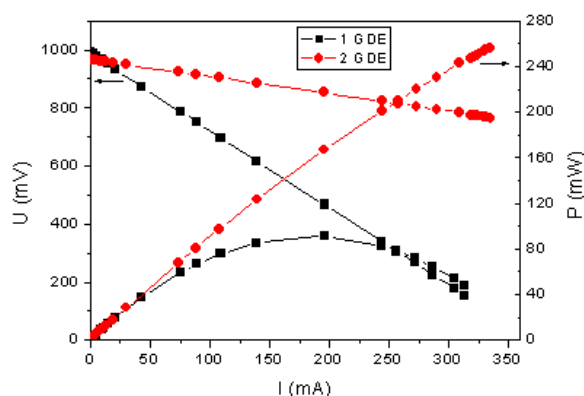
Fig. 4. Comparison of polarization and power curves obtained with DBFC by using CoNiMoW/Ni-foam anode and one or two air-cathodes.
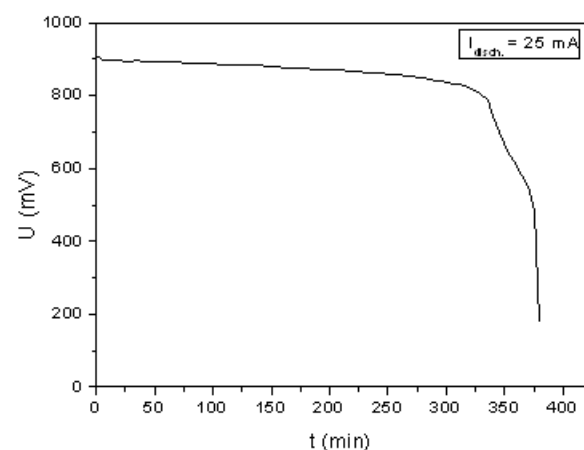
Fig. 5. Discharge curve obtained with the studied DBFC.

Catalytic studies

To evaluate the catalytic activity of the investigated CoNiMoW electrodeposits towards borohydride hydrolysis reaction, kinetic experiments for determination of the hydrogen generation rate and activation energy of the process were carried out at different temperatures. The catalytic studies were performed in the temperature range from 288 to 315 K, where the alkaline sodium borohydride solution is relatively stable in the absence of catalyst. Typically, as seen from Fig. 6, the reaction starts instantly after the catalyst comes into contact with the solution and a constant-rate hydrogen evolution is observed during the whole experimental window.
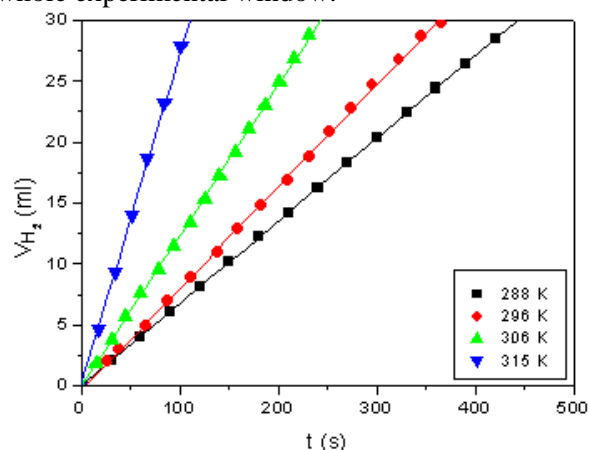
Fig. 6. Kinetic curves of catalyzed borohydride hydrolysis using CoNiMoW/Ni-foam (15 mA cm^{-2}) as catalyst and 5% (w/v) NaBH$_4$/6 M KOH solution.

From the slopes of the kinetic curves obtained at different temperatures the hydrogen evolution rate values were calculated and presented as Arrhenius plots (*ln k vs. 1/T*) – Fig. 7. The values of the activation energy, E_a, estimated from the slope of the Arrhenius plots, are shown in Table 2.

Table 2. Activation energy, E_a, of catalyzed borohydride hydrolysis depending on the current density, $i_{deposit.}$, applied during CoNiMoW catalyst preparation.

$i_{deposit.}$, mA cm^{-2}	E_a, kJ mol^{-1}
15	37.8
30	33.8
45	38.9
75	35.6

The analysis of the results obtained by the catalytic studies show that the rate of hydrogen evolution, as a product of borohydride hydrolysis, increases when CoNiMoW obtained at lower currents are applied as catalysts. The highest hydrogen generation rate of 15.0 ml min^{-1} (at 315 K) was achieved with CoNiMoW electrodeposited at 15 mA cm^{-2}. The close values of the activation energy indicate that the process takes

place via identical mechanism on all examined catalysts.
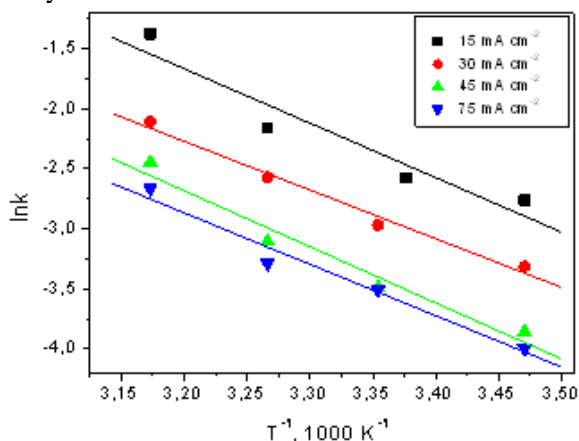
Fig. 7. Arrhenius plots of borohydride hydrolysis catalyzed by CoNiMoW electrodeposited on Ni-foam at different galvanostatic regimes.

CONCLUSION

The quaternary CoNiMoW alloys electrodeposited on nickel foam exhibit a promising performance as anodes in DBFC. A power of 250 mW was achieved by using two air cathodes. This value exceeds 2.5 times the maximum power obtained with one air cathode, which supposes that the overall electrochemical reaction is limited by hindrances connected with oxygen delivery to the cathode. The anode performance is improved by decrease of the current applied for electrocatalyst deposition. The same tendency was also observed when the studied materials have been investigated as catalysts for borohydride hydrolysis. Based on the results from both electrochemical and catalytic studies it can be concluded that the CoNiMoW electrodeposits are suitable for application in hybrid systems combining DBFC and Hydrogen-on-demand generator, which may further supply a low-power hydrogen fuel cell.

REFERENCES

1. S.J.C. Cleghorn, X. Ren, T.E. Springer, M.S. Wilson, C. Zawodzinski, T.A. Zawodzinski, S. Gottesfeld, *Int. J. Hydrogen Energy*, **22**, 1137 (1997).
2. A. Zuttel, *Naturwissenschaften*, **91**, 157 (2004).
3. B. Sundqvist, *Solid-State Phenom.*, **150**, 175 (2009).
4. F. Agresti, A. Khandelwal, A. Maddalena, G. Principi, S. Russo, *Int. J. Nucl. Hydrogen Prod. Appl.*, **2**, 122 (2009).
5. E.Y. Marrero-Alfonso, A.M. Beaird, T.A. Davis, M.A. Matthews, *Ind. Eng. Chem. Res.*, **48**, 3703 (2009).
6. Y. Kojima, T. Haga, *Int. J. Hydrogen Energy*, **28**, 989 (2003).
7. T. Kemmitta, G.J. Gainsford, *Int. J. Hydrogen Energy*, **34**, 5726 (2009).
8. S.C. Amendola, S.L. Sharp-Goldman, M.S. Janjua, M.T. Kelly, P.J. Petillo, M. Binder, *J. Power Sources*, **85**, 186 (2000).
9. S.U. Jeong, R.K. Kim, E.A. Cho, H.J. Kim, S.W. Nam, I.H. Oh, S.A. Hong, S.H. Kim, *J. Power Sources*, **144**, 129 (2005).
10. J. Ma, N. Choudhury, Y. Sahai, *Renew. Sust. Energ. Rev.*, **14**, 183 (2010).
11. H. Dong, R. Feng, X. Ai, Y. Cao, H. Yang, C. Cha, *J. Phys. Chem. B*, **109**, 10896 (2005).
12. H. Celikkan, M. Sahin, M.L. Aksu, T.N. Veziroglu, *Int. J. Hydrogen Energy*, **32**, 588 (2007).
13. E. Gyenge, *Electrochim. Acta*, **49**, 965 (2004).
14. H. Cheng, K. Scott, *Electrochim. Acta*, **51**, 3429 (2006).
15. M. Chatenet, F. Micouda, I. Roche, E. Chainet, *Electrochim. Acta,* **51**, 5459 (2006).
16. M. Simoes, S. Baranton, C. Coutanceau, *J. Phys. Chem. C*, **113**, 13369 (2009).
17. L. Wang, C. Ma, Y. Sun, S. Suda, *J. Alloys Compd.*, **391**, 318 (2005).
18. Y.P. Petrov, M.Y. Mitov, A.K. Popov, Bulg. *Chem. Commun.*, **38**, 217 (2006).
19. Z.P. Li, B.H. Liu, K. Arai, S. Suda, *J. Electrochem. Soc.*, **150**, A868 (2003).
20. S.M. Lee, J.H. Kim, H.H. Lee, P.S. Lee, J.Y. Lee, *J. Electrochem. Soc.*, **149**, A603 (2002).
21. J.Y. Lee, H.H. Lee, J.H. Lee, D.M. Kim, US Patent 5599640 (1997).
22. V. Kiran, S. Srinivasan, *J. Indian Inst. Sci.*, **89**, 447 (2009).
23. M. Mitov, R. Rashkov, N. Atanassov, A. Zielonka, *J. Mater. Sci.*, **42**, 3367 (2007).
24. M. Mitov, G. Hristov, E. Hristova, R. Rashkov, M. Arnaudova, A. Zielonka, *Environm. Chem. Lett.*, **7**, 167 (2009).
25. R. Rashkov, G. Hodjaoglu, N. Atanassov, A. Zielonka, in: Nanostructured Materials in Electroplating, D. Stoychev, E. Valova, I. Krastev, N. Atanassov (eds.), St. Kliment Ohridski University Press, Sofia, 2006, p. 190.
26. A. Kaisheva, I. Iliev, S. Gamburzev, *J. Power Sources*, **13**, 181 (1984).
27. E. Budevski, *J. Optoelectron. Adv. Mater.*, **5**, 1319 (2003).

КВАТЕРНЕРНИ ЕЛЕКТРОДЕПОЗИТИ ВЪРХУ ПЕНООБРАЗЕН НИКЕЛ ЗА ПРИЛОЖЕНИЕ В ХИБРИДНА СИСТЕМА ГОРИВЕН ЕЛЕМЕНТ С ДИРЕКТНО ЕЛЕКТРООКИСЛЕНИЕ НА БОРХИДРИД – ГЕНЕРАТОР НА ВОДОРОД

М. Й. Митов[1], Г. Й. Христов[1], Р. С. Рашков[2], Й. В. Хубенова[3]

[1]Катедра Химия, Югозападен университет „Неофит Рилски", Благоевград, България
[2]Институт по Физикохимия "Акад. Ростислав Каишев", Българска Академия на Науките, България
[3]Катедра Биохимия и Микробиология, Пловдивски Университет, Пловдив, България

(Резюме)

В настоящата разработка, CoNiMoW електроотложения, получени при различни галваностатични условия, са изследвани като анодни материали в Горивен елемент с директно електроокисление на борхидрид. Като тенденция, по-голяма мощност е получена с аноди, електроотложени при по-ниски плътности на тока. Максимална мощност от 250 mW е достигната с използването на CoNiMoW-анод, електроотложен при най-ниската плътност на тока (15 mA cm^{-2}) и два въздушни газо-дифузионни катода. Тази стойност надвишава 2.5 пъти достигнатата мощност със същия анод и един газо-дифузионен катод, което е указание, че редукцията на кислорода върху катода е скоростоопределяща за цялостния процес. Паралелно са изследвани каталитичните свойства на CoNiMoW електродепозити по отношение на „непроизводителната" борхидридна хидролиза. Най-голяма скорост на генериране на водород (15.0 ml min^{-1}) е постигната с CoNiMoW-електроотложения, получени при най-малката приложена плътност на тока. Близки стойности на активиращата енергия (36.5±2.7 kJ mol^{-1}) са получени с всички изследвани материали. Обобщавайки резултатите от проведените изследвания, електроотложените CoNiMoW материали се предлагат като потенциални кандидати за приложение в хибридна система Горивен елемент с директно електроокисление на борхидрид – Генератор на водород.

Electrocatalytic activity of Pd-Au co-deposits on Ni-foam towards hydrogen evolution reaction

E. Y. Chorbadzhiyska[1*], Y. V. Hubenova[2], G. Y. Hristov[1], L. Nalbandian[3], M. Y. Mitov[1]

[1]*Department of Chemistry, South-West University "Neofit Rilski", Blagoevgrad, Bulgaria*
[2]*Department of Biochemistry and Microbiology, Plovdiv University "Paisii Hilendarski",*
Plovdiv, Bulgaria
[3]*Laboratory of Inorganic Materials (LIM), Chemical Process & Energy Resources Institute,*
Center for Research and Technology - Hellas (CPERI / CERTH), Thermi-Thessaloniki, Greece

Pd-Au coatings were electrodeposited on Ni-foam from electrolytes with different contents of both metals. The morphology of the produced co-deposits was analyzed by scanning electron microscopy. Their electrocatalytic activity towards hydrogen evolution reaction from neutral phosphate buffer solution was explored by means of linear voltammetry. In addition, the current was monitored under potentiostatic polarization from -0.6 to -1.2 V (vs. Ag/AgCl) and the quantities of the produced hydrogen gas with the electrocatalysts were calculated. The highest hydrogen evolution rate was achieved with the electrocatalysts produced from an electrolyte with equal Pd and Au contents.

Keywords: Pd-Au electrocatalysts, hydrogen evolution reaction, neutral electrolyte, linear voltammetry, chronoamperometry.

INTRODUCTION

Hydrogen evolution reaction (HER) takes place at the cathode in many industrial electrolysis processes with aqueous electrolytes, as well as in bioelectrochemical systems, in particular – microbial electrolysis cells (MECs), where the production of hydrogen is the main target [1,2]. The development of MECs represents an exciting new area of the environmental biotechnological research. The MECs, commonly exploiting wastewater as a fuel source to produce hydrogen while accomplishing wastewater treatment, are closely related to two intensively developing technologies - microbial fuel cells (MFCs) and water electrolysis. As far as the anodic reactions, as well as the operational conditions in MECs are the same as those in MFCs, the achievements concerning development of the bioanodes could be directly transferred from the one technology to the other one. Although HER is the common cathodic reaction in MECs and water electrolyzers, the operating conditions in both systems are quite different. The use of microorganisms as biocatalysts in MECs requires mild conditions such as near neutral electrolytes and ambient temperatures, while most industrial water electrolyzers operate with acidic or alkaline electrolytes at elevated temperatures. By these reasons, the crucial point for the practical application of MECs as a feasible hydrogen production technology is to find cost effective and high catalytically active cathodes for near-neutral pH and moderate temperatures.

Platinum is well-known as the best electrocatalyst for HER, but it is too expensive [1, 2-6]. Partial substitution of Pt and decrease of catalyst amount are among the main strategies for cost reduction [7-9]. Kye et al. [10] have demonstrated that the Pt-Au electrocatalyst shows higher area-specific activity than platinum nanoparticles alone. Huang et al. [11] reported that Pd nanoparticles coated carbon cloth was almost 50 times more effective than Pt as cathode catalyst for HER in MEC. In our previous study [12], it was established that Pd-Au co-deposits, produced by electrodeposition on carbon felt, display electrocatalytic activity for HER in neutral electrolyte, increasing with augmentation of the gold content.

Ni-foam has been widely used as an electrocatalyst supporting material due to its well-developed porous structure, high conductivity, corrosion resistivity and good mechanical properties [13-16].

In this study, Pd-Au composites were synthesized by electrodeposition on Ni-foam and

---

* To whom all correspondence should be sent:
E-mail: elli_e1@swu.bg

their electrocatalytic activity towards HER was investigated in neutral phosphate buffer solution with a view to their possible application as cathodes in MECs.

EXPERIMENTAL

Electrodes were prepared by electrochemical co-deposition of Pd and Au on Ni-foam (RCM-Ni-4753.016). The electrodeposition was carried out in a three-electrode cell and the potential was controlled by PalmSens handheld potentiostat/ galvanostat. A round-shaped sample of Ni-foam with geometric area of 1.6 cm^2 was connected as a working electrode, platinum-titanium mesh was used as a counter electrode and the potential was measured against Ag/AgCl reference electrode. The electrolyte was a mixture of 2% PdCl$_2$ in 0.1M HCl and 2% HAuCl$_4$ in 0.1M HCl in different ratios (w/w %): 9:1, 7:3 and 1:1 [17]. The electrodeposition was performed in potentiostatic regime at E$_{deposit}$ = -500 mV (vs. Ag/AgCl) for 10 s.

The morphology of the produced electrodeposits, further denoted in the text as Pd$_{50}$Au$_{50}$/Ni-foam, Pd$_{70}$Au$_{30}$/Ni-foam and Pd$_{90}$Au$_{10}$/Ni-foam, was analyzed by scanning electron microscopy (SEM) and energy dispersive spectroscopy (EDS) using JEOL 6300 microscope.

The weight of the co-deposits was estimated from the current transients, obtained during electrodeposition, by using the Faraday's law and data for the molar percentage, determined in a previous study [12].

The electrocatalytic activity of the obtained materials towards HER was investigated in 67 mM phosphate buffer solution (pH 7.0) by means of linear voltammetry (LV). The experiments were carried out in a three-electrode cell. The explored sample was connected as a working electrode and a platinum-titanium mesh (10 cm^2) and Ag/AgCl (3 M KCl) were used as a counter and a reference electrode, respectively. The potential was swept from 0 to -1.2 V (vs. Ag/AgCl) with a scan rate of 2 mV.s^{-1}. Three subsequent scans were performed for each sample and the third scan was used for data analysis.

In parallel, chronoamperometric measurements were carried out under the same conditions. The working electrode was polarized from −0.6 to −1.2 V (vs. Ag/AgCl) with a voltage step of 0.1 V for 10 min at each step and the current was monitored. The quantity of the produced hydrogen was calculated by integration of the areas under the chronoamperometric curves at each potential and applying Faraday's law.

The voltammetric and chronoamperometric studies were performed by using potentiostat/ galvanostat PJT 35-2 with IMT-101 electrochemical interface.

RESULTS AND DISCUSSION

Scanning electron microscopy (SEM) observations show that the obtained Pd-Au electrodeposits are irregularly distributed over the Ni-foam, forming islands with varying size (Fig. 1). In all cases the distribution of the particles is not uniform. The bigger magnifications of the co-deposits reveal that the islands consist of nearly spherical complex structures sized up to 2.5 μm. The recorded EDS spectra confirm the co-presence of Pd and Au in the deposits (Fig. 2).
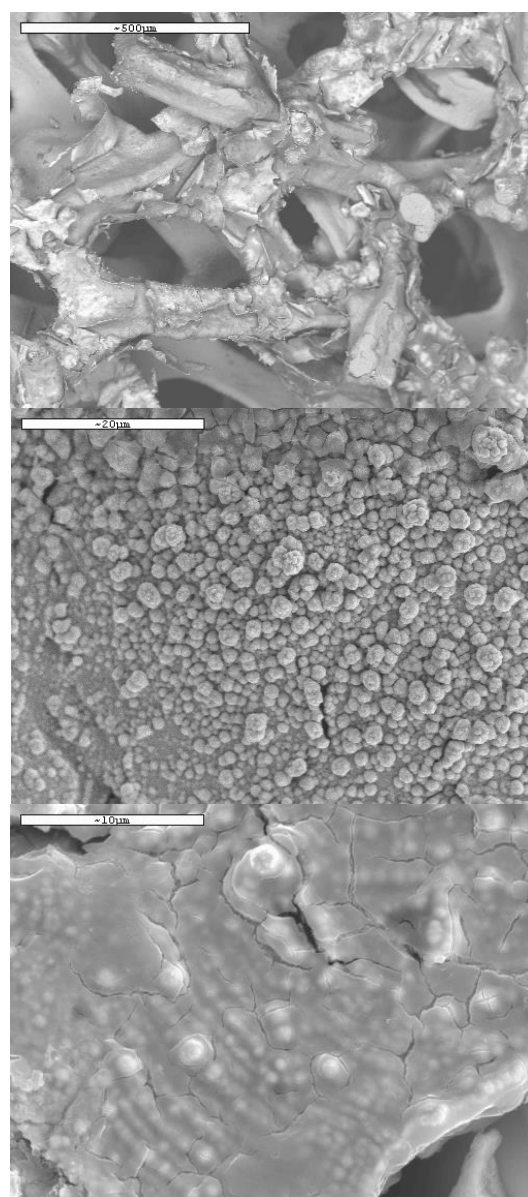
Fig. 1. SEM images of Pd-Au electrodeposits on Ni-foam, taken at different magnifications.

Earlier studies [18] have proved that each globular structure is formed by a large number of nanosized particles, whose shape is strongly affected by the percentage of gold in the deposit and changes from needle-like crystallites (as with the co-deposits with high Pd content) to cauliflower-like shape, observed with Au-enriched crystallites. In the same paper [18], the XRD spectra of Pd-Au co-deposits, produced in varied proportions of both metals, were compared with those of the pure Au and Pd electrodeposits. The 2Θ values of the deposits indicate the availability of fcc crystalline metal phases corresponding to (111), (200), and (220) facets. The diffraction peaks of the co-deposited metal phases were shifted to the lower 2Θ values as compared to that of the pure Pd. The lattice expansion caused by the inclusion of Au atoms into the Pd fcc structure is indicative for alloy formation.

Table 1. Values of V_e, V_h and current density at -1.2 V (vs. Ag/AgCl), estimated from LVs.

Material	V_e, V (vs. Ag/AgCl)	V_h, $A.V^{-1} \times 10^{-3}$	Current density, $mA.cm^{-2}$
Ni-foam	-0.63	3.42	1.32
$Pd_{90}Au_{10}$ / Ni-foam	-0.52	4.30	1.91
$Pd_{70}Au_{30}$ / Ni-foam	-0.48	5.25	2.47
$Pd_{50}Au_{50}$ / Ni-foam	-0.41	10.40	5.29
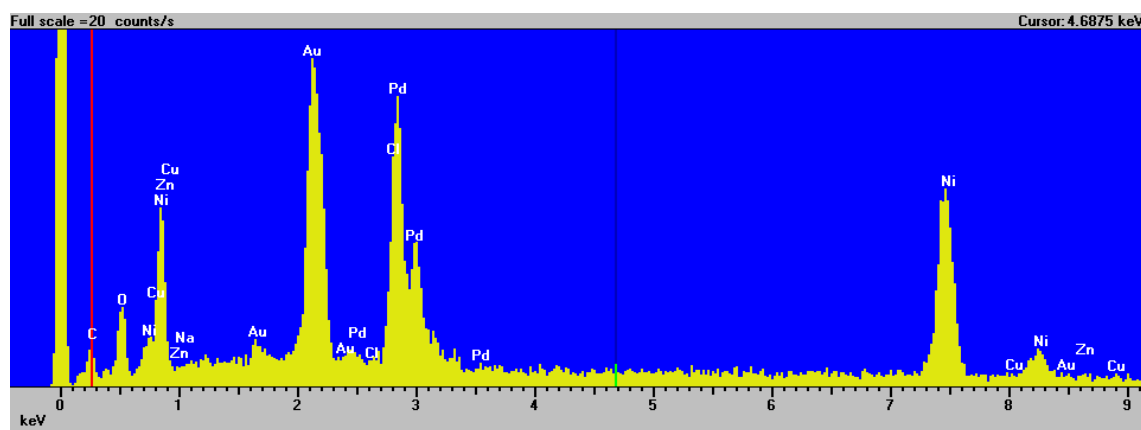
Fig. 2. EDS-spectrum of $Pd_{50}Au_{50}$/Ni-foam.
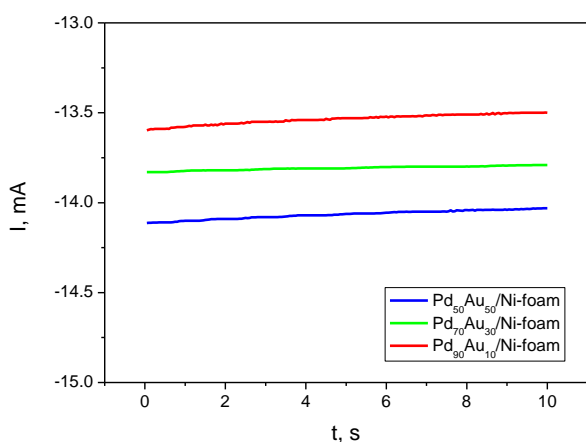
Fig. 3. Chronoamperograms obtained during co-electrodeposition of Pd and Au
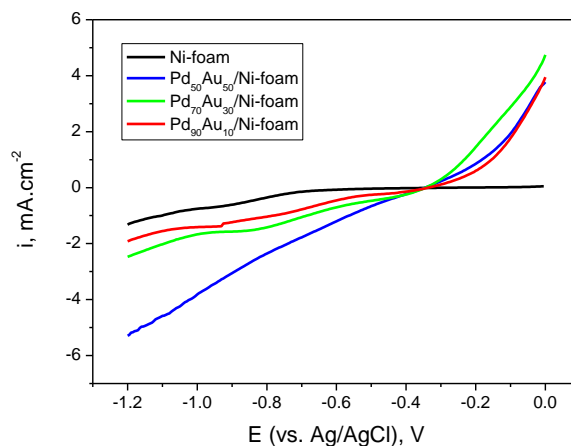
Fig. 4. Linear voltammograms obtained with Pd-Au in different ratios on Ni-foam in phosphate buffer (pH 7).

The amounts of the electrodeposits were calculated from the coulombs, obtained by integration of the current passed through the system during deposition (Fig. 3), applying the Faraday's law. The obtained values are of the order of 0.080 ± 0.004 mg, slightly increasing with augmentation of gold content in the electrodeposition bath.

Linear voltammograms (LVs) obtained with a Ni-foam and with the newly produced Pd-Au modified electrodes are plotted in Fig. 4. The evaluation of the electrocatalytic performance was based on the voltage needed to initiate hydrogen production (V_e) and the slope (V_h) of the first linear region in the voltammogram. The value of V_e indicates the relative overpotential, while V_h reflects the current production rate at an applied voltage. Better catalytic performance is achieved by a lower V_e and higher V_h [19]. The values of V_e and V_h estimated from LVs are summarized in Table 1. In addition, the current density values, derived from Fig. 3 at a potential of -1.20 V (vs. Ag/AgCl), are also presented.

a)

b)
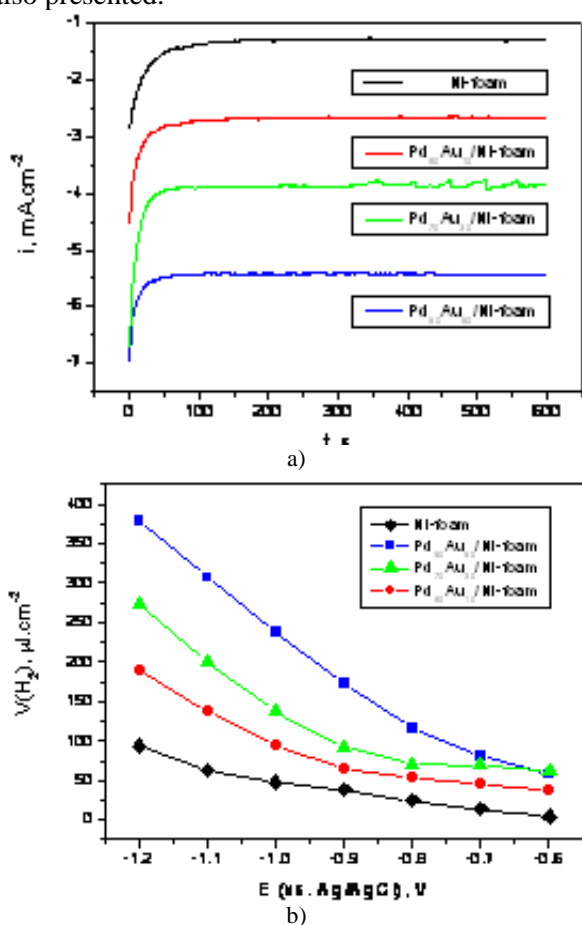
Fig. 5. a) Chronoamperograms obtained with Ni-foam and Pd-Au electrodeposits at potential -1.2 V (vs. Ag/AgCl); b) Quantities of evolved hydrogen at different applied potentials estimated from chronoamperometric measurements.

The obtained results indicate that the bare Ni-foam possesses a higher overpotential in respect to HER than the electrodeposited electrodes. The increase of gold content in the electroplating bath, resp. in the co-deposits [12], diminishes the overpotential; thus, the hydrogen production on $Pd_{50}Au_{50}$/Ni-foam begins at the lowest potential -0.41V (vs. Ag/AgCl). In the same direction, a tendency for increase in both V_h and current density values is observed, showing that the augmentation of gold content improves the cathodic reaction. The quantitative deviations between the ratios of V_h and current density at -1.20 V (vs. Ag/AgCl) for the different materials studied are due to the appearance of a cathodic hump in the LVs of deposited $Pd_{90}Au_{10}$ and $Pd_{70}Au_{30}$ electrodes, which could be assigned to possible hydrogen absorption and/or hydride formation in these samples [20]. We suppose that the decrease of palladium in the deposit lowers its capability for hydrogen absorption, thus making the competitive hydrogen evolution reaction more favourable.
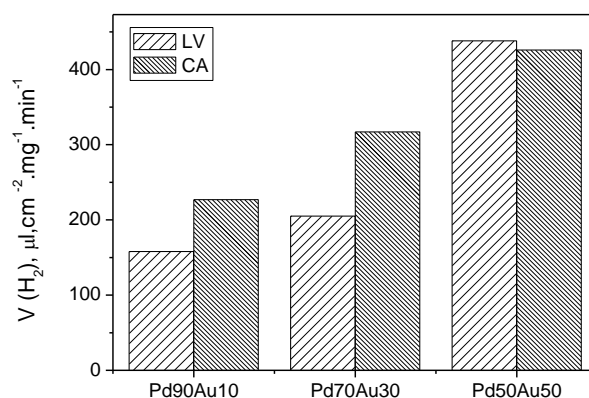
Fig. 6. Intrinsic electrocatalytic activity of the investigated Pd-Au electrodeposits towards HER, expressed as a volume of generated hydrogen per min normalized to the weight of the co-deposits and the geometric area of the support. The estimations were performed by using current density values from the linear voltammograms (LV) and chronoamperograms (CA) at potential -1.2 V (vs. Ag/AgCl).

In our previous study [12], it was verified that the estimations based on chronoamperometric measurements are related to the quantities of the evolved hydrogen detected by mass spectrometry. These findings allowed evaluation of the hydrogen production by monitoring the current response at different potentials. Considering the results from LVs, chronoamperometric experiments with the investigated materials were performed at potentials from -0.6 to -1.2 V (vs. Ag/AgCl). Chronoamperograms obtained with Pd-Au electrodeposits and Ni-foam at -1.2 V (vs.

Ag/AgCl) are presented in Fig. 5a. The estimated quantities of the produced hydrogen at different applied potentials are plotted on Fig. 5b.

In general, the results from chronoamperometric measurements confirm those obtained by LV. The hydrogen production rates on all electrodeposited electrodes are higher than those on the non-modified Ni-foam and a tendency for increasing the amount of generated hydrogen with the increase of gold content in the electrodeposited catalysts is observed.

To evaluate the intrinsic electrocatalytic activity of the explored Pd-Au electrodeposits, the quantities of generated hydrogen were normalized to the weight of the co-deposits. The estimations were done by using current density values at -1.2 V (vs. Ag/AgCl), derived from the corresponding LVs and chronoamperograms, and summarized in Fig. 6. The slight increase of the deposits' weight with the rise in the gold amount does not significantly influence the estimated intrinsic activity values, which enhance in the order $Pd_{90}Au_{10} < Pd_{70}Au_{30} < Pd_{50}Au_{50}$.

CONCLUSION

Palladium and gold could be co-deposited on Ni-foam by electrodeposition at -0.5 V (vs. Ag/AgCl). The increase of the gold content in the electrolyte bath enhances the electrocatalytic activity of the obtained Pd-Au electrodeposits towards HER in neutral phosphate buffer solution. The highest intrinsic electrocatalytic activity was achieved with $Pd_{50}Au_{50}$ electrodeposits. Based on the results obtained in this study we consider that Pd-Au co-deposits are promising electrocatalysts for hydrogen generation in microbial electrolysis cells.

REFERENCES

1. H. Liu, H. Hu, J. Chignell, Y. Fan, *Biofuels*, **1**, 129 (2010).
2. A. Jeremiasse, H. Hamelers, C. Buisman, *Bioelectrochemistry*, **78**, 39 (2010).
3. A. Bandyopadhyay, J. Stöckel, H. Min, L. Sherman, H. Pakrasi, *Nature Comm.*, **1**, 139 (2010).
4. S. Cheng, D. Xing, D. Call, B. Logan, *Environ. Sci. Technol.*, **43**, 3953 (2009).
5. S. Cheng, B. Logan, *PNAS*, **104,** 18871 (2007)
6. J. O. Ramirez, M. C. Cornelio, J. U. Godinez, E. B. Arco, R. Castellanos, *Int. J. Hydrogen Energy*, **32**, 3170 (2007).[\
7. Y. Fan, S. Xu, R. Schaller, J. Jiao, F. Chaplen, H. Liu, *Biosens. Bioelectron.*, **26**, 1908 (2011).
8. S. Freguia, K. Rabaey, Z. Yuan, J. Keller, *Environ. Sci. Technol.*, **41**, 2915 (2007).
9. M. D. Crespo, E. R. Meneses, A. T. Huerta, V. G. Febles, K. Philippot, *Int. J. Hydrogen Energy*, **37,** 4798 (2012).
10. J. Kye, M. Shin, B. Lim, J. W. Jang, I. Oh, S. Hwang, *ACS Nano,* **7,** 6017 (2013).
11. Y. Huang, X. Liu, X. Sun, G. Sheng, Y. Zhang, G. Yan, S. Wang, A. Xu, H. Yu, *Int. J. Hydrogen Energy*, **36**, 2773 (2011).
12. E.Chorbadzhiyska, M.Mitov, G.Hristov, N.Dimcheva, L.Nalbandian, A.Evdou, Y.Hubenova, *Int. J. Electrochem.*, Vol. 2014, Article ID 239270, 6 pages, (2014) http://dx.doi.org/10.1155/2014/239270
13. M. D. Crespo, A. T. Huerta, B. B. Sibaja, A. F. Vela, *Int. J. Hydrogen Energy*, **36,** 135 (2011).
14. R. Solmaz, A. Gundogdu, A. Doner, G. Kardas, *Int. J. Hydrogen Energy*, **37,** 8917 (2012).
15. P. Zhao, H. Zhang, H. Zhou, B. Yi, *Electrochim. Acta,* **51**, 1091 (2005).
16. J. Pu, Y. Tong, S. Wang, E. Sheng, Z. Wang, *J. Power Sources,* **250**, 250 (2014).
17. E. Horozova, T. Dodevska, N. Dimcheva, R. Mussarlieva, *Int. J. Electrochem.,* Article ID 697698, (2011).
18. T. Nagaiah, D. Schafer, W. Schuhmann, N. Dimcheva, *Anal. Chem.*, **85**, 7897 (2013).
19. Y. Zhang, M. Merrill, B. Logan, *Int. J. Hydrogen Energy,* **35**, 12020 (2010).
20. E. Crespo, M. Ruda, S. Ramos de Debiaggi, E. Bringa, F. Braschi, G. Bertolino, *Int. J. Hydrogen Energy*, **37,** 14831 (2012).

ЕЛЕКТРОКАТАЛИТИЧНА АКТИВНОСТ НА Pd-Au КО-ДЕПОЗИТИ ВЪРХУ ПЕНООБРАЗЕН НИКЕЛ ПО ОТНОШЕНИЕ ЕЛЕКТРОХИМИЧНОТО ОТДЕЛЯНЕ НА ВОДОРОД

Е. Й. Чорбаджийска[1*], Й. В. Хубенова[2], Г. Й. Христов[1], Л. Налбандиан[3], М. Й. Митов [1]

[1]Катедра Химия, Югозападен университет „Неофит Рилски”, Благоевград, България
[2]Катедра Биохимия и Микробиология, Пловдивски Университет, Пловдив, България
[3]Лаборатория по неорганични материали, Институт по химични процеси и енергийни ресурси, Научно-изследователски и технологичен център – Хелас, Терми-Солун, Гърция

(Резюме)

Тънки слоеве от Pd-Au са отложени върху пенообразен никел от електролити с различно съдържание на двата метала. Морфологията на получените електроотложения е анализирана чрез сканираща електронна микроскопия. Чрез линейна волтамперометрия е изследвана електрокаталитичната активност на материалите по отношение електрохимичното отделяне на водород от неутрален фосфатен буферен разтвор. Паралелно са проведени потенциостатични измервания в интервала от -0.6 до -1.2 V (vs. Ag/AgCl), от които е изчислено количеството водород, получавано с различните депозити. Най-висока скорост на отделяне на водород е постигната с електрокатализаторите, отложени от електролит с еднакво съдържание на Pd и Au.

Catalytic decomposition of N_2O, contained in waste gases originating from HNO_3 production

D. D. Stoyanova[*1], N. A. Kasabova[2], D. St. Shishkov[2], Tc. N. Velinova[2], D. Dimitrov [3]

V. Grancharov[4]

[1] *Institute of General and Inorganic Chemistry, Bulgarian Academy of Sciences, acad. G. Bonchev Str., bl.11, 1113Sofia, Bulgaria*
[2] *University of Chemical Technology and Metallurgy, Kl. Ohridski 8 blv., 1756 Sofia, Bulgaria*
[3] *Higher Institute of Agriculture, Department of Chemistry, 12 Mendeleev str., 4000 Plovdiv, Bulgaria*
[4]*NEOCHIM PLC, 6403 Dimitrovgrad, Bulgaria*

The object of the present investigations is a catalyst sample possessing a spinel-like structure, comprising copper, zinc and aluminum oxides in a ratio Cu:Zn:Al = 1:1:4. The conditions of co-precipitation of copper - zinc ammonia-carbonate solutions and a solution of aluminum nitrate ensure nano-size dimensions of the precursors and high dispersion degree after calcination of the contact masses at a temperature of 900^0C. This fact predetermines the high activity of the catalyst during the testing in kinetic and diffusion regime of operation at gaseous hourly space velocities of $W = 8500$ h^{-1} and 17000 h^{-1}, $T = 830^0C$ and inlet N_2O concentration $= 1100 \div 1400$ ppm, i.e. under conditions analogous to those in the industrial process. The degree of decomposition (α) is higher than 0.9. The catalytic sample having the above indicated composition is highly active in the reaction of decomposition of N_2O into N_2 and O_2 in the case of production of HNO_3 based on the method of Ostwald as early as in the first steps of the process – catalytic oxidation of NH_3, i.e. "secondary in sequence".

Keywords: Catalytic decomposition of N_2O, precursor, catalysts, catalytic activity.

INTRODUCTION

In view of the increasing importance of the chemical branch in developing industry, the issue of monitoring harmful emissions, liberated into the atmosphere, is becoming a hot topic of the day. The problem of reducing „the hot house effect" is occupying one of the first positions among the top priorities, as a consequence of the global warming. The nitrous oxide N_2O is among the several hot house gases, having 300 times higher coefficient of the hot house effect compared to that of CO_2.

The total amount of N_2O emitted into the atmosphere has been evaluated to be 7.2×10^6 tons per year, and out of this amount the emissions during the production of HNO_3 are 0.4×10^6 t/y.

In the course of producing HNO_3 based on „Ostwald's process" the following reactions are occurring:

$4NH_3 + 5O_2 \rightarrow 4NO + 6H_2O + 906,1$ kJ   /1/
$4NH_3 + 4O_2 \rightarrow 2N_2O + 6H_2O + 1287,2$ kJ   /2/
$4NH_3 + 3O_2 \rightarrow 2N_2 + 6H_2O + 1103,0$ kJ   /3/
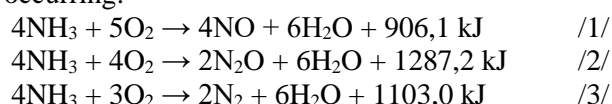
Among these three reactions it is only the reaction /1/, which is desirable. The purification of waste gases originating from the production of HNO_3 is accomplished by means of catalytic decomposition or reduction of the nitrogen oxides into elemental N_2. The current research and patent literature considers the problem of reducing the emissions of N_2O liberated in the production of HNO_3 through the „Ostwald's process" [1 - 4].

Some oxide catalysts have also been proposed for the decomposition of N_2O. Analyzing the available literature data it has been noted that the highest activity is manifested by the oxides of the transition metals belonging to Group VII (Rh, Ir, Co, Fe, Ni) and also by Group 1B – mainly Cu [5 - 9].

The authors of ref. [10] made a remark that the decomposition reaction of N_2O is sensitive with respect to the structure of the oxides. In some cases the oxygen vacancies are involved, while in other cases it is the coordinatively unsaturated transition metal ions that are taking part. High catalytic activity is displayed by zeolites of the Y – ZSM – 5 type (pentasil). In accordance with the mechanism of the reaction two classes of catalysts are being formed. The first ones are catalysts of the type Mn_2O_3, Fe_2O_3, NiO, $LaCoO_3$, Cu-ZSM-5, on which the decomposition is occurring on the oxygen vacancies / /:

$$N_2O + /\ /O_2 + N_2$$

---

* To whom all correspondence should be sent:
E-mail: dsto@svr.igic.bas.bg

(O) + (O)O$_2$ + 2/ /

The catalysts of the second class/group are the zeolites, such as Fe-HZSM-5 and Co-HZSM-5, where the decomposition of N$_2$O involves the participation of isolated ions of the transition metals [M^{n+}]:

N$_2$O + [M^{n+}]N$_2$ + [M^{n+}]O

N$_2$O + [M^{n+}]ON$_2$ + O$_2$ + [M^{n+}]
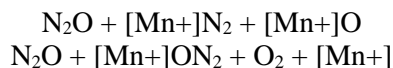
The catalytic properties of the catalysts of zeolite type are associated with the presence of α-sites, complexes of iron, stabilized in the matrix of the zeolite ZSM-5 [11, 12]. An iron oxide catalyst supported on Al$_2$O$_3$, prepared by the method of co-precipitation, manifested high catalytic activity and also mechanical stability during the reaction of N$_2$O conversion at T = 750^{0}C, in the presence of H$_2$O and NO [13]. Many oxide-supported catalysts for the above specified process contain oxides or spinels of Cu or Co as the active phase [6, 7, 9, 14]. Analyzing the variety of catalytic compositions it is stated that both the effect of the active spinel phase, as well as the influence of the nature of the support, should be taken into account [14 - 18].

The catalytic decomposition of N$_2$O using a model gas mixture analogous to that liberated in the production of HNO$_3$ is commented on in ref. [19, 20]. It is only a small number of the studied catalysts that have been tested under the actual industrial conditions in the N$_2$O decomposition reaction.

On the basis of the above presented survey of literature one can draw the conclusion that the most promising catalysts for N$_2$O decomposition are those based on oxides of the transition metals Rh, Ir, Co, Fe, Ni and copper oxide catalysts.

In this aspect the aim of our studies was to establish the optimal conditions for synthesizing a Cu-Zn-Al catalyst of spinel-type for decomposition of N$_2$O to N$_2$ and O$_2$, as an accessible and economically advantageous catalyst. The decomposition reaction is expected to occur at certain fixed values of the thermodynamic, kinetic and technological parameters, immediately after the contact mesh, in accordance with the industrial operation conditions.

EXPERIMENTAL

Preparation of the catalyst samples

The synthesis of the catalyst samples was described in the patent application [21]. The spinel-like structure is based on the oxides of Cu, Zn and Al at a ratio Cu:Zn:Al = 1:1:4, the phase composition comprising CuAl$_2$O$_4$ and ZnAl$_2$O$_4$. The initial precursors are in the form of solutions of dissolved (electrolytic) Cu, ZnO and metallic Al.

Copper and zinc are in the form of a copper-ammonia, respectively zinc-ammonia carbonate solution. Upon mixing the two solutions of Cu and Zn a copper-zinc ammonia-carbonate solution is obtained, which is the precipitating agent in the reaction system. The homogeneity of precipitation is achieved by a fixed set of conditions: pH factor – 5, 2÷7; temperature 60÷80^{0}C; time interval of precipitation 15÷30 min and aging time of the precipitate from 30 to 60 min. The so obtained system possesses a high degree of dispersion and the chemical and phase compositions are homogeneously distributed. The consecutive steps of the synthesis are trivial: filtering, washing until the absence of NO$_3^-$ ions, drying at T = 120 ÷ 150^{0}C, calcination at T = 350 ÷500^{0}C for 4 to 8 hours, forming of tablets or extruding the material, followed by calcination at a higher temperature T = 800 ÷ 1000^{0}C for 4 to 6 hours. This technological scheme ensures absence of any waste material and high catalytic activity and selectivity.

The catalyst sample **S** was prepared by the above described technology and then it was characterized after calcination at different temperatures. Another supported type of catalyst sample was synthesized for comparison. The support was α-Al$_2$O$_3$, while the supported phases were the oxides of Cu, Zn and Al at a ratio 1:1:4 (catalyst sample **S$_1$**).

Characterization of the catalyst samples

The structure and the phase composition of the catalyst samples were identified on a XRD apparatus Bruker Advance, using CuKα radiation and SolX Detector with 2θ ranging from 20^0 to 80^0 at a scan step of 0.04^0. The degree of dispersion of the phases was determined on the basis of the XRD analysis and in accordance with Scherrer's rule L = k.λ/β.cos θ).

The express BET method was applied to measure the specific surface area, based on low-temperature adsorption of nitrogen – i.e. at the boiling temperature of liquid nitrogen 77K. The relative error of the method amounts to about 8%. The specific surface area and the pore size distribution of the two catalyst samples were measured on an automated apparatus NOVA Win/Nova Win – CFR Quantachrom – Gas Sorption System. The calculation of the surface area was done using the BET equation, whereupon the pore size distribution, as well as the average pore diameter were evaluated by DFT assuming a cylindrical model of the pores. The total pore volume was estimated in accordance with the rule of Gurvich ata relative pressure of 0.96.

The derivatographic analysis was realized using the STAPT 1600 TG-DTA/DSC apparatus, manufactured by LINSEIS Messgeräte GmbH, Germany; the monitored temperature interval was $20 \div 1550^0$C.

The catalytic activity testing was carried out in a three-channel integral isothermal reactor under kinetic control conditions. The space velocity was equivalent to 100 mm, respectively 200 mm height of the catalyst bed (i.e. 16 000 h^{-1}, respectively 32 000 h^{-1}). Under these hydrodynamic conditions the ratio H/D > 2 and D/dz > 3, the Peclet number was Pe > 120, i.e. conditions determining a plug flow reactor, which is most often occurring under industrial conditions of heterogeneous catalytic processes. In the ratio H/D and D/dz H is the height of the catalyst bed, D is the diameter of the reactor tube, while dz is the diameter of the catalyst granule. The concentration of N_2O was determined using a gas chromatograph equipped with a thermal conductivity detector (hot-wire detector HWD) and a packed-bed GC column of „Porapack Q" (the feed gaseous mixture was purified from NOx prior to the experiment). The catalytic activity was studied also on a pilot-plant scale reactor, under conditions analogous to those in the industrial process – catalyst grain size, catalyst loading (space velocity), height of the catalyst bed (100 mm and 200 mm), temperature 830^0C and pressure up to 100 mm H_2O column. The reaction mixture under consideration in this study, consisting of NOx, N_2O,

N_2 and O_2, was sampled out immediately after the contact meshes in the industrial installation.

RESULTS AND DISCUSSION

The process of the formation of the precursor, as well as the thermal transitions inside, are both of special importance in view of obtaining different structures and textures of the contact masses. Having this in mind we carried out differential thermal analysis (DTA), in order to trace the processes of phase transformations within a specific temperature interval. The phase transitions inside the S catalyst sample were observed within the T = $0 \div 1150^0$C temperature interval. The selected parameters of precipitation – pH factor, time interval of precipitation and aging time of the residue predetermine the nature of the precipitate - mainly malachite and some isomorphous admixtures in the hydrozincite, $(Cu,Zn)_5(OH)_6(CO_3)_2$, established in our previous investigations [22]. The high percentage of Al_2O_3 content in the system and the initial lower pH value of precipitation pH = $6 \div 6.5$ – all these create conditions for precipitation of scarboite phase having composition $12Al(OH)_3.Al_2(CO_3)_3$, which is stable up to ~130^0C and passes over to metascarboite phase thereafter. The first observed endothermal effect in the course of the thermal analysis in the interval $150 \div 205^0$C is an indication of the presence of this phase.
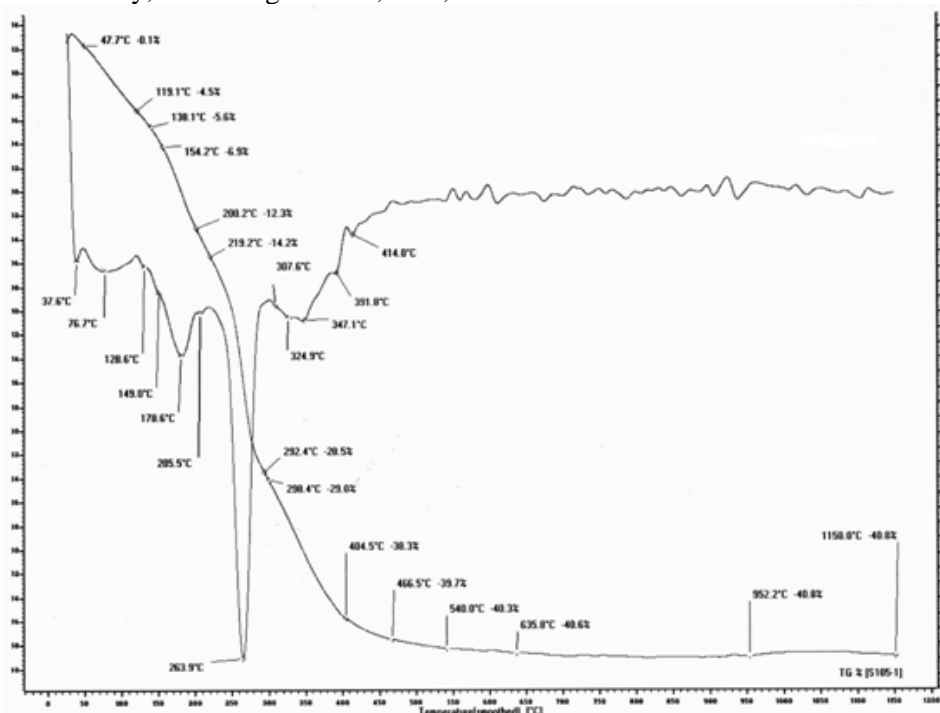
Fig.1. DTA and TG curves of the catalyst sample precursor S within the temperature interval T = $0 \div 1150^0$C

The hydroxyl-carbonate groups are decomposed upon increasing the temperature from 250^0C to 400^0C – this is the second endothermal effect with a maximum at $T = 264^0C$. In view of the combined process of co-precipitation of copper and zinc, it is most probable that there occurs isomorphous substitution in the hydrozincite - $(Zn,Cu)_5(OH)_6(CO_3)_2$ (Figure 1).

This substitution predetermines the nanometer-sized dimensions of the phases after calcination at considerably higher temperatures.

The phase composition, the particle sizes of the different phases and the pore size distribution in the system are factors of essential importance for the catalytic activity and for the stability of the composite catalyst sample. For this purpose we followed the changes occurring with the increase in the temperature and prolonging the duration of the calcination treatment of sample S in regard to the specific surface area variation and the degree of dispersion of the phases (Table 1, Figure 2). The dispersity was evaluated by the above indicated method.

Table 1. Specific surface area and degree of dispersion as functions of the calcination time interval and calcination temperature

Samples-τ(h)-T (^0C)	Specific surface area S (m^2g^{-1})	Dispersion, D (nm)
S – 4 - 400	203	3÷4
S – 2 - 830	112	7÷8
S – 4 - 830	102	12
S – 6 - 830	96	18
S – 8 - 1000	23	50

Figure 2 illustrates the XRD patterns of the catalyst sample **S** calcined at $T_{calc.}$ varying from 400 to 1000^0C and various time intervals of maintaining the calcination temperature. A characteristic feature, observable for this system, is that as early as $T = 400^0C$ spinel phases of Cu and Zn are appearing: 01-070-8181 (Gahnite – $ZnAl_2O_4$); 00-033-0448 ($CuAl_2O_4$). A limited presence of CuO phase max lines is observed. The high specific surface area of the catalyst sample is due not only to the homogenizing conditions of preparation during the precipitation of the precursor, but also to the content of Al_2O_3. The latter is the structure-forming and dispersing component in the system. This high surface area is preserved, in spite of the drastic increase in the temperature of calcination (up to 1000ºC) and the long time interval of maintaining such high temperature. Although spinel-phase formation is occurring at low temperatures the nanosize dimensions of the particles in the contact mass are preserved and this

fact is in correlation with the data reported in [23, 24]. It is probably the precursor of the studied catalyst that determines the high degree of dispersion of the phases. On the other side the presence of the two spinel phases of copper and zinc is the inhibiting factor causing the preservation of the nanosize crystallinity [25].
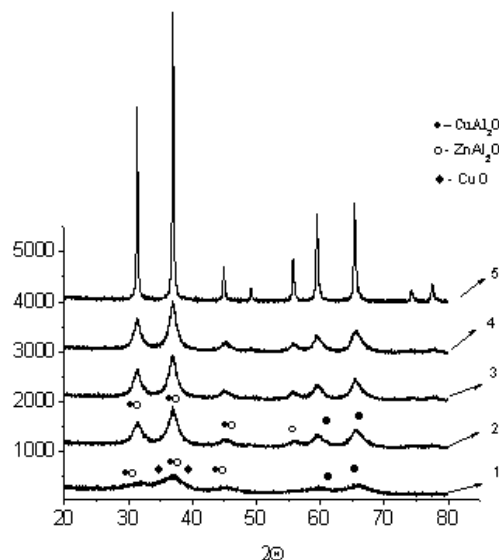
Fig.2. XRD patterns of the catalyst samples: 1 - S-4-400, 2 - S-2-830, 3 - S-4-830, 4 - S-6-830, 5 - S-8-1000

The adsorption isotherms of the samples S-4–400 and S-2–830 show the presence of mesopores. In the catalyst sample calcined at the lower temperature $T = 400^0C$, the system is monodisperse and the prevailing pore volume is within the interval $3 \div 9$ nm. Upon increasing the temperature the appearance of bidispersity becomes observable, whereupon the peak at $4 \div 6$ nm is comparatively narrow, while the second peak at $6 \div 14$ nm demonstrates an increase in the relative share of pores of larger dimensions. The type of the adsorption isotherms can be classified as type IV, while the hysteresis loops belong to the type H2 according to the classification of IUPAC. There is very good coincidence between the calculated specific surface area, based on the isotherms, and that determined by the express method (Table 2, Figure 3).

The phase structural and physicochemical characteristics of the contact mass **S**, calcined at various temperatures and different time intervals of thermal treatment gave us the reason to expect a high catalytic activity in the reaction of N_2O decomposition in the reaction mixture NO_x, N_2O, N_2 and O_2, immediately after the contact meshes.

Table 2. Total pore volume and specific surface area of the catalyst samples

Samples	Specific surface area $S(m^2g^{-1})$	Total pore volumeVt (cm^3g^{-1})	Average pore diameter τav (nm)
S-4-400	213	$2.038.10^{-1}$	3.82396
S-2-830	111	$2.323.10^{-1}$	8.38132

The tabletted catalyst sample calcined at T = 900^0C for 4 hours contains nanosize particles of diameter D ~ 25 nm and specific surface area S = 62 m^2/g. The catalyst granules have dimensions D × d × h = 11 × 5 × 5 ± 1 mm. The degree of conversion of N_2O to N_2 and O_2 was taken as the measure of the catalytic activity and it was measured under the following conditions:

	Laboratory reactor	Pilot plant Reactor
Catalyst bed volume, ml	4	100
Size of granules, mm	0.63÷0.8 Kinetic regime	11 × 5 × 5 Diffusion regime
Catalyst bed temperature,(^{0}C)	830	830
Pressure, bar	0.96	0.96
N_2O inlet conc., (ppm)	1100 ÷ 1400	
Space velocity, (W, h^{-1})	8 500 17 000	8 500 17 000
Degree of decomposition, α_p	0.98 0.95	0.92 0.90

The gas mixture sample for this study was taken after the contact meshes of the industrial installation for the production of HNO_3 based on the method of Ostwald.

The catalyst sample **S_1** was studied under analogous conditions - this is the supported type of sample, which was tabletted into dimensions d × h = 12 × 12 mm and respectively its activity, taken as degree of decomposition of N_2O, is as follows:

- kinetic regime
  W = 16 000 h^{-1}
  α_p = 0.83
- diffusion regime
  W = 8 000 h^{-1} W = 16 000 h^{-1}
  α_p = 0.62 α_p = 0.46

The drastic difference in the activities of the two contact masses shows the importance of the method of preparation of the synthesized precursor, as well as the effect of the genesis of different phases (phase formation) and the formation of different structures. The investigation proves that the low-temperature spinel formation process in the early stage of phase formation predetermines the high

dispersion degree of the phases, respectively the high specific surface area. Moreover, the isomorphous precursor phases of the synthesis by the method of co-precipitation of the composites are leading to Cu, Zn spinel phase formation, whereupon the alumina is the stabilizing component, which also causes dispersion and formation of specific structure.
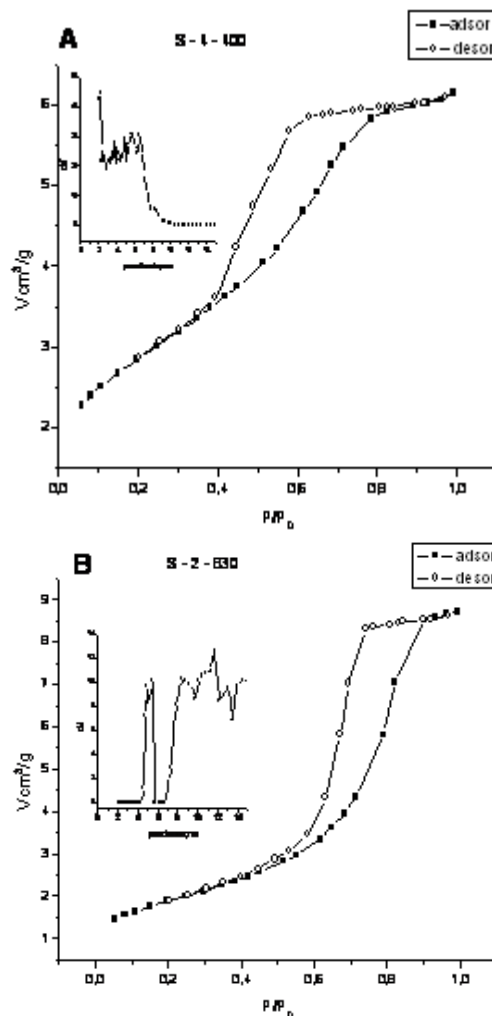
Fig.3. Adsorption isotherms and pore size distribution of catalyst samples: **A** – S-4-400 and **B**- S-2-830.

CONCLUSION

This gives us the reason to draw the following conclusions:

The catalyst composition having the ratio Cu : Zn : Al = 1 : 1 : 4, prepared by the method of co-precipitation from copper-zinc-ammonia carbonate solution and aluminum nitrate is a highly active catalyst for the decomposition of N_2O to N_2 and O_2, under industrial operation conditions from the production of HNO_3 by the method of Ostwald, as early as in the first stage – the catalytic oxidation of NH_3, i.e. "secondary in sequence".

REFERENCES

1. M. Schwefer, R. Siefert, M. Groves, Krupp Uhde GmbH, *Nitrogen* 60 (2000).
2. M. Groves, R. Maurer, M. Schwefer, R.Siefert, Uhde GmbH, *Nitrogen* 121, (2006).
3. G. Lenoir, J. France, T. Kopperud, N. Oystein, International ASA Norway, *Nitrogen,* 113 (2006).
4. BASF AG "Verfahzen zur katalytischen Zersetzung von N₂O DE", **198,** 19 882.5 (1999).
5. K. Terterian, L. Peshkov, A. Novojilov, Materials XIII NTC „University Science – Severokavkazkomu region", vol. 1 Natural Sciences, Stavropol, North Kavkaz GTU, 2009, 116
6. J. Dedecek, L. Capek, P.SAzana, Z.Sobalik, B. Wichterlova, *Appl. Catal. A: General,* **391**, 244 (2011).
7. Q. Shen, L. Li, J. Li, H. Tian, Z. Hao, *J. of Hazardus Materials*, **163**, 1332 (2009).
8. S. N. Orlyk, T.M. Pidruchina, *Theoret. and experiment. Chemistry*, **41** (1), 35 (2005), (Russ).
9. E. Wilczkowska K. Krawczyk, J. Petryk, J. W. Sobczak, Z. Kaszkur, *Appl. Catalysis A: General,* **389** (1–2), 1 (2010).
10. A. Kubassov, *Sarosovskogo Educational Journal*, **7, 70** (1998).
11. E. Starakon, K. Dubkov, H. Ovasian, A. Sheinman, G. Panov,VI Russian Conference „Mechanisms of catalytic reaction", Moskow, 168, 2002.
12. BG Patent № 5025641, 2007.
13. G. Giesko, T. Borowiecki,W. Gas, J. Kruk, *Catalysis Today* , 137, (2-4) 403 (2008).
14. J. P. Dacquin, C. Lancelot, C. Dujardin, P. Da Costa, G. Djega-Mariadassou, P. Beaunier, S. Kaliaguine, S. Vaudreuil, S. Royer, P. Granger*, Appl. Catalysis B: Environ.*, **91**, 596 (2009).
15. L. Xue, C. Zhang, H. He, Y. Teraoka, *Applied Catalysis B: Environmental,* **75,** 167 (2007).
16. L. Yan, T. Ren, X. Wang, D. Ji, J. Suo, *Applied Catalysis B: Environmental,* **45,** 85 (2003).
17. L. Yan, T. Ren, X. Wang, Q. Gao, D. Ji, J. Suo, *Catal. Comm.*, **4** (10), 505 (2003).
18. Z. Liu, M. Amiridis, Yi Chen, *J. Phys. Chem. B*, **109,** (3), 1251 (2005).
19. G. Mul, Perez-Ramirez, F. Kapteijn, J. Moulijn, Catal. Lett., **77,** 7 (2001).
20. J. Perez-Ramirez, J. M. Garcia-Cortes, F. Kapteijn, M. J. Шan-Gomez, A. Ribera, C. Salinas-Martinez de Lecea, J. A. Moulijn, *Appl. Catal. B*, **25** (2-3), 191 (2000).
21. BGPatent Application № 111654/16.12.2013.
22. D.St. Shishkov, D. A. Stavrakeva, N. A. Kasabova, *Kinetika I kataliz*, **XXI** (6), 1559 (1980) (Russ).
23. J. Wang, C. Zeng, *Journal of Natural Gas Chemistry,* **14,** 156 (2005).
24. R. Amrousse, A. Tsutsumi, A. Bachar, D. Lahcene, *Appl. Catal. A: General,* **450,** 253 (2013).
25. M. S. Niasari, F. Davar, M. Farhadi, *J. Sol. Gel. Sci Technol.*, **51,** 48 (2009).

КАТАЛИТИЧНО ДЕКОМПОЗИРАНЕ НА N₂O ОТ ОТПАДНИ ГАЗОВЕ ПРИ ПРОИЗВОДСТВОТО НА HNO₃

Д. Д. Стоянова[1], Н. А. Касабова[2], Д. С. Шишков[2], Цв. Н. Велинова[2], Д. Димитров[3], В. Грънчаров[4]

[1] Институт по обща и неорганична химия, Българска академия на науките, ул."акад. Г. Бончев" бл. 11, 1113 София, България
[2] Химикотехнологичен и Металургичен Университет, бул."Кл. Охридски" №8, 1756, София, България
[3] Висш институт по селско стопанство-Департамент по химия, бул. „Менделеев №12", 4000 Пловдив, България
[4]НЕОХИМ-АД, 6403, Димитровград, България

(Резюме)

Обект на изследванията е катализатор с шпинелоподобна структура на мед, цинк, алуминиеви оксиди в съотношение Cu:Zn:Al = 1:1:4. Условията на съутаяване от мед, цинк амонячно-карбонатни разтвори и разтвор от алуминиев нитрат осигуряват наноразмерност на прекурсорите и висока дисперсност след накаляване на контактните маси при температура 900⁰C. Това предопределя високата активност на катализатора при изследване в кинетичен и дифузионен режим при обемни скорости, W = 8500, 17000h⁻¹, T = 830⁰C и N₂O на вход = 1100 ÷ 1400ppm т.е. условия аналогични на промишлените. Степента на разлагане (α) е по-голяма от 0.9. Каталитичната композиция с посочения състав е високоактивен катализатор за декомпозиране на N₂O до N₂ и O₂ при производството на HNO₃ по метод Освалд още в първия стадий – каталитично окисление на NH₃, т.е. "secondary".

Effect of DC magnetic field on some physical and catalytic properties of Fe- and Fe/Pt- nanoparticles synthesized by BH method

E. D. Lefterova[1], A. E. Stoyanova[1*], H. Kolev[2], G. Tyuliev[2], D. Paneva[2],
G. R. Borisov[1], I. Dragieva[1]

[1]*Acad. Evgeni Budevski Institute of Electrochemistry and Energy Systems, Bulgarian Academy of Sciences, 1113, Sofia Bulgaria*
[2]*Institute of Catalysis, Bulgarian Academy of Sciences, 1113, Sofia Bulgaria*

The influence of dc magnetic field on some physical and catalytic properties of iron and platinum/iron nanoparticles is investigated. The nanoparticles are produced by a borohydride (BH) reduction process, as the dc magnetic field is applied during their synthesis. Structural differences between Fe powders are not observed. XRD and Mössbauer data show the presence of metallic iron and iron oxides (γ-Fe_2O_3/Fe_3O_4). In the Pt-Fe powders fcc-Pt and iron oxide-hydroxides are identified. XPS investigations confirm the availability of the iron oxides and metallic Pt. Pt^{2+} is identified too. A comparison of the XRD and the XPS data suggests the formation of core (metal)/shell (oxide) structure of the nanoparticles. The samples untreated with magnetic field show better electrocatalytic activities in PEM water electrolysis compared to the treated nanoparticles. For Pt-Fe samples, in which the iron content is about 50%, the influence of the magnetic field is weak. The observed effect can be explained with the influence of the magnetic field on the capability of their self-organization.

Key words: nanoparticles, borohydride (BH) reduction, PEM water electrolysis, XRD, XPS

INTRODUCTION

Iron oxide nano-particles are of considerable interest due to their wide range of applications. Nanotechnology has great potential and its development has allowed the synthesis of iron based nanoparticles with desired properties and expanded the range of their usage in different fields as magnetic recording, magnetic data storage devices, toners and inks for xerography, catalysts, sorbents, pigments, coatings, gas sensors, wastewater treatment[1], biomedical application, magnetic resonance imaging in medicine [2,3], etc. Ferrimagnetic particles are promising materials as sorbents in medical practice. Fe and $CoFe_2O_4$ nanoparticles can efficiently adsorb antigens, and viruses [4]; nanodispersive magnetite (Fe_3O_4) could be used for detoxification of cellular physiological fluids such as lymph or blood plasma [4-7]. Investigations on the use of magnetic nanoparticles for targeted drug delivery and for localized heating by absorption of electromagnetic radiation for efficiently eradication of cancerous cells are in progress [8-11].

Iron based materials are also cheap and efficient catalysts for many applications, as for the oxidation of CO, the oxidative pyrolysis of biomass, oxidation/reduction and acid/base reactions [12-15]. Iron oxide mixed with other metals has been shown to be a very active catalyst for the oxygen evolution reaction in water splitting, as well as other related processes. It is known that the best electrocatalyst toward oxygen evolution reaction among the pure metals is platinum. Alloying of Pt with various transition metals is often used in order to improve the catalytic activity toward the anodic reaction. It has been proven that carbon and Ti-oxide supported binary alloys of Pt with Fe and Co offer good performance mainly in direct methanol and polymer electrolyte fuel cells. The results obtained showed changes in particle size, distribution and electronic structure of the catalyst that are expected to be beneficial for catalytic activity of these materials toward the OER in water electrolysis as well [16-22].

It should be borne in mind that nano-particles of iron oxide are significantly more effective in many cases than conventional micron-sized iron oxide. These effects may arise from the high activity of the nano-particles having high surface areas and a better coordination of unsaturated sites on the

* To whom all correspondence should be sent:
E-mail: antonia.stoyanova@gmail.com

surfaces. Chemical and electronic properties, such as phase changes, OH content, band gap changes etc., could also have contributed to their high reactivity [23].

Furthermore, each application requires different material properties - thermal, chemical, and colloidal stability, magnetic characteristics, particle shape and size, and non-toxicity. These requirements determine the methods of preparation [1, 24]. With time the synthesis procedures for preparation of iron oxides in the nano range have gone through innovation, such as applying dc magnetic and electric fields that may set in a long-range ordering in the assembly and orientation during synthesis itself. The effect of magnetic field on the biomimetic synthesis, for example, leads to reduction in particle size and a directional assembly of synthesized super paramagnetic particles into a regular pattern in the protein film [25].

The aim of this work is to investigate the effect of the dc magnetic field applied during synthesis of iron and platinum/iron containing nanoparticles towards some physical and catalytic properties.

MATERIAL AND METHODS

Four samples containing Fe and Pt-Fe are prepared using the borohydride wet chemical reduction (BH) process with (marked with +) and without (-) dc magnetic field. The synthesis of the Fe nanoparticles is carried out with an aqueous solution of the salt $FeCl_2.4H_2O$, placed in the reactor with or without a dc magnetic field and reduced by addition of sodium borohydride solution under continuous stirring at 40°C for several min. The synthesis of the Pt-Fe nanoparticles required first synthesizing of platinum ethylenediamine complexes serving as metal precursors according to a previously developed preparation procedure [26, 27]. In a second stage, the prepared and mixed aqueous solutions of the precursors (Pt-complex and Fe-salt) are reduced by addition of sodium borohydride solution. After repeated washing of the obtained precipitate it was dried in a vacuum desiccator at room temperature.

Structural characterization was performed using XRD, XPS and Mössbauer spectroscopy. X-ray diffraction (XRD) patterns were recorded by X-ray diffractometer Philips APD15. The diffraction data were collected at a constant rate of 0.02 $^{\circ}.s^{-1}$ over an angle range of 2θ = 10 – 90 degrees with CuKα radiation (λ=1.54178 Å). The size of Pt crystallites was determined by the Scherrer equation [28]. The identification of crystalline phases was made by comparison with data on the JCPDS-ICDD files.

The Mössbauer spectra were obtained with an electromechanical spectrometer (Wissenschaftliche Elektronik GMBN, Germany) working in a constant acceleration mode. A 57Co/Rh (activity @50 mCi) source and α-Fe standard were used. The experimentally obtained spectra were subjected to mathematical processing according to the least squares method. The parameters of hyperfine interaction such as isomer shift (IS), quadrupole splitting (QS) and magnetic hyperfine field (Hhf), as well as the line widths (FWHM) and the relative spectral area (G) of the partial components of the spectra were determined. X-ray photoelectron spectroscopy measurements were performed on the ESCALAB MkII (VG Scientific) electron spectrometer at a base pressure in the analysis chamber of 5×10^{-10} mbar using twin anode MgKα/AlKα X-ray source with excitation energies of 1253.6 and 1486.6 eV, respectively. The peak fitting of the core-level XPS lines was carried out using Casa XPS Processing Software (Casa Software Ltd.) with a Gaussian–Lorentzian product function and a non-linear Shirley background [29]. The energy scale was calibrated by normalizing the C1s line of adsorbed adventitious hydrocarbons to 285.0 eV.

The electrochemical tests were performed on membrane electrode assemblies (MEAs) with a commercial polymer membrane Nafion 117 (Alfa Aesar), as an electrolyte. MEA was prepared by hot pressing of the electrodes for hydrogen (HER) and oxygen evolution (OER) on both sides of the membrane using a 5% Nafion solution as a binder. The electrodes with geometric area of 0.5 cm^2 had a double layered structure, consisting of a hydrophobic backing layer (GDL) and an active catalytic one (metal loading of 5 mg.cm^{-2}). The preparation procedure is described elsewhere [22].

The performance characteristics of the prepared MEA were investigated in a self made laboratory PEM electrolytic cell, consisting of two gas compartments where hydrogen and oxygen evolution take place, separated by the membrane electrode assembly under study. A reference electrode (commercial E-TEK catalyst containing 20% Pt on carbon support) was situated in the hydrogen evolution compartment. The catalytic activity of the prepared catalysts was studied using the techniques of cyclovoltammetry and steady state polarization at temperatures of 20ºC and 80ºC. All electrochemical measurements were carried out with a commercial galvanostat/potentiosat POS 2 Bank Electronik, Germany.

RESULTS AND DISCUSSION

For clarifying of the observed effects physical analyses were performed to trace the changes in the structure of the obtained nanoparticles with and without a magnetic field.

X-ray diffraction

The X-ray diffractograms of the synthesized Fe and Pt-Fe powders are presented in Figs. 1 and 2, respectively. XRD patterns of Fe powders (samples Fe(+) and Fe(-)) (Fig. 1) are almost identical. The phase analysis shows a presence of metallic iron (α-Fe) with crystallite size of 6 nm and iron oxides $Fe_3O_4/\gamma-Fe_2O_3$ with crystallite size of $8\div10$ nm, respectively. X-ray diffractograms for Pt-Fe powders (samples Pt-Fe(+) and Pt-Fe(-)) are more complicated (Fig. 2a). No metallic iron (α-Fe) is registered, but fcc-Pt is additionally identified. Pt cell parameter was determined using a nonlinear regression analysis with the "UnitCell" software [30].The calculated cell parameters for Pt (3.920 and 3.919 Å) correspond to pure Pt (a=3.920 Å [31]). It means that there is no common Pt-Fe crystal cell. Hence, there is no alloying between

platinum and iron. The goethite (α-FeOOH) diffraction peaks are clearly distinguishable on the X-ray pattern of the sample synthesized with dc magnetic field. The broadened and strong peak at 2Θ ~53-54 degrees is connected with other iron hydroxide-feroxyhite (δ'-FeOOH)[32-34].
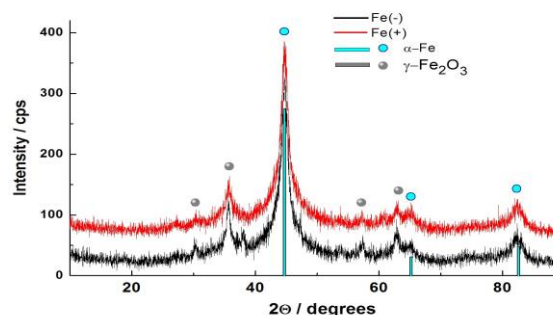
Fig. 1. XRD patterns of Fe nanopowders synthesized with Fe(+) and without Fe(-) magnetic field

The XRD 2Θ position of feroxyhite is presented with bargrams on Fig. 2. Some of these positions are close to or coincide with the positions of $Fe_3O_4/\gamma-Fe_2O_3$ and Pt. Hence, these peaks are superposition of sharper Pt (cryst. size 20 nm) or

Table1. Calculated Mössbauer parameters

Sample	Components	IS, mm/s	QS, mm/s	H_{eff}, T	FWHM, mm/s	G, %
Fe(+)	Sx1 – Fe^0	0.03	-0.01	33.3	0.53	21
	Sx2 – Fe^0	0.06	-0.03	29.7	0.69	18
	Sx3 – Fe^0	0.06	0.00	26.1	0.77	26
	Sx4 – Fe^0	0.02	0.00	21.8	0.92	3
	Db – Fe^{3+}	0.33	0.78	-	0.52	32
Fe(-)	Sx1 – Fe^0	0.02	-0.01	33.3	0.53	21
	Sx2 – Fe^0	0.07	-0.03	29.5	0.69	21
	Sx3 – Fe^0	0.07	0.02	26.1	0.77	24
	Sx4 – Fe^0	0.04	0.00	21.8	0.92	4
	Db – Fe^{3+}	0.33	0.80	-	0.52	30
FePt(-), RT	Sx - $\gamma-Fe_2O_3$-HD	0.34	0.02	33.0	2.00	71
	Db – Fe^{3+}	0.36	0.70	-	0.53	29
FePt(+), RT	Sx1 – $\gamma-Fe_2O_3$	0.33	0.01	49.3	0.82	9
	Sx2 – α-FeOOH	0.34	-0.11	34.2	0.76	11
	Sx3 - α-FeOOH-HD	0.34	-0.11	27.7	1.86	44
	Db – Fe^{3+}	0.37	0.67	-	0.52	36
Pt-Fe(-), LNT	Sx1 - $\gamma-Fe_2O_3$	0.47	0.01	50.1	0.56	33
	Sx2 – $\gamma-Fe_2O_3$-HD	0.46	0.02	46.4	1.30	59
	Db – Fe^{3+}	0.45	1.02	-	0.90	8
Pt-Fe(+), LNT	Sx1 - $\gamma-Fe_2O_3$	0.47	0.05	49.1	0.60	30
	Sx2 - $\gamma-Fe_2O_3$-HD	0.48	0.07	47.2	0.48	15
	Sx3 - α-FeOOH	0.45	-0.10	44.5	0.74	25
	Sx4 - α-FeOOH-HD	0.45	-0.11	39.1	1.63	30
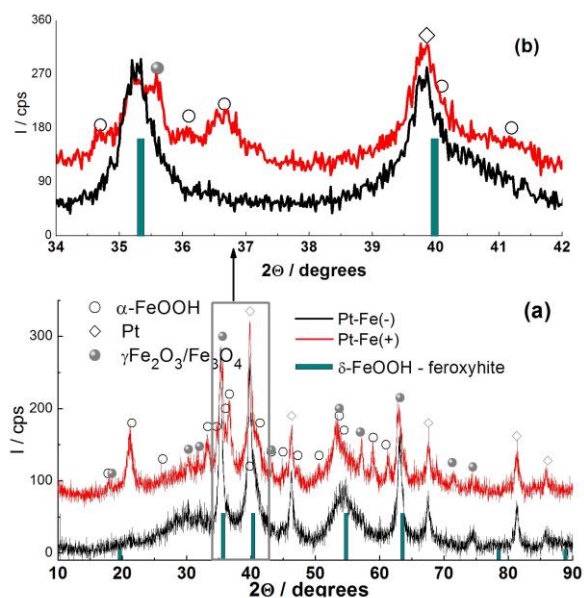
Fig. 2. XRD patterns of Pt-Fe nanopowders synthesized with (+) and without (-) magnetic field in the range (a) $2\Theta = 10 \div 90°$; (b) $\Theta = 34 \div 42°$.

Fe_3O_4/γ-Fe_2O and broadened feroxyhite. This leads to additional broadening in the lower part, splitting and/or asymmetry of these peaks (Fig. 2b). The diffuse maximum between 22-32° 2Θ could be explained with ultra dispersed iron oxides.

Mössbauer spectroscopy

All Mössbauer spectra measured at room temperature consist of a pronounced doublet in the center and complex broadening and overlapping sextet components (Fig. 3).
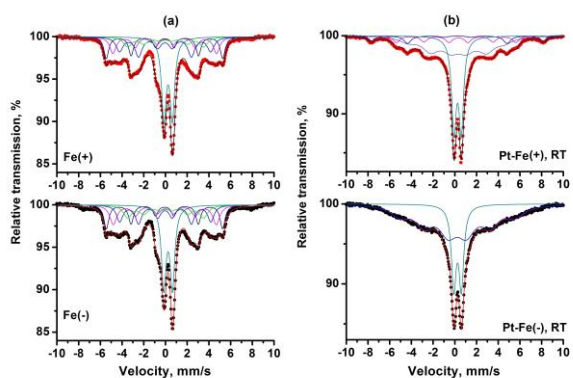
Fig. 3. Mössbauer spectra of Fe and Pt-Fe nanopowders synthesized with (+) and without (-) magnetic field, measured at room temperature (RT).

Both Fe samples (Fe(+) and Fe(-)) have similar Mössbauer spectra (Fig. 3a). The best mathematical processing is achieved using the model including 4 sextets and one doublet. Calculated Mössbauer

parameters are included in Table 1. All sextet components are due to Fe^0– isomer shift and quadrupole splittings are close to zero values. The different values of the effective magnetic field can be attributed to the components in which iron ions are neighbors of different chemical nature. The doublet is due to Fe^{3+} ions in octahedral coordination in the maghemite crystal structure.

The sextet components of Pt-Fe Mössbauer spectra (Fig. 3b.) obtained at room temperature are with stronger broadening and non-Lorenzian lines. For the sample Pt-Fe(-) the mathematical processing shows that Fe^{3+} ions in the octahedral coordination are incorporated into maghemite particles with different dispersity - a sextet for larger and a doublet for the smaller particles, respectively. The doublet with the same parameters could be connected with the presence of feroxyhite too [36]. Additional two sextets caused by octahedral coordinated Fe^{3+} ions with parameters of iron hydroxide - goethite with different dispersity are observed in the sample Pt-Fe(+), Sx2 for larger and Sx3 - HD to smaller particles. For a more detailed survey the Mössbauer spectra were measured at liquid nitrogen temperatures (LNT) (Fig. 4).
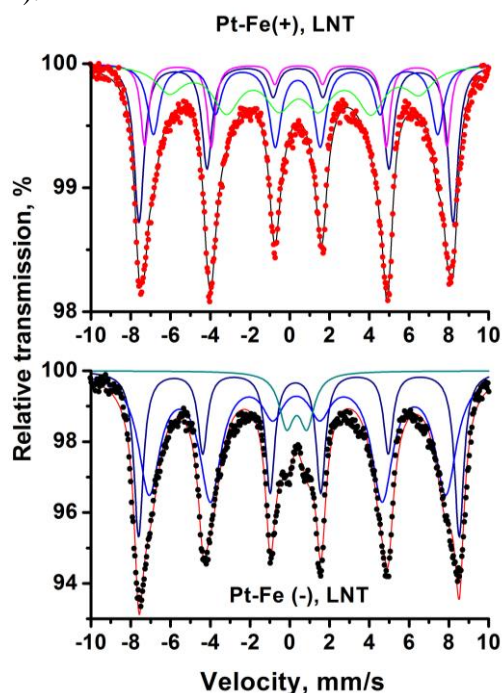
Fig. 4. Mössbauer spectra of Pt-Fe(+) and Pt-Fe(-) nanopowders, measured at liquid nitrogen temperature (LNT).

The lowering of temperature blocks the magnetic vector fluctuations induced by thermal motion and allows registration of superfine interactions in superparamagnetic materials. Both spectra at LNT contain mainly sextet components

with maghemite and goethite parameters. The introduction of the components of smaller and larger particles of the hydroxides and maghemite is connected with the particle size distribution in a very wide range.

X-ray photoelectron spectroscopy

Figure 5 presents high resolution of Fe2p core-shell spectra for all samples. There is no significant difference between the corresponding photoelectron spectra of the samples obtained with and without magnetic field. The Fe2p photoelectron spectra have a complex nature due to spin-orbital coupling, satellite structure and multiplet splitting of the oxidation states, as well as the low difference between Fe^{2+} and Fe^{3+} binding energies. But energy separation of the shake-up satellites is sensitive to the iron chemical state. Therefore, the satellite structure can be used to identify the oxide phases [36-37].

Fig. 6. High-resolution X-ray photoelectron spectra of Pt4f core-level.

Fig. 5. High-resolution X-ray photoelectron spectra of Fe2p core-level.

In iron oxides the satellite located at ~8 eV (around 719 eV) above the main line is connected with Fe^{3+} while that at 714-715 eV is ascribed to the existence of Fe^{2+}. The registered Fe2p peaks at ~711, ~719, and ~725 eV represent the binding energies of Fe $2p_{3/2}$, shake-up satellite Fe $2p_{3/2}$ of Fe^{3+}, and Fe $2p_{1/2}$, respectively. The XPS study does not show the presence of Fe^0 on the surface of the samples. For samples Pt-Fe the Pt4f core-shell spectra (Fig. 6) confirm the availability of Pt in Pt^0 (~70.5 eV). The component at ~72.5 eV reveals additional Pt^{2+} states, most probably as $Pt(OH)_2$. The ratio Pt^0: Pt^{2+} is ~1:1 for both samples.

The O1s peak (Fig. 7) is fitted with three components: (1) the component situated at 529-530 eV is due to the oxygen in the Me-O bonds in FeO_x; (2) the component around 531-532 eV corresponds to Me–OH bonds; (3) the highest energy component (532.5-534 eV) can be assigned

Fig. 7. High-resolution X-ray photoelectron spectra of O1s core-level.

to adsorbed H_2O and/or B-O bonds. Iron oxide-hydroxide (α-FeOOH) availability in sample Fe-Pt(+) reflects on the O1s peak. As a result, the component (2) dominates.

Electrochemical tests

The effect of the dc magnetic field applied during the synthesis is investigated towards the electrocatalytic properties of the Fe- and Pt-Fe-containing nanoparticles in PEM water electrolyses using cyclic voltammetry and steady state polarization techniques.

Cyclic voltammograms (CV) performed in the whole potential range between hydrogen and oxygen evolution give qualitative information about the nature of the processes occurring on the catalyst surface (Fig. 8).
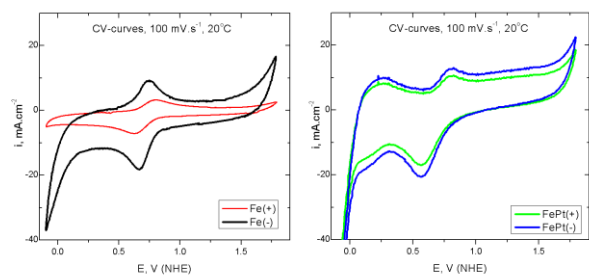
Fig. 8. Cyclovoltammetric curves of the samples under study at a scan rate of 100 mV.s^{-1} and temperature 20°C.

On the CV of the samples distinct, nearly reversible anodic and cathodic peaks situated in the potential range 0.7 – 0.75 V are observed. These peaks are due to the redox transition Fe^{3+}/Fe^{2+} and indicate an existence of Fe_3O_4/Fe_2O_3 phase [22]. In the unfolding of the potential in the opposite direction the cathode peak seems similar in shape and size at approximately the same values of the potential. The presence of these peaks means that in the cycling of the selected potential field, the catalytic material reversibly changes its valence state. For the Pt-based catalyst, peaks corresponding to hydrogen adsorption/desorption processes are situated in the potential range between 0.12 and 0.35 V (Fig. 8b) [19]. The shapes of the CV-curves of the catalysts treated and untreated with magnetic field are similar. The area (surface) of the curves of the untreated sample is greater in both cases, as in non-platinum-containing samples, it is essential. In iron-containing samples the difference in the active surface area is about 65%, while in the platinum-iron samples it is stationed around 18%. This result may be explained by the twice lower content of iron in the Pt-Fe composition and hence the much lower effect of the magnetic field. As may reasonably be expected, the active surface in a platinum-containing nanoparticle is higher in both cases.

The main results from the steady state electrochemical characterisation of the prepared catalysts, incorporated in MEAs are summarised in Fig. 9.
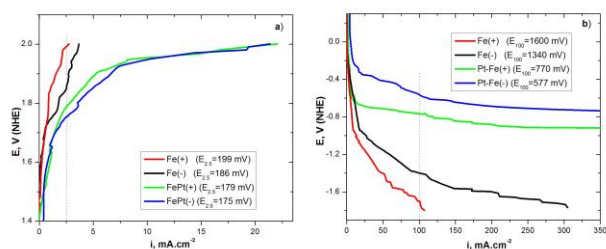
Fig. 9. Anodic (a) and cathodic (b) polarization curves of the samples under study at scan rate 1 mV.s^{-1} and temperature 80°C.

The polarization curves of the partial electrode reactions (OER and HER) involved in the electrolytic water splitting are recorded at a typical PEMWE operation temperature of 80°C. A significantly higher activity of the untreated catalyst to the magnetic field can be seen, as in the reaction of oxygen evolution, and in relation to that of the hydrogen evolution. The order of the catalytic activity for hydrogen and oxygen evolution of the studied composition is the following: Pt-Fe(-) > Pt-Fe(+) > Fe(-) > Fe(+). The influence of the magnetic field on the HER is more pronounced.

The observed effects can be explained with the influence of the magnetic field on the self-organization of the magnetic nanoparticles. Dragieva et al. [38-42] have observed self organization into chains of magnetic nanoparticles produced by the borohydride reduction method. The application of dc magnetic field during the synthesis reduces the space (pores) between the particles and densifies the chain structure. This leads to a decrease in the specific surface and hence, to a decrease in catalytic activity.

CONCLUSIONS

Structural studies showed no differences between Fe powders synthesized with and without dc magnetic field. A comparison of XRD, Mössbauer and XPS data suggests the formation of core (metal Fe)/shell (Fe-oxides) structure of the nanoparticles. In Pt-Fe powders Pt is in metal and oxide states. Iron is present mainly as Fe^{3+} ions in octahedral positions in the oxide and oxyhydroxide structures. The particles size distribution is within a very wide range.

It was found that the dc magnetic field applied during the synthesis of Fe- and Pt-Fe nanoparticles affects their electrocatalytic properties in PEM water electrolysis, as untreated samples showed a greater activity. In Pt-Fe compounds, in which the iron content is about 50% less, the influence of the magnetic field is weak. The observed effects can be explained with the influence of the magnetic field on the capability of their self-organization including the effects of the OH-groups.

REFERENCES

1. M. Mohapatra, S. Anand, *IJEST,* **2**, 127 (2010).

2. S. Mornet, S. Vasseur, F. Grasset, P. Veverka, G. Goglio, A. Demourgues, J. Portier, E.Pollert, E. Duguet, *Prog. Solid State Chem*., **34**, 237 (2006).

3. Lin M.M, Kim, H., and Mohammad M., *Nano Reviews*, **1**, 1 (2010).

4. Ю. Г. Яновский, *Технологии живых систем*., **4**, 73 (2007).

5. K. Cai, *Chem. Commun*. (Cambridge, U. K.), **27**, 7719 (2011).

6. M. Bhaumik, *J. Hazard. Mater.,* **186**, 150 (2011).

7. N. Y. Anisimova, F. S. Senatov, S. I. Milyaeva, M. V. Kiselevsky, *Medical Sciences*, **11**, 263 (2011).

8. D. Ho, X. Sun, S. Sun, *Acc. Chem. Res*., **44**, 875 (2011).

9. Q. A. Pankhurst, N. T. K. Thanh, S. K. Jones and J. Dobson, *J. Phys. D: Appl. Phys*., **42**, 224001. (2009)

10. I. Hilger, K. Fruhauf, W. Andra, R. Hiergeist, R. Hergt, W. A. Kaiser, *Academic Radiology*, **9**, 198 (2002).

11.C. H. Li, P. Hodgins, G. P. Peterson, *J. Appl. Phys*., **110**, 054303 (2011).

12. T. Miyata, Y. Ishino, T. Hirashima, *Synthesis* I, 834 (1978).

13. J. S.Walker, G. I.Stragauzzi, W. H. Manogue, G. C. A. Schuit, *J. Catal*., **110**, 298 (1988).

14. P. Li, D. Miser, S. Rabiei, R. Yadav, M. R.Hajaligol, *Appl. Catal. B: Environ*., **43**, 151 (2003).

15. P. Li, E. J. Shin, D. Miser, M. R. Hajaligol, F. Rasouli, B. In: Nanotechnology in Catalysis Zhou, S. Hermans and G.A. Somorjai (eds.), Kluwer Academic/Plenum, New York, 2004, p.515.

16. C. Medard, M. Lef˘evre, J.P. Dodelet, F. Jaouen, J. Lindbergh, *Electrochim. Acta,* **5**, 3202 (2006).

17. F. Charreteur, R. Stephane, J. Frederic, J. P. Dodelet, *Electrochim Acta*, **53**, 6881 (2008).

18. W. Li, X. Qin, Y. Yushan, *Int. J. Hydrogen Energy,* **35**, 2530 (2010).

19. S. Mukerjee, C. Srinivasan, M. Soriaga, *J. Electrochem Soc*., **142**, 1409 (1995).

20. W. Li, W. Zhou, H. Li, Zh. Zhou, B. Zhou, G. Sun, Q. Xin, *Electrochim. Acta,* **49**, 1045 (2004).

21. L. Xiong, A. Manthiram, *Electrochim. Acta,* **50**, 2323 (2005).

22. A. Stoyanova, G.Borisov,E. Lefterova, E.Slavcheva, *Int. J. Hydrogen Energy,* **37**, 16515 (2012).

23. P. Li, D. Miser, S. Rabiei, R. Yadav, M. R. Hajaligol, *Appl. Catal. B: Environ.* **43**, 151 (2003).

24. A. I. Martinez, M. A. Garcia-Lobato, D. L. Perry, In: Research in Nanotechnology Developments, Armando Barrañón (ed.), © Nova Science Publishers, Inc., 2009, p.183.

25. A. Sinha, S. Nayar, B.K. Nath, D. Dasb, P.K. Mukhopadhyayc, *Colloids and Surfaces B: Biointerfaces*, **43**, 7 (2005).

26. I. Dragieva, S. Stoeva, P. Stoimenov, E. Pavlikianov, K. Klabune, *Nanostruct. Mater*., **12**, 267 (1999).

27. I. Dragieva, S. Stoeva, P. Stoimenov, Z. Stoynov, Bg Patent No 103629 (03.08.1999).

28. J. Lanfgord, A. A. Wilson, *J. Appl. Crystallogr*., **11**, 102 (1978).

29 D. Shirley, *Phys. Rev. B***, 5**, 4709 (1972).

30. T. Holland, S. Redfern, *Mineral Mag*., **61**, 65 (1997).

31. JCPDS International Center for Diffraction Data, *Power Diffraction* File #87-0646.

32. V. A. Drits, B. A. Sakharov, A. Manceau, *Clay Minerals*, **28**, 209 (1993).

33. L. Carlson, U. Schwertmann, *Clays and Clay Minerals,* **28**, 272 (1980).

34. JCPDS International Center for Diffraction Data, *Power Diffraction File* # 13-0087

35. Mössbauer Spectroscopy: Tutorial Book, Yutaka Yoshida, Guido Langouche (eds.), Springer-Verlag Berlin Heidelberg, 2013.

36. M. Aronniemi, J. Sainio, J. Lahtinen, *Surf. Sci*., **578**, 108 (2005).

37. M.C.Biesinger, B.Payne, A.Grosvenor, L.Lau, A. Gerson, R. Smart, *Appl. Surf. Sci.,* **257**, 2717 (2011).

38. I. Dragieva, D. Buchkov, D. Mehandjiev, M. Slavcheva, *J. Magn. Magn. Mater.*, **72**, 109,(1988).

39. I. Dragieva, M. Slavcheva, D. Buchkov, D. Mehandjiev, *J. Magn. Magn. Mater.*, **89**, 75(1990).

40. I. Dragieva, D. Mehandjiev, D. Buchkov, M. Slavcheva, *J. Magn. Magn. Mater.*, **83**, 460(1990).

41. D. Mehandjiev, I. Dragieva, *Journal of Magnetism and Magnetic Materials*, **101**, 167 (1991)

42. I. Dragieva, C. Deleva, M. Mladenov, *Monatshefte fur Chemie*, **133**, 807 (2002).

ВЛИЯНИЕ НА МАГНИТНОТО ПОЛЕ ВЪРХУ НЯКОИ ФИЗИЧНИ И КАТАЛИТИЧНИ СВОЙСТВА НА Fe- И Fe/Pt НАНОЧАСТИЦИ СИНТЕЗИРАНИ ПО БХ МЕТОД

Е. Д. Лефтерова[1], А. Е. Стоянова[1]*, Х. Колев[2], Г. Тюлиев[2], Д. Панева[2], Г. Р. Борисов[1], Й. Драгиева[1]

[1]Институт по електрохимия и енергийни системи «Евгени Будевски», Българска академия на науките, 1113, София, България
[2]Институт по катализ, Българска академия на науките, 1113, София, България

(Резюме)

Изследвано е влиянието на постоянно магнитно поле върху някои физични и каталитични свойства на наночастици, съдържащи желязо и платина/желязо. Наночастиците са синтезирани чрез борохидридна редукция, като магнитното поле е прилагано по време на синтеза. Не се регистрира разлика в структурата между Fe-праховете, синтезирани с и без магнитно поле. Рентгеновата дифракция и Мьосбауеровата спектроскопия показват наличие на железни оксиди (γ-Fe_2O_3/Fe_3O_4). В Pt-Fe праховете са идентифицирани fcc-Pt и железни оксиди-хидроксиди. Рентгеновата фотоелектронна спектроскопия (РФС) потвърждава наличието на железни оксиди и метална Pt, както и на OH-групи. Допълнително е идентифицирана и Pt^{2+}. Анализирането на данните от структурните изследвания подсказва формирането на core/shell структура (метална сърцевина и оксидна обвивка) на наночастиците. Образците без приложено магнитно поле проявяват по-добра електрокаталитична активност при ПЕМ електролиза на вода, като неговото въздействие върху Pt-Fe проби, в които съдържанието на желязо е около 50%, е значително по-слабо изразено. Наблюдаваният ефект може да се обясни с влиянието на магнитното поле върху способността за самоорганизация на наночастиците.

Synthesis, characterization and DFT studies of hydrazones of cycloalkanespirodithiohydantoins

M. N. Marinov [1*], P. E. Marinova [2], N. V. Markova [3], N. M. Stoyanov [4]

[1]Agricultural University – Plovdiv, Faculty of Plant Protection and Agroecology, Department of General Chemistry, 4000 Plovdiv, 12 "Mendeleev" Blvd, Bulgaria

[2]University of Plovdiv, Faculty of Chemistry, Department of General and Inorganic Chemistry with Methodology of Chemistry Education, 4000 Plovdiv, 24 "Tzar Asen" St, Bulgaria

[3]Institute of Organic Chemistry, Bulgarian Academy of Sciences, 1113 Sofia, Bulgaria

[4]University of Ruse – Razgrad Branch, Department of Chemistry and Chemical Technologies, 7200 Razgrad, 47 "Aprilsko Vastanie" Blvd, Bulgaria

This article presents a method for synthesis of hydrazones of cycloalkanespirodithiohydantoins. The initial spirodithiohydantoins were prepared by an interaction of cycloalkanespiro-5-hydantoins with P_4S_{10} and hexamethyldisiloxane. This method yielded products with a higher yield, compared to the known methods in the literature. The spirodithiohydantoins obtained were subjected to an interaction with hydrazine hydrate. As a result 4-hydrazones of the corresponding spirodithiohydantoins were obtained. The structures of all obtained products were verified *via* ^{1}H, ^{13}C NMR and IR spectroscopy. The structures of 4-hydrazinylidene-1,3-diazaspiro[4.4]nonane-2-thione, 4-hydrazinylidene-1,3-diazaspiro[4.5]decane-2-thione, 4-hydrazinylidene-1,3-diazaspiro[4.6]undecane-2-thione and 4-hydrazinylidene-1,3-diazaspiro[4.7]dodecane-2-thione were optimized using Density Functional Theory (DFT) methods at B3LYP/6-31G(d,p) level. The theoretical IR and NMR spectra of the compounds were calculated at B3LYP/6-31G(d,p) and B3LYP/6-31+G(2d,p) levels, respectively and were compared to experimental data. A good agreement between the DFT predicted and the experimentally measured IR and NMR spectra of the hydrazones was found.

Key words: Hydrazones, cycloalkanespiro-5-(2,4-dithiohydantoins), DFT

INTRODUCTION

In a previous work we reported two methods for cycloalkanespiro-5-hydantoins thionation [1]. These methods were based on the reaction of the respective spirohydantoins (with five-, six-, seven-, eight- and twelve-membered cycloalkane substituent at 5th position in the hydantoin ring) with Lawesson's reagent (2,4-bis(4-methoxyphenyl)-1,3,2,4-dithiadiphosphetane-2,4-disulfide, LR) or P_4S_{10}. Thionation of spirohydantoins with LR as cited above was performed in toluene medium under refluxing for six hours. This procedure led to obtaining of products with high yields (82 – 96 %). On the other hand, the use of P_4S_{10} as a thionation reagent (refluxing for five hours in xylene medium) resulted in formation of spirodithiohydantoins with 7 – 28 % lower yields of products as compared to those obtained through the method previously commented [1]. Recently, we reported a method for synthesis of cyclopentanespiro-5-(2,4-

dithiohydantoin), based on the interaction of cyclopentanespiro-5-hydantoin with a combination of P_4S_{10} and hexamethyldisiloxane (HMDO), following a modification of a procedure developed by Curphey [2]. This technique led to a significant reduction of the reaction time (1.5 hours) and to obtaining a product of higher yield (92 %), compared to the thionation methods mentioned above [1]. It was also found out that this compound showed an *in vitro* insecticidal activity against *Cladius pectinicornis* [3], Mealy plum aphid (*Hyalopterus pruni*) [4] and Oleander aphid (*Aphis nerii*) [5], as well as an *in vitro* fungicidal activity towards *Blumeria graminis* f. sp. *tritici* [6]. This work is a continuation of our previous studies for the development of more effective spirohydantoins thionation techniques. The current study presents the thionation of a series of cycloalkanespiro-5-hydantoins with a combination of P_4S_{10} and HMDO, as well as the interaction of the dithio analogues obtained with hydrazine hydrate, resulting in formation of the corresponding 4-hydrazones.

---

* To whom all correspondence should be sent:
E-mail: m_n_marinov@abv.bg

EXPERIMENTAL

General

All chemicals used were purchased from Merck and Sigma-Aldrich. The melting points were determined with a digital melting point apparatus SMP 10. The elemental analysis data were obtained with an automatic analyzer Carlo Erba 1106. The purity of the compounds was checked by thin layer chromatography on Kieselgel 60 F_{254}, 0.2 mm Merck plates, eluent systems (vol. ratio): (a) chloroform : acetone = 9 : 1, (b) ethylacetate : petroleum ether = 1 : 5. IR spectra were taken on spectrometers Bruker-113 and Perkin-Elmer FTIR-1600 in KBr discs. NMR spectra were taken on a Bruker DRX-250 spectrometer, operating at 250.13 and 62.90 MHz for ^1H and ^{13}C, respectively, using the standard Bruker software. Chemical shifts were referenced to tetramethylsilane (TMS). Measurements in DMSO-d_6 solutions were carried out at ambient temperature (300 K). The initial cycloalkanespiro-5-hydantoins 1a-4a (Scheme 1) were synthesized *via* the Bucherer-Lieb method [7]. The compounds 1a-4a were thionated with the combination of P_4S_{10} and hexamethyldisiloxane (HMDO), following a modification of a procedure developed by Curphey [2] (Scheme 1).

Synthesis of cycloalkanespirodithiohydantoins 1b-4b (a modification of the method reported by Curphey [2]) (Scheme 1)

A mixture of 0.03 mol of the corresponding cycloalkanespiro5-hydantoin (1a-4a), 4.89 g (0.011 mol) of P_4S_{10}, 21 ml (0.1 mol) of hexamethyldisiloxane (HMDO) and 60 ml of xylene was refluxed for an hour and a half. After cooling, the obtained crystalline product (1b-4b) was filtered off and recrystallized from methanol/water solution. The physicochemical parameters and the IR and NMR spectral data of the compounds were identical with the previously published data [1, 3].
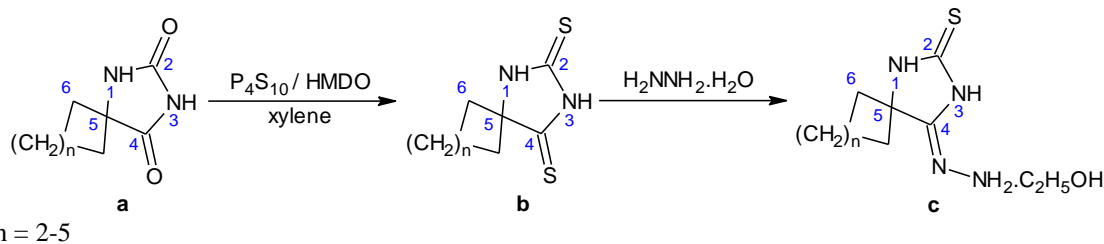
Synthesis of 4-hydrazones of cycloalkanespirodithiohydantoins 1c-4c (Scheme 1)

5.15 g (0.1 mol) of 95 % hydrazine hydrate was added to 0.004 mol of the corresponding cycloalkanespiro-5-(2,4-dithiohydantoin) (1b-4b) at room temperature. A small quantity of crushed ice was added to the reaction mixture. The crystalline product (1c-4c) obtained was filtered off and recrystallized from ethanol. The physicochemical parameters and the IR and NMR spectral data of the compounds (including an ethanol molecule in their structure) are listed in Tables 1 and 2, respectively.

COMPUTATIONAL DETAILS

The optimized geometries of the compounds 1c-4c (Fig. 2) were located by Density Functional Theory (DFT) using GAMESS (US) quantum chemistry package [8]. Geometry optimization of these structures was carried out by the hybrid B3LYP functional which combines the three-parameter exchange functional of Becke [9] with the LYP correlation one [10] using 6-31G(d) basis set. The calculations were carried out without symmetry constraints by the gradient procedure. A gradient convergence threshold of 1×10^{-4} hartree Bohr^{-1} was used.

The proton and carbon chemical shieldings were calculated with the B3LYP functional and 6-31+G(2d,p) basis set using the gauge-including atomic orbitals (GIAO) approach [11, 12] and B3LYP/6-31G(d) optimized geometry. The including of the solvent as dielectric (polarizable continuum model) in GIAO NMR calculations was used to estimate the effect of the medium (DMSO) on the chemical shifts of 1c-4c compounds. In order to compare with the experimental data, the calculated absolute shieldings were transformed to chemical shifts using the reference compound tetramethylsilane (TMS): $\delta = \delta_{calc}(TMS) - \delta_{calc}$. Both $\delta_{calc}(TMS)$ and δ_{calc} were evaluated with the same method and basis set. The NMR calculations were carried out using GAUSSIAN 09 program package [13].

1-4 n = 2-5

Scheme 1. Synthesis of 4-hydrazinylidene-1,3-diazaspiro[4.4]nonane-2-thione (1c), 4-hydrazinylidene-1,3-diazaspiro[4.5]decane-2-thione (**2c**), 4-hydrazinylidene-1,3-diazaspiro[4.6]undecane-2-thione (**3c**) and 4-hydrazinylidene-1,3-diazaspiro[4.7]dodecane-2-thione (**4c**)

RESULTS AND DISSCUSION

The synthesis of the compounds was performed in accordance with Scheme 1. The cycloalkanespiro-5-hydantoins 1a-4a were synthesized by the Bucherer-Lieb method [7], based on the interaction between the corresponding ketone, sodium or potassium cyanide, ammonium carbonate and ethanol. The compounds obtained (1a-4a) were subjected to thionation with the combination of P_4S_{10} and hexamethyldisiloxane (HMDO), following a modification of the procedure developed by Curphey [2]. The advantage of this method is the significant reduction of the reaction time (from 5 or 6 hours to 1.5 hours), and obtaining products of higher yield compared to previously used thionation methods [1]. Yields of the spirodithiohydantoins obtained were as follows: 1b - 92 % [3]; 2b - 96 %; 3b - 99 %; 4b - 98 %. The physicochemical parameters and the IR and NMR spectral data of the compounds 1b-4b were identical with the previously published data [1, 3].

The compounds 1b-4b were subjected to an interaction with hydrazine hydrate. The literature data available showed that the refluxing of cycloalkanespiro-5-hydantoins with hydrazine hydrate led to obtaining of the relevant 3-amino derivatives [14]. Additionally, the treatment of cyclohexanespiro-5-(2-thiohydantoin) with hydrazine hydrate at different reaction conditions was studied [15]. It was found that refluxing of cyclohexanespiro-5-(2-thiohydantoin) with hydrazine hydrate resulted in formation of the relevant 3-amino derivative. On the other hand, when the reaction was done at normal conditions, the corresponding 2-hydrazone was obtained. Now, we examined the interaction of four cycloalkanespirodithiohydantoins with hydrazine hydrate (Scheme 1) at room temperature. The spectral data obtained clearly showed that in this case the substitution was realized at C^4 of the dithiohydantoin ring, and an ethanol molecule was present in the structures of the compounds 1c-4c. The spectral data obtained were in compliance with previously published results about synthesis of hydrazones of cyclododecanespiro-5-(2,4-dithiohydantoin) and spiro-(fluorene-9,4'-imidazolidine)-2',5'-dithione [16]. The physico-chemical parameters and the IR and NMR spectral data of the compounds 1c-4c are listed in Table 1 and Table 2. The structural formulas and atom numbering of the compounds synthesized are presented in Figure 1.
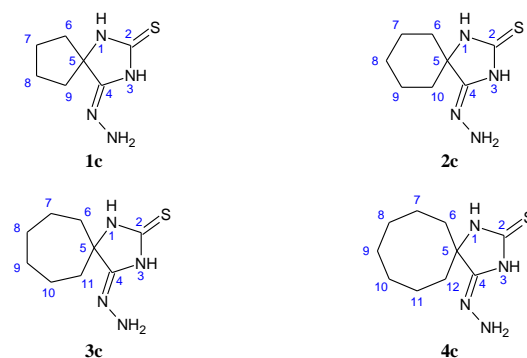
Fig. 1. Structural formulas and atom numbering of the compounds synthesized.

It is well known that DFT often gives calculated magnetic shieldings in large systems of a quality comparable or even better than MP2 for a cost that is of the same order as Hartree–Fock, substantially less than that of traditional correlation techniques [17-19]. Exchange–correlation functionals are believed to be superior in predicting molecular properties [20, 21]. We carried out calculations using B3LYP and BPW91 functionals, and found the B3LYP results to be closest to experimental data. Therefore, we present only the B3LYP results in GIAO NMR calculations in DMSO. Because of the sensitivity of ^{13}C NMR chemical shifts to the presence of polarization and diffuse functions in the basis set, the 6-31+G(2d,p) basis set was employed [22, 23]. Our theoretical results are in agreement with the ^{1}H and ^{13}C NMR measurements in DMSO-d_6 solution of compounds 1c-4c.

The vibrational spectra of the 4-hydrazinylidene-1,3-diazaspiro[4.4]nonane-2-thione (1c), 4-hydrazinylidene-1,3-diazaspiro[4.5]decane-2-thione (2c), 4-hydrazinylidene-1,3-diazaspiro[4.6]undecane-2-thione (3c) and 4-hydrazinylidene-1,3-diazaspiro[4.7]dodecane-2-thione (4c) were computed at B3LYP/6-31G(d,p) level. Available experimental data for the vibrational frequencies of the four compounds in KBr are presented for comparison. All results are listed in Table 2. Our assignments for the DFT calculated frequencies are based upon the analysis of the corresponding vibrational eigenvectors. Some modes such as NH, C=S, C=N stretching and NH_2 deformation were found to be characteristic. The analysis of the theoretical spectra of the four compounds shows that there is a good agreement with experimental data.

On the base of the good accordance in theoretically found molecular properties we have investigated the performance of the hybrid density functional B3LYP for predicting geometrical parameters of the 1c-4c compounds. The B3LYP/6-

31G(d,p) optimized geometries and interatomic distances of the 1c-4c molecules are presented in Figure 2. The augmentation of the cycloalkane ring in the hydrazone molecules from 4-hydrazinylidene-1,3-diazaspiro[4.4]nonane-2-thione (1c) to 4-hydrazinylidene-1,3-diazaspiro[4.7]dodecane-2-thione (4c) induces some changes in the geometrical parameters of the imidazolidine moiety. They are mainly related to the changes in C-C bonds. According to calculations at B3LYP/6-31G(d,p) level the C–C

bond in the imidazolidine ring is lengthened from 1.522 Å in 1c to 1.534 Å in 4c. The lengthening of this bond in 2c is by 0.007 Å while in 3c and 4c it is 0.009 Å and 0.012 Å, respectively. There is little change in the C-C bonds in the cycloalkane moiety. The bonds that connect the cycloalkane ring to the imidazolidine moiety are shortest in the 1c molecule and longest in the 2c one. There is no alteration in the rest of bonds in the hydrazone molecules as a result of cycloalkane ring augmentation.

Table 1. Physico-chemical parameters and elemental analysis data of compounds 1c-4c

№ [a]	Yield, %	M.p., °C	R_f [b]		Anal. calcd. (found) / %			
			i	ii	C	H	N	S
1c	54	231-232	0.53	0.11	46.93 (46.87)	7.88 (7.85)	24.32 (24.13)	13.92 (13.26)
2c	55	206-207	0.63	0.19	49.15 (49.02)	8.25 (8.18)	22.93 (22.78)	13.12 (12.99)
3c	69	193-194	0.60	0.15	51.13 (51.00)	8.58 (8.49)	21.68 (21.58)	12.41 (12.07)
4c	66	265-266	0.68	0.34	52.91 (52.78)	8.88 (8.81)	20.57 (20.48)	11.77 (11.37)

[a] The compounds numbering is in accordance with Scheme 1.
[b] Eluent systems (vol. ratio): i) chloroform : acetone = 9 : 1; ii) ethylacetate : petroleum ether = 1 : 5.
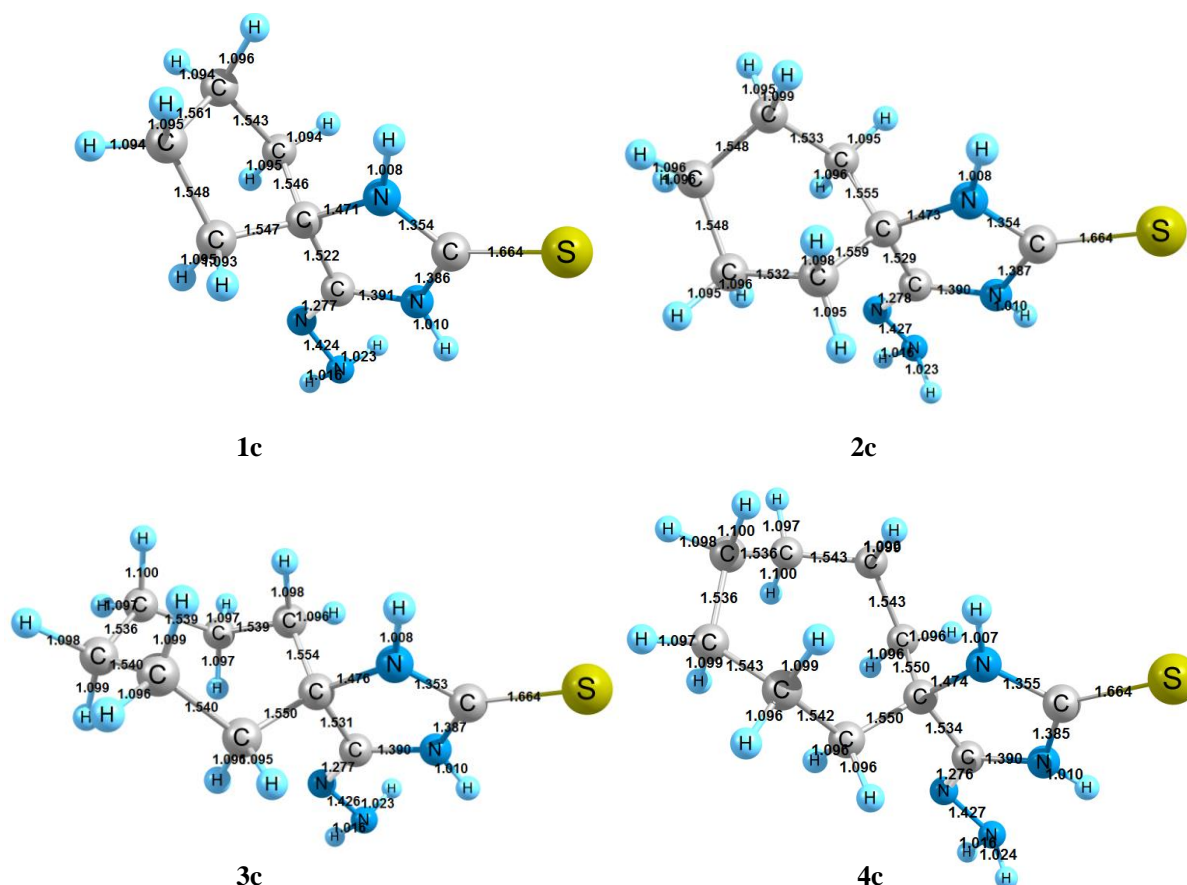
Fig. 2. B3LYP/6-31G(d,p) optimized structures of compounds 1c–4c. The bond lengths (in Å) are also given.

Table 2. Experimental IR, ^1H and ^{13}C NMR data of compounds 1c–4c[a]. Selected IR frequencies calculated at B3LYP/6-31G(d,p) level and GIAO ^1H and ^{13}C chemical shifts calculated (in italic) at B3LYP/6-31+G(2d,p) level. The frequencies are scaled by 0.945

№	IR (KBr) ν_{max} / cm^{-1}	^{1}H NMR (DMSO-d$_6$) δ / ppm	^{13}C NMR (DMSO-d$_6$) δ / ppm [b]
1c	3289, 3256, 3178 *3480, 3457, 3372, 3234* (NH, NH$_2$); 2972-2889 *2957- 2886* (CH$_2$); 1697 *1673* (C=N); 1519, 1161 *1454, 1185* (C=S)	1.00-1.05 (m, 3H, CH$_3$/EtOH), 1.67-1.91 *1.87-2.08* (m, 8H, CH$_2$), 5.24 (s, 1H, OH/EtOH), 9.58 *8.63* (s, 2H, NH$_2$), 10.49 (s, 1H, N^3-H)	18.8 (CH$_3$/EtOH), 23.8 *26.8* (C^7, C^8), 39.5 *43.1* (C^6, C^9), 56.2 (CH$_2$/EtOH), 70.3 *77.4* (C^5), 178.1 *177.1* (C^2), 145.9 *152.6* (C^4)
2c	3432, 3347, 3319, 3198 *3476, 3453, 3371, 3236* (NH, NH$_2$), 2939-2792 *2937-2859* (CH$_2$), 1703 *1670* (C=N), 1542, 1093 *1455, 1092* (C=S)	1.00-1.06 (m, 3H, CH$_3$/EtOH), 1.42-1.73 *1.50-2.07* (m, 10H, CH$_2$), 5.25 (s, 1H, OH/EtOH), 9.72 *8.57* (s, 2H, NH$_2$), 10.52 (s, 1H, N^3-H)	18.6 (CH$_3$/EtOH), 20.8 *21.3* (C^7, C^9), 24.7 *24.3* (C^8), 36.2 *36.6* (C^6, C^{10}), 56.1 (CH$_2$/EtOH), 64.0 *68.6* (C^5), 178.7 *177.0* (C^2), 145.7 *156.8* (C^4)
3c	3348, 3223, 3155 *3476, 3453, 3372, 3235* (NH, NH$_2$), 2931-2848 *2928, 2846* (CH$_2$), 1703 *1670* (C=N), 1532, 1090 *1452, 1113* (C=S)	1.00-1.06 (m, 3H, CH$_3$/EtOH), 1.22-1.99 *1.32-2.02* (m, 12H, CH$_2$), 5.26 (s, 1H, OH/EtOH), 9.90 *8.50* (s, 2H, NH$_2$), 11.01(s, 1H, N^3-H)	18.8 (CH$_3$/EtOH), 21.5 *26.9* (C^7, C^{10}), 29.6 (C^8, C^9), 39.6 *43.4* (C^6, C^{11}), 56.4 (CH$_2$/EtOH), 66.8 *72.4* (C^5), 178.2 *176.8* (C^2), 147.1 *156.2* (C^4)
4c	3329, 3208, 3163 *3490, 3457, 3370,3232*, (NH, NH$_2$); 2919-2847 *2922-2843* (CH$_2$); 1689 *1673* (C=N); 1538, 1194 *1450, 1125* (C=S)	1.00-1.05 (m, 3H, CH$_3$/EtOH), 1.45-1.67 *1.25-2.12* (m, 14H, CH$_2$), 5.10 (s, 1H, OH/EtOH), 9.64 *8.44* (s, 2H, NH$_2$), 10.30 (s, 1H, N^3-H)	18.6 (CH$_3$/EtOH), 20.8 *28.0* (C^7, C^{11}), 24.1 (C^9), 27,7 (C^8, C^{10}), 34.1 (C^6, C^{12}), 56.1 (CH$_2$/EtOH), 66.6 *71.3* (C^5), 178.5 *177.8* (C^2), 148.0 (C^4)

[a] Atom numbering is in accordance with Figure 1.

[b] These assignments are confirmed by the DEPT-135 spectral data.

REFERENCES

1. M. Marinov, S. Minchev, N. Stoyanov, G. Ivanova, M. Spassova, V. Enchev, *Croat. Chem. Acta*, **78**, 9 (2005).
2. T. J. Curphey, *J. Org. Chem.*, **67**, 6461 (2002).
3. M. Marinov, D. Ganchev, P. Marinova, S. Krustev, N. Atanasova, M. Zlateva, N. Stoyanov, *Bulg. J. Agric. Sci.*, **18**, 929 (2012).
4. D. Ganchev, M. Marinov, M. Zlateva, R. Prodanova, A. Nikolov, S. Krustev, N. Stoyanov, *University of Ruse "Angel Kanchev" Proceedings*, **52** (10.2), *Biotechnologies and food technologies*, 16 (2013).
5. M. N. Marinov, D. H. Ganchev. P. E. Marinova, A. S. Nikolov, R. Y. Prodanova, S. V. Krustev, M. R. Zlateva, N. M. Stoyanov, *J. Sci. Appl. Res.*, **4**, 171 (2013).
6. M. Marinov, D. Ganchev, A. Nikolov, P. Marinova, S. Krustev, V. Madzharova, N. Stoyanov, *Agric. Sci.*, **12**, 97 (2013).
7. H. T. Bucherer, V. A. Lieb, *J. Prakt. Chem.*, **141**, 5 (1934).
8. M. W. Schmidt, K. K. Baldridge, J. A. Boatz, S. T. Elbert, M. S. Gordon, J. H. Jensen, S. Koseki, N. Matsunaga, K. A. Nguyen, S. Su, T. L. Windus, M. Dupuis, J. A. Montgomery, *J. Comput. Chem,* **14**, 1347 (1993).
9. A. D. Becke, *J. Chem. Phys.*, **98**, 5648 (1993).
10. C. T. Lee, W. T. Wang, R. G. Pople, *Phys. Rev.*, **B 37**, 785 (1988).
11. R. Ditchfield, *Mol. Phys.,* **27**, 789 (1974).
12. K. Wolinski, J. F. Hilton, P. Pulay, *J. Am. Chem. Soc.*, **112**, 8251 (1990).
13. M. J. Frisch, G. W. Trucks, H. B. Schlegel, G. E. Scuseria, M. A. Robb, J. R. Cheeseman, G. Scalmani, V. Barone, B. Mennucci, G. A. Petersson, H. Nakatsuji, M. Caricato, X. Li, H. P. Hratchian, A. F. Izmaylov, J. Bloino, G. Zheng, J. L. Sonnenberg, M. Hada, M. Ehara, K. Toyota, R. Fukuda, J. Hasegawa, M. Ishida, T. Nakajima, Y. Honda, O. Kitao, H. Nakai, T. Vreven, J. A. Montgomery, Jr., J. E. Peralta, F. Ogliaro, M. Bearpark, J. J. Heyd, E. Brothers, K. N. Kudin, V. N. Staroverov, R. Kobayashi, J. Normand, K. Raghavachari, A. Rendell, J. C. Burant, S. S. Iyengar, J. Tomasi, M. Cossi, N. Rega, J. M. Millam, M. Klene, J. E. Knox, J. B. Cross, V. Bakken, C. Adamo, J. Jaramillo, R. Gomperts, R. E. Stratmann, O. Yazyev, A. J. Austin, R. Cammi, C. Pomelli, J. W. Ochterski, R. L. Martin, K. Morokuma, V. G. Zakrzewski, G. A. Voth, P. Salvador, J. J. Dannenberg, S. Dapprich, A. D. Daniels, O. Farkas, J. B. Foresman, J. V. Ortiz, J. Cioslowski, and D. J. Fox, (2009), GAUSSIAN 09 Revision A.1, Gaussian, Inc., Wallingford CT.
14. E. Naydenova, N. Pencheva, J. Popova, N. Stoyanov, M. Lazarova, B. Aleksiev, *Farmaco*, **57**, 189 (2002).
15. M. N. Marinov, *J. Sci. Appl. Res.*, **2**, 66 (2012).

16. N. Stoyanov, M. Marinov, S. Minchev, *Compt. Rend. Acad. Bulg. Sci.*, **55**, 61 (2002).
17. C. Ochsenfeld, J. Kussmann, F. Koziol, *Angew. Chem. Int. Ed.*, **43**, 4485 (2004).
18. J. Kussmann, C. Ochsenfeld, *J. Chem. Phys.*, **127**, 204103 (2007).
19. M. Beer, C. Ochsenfeld, *J. Chem. Phys.*, **128**, 221102 (2008).
20. J. C. Facelli, *Prog. NMR Spectroscopy*, **58**, 176 (2011).
21. J. R. Cheeseman, G. W. Trucks, T. A. Keith, M. J. Frisch, *J. Chem. Phys.*, **104**, 5497 (1996).
22. B. Blicharska, T. Kupka, *J. Mol. Struct.*, **613**, 153 (2002).
23. P. d'Antuono, E. Botek, B. Champagne, J. Wiem, M. -F. Reyniers, G. B. Marin, P. J. Adriaensens, J. M. Gelan, *Chem. Phys. Lett.*, **41**, 207 (2005).

СИНТЕЗ, ОХАРАКТЕРИЗИРАНЕ И КВАНТОВО-ХИМИЧНИ ИЗЧИСЛЕНИЯ С ПОМОЩТА НА ТЕОРИЯТА НА ФУНКЦИОНАЛА НА ПЛЪТНОСТТА НА ХИДРАЗОНИ НА ЦИКЛОАЛКАНСПИРОДИТИОХИДАНТОИНИ

М. Н. Маринов[1*], П. Е. Маринова[2], Н. В. Маркова[3], Н. М. Стоянов[4]

[1]*Аграрен университет – Пловдив, Факултет по растителна защита и агроекология, Катедра „Обща химия", 4000 Пловдив, бул. „Менделеев" 12, България*

[2]*Пловдивски университет, Химически факултет, Катедра „Обща и неорганична химия с методика на обучението по химия", 4000 Пловдив, ул. „Цар Асен" 24, България*

[3]*Институт по органична химия с център по фитохимия, Българска Академия на Науките, 1113 София, ул. „Акад. Г. Бончев", бл. 9, България*

[4]*Русенски университет, Филиал – Разград, Катедра „Химия и химични технологии", 7200 Разград, бул. „Априлско въстание" 47, България*

(Резюме)

Статията представя метод за синтез на хидразони на циклоалканспиродитиохидантоини. Изходните спиродитиохидантоини бяха получени при взаимодействие на циклоалканспиро-5-хидантоини с P_4S_{10} и хексаметилдисилоксан. Този метод води до синтез на продукти с по-висок добив, в сравнение с известни литературни данни. Спиродитиохидантоините бяха подложени на взаимодействие с хидразин хидрат, в резултат на което бяха получени съответните 4-хидразони. Структурата на продуктите беше потвърдена чрез ^{1}H, ^{13}C ЯМР и ИЧ спектроскопия.

Структурите на 4-хидразинилиден-1,3-диазаспиро[4.4]нонан-2-тион, 4-хидразинилиден-1,3-диазаспиро[4.5]декан-2-тион, 4-хидразинилиден-1,3-диазаспиро[4.6]ундекан-2-тион и 4-хидразинилиден-1,3-диазаспиро[4.6]додекан-2-тион бяха оптимизирани с помощта на теорията на функционала на плътността на ниво B3LYP/6-31G(d,p). Със същия функционал бяха изчислени теоретичните ИЧ и ЯМР (протонни и въглеродни) спектри на съединенията, като за предсказване на ^{1}H и ^{13}C ЯМР спектри беше използван 6-31+G(2d,p) базисен набор, а за предсказване на ИЧ спектрите - 6-31G(d,p) базисен набор. Намерено беше добро съответствие между теоретичните и експерименталните резултати.

Extracts of the plastic layer of coals of different reductivity type and their blends

L. Butuzova[1], S. P. Marinov[2*], R. Makovskyi[1], G. Butuzov[1]

[1] Donetsk National Technical University, 58 Artema str., Donetsk 83000, Ukraine
[2] Bulgarian Academy of Sciences, Institute of Organic Chemistry, Acad. G.Bonchev str., Bl.9, Sofia 1113, Bulgaria.

Extracts of the plastic layer of fat (J-grade) and gas (G-grade) coals of different genetic types by reductivity (GTR) and their blends were comprehensively studied. It was shown that the coking capacity of coals implies a certain balance between the mobile liquids and the macromolecular phases in the plastic state. A new indicator of the coking capacity, was proposed, namely, the proportion of carbenes+carboides/maltenes in the extracts of liquid mobile products of thermal filtration of coals and blends which linearly correlates with the yields of the above products responsible for the coking processes. An optimal blend composition (G - low-reduced ÷ J - reduced coals) which gives a maximum yield of fluid non-volatile products (FNP) saturated with aliphatic components was found.

Key words: Plastic layer, Extracts, Coal, Blends, Coking

INTRODUCTION

A study of coal properties in the plastic state is of great practical and theoretical importance for scientifically based development of optimal coal blends. Penetration and dilatometric conventional methods for characterization of the coal plastic mass are based on determining the width of the plastic state zone, the plastic mass viscosity, resistance, the rate of movement of the metal plate in the coal charge and other physical properties [1]. These methods give no way of assessing the nature of the substances responsible for plastic layer formation and coking.

Very important information can be derived from direct observations of the mesophase. Such data were described by Zubkova [2-4], using a special laboratory unit consisting of a furnace and coking chamber with contrasting elements embedded into the coal charge. The coal charge was irradiated with X-rays during carbonization and all the changes in the charge were registered on a film. The macrostructure of the coal plastic layer and the processes of formation of a solid carbonization residue were described for coals of different rank and caking capacity in different conditions [3, 4].

Extraction is another advanced method of studying the structure of solid fossil fuels, which permits to determine the differences in the composition of products obtained upon their processing [5-8].

Differences in the yield and composition of coal extracts are due to coalification degree and specified coal genetic types by reductivity (GTR). A particular characteristic of seams from Donetsk coal basin in Ukraine is the occurrence of high- and low-sulfur coals of the same rank differing by some physicochemical properties [9-14]. These differences are due to specified genetic types by reductivity formed in alluvial or marine depositional environments during diagenesis processes [11]. Earlier, high reactivity for sulfur coals in coking and lacing processes was established [15].

Previous work has demonstrated that heating of blends with high-sulfur coking coal in the plastic temperature range in a centrifugal field leads to a substantial increase in the yield of fluid non-volatile products in comparison with the blends containing low-sulfur coking coal. An apparent relation between the content of sulfur in coal, the concentration of paramagnetic sites in the fluid non-volatile products and coal coking ability was discovered [16].

The first experimental task in the present study was to isolate the fluid non-volatile products by the method of centrifugal thermal filtration. Then the obtained mobile products should be appropriately separated into characteristic fractions.

The aim of this research was to study the influence of components in fluid non-volatile products of the plastic layer from coals of different type by reluctivity and their blends on the yields of liquid mobile products responsible for the coking processes.

* To whom all correspondence should be sent:
E-mail: stif@bas.bg

EXPERIMENTAL

Two pairs of isometamorphic Donetsk coals of different genetic types by reductivity, formed under reductive and less reductive conditions (low reduced – LRC and reduced coals – RC) and their blends, were used as objects of research. Characteristics of the initial coals are given in Table 1. As it is seen, the two coal types G and J-grade coals ($\approx$83-88 % C^{daf}) according to Ukrainian classification differ mainly by their carbon, volatile and ash contents and their pairs with low and higher sulphur contents.

The ratio of different grades of coal in the composed blends was chosen as conventional blend (J:G=70:30) and as J:G=50:50 to assess the feasibility of increasing the share of low coking coals. A distinctive feature of the blends under analysis is the use of all possible combinations of coals of different genetic types by reluctivity, i.e., low-reduced (J_{LRC}, G_{LRC}) and reduced types (J_{RC}, G_{RC}). These coals and their blends are thermally treated up to 600 °C at a rate of 1500 rev/min using the method of centrifugal thermal filtration with separation of the fluid non-volatile products (FNP). This method enables the immediate separation of the primary products that form the plastic mass, thus preventing their secondary transformations [17]. The amount and composition of FNP largely determine the processes of caking and coking.

The following methods of research were used: thermal filtration (National State Standard 17621-89), technical (National State Standard 11014-89, National State Standard 11022-95, National State Standard 2059-95, National State Standard 6382-91) and elemental (National State Standard 24081-95) analyses, and Fourier transform infrared spectroscopy.

Infrared spectra were recorded on a Bruker FTS-7 spectrometer using the DRIFT technique. Semi quantification of the infrared spectra was made using the Origin 6.1 software package by basic-line technique.

Fluid non-volatile products were separated into components (Fig. 1) using the following procedure: first water was removed, then asphaltenes were separated. Hexane-soluble compounds were resolved into alkalis, carboxylic acids, phenols, neutral oils by their consecutive treatment with 10% H_2SO_4, 3% $NaHCO_3$, and 5% NaOH. Neutral oils were chromatographed on silica gel using hexane, benzene or acetone as eluents, with subsequent separation of paraffin-naphthene, aromatic and polar hydrocarbons.
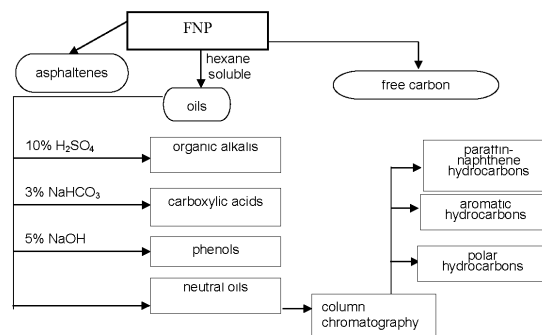
Fig. 1. Scheme of FNP separation into components.
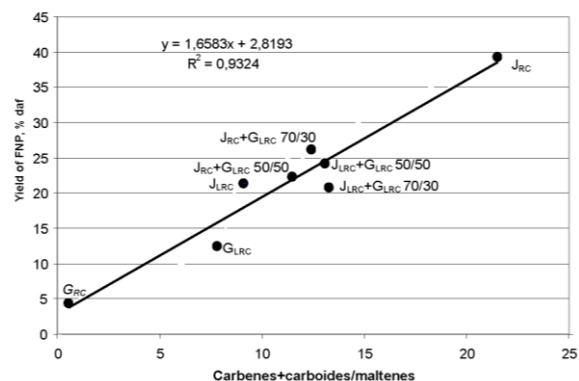
Fig.2. Dependence of the plastic mass yield on the carbenes+carboides/maltenes ratio.

RESULTS AND DISCUSSION

As seen from Table 2, the elemental composition of the thermal filtration products is different for coals and blends. In particular, the hydrogen content in FNP is 2-3 times as much as that in over-sieve residues (OR), which permits to form a plastic layer enriched with a liquid component. The analysis of the sulfur content in the blends showed that in the blend $J_{RC} \div G_{LRC}$ the ratio between J and G components (J : G = 50% / 50% and 70% / 30%) permits to lower the sulfur content in FNP and OR. Accordingly, sulfur-containing components will migrate to the vapour-gas phase.

The method of DRIFT-spectroscopy corroborates the processes of hydrogen redistribution. As can be seen from Table 3, the ratio of the aromatic to the aliphatic hydrogen (I_{1600}/I_{1440}) is dozen times as much for OR compared to FNP. These data convincingly demonstrate that the processes ensuring the formation of the plastic layer proceed most intensively in the blend containing G_{RC} coal. The plastic layer of J-grade coals is saturated with the optimal number of aliphatic and polycyclic aromatic fragments, which are able to form the liquid crystalline state, i.e., the mesophase. Stabilisation of the formed radicals is likely to occur at the expense of the hydrogen of over-grid residues (See Tables 2, 3).

Table 1. Characterization of analysed coals

Mine	Coal grade	Type	Technical analysis, %				Elemental analysis, % daf		
			W^a	A^d	S^d_t	V^{daf}	C	H	O+N
Tsentralnaya	G, k_7	LRC	2.2	5.2	1.22	36.0	85.1	5.11	8.71
Dimitrova	G, l_1	RC	2.1	4.4	2.49	38.,7	83.8	5.34	9.50
Zasiadko	J, l_4	LRC	1.4	2.6	1.09	31.6	87.8	5.16	7.00
Zasiadko	J, k_8	RC	0.8	2.7	2.81	31.7	87.3	5.23	7.20

Table 2. Elemental composition of the centrifugal thermal filtration products of coals and blends

Thermal filtration products of coals and blends		The ratio of J / G components, %	C	H	S
Fluid non-volatile products	G_{LRC}		84.04	6.55	1.11
	G_{RC}		82.50	7.08	2.28
	J_{LRC}		86.57	4.40	1.05
	J_{RC}		84.68	6.34	1.76
	$J_{LRC} \div G_{LRC}$	70 / 30	70.69	4.45	0.75
	$J_{LRC} \div G_{RC}$	70 / 30	86.47	4.43	1.95
	$J_{RC} \div G_{RC}$	50 / 50	84.72	6.26	2.15
		70 / 30	83.79	5.44	2.,55
	$J_{RC} \div G_{LRC}$	50 / 50	85.16	5.27	1.86
		70 / 30	83.81	5.85	1.84
Over- sieve residues	G_{LRC}		86.98	2.70	0.88
	G_{RC}		87.25	2.78	0.85
	J_{LRC}		89.91	2.39	1.04
	J_{RC}		91.47	1.02	2.81
	$J_{LRC} \div G_{LRC}$	70 / 30	81.44	2.25	1.25
	$J_{LRC} \div G_{RC}$	70 / 30	91.19	1.38	0.90
	$J_{RC} \div G_{RC}$	50 / 50	87.86	2.36	1.79
		70 / 30	83.79	2.44	1.68
	$J_{RC} \div G_{LRC}$	50 / 50	68.68	2.82	2.24
		70 / 30	82.89	2.82	1.30

A comparison of two over-grid residues (OR) obtained from blends with different reductivity type of of J-grade coal ($J_{LRC} \div G_{LRC}$ and $J_{RC} \div G_{LRC}$) shows that in the latter case the solid residue is characterised by virtually ten times as high relative content of the aromatic hydrogen. Thus, when J-grade reduced coal is added to the blend, FNP is intensively saturated with hydrogen (C-H_{aliph}). The solid residue is enriched with aromatic fragments, i.e., gives up hydrogen. Judging by the experimental and theoretic yield of the plastic layer [16], there is a sufficient number of aromatic and aliphatic components in FNP of the blend ($J_{LRC} \div G_{LRC}$) to achieve stabilisation of the products of

bridge bonds destruction with hydrogen. The ratio C-H_{ar} / C-H_{aliph} (I_{1600}/I_{1440}) is much the same for FNP and OR. In FNP of other blends, a part of aromatic hydrogen carriers formed from J-grade coal, is spent on stabilisation of gas (G-grade) coal decomposition products, which is confirmed by a decrease in the experimental, as compared to the theoretic yield of FNP products [18]. The maximum difference between the I_{1600}/I_{1440} values in OR and FNP was recorded for the $J_{RC} \div G_{LRC}$ blend, which corroborates maximum hydrogen transfer in this system.

Table 3. The ratios of characteristic absorption bands in DRIFT spectra

Coals, fluid non-volatile products, over-sieve residues of coals and blends (F:G=70:30)		Relative intensity I_{1600}/I_{1440}
Coals	G_{LRC}	1.894
	G_{RC}	1.804
	J_{LRC}	1.638
	J_{RC}	1.321
Fluid non-volatile products	G_{LRC}	1.458
	G_{RC}	0.928
	J_{LRC}	2.071
	J_{RC}	1.671
	$J_{RC} \div G_{RC}$	1.586
	$J_{RC} \div G_{LRC}$	0.179
	$J_{LRC} \div G_{LRC}$	2.417
	$J_{LRC} \div G_{RC}$	2.253
Over- sieve residues	G_{LRC}	13.540
	G_{RC}	5.002
	J_{LRC}	-
	J_{RC}	-
	$J_{RC} \div G_{RC}$	7.638
	$J_{RC} \div G_{LRC}$	20.352
	$J_{LRC} \div G_{LRC}$	2.165
	$J_{LRC} \div G_{RC}$	17.155

The differences in the sulfur and ash content and the elemental composition of the reduced and low-reduced coals account for their different behaviour during thermal processing. Notably, the impact of the genetic type by reductivity is dissimilar in coals of different ranks.

Extracts of fluid mobile products were taken and their structural-group composition (SGC) was thoroughly examined to extend knowledge of the mechanism of the coking process. The structural-group composition (SGC) of the extracts of liquid mobile products (Table 4) is presented by a group of hexane-soluble (maltenes or oil), hexane–insoluble, but toluene–soluble (asphaltenes) compounds, and a sediment formed upon washing of asphaltenes with hot toluene (carbenes and carboides). FNP composition essentially depends on the coal genetic type by reductivity, as is evident from the results of the structural-group analysis. The proportion of asphaltenes in the extracts of reduced gas coals is three times as much as that of low-reduced G-Grade coals. An inverse dependence is observed for FNP extracts of fat coals. The content of asphaltenes decreases twice from 9.30% in FNP of J_{LRC} coal down to 4.51% in FNP of J_{RC} coal. A similar picture is seen in the content of maltenes for the pairs $G_{LRC} \div G_{RC}$ and $J_{LRC} \div J_{RC}$. Maltenes of G_{RC} coals yield 4 times more, and those of J_{RC} coals half as much hexane-soluble products compared to low-reduced coals.

Thus, genetic type by reductivity (GTR) of coals has a great impact on the yields of particular soluble compounds. A detailed analysis of maltenes composition in the $G_{LRC} \div G_{RC}$ pair (Table 4) has shown that in the hexane-soluble part of the extract of fluid mobile products of the G_{RC} coal there are more phenols (7.1 times) and organic alkalis (6 times), more carboxylic acids and neutral oil in comparison with the G_{LRC} extract. For the $J_{LRC} \div J_{RC}$ pair the difference in maltenes composition basically shows in a decreased content of organic alkalis and decreased content of carboxylic acids (1.2 times) in the FNP extract of J_{LRC} as compared to J_{RC} coals (Table 4).

The differences in the structural-group FNP composition of the blends made up of fat and gas coals (J- and G-grade) primarily consist in a substantially higher (~ two-fold) content of asphaltenes in the extracts of the blends containing low-reduced fat coals.

The fluid non-volatile products extracts of the blends with different component ratios also differ in their SGC, first and foremost, by the content of mobile low-molecular products (maltenes) and by the content of high-molecular components (carbenes/carboides and asphaltenes). It follows from the data obtained that the caking properties of the blends are related to both the amount and the composition of FNP.

Close linear correlation between the carbenes+carboides/maltenes ratio and the yield of liquid mobile products from coals and blends was established. The graphical representation of this function can be found in Fig. 2. The correlation coefficient value is $R^2=0.9324$. The data prove conclusively that the coking capacity of coals presupposes a balance in the system between the mobile phase, i.e., hydrogen carrier, and its donor, i.e., the macromolecular phase.

Table 4. Results of structural-group analysis of liquid non-volatile thermal filtration products of the coals and blends, wt.% from FNP amount

Coal grade, type, percent composition of components	FNP yield, % daf	Maltenes					Asphaltenes	Carbenes + carboides
		Organic alkalis	Carboxylic acids	Phenols	Neutral oils	Σ Maltenes		
G_{LRC}	12.44	0.30	0.38	1.87	7.62	10.17	10.38	79.45
G_{RC}	4.28	1.79	0.58	13.26	29.5	45.13	30.45	24.42
J_{LRC}	21.33	0.27	0.19	1.40	7.3	8,9	9.0	81.71
J_{RC}	39.28	0.34	0.23	0.57	3.0	4.24	4.1	91.25
$J_{RC} \div G_{LRC}$ 50/50	22.22	0.24	0.40	0.92	6,.1	7.87	1.0	90.23
$J_{RC} \div G_{LRC}$ 70/30	26.19	0.27	0.60	0.88	5,.6	7.31	1.3	90.96
$J_{LRC} \div G_{LRC}$ 50/50	24.11	0.34	1.50	0.17	4,.2	6.63	6.7	86.70
$J_{LRC} \div G_{LRC}$ 70/30	20.71	0.65	0.51	1.35	4.0	6.61	5.51	87.88

Table 5. The composition of neutral oils obtained from the plastic layer of coals of different types by reductivity and blends on their basis, wt.%

Coal grade, type, percent of components	Paraffin-naphthene fraction	Aromatic fraction	Polar fraction	Losses
G_{LRC}	55.5	27.7	12.4	4.4
G_{RC}	55.4	27.8	15.0	1.8
$J_{RC} \div G_{LRC}$ 50/50	54.6	29.1	15.1	1.2
$J_{RC} \div G_{LRC}$ 70/30	52.7	31.6	12.2	3.5
$J_{LRC} \div G_{LRC}$ 50/50	57.4	27.6	15.0	-
$J_{LRC} \div G_{LRC}$ 70/30	52.9	31.4	15.6	0.1

A comparison of the blends (J / G = 70 / 30) including fat (J-grade) coals of different GTR shows that the J_{RC} component promotes a decrease in the neutral oil content in maltenes regardless of its relatively low content in FNP of the initial coal. These data are in excellent agreement with the IR-spectroscopy results of the respective FNP. The concentration of CH_{aliph} groups is 13.5 times higher in FNP of the $J_{RC} \div G_{LRC}$ blend in comparison with the $J_{LRC} \div G_{LRC}$ blend (Table 3). Accordingly, the method of structural-group analysis substantiates the leading role of GTR of J-grade coals at the stage of plastic layer formation in a blend. The data obtained unambiguously indicate that it is necessary to take into account the GTR of coals when making coking blends.

Fractional composition of neutral oils in Table 5 demonstrates that the composition of neutral oils of gas coals (G-grade) of different GTR is similar and appears to have little effect on the composition of the blend extracts, which is sufficiently homogeneous and differs little from the

composition of gas coal extracts. However, it is noteworthy that when the proportion of fat coal (J-grade) in the blend increases, the share of the paraffin-naphthene fraction decreases, whereas that of the aromatic fraction of neutral oils increases.

CONCLUSION

The results of a detailed study of the extracts from the plastic layer of coals of different genetic types by reductivity and their blends are described. The main part of the extracts is composed of carbenes+carboides (24-91%) and maltenes. Quantity of carbenes+carboides increases during coalification processes and is much higher for blends, containing middle-rank coal of reduced type. Obviously, their segregation at the early stages of thermal decomposition is very important for the formation of a plastic layer and subsequent formation of the coke structure. DRIFT-spectroscopy analysis of the extracts revealed significant quantitative differences in the

composition of components extracted from different coals and blends.

The extracts obtained from J-grade coals are characterized by a higher content of carbenes+carboides in comparison with G-grade coals, which corresponds to their higher FNP yield and higher caking ability.

It was shown that the caking ability of coals requires some balance between the mobile and the macromolecular phases in a plastic state. A new indicator of caking – the ratio of carbenes+ carboides/maltenes in extracts of liquid products of coals and blends was suggested. This indicator correlates with the yield of plastic layer which is responsible for the caking process. The optimal composition of the blends which gives the highest yield of plastic layer, saturated with aliphatic components, was cleared. Therefore, for good caking capacity of a blend during pyrolysis a certain correlation between the amount of relatively higher-molecular FNP components insoluble in neutral low-boiling solvents and the amount of relatively low-molecular maltenes, is needed to ensure the mesophase mobility.

Excessive amount of asphaltenes in FNP is highly undesirable and can be avoided by varying the proportion of strongly coking coals in a blend.

REFERENCES

1. H. Schobert, Chemistry of Fossil Fuels and Biofuels, Cambridge Univ. Press. (2013).
2. V.V. Zubkova, *Fuel Processing Technology,* **76**, 105 (2002).
3. V.V. Zubkova, *Fuel,* **84**, 755 (2005).
4. V.V. Zubkova, *Fuel*, **84**, 741 (2005).
5. D.W. Van Krevelen, Coal, III-edition, Elsevier. (1993).
6. O.A. Radchenko, *Academic Press of the Academy of Sciences of the USSR*, **3**, 172 (1962).
7. L. Butuzova, L. Isaeva, O. Turchanina, A. Krzton, *Fuel Processing Technology,* **77- 78**, 145 (2002).
8. J. Yang, P.G. Stansberry, J.W. Zondlo, A.H. Stiller, *Fuel Processing Technology,* **79**, 207 (2002).
9. L.F. Butuzova, S. Marinov, V.N. Minkova, V.A. Safin, M. Stefanova, V. Stamenova, *Bulletin of Geosciences*, **80**, 15 (2005).
10. L. Butuzova, O. Turchanina, S. Shakir, G. Butuzov, A. Bechtel, A. Castelbranco, *China-USA Business Review*, **12**, 1033 (2013).
11. A. Bechtel, L. Butuzova, O. Turchanina, *Fuel Processing Technology* ,**77-78**, 45 (2002).
12. L. Butuzova, A. Bechtel, O. Turchanina, V.A. Safin, G. Butuzov, L. Isaeva, *Bulletin of Geosciences,* **80**, 3 (2005).
13. L. Butuzova, L. Isayeva, O. Bulyga, O. Turchanina, A. Krzton, G. Matsenko, *Bulletin of Geosciences,* **80**, 9 (2005).
14. L.Butuzova, S. Rozhkov, R. Makovskyi, N. Rozhkova, G. Butuzov, *GeoLines,* **22**, 9 (2009).
15. L.F. Butuzova, V.N. Minkova, V.A. Safin, S. Marinov, V. Stamenova, *Polish Journal of Environmental studies,* **14**, 75 (2005).
16. L. Butuzova, R.V. Makovskiy, T. Budinova, S.P. Marinov, *Fuel Processing Technology,* **125**, 246 (2014).
17. Yu.V. Birukov, Metallurgiya, Moskow, 1980, p. 120.
18. R.V. Makovskiy, L.F. Butuzova, S. Marinov, V.A. Safin, A.O. Nalivkina, *Transactions of Donetsk National Technical University. Series: Chemistry and Chemical Technology*, **162**, 97 (2010).

ЕКСТРАКТИ НА ПЛАСТИЧНИЯ ПЛАСТ ОТ ВЪГЛИЩА С РАЗЛИЧЕН ТИП ПО РЕДУКТИВНОСТ И ТЕХНИ СМЕСИ

Л. Бутузова[1], С. П. Маринов[2*], Р. Маковски[1], Г. Бутузов[1]

[1]*Донецки Национален Технически Университет, ул. Артьом 58, Донецк 83 000, Украйна*
[2]*Институт по Органична химия с Център по Фитохимия, Българска Академия на Науките, ул. Акад. Г.Бончев, бл.9, 1113 София, България*

(Резюме)

Изучени са екстрактите на пластичния пласт от тлъсти (J-ранк) и газови (G-ранк) въглища с различен генетичен тип по редуктивност (ГТР) и техни смеси. Показано е, че коксуващият капацитет на въглищата предполага определен баланс между подвижната течна и макромолекулната фаза в пластично състояние. Предложен е нов индикатор за коксуващия капацитет, а именно отношението карбени + карбоиди / малтени в екстрактите на течните подвижни продукти от термичната филтрация на въглища и техни смеси, което линейно корелира с добивите на по-горе споменатите продукти, отговорни за коксуващите процеси. Намерен е оптимален състав на сместа (G- ниско редуцирани ÷ J- редуцирани въглища), който дава максимален добив на флуид нелетливите продукти (ФНП), наситени с алифатни компоненти.

An easy and fast one-pot preparation of 2-thiomethyl and 2-thioacyl benzothiazoles, benzoxazoles, and benzimidazoles

T. G. Deligeorgiev, A. A. Kurutos*, N. I. Gadjev, A. A. Alexiev

University of Sofia, Faculty of Chemistry and Pharmacy, 1 J. Bourchier blvd., 1164 Sofia, Bulgaria

A one-pot preparation of 2-thiomethyl and 2-thioacyl benzazolium derivatives using *o*-aminothiophenol, *o*-aminophenol or 1,2-phenilenediamine as starting material is reported in the present paper. This novel method involves a combination of microwave heating and ultrasound irradiation, affording the title compounds with good to excellent yields, without isolating the intermediate products.

Keywords: 2-thiomethylbenzothiazoles, 2-thiomethylbenzoxazoles, 2-thiomethylbenzimidazoles, 2-thioacylbenzothiazoles, 2-thioacylbenzoxazoles, 2-thioacylbenzimidazoles.

INTRODUCTION

Quaternary 2-thiomethylbenzazoles are important class of intermediates involved in the synthesis of symmetric and asymmetric monomethine cyanine dyes. In addition to, 2-methylmercaptobenzothiazole, and 2-methylmercaptobenzoxazole derivatives represent an essential group of compounds for the synthesis of cyanine dyes [1–3]. S-Alkylated heterocyclic derivatives are known as key compounds, finding application in copper and copper alloys protection against corrosion [4–6].

Thiocarboxylic acid esters (2-thioacyl derivatives) can be used in various chemical transformations, such as asymmetric aldol reactions [7], and as cephalosporin derivatives [8]. Thioethers play an important role in the development of thiol drugs, especially in masking the unpleasant odor and taste of the native thiol [9]. Recently we have published two methods as an environmentally benign ways the former of which involves the synthesis of substituted 2-thiobenzothiazoles, 2-thiobenzoxazoles, 2-thiobenzimidazoles, and 1,3-oxazolopyridine-2-thiols [10], as well as an easy and fast ultrasonic selective S-alkylation of hetaryl thiols proceeding at room temperature as presented in the latter publication [11].

Herein we report that those two methods mentioned above can be joined together in a novel synthetic procedure, for an easy and fast one-pot preparation of 2-thiomethylbenzothiazoles, 2-thiomethylbenz- oxazoles, 2-thiomethylbenzimid- azoles or 2-thioacylbenzothiazoles, 2-thioacylbenzoxazoles and 2-thioacylbenzimidazoles.

EXPERIMENTAL

All reagents and solvents were purchased from Sigma-Aldrich, Organica Feinchemie GmbH Wolfen, Fluka, Alfa-Aesar, and were used without further purification. The deuterated solvents were purchased from Deutero GmbH. The target 2-thioalkyl and 2-thioacyl benzazolium derivatives were compared to previously reported ones. Melting point temperatures were determined on a Kofler bench and are uncorrected. ^{1}H-NMR spectra were recorded on a Bruker Avance III HD, 500 MHz in DMSO-d_6 at room temperature. The chemical shifts were reported in ppm in δ-values with respect to tetramethylsilane (TMS) as an internal standard.

Synthesis of potassium salts of substituted or unsubstituted 2-mercaptobenzazoles 7a-7k

3.7 g. potassium hydroxide **1** (0.066 mol) was dissolved in 20 ml of 2-methoxyethanol **2** upon heating in a microwave oven at 450 W for 45 sec. The experiment was held in a well-ventilated hood. At this stage, the solution turned yellowish, indicating the formation of intermediate **3**. After allowing it to cool down to room temperature, 3.9 ml of carbon disulfide **4** (0.066 mol) was added to the solution. Normally, the formation of a white precipitate of 2-methoxyethyl xanthate **5** can be observed. The reaction mixture is self-warmed. The content of the flask was allowed to cool down again, and substituted or unsubstituted 2-aminothiophenol, 2-aminophenol or 1,2-diaminobenzene **6a-6k** (0.066 mol) were added to it with stirring. The resulting mixture was heated up

* To whom all correspondence should be sent:
E-mail: ohtak@chem.uni-sofia.bg

in a microwave oven at 450 W for 2 min (note, the heating was stopped for about 15 sec on every 30 seconds, in order to avoid overheating of the sample). The potassium salt 7a-7k of the corresponding hetaryl thiol crystallizes and the solvent is almost evaporated (Scheme 1).

Preparation of 2-thioalkyl and 2-thioacyl benzazolium derivatives 8a-8k

Procedure A: The resulting potassium salt **7a-7k**, was dissolved in 50 ml water (in case of undissolved particles, the solution was filtered), followed by addition of ice and 6.25 ml dimethylsulfate (0.066 mol) to the filtrate. The solution was stirred for 15-30 min and the precipitate was filtered off. The pH of the final reaction mixture was maintained between 8–9. The resulting precipitate was dried. In the case of product **8f,** the reaction mixture was extracted with dichloromethane, and dried over anhydrous sodium sulfate. The product was filtered off, and the solvent was evaporated, yielding an oily product. The corresponding yields and melting point temperatures of the products are given in Table 1.

Procedure B: similar to the procedure reported above, except that the alkylation step was carried out with methyl iodide instead of dimethylsulfate. In addition, ultrasound irradiation was performed for 5 min in the presence of 50 ml acetone which was added to the aqueous solution of the potassium salt **7a-7k**. The resulting precipitate was filtered off. Again, the pH of the final reaction mixture should be in between 8-9. The precipitate was dried.

Procedure C: performed as procedure B. Herein S-acylation occured using benzoyl chloride. The reaction conditions and sonication time remained unaltered. Product **8h** is reported as novel.

2-(methylthio)-5-phenylbenzo[d]oxazole (**8h**):
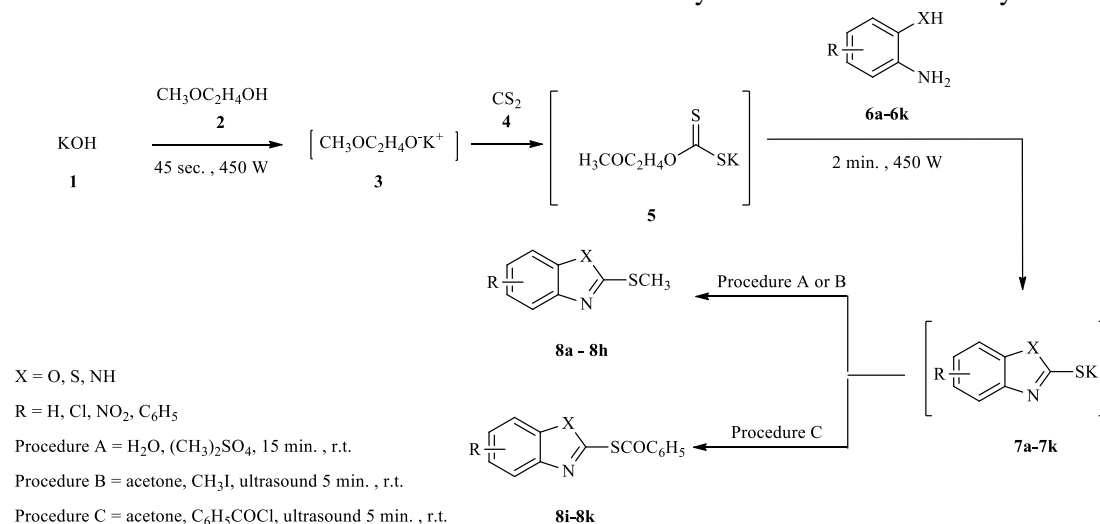
^{1}H NMR (500 MHz, DMSO-d$_6$, δ/ppm):2.79 (s, 3H, CH$_3$-S), 7.37-7.40 (m, 1H, ArH), 7.47-7.50 (m, 2H, 2 x ArH), 7.60 (dd, 1H, J 1.7, 8.4, ArH), 7.70-7.73 (m, 2H, 3 x ArH), 7.89-7.90 (*m*, 1H, ArH);
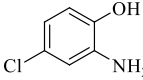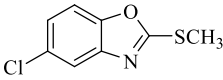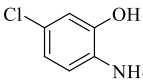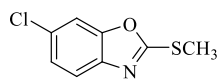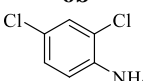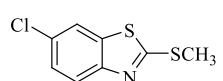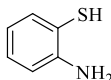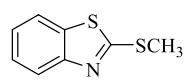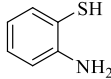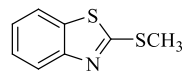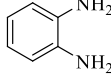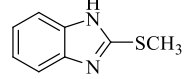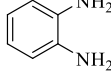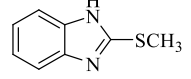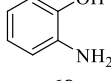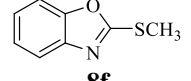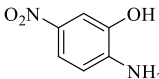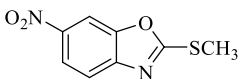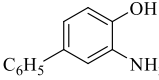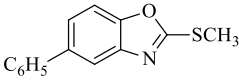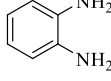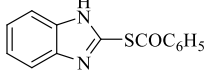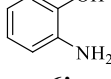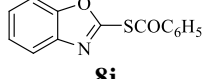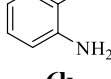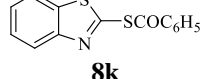
^{13}C NMR (125 MHz, DMSO-d6, δ/ppm): 14.7; 110.8; 116.7; 123.6; 127.6; 127.6; 127.8; 129.4; 129.4; 137.8; 140.4; 142.6; 151.5; 166.4;

RESULTS AND DISCUSSION

Based on the experimental part of the present work, we achieved the preparation of potassium salts of different benzothiazoles, benzoxazoles and benzimidazoles, which can subsequently be selectively S-alkylated or S-acylated. The reaction (four steps) can be run in one reaction vessel without isolating the intermediates. The first step involves the preparation of 2-methoxyethyl xanthate in 2-methoxyethanol, followed by the formation of potassium salts of substituted or unsubstituted benzothiazoles, benzoxazoles and benzimidazoles under microwave irradiation for a relatively short time. Due to the fact that the potassium salts of substituted or unsubstituted 2-mercaptobenzothiazoles, 2-mercaptobenzoxazoles and 2-mercaptobenzimidazoles are readily water soluble compounds, the final step (S-alkylation or S-acylation), is carried out using suitable alkylating or acylating agents in an aqueous solution at room temperature. The alkylation step using methyl iodide (**Procedure B**) or acylation (**Procedure C**), can be performed under ultrasound irradiation, in order to accelerate the experimental outcome.

To the best of our knowledge, the S-alkylation and S-acylation of hetaryl thiols at room temperature, promoted by the combination of microwave heating and ultrasound irradiation for the preparation of hetaryl thiols in a one-pot synthesis has not been reported. Herein, we present a highly reproducible one-pot synthesis of 2-thiomethylbenzazoles and 2-thioacylbenzazoles.

X = O, S, NH

R = H, Cl, NO$_2$, C$_6$H$_5$

Procedure A = H$_2$O, (CH$_3$)$_2$SO$_4$, 15 min. , r.t.

Procedure B = acetone, CH$_3$I, ultrasound 5 min. , r.t.

Procedure C = acetone, C$_6$H$_5$COCl, ultrasound 5 min. , r.t.

Scheme 1. One-pot preparation of 2-thioalkyl and 2-thioacyl benzazolium derivatives

Table 1. 2-Thiomethyl- and 2-thioacylbenzothiazoles, benzoxazoles and benzimidazoles

Entry	Starting compound (6)	Product (8)	Yield[a] (%) Procedure	Mp. / lit. Mp. (°C)
1	6a	8a	70 A	87-88 / 89 [12]
2	6b	8b	78 A	90-91 / 88-90 [11]
3	6c	8c	85 A	93-95 / 95 [13]
4	6d	8d	84 A	45-46 / 46 [14]
5	6d	8d	85 B	45-46 / 46 [14]
6	6e	8e	70 A	200-201 / 201-203 [15]
7	6e	8e	75 B	200-201 / 201-3 [15]
8	6f	8f	75 A	Oil [11]
9	6g	8g	75 A	191-192 / 193 [16]
10	6h	8h	89 A	75-77 [b]
11	6i	8i	95 C	264 / 265 [17]
12	6j	8j	85 C	84-85 / 83-85 [18]
13	6k	8k	87 C	130 / 129-131 [17]

[a] Isolated yield of crude product
[b] Novel compound

The final step to the synthesis of the title compounds involves an effectively accelerated selective S-alkylation or S-acylation reaction using ultrasonic irradiation with methyl iodide and benzoyl chlorides under mild conditions at room temperature. Such a unique combination of microwave heating and ultrasound irradiation is notably applied in the organic synthesis [19]. As an example, such a synthetic approach is applied for the preparation of biodiesel. The transesterification reaction in the study mentioned above was promoted by ultrasonic mixing and microwave irradiation of soybean oil. In the present work, the total reaction time was found to be significantly reduced compared to former studies [20].

Last but not least, such a combination is used in analytical processes [21], or applied in municipal and industrial wastewater treatment plants, in order to stabilize organic matter [22]. This process comprises four major microbiological degradation steps, such as hydrolysis, acidogenesis, acetogenesis and methanogenesis. Various patented constructions of microwave and ultrasonic apparatuses can also be found in the literature. This equipment is capable of performing numerous functions, which include ways of emitting microwave energy for heating, ultrasound energy to a given workload, whereas an overall control of both the microwave and the ultrasonic sources can be achieved [23].

For product **8h**, there are insufficient data in the literature. The only report [24] of this compound mentions its usage for the preparation of monomethine cyanine dyes, without providing any further information about it. This product was evaluated by ^{1}H –NMR, and ^{13}C -NMR spectra, as well as melting point temperature.

CONCLUSION

The newly developed synthetic approach has the following advantages: i) the reaction overall takes not more than 30 min; ii) the procedure is energy efficient, because of the application of MW heating and ultrasonic irradiation; iii) it combines selective S-alkylation and S-acylation reactions, therefore it can be applied to a wide range of hetaryl thiol derivatives; iv) it is carried out under mild conditions; v) the final products can readily be isolated; vi) the target products are obtained with high purity in good to excellent yields; vii) a small reaction volume is used.

REFERENCES

1. X. Fei, Y. Gu, Y. Ban, Zh. Liu, B. Zhang, *Bioorg. Med. Chem.*, **17**, 585 (2009).
2. T. G. Deligeorgiev, N. I. Gadjev, A. A. Vasilev, V. A. Maximova, I. I. Timcheva, H. E. Katerinopoulos, G. K. Tsikalas, *Dyes and Pigments,* **75**, 466 (2007).
3. Y. L. Fu, B. R. Zhang, S. Wang, X. X. Gao, L. Y. Wang, *Bull. Korean Chem. Soc.,* **34** (2), 489 (2013).
4. J. C. Marconato, L. O. Bulhões, M. L. Temperini, *Electrochim. Acta,* **43**, 771 (1998).
5. C. W. Yan, H. C. Lin, C. N. Cao, *Electrochim. Acta*, **45**, 2815 (2000).
6. M. Benmessaoud, K. Es-Salah, N. Hajjaji, H. Takenouti, A. Srhiri, M. Ebentouhami, *Corros. Sci.*, **49**, 3880 (2007).
7. S.-I. Fujiwara, N. Kambe, *Top. Curr. Chem.*, **251**, 87 (2005).
8. M. Alpegiani, A. Baici, P. Bissolino, P. Carminati, G. Cassinelli, S. Del Nero, G. Franceschi, P. Orezzi, E. Perrone, V. Rizzo, N. Sacchi, *Eur. J. Med. Chem.*, **27**, 875 (1992).
9. A. Duarte, W. Cunico, C. M. P. Pereira, A. F. C. Flores, R. A. Freitag, G. M. Siqueira, *Ultrasonics Sonochem.*, **17**, 281 (2010).
10. T. G. Deligeorgiev, S. S. Kaloyanova, N. Y. Lesev, J. J. Vaquero, *Monatsh. Chem.,* **142**, 895 (2011).
11. T. Deligeorgiev, S. Kaloyanova, N. Lesev, J. J. Vaquero, *Ultrasonics Sonochem.,* **17**, 783 (2010).
12. D.M. Fabricius, *US Patent 5707794* (1988).
13. M. Pays, M. Beljean, *Bull. Soc. Chim. France*, **11**, 3044 (1973).
14. B. R. Rani, U. T. Bhalerao, M. F. Rahman, *Synth. Commun.,* **20**, 3045 (1990).
15. J. Valdes, R. Cedillo, A. Hernandes-Campos, L. Yepez, F. Hernandes-Luis, G. Navarrete-Vazquez, A. Tapiq, R. Cortes, M. Hernandes, R. Castillo, *Bioorg. Med. Chem. Lett.* **12**, 2221 (2002).
16. H. Zinner, R. Reimann, A. Weber, *Chem. Ber.,* **93**, 2035–2040 (1960).
17. D. S. Dalal, N. S. Pawar and P. P. Mahulikar, *Organic Preparations and Procedures International,* **37** (6), 539 (2005).
18. M. Ueda, K. Seki, Y. Imai, *Synthesis*, 991, (1981).
19. D. S. Arun, B. M. Sudesh, C. P. Balkrishna, I. K. Bhanudas, *Inter. J. Pharma Sciences and Research*, **5** (6), 241 (2014).
20. M.-C. Hsiao, C.-C. Lin, *Inter. J. Energy and Power Engineering*, **2** (2) 54 (2013).
21. Z. X. Lou, H. X. Wang, S. Zhu, S. W. Chen, M. Zhang, Z. P. Wang, *Analytica Chimica Acta*, **716**, 28 (2012).
22. A. M. Yeneneh, T. K. Sen, S. H. Chong, H. M. Ang, A. Kayaalp, *Energy and Environmental Engineering*, **2**, 7 (2013).
23. M. L. Levinson, *US Patent 3419116* (1968).
24. G. E. Ficken, D. J. Edwards, C. W. Mowforth, T. J. Maternaghan, R. S., V. W. Dolden, *EP Patent* 324717 (1989).

ЛЕСЕН И БЪРЗ МЕТОД ЗА ПОЛУЧАВАНЕ В ЕДИН СЪД НА 2-ТИОМЕТИЛОВИ И 2-ТИОАЦИЛОВИ БЕНЗОТИАЗОЛИ, БЕНЗОКСАЗОЛИ И БЕНЗИМИДАЗОЛИ

Т. Г. Делигеоргиев, А. А. Курутос, Н. И. Гаджев, А. А. Алексиев

Софийски университет, Факултет по химия и фармация, 1 Дж. Баучер бул., 1164 София, България

(Резюме)

В настоящата статия е представен нов метод за получаване на 2-тиометил и 2-тиоацил бензазолиеви производни в един реакционнен съд. За целта са използвани о-аминотиофенол, о-аминофенол, и 1,2-фенилендиамин като изходни вещества. Новопредставения метод включва комбинация от микровълново нагряване и облъчване с микровълни, което води до изолиране на целевите продукти с високи до отлични добиви, без да е необходимо изолирането на междинни съединения.

A superhydrophobic quartz crystal microbalance based chemical sensor for NO$_2$ detection

K. D. Esmeryan*, V. Georgieva, L. Vergov, J. Lazarov

Georgi Nadjakov Institute of Solid State Physics, 72, Tzarigradsko Chaussee Blvd., 1784 Sofia

The gas sensitivity of 16 MHz carbon soot coated quartz crystal microbalances (QCMs) towards various NO$_2$ concentrations is investigated. The Scanning Electron Microscopy measurements reveal that the soot is deposited on the sensor surface irregularly, forming carbon nanospheres separated by nanoscale cavities. The inherent non-polar nature of the soot, along with its estimated root mean square roughness (R_{rms}) of 130 nm, transform the quartz surface into a superhydrophobic (SH) one, characterized with high static contact angle (~153 °) and low contact angle hysteresis (~1 °). Such surface configuration induces 15 Hz resonance frequency downshift of the SH QCM at low NO$_2$ concentrations up to 500 ppm. Furthermore, the sensor demonstrates reversible gas sorption ability in the same gas range. Further gradual increase in the NO$_2$ concentration up to 5000 ppm leads to an additional sensor response of 38 Hz; however, after dry air scavenging the sensor reaches its baseline with a slow rate of ~0.33 Hz/min. In addition, upon ambient humidity increase of 45 %, the SH QCM shifts down its resonance with 45 Hz, whereas the 16 MHz WO$_3$ coated counterpart with 212 Hz. These results clearly indicate the advantage of the soot coated QCM, which could be used for continuous *in situ* monitoring of air pollutants with negligible cross sensitivity to humidity of 1Hz/% RH.

Key words: Quartz Crystal Microbalance, Superhydrophobicity, Gas-sensitivity, Carbon soot.

INTRODUCTION

Nowadays, one of the major problems related with the environmental protection is the air pollution by toxic gases [1]. In particular, the nitrogen dioxide (NO$_2$) is an irritant gas released during fuel combustion, which at high concentrations is responsible for the formation of acid rain, ground-level ozone and enhancement of the global green house effect [2]. Therefore, over the last few years, the detection of NO$_2$ has been an aim of various research groups around the world [3-5]. The methods for gas analysis are based on gas chromatography, mass spectrometry, infrared spectrometry and cavity enhanced absorption spectroscopy (CEAS). Each sensing mechanism has advantages such as high sensitivity and low detection limit, and disadvantages, e.g.., requirement of grab-samples and off-site analysis, time consumption, etc. As an alternative, many researchers have focused on the use of quartz crystal microbalance (QCM) based chemical sensors due to their miniature size, low power consumption, high sensitivity and resolution, fast response-recovery time and relatively low cost [6-10]. During "real-world" monitoring of the quality of air, two external factors are of crucial importance

for the accurate QCM performance, namely the ambient temperature and humidity. While the methods of temperature control are sufficiently well documented [11-13], a very few is known about the compensation of relative humidity (RH). The latter has an interfering influence on the sensor resolution and sensitivity, as the adsorbed water vapor impedes the interaction between the gas analyte and the sensitive layer [14]. Furthermore, the changes in ambient humidity induce cross sensitivity of the QCM, which cause measurement errors, similar to the temperature effect [15, 16]. Recently, the humidity compensation has been implemented by means of a dual QCM oscillator circuit [17] or computational algorithms [18]. Such techniques are accurate, but they are insufficient in regard to the reduced gas sensitivity, caused by the water vapor-occupied active adsorption sites of the sensing surface [14]. This drawback could be overcome by utilizing a superhydrophobic (SH) sensitive coating. With their extreme non-wettability, expressed through static water contact angle greater than 150° and contact angle hysteresis ≤5° [19], the superhydrophobic coatings stand out as facile solution, because they inhibit the accumulation of water vapor on solid surfaces. This phenomenon may be explained through the heterogeneous nucleation theory [20] and has been verified for QCM coated with SH

silica film [21]. Unfortunately, these experiments are inconsistent with the theory, showing higher frequency shifts of the SH QCM compared to an uncoated device. According to Sauerbrey's equation [22], this is associated with larger amount of water vapor adsorbed on the SH sensor surface.

Therefore, the primary objective of this paper is to investigate the applicability of 16 MHz superhydrophobic carbon soot coated QCMs for *in situ* detection of various NO_2 concentrations. In addition, our experiments will be used to validate the hypothesis that superhydrophobicity inhibits the accumulation of water vapor on solid surfaces. The latter is crucial if the sensor is intended to operate in "real-world" environmental conditions. Section 2, gives brief description of the fabrication process and surface characterization of the soot coatings. Furthermore, the gas sensing measurement setup is discussed. Section 3, summarizes the experimental results for the gas sorption-desorption ability of the sensitive layer. Also, the relation between the surface wettability and humidity sorption is considered in terms of the heterogeneous nucleation theory.

EXPERIMENTAL

Surface coating fabrication

The technique we used is based on the incomplete combustion of carbon nanoparticles contained in a rapeseed oil mixture [23]. Firstly, 100 ml of rapeseed oil are added to an evaporating glass dish. A gauze based wick is immersed in the oil and then ignited until a black c a r b o n fume occurred. In this study, a few microscope glass slides and 16 MHz AT-cut QCMs were exposed over the fume, which caused deposition of carbon soot on the substrate surface. The wettability of soot coatings is investigated through static contact angle, contact angle hysteresis and roll-off angle measurements for droplets of water, by using a high speed camera Nac Memrecam HX-6. These were found to be in the range of 151-154 °, 0.2-4 ° and 2-10 °, respectively, confirming superhydrophobic surfaces with mobile droplet behavior [19].

Surface characterization

The surface morphology and roughness were examined by Scanning Electron Microscopy (SEM) and Atomic Force Microscopy (AFM). The experiments were carried out using a JSMT 200 (Jeol) SEM with magnification of 50k and an AFM Multimode V (Bruker, Santa Barbara, CA). During SEM analysis, the samples were studied and imaged in secondary electron mode. The observations were preceded by a vacuum

deposition of several nanometer thick films of carbon and gold. AFM imaging was performed in tapping mode and height, amplitude and phase images were recorded. At least two different points on the sample surface were explored. For all measurements, the image resolution was 512 lines per scan direction. Silicon cantilevers for soft and fragile surfaces with a cantilever length of 125 μm and Al reflective coating on the backside (HQ-NSC19-Al BS, MikroMasch) were used in the experiments. These cantilevers have a nominal resonance frequency of ca. 65 kHz and a typical force constant of 0.5 N/m. The tip nominal radius is less than 8 nm. For 1 μm scan, the used scan rate was 0.45 Hz.

Gas sensing measurement setup

The gas sensing properties of 16 MHz carbon soot coated QCMs were studied by exposure to different NO_2 concentrations. The QCMs were fabricated on AT-cut quartz plates. On both sides of the quartz substrate were deposited gold electrodes with thickness t~60 nm and diameter d~4 mm. A detailed description of the gas experimental setup is given elsewhere [24. In s u m m a r y, the sensor was placed in a gas-test chamber, whose temperature was kept constant at 26 °C. The concentration of NO_2, flowing into the thermally-stabilized measurement chamber, was varied between 10-5000 ppm. The sorption ability of the soot layers was investigated after initial resonance frequency stabilization as a result of dry air scavenging. Afterwards, the desired NO_2 concentration was added in the chamber and subsequent gas sorption on the sensor surface was observed via resonance frequency downshifts. This process was monitored until the system reached dynamic equilibrium and the frequency fluctuations remained within ±0.5 Hz. Finally, the gas chamber was scavenged again and a frequency backshift was observed. During the gas experiments, the QCM's resonance behavior was monitored via frequency counter HM8123 Hameg instruments and all experimental data were recorded on a personal computer. The measurement accuracy was found to be ~0.1 Hz.

RESULTS AND DISCUSSIONS

Electrical characteristics of an uncoated and SH QCM in air

The measurements were carried out using two quartz crystal resonators, intended to operate as QCMs, with a resonance frequency f_r ~16 MHz,

dynamic resistance R_S=16.5–18.5 Ω and Q-factor of 19385–22185. Table 1 summarizes these electrical characteristics in air, prior to and after superhydrophobization. The deposition of carbon soot causes a proportional frequency downshift in the range of 643–814 Hz, a decrease in the Q-factor to 7913–8292 and a corresponding dynamic resistance increase of 37.4–43 Ω.

Table 1. Electrical characteristics of 16 MHz QCMs prior to and after superhydrophobization

QCM №	QCM status	f_r (MHz)	Q factor	R (Ω)
1	Prior to	15.958339	19385	18.5
	After SH	15.957525	8292	37.4
2	Prior to	16.022646	22185	16.5
	After SH	16.022003	7913	43

Gas sensing properties of the SH QCM

The sorption properties of the carbon soot coatings were investigated for NO₂ concentrations in the range of 10–5000 ppm. The initial gas-sensitivity of the SH QCM was determined at a concentration of 100 ppm and its real-time frequency response is illustrated in Figure 1.
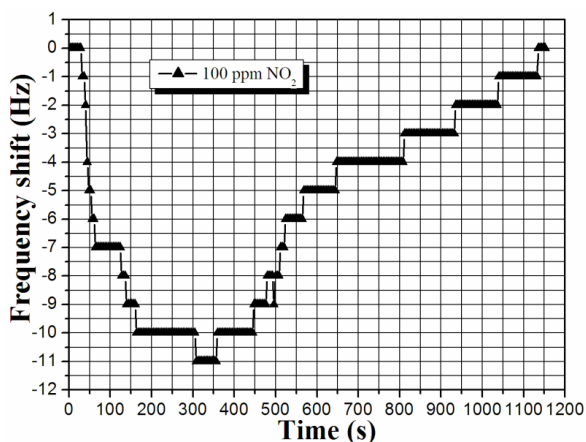
Fig. 1. Real-time frequency response of a SH carbon soot coated QCM at NO₂ concentration of 100 ppm.

As seen from Fig. 1, during the gas sorption there are two main areas, namely fast and slow one. In the first 52 s, the resonance frequency decreases with 7 Hz, while in the next 242 s the changes are within 4 Hz. The measured sorption rate is 2.19 Hz/min, which corresponds to 2.65 times faster process of sorption compared to the desorption one (~0.85 Hz/min). Similar fast and slow areas are registered when the adsorbed NO₂ gas is flushed away with a dry air flow. At the beginning of desorption, the resonance frequency recovers with 7 Hz for 300 s, while for the next 500 s the frequency

shift is only 4 Hz.
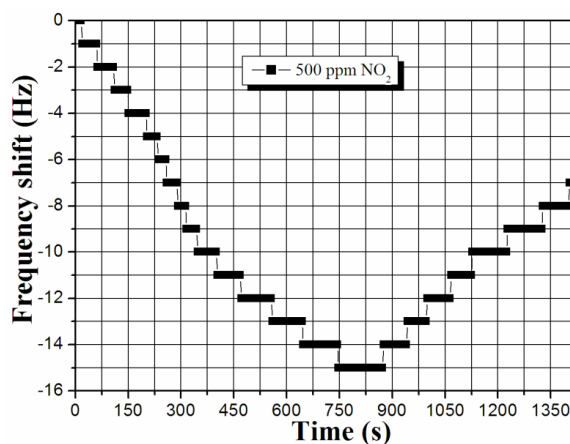
Fig. 2. Time-frequency characteristic of a SH QCM towards NO₂ concentration of 500 ppm.

Figure 2 represents the time-frequency characteristic of the SH QCM at higher NO₂ concentrations of 500 ppm.

In this case, the desorption rate is very slow (0.33 Hz/min); therefore, the recovery of resonance frequency is terminated at 1400 s. As evident from Figs. 1 and 2, the increased gas concentration (from 100 to 500 ppm) leads to an increase in the time for which the sensor system reaches dynamic equilibrium. This is expected since more gas molecules provided in the test chamber, more molecules would be adsorbed at the expense of a longer sorption time. The sorption-desorption analyses for the above range of gas concentrations are conducted for a period of 12 min. Figure 3 shows the resonance behavior of the SH QCM towards the entire NO₂ concentration range of 50-5000 ppm.
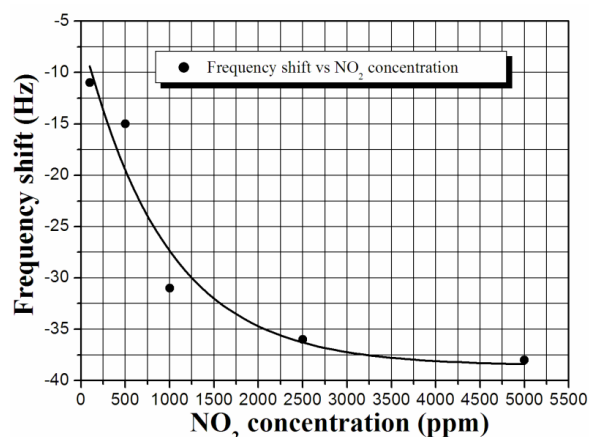
Fig. 3. Resonance frequency shift of a 16 MHz SH QCM towards NO₂ concentrations in the range of 50-5000 ppm.

For the chosen gas range, the SH QCM exhibits exponential resonance behavior with an overall

1041

downshift of 38 Hz. At low concentrations, up to 500 ppm, the sorption process is reversible and the sensor system recovers its initial electrical parameters (f_r, R_S and Q-factor). However, at higher concentrations (above 500 ppm), the sensor responds to the gas analyte, but the recovery time is significantly slower (0.33 Hz/min). These results reveal that the SH carbon soot coated QCM is appropriate for multiple measurements at low NO₂ concentrations, while above 500 ppm the sensor system can be used only for single NO₂ detection. For the sake of completeness, the coating's wettability was verified again through static contact angle, contact angle hysteresis and roll-off angle measurements. The obtained numerical values were 153 °, 1 ° and 4 °, respectively, thereby showing that after several sensor cycles, the layer is still superhydrophobic and shows no aging.

Humidity sorption and surface-characterization of the SH QCM

In order to validate the hypothesis that superhydrophobicity mitigates the condensation of water vapor on solid surfaces, further experiments were performed. The humidity-frequency responses of the SH QCM and a WO₃ coated hydrophilic QCM were recorded after saturation in a dry synthetic air flow and subsequent exposure to 45 % ambient humidity, and temperature T of 25 °C. The inclusion of a hydrophilic QCM allowed us to assess the extent to which superhydrophobicity inhibits the sorption of water vapor. Figure 4 shows the real-time frequency response of both devices towards 45 % RH.
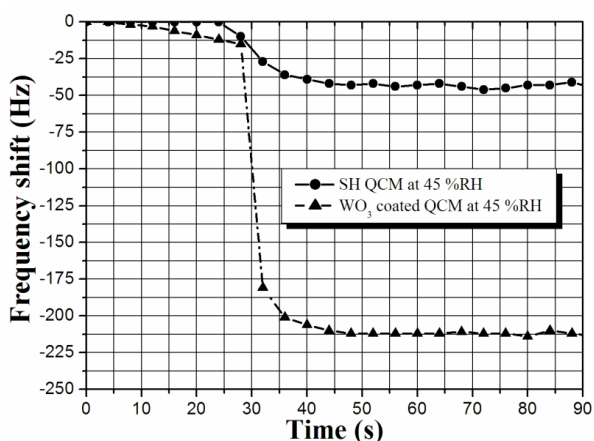
Fig. 4. Humidity-frequency response of a SH QCM and a WO₃ coated QCM in dry synthetic air and after exposure to 45 % RH.

As evident, upon exposure to 45 % RH and T ~25 °C, the resonance frequency of the SH QCM shifts down with approximately 45 Hz, against

212 Hz reduction for the WO₃ coated QCM. These data indicate ~5 times higher humidity sensitivity of the latter in comparison with the SH QCM. Therefore, our sensor device may operate in "real-world" environmental conditions with negligible cross sensitivity to humidity of 1Hz/% RH. In turn, this would substantially improve its sensor performance towards those of the commonly used metal oxide film coated QCMs. These observations are in good agreement with the heterogeneous nucleation theory [20]. It states that at equal other conditions the process of condensation depends on the surface wettability. For hydrophilic surfaces the energy barrier determining the phase transition is low due to the high surface free energy. For the superhydrophobic coatings; however, the latter is low. Therefore, the energy barrier is sufficiently high to ensure low nucleation (condensation) rate [20].

To compare the moisture sorption capacity of soot layers with their surface morphology, we performed SEM and AFM analyses. Figure 5 a) and b) shows 2-D and 3-D images of the carbon soot coated sensor surface.

a)

b)
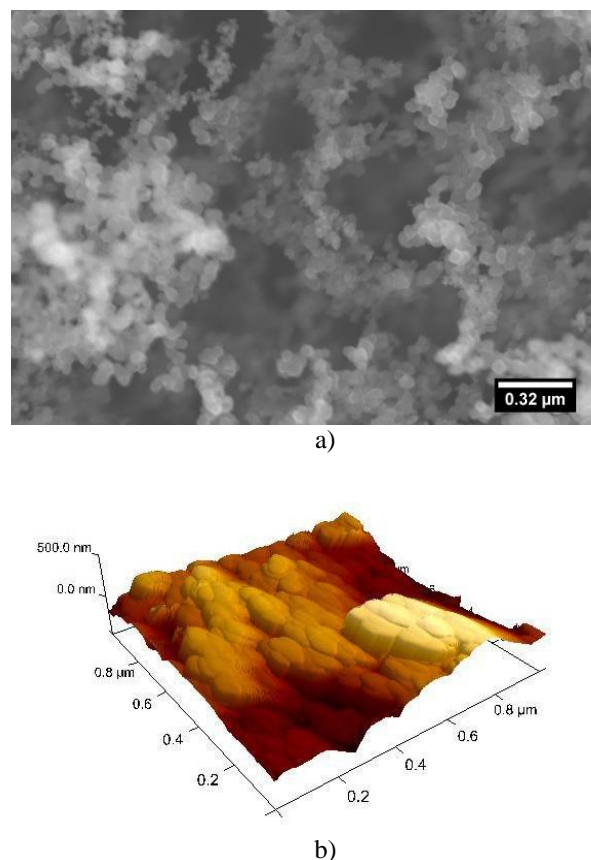
Fig. 5. a) 2-D SEM and b) 3-D AFM images of the carbon soot coated QCM.

The images above clearly illustrate that the soot precipitates on the crystal surface irregularly,

forming islands and cavities in the nanometer scale. This leads to an irregular surface topography composed of nanospheres and nanocavities. The root mean square roughness (R_{rms}) of the non-polar soot layer is estimated to be 130 nm, which converts the sensor surface into a superhydrophobic one. Similar results are achieved in [23] and [25], where carbon soot is deposited on glass slides and underlying epoxy resin coatings.

CONCLUSIONS

In this paper we presented systematic experimental investigations on the gas sorption ability of superhydrophobic carbon soot coated QCMs. The surface characterization analyses show that the non-polar and rough soot coating alters the sensor surface into a superhydrophobic one. As a result, superhydrophobicity induces approximately 5 times lower humidity sensitivity of the carbon soot coated QCM compared to a WO_3 coated QCM. Furthermore, the SH QCMs demonstrate reversible gas sorption at low NO_2 concentrations, up to 500 ppm, and insufficient desorption at higher concentrations. These results validate the hypothesis that superhydrophobicity mitigates the sorption of water vapor on the sensor surface. In turn, this opens a new venue in chemical sensing for the development of QCM based NO_2 detectors with negligible cross sensitivity to the ambient humidity.

REFERENCES

1. G. P. Macey, R. Breech, M. Chernaik, C. Cox, D. Larson, D. Thomas, D. O. Carpenter, *Environ. Health*, **13**, 82 (2014).
2. P. Schneider, W. A. Lahoz, R. van der A, *Atmos. Chem. Phys.*, **15**, 1205 (2015).
3. S. R. Drescher, S. D. Brown, *J. Chrom. A*, **1133**, 300 (2006).
4. J. Liu, F. Zhang, B. L. Zhu, C. Y. Xia, *Chin. J. Ind. Hyg. Occup. Desea.*, **11**, 862 (2011).
5. J. Wojtas, Z. Bielecki, T. Stacewicz, J. Mikolajczyk, R. Medrzycki, B. Rutecka, *Proc. in PIER Symp.* 2012, p. 87
6. M. Matsuguchi, Y. Kadowaki, M. Tanaka, *Sens. Act. B Chem.*, **108**, 572 (2005).
7. A. Fort, M. Innocenti, M. L. Foresti, M. Mugnaini, I. Pasquini, L. Pigain, S. Rocchi, V. Vignoli, *Proc. in IEEE Adv. Sens. Interfaces*, 184 (2009).
8. C. Y. Yang, M. J. Hwang, D. W. Ryu, J. H. Park, M. S. Ryu, H. Moon, *J. Nanosci. Nanotechnol.*, **11**, 7189 (2011).
9. A. L. Ndiaye, J. Brunet, C. Varenne, P. Bonnet, A. Pauly, M. Dubois, K. Guerin, B. Lauron, *Key Eng. Mater.*, **605**, 75 (2014).
10. V. Georgieva, M. Alexandrova, P. Stefanov, A. Grechnikov, V. Gadjanova, T. Dilova, Ts. Angelov, *J. Phys. Conf. Series*, **558**, 012037 (2014).
11. M. Kimura, Y. Liu, R. Sakai, S. Sato, T. Hirai, T. Fukawa, T. Mihara, *Sens. and Mater.*, **23**, 359 (2011).
12. Y. Kim, D. E. Pierce, Joint meeting *EFTF-IEEE IFCS*, **2**, 1001 (1999).
13. S. Bruckenstein, M. Michalski, A. Fensore, A. Hillman, *Anal. Chem.*, **66**, 1847 (1994).
14. M. Boutamine, A. Bellel, S. Sahli, Y. Segui, P. Raynaud, *Thin Solid Films*, **552**, 196 (2014).
15. V. V. Quang, V. N. Hung, L. A. Tuan, V. N. Phan, T. Q. Huy, N. V. Quy, *Thin Solid Films*, **568**, 6 (2014).
16. P. Sun, Y. Jiang, G. Xie, X. Du, J. Hu, *Sens. and Act. B-Chem.*, **141**, 104 (2009).
17. Y. Ushimi, Y. Ito, H. Horiuchi, M. Kadota, Y. Nozaki, Y. Hotta, S. Shiratori, *IEEJ Trans. Sens. and Micromach.*, **133**, 184 (2013).
18. B. Mumyakmaz, A. Özmen, M. A. Ebeoglu, C. Tasaltin, I. Gűrol, *Sens. and Act. B-Chem.*, **147**, 277 (2010).
19. P. Roach, N. J. Shirtcliffe, M. I. Newton, *Soft Mater*, **4**, 224 (2008).
20. R. P. Sear, Nucleation: *J. Phys: Condens. Matter*, **19**, 3 033101, (2007).
21. N. Andreeva, T. Ishizaki, P. Baroch, N. Saito, *Sens. and Act. B-Chem.*, **164**, 15 (2012).
22. G. Z. Sauerbrey, *Physics*, **155**, 206 (1959).
23. M. Qu, J. He, B. Cao, *Appl. Surf. Sci.*, **257**, 6 (2010).
24. V. Georgieva, P. Stefanov, L. Spassov, Z. Raicheva, M. Atanassov, T. Tincheva, E. Manolov, L. Vergov, *J. Optoelect. Adv. Mater.*, **11**, 1363 (2009).
25. K. D. Esmeryan, G. McHale, C. L. Trabi, N. R. Geraldi, M. I. Newton, *J. Phys. D: Appl. Phys.*, **46**, 345307 (2013).

ХИМИЧЕСКИ СЕНЗОР ЗА ОТКРИВАНЕ НА NO_2, БАЗИРАН НА СВРЪХХИДРОФОБНА КВАРЦОВА МИКРОВЕЗНА

К. Д. Есмерян, В. Георгиева, Л Вергов, Й. Лазаров

Георги Наджаков Институт по физика на твърдото тяло, 72, Цариградско шосе, бул 1784 София

(Резюме)

Изследвана е газочувствителността на 16 МХц Кварцови Микровезни (КМВ), покрити със слой от въглеродни сажди, спрямо различни концентрации на NO_2. Анализите от сканиращ електронен микроскоп показват, че саждите се характеризират с неправилна подредба върху сензорната повърхност, образувайки въглеродни наносфери разделяни от наноразмерни пори и празнини. Неполярната природа на въглеродните наночастици заедно със средноквадратичната награпавеност на покритието от 130 nm преобразуват кварцовата повърхност в свръххидрофобна, характеризираща се със стойности на ъгъла на омокряне и хистерезис на ъгъла на омокряне от съответно 153 ° и 1 °. Подобна конфигурация на покритието предизвиква 15 Хц понижение в резонансната честота на свръххидрофобната КМВ при ниски концентрации на NO_2 до 500 ppm. Освен това, сензорът демонстрира обратима газосорбционна способност в същия диапазон от газови концентрации. Последващото постепенно увеличение на количеството NO_2 до 5000 ppm води до допълнителен сензорен отклик от 38 Хц. Въпреки това обаче, след продухване със сух въздух сензорът възстановява своята честота с много ниска скорост (~0.33 Хц/мин.). В допълнение, при промяна на относителната влажност на въздуха с 45 %, свръххидрофобната КМВ понижава честотата си само с 45 Хц, докато нейният аналог покрит с WO_3 с цели 212 Хц. Тези резултати ясно показват преимуществото на КМВ покрита с въглеродни сажди, изразяващо се в това, че тя може да бъде използвана за постоянен контрол на съдържанието на азотен диоксид във въздуха, при пренебрежима чувствителност на резонансната ѝ честота към промени във влажността на околната среда.

Silver nanoparticle forms with new organometallic compounds enhance antimicrobial activities

E. A. El-Sawi[*], M. A. Hosny

*Department of Chemistry, Faculty of Women for Arts, Science and Education
Ain Shams University, Heliopolis, Cairo, Egypt*

Metallated heterocyclic compounds (4-9) were obtained from the reaction of 2-(2-oxo-2*H*-pyrano[3,2-*h*] quinolin-4-yl) acetic acid (1) and 4-(2,2-dihydroxy-vinyl)-2*H*-pyrano[3,2-*h*] quinolin-2-one (2) and their derivative (3) with Co(II) and Cu(II) acetates. Elucidation of the structures were based on their elemental analyses, IR, ^{1}HNMR, and MS. The prepared silver nanoparticles were confirmed by transmission electron microscopy (TEM) and UV spectra. The antimicrobial activities of the all products with their silver nanoparticle forms were investigated to compare their effect with respect to the parent new compounds. The results indicated that silver nanoparticles increased by 12-170% and can be used as effective growth inhibitors for microorganism.

Key words: pyrano-quinoline-metallation-antimicrobial- Silver nanoparticles.

INTRODUCTION

The antimicrobial activity of silver nanoparticles (Ag-NPs), gold nanoparticles and platinum nanoparticles (Pt-NPs) in aqueous solution were investigated. The minimum inhibitory concentration (MIC) of (Ag-NPs) for *S.aureus* and *E.coli* were 5 and 10 ppm, respectively, but the (Au-NPs) stabilized with sodium dodecylsulfate (SDS) did not show antimicrobial activity. Also the (Pt-NPs) stabilized with poly-(N-vinyl-2-pyrrolidone) (PVP) or (SDS) did not show antimicrobial activity for the test organisms [1]. Silver had been in use in the form of metallic silver, silver nitrate, silver sulfadiazine for the treatment of burns, wounds, several bacterial infections and metallic silver in the form of silver nanoparticles had made a remarkable comeback as a potential antimicrobial agent [2]. Jiang et al. [3] reported that gold and silver nanoparticles coated with antibodies can regulate the process of membrane receptor internalization. The silver nanoparticles were found to accumulate in the bacterial membrane.

A membrane with such morphology exhibited a significant increase in permeability, resulting in death of the cell [4]. The antimicrobial activity of silver nanoparticles was investigated against yeast, *Escherichia coli*, and *Staphylococcus aureus* [5]. Quinolines form an interested and important group of compounds; they possess excellent application for their pharmacological properties. Quinoline derivatives 2-(2-oxo-2*H*-pyrano[3,2-*h*]quinolin-4-

yl) acetic acid , 4-(2,2- dihydroxy-vinyl)-2*H*-pyrano[3,2-*h*]quinolin-2-one, their derivatives obtained via their reactions with N-(2-amino ethyl) propane-1,3-diamine and their palladated products exhibited antimicrobial activity as well as their silver nanoparticle forms also some exhibit anticancer activity against breast cancer [6]. Quinolines showed antimicrobial [7], antimalarial [8], anti-inflammatory [9], antitumor [10], antioxidant [11], and antiplatelet [12] activity. Pyranoquinoline also showed antimicrobial activities [13]. Many derivatives of this heterocyclic compounds are biologically active and are found to be useful intermediates for many medicinal products [14], [15], as well as derivatives containing pyrazole and indoline moieties have excellent antibacterial and antifungal activities [16]. Schiff base 2-(4-methoxybenzylidene amino) benzene-thiol, its metallation with mercury (II), nickel (II), palladium (II) gave compounds exhibited antimicrobial and anticancer activity [17]. Organo-mercury compounds via metallation of some new Schiff bases were also synthesized [18], [19].

In continuation to our previous work the study was directed to synthesize new organometallic compounds containing Co (II) and Cu (II) to study the effect of silver nanoparticles on their antimicrobial activity.

RESULTS AND DISCUSSION

New compounds (4) and (5) were obtained from the reactions of compounds 2-(2-oxo-2*H*-pyrano[3,2-*h*] quinolin-4-yl) acetic acid (1) and 4-

---

(2,2- dihydroxy-vinyl)-2*H*-pyrano[3,2-*h*] quinolin-2-one (2) [6] with cobalt acetate. The reactions may proceed as follows, cf. Scheme (1).

Elucidation of the structures based on their elemental analyses, IR, ^{1}HNMR and MS spectra. The IR spectra showed ν_{OH} at 3424 cm^{-1}, $\nu_{C=O}$ for carboxylate attached to cobalt at 1610 cm^{-1} (antisymmetrical) & 1420 cm^{-1} (symmetrical stretching), ν_{Co-C} at 536 cm^{-1} and ν_{Co-o} at 458 cm^{-1} for compound (4), and broad absorption band at 3650- 2600 cm^{-1} for ν_{OH} & at 1710 cm^{-1} for $\nu_{C=O}$ due to carboxylic group and ν_{Co-C} at 529 cm^{-1} and ν_{Co-C} at 469 cm^{-1} for compound (5).
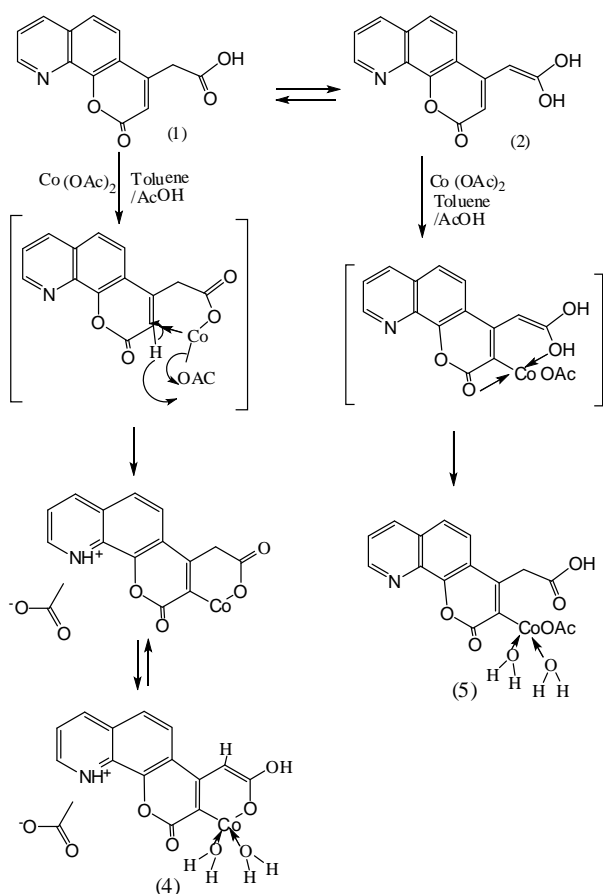
Scheme 1.

The ^{1}HNMR spectrum for compound (4) showed δ 11.93 ppm (1H, for OH), δ 9.46 - 7.01 ppm (5H, for aromatic protons) and δ 6.8 ppm (1H, for methine proton) and δ 2.20 ppm (3H, for methyl protons). The ^{1}HNMR spectrum for compound (5) showed δ 12.0 ppm (1H, for OH), δ 8.40-7.01 ppm (5H, for aromatic protons) and δ 2.80 ppm (2H, for methylene protons).

The MS spectra for compounds (4) & (5) showed $M^{\rceil +}$· at m/z 372 (40.60%), the base peak at 57 (100%) can be attributed to $C_3H_7N^{\rceil +}$· &

$M+1^{\rceil +}$ at m/z 373 (1.02 %)) the base peak at 370 (100%). can be attributed to $M-2^{\rceil +}$. Compounds (6) and (7) were obtained from the reactions of compounds (1) and (2) with copper acetate. The reactions may proceed as follows cf. Scheme (2). The structures were inferred from their elemental analyses, IR, ^{1}HNMR and MS spectra. The IR spectrum for compounds(6) showed ν_{OH} at 3394 cm^{-1}, $\nu_{C=O}$ for carboxylate ion at 1610 cm^{-1} (antisymmetrical) & 1405 cm^{-1} (symmetrical stretching)and ν_{Cu-C} at 577 cm^{-1}, while compound (7) showed two absorption bands at 3500& 3398 cm^{-1} for two ν_{OH} & at 1633 cm^{-1} for $\nu_{C=O}$ due to carboxylic group and ν_{Cu-C} at 580 cm^{-1}.

The ^{1}HNMR spectrum for compound (6) showed δ 11.90 ppm (1H, for OH), δ 9.50- 7.45 ppm (5H, for aromatic protons) and δ 6.27 ppm (1H, for methane proton) and δ 2.39 ppm (3H, for methyl protons).
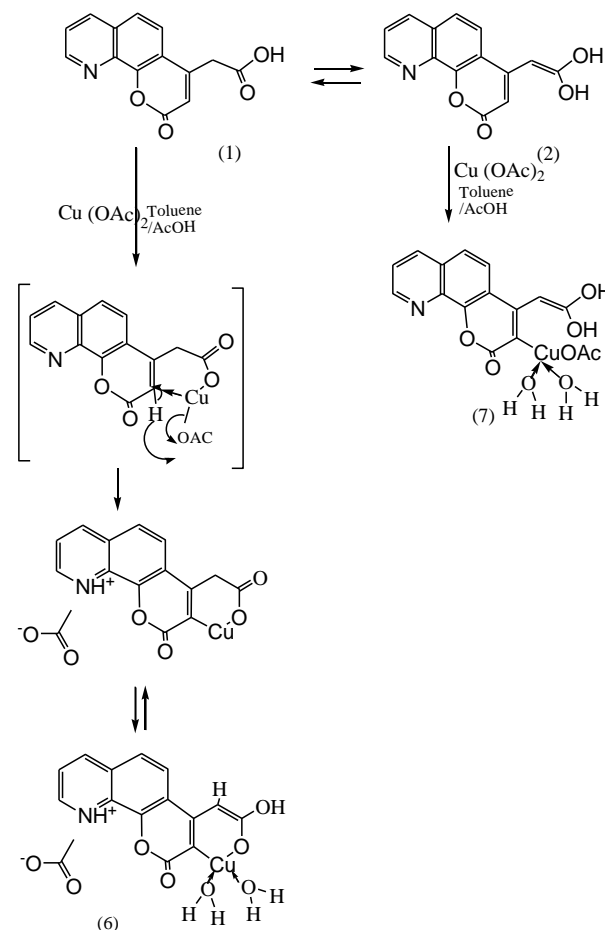
Scheme 2.

The ^{1}HNMR spectrum for compound (7) showed δ 11.84 ppm (2H, for2 OH), δ 9.79-7.04 ppm (5H, for aromatic protons), δ 6.44 ppm (1H, for methine proton) and δ 2.28 ppm (3H, for CH₃).

The MS spectrum for compounds (6) showed M at m/z 377 (24.53%), the base peak at 353 (100%) can be attributed to $M-24^{+}$ and the MS spectrum for (7) showed M at m/z 377(8.97 %)) the base peak at 69 (100%) can be attributed to $C_4H_7N^{+}$.

Metallation of compound (3) [6] with cobalt acetate and copper acetate.

The metallation of compound (3) [6] with cobalt acetate and copper acetate gave rise to new metallated compounds (8) and (9) via coordination to nitrogen then followed by electrophilic substitution in the o-position cf. Scheme (3).

Elucidation of the structure of compound (8) based on IR, ¹HNMR and MS spectra. The IR spectrum showed new absorption bands two bands for v_{NH2} at 3494, 3420 cm⁻¹, v_{NH} at 3321 cm⁻¹ ,v_{CHstr} at 2953 cm⁻¹, $v_{C=O}$ at 1653 cm⁻¹, $v_{C=C\ Alken}$ at 1614 cm⁻¹, $v_{C-H\ bending}$ at 1463 cm⁻¹ , v_{C-Co} at 548 cm⁻¹, v_{O-Co} at 463 cm⁻¹. The ¹HNMR spectrum showed δ 7.8-6.67 ppm (4H, for aromatic protons), δ 6.63ppm (1H, for=C-H proton), δ 3.96 ppm (1H, for O-C-C= CH proton), δ 2.7, 2.8 ppm (4H, for2 CH₂ protons attached to NH and NH₂), δ 1.6, 2.3, 2.6 ppm (6 H, for 3CH₂ protons), δ2.1 ppm (3H, for 3 OH protons). The absence of 8.9 ppm indicated that substitution reaction took place at this position via coordination with N in the pyridine ring followed by electrophilic substitution in the aromatic moiety.The MS spectra showed the M+2
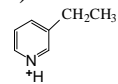
at m/z 431(1.25%) and the base peak at m/z 108(100%) due to

The IR spectrum of compound (9) indicated the presence of new absorption bands for v_{NH2} two bands at 3493,3419 cm⁻¹, $v_{C=O}$ at 1657 cm⁻¹, v_{C-Cu} at 549 cm⁻¹ and v_{O-Cu} at 463 cm⁻¹. The ¹HNMR spectrum showed δ 7.8-7.2 ppm (4H, for aromatic protons), δ 6.70 ppm (1H, for =C-H proton), δ 4.3 ppm (1H, for O-C-C= CH proton), δ 2.7, 2.9 and 3.2 ppm (4H, for2 CH₂ protons attached to NH and NH₂ , and 4H for 2CH₂ attached to N-C=O), δ2.1 ppm (3H, for 3 OH protons) [20] and δ 1.8 ppm (2 H, for CH₂ protons). The MS spectrum showed the $M+1^{+}$ at m/z 435 (36.32%) and the base peak at

m/z 108(100%) due to .

BIOLOGICAL ACTIVITY

Measurement of Antimicrobial Activity using Diffusion disc Method

A filter paper sterilized disc saturated with measured quantity of the sample is placed on a plate containing solid bacterial medium (nutrient agar broth) or fungal medium (Doxs medium) which has been heavily seeded with the spore suspension of the tested organism. After incubation, the diameter of the clear zone of inhibition surrounding the sample is taken as a measure of the inhibitory power of the sample against the particular test organism [21-24].
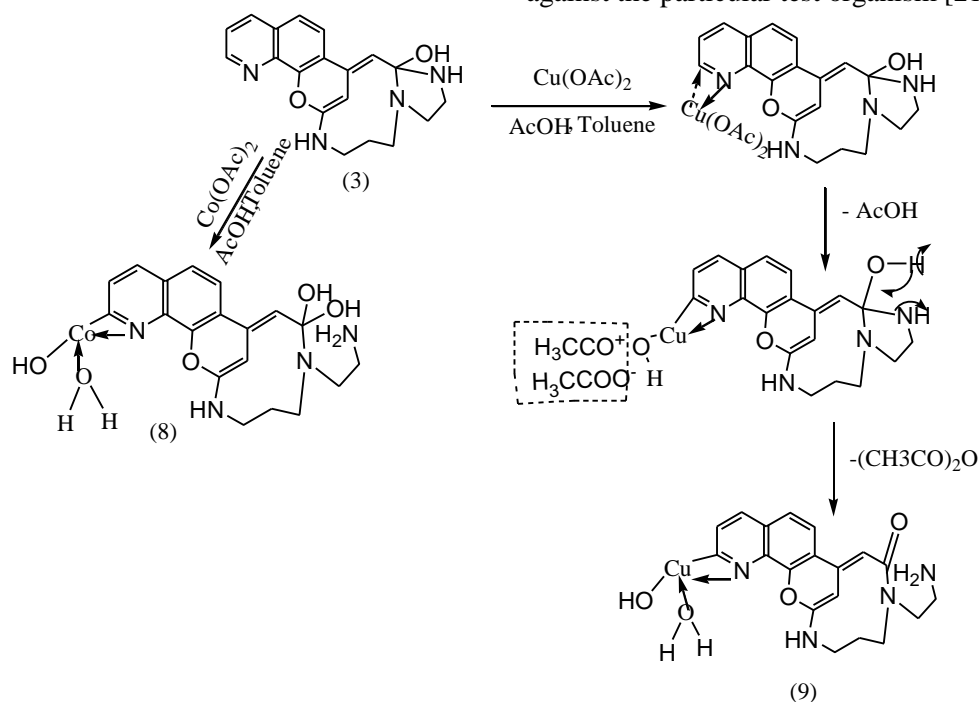
Sheme 3.

Table 1. The antimicrobial activities of the compounds (5-8 & 10-11) and their silver nano-forms.

Compds. No.	Candida albicans	Fold increase% (nano.-parent)/ parent X100=	Aspergillus Niger	Fold increase% (nano.-parent)/ parent X100=	Staphylococcus aureus (G+)	Fold increase% (nano.-parent)/ parent X100=	Escherichia coli (G-)	Fold increase% (nano.-parent)/ parent X100=
Tetracycline Antibacterial	------		------		20		22	
Amphotericin Antifungal	20		20		------		------	
4	14		11		0.0		0.0	
4 nano-form	24	71.42	23	102.09	22		22	
5	26		26		27		27	
5 nano-form	32	23.07	32	23.07	33	22.22	33	22.22
6	19		18		14		8	
6 nano-form	29	52.63	29	61.11	26	85.71	26	225
7	25		25		25		25	
7 nano-form	28	12	28	12	29	16	29	16
8	23		22		23		22	
8 nano-form	31	34.78	31	40.90	32	39.13	32	45.45
9	10		11		12		14	
9 nano-form	27	170	27	145.45	28	133.33	28	100

Weakly active: less than 10mm, Moderately active: 10-20 mm, Highly active: 20-25 mm, Strong active: more than 25 mm

The antimicrobial activities of all compounds were tested. Compound (5) showed strong activity towards bacteria and fungi under investigation and compounds (7) and (8) showed high activity. The effect of silver nanoparticles on the biological activity efficiency was investigated using chemical reduction method [25-28]. TEM and SEM images of silver nanoparticle are shown in Fig. 1a and Fig. 1b and TEM for nanoforms of compounds (5), (7), (8) and (9) are shown in Figures 2a, 3a, 4 and 5. The SEM images for the nanoforms of compounds (5),(8) are shown in Fig. 2b and Fig. 3b. Generally the nanoforms of compounds (5-9) exhibit strong activities and the nanoform of compound (4) showed high activity. The highest fold increases in area were observed for (9) in presence of Ag-NPs solution against *Candida albicans, Aspergillus Niger* and *Staphylococcus aureus* (G+), and the highest fold increases in area were observed for(6) in presence of Ag-NPs solution against *Escherichia coli*(G-) Table 1.

Transmission electron microscopy (TEM) and (SEM) images of the Ag-NPs solution and the Ag-NPs of the compound (4) and (5)
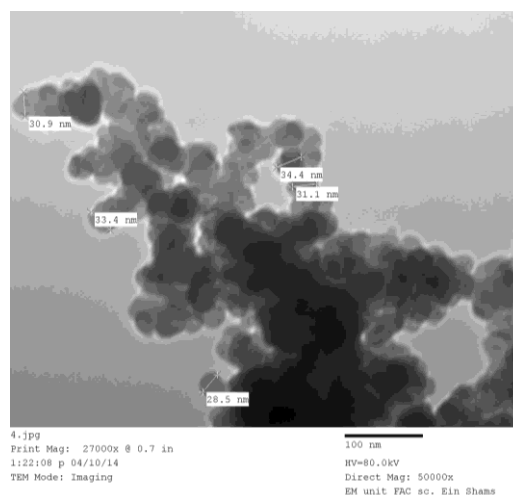
Fig. 1a. TEM Ag-NPs.
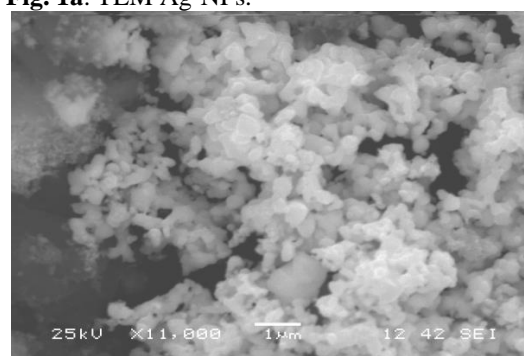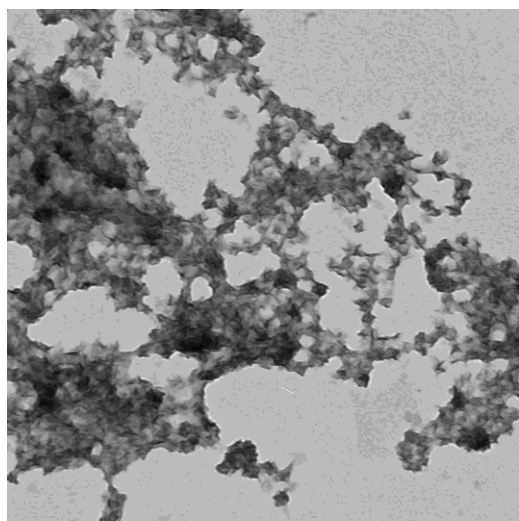
Fig.1b. SEM Ag –NPs.

Fig. 2a. TEM micrograph of compound (5).
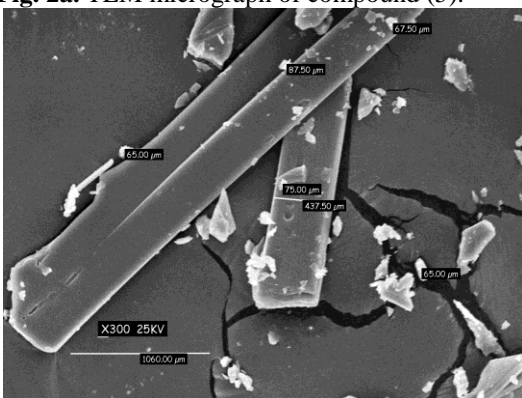
Fig. 2b. SEM of compound (5) after addition of Ag-NPs solution,after addition of Ag-NPs solution
Scale bar = 100 μm
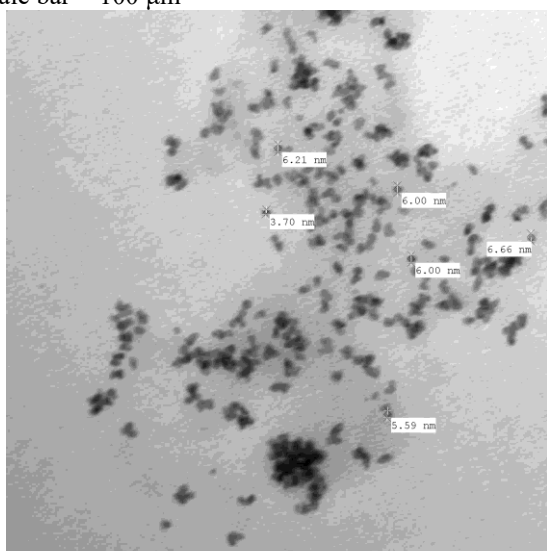
Fig. 3a. TEM micrograph of compound (8) after addition of Ag-NPs solution, Scale bar = 100 μm,
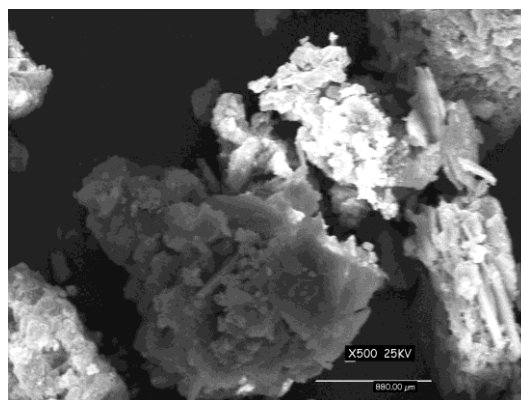
Fig. 3b. SEM of compound (8) after addition of Ag-NPs solution
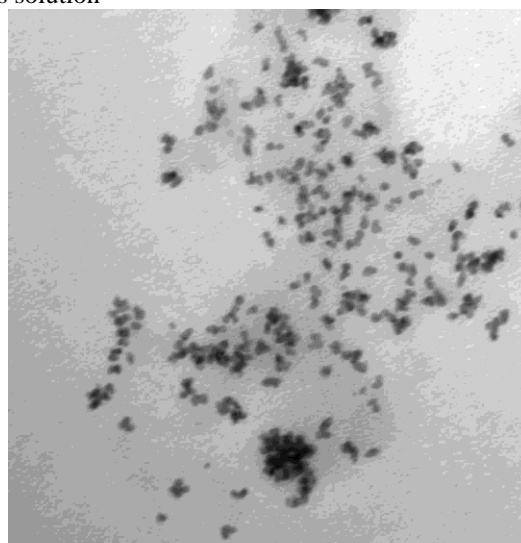
Fig. 4. TEM micrograph of compound (7) after addition of Ag- NPs solution.
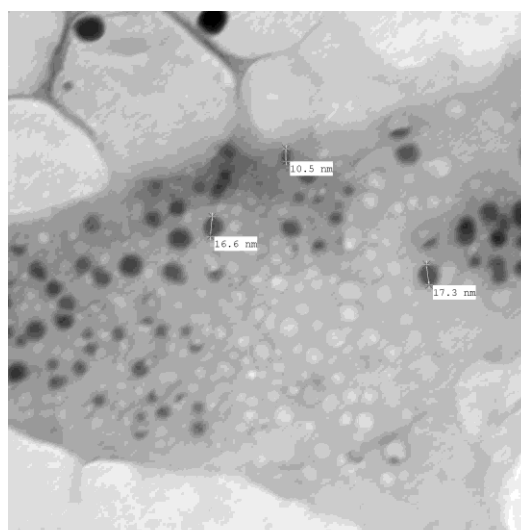
Fig. 5. TEM of compound (9) after addition of Ag-NPs solution.

EXPERIMENTAL

Melting points were measured by a Gallen Kamp melting point apparatus. Thin layer chromatography was performed with fluorescent silica gel plates HF254 (Merck), and plates were viewed under UV light at 254 and 265 nm. Infrared spectra (v cm^{-1}) were recorded on Bruker Vector Germany and on Mattson FT-IR 1000, using KBr disks. Mass spectra were measured on GCQ Finnigan MAT in Micro Analytical Centre, Cairo University, Giza, Egypt. 1H-NMR spectra were recorded on Gemini 200 MHZ NMR spectrometer, in DMSO-d6 solution with TMS as internal standard. It was determined in microanalytical centre in main defence chemical laboratory of the Egyptian Accreditation council. The antibacterial activity was determined in microanalytical center in main defence chemical laboratory of the Egyptian Accreditation Council. Transmission electron microscopy (TEM) images and scanning electron microscopy (SEM) were taken on (JEOL; model 1200 EX) at an accelerator voltage of 80 kV, in Central lab., Ain Shams University.

Metallation of compound (1a),(1b)& (2b) with cobalt acetate and copper acetate

General Procedure

The cobalt or nickel acetate (1mmol) reacts with (1a) or (1b) & or (2b) [6] (1mmol) in 50 mL of toluene in the presence of few drops of acetic acid under reflux for 3h. The precipitated crystals (compounds 4-9) are filtered, dried, and crystallized from acetic acid.

Compound (4): Pale brownish white crystals, (yield: 85 %), m.p.340-341 °C, IR (KBr) (cm^{-1}): showed v_{OH} at 3424, $v_{C=O}$ for carboxylate (attached to cobalt) at 1635 (antisymmetrical) & 1420 (symmetrical stretching) and 536 and 458 for v_{Co-C} and v_{Co-o} respectively. The ^{1}HNMR spectrum for compound (4) showed δ 11.93 ppm (1H,for OH), δ 9.46- 7.01 ppm (5H, for aromatic protons) and δ 6.8 ppm (1H, for methine proton) and δ 2.20 ppm (3H, for methyl protons). The MS spectrum showed the molecular ion peak $M^{\rceil +}_{\cdot}$ at m/z 372 (40.60%) the base peak at 57 (100%) can be attributed to $C_3H_7N^{\rceil +}_{\cdot}$.

Compound (5): Pale brownish crystals, (yield: 86 %), m.p. d.240 °C, IR (KBr) (cm^{-1}): at 1710 cm^{-1} for $v_{C=O}$ due to carboxylic group, 529 and 469 for v_{Co-C} and and v_{Co-O}. The ^{1}HNMR spectrum for compound (5) showed δ 12.0 ppm (1H,for OH), δ 8.40-7.01 ppm (5H, for aromatic protons) and δ 2.80 ppm (2H, for methylene protons). The MS

spectrum showed $M+1^{\rceil +}$ at m/z 372(1.02%), the base peak at 370 (100%) can be attributed to $M-2^{\rceil +}$.
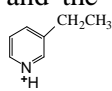
Compound (6): Pale brownish white crystals, (yield: 81 %), m.p.d.340 °C, IR (KBr) (cm^{-1}): showed v_{OH} at 3394 cm^{-1}, $v_{C=O}$ for carboxylate ion at 1610 cm^{-1} (antisymmetrical) &1405 cm^{-1} (symmetrical stretching)and v_{Cu-C} at 577 cm^{-1} The ^{1}HNMR spectrum for compound (6) showed δ 11.90 ppm (1H,for OH), δ 9.50- 7.45 ppm (5H, for aromatic protons) and δ 6.27 ppm (1H, for methane proton) and δ 2.39 ppm (3H, for methyl protons). The MS spectrum showed $M^{\rceil +}_{\cdot}$ at m/z 377(24.53%), the base peak at 353 can be attributed to $M-24^{\rceil +}$

Compound (7): Pale brownish white crystals, (yield: 83 %), m.p.120-121 °C, IR (KBr) (cm^{-1}): showed two absorption bands at 3500& 3398 cm^{-1} for two v_{OH} &at 1633 cm^{-1} for $v_{C=O}$ due to carboxylate ion. The ^{1}HNMR spectrum for compound (7) showed δ 11.84 ppm (2H, for 2 OH), δ 9.79-7.04 ppm (5H, for aromatic protons), δ 6.44 ppm (1H, for methine proton) and δ 2.28 ppm (3H, for CH$_3$). The MS spectrum showed $M^{\rceil +}_{\cdot}$ at m/z 377(8.97 %)) and the base peak at 69 (100%) can be attributed to $C_4H_7N^{\rceil +}$

Compound (8): Pale brownish white crystals, (yield: 71 %), m.p.250-251 °C, IR (KBr) (cm^{-1}): showed new absorption bands: two bands for v_{NH2} at 3494, 3420 cm^{-1}, v_{NH} at 3321 cm^{-1} ,v_{CHstr} at 2953 cm^{-1}, $v_{C=O}$ at 1653 cm^{-1}, $v_{C=C\ Alkene}$ at 1614 cm^{-1}, $v_{C-H\ bending}$ at 1463 cm^{-1}, v_{C-Co} at 548 cm^{-1}, v_{O-Co} at 463 cm^{-1}. ^{1}HNMR spectrum showed δ 7.8-6.67 ppm(4H, for aromatic protons), δ 6.63ppm (1H,for =C-H proton), δ 3.96 ppm(1H,for O-C-C= CH proton), δ 2.7, 2.8 ppm (4H, for2 CH$_2$ protons attached to NH and NH$_2$), δ 1.6, 2.3, 2.6 ppm (6 H, for 3CH$_2$ protons), δ2.1 ppm (3H, for 3 OH protons).The absence of 8.9 ppm indicated that substitution reaction took place at this position via coordination with N in the pyridine ring followed by electrophilic substation in the aromatic moiety. The MS spectra showed the $M+2^{\rceil +}_{\cdot}$ at m/z 431(1.25%) and the base peak at m/z 108(100%) attributed to .

Compound (9): brownish crystals, (yield: 70 %), m.p.184-185 °C, IR (KBr) (cm^{-1}): The IR spectrum indicated the presence of new absorption bands for v_{NH2} two bands at 3493, 3419 cm^{-1}, $v_{C=O}$ at 1657

cm^{-1}, ν_{C-Cu} at 549 cm^{-1} and ν_{O-Cu} at 463 cm^{-1}. The ^{1}HNMR spectrum showed δ 7.8-7.2 ppm (4H,for aromatic protons), δ 6.70 ppm (1H,for =C-H proton), δ 4.3 ppm (1H, for O-C-C= CH proton), δ 2.7, 2.9 and 3.2 ppm (4H, for2 CH$_2$ protons attached to NH and NH$_2$,and 4H for 2CH$_2$ attached to N-C=O), δ2.1 ppm (3H, for 3 OH protons) [20] and δ 1.8 ppm (2 H, for CH$_2$ protons). The MS spectrum showed the $\overline{M+1}^+$ at m/z 435(36.32%) and the base peak at m/z 108(100%) due to
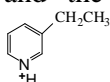
Preparation of silver nanoparticles:

Silver nanoparticles were prepared by chemical reduction method [28]. All solutions were prepared in distilled water. 50 ml of 0.001 M silver nitrate was heated to boiling using hot plate magnetic stirrer. To this solution 5 ml of 1% trisodium citrate was added drop by drop. During this process solution was mixed vigorously. Solution was heated until colour change is evident (yellowish brown). Then it was removed from the heating element and stirred until cool to room temperature. UV/Visible spectrum for the silver nanoparticles in the solution showed λ max at 420 nm due to the surface plasmon resonance effect.

CONCLUSION

Metallated heterocyclic compounds (4-9) were synthesized from the reaction of 2-(2-oxo-2*H*-pyrano[3,2-*h*]quinolin-4-yl) acetic acid (1) and 4-(2,2-dihydroxy-vinyl)-2*H*-pyrano[3,2-*h*]quinolin-2-one (2) and their derivative (3) with Co(II) and Cu(II) acetates. The antimicrobial activities of the all products and their silver nanoparticle forms were examined. The antibacterial and antifungal activities of the silver nano forms (Ag-NPs) of the compounds were screened to compare their effect with respect to the parent new compounds. Compound (5) showed strong activity towards bacteria and fungi under investigation and compounds (7) and (8) showed high activity. The nanoforms of compounds (5-9) exhibit strong activities and the nanoform of compound (4) showed high activity. The highest fold increases in area were observed for (9) in presence of Ag-NPs solution against *Candida albicans*, Aspergillus Niger and staphylococcus aureus (G+), and the highest fold increases in area were observed for (6) in presence of Ag-NPs solution against escherichia coli (G-) Table 1.

REFERENCES

1. K. H. Cho, J. E. Park, T. Osaka, S. G. Park, *Electrochimica Acta*, **51**: 956 (2005).
2. M. Rai, A. Yadav, A. Gade, *Biotechnology Advan*ces, **27, **76 (2009).
3. W. Jiang, B. Y. S Kim., J. T. Rutka, C. W. Chan Warren, *Nature Nanotechnology*, **3**, 145 (2008).
4. I.Sondi, B. Salopek-Sond., *Journal of Colloid and Interface Scie*nce, **275**, 177 (2004).
5. J.S. Kim, E. Kuk, K.N Yu., J. H. Kim, S. J. Park, H. J. Lee, S.H. Kim., Y. K. Park., Y. H. Park., C.Y. Hwang, Y. K. Kim, YS. Lee, D.H. Jeong, MH. Cho, *Nanomedicin: Nanotechnology, Biology and medicine*; **1**, 95, (2007).
6. E. A. El-Sawi, M. A. Hosny, T. M. Sayed, *International Journal of Engineering Research and Technology* (IJERT), **3** (5): 770 (2014).
7. G. Madhu, K. Jayaveera, L. Ravindra, B. Kumar and P. Reddy, *Der Pharma Chemica*, **4 (**3), 1033 (2012).
8. K. Kaur, M. Jain, R. Reddy and R. Jain, *European Journal of Medicinal Chemistry,***45** (8), 3245 (2010).
9. A. Abadi, G. Hegazy and A. El-Zaher, *Biorganic and Medicinal Chemistry* **13**, 5759 (2005).
10. A. Abu-Hashem and A. Aly , *Arch Pharm Res*, **35** (3), 437 (2012).
11. L. Korrichi, B. Dalila and S.Dalila, *European Journal of biological Sciences*, **1** (3), 32 (2009).
12. L. Chen, I. Chen, C.Huang, C. Liao, C.Chen and T.Wang, *Journal of the Chinese Chemical Society*, **57**, 1331 (2010).
13. H. Hassanin, M. Ibrahim and Y.Alnamer, *Turkish Journal of Chemistry,* **36,** 682 (2012).
14. A. B. Ahvale , H. Prokopcova, J. Sefoviova , W. Steinschifter, A. E.Taubl, G.Uray, W. Stadlbauer, *Eur. J. Org. Chem.*, 563 (2008).
15. I. V. Ukrainets, A. A. Tkach and L. Y.Yang, *Chem. Heterocycl.Compds.*, **44**, 1347 (2008).
16. M.S. Mostafa, *Chemistry and Materials Research*, **3** (9):125 (2013).
17. E. A. El-Sawi, M. A. Hosny, W. A. Mokbel, T. M Sayed., *Synth. React. Inorg. Met. Nano- Met. Chem.*, **40**, 934 (2010).
18. E. A. El-Sawi , W. A. Mokbel and T. M. Sayed, *Bulg. Chem. Commun.*, **39**, 281 (2007).
19. E. A El-Sawi .and T. M. Sayed, *Synth. React. Inorg. Met.-Org. Nano- Met.Chem*, **41**,992 (2011).

20. D. H. Williams, I. Fleming,*Spectroscopic methods in organic chemistry*,2 nd. edition, McGraw-Hill Book Company(UK) limited, 1993, p. 1348.

21. E. Jawetz, J. L. Melnick, E. A. Adelberg, *Review of Medical. Microbiology, 14th ed, Lange Medical Publication, Los. Altos*, CA, 1980, p 45.

22. D. N. Muanza, B. W. Kim, L. L. Euler, L. Williams, *Int. J. Pharmacog.*, **32**, 337 (1994).

23. O. N. Irob, M.moo-Young, W. A. Aperson, *Inter. J. Pharmacol.*, **34**, 87 (1996).

24. A. Sileikaite, I. Prosycevas, J. Puiso, A. Juraitis and A. Guobienė, *Material Science,* **12**, 1320 (2006).

25. M. Sastry, K. S Mayya, K. Bandyopadhyay, *Colloid. Surf.* A, 127-221 (1997).

26. M. Sastry, V. Patil.and S. R. Sainkar, *J Phys Chem B.* **102**, 1404 (1998).

27. V. Vichai and K. Kirtikara, *Sulforhodamine B colorimetric assay for cytotoxicity screening.*, **1**, 1112 (2006)

A. Henglein, *J. Phys. Chem.* **97**, 5457 (1993).

СРЕБЪРНИ НАНОЧАСТИЦИ С НОВИ ОРГАНОМЕТАЛНИ СЪЕДИНЕНИЯ ПОДОБРЯВАТ АНТИМИКРОБНАТА АКТИВНОСТ

Е. А. Ел-Сауи[*] , М. А. Хосни

Департамент по химия, Девически факултет по изкуства, наука и образование

Университет Ейн Шамс Хелиополис, Кайро, Египет

(Резюме)

Металираните хетероциклени съединения (4-9), получени при реакцията на 2-(2-оксо-2*H*-пирано[3,2-*h*] хинолин-4-ил) оцетна киселина (1) с 4-(2,2-дихидрокси-винил)-2*H*-пирано[3,2-*h*] хинолин-2-он (2) и техни производни (3) с ацетати на Co(II) и Cu(II). Изясняването на структурите им е направено с помощта на елементен анализ, IR, ¹HNMR и MS. Приготвените сребърни наночастици са изучени с трансмисионна електронна микроскопия (TEM) и UV-спектри. Изследвана е антимикробната активност на всички продукти, дотирани със сребърни наночастици спрямо основните съединения. Резултатите показват, че наночастиците повишават тази активност с 12-170% и може да се използват като инхибитори на растежа.на микроорганизмите

Evaluation of the *in vitro* antioxidant effect of novel 3-methoxysalicylaldehyde derived hydrazones

N. G. Hristova-Avakumova[1], B. I. Nikolova-Mladenova[2], V. A. Hadjimitova[1*]

[1]Department of Medical Physics and Biophysics, Medical University – Sofia, Bulgaria
[2]Department of Chemistry, Faculty of Pharmacy, Medical University – Sofia

In an effort to continue the exploration of hydrazone analogues with highly diverse structural features based on variation in the skeleton we present a comparative evaluation of the antioxidants properties of novel 3-methoxy hydrazones derived from salicylaldehyde benzoylhydrazone. The determination of the antioxidant properties was performed *in vitro* in biologically relevant cell-free model systems with different mechanism of generation of ROS using chemiluminescent (potassium superoxide (KO_2)-produced superoxide and luminol-dependent CL in a system of iron dependent hydroxyl radical formation) and spectrophotometric (ABTS, DPPH) methods to monitor and compare the investigated properties. We demonstrated that the initial compound salicylaldehydebenzoylhydrazone and its 3-methoxy derivatives exhibited antioxidant activity with variable efficiencies in relation to the experimental model system and the used method for registration. In both chemiluminescent model systems the incorporation of the electron donating methoxy group had increased considerably the studied properties, while in the ABTS assay we observed a slight but significant decrease. According tothe obtained by the ABTS method results of TEAC the four hydrazones have demonstrated better scavenging properties compared to the reference Trolox. All the studied compounds have demonstrated high antioxidant activity in terms of oxidation inhibition and free radical scavenging activity, thus indicating their potential direct or indirect beneficial effect in case of oxidative stress processes.

Key words:Hydrazones, antioxidant activity, ABTS, DPPH,chemiluminescence

INTRODUCTION

In medical chemistry hydrazones derivatives have been very well known for their vast spectrum of biological activities, coordinative capability and applications in analytical chemistry.The scientific interest in this group of compounds, as an alternative for the development and design of new therapeutic agents with improved toxicity profile and increased efficiency is determined by the combination of the relatively easy and cheap technology of synthesis, their physicochemical properties and their pharmacological activities.Scientific evidences obtained during the extensive investigations of these compounds have proved their capability for versatility in coordination, tendency to yield stereochemistry of higher coordination number, ability to behave as deprotonated or neutral ligands and capacity to generate flexible molecular architecture in assuming different conformations[1, 2].It has been reported that derivatives of this class of organic compounds possessing different functional moieties in the aldehyde or hydrazide part of the molecule exhibit antimicrobial, antimalarial, analgesic, anti-inflammatory, antitumoral and antioxidant properties[3]. All those effects are connected with opportunity of hydrazones to influence directly or indirectly free radicals processes.

In an effort to continue the exploration ofhydrazone analogues with highly diverse structural features based on variation in the skeleton we present a comparative evaluation of the antioxidants properties of novel hydrazones derived from salicylaldehyde benzoylhydrazone.We determined their antioxidant activity in *in vitro* biologically relevant cell-free model systems with different mechanism of generation of ROS using various methods to monitor and compare the investigated properties. This offersthe unique advantages to delineate the chemical and molecular mechanisms of action of these compounds and to investigate the correlation of their reactivity in radical reactions with their composition and molecular structure.The studied molecules have more drug-like structures compared to the initial compound and the current investigation was carried out in order to establish their value as prospective multifunctional antioxidant candidates.

MATERIALS AND METHODS

Materials

All the reagents used in the antioxidant model systems were analytical grade. 1,1-Diphenyl-2-picryhydrazyl (DPPH), 2,2'-azinobis-(3-ethyl-

---

benzothiazoline-6-sulfononic acid), and Trolox(6-hydroxy-2,5,7,8-tetra-methylchroman-2-carboxyl acid) were obtained from Sigma-Aldrich. Ethylenediamine-tetraacetic acid(EDTA) and $FeCl_3.6H_2O$ were purchased from Genaxxon.

The derivatives of SBH used in the present work - 3-methoxysalicylaldehydebenzoylhydrazone (3mSBH), 3-methoxysalicylaldehyde-4-hydroxybenzoylhydrazone (3mShBH) and 3-methoxysalicylaldehydeisonicotinoylhydrazone (3mSIH)were synthesized and characterized in the Faculty of Pharmacy at the Medical University of Sofia by assistant professor B. Nikolova-Mladenova. The hydrazones were obtained by Schiff base condensation. Their structure was confirmed by elemental and thermo-gravimetric analysis, IR, ^{1}H-NMR and ^{13}C-NMR spectroscopy[4].

Methods

Evaluation of the antioxidant properties in chemiluminescent model systems

Luminol-dependent CL was used for registrationof ROS [5-7].The fundamental chemistry of CL assay is based on the two-electron oxidation of the luminol molecule and formation of endoperoxide. This compound is unstable and upon decomposition yields an electronically excited 3-aminophthalate, emitting photons on its return to the ground sate whichare amplified by the phototube of the luminometer. The chemiluminescent response is determined by calculating the area under the obtained chemiluminescent light curves. We assumed that the CL ratio in the presence and in the absence of the tested compound should indicate the scavenging properties of the derivatives. Therefore, this ratio was termed chemiluminescence scavenging index (CL-SI).

Two types of CL model systems were chosen - luminol-dependent CL in a system of potassium superoxide (KO_2)-produced superoxide and luminol-dependent CL in a system of irondependent hydroxyl radical formation. For the purpose of these methods an LKB 1251 luminometer (BioOrbit, Turku, Finland) set at 37°C was used. It was connected with an AT-type computer via serial interface and MultiUse program ver. 1.08 (Bioorbit, Turku, Finland) which was used for collection of the experimental data.

For both assaysthe chemiluminescent reagent was prepared by dissolving luminol in a small amount of 0.01 M NaOH. Then the solution was diluted to luminol concentration of 1 mMwith a 50mMphosphate buffer solution (PBS) and the pH

was adjusted to 7.4 with 0.01 M HCl. Drugs were dissolved in 10mMNaOH. Their final concentrations in the investigated samples are shown in the figure legends.

*Luminol-dependent CL in a system of potassium superoxide (KO_2)-produced superoxide.*The assay was carried out using 1 ml samples of phosphate buffer solution, pH 7.4, containing 0.1 mMluminol, and the studied hydrazone derivative. In the control sample hydrazones were omitted. The release of the superoxide is a fast process. Therefore, the CL response was measured immediately after addition of 20 μl KO_2 solution using the "flash assay" option of the MultiUse program, every 50 milliseconds.

*Luminol-dependent CL in a system of irondependent hydroxyl radical formation.*One ml samples of PBS, pH 7.4, contains 0.1 mMluminol, 0.1 mM Fe^{3+} ($FeCl_3$), 0.1 mM EDTA, 0.1 mM ascorbate, 1mM H_2O_2 and any of the tested hydrazones at concentrations between 0.1 and 100 μM, or buffer for the controls. The CL was measured using the "flash assay" option of the MultiUse program, every 50 milliseconds.

Evaluation of the radical scavenging activity against stable free radicals

The total antioxidant capacity of the tested hydrazones was measured spectrophotometricallyby using the stable 1,1-diphenyl-2-picrul-hydrazilor 2,2'-azinobis-(3-ethylbenzothiazoline-6-sulfononic acid)free radicals in vitro assays. $DPPH^•$ and $ABTS^{+•}$ have different mechanism of neutralizing their free radical character.$DPPH^•$ absorbance decreases in presence of hydrogen-donating antioxidants due to the formation of the stable DPPH-H compound and ABTS is involved in an electron transfer processes.Unicam UV 500 Spectrophotometer (ThermoSpectronic, UK) and 1 cm disposable cuvettes (Brandt, Germany) were used for all the absorption measurements.

The antioxidant activity was calculated by the formula:

$$AOA\% = \frac{Abs_{control} - Abs_{hydrazone\ probe}}{Abs_{control}}.100$$

The procedure followed the method as described by Re et al., [8]. The $ABTS^{•+}$working solution was produced by the mixing of 14 mM ABTS stock solutions with potassium persulfate 2.45 mM (final concentration), allowing the mixture to stand in the dark at room temperature for 12–16 h before use. The suspension was then diluted by mixing 1 ml $ABTS^{•+}$with PBS to obtain final solution with absorbance 0.70 ± 0.01 units at 734 nm. The reduction in absorbance of 2 ml of $ABTS^{•+}$ after

adding the hydrazones derivatives was recorded at 734 nm exactly 60 min after the mixing. Fresh ABTS$^{\bullet+}$solution was prepared for each assay.

Trolox was used as a reference compound. The concentration that provides 50% AOA (C-50) for different hydrazone derivatives andTrolox equivalent antioxidant capacity (TEAC) were calculated to quantify the antioxidant capacity. The DPPH freeradical-scavengingactivityofthehydrazoneswasdetermineda ccordingtothemethoddescribedbyGoupy*etal.*[9].For this experiment all studied compounds were dissolved in ethanol to a concentration of 1 mM/L. DPPH$^{\bullet}$ solution in ethanol was prepared with initial optical absorbance of 1 at 518 nm.2 mL of DPPH$^{\bullet}$ solution were allowed toreact with 200 µl sample solution. The probes were left to stay at room temperature in the dark. After 1 hour of incubation, the absorbanceof the solution was measured at 518 nm. The scavenging activity was expressed as a percentage of the absorbance of the control DPPH$^{\bullet}$ solution containing ethanol instead of hydrazones derivatives solution.

The concentration that corresponds to 50% decreasing of radicals was termed C-50. Its value was calculated, using the following equation:

$$AOA = 100/[1 + 10^{B(logC - \log(C-50))}]$$

The data processing included fitting of the experimental results to sigmoid dose-response curves, whereby B is the coefficient (hill slope) and C is the substrate concentration. The formula was used to calculate C-50 for the data obtained by all experimental model systems.

All statistical analyses were performed using IBM SPSS Statistics v.19.0. for Windows (Chicago, Illinois, USA, 2010). The assays were carried out in triplicate and the quantitative variables are presented as mean ± standard deviation. P-values lower than 0.05 were considered statistically significant.

RESULTS

The effects of the studied 3-methoxy derivatives on the luminol-dependent CL in a system of KO$_2$ generated O$_2^{-\bullet}$ (assay 1) are shown on figure 1. The chemiluminescent luminosity is dependent on the quantity of the generated O$_2^{-\bullet}$ in the reaction system. Therefore this CL reaction system can be used to evaluate the scavenging activity of the tested derivatives on O$_2^{-\bullet}$.SBH had the lowest inhibitory effect among the studied hydrazones. It didn't demonstrate any antioxidant properties at concentrations above 1µmol/L and with increasing its concentration to 100 µmol/L the inhibition effect exhibited slight but significant escalation to

74%.Due to the strong inhibitory effect of the rest of the tested compounds under investigation their antioxidantpropertieswerefollowedover a wide
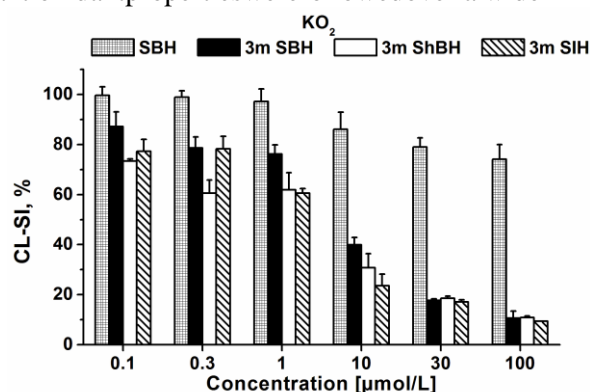
Fig. 1. Effect of SBH and its 3-methoxy derivatives on the luminol-dependent chemiluminescence scavenging index in the presence of KO$_2$ generated O$_2^{\bullet-}$. The solution in the sample cuvette comprises 1 ml phosphate buffer solution pH 7.4, containing 0.1 mMluminol and the hydrazone derivatives at concentration as indicated. In the control sample the studied hydrazones were omitted.

concentration range from 0.1 to 100 µmol/L. A small and not statistically significant difference was observed between the obtained values for their chemiluminescent scavenging index at concentrations upper than 30 µmol/L, suggesting no influence and involvement of the incorporation of the electron-donating atoms or groups in their molecular structureon the radical scavenging activity.At the maximal studied concentration of 100 µmol/L the chemiluminescent response in percentage for SBH is equal to 74,09 %, for 3mSBH = 10.62 %, for 3mShBH = 10.94 % and for 3mSIH = 9.39%. The diminished SBHs' effectiveness is due to the lack of methoxy substitution in its structure which is required for the high antioxidant activity in the experimental chemiluminescent model system.

We investigated the ability of the selected drugs to interact with OH$^{\bullet}$ in a system containing the Fe^{2+}-EDTA complex (Figure 2). In this system the OH$^{\bullet}$ are formed in the water phase in which are located the rest of the participants of the system– luminol and the studied hydrazones.The tested compounds exhibit different antioxidant activities in a concentration-dependent manner. At the lowest tested concentration 3µmol/L the obtained results for the studied parameter for all compounds except 3mSIH were almost identical to those of the untreated control sample. Further increasing of the concentrations to 10 µmol/L decreased moderately the CL-SI index. In the whole studied concentration range the initial compound SBH again

demonstrated the lowest antioxidant properties. At the highest tested concentration the 3mSBH, 3mShBH and 3mSIH values of the CL-SI were respectively 78,4%, 58,3% and 25,7% from the one obtained from the initial SBH compound. In this experimental chemiluminescent model system we can observe again the effect of diminished activity of the initial compounds due to the absence of methoxy group in its molecular structure.
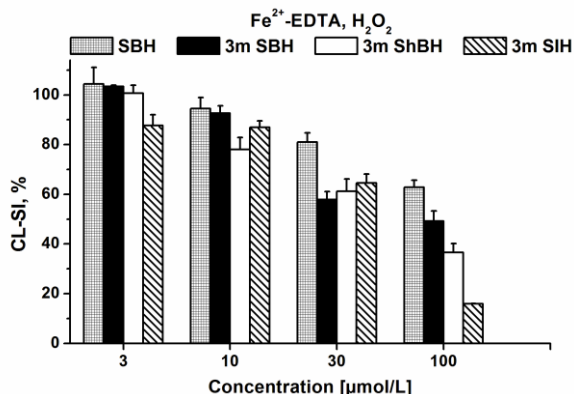
Fig. 2. Effect of SBH and its 3-methoxy derivatives on the luminol-dependent chemiluminescence scavenging index in a system of iron-dependent hydroxyl radical formation. The solution in the sample cuvette comprises 1 ml phosphate buffer solution pH 7.4, containing – 0.1 mMluminol, 0.1 mM Fe^{3+}, 0.1 mM EDTA, 0.1 mM ascorbate, 1mM H_2O_2 and the hydrazonesat concentrations as indicated. The control sample contained solvent in place of the studied hydrazones.

The C-50 values for all the studied 3-methoxy derivatives in both chemiluminescent model systems were determined and reported in Table 1.

Table 1. C-50 inhibition values of the chemiluminescence scavenging index for the investigated SBH derivatives in the studied model systems. SBH C-50 values are not presented due its weak effect on the tested systems they were out of investigated concentration range.

	C-50 [µmol/L] CL system of KO_2-produced superoxide	C-50 [µmol/L] CL system of iron dependent hydroxyl radical formation
SBH	*	*
3mSBH	3.58 ± 0.13	79.86 ± 5.61
3mShBH	1.43 ± 0.04	50.12 ± 0.001
3mSIH	1.89 ± 0.07	54.00 ± 0.43

SBH values are not reported because of its relatively weak inhibition activity in order to avoid extrapolation error. Comparing the structures and the demonstrated activities of the studied compounds it is inferred that the presence of a methoxy group in the molecular structure of the studied compounds is a crucial factor affecting the

1056

antioxidant behavior of these compounds in the tested chemiluminescent systems.The values of C-50 suggested that the strength of the radical-scavenging effect decrease in the order $O_2^{-\bullet} > OH^{\bullet}$.In both assays the 3-methoxy derivatives containing hetero atom or hydroxyl group (3mShBH and 3mSIH) exhibited lower C-50 values, compared to 3mSBH. The results obtained for these two compounds in each of the tested systems lead to the assumption that these types of molecular modifications seems to have slight but significant influence on the studied properties.

Scavenging potential

The free radical scavenging potential of the studied hydrazones derivatives and the initial compound were tested by the ABTS and DPPHdecolorization assays – operationally simple, reproducible, sensitiveand relatively cheap methods. The most important advantages of these model systems are their flexibility allowing to use the preformed stable radicals in aqueous and nonpolar organic solvents and the possibility to determinesimultaneouslythe antioxidants capacity of both hydrophilic and lipophilic constituents of the tested sample[10]. Both assays are considered as representative methods for preliminary screening of broad spectrum of complex samples (plant and food extracts, dietary supplements, biologic fluids, natural and synthetic compounds).

ABTS method

In the investigated concentration range (from 0.9 to 9 µmol/L) a significant decrease in the concentration of ABTS radical due to the demonstrated excellent scavenging effect of the tested compounds was observed. From the analysis represented at Figure 3 it can be concluded that the scavenging activity of all derivatives compounds on ABTS rises with increase in the concentration.
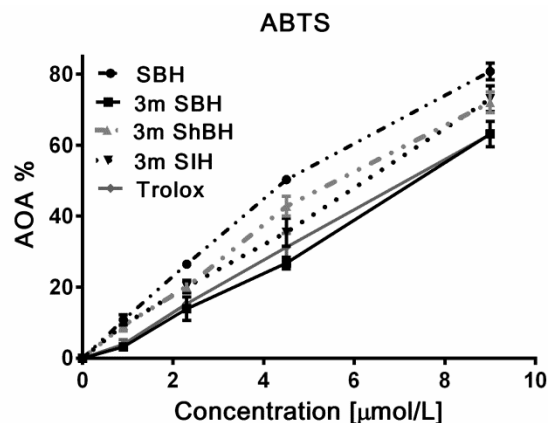
Fig. 3. Antioxidant activity of salicylaldehydebenzoylhydrazone and its 3-methoxy derivatives measured by the ABTS assay.

The initial compound SBH demonstrated higher effect compared to the 3-methoxy derivatives and the reference Troloxfor all of the applied concentrations. According to the results presented at figure 1 and the performed calculation the C-50 values decrease in the following order – trolox (C-50 = 8.53 µmol/L) < 3mSBH (C-50 = 7.44µmol/L) < 3mSIH (C-50 = 6.16µmol/L) < 3mShBH (C-50 = 5.98 µmol/L) < SBH (C-50 = 5.17 µmol/L).

The C-50 values from the antioxidant activity in the ABTS spectrophotometric model system were evaluated by measuring the Trolox equivalent antioxidant capacity (TEAC). The method allow to determine the relative of antioxidant substances to scavenge the radical action 2,2'-azinobis-(3-ethylbenzthiazoline-6-sulfonic acid) compared with a standard amount of the synthetic antioxidant Trolox. In this experiment TEAC values are defined as concentrations of standard Trolox with the same antioxidant capacity as 1 mMconcentration of the hydrazone under investigation.

Table 2 summarized the obtained results in terms of Trolox equivalent capacity. Because the initial compound has demonstrated strongest antioxidant effect in the studied model system its TEAC value is the smallest one. From the presented in table 2 results we can conclude that the electron donating properties of the studied hydrazones and the reference trolox increase in the following order:Trolox< 3mSBH < 3mSIH < 3mShBH < SBH.

Table 2. Determination of antioxidant activity as TEAC of the studied hydrazones by ABTS.

Compound	TEAC
SBH	1.65 ± 0.028
3mSBH	1.16 ± 0.007
3mShBH	1.44 ± 0.013
3mSIH	1.40 ± 0.002

Contradictory to the chemiluminescent model system the obtained by the ABTS assay results demonstrate only slight but significant variation in the studied properties due to the studied structural modifications. The scavenging activity of the studied compounds diminished with the incorporation of the electron donating methoxy group in the molecular structure of the initial structure of SBH. The subsequent alterations in the structure of 3mSBH by the addiction of hydroxyl group or hetero atom have increased equally the AOA of 3mShBH and 3mSIH but the obtained values were still smaller compared to SBH.

DPPH method

The results of the antioxidant activity using the DPPH radical scavenging assay indicate that the studied hydrazone derivatives demonstrate very weak (3mSBH, 3mShBH and 3mSIH) or absence (SBH) of antioxidant properties compared to the reference Trolox (). The tested hydrazones were used at final concentration 90 µmol/L. The scavenging effect of the compounds and the reference antioxidant on DPPH decreases in the following order: Trolox> 3mSIH >3mSBH > 3mShBH>SBH. The 3-methoxy derivatives have demonstrated close but not similar antioxidant activity compared with the initial compound SBH. There was no statistically significant difference between the obtained values for these structural analogues - 3mSIH = 88.4%, 3mShBH = 94.7% and 3mSBH = 92.7%.
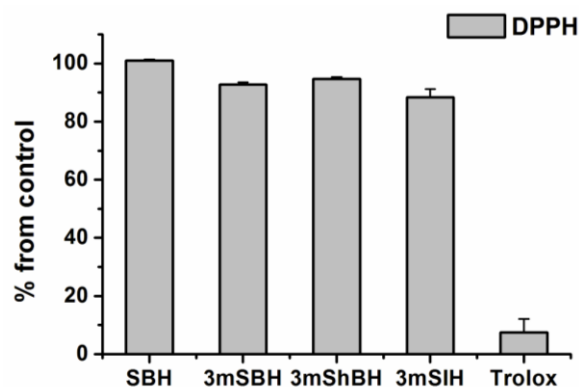
Fig. 4. Antioxidant activity of salicylaldehydebenzoylhydrazone and its 3-methoxy derivatives measured by the DPPH assay. The concentration of the studied hydrazones in the sample cuvette is 90 µmol/L. Trolox at concentration 46 µmol/L was used as reference.

The obtained results could be explained by the quite difficult possibility of abstraction of hydrogen atom from the phenolic ring of the studied compounds under the examined conditions. This is due to the strong intermolecular bonds with the adjacent methoxy group. According to the recent work of Dolens et al. regarding the autoxidation processes ofhydrazone derivatives and the results obtained by Belkheiri et al., as a consequence of the interaction with the DPPH radical may be produced a nitrogen radical of the investigated compound[11]. After studying the influence of the incorporation of different functional moieties in the structure of the initial hydrazone compound these authors proposed the formation of N• centered hydrazonyl radical which is stabilized through formation of delocalised C• centered radicals.

The modest increase of the scavenging properties of the studied derivatives compared to the initial compound could be due to the increased ability of N-H hydrogen atom extraction due to the incorporation of the methoxy group in the molecular structure.

CONCLUSION

Using four experimental methods, we demonstrated that the studied 3-methoxy derivatives of salicylaldehyde benzoylhydrazones exhibited antioxidant activity with variable efficiencies in relation to the experimental model system and the used method for registration of the studied properties. The compounds have demonstrated high antioxidant activity in terms of oxidation inhibition and free radical scavenging activity, thus indicating their potential direct or indirect beneficial effect in case of oxidative stress processes.

REFERENCES

1. N. Mangalam, S. Sheeja, M. Kurup,*Polyhedron,***29**, 3318 (2010).
2. S. Naskar, S. Naskar, R. Butcher, S. Chattopadhyay, *Chim. Acta.,***363**, 3641 (2010).
3. G. Verma, A. Marella, M. Shaquiquzzaman, M. Akhtar, M. Ali, M. Alam, *JPharmBioallSci,***6**, 69 (2014).
4. B. Nikolova-Mladenova, N. Halachev, R. Iankova, G. Momekov, D. Ivanov, *Arzeimittelforschung/drug research,***12-F**, 714 (2011).
5. R. Allen , Biochem. *Biophys. Res. Com.,***63**, 684 (1975).
6. R. Allen, L. Loose, *Biochem. ura, Sofia.Biophys. Res. Commun.,***69**, 245 (1976).
7. K. Itoh, T. Majima, K. Edo,M. Mizugaki,N. Ishida, *Tohoku J. Exp. Med.,***157**, 205 (1989).
8. R. Re, N. Pellegrini, A.Proteggente, A.Pannala, M.Yang, C.Rice-Evance,*Free radical biology and Medicine*, 1231 (1999)
9. P. Goupy, C.Dufour, M. Loonis, Dangles,*Journal of agriculture and foods chemistry*, 615 (2003).
10. R. Prior, X. Wu, K. Schaich,*J Agri Food Chem.,***53**,4290 (2005).
11. N. Belkheiri, Bouguerne B, Bedos-Belval F, Duran H, Bernis C, SalvayreR,Nègre-Salvayre A, Baltas M. *Eur J Med Chem.*;**45**3019 (2010)

АНТИОКСИДАНТИ СВОЙСТВА НА НОВОСИНТЕЗИРАНИ 3-МЕТОКСИ САЛИЦИЛ-АЛДЕХИДБЕНЗОИЛХИДРАЗОНИ В *in vitro* ТЕСТ СИСТЕМИ

Н. Г. Христова-Авакумова[1], Б. И. Николова-Младенова[2], В. А. Хаджимитова[1]*

[1]Катедра медицинска физика и биофизика, Медицински факултет, МУ-София, България
[2]Катедра химия, Фармацевтичен факултет, МУ-София, България

(Резюме)

В настоящата статия са представени резултатите от сравнително проучване на антиоксидантните свойства на три новосинтезирани 3-метокси структурни аналози на активния хелаторсалицилалдехидбензоилхидразон. Антиоксидантната и радикал-улавящата активности на съединенията са изследвани в биологично релевантни тест системи на генериране на АФК. За регистриране на радикалите са използвани спектрофотометрични и хемилуминесцентни методики. Получените резултати показват, че новосинтезираните аналози проявяват различна от базисното съединение антиоксидантна активност. В системата с хидроксилни радикали и в тази със супероксидни радикали се наблюдава значително нарастване на инхибиращият ефект върху луминол-зависимата хемилуминесценция при наличие на електрон донорен заместител в алдехидното ядро на молекулата. Съединенията проявяват силни редукционни свойства спрямо ABTS радикала. Отчетеният антиоксидантен ефект надвишава този на използваният референт Trolox, като въвеждането на метокси група е съпроводено със слабо статистически значимо потискане на изследваните свойства.

Въз основа на получените експериментални данни може да заключим, че изследваните съединения проявяват мощен антиоксидантен ефект по отношение на HO$^\bullet$ и O$_2^{-\bullet}$ и спрямо стабилният ABTS радикал. Получените резултати ще са от значение за рационалния лекарствен дизайн на фармакологично активни агенти притежаващи антиоксидантни свойства на основата на хидразоните.

Selected papers presented at the 3rd Asia-Pacific Conference on Engineering Technology (APCET 2015), March 27-30, 2015, Beijing, China.

Bioconjugated carbon nanotubes for cancer targeting and near-infrared laser photothermal therapy

Jun Li, Yaodong Dai[*]

College of Material Science and Technology, Nanjing University of Aeronautics and Astronautics, Nanjing 210016, China

Cancer targeting and selective photothermal destruction were achieved by using folate conjugated carbon nanotubes and a near-infrared continuous wave laser (800 nm). By functionalizing the nanotubes with folate, a photothermal agent was developed to selectively enter into the cancer cells and kill them through generating heat inside the cells under laser irradiation. The results of confocal fluorescence imaging showed that the functionalized nanotubes can specifically enter into the cancer cells via a folate receptor mediated pathway without significant internalization into normal cells. Under the irradiation of an 800 nm laser, cancer cells were selectively killed by the heat generation from carbon nanotubes inside the cancer cells, while the normal cells still remained alive. The photothermal technique combined with nanotubes and near infrared laser irradiation might afford a promising potential way for cancer targeting and selective therapy without causing toxicity and side effects.

Key words: Carbon nanotubes, cancer targeting, photothermal therapy, near-infrared laser

INTRODUCTION

Applying controlled and targeted therapeutics to cancer may provide a more efficient and less harmful solution to overcome the limitations of conventional techniques [1]. Over the past decade, there has been increasing interest in using nanotechnology for new potential therapeutics of cancer. Nanoparticles [2-4], nanoshells [5, 6], nanorods [7, 8], and recently nanotubes [9-11] have been shown to be applicable to cancer imaging and therapy. The subcellular size and unique physical properties of nanostructures make them very attractive for molecular transporters [11], anticancer drug delivery [12], and new therapeutic mechanisms [6, 13]. For active targeting to cancer cells, nanomaterials were functionalized with ligands such as antibodies, peptides, nucleic acid aptamers, carbohydrates, and small molecules [13], among which, folic acid (FA) is appealing as a small molecular ligand for targeting cancer cell membrane and allows for its use for specific cancer targeting [14].

In the attractive field of nanotechnology-based cancer therapy, nanostructures with unique photophysical properties have been considered as an interesting and promising approach for the destruction of cancer cells [5, 9, 10]. Single walled carbon nanotubes (SWNTs) are very suitable for these techniques due to their strong optical absorbance in the near infrared (700–1100 nm)

region [15, 16]. This intrinsic property stems from the electronic band structures of the nanotubes. Strong optical absorbance originates from the electronic transitions from the first or second van Hove singularities [17]. The van Hove-like singularity in the density of states (DOS) moves towards the top of the valence band, enhancing the effective DOS near the Fermi energy and results in an increase in the electron–phonon interaction, thereby increasing the temperature of the nanotubes [18].

In the current work, we studied the cancer targeting of folate conjugated carbon nanotubes and the selective cancer destruction by using a cheap and simple near-infrared continuous wave (CW) laser (800 nm). By functionalizing the SWNTs with folate, we developed a photothermal agent that can selectively enter into the cancer cells that overexpress folate receptor on the surface of the cell membrane and kill them through generating heat inside cells under the excitation of CW laser. The uptake of folate-conjugated SWNTs into cells is investigated via a confocal fluorescence imaging route, and it is found that the functionalized SWNTs can enter into the cancer cells selectively via a folate-folate receptor-mediated pathway. Under the treatment of an 800 nm CW laser, cancer cells were selectively killed by the heat generation from carbon nanotubes inside cancer cells, while the normal cells still remained alive. These results demonstrated that biofunctionalized carbon nanotubes could be potential agents for cancer targeting and selective photothermal therapy.

* To whom all correspondence should be sent:
E-mail: yaodong_dai@163.com

EXPERIMENTAL DETAILS

Single walled carbon nanotubes (SWNTs) with a diameter of 1-3 nm and an average length of 200 nm were made by a CVD approach, followed by purification and cutting process [19, 20]. Oxidized SWNTs were obtained by refluxing in 2.6 M nitric acid, and -COOH groups were formed on the side walls of the nanotubes [21]. Chitosan oligomers (CS) with molecular weight of 3000-5000, folate, 1-ethyl-3-(3-dimethylamino-propyl) carbodiimide hydrochloride (EDC), N-hydroxysulfosuccinimide (Sulfo-NHS) were purchased from Sigma-Aldrich Corp. FITC fluorescence dye, dimethyl sulfoxide (DMSO), and 4-6-diamidino-2-phenylindole (DAPI) were purchased from Invitrogen Corp. All other chemicals used in this work were of analytical grade.

The conjugation of chitosan on SWNTs was achieved by a simple noncovalent approach [22]. The SWNTs were sonicated for 1 h in a phosphate buffer saline (PBS) solution (0.5 mM) of chitosan (CS); the initial concentration of SWNTs was 1 mg/ml. The solution was centrifuged at 15000 g for 1 h to remove aggregated and large bundled nanotubes. The supernatant was collected and filtered through a 10 kDa MWCO membrane (Millipore Amicon) to remove excess chitosan, washed several times with water, and resuspended in PBS. For conjugation of folate and FITC on CS-SWNTs, folate (2.5 mM) was added to a solution of CS-SWNTs in PBS buffer (5 ml) at pH 7.4; to this solution 100 μl of FITC solution in DMSO (80 μM) was added, and then EDC (3.5 mM) and sulfo-NHS (3.5 mM) were added. The mixture was allowed to react overnight at room temperature with protection from light. The solution was subsequently dialyzed three times to ensure complete removal of excess unconjugated molecules. The remaining functionalized SWNTs (f-SWNTs) were dispersed in PBS buffer or DMEM cell medium for several days at room temperature to test the solution stability. UV-vis and fluorescence spectra were used to record the functionalization process. The concentration of final f-SWNTs was estimated via a concentration-dependent UV-vis spectroscopic route [23, 24].

Human hepatocellular carcinoma cells (Hep G2, an adherent cell line), used as the cancer cell model here, were cultured in DMEM without folate in cell medium. The folate-starved cells overexpress folate receptors on the cell membrane surface. Hep G2 cells were passed three rounds in the folate free medium before use to ensure overexpression of FA receptor on the cell surface. Normal cell model was constructed by culturing cells in DMEM medium with abundant free folate to block the folate receptors on the cell membrane surface. Both cancer and normal cell models were cultured in 6-well plates containing DMEM supplemented with 10% (v/v) fetal calf serum (FCS, Minghai Bio., China), 100 units/ml penicillin and 100 μg/ml streptomycin at 37 °C in humidified air containing 5% CO_2. When the cells were grown to 80% confluence, nanotube solution was added to each well at a final concentration of 50 μg/ml. The incubations were carried out at 37 °C and in 5% CO_2 atmosphere for 5 h. After incubation, all cells were washed with PBS to remove excess SWNTs and placed in fresh medium before any assays described here.

For confocal imaging, the adherent Hep G2 cells were directly imaged by an Olympus FV-1000 laser scanning confocal microscope (LSCM). Before examination, Hep G2 cells were fixed with 4% paraformaldehyde for 15 min, and then washed three times with PBS buffer. The laser wavelength of excitation was 488 nm for fluorescence channel imaging and the detected wavelength was from 500 nm to 550 nm. The TD channel imaging was done using a 488 nm laser.

To measure the cell viability after various laser and nanotube treatments, cell samples were planted into 96-well plates and went through the microtiter tetrazolium (MTT) array. For test, 20 μl MTT (5 mg/ml, contained in 0.01 M PBS) was added into each well and incubated for 4 h at 37 °C, then the medium was replaced with DMSO (200 μl in each well). A492 was detected to measure the proliferative capacity of each group. The relative proliferation ratio of the treated groups was calculated based on the intensity compared to controls.

RESULTS AND DISCUSSION

Our starting materials were short oxidized CVD SWNTs with -COOH groups on the side wall, which were generated by refluxing in nitric acid. Fig. 1 shows a schematic drawing of SWNT functionalization. Oxidized SWNTs were firstly noncovalently functionalized with chitosan (CS), and then the CS-SWNTs were conjugated with folate and FITC. SWNTs functionalized by both folate and FITC were denoted as f-SWNTs. The final f-SWNTs were highly stable in PBS buffer, as well as in cell culture medium without aggregation even after 1 week. The unbound folate and FITC were removed from the solution by centrifugation and repeated filtering.

Receptor-mediated endocytosis through clathrin-coated pits is the most common pathway of endocytosis [25]. It provides a means for the

selective and efficient uptake of macromolecules and particles that may be present at relatively low concentrations in the extracellular medium.
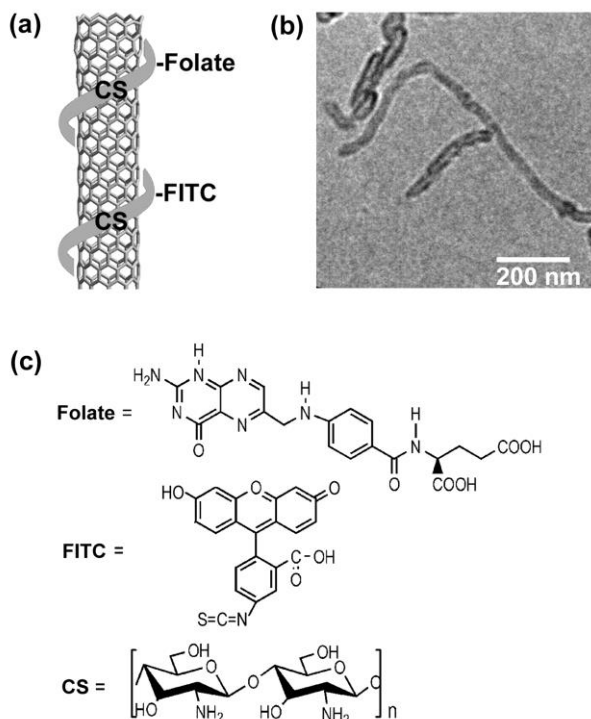
Fig. 1. (a) Schematic drawing of the functionalization of SWNTs with CS, folate and FITC. (b) TEM image of oxidized SWNTs. (c) Molecular structures of folate, FITC and CS.

Cells have receptors for the uptake of many different types of ligands, including hormones, growth factors, enzymes, and plasma proteins [26]. Herein, we conjugated the SWNTs with a kind of folate, which can specifically bind to folate receptors that overexpressed on the surface of cancer cells membrane. The selective internalization and uptake of SWNTs into Hep G2 cells were recorded by confocal imaging (Fig. 2). After incubating the cells together with 50 µg/ml FA-SWNTs for 3 h, strong fluorescence was observed in the cytoplasm of cancer cells, indicating that SWNTs entered into the cancer cells. However, for normal cells where the folate receptors on the surface of the cell membrane were blocked with free folate before incubation with FA conjugated nanotubes, just a weak fluorescence was observed in the cytoplasm. These results demonstrated that cancer cells were able to specifically internalize folate conjugated SWNTs via a folate receptor-mediated pathway while the normal cells were not.

The selective uptake of f-SWNTs inside cancer cells is due to the specific receptor-mediated interaction between the folate and the folate receptor on the cell membrane. Fig. 3 shows the magnified confocal images of the cell membrane of normal and cancer cells incubated with f-SWNTs. Bright green spots were observed on the surface area of the cell membrane of cancer cells, indicating the specific binding of f-SWNTs on the cancer cell membrane. For normal cells, no green spots were seen to show the specific binding.
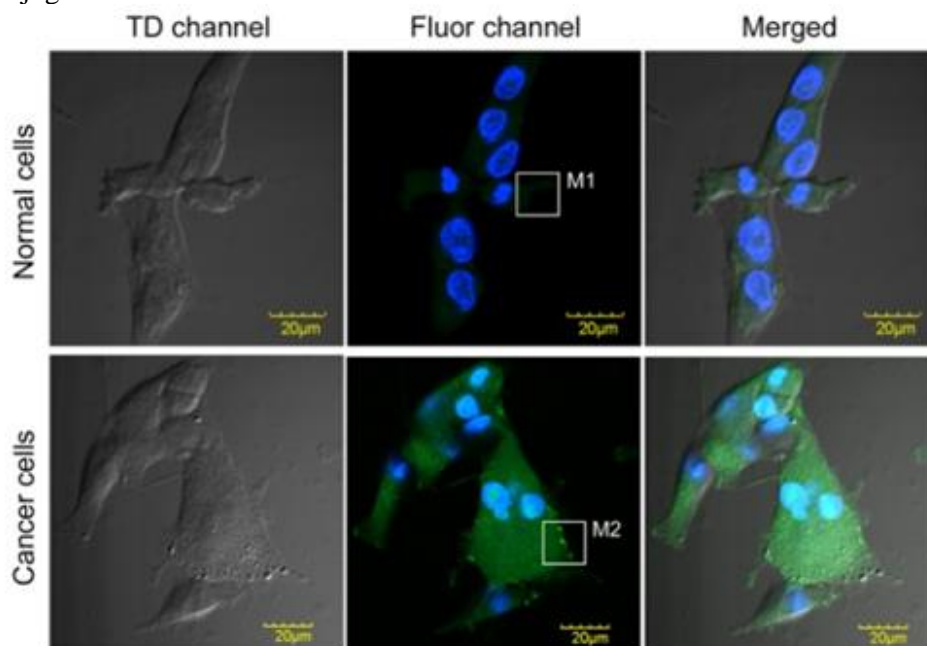
Fig. 2. Multi-channel confocal microscopy images of normal and cancer cells incubated with 50 µg/ml bioconjugated carbon nanotubes for 3 h. The magnified images of M1 and M1 are shown in Fig. 3.
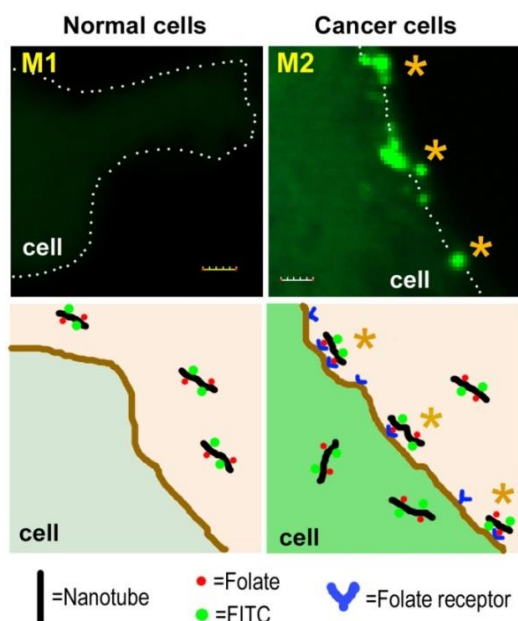
Fig. 3. Confocal images and representative schematic illustrations showing the selective targeting of folate conjugated carbon nanotubes to cancer cells through the specific receptor-mediated interaction. Both normal and cancer cells were incubated with 50 μg/ml bioconjugated carbon nanotubes for 3 h. The yellow stars indicate the specific binding of f-SWNTs to the cell membrane. M1 and M2 were magnified from Fig. 2, the scale bar is 2 μm.

To quantitatively analyze the targeting rate, we used flow cytometry to record the fluorescence intensity of cells, which denoted the relative amount of f-SWNTs in the cells (Fig.4). The targeting capability was defined as the ratio of FA-SWNTs in cancer cells and in normal cells. Strong fluorescence was observed in cancer cells incubated with f-SWNTs, whereas in untreated cells and normal cells with f-SWNT incubation, the fluorescence intensity was much lower (Fig.4). This clearly confirmed the high selective targeting of f-SWNTs to cancer cells. The targeting capability is about 6 times higher at a concentration of f-SWNTs of 50 μg/ml.
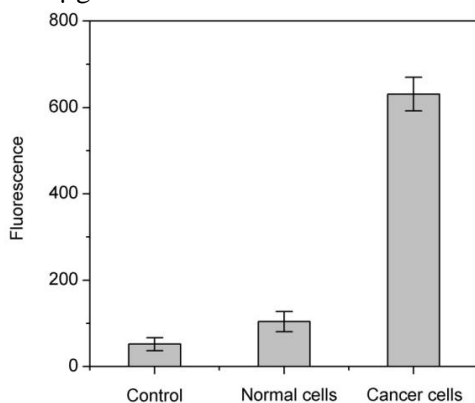
Fig. 4. Analysis of the targeting capability of folate conjugated carbon nanotubes to cancer cells.

To investigate the destructive effect of SWNTs combined with laser excitation on living cancer cells both normal and cancer cells incubated with SWNTs were exposed to an 800 nm near-infrared CW laser for 5 min. From the confocal images of cancer cells with SWNT uptake before and after laser treatment, as shown in Fig.5, one can clearly see the cracks of cancer cells due to the photothermal effect of SWNTs inside cells under laser excitation. Before laser treatment, the cancer cells have a clear dividing line at the edge of the cell membrane. After laser treatment, it is hard to distinguish the cytoplasm of the different cells since all cancer cells show a cracked and atrophic form. In the confocal images of normal cells treated with f-SWNTs and laser irradiation, normal cells survived after the same laser irradiation due to the low uptake of f-SWNTs. This result clearly shows the high selectivity of f-SWNTs on the photothermal destruction of cancer cells.
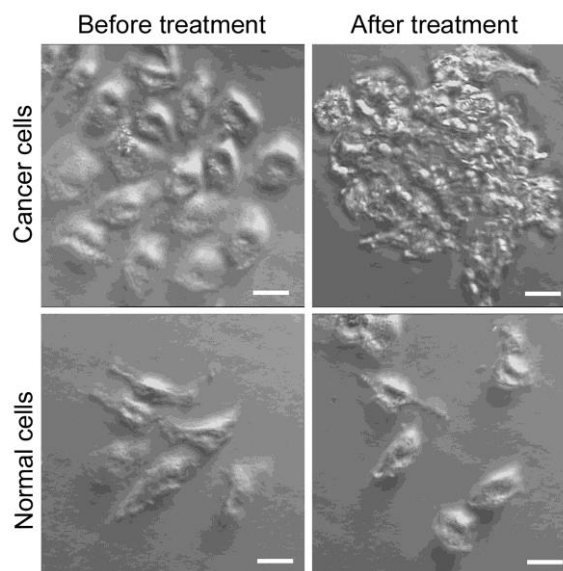
Fig. 5. Targeted cancer therapy by using carbon nanotubes and NIR laser. Both normal and cancer cells were incubated with 50 μg/ml nanotube for 3 h, followed by an 800 nm NIR laser irradiation for 5 min at a power density of 2.5 W/cm^2.

The selective destruction of cancer cells was further quantitatively analyzed through measuring the cell viability of cells with a MTT method. As shown in Fig.6, the cell viability of cells only with 50 μg/ml f-SWNTs (NTs) or 5 min laser treatment (laser) shows no obvious differences from the control cells (Control). Yet, the cancer cells with both f-SWNTs and laser treatment showed a remarkable decrease in cell viability. These results clearly demonstrated that the bioconjugated cancer nanotubes might act as potential agents for cancer-targeted near-infrared photothermal therapy.
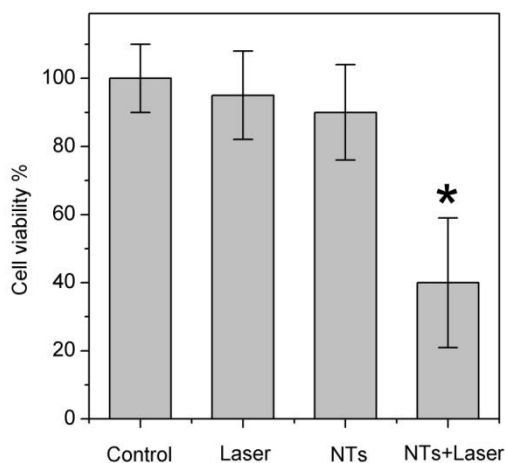
Fig. 6. Cell viability of cancer cells after different treatments: (Control) Control cells without any treatment; (Laser) Cancer cells irradiated with a 800 nm CW laser for 5 min in the absence of nanotubes; (NTs) Cancer cells incubated with 50 μg/ml nanotube for 3 h; (NTs+Laser) Cancer cells irradiated with the laser for 5 min in the presence of 50 μg/ml nanotube. Power density of 2.5 W cm^{-2} was used for all of these studies. Under a significance level of 5% (a = 0.05), the p values are shown as p < 0.05(*).

CONCLUSIONS

We studied the cancer targeting of folate conjugated carbon nanotubes and the selective cancer destruction by using a near-infrared continuous wave (CW) laser (800 nm). By functionalizing the SWNTs with folate, we developed a photothermal agent that can selectively enter into cancer cells that overexpress folate receptors on the surface of cell membrane and kill them through generating heat inside the cells under the excitation of a CW laser. The uptake of folate-conjugated SWNTs into the cells was investigated via a confocal fluorescence imaging route, and it is found that the functionalized SWNTs can enter into the cancer cells selectively via a folate-folate receptor-mediated pathway. Under the treatment of an 800 nm CW laser, cancer cells were selectively killed by the heat generation from carbon nanotubes inside the cancer cells, while the normal cells still remained alive. These results demonstrated that biofunctionalized carbon nanotubes could be potential agents for cancer targeting and selective photothermal therapy. Our current photothermal technique combined with nanotubes and near infrared laser might afford a promising potential way for cancer killing without causing toxicity and drug resistance since such a photothermal process is an instantaneous physical effect. These finds will be useful for the application of the structural properties of SWNTs for future therapeutic approaches.

REFERENCES

1. T. M. Allen, P. R.Cullis, *Science*, **303**, 1818 (2004).
2. C. K. Huang, C. L. Lo, H. H. Chen, G. H. Hsiue, *Adv. Funct. Mater.,* **17**, 2291 (2007).
3. M. Das, S. Mardyani, W. Chan, E. Kumacheva, *Adv. Mater.*,**18**, 80 (2006).
4. E. Patrikiadou, V. Zaspalis, L. Nalbandian, E. Chorbadzhiyska, M. Mitov, Y. Hubenova, *Bulg. Chem. Commun.*, **45**, 227 (2013).
5. L. R. Hirsch,R. J. Stafford,J. A. Bankson, S. R. Sershen, B. Rivera, R. E. Price, J. D. Hazle, N. J. Halas, J. L. West, *P. Natl. Acad. Sci. USA*, **100**, 13549 (2003).
6. J. M. Stern, J. Stanfield, J. T. Hsieh, J. A. Cadeddu, *J. Urology*, **177**, 210 (2007).
7. X. H. Huang,I. H. El-Sayed,W. Qian,M. A. EI-Sayed, *J. Am. Chem. Soc.,* **128**, 2115 (2008).
8. X. H. Huang, I. H. El-Sayed, W. Qian,M. A. EI-Sayed, *NanoLett.*, **7**, 1591 (2007).
9. N. W. S. Kam, M. O'Connell, J. A. Wisdom, H. J. Dai, *P. Natl. Acad. Sci. USA*, **102**, 11600 (2005).
10. N. Shao, S. Lu, E.Wickstrom, B. Panchanpakesan, *Nanotechnology*, **18**, 315101 (2007).
11. N. W. S. Kam, Z. Liu, H. J. Dai, *Angew.Chem. Int. Edit.*, **45**, 577 (2006).
12. Z. Liu, X. M. Sun, N. Nakayama-Ratchford, H. J. Dai, *AcsNano*, **1**, 50 (2007).
13. X. Wang, L. L. Yang, Z. Chen, D. M. Shin, *CA Cancer J. Clin.,* **58**, 97 (2008).
14. J. Sudimack, R. J. Lee, *Adv. Drug Deliver.Rev.*,**41**, 147(2000).
15. S. M. Bachilo, M. S. Strano, C.Kittrell, R. H. Hauge, R. E. Smalley, R. B. Weisman, *Science*, **298**, 2361 (2002).
16. M. J. O'Connell, S. M. Bachilo, C. B. Huffman,V. C. Moore, M. S. Strano, E. H. Haroz, K. L. Rialon, P. J. Boul, W. H. Noon, C. Kittrell, J. P. Ma, R. H. Hauge, R. B. Weisman, R. E. Smalley, *Science*, **297**, 593 (2002).
17. P. Cherukuri, C. J. Gannon, T. K.Leeuw,H. K. Schmidt, R. E. Smalley, S. A. Curley, R. B. Weisman, *P. Natl. Acad. Sci. USA*, **103**, 18882 (2006).
18. P. Kim, T. W. Odom, J. L. Huang, C. M. Lieber, *Phys. Rev. Lett.*, **82**, 1225 (1999).
19. N. W. S. Kam, H. J. Dai, *J. Am. Chem. Soc.*, **127**, 6021 (2005).
20. J. Peng, X. X. Qu, G. S. Wei,J. Q. Li, J. L. Qiao, *Carbon*, **42**, 2741 (2004).

21. J. Chen, M. A.Hamon,H. Hu,Y. S. Chen, A. M. Rao, P. C. Eklund, R. C. Haddon, *Science*, **282**, 95 (1998).
22. N. Nakayama-Ratchford, S. Bangsaruntip, X. M. Sun, K. Welsher, H. J. Dai, *J. Am. Chem. Soc.*, **129**, 2448 (2007).
23. B. Kang, D. C. Yu, S. Q. Chang, D. Chen, Y. D. Dai, Y. T. Ding, *Nanotechnology*, **19**, 375103 (2008).
24. Z. Liu, W. B. Cai, L. N. He, N. Nakayama, K. Chen, X. M. Sun, X. Y. Chen, H. J. Dai, *Nat. Nanotechnol.*, **2**, 47 (2007).
25. R. D. Singh, V. Puri, J. T. Valiyaveettil, D. L. Marks, R. Bittman, R. E. Pagano, *Mol. Biol. Cell*, **14**, 3254 (2003).
26. R. D. Singh, V. Puri, C. L. Wheatley, J. T. Valiyaveettil, D. L. Marks, R. Bittman, R. E. Pagano, *Mol. Biol. Cell,* **13**, 230A (2002).

БИО-СПРЕГНАТИ ВЪГЛЕРОДНИ НАНОТРЪБИ ЗА ОТКРИВАНЕ НА РАК И ФОТОТЕРМАЛНА ТЕРАПИЯ С ЛАЗЕР В БЛИЗКАТА ИНФРА-ЧЕРВЕНА ОБЛАСТ

Джун Ли, Яаодонг Даи[*]

Колеж по материалознание и технологии, Университет по аеринавтика и астронавтика в Нанджинг, Китай

(Резюме)

Откриване на ракови клетки и селективното им фототермичното разграждане е постигнато чрез фолат-спрегнати въглеродни нанотръби и вълнов инфра-червен лазер (800 nm) с непрекъснато действие. Така е създаден фототермичен агент, който прониква селективно в раковите клетки и ги убива чрез генерирането на топлина в тях след лазерно възбуждане. Резултатите, получени чрез конфокално флуоресцентно изобразяване показват, че функционализираните нанотръби могат специфично да проникнат в раковите клетки чрез фолат-модифицирани рецептори без съществено проникване в нормалните клетки. При облъчването с лазер при 800 nm раковите клетки селективно се убиват от топлината, генерирана във въглеродните нанотръби, докато нормалните клетки остават живи. Фототермичният метод с нанотръби и облъчването с инфрачервен лазер може да разкрият обещаващ начин за откриване на рак и селективна терапия без предизвикана токсичност и странични ефекти.

Numerical simulation of the transport process of biomolecules and ions at molecular level in parallel carbon-wall nanofluidic channels

K. Liu[1*], Y. C. Ning[1], D. C. Ba[1*], S. W. Xiao[2], X. L. Zhang[3], D. Y. Wang[1], G. Y. Du[1], Y. S. Ba[1]

[1]*School of Mechanical Engineering and Automation, Northeastern University, Shenyang, 110089, China;*
[2]*Institute of High Energy Physics Chinese Academy of Sciences, 100049 Beijing, China;*
[3]*Capital Aerospace Machinery Company, Beijing, 100076, China,*

The manipulation of biomolecules in nano-scale channels is quite interesting but full of challenge. One of the preconditions is to understand the transport process of biomolecules and ions in nanofluidic channels. In this issue, numerical simulations were carried out at a molecular level. The model of polypeptide GNNQQNY was introduced as a protein molecule under different conditions varying the driving factors like channel height, solution concentration and electric field intensity. The simulated results were discussed and analysed by comparing the molecular distribution, protein molecules' movement amplitude and potential energy. The decreasing channel height greatly influences the movement of proteins due to the more obvious electric double layer (EDL) effect. The increasing ionic concentration helps the passage of protein molecules while the layered concentration phenomenon of molecules and ions nearby the channel wall aggravates with the average ionic density. The electric field strength was also found to be an effective tool to control the passage of protein molecules. The results were helpful to understand the transport of biomolecules in nanofluidic channels.

Keywords: Molecular simulation, nanofluidic channel, protein molecules, transport process, GROMACS

INTRODUCTION

Nanofluidic chips are widely used in the detection [1], separation [2] and manipulation [3] of biomolecules in solutions with the rapid progress of nanoscale fabrication [4]. Due to the complex structure and high surface activity, it is quite difficult to control the movement of biomolecules in nanofluidic research [5]. Researchers focus their interest on electrophoresis and electroosmotic flow in the research of the electrokinetic phenomenon in parallel plates. Qiao and Aluru [6, 7] simulated the electric double layer (EDL) structure and electroosmotic flow in nanoscale channels. R. Karnik [8, 9] manipulated the concentration and transport of ions and biomolecules on changing the wall surface charge of 35 nm high nanofluidic diodes. Kun Liu and Dechun Ba [10] built a 1-D model of ion transport in rectangular nanofluidic channels using the Poisson-Boltzmann equation, which proves that potential control is an effective way to manipulate the movement of protein molecules.

MODEL AND SIMULATION DETAILS

The simulation system is built in the channel between two parallel plates, supposed with nanoscale distance and unlimited length. Assume that the solution between the parallel plates is sufficient and free without any initial external pressure gradient. The geometrical model is built as shown in Fig.1.
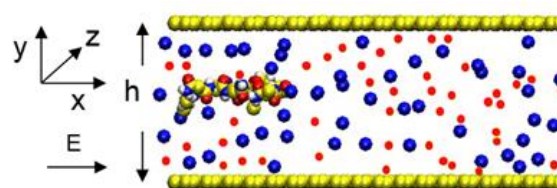
Fig.1. The geometrical model of biomolecules and ions transport in nanoscale channels.

The direction along the height is marked as *y* axis and the direction along the biomolecules' flow is marked as *x* axis. The channel is full of electrolyte solution mixed with protein molecules, the polypeptide *GNNQQNY*. For the sake of a clear display, the water molecules are hidden in Fig.1. The channel along the *x* and *y* axes is divided into tiny units with the scale of 7.60 nm×2.34 nm. The channel wall per unit is composed of 72 monolayer carbon atoms in every unit. One protein molecule is initially located in the left side of the channel. Larger (blue) and smaller (red) spheres represent Na^+ and Cl^- ions, respectively.

The flow in the channel is limited along the *y* axis. Periodic boundary conditions are brought to the flow along the x and z axis. The wall is charged with an average density of $0.05 C/m^2$. The water molecular model is simplified as a SPC model [13-15]. In the simulation system, two kinds of potential energy are mainly considered, Lenard-

Jones (LJ) interaction and electrostatic interaction. LJ atomic model is adapted to the charged ions in the channel. All LJ parameters are derived from Gromos96 force field.

GROMACS program packages are used to simulate the protein molecules in an aqueous solution of sodium chloride. First, one GNNQQNY molecule was put into the left entrance of the channel, followed by water molecules and ions. The initial speeds were generated under Maxwell-Boltzmann distribution at 300K. Energy minimization was done after 400 steps by the steepest descent method. Then molecular hot bath was carried out based on Berendsen methods after 200 steps without external voltage until the system reached balance. 400 ps molecular simulation was performed with external electric field along the x axis.

As time step was set to be 2.0 fs, the simulation steps were up to 300,000. The Newton motion equation was solved with leap-frog algorithm [16,17]. The results were tracked every 100 steps. A series of such simulations was carried out varying the channel height, number of positive and negative ions and external electric field strength. Table 1 lists the simulation parameters.

RESULTS AND DISCUSSION

Fig.2 shows the key frames of the transport movement of protein biomolecules. The protein molecule moved to the right according to the direction of the external electric field. Since the room was enlarged, the protein molecule turned over to a large extent. In the whole process, the positive Na^+ ions were mainly concentrated in the central channel while the negative Cl^- ions were mainly located near the wall.

Root-mean-square deviations (RMSD) [14] were here used to measure the oscillating amplitude of the molecules. Larger RMSD value means more dramatic changes of molecular position and better transport of protein molecules in the simulation process. Fig.3 shows the RMSD analysis results in No.1 ~ No.3 simulation systems listed in Table 1.

With the decrease in channel height, the RMSD value changed drastically till 100 ps ～ 150 ps reaching a dynamic balance. This is because the EDL's effect was stronger with the decreasing and resulted in greater influence on the ions' movements. Under the drive of electric field generated by EDL, the chloride ions moved directionally. The protein molecules, which were negatively charged after absorbing electrons in the solution, were excluded at a certain distance from

the chloride ions and then moved to the same direction as the chloride ions.

(a)

(b)

(c)

(d)

(e)

(f)
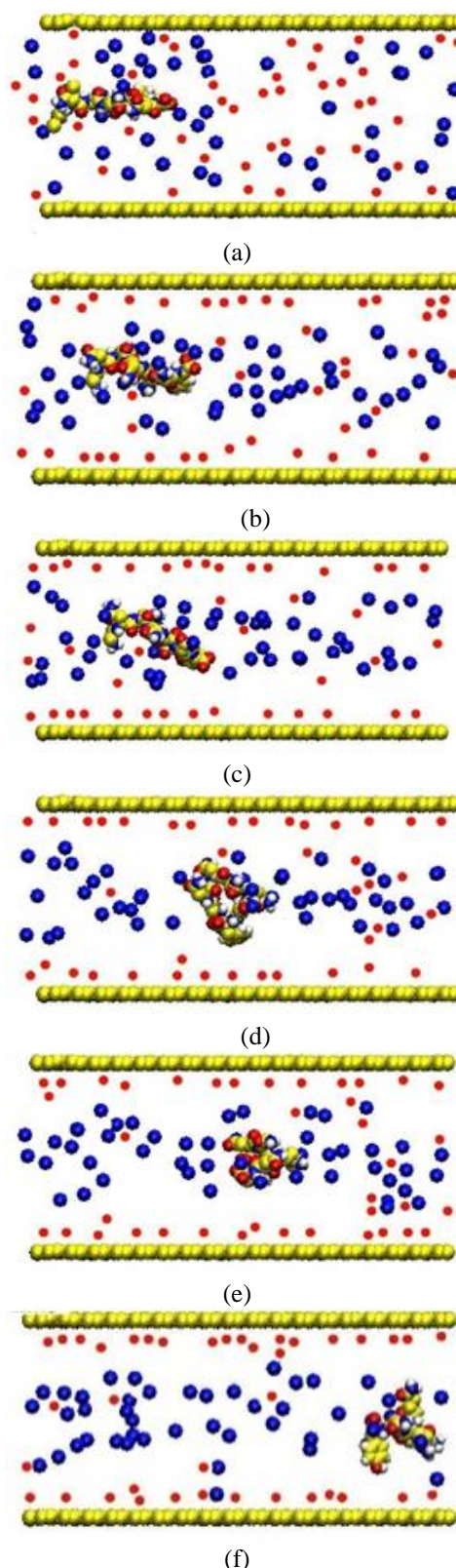
Fig.2. Simulation movement snaps of a biomolecular transport process (a) 1st step; (b) 4000th step; (c) 25000th step; (d) 100000th step; (e) 150000_t^h step; (f) 200000th step.

Table 1. List of the simulation parameters

Simulation system	No.1	No.2	No.3	No.4	No.5	No.6	No.7
Channel height (nm)	3.1	3.4	2.7	3.1	3.1	3.1	3.1
Number of Na^+ ions (per unit)	50	50	50	20	70	50	50
Number of Cl^- ions (per unit)	50	50	50	20	70	50	50
External electric field strength (V/nm)	1	1	1	1	1	0.5	2
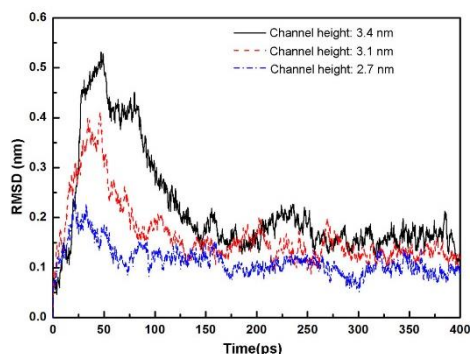
Fig.3. Oscillating amplitude of protein molecules at different channel heights

On the contrary, the stretch room of the protein became larger with the increase in channel height. RMSD value changed drastically at the very beginning. However, the movements tended to be weaker and the passage time turned shorter because of the conjunct action of surrounded ions, water molecules and the channel wall.

The density distribution of ions and water molecules along the height direction is given in Fig.4. The curve of water molecule distribution has two peaks nearby the wall. The chloride ions were attracted by the wall charge and gathered near the wall. There were few chloride ions but a large number of sodium ions around the protein molecules. However, the sodium ions were neither concentrated on the protein molecules nor absorbed by them. They just moved regularly and induced the movements of protein molecules. The width of EDL decreased with the increase in channel height because the motive force exerted on the protein molecules from the ions was weakened.

Fig.5 shows the comparisons of the oscillating status under different ion concentrations in No.1, No.4 and No.5 simulation systems. The ion concentration greatly influenced the RMSD value of protein molecules. When the number of ions increased to 70 per unit, the RSMD value strongly changed and hardly got up to a balance in a quite long time of 400 ps. When the ion's number decreased to 50 per unit, the balance time could be about 200 ps. When the ion's number further decreased to 20 per unit, the balance time correspondingly decreased to 100 ps. With the help

of the viewer toolbox, it could be observed that the protein molecules obviously interacted with ions and moved rapidly through the channel at a high concentration, and *vice versa*.
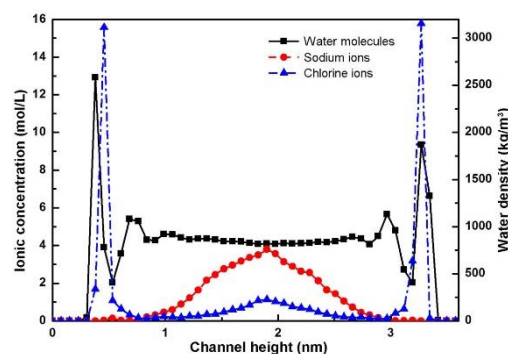
Fig.4. Density distribution of molecules and ions along the y axis at a channel height of 3.4 nm
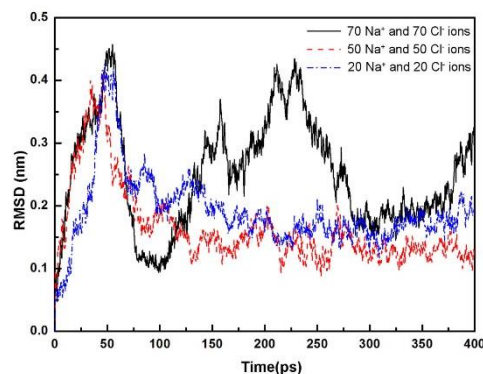
Fig.5. Oscillating amplitude of protein molecules at different concentrations

Fig.6 shows the density distribution of water molecules and ions in simulation system No.5. The water molecules and the negative ions mainly gathered on the two sides near the channel wall and displayed two peaks.

But the positive ions looked quite different. Many sodium ions concentrated in the center of the channel. With the increase of ionic concentrations, the central ionic concentration also increased, which favored the movement of protein molecules. Meanwhile, the layered concentration phenomenon of molecules and ions nearby the channel wall aggravated with the average ionic density. The RMSD comparison of different electric field strength in simulation systems No.1, No.6 and No.7 is shown in Fig.7.
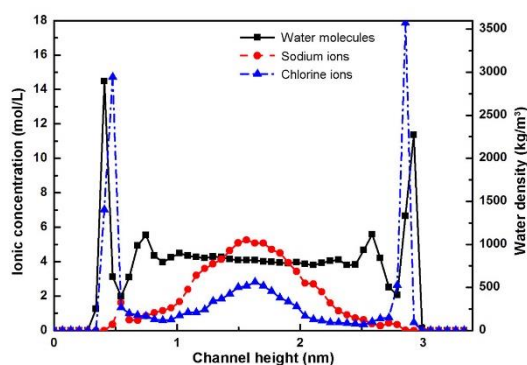
Fig.6. Density distribution of molecules and ions at 70 Na^+ ions and 70 Cl^- ions per unit
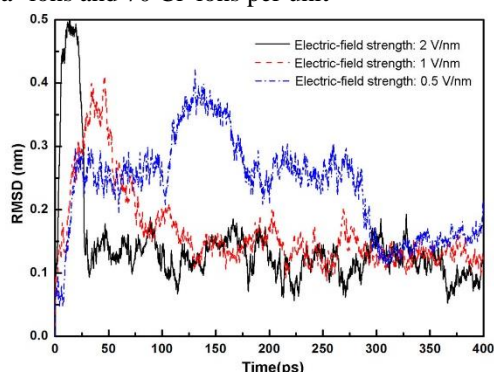
Fig.7. RMSD values of protein molecules at different electric field strength

When electric field of 2 V/nm strength was exerted along the *x* direction, the RMSD value strongly oscillated and then quickly relaxed, which showed that the conformations of the protein molecules were easy to get to balance. However, with the decrease of exerted voltage, the RMSD value still oscillated but the amplitude weakened. Meanwhile, the balance time was extended with reduced electric field strength. The proteins moved so rapidly that those of them with no charge on the side chain could not force the whole peptide chain to interact with ions. Although the far side chain had the trend to move to the wall, it could not approach the wall surface due to steric hindrance. The stronger the electric field force, the faster moved the ions, hence the more quickly the protein molecules passed thought the channel. Large initial RSMD value and reduced balance time helped the transport of protein molecules.

Fig.8 shows the density distribution of water molecules and ions under electric field in system No.7. The water molecules distribution was almost unchanged at different electric field strengths. With the increase in electric field strength, the negative ions concentrated in the two sides while the positive ions moved to the centre of the channel.
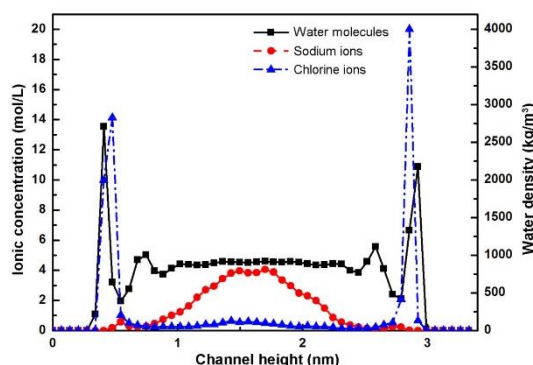
Fig.8. Density distribution of molecules and ions at electric field strength of 2 V/nm

The chloride ions moved quickly and came close to the wall surface while the sodium ions moved along the electric field direction in the central channel with a high flow rate. That is because the electroosmotic flow formed in the channel was strengthened by the strong electric field. The accelerated flow carried over more ions around the protein molecules and weakened the interaction between the ions and protein molecules. So the electric field force was prior to the LJ impact and the Coulomb force at strong electric field.

CONCLUSIONS

The transport process of biomolecules and ions in nanoscale channels was investigated using seven groups of parameters. Based on the simulated results, several conclusions could be drawn, as follows:

(1) The channel height greatly influenced the transport of proteins. With the decrease in channel height, the EDL effect became more obvious, so the moving proteins received more repulsive force from the counter chloride ions. As the transport direction of protein molecules was the same as that of the counter ions, the transport became more difficult, and *vice versa*.

(2) The ionic concentration also influenced the transport of protein molecules. At higher ionic concentration, the interaction between ions and protein molecules became stronger, which forced the protein molecules to move more rapidly and pass through the channel more quickly, and *vice versa*. Meanwhile, the layered concentration phenomenon of molecules and ions nearby the channel wall aggravated with the average ionic density.

(3) The electric field strength played an important role on the transport of protein molecules. The protein molecules passed more easily and more quickly with the increase in electric field strength because the flow velocity turned higher and the electric field force prevailed over other forces such as LJ impact and Coulomb force.

REFERENCES

1. T. Yamamoto, T. Fujii. *Nanotechnology*, **21**, 395502(2010).
2. S. L. Levy, H. G. Craighead. *Chem. Soc. Rev.*, **39**, 1133(2010).
3. S. M. Stavis, J. Geist, M. Gaitan, L. E. Locascio, E. A. Strychalski. *Lab Chip*, **12**, 1174 (2012).
4. C.H. Duan, W. Wang, Q. Xie. *Biomicrofluidics.* **7**, 026501 (2013).
5. M. Napoli, J. C. T. Eijkel, S. Pennathur., *Lab chip*, **10**, 957 (2010).
6. R. Qiao, N. R. Aluru, *J. Chem. Phys.*, **118**, 4692 (2003).
7. R. Qiao, N. R. Aluru, *Phys. Rev. Lett.,* **92(19)**, 1 (2004).
8. R. Karnik, R. Fan, M. Yue, D. Li, P. Yang, A. Majumdar, *NanoLett.*, **5**, 943(2005).
9. R. Karnik, K. Castelino, *Appl. Phys. Lett.*, **88**, 123 (2006).
10. K. Liu, D.C.Ba, X.G.Gu, G.Y.Du, Z.Lin, X. H. Liu, Z. X. Wang, S.W.Xiao. *Appl. Surf. Sci.*, **258**, 2157 (2012).
11. D.V.D. Spoel, E. Lindahl, B. Hess, G. Groenhof, A.E. Mark, H. J. C. Berendsen. *J. Comput. Chem.,* **26,** 1701 (2005).
12. B. Hess, C. Kutzner, D. Spoel, E. Lindahl, *J. Chem. Theory and Comput.***, 4**, 435 (2008).
13. W. D. Cornell, P. Cieplak, C.I. Bayly, I. R. Gould, K. M. Merz, D. M. Ferguson, D. C. Spellmeyer, T. Fox, J. W. Caldwell, P. A. Kollman. *J. Am. Chem. Soc*, **117**, 5179 (1995).
14. B. R. Rooks, R. E. Bruccoleri, B. D. Olafson, D. J. States, S. Swaminathan, M. Karplus. *Journal of Comput. Chem.*, **4**, 187(1983).
15. I. D. Kuntz, J. M. Blaney, S. J. Oatley, R. Langridge, T. E. Ferrin. *J. Mol. Biol.,* **161**, 269 (1982).
16. W. L. Jorgensen, J. Chandrasekhar, J. D. Madura, R. W. Impey, M. L. Klein. *J. Chem. Phys.*, **79**, 926 (1983).
17. H. J. C. Berendsen, J. R. Grigera, T. P. Straatsma. *J. of Chem. Phys.*, **91**, 6269 (1987).

ЧИСЛЕНО СИМУЛИРАНЕ НА ТРАНСПОРТНИ ПРОЦЕСИ НА БИОМОЛЕКУЛИ И ЙОНИ НА МОЛЕКУЛЯРНО РАВНИЩЕ В УСПОРЕДНИ КАНАЛИ С НАНОРАЗМЕРИ СЪС СТЕНИ ОТ ВЪГЛЕРОД

К. Лю[1*], Й. Ч. Нинг[1], Д. Ч. Ба[1*], С. У. Ксиао[2], Кс. Л. Жанг[3], Д. Ю. Уанг, Г. Ю. Ду[1], Я. Ш. Ба[1]

[1]*Училище по механо-инженерство и автоматизация, Североизточен университет, Шенянг, Китай*
[2]*Институт по физика на високите енергии, Китайска академия на науките, Бейджин, Китай*
[3]*Столична компания по космическо машиностроене, Бейжин, Китай*

(Резюме)

Манипулирането на био-молекули в канали с нано-размери е твърде интересно и предизвикателно. Едно от пред-условията е да се разберат транспортните процеси на биомолекули и йони в нано-размерни канали. В настоящата работа е извършено числено моделиране на молекулно ниво. Въведен е модел на полипептида GNNQQNY като молекула на протеин за изследване на поведението му спрямо движещи фактори като височина на каналите, концентрацията му и интензитета на електрично поле. Резултатите от симулирането са обсъдени и анализирани чрез сравнение на разпределението на молекулите, амплитудите на движението на протеиновите молекули и потенциалната енергия. Намаляването на височината на каналите влияе значително на движението на молекулите главно чрез ефекта на двойния електричен слой (EDL).Повишаването на йонната концентрация спомага за преминаването на протеиновите молекули, докато слоистото концентриране на молекулите и йоните в близост до стените на каналите се влошава със средната йонна плътност. Силата на електричното поле също е ефективно средство за контролиране на преминаването на протеиновите молекули. Резултатите са полезни за разбирането на преноса на био-молекули в нано-флуидни канали.

Preparation and research of a novel cellulose-based heavy metal adsorbent

H. X. Zhu[1], Q. P. Kong[1], X. J. Cao[1], H. He[2], J. Wang[3,*], Y. C. He[4]

[1]*College of Light Industry and Food Engineering, Guangxi University, Nanning, 530004, China*
[2]*PCFM Lab, School of Chemistry and Chemical Engineering, Sun Yat-Sen University, Guangzhou 510275, China*
[3]*College of Agriculture and Biology, Shanghai Jiao Tong University, Shanghai, 200240, China*
[4]*College of Pharmaceutical Engineering and Life Sciences, Changzhou University, Changzhou 213164, China*

This paper describes a novel cellulose-based heavy metal adsorbing material. The bamboo cellulose was pretreated by plasma (150 V, 120 s), then subjected to epoxidation, amination and ultrasonic enhancement sulfonation reaction to prepare the cellulose-based heavy metal adsorbing material which grafted heavy metal adsorbing groups of N, S into the bamboo cellulose. The treated materials were characterized by FTIR and NMR analysis. The analyses showed that O-containing epoxy groups, N-containing amine group, and S-containing sulfo groups were successfully grafted into the bamboo cellulose.

Keywords: Adsorbption, Bamboo fibers, Plasma, Cr(VI), FTIR, NMR

INTRODUCTION

With the rapid development of industry, the problem of heavy metal ion pollution has become increasingly serious. Many technologies and methods have been applied in the removal of heavy metal ions, such as flotation [1], adsorption [2], ion exchange, chemical precipitation, membrane separation [3], electrochemical [4], oxidation/ reduction [5], ultra-filtration, and so on. Recent research work has focused on the bio-adsorbent properties of natural cellulose to remove metal ions from wastewater. Cellulose, a polysaccharide polymer, has many reactive surfaces with -OH groups that allow it to participate in a variety of chemical reactions [6], such as esterification [7], etherification [8], oxidation [9], and polymer grafting [10]. Yu [11] reported the magnetically modified sugarcane bagasse with a higher adsorption capacity and a rapid adsorption rate. Experimental results showed that the adsorption capacities of the magnetic sorbent for Pb^{2+} and Cd^{2+} were 1.2 and 1.1 mmol/g, respectively. Esfandiar [12] studied the removal of Mn(II) from groundwater by modified sugarcane bagasse with response surface methodology (RSM). The effects of pH, adsorbent dosage and initial metal concentration on the adsorption of Mn(II) were investigated using response surface methodology (RSM) based on Box-Behnken design. A maximum experimental Mn(II) removal efficiency of 63% for SCB was obtained.

Bamboo is widely cultured in tropical and subtropical areas, especially in Guangxi, China. It has a lot of active hydroxyl groups and can be modified to obtain new properties, such as adsorption of heavy metals. Researchers [13] have found that carboxylated bamboo fibers treated with citric acid have a higher adsorption capacity of Pb^{2+} (127.1 mg/g). Carboxyl group content between 1.99 and 4.13 mmol/g could be obtained by changing the ultrasonic pretreatment time, reaction temperature, reaction time, and the amounts of catalyst and citric acid. Bamboo root biomass [14] was shown to be suitable for the adsorption of Cu^{2+} and Zn^{2+} ions from wastewater. The effects of contact time, adsorbent dose, and initial concentration of the metal solution on metal uptake were evaluated. Equilibrium was reached after 15 to 20 min for both Cu^{2+} and Zn^{2+}. The endothermic adsorption process was measured, but its chemical and physical mechanism was not studied.

In the present work, we prepared a bamboo cellulose-based heavy metal adsorbing material for Cr(VI) adsorption. The cellulose was prepared by using plasma treatment, epoxidation, amination, and ultrasonic enhancement sulfonation reactions to graft N and S groups. The surface morphology, and the chemical structure of the bamboo fibers before and after modifications were characterized by Fourier transform infrared (FTIR) spectroscopy and nuclear magnetic resonance (NMR).

Materials

Natural cellulose (bleached bamboo pulp) was supplied by Guangxi Hwagain Paper Industry of

---

China. Diethylenetriamine (DETA), epoxy chloropropane, carbon disulfide, anhydrous cupric sulfate, hydrochloric acid, sodium hydroxide, absolute ethyl alcohol and acetone were purchased from Tianjin Kermel Chemical Reagent Co., Ltd. All these reagents were of analytical grade and used without further purification.

SYNTHESIS OF ADSORBENT

Plasma pretreatment

5 g of bamboo fibers and a certain amount of 2% NaOH were added into a beaker. The moisture content was controlled at 60%. After defibering for 10 min, the mixture was pretreated with plasma (120 s, 150V, 160Pa).

Epoxidation reaction

5 g of plasma-pretreated bamboo fibers and 200 mL of 10% NaOH solution were added into a 250-mL three-stoppered flask. After shaking for 15 min, 15 mL of epichlorohydrin (ECH) solution was added to the flask. The mixture was stirred for 150 min at 50 °C. As a result, epoxy bamboo fibers with an epoxy value of 7.3 mmol/g were obtained.

Amination reaction

5 g of the epoxy bamboo fibers and 200 mL of 3% NaOH solution were then added into a 250 mL three-stoppered flask fitted with a magnetic stirrer. After defibering for 15 minutes, 7 g of diethylenetriamine (DETA) solution was added into the mixture and stirred at 70 °C for 120 min. Zeta potential of the final amino-bamboo fibers was 30.4 mV.

Ultrasonic sulfonation reaction

The amino-bamboo fibers were then treated by an ultrasonic sulfonation reaction as follows: 5 mL of CS_2, reaction temperature of 25 ℃, reaction time of 60 min, 14% alkali solution and 200 W of ultrasonic energy.

CHARACTERIZATION OF UNTREATED AND TREATED BAMBOO FIBERS

Fourier transform infrared spectroscopy

The Fourier transform infrared (FTIR) spectra of untreated and treated bamboo fibers were recorded on an attenuated total reflection FTIR spectroscope (HP Nexus470,USA) equipped with smart omni-transmission in the range of 650-4000 cm^{-1}. Untreated and treated bamboo fibers were dried in an air-circulating oven at 50 °C overnight. Finally, the samples were prepared by mixing 1 mg of untreated or treated bamboo fibers with 100 mg of KBr followed by pressing the mixture into ultra-thin pellets.

NMR analysis

A common testing method for cellulose structural analysis,^{13}C-NMR analysis was applied to study the structure of untreated and treated bamboo fibers. ^{13}C-NMR spectra of the samples were obtained on a Bruker (Germany) AVANCE III equipment at room temperature. Measurements were performed by applying the Carr-Purcel-Meiboon-Gill (CPMG) pulse sequence with an interpulse spacing of 200 ms.

ADSORPTION MEASUREMENT OF Cr^{6+}

The adsorption of Cr(VI) onto grafted bamboo fibers was carried out with a selected amount of adsorbent in 160 mL of Cr(VI) solution at various concentrations. The initial pH of the Cr(VI) solution was adjusted with 0.1 M HCl and NaOH. Then, the adsorption step occurred at 30 °C for 2 h at 150 rpm. Afterwards, the reaction mixture was filtered and the concentration of Cr(VI) in the filtrate was measured by inductively coupled plasma optical emission spectrometry with an Agilent (US) ICP-700 Series OES. The calculation of formaldehyde adsorption on grafted cellulose was following Eq. (1):

$$Q = \frac{(C_0 - C_t)V}{m} - Q_0 \qquad (1)$$

Where Q is the adsorption capacity of treated cellulose, mg/g; Q_0 is the adsorption capacity of native cellulose, mg/g; C_0 is the initial Cr^{6+} concentration, mg/L; C_t is the subsequent Cr^{6+} concentration, mg/L; V is the volume of Cr^{6+} solution, mg/L; m is the weight of treated cellulose, g.

RESULTS AND DISCUSSION

FTIR analysis

The FTIR spectra of untreated and pretreated bamboo fibers are presented in Fig.1. The featured structures are listed in Table 1. As shown in Fig.1, the new absorption peaks at 1,277.34 cm^{-1}, 993.57 cm^{-1}, and 856.38 cm^{-1} are due to the presence of an epoxy group, indicating that epoxidation was successful.

The hydroxyl absorption peak at 3000 to 3400 cm^{-1} was slightly strengthened and widened. This may have been caused by a primary amine N-H stretching vibration and weak absorption from the secondary amine. The IR spectrum of the modified cellulose-based adsorbent displayed an N-H stretching vibration adsorption at 3,332.56 cm^{-1}, a C-H stretching vibration adsorption at 2,934.96 cm^{-1}, the amines of -NH bending vibration adsorption at 1,639.59 cm^{-1} and 1,456.01 cm^{-1}, as well as a C-N stretching vibration at 1,497.92 cm^{-1}. These

absorption peaks were present in the diethylenetriamine monomer molecule, but were not found in tests of untreated bamboo cellulose.

The peaks at 1,497.92 cm^{-1}, 1,456.01 cm^{-1}, and 1,324.56 cm^{-1} correspond to bending vibrations of I type C-S, II type C=S, and the presence of a CS$_2$-NR$_2$ group, respectively. These molecules indicate that the modified cellulose-based adsorbent was successfully sulfonated.
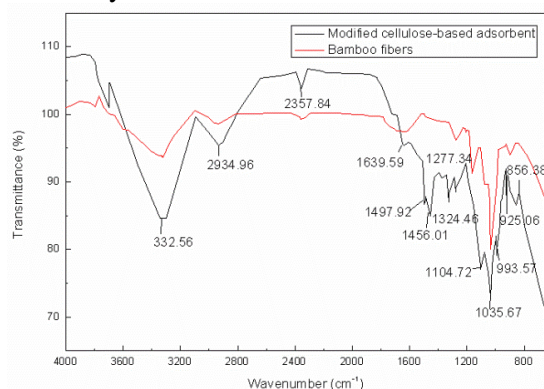
Fig. 1. FTIR spectra of untreated and treated bamboo fibers

Table 1. FTIR spectra peaks of untreated and treated bamboo fibers.

Characteristics	Δν (cm^{-1})		Δν (cm^{-1})/ absorbance change	Assignment
	Bamboo fibers	cellulose-based heavy metal adsorbent		
	3331	3332	+1/Δ	δ O-H
	2930	2934	+4/Δ	δ C-H (methyl and methylene)
	1640	1639	-1/▽	η N-H (in plane) ; δ C=O
		1496	new	I type ε C-S (CS$_2$-NR$_2$); ε C-H
	1455	1456	+1/Δ	ε CH; ζ methyl; ζ methylene
	1373	1373	0	ε C-H; ε C-O-H
	1337	1336	-1/▽	γ OH
		1324	new	II type γ C=S (CS$_2$-NR$_2$); γ C-H
	1319	1320	+1/Δ	γ CH$_2$
	1281	1277	-4/Δ	ε CH
	1166	1164	-2/▽	ζ C–O–C
	1104	1104	0	δ C-C; δ C-O
	1034	1035	+1/Δ	δ C-O (cellulose ether bond)
		993	new	δ C–O–C
	918	925	+7/Δ	δ C–OH (out-of-plane)
		856	new	δ C-O

Key to symbols: γ: wagging vibration; δ: vibration; ε: deformation vibration; ζ: asymmetrical vibration; η: bending vibration; Δ: increase; ▽: decrease.

NMR analysis

Details of the NMR analysis are shown in Table 2 and Fig. 2. The analysis of the treated

1074

bamboo fibers indicated that the peak shifts from 150 to 200 ppm correspond to C=S and C-S. Chemical shifts at 196, 169, 162, and 150 ppm indicated that C=S and C-S were successfully grafted in the treated fibers. The 100 to 150 ppm shift was caused by C-O. New chemical shifts corresponding to an ether bond in the treated bamboo cellulose occurred at 134, 126, 118, and 103 ppm. The 50 to 100 ppm shift was caused by C-N. A new chemical shift at 83 ppm occurred in the treated bamboo fiber sample. The chemical shift at 56 ppm was strengthened, while the shift at 75 ppm was weakened. This might indicate that the cellulose had a C-N linkage. All NMR analyses of the treated bamboo suggested that the fibers were modified by grafting. In other words, the epoxidation, amination, and sulfonation reactions were successful.
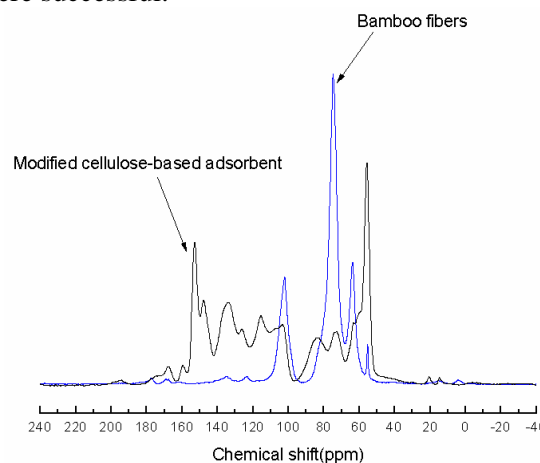
Fig. 2. ^{13}C-NMR spectra of untreated and treated bamboo fibers.

Table 2. ^{13}C-NMR chemical displacement of untreated bamboo fibers and treated bamboo fibers

Peak shift (ppm)	Bamboo fibers (ppm)	Modified cellulose-based adsorbent (ppm)	Assignment
200-180		196	C=S
180-165		168	C=S and C-S
165-140		159-150	C-S
140-120		132and129	C-O
120-110		116	C-O-C
105-100	101	102	C1, C=N
95-80		82	C-N
80-70	72	71	C-N, C2, C3, C5
70-60	61	61	C6, C-O
60-50	58	58	C4, sugar terminal group C

REGENERATION EXPERIMENTS

The treated bamboo fibers had the advantage of being biodegradable and recyclable. To obtain the

material for regeneration, the treated bamboo fibers after adsorption were dried and treated with a certain amount 0.1 mol/L HCl solution and then neutralized with 0.1 mol/L NaOH. As shown in Table. 3, with the increase in adsorption time, the adsorption capacity to Cr^{6+} decreased. After two cycles of adsorption, the regeneration rate was 46.9%. The proposed process and mechanism of Cr(VI) adsorption by the bamboo cellulose adsorbent from an aqueous solution is shown in Fig. 3.
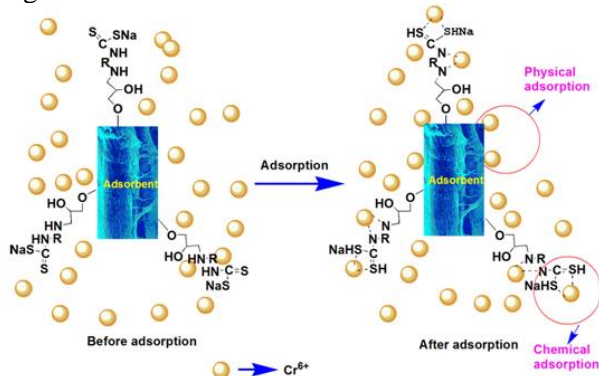
Fig. 3. Proposed process and mechanism for adsorption of Cr(VI) by treated bamboo fibers from an aqueous solution.

Table 3. The adsorption material regeneration experiment.

	Adsorption cycles			
	1	2	3	4
Adsorption capacity/(mg/g) (Cr^{6+})	32.4	15.2	7.2	5.5
Regeneration rate （%）		46.9	22.2	17.0

CONCLUSIONS

The FTIR and NMR analyses showed that O-containing epoxy groups, N-containing amine groups, and S-containing sulfo groups were successfully grafted. The analysis showed that the structure of treated bamboo fibers greatly changed, compared with untreated bamboo fibers. The treated bamboo fibers are an attractive alternative adsorbent in wastewater treatment.

REFERENCES

1. N. Reynier, J-F. Blais, G. Mercier, S..Besner, *Water. Air.Soil.Poll.*, **224**(4), 1514 (2013).
2. X. Sun, L. Yang, Q. Li, Z. Liu, T. Dong, H. Liu, *Chem. Eng. J.*, **262**, 101 (2015).
3. A. K. Basumatary R. V. Kumar, A. K. Ghoshal, G. Pugazhenthi, *J. Membrane Sci.*, **475**, 521 (2015).
4. H. Wang, C. Na, *Appl. Mater. Inter.,* **6**(22), 20309 (2014).
5. I. M. Dittert, H. de Lima Brandão, F. Pina, E. A. B. da Silva, S.M.A.G.U. De Souza, A.A.U. de Souza, C.M.S. Botelho, R.A.R. Boaventura, V.J.P. Vilar, *Chem. Eng. J.,* **237**, 443 (2014).
6. S. Boufi, M. N. Belgacem, *Cellulose*, **13**(1), 81(2006).
7. A. M. Senna, K. M. Novack, V. R. Botaro, *Carbohydr.Polym.,* **114**, 260 (2014).
8. T.T.T. Ho, T. Zimmermann, R. Hauert, W. Caseri, *Cellulose*, **18**(6), 1391 (2011).
9. S. Takaichi, A. Isogai, *Cellulose*, 20(4), 1979 (2013).
10. J. Zhuo, G. Sun, *Carbohydr. Polym.*, **112**, 158 (2014).
11. J. X. Yu, L. Y. Wang, R. A. Chi, Y. F. Zhang, Z. G. Xu, J. Guo, *Appl. Surf. Sci.,* **268**, 163 (2013).
12. N. Esfandiar, B. Nasernejad, T. Ebadi, *J. Ind. Eng.Chem.*, **20**(5), 3726 (2014).
13. S. Wang, L. Wang, W. Kong, J. Ren, C. Liu, K. Wang, R. Sun, D. She, *Cellulose*, **20**(4), 2091 (2013).
14. A. I. Babatunde, O. K. Abiola, O. A. Osideko, O. T. Oyelola, *Afr. J. Biotechnol.*, **8**(14), 3364 (2009).

ПОЛУЧАВАНЕ И ИЗСЛЕДВАНЕ НА НОВ АДСОРБЕНТ НА ТЕЖКИ МЕТАЛИ НА ЦЕЛУЛОЗНА ОСНОВА

Х. Кс. Жу[1], К. П.Конг[1], Кс. Дж. Цао[1], Х. Хе[2], Дж. Ванг[3,*], Ю. Хе[4]

[1]Колеж по лека промишленост и хранително инженерство, Университет Гуанкси, Нанинг, Китай
[2]Лаборатория PCFM, Училище по химия и химично инженерство, Университет Сун Ят-сен, Гуанчжоу, Китай
[3]Колеж по земеделие и биология Университет Джиао Тонг, Шанхай, Китай
[4]Колеж по фармация и науки за живота, Университет в Чангжоу, Китай

(Резюме)

В работата се описва нов материал за адсорбция на тежки метали на целулозна основа. Бамбукова целулоза се третира с плазма (150 V) за 120 секунди, следват епоксидиране, аминиране и ултразвуково ускорено сулфониране за получаването на адсорбента, който е в състояние на вгради тежките метали. Получените материали са изследвани с инфрачервена спектроскопия(FTIR) и ядрено-магнитен резонанс.Анализите показват, че кислород-съдържащите сулфо-групи са успешно включени в целулозата.

Study of the influence of acidic tailings water with a large number of chemical substances on the granular medium and slope stability in the dump

Guangjin Wang[1,2]*, Xiangyun Kong[2], Chunhe Yang[1]

[1]*State Key Laboratory of Geomechanics and Geotechnical Engineering，Institute of Rock and Soil Mechanics, Chinese Academy of Sciences，Wuhan,430071, China*
[2]*Kunming University of Science and Technology, Kunming 650093, China*

The long-term soaking of the granular medium with acidic tailings water which contains a large number of chemical substances is an important factor that affects the structural composition of copper waste ore with copper compounds and the slope stability in the dump. Therefore, based on the project example that part of the granular material of the mine dump at the bottom is soaked by the acidic tailings water for a long time, in the present work indoor direct shear tests of the granular medium under long-term soaking were performed and the influence of long-term soaking on the particle breakage of granular medium and strength parameters was analyzed. The dump slope stability was studied at different water levels of the tailings pond and was compared to the indoor test results. The research results show that the breakage rate of the soaked samples is obviously higher than that of saturated and *on-situ* samples when the granular medium is soaked by the tailings water for a long time. The change in the value of the safety coefficient is small as the water level of the tailings pond is below 230 m. But the safety coefficient obviously decreases after the water level of the tailings pond is up to 230 m and it increases with the increase of the water level of the tailings pond. Moreover, the slope sliding surface moves down with the increase in the water level of the tailings pond.

Key words: acidic tailings water, copper and iron compounds, chemical reaction, slope stability

INTRODUCTION

The long-term soaking of the granular medium is an important factor that impacts the dump stability. However, in the process of experiment, the decrease in strength parameters mainly results from particle breakage. Based on a number of tests, the articles [1-3] point out that the particle breakage can change the particle size, gradation curve and density degree, resulting in changes of the physical and mechanical properties of the soil samples. Hall and Gordon [4-5] find that under a certain amount of stress, the breakage rate of sands with good grading is smaller than that of sands with poor grading. The articles [6-8] find that by the triaxial test the increment of the particle breakage leads to the reduction of the shear strength of the coarse aggregates, and the peak friction angle within the peak values is a power function of the particle breakage rate. Wei Song [9] points out through the triaxial test of wet particle breakage that the particle breakage caused by wetting increases with the increment of the confining pressure and the wet stress, and a linear relationship approximately presents between the wet- axis variation and the wet particle breakage. Therefore, the long-term soaking of tailings water can affect the breakage of the dump granules and then the granular strength parameters. In fact, the particle breakage test is of

actual engineering significance in the dump and rockfill dam. In particular, when the bottom granular medium of the dump is soaked in the tailings water, the particle breakage is quite obvious because of the long-term soaking of the granular medium in the acidic tailings water which contains a lot of chemicals.

The XRD patterns of the original tailing sample and after leaching at pH=2, 4.5, and 7.0 are shown in Fig. 1. XRD data were collected in the angular range (10°−90°). The tailings mainly consist of quartz, despujolsite and muscovite-3T, with trace palygorskite O, pectolite and manganoan [10].

The previous studies were rarely related to the influences of the particle breakage in the long-term soaking of the tailings water on the shear strength. However, the large-scale direct shear test is one of the conventional indoor test methods for coarse grained soil because the large-scale direct apparatus is characterized by a large specimen size used in it that can retain the original grading of the soil samples to a maximum extent and weaken the size effect. As the direct shear test is easy to operate and applicable in a wide range, it is the most widely used method [11] that is economical and practical for small and medium-size engineering projects. Therefore, in our work, the modified large-scale strain-controlled direct dual-purpose shear apparatus of indoor and field use, developed jointly by Wuhan Institute of Rock and Soil Mechanics,

---

Chinese Academy of Sciences and Hongkong University, was used to test the particle breakage of the dump granules and its influences on the strength parameters. On the basis of the experimental results, the slope stability of the mine dump was studied by means of FLAC software.

DIRECT SHEAR TEST

Test equipment

The dual-purpose direct shear apparatus used in this test is of assembled structure, and mainly composed of an overall removable outer frame, horizontal loading system, vertical loading system, a shear box, etc. The clearance dimension of the shear box is: L×W×H = 500 m×500 m×410 mm. The lower shear box is connected with the overall framework, and the largest slit width between the upper shearing box and the lower one is 10 mm. Since the lower shear box is fixed in the shearing process of the direct shear apparatus, the upper shear box can only be moved in the horizontal plane and then the shear slits do not change due to the dilatation of the specimens. The deformation of the specimens by the above dual-purpose direct shear apparatus is more uniform than that by using the conventional one. Compared with the stress-controlled field-use direct shear apparatus, this

device can show the whole process of rock mass deformation, and the maximum shear displacement can be up to 140 mm.

Test method and test grading

A large number of experimental studies performed by Yangtze River Scientific Research Institute [12] has shown that the sample size effect can be almost eliminated only when the D/dmax is 4-6mm (D is the size of the shear box and dmax is the largest tested particle diameter). According to the designed size of the above direct shear apparatus, the maximum particle diameter of the samples is selected to be 60 mm. The tested grain size range groups are shown in Table 1.

Table 1. Test grading of coarse grained soil.

Range of grain size(mm)	40-60	20-40	10-20	5-10	2-5
Percent (%)	22.5	14.5	9.5	7.5	10.0
Range of grain size(mm)	1-2	0.5-1	0.25-0.5	0.074-0.25	<0.074
Percent (%)	6.0	5.1	6.9	12.0	6.0
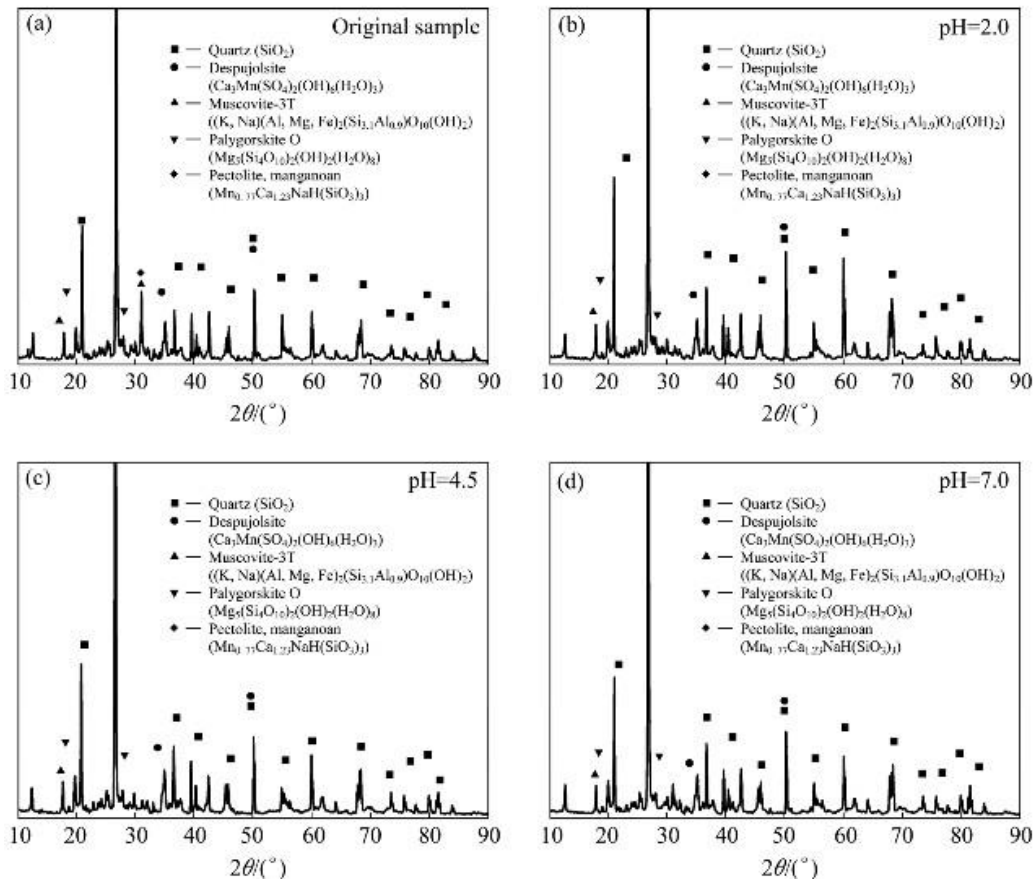
Fig. 1. XRD patterns of tailings samples before (a) and after leaching at pH 2 (b) [10].

In order to study the effect of the tailings water on the particle breakage of the coarse grained soil, the *on-situ* samples (with water content of 4%), saturated samples and soaked samples with a dry density of 1.90 g/cm^3 were selected for each group's tests under different vertical pressures (0.05, 0.1, 0.2, 0.4, 0.7, 1.0, 1.3MPa, respectively). The granular samples soaked in the tailings water and the pictures of their direct shear tests are shown in Figures 2(a) and 2(b).

(a)

(b)
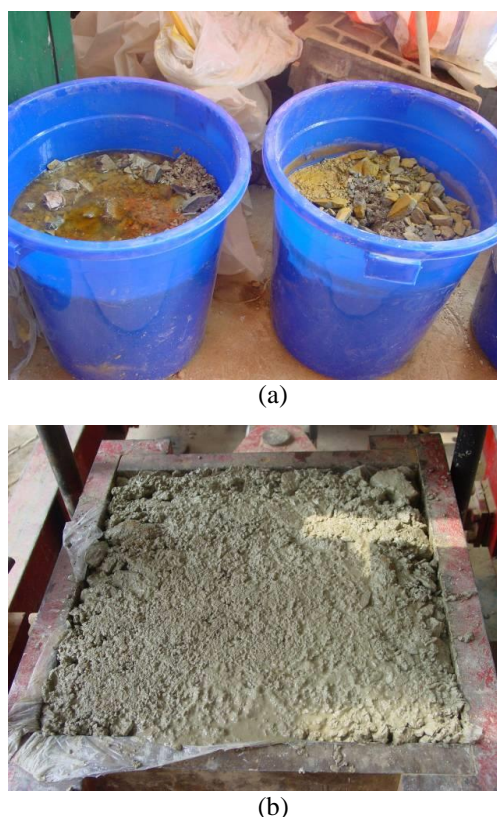
Fig. 2. (a) Samples soaked in the tailings water and (b) Direct shear test of the soaked samples.

The soaked samples refer to the soil samples that were put into the water containers after weight proportioning and air drying and maintained to be in fully-saturated state without external forces and sealed for a month. Before the test, the soil samples were taken out from the site, dried at ambient temperature, separated by sieving, weighed, then added water as required, mixed evenly (saturated samples needed to add water to maintain the full saturation state), and loaded in 3 tiers for compaction. Then artificial consolidation was conducted for the samples and the consolidation stability was controlled to be 0.0025 mm/min. After the deformation was stable, the direct shear test was operated at a horizontal shear rate of 1.4 mm/min and it was stopped when the shear strain was 20%. After finishing the test, the soil samples were dried again at ambient temperature and then screened.

The pH value of the tailing water is 2.1~2.5 and its physicochemical composition is shown in Table 2.

Table 2. Physical and chemical composition of the tailing water

Item	COD	Fe	Ca	Zn	Mn	Al
Concentration (mg/L)	19.50	0.82	498.80	0.18	4.70	0.42
Item	Mg	Cu	Na	K	Cd	As
Concentration (mg/L)	67.30	≤0.02	54.80	23.40	≤0.02	≤0.02

The main ingredients of mine waste rock which can participate in chemical reactions were chalcopyrite ($CuFeS_2$), chalcocite (Cu_2S), oxidized copper ore ($CuCO_3 \cdot Cu(OH)_2$) and pyrite (FeS_2). The chemical reaction is as follows:

① Chalcopyrite
$$2CuFeS_2+H_2SO_4+O_2 \rightarrow 2CuSO_4+Fe_2(SO_4)_3+H_2O$$
$$CuFeS_2+2Fe_2(SO_4)_3 \rightarrow CuSO_4+5FeSO_4+2S$$
$$2FeSO_4+H_2SO_4+O_2 \rightarrow Fe_2(SO_4)_3+H_2O$$

② Chalcocite
$$Cu_2S+Fe_2(SO_4)_3 \rightarrow CuS+CuSO_4+2FeSO_4$$
$$CuS+Fe_2(SO_4)_3 \rightarrow S+CuSO_4+2FeSO_4$$

③ Oxidized copper ore
$$2CuCO_3 \cdot Cu(OH)_2+H_2SO_4 \rightarrow 3CuSO_4+4H_2O+2CO_2$$
$$CuO+H_2SO_4 \rightarrow CuSO_4+H_2O$$
$$Cu_2O+H_2SO_4 \rightarrow CuSO_4+Cu+H_2O$$

④ Pyrite
$$2FeS_2+3O_2+2H_2O \rightarrow 2FeSO_4+2H_2SO_4$$
$$4FeSO_4+H_2SO_4+O_2 \rightarrow 2Fe_2(SO_4)_3+2H_2O$$
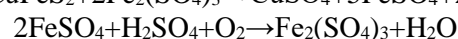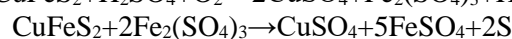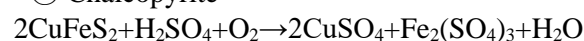
⑤ Other reactions
$$Fe_2O_3 +3H_2SO_4 \rightarrow Fe_2(SO_4)_3+3H_2O$$
$$Al_2O_3+3H_2SO_4 \rightarrow Al_2(SO_4)_3+3H_2O$$
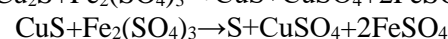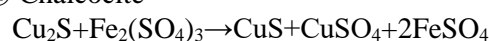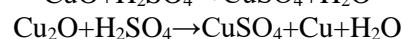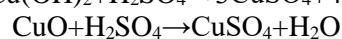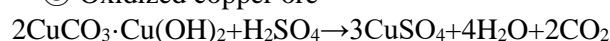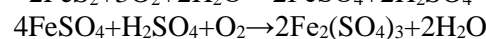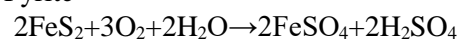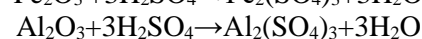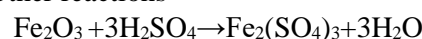
ANALYSIS OF TEST RESULTS

According to Hardin's definition, the relative particle breakage rate Br is the area Bt between the grading curve before and after the test divided by the initial crushing potential Bp, i.e., Br=Bt/Bp. As the relative particle breakage rate can reflect the variation of the various particle sizes of the sample before and after the test, the direct shear tests were conducted in our work for the *on-situ* samples (with water content of 4%), saturated samples and soaked samples to obtain the relative particle breaking rate Br as shown in Table 3.

From Table 3, it can be seen that the breakage rate Br of the saturated samples increases but not clearly, compared with the *on-situ* samples. On the contrary, that of the coarse-grained samples soaked in the tailings water for a month increases obviously and is much higher than that of *the on-situ* samples and the saturated ones. In the long run, tailings water has a striking softening effect on the

coarse-grained soil while not in the short-term water flow. The typical SEM images of the granular medium before and after soaking are shown in Figure 3.

Table 3. Relationship between σ and Br at different water contents

Sample	Breakage rate (Br)at different vertical pressures(MPa)						
	0.05	0.1	0.2	0.4	0.7	1.0	1.3
Soaked sample (%)	1.34	2.04	4.56	7.57	9.14	11.19	11.91
Saturated sample (%)	0.34	0.46	0.788	1.87	5.15	6.60	7.23
On-situ sample (%)	0.24	0.23	0.77	1.50	4.33	5.29	6.56
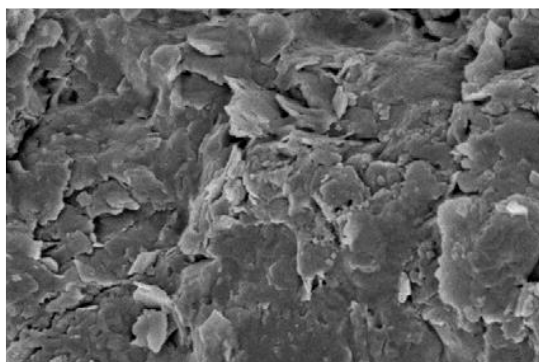
(a) SEM images before soaking
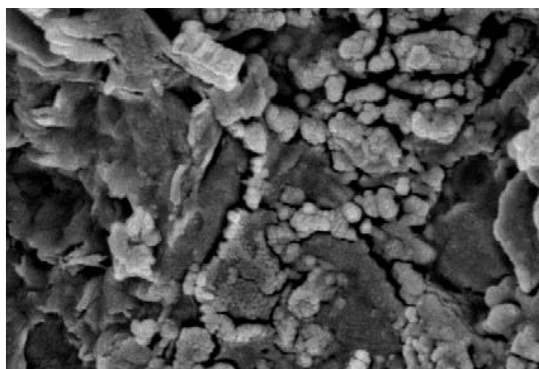
(b) SEM images after soaking

Fig. 3. Typical SEM images of the granular medium before and after soaking.

ANALYSIS OF DUMP SLOPE STABILITY

Slope model

A mine dump is very close to the tailings pond and its bottom granular medium is under the water surface of the tailings pond. See Figure 4 for the site photos. Landslides of the dump may affect the safety of the tailings dam of the mine. Therefore, the dump slope stability was analyzed by means of the ANSYS and FLAC software based on the results of the indoor direct shear test for the dump granular medium.

Fig. 4. *On-site* dump granular in the tailings pond.

According to the original and current topographic maps of the dump, the three-dimensional geological model was created and shown in Figure 5, which was divided into 6 layers with 20 m each and 120 m in total.
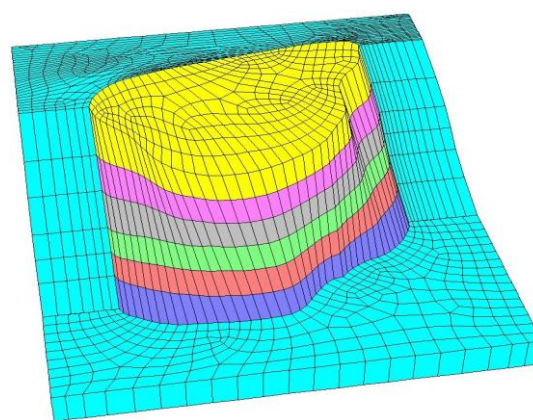
Fig. 5. Three-dimensional geological model of the dump.

Table 4. Material parameters of granular accumulation.

Sample	Density (kg.m^{-3})	Bulk modulus K (Gpa)	Shear modulus G (Gpa)	Cohesion C (Mpa)	Internal frictional angle φ(°)	Dilation angle ψ(°)	Tensile strength σ_t(Mpa)
Long-term soaked sample	1900	0.03	0.02	0.03	22.90	4.80	0.03
On-situ sample	1900	0.15	0.10	0.09	33.89	7.60	0.05
Rock	1900	13.600	9.800	0.40	46.00	14.00	2.15

Calculation parameters and schemes

The Mohr-Coulomb criterion was used for the calculation of the model. The top surface was set to be a free boundary, the bottom - a fixed restricted boundary and the four sides - roller bearing boundary. Under the initial conditions, only the dead weight was considered in the entire process of the calculation. The parameter values of the dump materials are shown in Table 4.

Based on the indoor experimental research of the long-term soaking of the dump granules in the mine tailings water, five schemes were selected to make the analysis of the dump stability, i.e., Scheme 1 for the dump granules which are not soaked in the tailings water (i.e., the water level of the tailings pond is <190m), Scheme 2 for the current water level of the tailings pond and the rest schemes for the water level of 230 m, 250 m and 270 m, respectively. See Table 5 for the specific calculation schemes.

Table 5. Calculation schemes.

Calculation scheme	1	2	3	4	5
Water level of tailings pond (m)	<190	210	230	250	270

RESULTS ANALYSIS

Table 6 shows the computed results of the slope safety coefficient of the dump in the different schemes, from which the slope safety coefficient follows the order: Scheme 1 > Scheme 2 > Scheme 3 > Scheme 4 > Scheme 5. The value of the safety coefficient changes little in Scheme 1 and Scheme 2 while it obviously decreases after the water level of the tailings pond increases up to 230 m. It is not obvious for the long-term soaking of the dump granular medium at the bottom of the dump to impact the safety coefficient of the dump slope because the slope sliding surface is still above the water level of the tailings pond when the water level of the tailings pond is 210 m. However, when the water level of the tailings pond is up to 230 m, the slope sliding surface has already been below the surface of the tailings pond partly and then the change value of the safety coefficient increases. In addition, with the increment of the water level of the tailings pond, the change value of safety coefficient continues to increase.

Figure 6 indicates the displacement vector cloud in Scheme 1 and Scheme 5, from which it can be seen that the slope sliding surface moves downward with the increment of the water level of the tailings pond and as a result the change value of slope safety coefficient also increases. The above analysis shows that long-term soaking of the dump granular medium is adverse to the stability of the dump slope. In particular when part of the slope sliding surface is under the water level of the tailings pond, the long-term soaking of the dump granular medium greatly affects the stability of the dump slope. Thus, separate tailings dam and dump should be built as far as possible.

Table 6. Calculation results of slope reliability.

Calculation scheme	1	2	3	4	5
Safety coefficient	1.26	1.24	1.19	1.10	0.98

CONCLUSION

Compared with the *on-situ* samples, the breakage rate Br of the saturated samples increases but not distinctly. On the contrary, that of the coarse-grained samples soaked in the tailings water for a month obviously increases and is much higher than that of the *on-situ* samples and the saturated ones. The tailings water has a striking softening effect on the coarse-grained soil in long term while it has not in short term. The safety coefficient of the slope calculated for the dump decreases with the increment of the water level of the tailings pond.

(b)
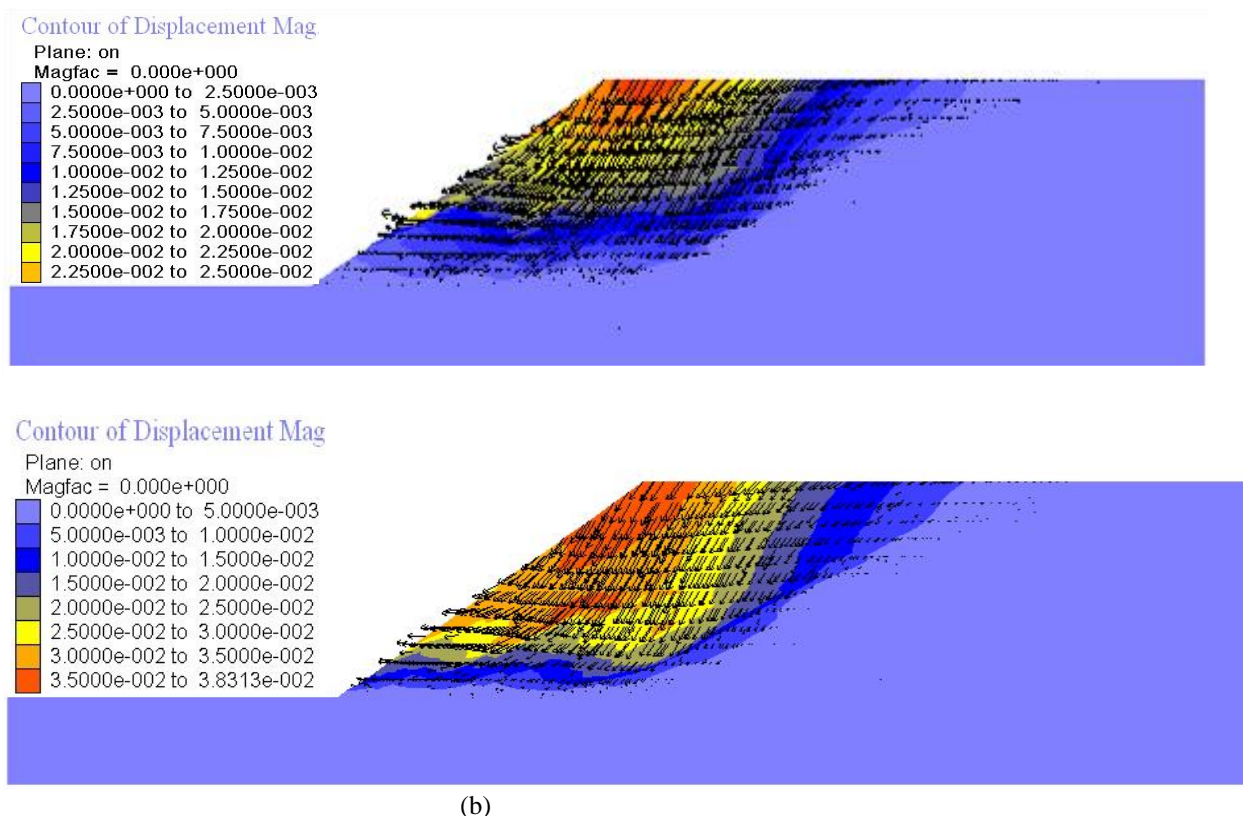
Fig. 6. (a) Displacement vector cloud of Scheme 1; (b) Displacement vector cloud of Scheme 5.

It changes little when the water level of the tailings pond is below 230 m; while it obviously decreases when the water level is above 230 m. The value of the change continues to increase with the increment of the water level of the tailings pond. Meantime, with the increment of the water level of the tailings pond, the slope sliding surface moves downward, resulting in increased change value of the slope safety coefficient of the dump. It is concluded that long-term soaking of the dump granular medium is unfavorable to the stability of the dump slope; in particular, it affects the stability of the dump slope significantly when part of the slope sliding surface is under the water level of the tailings pond.

REFERENCES

1. R J. Marsal, *Journal of the Soil Mechanics and Foundations Division*. **93**(SM2), 27 (1967).
2. L.Xiaoli, L.Hongyan, L.Zhonggang. *Disaster Advances*, **6** (S2) , 46 (2013).
3. Z. Qing, G. Yue, C. H. Ming, C. Jing, Y. ZhiHua, *Research Journal of Chemistry and Environment*, **16**(S2), 1 (2012).
4. E. B. Hall, B. B. Gordon, American Society for Testing and Materials, Philadelphia, Penn. Special Technical Publication STP-361, 1964, p. 315
5. W. Guangjin, K. Xiangyun, Y.Chunhe, R.Zhaoying. *Disaster Advances*, **6** (S4), 102 (2013).
6. L. Hanlong, Q. Hongyu, G. Yufeng, Y. D. Zhou, *Rock and Soil Mechanics*, **26**(4) ,562 (2005).
7. Wang Feiyue. *Research Journal of Chemistry and Environment*, 17(S1), 163 (2013).
8. Y. Gui, L. Kunlin, L. Yanchen. *Disaster Advances*, **6** (S1), 9 (2013).
9. W. Song , Z. Jungao, *Chinese Journal of Rock Mechanics and Engineering* , **25**(6), 1252 (2006).
10. Y. Guo, P. Huang, W. Zhang, X. Yuan, F. Fan, H. Wang, J. Liu, Z. Wang, *Transactions of Nonferrous Metals Society of China*, **23**, 3068 (2013).
11. W. Houzhen, W. Ren, H. Mingjian,et al. *Rock and Soil Mechanics*, **29**(1), 48 (2008).
12. Z. Xiaowen, G. Biwei, D. Hongshun, R. Xibao, *Chinese Journal of Geotechnical Engineering,* **27**(8), 876 (2005).

ИЗСЛЕДВАНЕ НА ВЪЗДЕЙСТВИЕТО НА КИСЕЛИННИТЕ ОСТАТЪЧНИ ВОДИ В ДЕПО ЗА ОТПАДЪЦИ, СЪДЪРЖАЩИ РАЗЛИЧНИ ХИМИЧЕСКИ ВЕЩЕСТВА ВЪРХУ ГРАНУЛИРАНА СРЕДА

Гуангджин Ванг[1,2] , Ксиангюн Конг[2] ,Чунхе Янг[1]

[1]*Държавна лаборатория по геомеханика и геотехническо инженерство，Институтпоскална и почвенамеханика, Китайска академия на науките, Ухан, Китай*
[2]*Научно-технологичен университетв Кунминг, Китай*

(Резюме)

Продължителното промиване на гранулирана среда с киселинни отпадъчни води, съдържащи голям брой химически вещества е важен фактор, който влияе на структурата на отпадъци, съдържащи медни съединенияи на ъгъла на откоса на депото.В тази работа са направени изпитания в лабораторни условия върху срязващото напрежение в гранулирана среда при продължително промиване и върху разрушаването на твърдите частици и здравината на средата. Стабилността на насипа и ъгъла на откоса са изследвани при различни нива на водите в хвосто-хранилището. Изследването показва, че скоростта на разрушаване при продължително промиване очевидно е по-висока отколкото при реални проби от хранилището. Промяната на коефициента на сигурност е малка, когато нивото на водите е под 230 м. Този коефициент намалява значително, когато нивото на водите достига 230 м. и продължава да намалява, когато нивото на водите в хвосто-хранилището се покачва. Освен това наклона на насипа от твърди отпадъци започва да се свлича с повишаване на водното ниво в хвосто-хранилището.

Physical model and industrial test of small inclusions removal by bubble adhesion

C. Yang[1*], F. Tang[2], M. Shen[1], H. Yu[1]

[1]*University of Science and Technology Liaoning, Anshan City 114053, Liaoning, China*
[2]*Anshan Iron and Steel Group Company, Anshan City 114014, Liaoning, China*

A variety of methods have been used to reduce the content of inclusions in metals. As one of the important refining equipments between steelmaking and continuous casting, RH vacuum refining plays an important role in removing inclusions from the molten steel. In this paper, a physical model is established at a geometric similarity ratio of 1:4, to simulate a real 180-t RH vacuum refining device. Inclusions removal from molten steel by bubble adhesion in an RH degasser is analyzed using the physical model. The effects of variables such as bubble size, treatment time, lift-gas flow rate, amount of added NaHCO₃, are investigated. The results of the 180-t RH industrial test reveal that bubbles of carbon dioxide are formed by the decarburization reaction of calcium hydrogencarbonate, which effectively removed inclusions from the molten steel.

Key words: Bubble adhesion, inclusion removal, physical model, industrial test.

INTRODUCTION

It is generally known that nonmetallic inclusions in molten steel can lead to serious defects in the final product. In order to satisfy the requirements for the degree of cleanliness of steel, controlling the amount, size distribution and shape of inclusions is of great importance in the steelmaking process. Inclusions in steel greatly affect its physical and chemical properties, such as fatigue life, machinability and corrosion resistance [2]. Big size inclusions are primarily removed by Stokes floating. However, inclusions less than 50 μm in diameter cannot rise rapidly and tend to remain in the steel [3-5]. During steel secondary refining aided by surface tension forces from non-wetting contact, some solid inclusions, such as alumina and silica tend to collect on surfaces such as bubbles [6,7] and therefore can adhere to the bubbles and be transported to the surface of molten steel [9].

Technologies for clean steelmaking are being continuously developed to fulfil the ever increasing demands on material properties [10]. The composition, quantity and size distribution of non-metallic inclusions are important in influencing the physical properties of steel. RH refining process to a significant degree has become the main refining operation for removing inclusions from liquid steel in order to minimize the inclusions that could potentially form defects in the finished product or adversely affect the product properties [10, 11].

Therefore, special methods have been developed to remove non-metallic inclusions from molten steel [12,13]. Furthermore, Miki [7] and Thomas in [5, 6, 23] developed a mathematical model to predict the removal of alumina inclusions from molten steel in a continuous casting tundish. Although several papers have been written on inclusion removal by gas bubbles flotation in water modeling [14-17] there are few papers systematically studying the fundamentals of inclusion removal by bubble attachment in liquid steel in an RH vacuum degasser and the effects of bubble size, treatment time, lift-gas flow rate, etc.

This paper presents fundamental models to quantify the removal of inclusions by bubbles in molten steel. A water model is used to study the influences on fine inclusions removal in a 180-t RH vacuum refiner. The industrial test proved that the inclusions in molten steel can be removed effectively by the addition of calcium carbonate.

EXPERIMENTAL PRINCIPLE AND METHOD

To make the prototype and the model identical in both geometry and dynamics, a physical model of a 180-t RH vacuum degasser was established with a geometric similarity ratio of 1:4. Table 1 shows the operational and geometrical parameters of the prototype and the physical model.

A diagram of the experimental apparatus is shown in Fig.1. Liquid steel was simulated by 400 L of acidified water, and fine inclusions - by 20 g of high-density polypropylene beads; compressed air was used as the lift gas. The inclusions are put into 500 ml water in a beaker and stirred using an ultrasonic stirrer to make sure the inclusions were fully wetted. The water with inclusions is then

* To whom all correspondence should be sent:
E-mail: chunjieyang_utsl@126.com

transferred into the experimental vessel. The snorkels are dipped into the liquid in the ladle to a depth of 100 mm.

The relevant parameters of the media (namely, the densities ρ of the liquid and the inclusions) for the model and prototype are shown in Table 2.
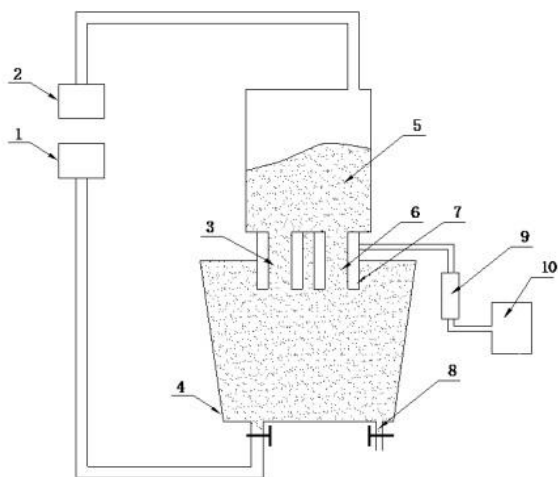
Fig. 1. Schematic drawing of the experimental apparatus – 1 water tank; 2 vacuum pump; 3 downleg snorkel; 4 ladle; 5 vacuum chamber; 6 upleg snorkel; 7 distribution chamber for lift-gas; 8 valve; 9 velocity-meter; 10 air cylinder.

Table 1. Main parameters of the prototype and the physical model (in mm).

Equipment	Dimensions	Prototype	Model
	Height	4450	1112
Ladle	Upper internal diameter	3130	782
	Lower internal diameter	2800	700
Vacuum vessel	Internal diameter	1786	446
	Length	900	225
Snorkel	Internal diameter	560	140

Table 2. Relevant parameters of the media for the model and prototype

Density	Prototype	Model
ρ_{liquid}/kg m^{-3}	7.0×10^3 (steel)	1.0×10^3
ρ_{inc}/ kg m^{-3}	3.9×10^3 (Al$_2$O$_3$) or 2.7×10^3 (SiO$_2$)	0.91×10^3 (polypropylene)

The contact angle of the inclusions with water is 118°, particle size (μm) distribution curves are shown in Fig.2.

The morphology of the inclusions in the water model is shown in Fig.3.
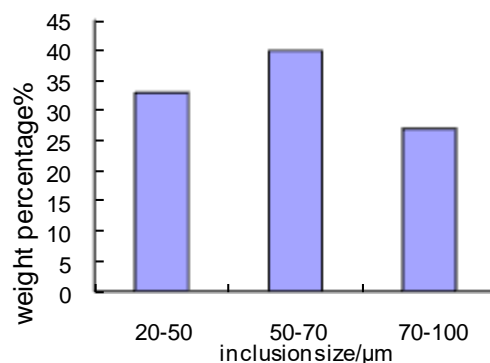
Fig. 2. Inclusions particle size distribution.
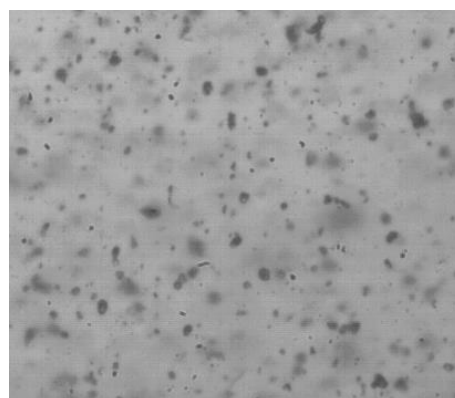
Fig. 3. Morphology of the polypropylene beads in the water model.

The inclusion removal rate after the first *j* time intervals is calculated from the formula

$$\eta_j = \frac{\sum_{i=1}^{j} m_{ti}}{m_0}$$

Where m_{ti} is the removed amount of inclusions in the *i*th time interval, and m_0 is the total amount of inclusions.

Acidified NaHCO$_3$ was used to produce fine bubbles of CO$_2$ according to the reaction:

$$HCl(aq) + NaHCO_3(aq) = NaCl(aq) + H_2O(l) + CO_2(g)$$

or:

$$HCO_3^-(aq) + H^+(aq) = CO_2(g) + H_2O(l)$$
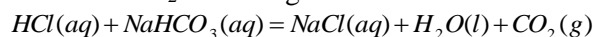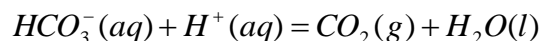
The fine bubbles of CO$_2$ were distributed evenly over the water, thus increasing mechanical collisions between bubbles and inclusions.

Hydrolysis equilibrium exists and the ionization equilibrium reaction is as follows:

$$HCO_3^- = H^+ + CO_3^{2-}$$
$$HCO_3^- + H_2O = H_2CO_3 + OH^-$$
$$H_2CO_3 = H_2O + CO_2$$
$$H^+ + OH^- = H_2O$$

Overall reaction:

$$2HCO_3^-(aq) = CO_3^{2-}(aq) + CO_2(g) + H_2O(l)$$
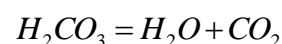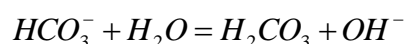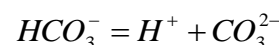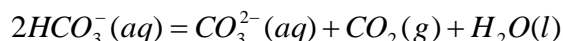
Bubble shape changes with size [18]; bubbles smaller than 3 mm are spherical, bubbles 3 to 10 mm are spheroidal, and bubbles larger than 10 mm are spherical-cap shaped [19-21]. Almost all of the bubbles produced by adding $NaHCO_3$ to acidified water are spherical due to their size of 0.5~1.5 mm.

The influence of treatment time, flow rate and method of addition of lift-gas, and amount and time of $NaHCO_3$ addition on the inclusion removal rate was examined.

RESULTS AND DISCUSSION

The process of inclusions adhesion to bubble

The process of inclusions adhesion to bubble is shown in Fig.4. Finer bubbles provide a larger gas/liquid interfacial area and higher attachment probability of inclusions to bubbles [22]. Inclusions tend to pass the midpoint of the bubble and first touch the bubble surface toward the bottom side. If the normal distance from the inclusion center to the surface of the bubble quickly becomes less than the inclusion radius, then collision attachment takes place [23]. Bubbles capturing inclusions move within the molten steel, and remove some of them to the top [24, 25].
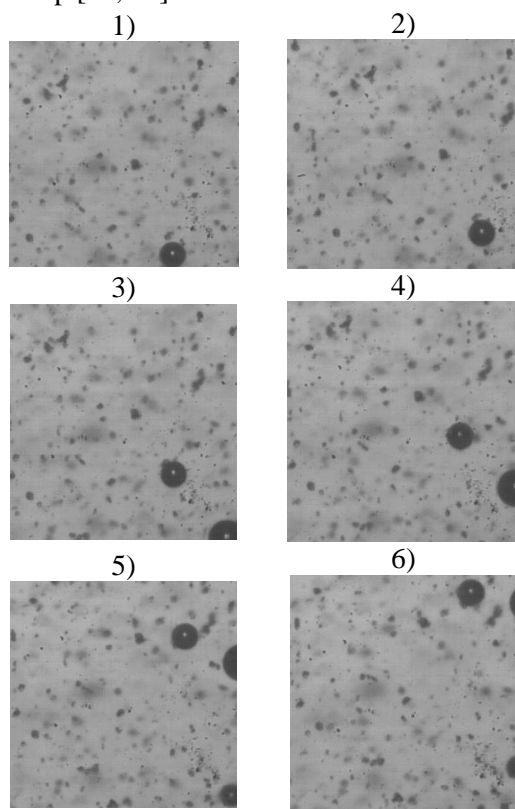
Fig.4. The process of inclusions adhesion to bubble.

It can be concluded that the smaller bubbles have a greater rate of inclusions removal. This conclusion is in agreement with Zhang's fundamental analysis [22]. The average equivalent size of bubbles is estimated to be 0.5~1.5 mm in diameter in the mold investigated in this work.

Effect of treatment time on inclusion removal rate

The relationship between inclusion removal rate and treatment time is show in Fig.5. The inclusion removal rate increased gradually with increasing treatment time, and most inclusions were removed between 0 and 15 min.
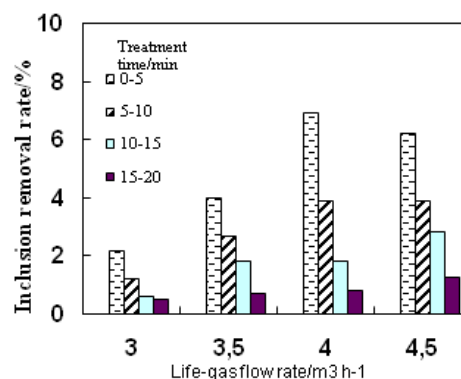
Fig. 5. Relationship between inclusion removal rate and treatment time

Effect of lift-gas flow rate on inclusion removal rate

As can be seen from Fig.6, for a treatment time of 20 min, the inclusion removal rate increased rapidly as the lift-gas flow rate was raised from 3.0 m^3 h^{-1} to 5.0 m^3 h^{-1}, after which it tended to stabilize.
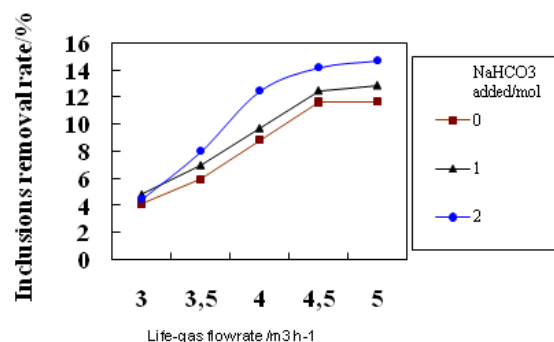
Fig. 6. Relationship between inclusion removal rate and lift-gas flow rate

With increasing lift-gas flow rate, the circulation rate initially increases, and consequently so does the inclusion removal rate. However, if the lift-gas flow rate becomes too high, the flow pattern of the liquid steel alters. Over-rapid flow of liquid steel inhibits the flotation and removal of inclusions. There is, therefore, an optimum value of the lift-gas flow rate: in this experiment, the highest inclusion

removal rate was registered when the lift-gas flow rate was about 4.5 m^3 h^{-1}.

Effect of amount and time of NaHCO$_3$ addition on inclusion removal rate

Figure 7 shows the relationship between inclusion removal rate and the amount and time of NaHCO$_3$ addition for a treatment time of 20 min at the optimum value of the lift-gas flow rate of 4.5 m^3 h^{-1}. It can be seen that the inclusion removal rate increases gradually with the addition of greater amounts of NaHCO$_3$, although, under conditions of industrial production, to avoid the introduction of excessive amounts of impurities, various factors need to be considered. The effect is greatest at the beginning of NaHCO$_3$ addition.
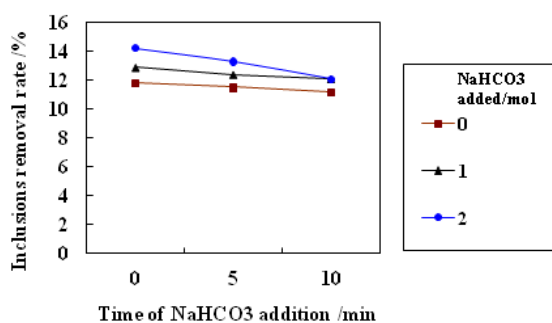
Fig. 7. Relationship between inclusion removal rate and amount and time of NaHCO$_3$ addition.

CONCLUSIONS

The influence of treatment time, lift-gas flow rate and amount and time of NaHCO$_3$ addition on the inclusion removal rate was investigated using a water model of 1:4 linear scale for a 180-t RH-TB degasser. The following conclusions can be drawn from the results:

1. The average equivalent size of bubbles is estimated to be 0.5~1.5 mm in diameter in the mold investigated in this work.

2. The inclusion removal rate increases gradually with increasing treatment time, with most inclusions being removed between 5 and 18 min. In this water model experiment, the treatment time was chosen as 20 min to obtain the best effect.

3. The inclusion removal rate increases with increasing lift-gas flow rate until an optimum value is reached, which in this experiment was 4.5 m^3 h^{-1}.

4. The inclusion removal rate increases gradually with the addition of NaHCO$_3$, and the effect is greatest at the beginning of NaHCO$_3$ addition.

5. Industrial test results indicate that bubbles of carbon dioxide are formed by the decarburization reaction of calcium hydrogencarbonate, thus inclusions can be effectively removed from molten steel.

REFERENCES

1. M.Y. Zhu, Z.Q. Xiao, Simulation on the secondary refining process, Beijing, Metallurgy Industry Press., 1998, p.320
2. J. Cheng, R. Eriksson, P. Jonsson, *Ironmaking and Steelmaking*, **30**, 66 (2003).
3. R. Dekkers, PhD thesis, Katholieke Universiteit Leuven, 2002; http://members.home.nl/rob.dekkers/pdf-files/contents.pdf
4. A. W. Cramb: 1998, http://neon.mems.cmu.edu/afs/afs2/form.html.
5. L. F. Zhang, B. G. Thomas, Proc. 7th European Electric Steelmaking Conf., Venice, Italy, May 2002, AIM, p. 277.
6. L. Zhang, B. Rietow, K. Eakin, and B.G. Thomas: *ISIJ Inter.*, **46**, 2006, , in press.
7. Y. Miki, S. Takeuchi, *ISIJ Int.*, **43**, 1548 (2003).
8. F. Tang, Z. Li, X. Wang, B. Chen and P. Fei, *Int. J. Miner. Metall. Mater.*, **18**, 144 (2011).
9. M. Söder, Licentiate Thesis, Royal Institute of Technology, Stockholm, Sweden, 2000.
10. P. Kaushik, M. Lowry, H. Yin, H.Pielet, *Ironmaking and Steelmaking*, **39**, 284 (2012).
11. J. H. Wei, H. T. Hu, *Ironmaking and Steelmaking*, **32**, 427 (2005).
12. T. Lee, H. J. Kim, B. Y. Kang, S. K. H-Wang, *ISIJ Int.*, **40**, 1260 (2000).
13. H. Yin, H. Shibata, T. Emi, M. Suzuki, *ISIJ Int.*, **37**, 946 (1997).
14. H. J. Schulze, *Developments in Mineral Processing*, **4**, 65 (1984).
15. L. Wang, H.-G. Lee, P. Hayes, *ISIJ Int.*, **36**, 7 (1996).
16. X. Zheng, P. Hayes, H.-G. Lee, *ISIJ Int.*, **37**, 1091 (1997).
17. N. Ahmed, G.J. Jamson, *Metall. Rev.*, **5**, 77 (1989).
18. R.M. Wellek, A.K. Agrawal, A.H.P. Skelland, *AIChE J.*, **12**, 854 (1966).
19. Y. Sahai, R.I.L. Guthrie, *Metallurgical Transactions B*, **13**, 193 (1982).
20. H. Tokunaga, M. Iguchi, H. Tatemichi, *Metallurgical and Materials Transactions B*, **30**, 61 (1999).
21. M. Iguchi, H. Tokunaga, and H. Tatemichi: *Metallurgical Transactions* B., 1997, 28, 1053-1061.
22. L. F. Zhang, S.Taniguchi, K.Matsumoto, *Ironmaking and Steelmaking*, **29**, 326 (2002).
23. L. F. Zhang, J.A. Brian, G. Thomas, *Metallurgical and Materials Transaction B*, **37B,** 361 (2006).
24. L. Zhang, S. Taniguchi, *International Materials Reviews*, **45**, 59 (2000).
25. G. Abbel, W. Damen, G. de Dendt, W. Tiekink: *ISIJ International*, **36**, 219 (1996).

ФИЗИЧЕН МОДЕЛ И ПРОМИШЛЕН ТЕСТ ЗА ОТСТРАНЯВАНЕ НА ГАЗОВИ ВКЛЮЧВАНИЯ ЧРЕЗ АДХЕЗИЯ НА МЕХУРИ

Ч. Янг[1*], Ф. Танг[2], М. Яен[1], Х. Ю[1]

[1]Научно-технологичен университет Ляолинг, Аншан сити, Ляолинг, Китай
[2]Аншанска компания за желязо и стомана, Аншан сити, Ляолинг, Китай

(Резюме)

Използвани са различниметоди за намаляване съдърванието на включвания в металите. RH-вакуумното рафиниране, приложено между добиването на стоманата и непрекъснатото й изливане, има важна роля за отстраняването на включванията в разтопената стомана. В настоящата работа е създаден физичен модел при геометрично отношение на подобие 1:4 за симулирането на реален180-t RH-уред за вакуумно рафиниране. Анализирано е отстраняването на включвания от разтопена стомана чрез адхезия на мехури. Изследван е ефекта на различни параметри вRH-дегазера (размер на мехура, време за третиране, дебит на газа, колиество добавен $NaHCO_3$).При промишления 180-t RH-тест се оказва, че се образуват мехури от въглероден диоксид при разлагането на калциев карбонат, при което става ефективно отстраняване на включванията.

Heat and mass transfer modeling of vacuum cooling for porous food material

Z. Zhang[1*], J. Gao[1], S. Zhang[1], Y.Xie[1], L. Zhao[2]

[1]School of Mechanical Engineering and Automation, Northeastern University,
Shenyang 110004, China
[2] School of Mechanical Engineering,Shenyang University, Shenyang 110044, China

Vacuum cooling is afast cooling method in food chemistry industrial processes. A lot of modeling methods and simulation technologies has been used to reveal the heat and mass transfer process. Based on the theory of heat and mass transfer, a coupled model for a vacuum cooling process of porous food materialis constructed. The model is implemented and solved using COMSOL software. The effects of food materialinitial temperature, vacuum chamber pressure, chamber temperature and relative humidity on the vacuum cooling process were examined. The results showed that food materialinitial temperature and chamber temperature have little effect on the vacuum cooling process. The chamber pressure affected the core and surface temperature of the porous food material. The relative humidity affected the surface temperature. The vacuum cooling process of the porous medium is anoutside controlled process.

Key words:vacuum cooling,porous food material, heat and mass transfer, COMSOL.

INTRODUCTION

Vacuum cooling, as a rapid cooling process,has huge ability of cooling porous food materials [1-5]. Its heat and mass transfer is a complicated process, which has been investigated by many researchers [6-17]. Jin et al. [6-8] developed and validated a moisture movement model for vacuum cooling of cooked meat. The vacuumcooling of cylindrically shapedcooked meat was carried out to find out the effects of the variations of temperature, moisture content and evaporationrate. Sun et al. [9-13] developed a series of models of simultaneous transient heat and mass transfer with inner heat and mass generation for analyzingthe performance of vacuum cooling of cooked meat. In addition, a mathematical model is developed to analyze the performance of a vacuum cooler [14]. Dostal et al.[15] gave a simple mathematical model of the vacuum cooling process which enables to predict the temperature evolution considering the equipment size, vacuum pump parameters and properties of the cooled liquid. He et al. [16] developed a model for predicting the temporal temperature and the mass of spherical solid food materials during vacuum cooling. It discusses the effects of product thermophysical properties, convection heat transfer coefficient, latent heat of evaporation, as well as vacuum environmental parameters that govern the heat and mass transfer of the product. The temporal trends of total system pressure, product temperature

such as surface temperature, core temperature, mass-average temperature, and mass of product were predicted.

The vacuum cooling has been used for many kinds of food material, for example, ham[17], chicken breast [18,19], beef [20-23], potatoes [24], cherries [25], pork[26,27], mussels[28], carrots [29], roses [30],purslane[31], lettuce[32], etc. [1-4]. Compared with experiment, the simulation shows an excellent ability in time and economy. However, little research was performed on the effect on food materialinitial temperature, and vacuum chamber pressure, by modeling and simulation.

In this paper, heat and mass transfer of porous food material in a vacuum cooling process is implemented by using a non-equilibrium method. The effects of initialtemperature, vacuum chamber pressure, chamber temperature, and relative humidity were studied.

MODEL DEVELOPMENT

Aphysical two-dimensional axissymmetry model that explains the vacuum cooling process is shown in Fig.1. The total length of the porous food material is 310mm. The diameter is 130mm. In order to simplify the calculation, half of the food material was used.

The porous food material consists of a continuous rigid solid phase and a continuous gas phase considered as an ideal gas. For a mathematical description of the transport phenomenon in a porous medium, we adopted a continuum approach, wherein macroscopic partial differential equations are achieved through the volume averaging of the

* To whom all correspondence should be sent:
E-mail:zhj_zhang@126.com

microscopic conservation laws. The value of any physical quantity at a point in space is given by its average value on the averaging volume centered at this point.
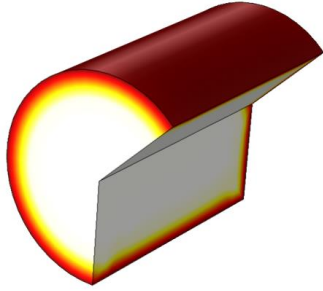
Fig.1. 2D Axissymmetry model of porous food material

The moisture movement of the inner porous medium is vapor movement; that is, the liquid H_2O could become vapor, and the vapor is moved by the pressure gradient. The heat and mass transfer theory could be found elsewhere [6-17].

The compressibility effects of the solid phase are negligible, and the phase is homogeneous:

$$\bar{\rho}_m = cste \tag{1}$$

The gaseous phase is considered an anideal gas. This phase ensures that

$$\bar{\rho}_v = \frac{m_v \bar{P}}{R\bar{T}} \tag{2}$$

Mass conservation equations are written for each component in each phase. For arigid solid phase, the following is given:

For vapor,

$$\varphi \frac{\partial(\bar{\rho}_v)}{\partial t} + \nabla \cdot (\bar{\rho}_v \bar{V}_v) = \dot{I} \tag{3}$$

Where the gas velocity is given by

$$\bar{V}_v = -\frac{k_v}{\mu_v} \cdot \nabla \bar{P} \tag{4}$$

$$k_v = \frac{d^2}{32}$$

By considering the hypothesis of the local thermal equilibrium, the energy conservation is reduced to a unique equation:

$$\rho_m c \frac{\partial \bar{T}}{\partial t} - \nabla(k \cdot \nabla \bar{T}) = -\lambda \cdot \dot{I} \tag{5}$$

BOUNDARY AND INITIAL CONDITIONS

B.C. for Eq. (10) on the symmetric surface,

$$\frac{\partial \bar{P}}{\partial n} = 0 \tag{6}$$

B.C. for Eq. (10) on the outer surface,

$$P = \bar{P}_{vc} \tag{7}$$

B.C. for Eq. (5) on the symmetric surface,

$$\frac{\partial \bar{T}}{\partial n} = 0 \tag{8}$$

B.C. for Eq. (5) on the outer surface,

$$-k \frac{\partial T}{\partial n} = h_r(T_s - T_{vc}) - \lambda \cdot \dot{m}_s \tag{9}$$

$$hr = \sigma \varepsilon (T_s^2 + T_{vc}^2)(T_s + T_{vc}) \tag{10}$$

The initial pressure of vapor,
I.C. for Eq. (3):

$$\bar{P} = P_{sat,0} \tag{11}$$

The initial temperature of porous food material,
I.C. for Eq. (5):

$$\bar{T} = T_0 \tag{12}$$

PHASE CHANGE

The evaporation rate is a complex function of the drying process in the porous medium. The phase change can be formulated in two ways, equilibrium and non-equilibrium. Evaporation of liquid H_2O was implemented using an equilibrium formulation where liquid H_2O in the solid matrix is assumed to be in equilibrium with water-vapor in the surrounding air. However, recent studies have shown that evaporation is not instantaneous and non-equilibrium exists during rapid evaporation between water-vapor in gas phase and liquid H_2O in solid phase. Furthermore, the equations resulting from an equilibrium formulation cannot be implemented in any direct manner in the framework of most commercial software. The more general expression of non-equilibrium evaporation rate used for modeling of phase change in porous media that is consistent with studies on pure H_2O just mentioned, is given by [6-17]:

$$\dot{I} = 4\frac{\varphi}{d} h_m (a_W P_{sat} - P) \tag{13}$$

$$\dot{m}_s = h_m (a_W P_{sat} - RH \cdot P_{vc}) \tag{14}$$

Here I is a parameter signifying the rate constant of evaporation. The non-equilibrium formulation, given by equation (13), allows precisely this, i.e., it can express the evaporation rate explicitly and therefore would be preferred in a commercial software. Therefore itis used in our model.

NUMERICAL SOLUTION

COMSOL Multiphysics 3.5a was used to solve the set of equations. COMSOL is an advanced software used for modeling and simulating any physical process described by partial derivative equations. The set of equations introduced above was solved using the relative initial and boundary conditions of each. COMSOL offers three possibilities for writing the equations: (1) using a template (Fick Law, Fourier Law), (2) using the

coefficient form (for mildly nonlinear problems), and (3) using the general form (for most nonlinear problems). Differential equations in the coefficient form were written using an unsymmetrical-pattern multifrontal method. We used a direct solver for sparse matrices (UMFPACK), which involves significantly more complicated algorithms than solvers used for dense matrices. The main complication is the need to efficiently handle the fill-in in factors L and U.

A two-dimensional (2D) axis symmetry grid was used to solve the equations using COMSOL Multiphysics 3.5a. The mesh consists of 4224 elements (2D), and time stepping is free taken by the solver. Several grid sensitivity tests were conducted to determine the sufficiency of the mesh scheme and to ensure that the results are grid-independent. A backward differentiation formula was used to solve time-dependent variables. Relative tolerance was set to 1×10^{-4}, whereas absolute tolerance was set to 1×10^{-6}. The simulations were performed using a Tongfang PC with Intel Core 2 Duo processor with 3.0 GHz processing speed, and 4096 MB of RAM running Windows 7.

INPUT PARAMETERS

The detailed parametersare given in Table 1.

Table1. Parameters used in the simulation process

Parameter	Value	Source	Unit
ρ_v	Ideal gas		kg m^{-3}
ρ_m	1072	[13]	kg m^{-3}
c	3439	[13]	J kg^{-1} K^{-1}
k	0.59	[13]	W m^{-1} K^{-1}
μ_v	1.8×10^{-5}		Pa s
h_m	8.4×10^{-7}	[13]	KgPa^{-2}m^{-2} s^{-1}
λ	2791.2×10^{3}	[8]	J kg^{-1}
φ	6	[13]	%
T_0	74+273.15	[13]	K
T_{vc}	25+273.15	[13]	K
d	2.5×10^{-3}	[13]	m

RESULTS AND DISCUSSION

Fig. 2 presents the simulation result using the parameters of Table 1. It is compared with the result from Ref [14]. The temperature of the surface agrees well, while the core temperature does not agreewell. The difference is because the liquid H$_2$O activity a_w has changed, but our parameter $a_w = 0.66$ is used and *RH* is 0.53 at the end. The temperature is lowered when the pressure is lowered until core temperature is higher than 0 ℃ and surface temperature is lower than 0 ℃. According to

Eq.(14), surface liquid H$_2$O could be evaperated by the vapor pressure difference[14].

Fig.3. shows the total, core and surface weight loss.The results show that the inner weight loss is the major part of the temperature cooling function. The pressure difference is given by the vacuum system between the vacuum chamber and the inner porous medium that enhances the mass transfer and heat transfer. It is the vacuum cooling method superiority.

Fig.4. shows the initial temperature effect on the vacuum cooling process. The initialtemperature is 74, 84 and 94ºC, respectively. The vacuum cooling temperature is almost the same. It should be concluded that the initial temperature has little effect on the vacuum cooling process if the vacuum is high enough. That is why the vacuum system including the condenser is sufficient, the pressure, especially the vapor pressure in the vacuum chamber is not affected by the vacuum cooling process. In our simulation process, the chamber pressure is given by Eq.(7) that is not changed in all simulations. The vacuum cooling process is controlled by the vacuum chamber conditions, i.e.,the outside conditions controlled the porous food material.
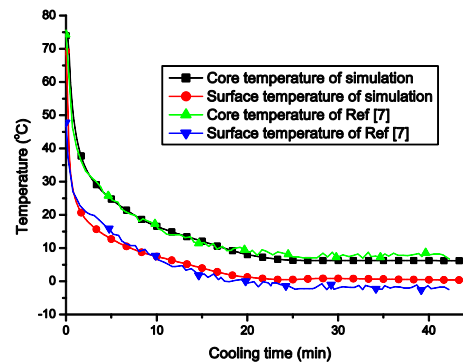
Fig.2. The simulation and experimentalresults compared with Ref [7] for porous food material.

Fig.5. presents the effect of vacuum chamber pressure on the vacuum cooling process. The end pressure is 650, 725 and 825 Pa, respectively. The vacuum pressure before the end pressures is the same. The temperature of core and surface is the same at different simulations until the end pressure is achieved. The temperature of core and surface has little effect at the end pressure stage. The higher the end pressure, the higher is the temperature including the core and surface. It shows that the vacuum cooling process is affected by the end pressure before the end pressure stage. So the vacuum cooling process is controlled by outside conditions of porous food material.

1091
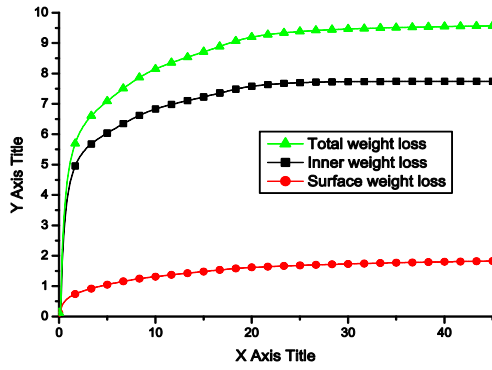
Fig.3. The total weight loss, inner weight loss and surface weight loss in the vacuum cooling process of porous food material.
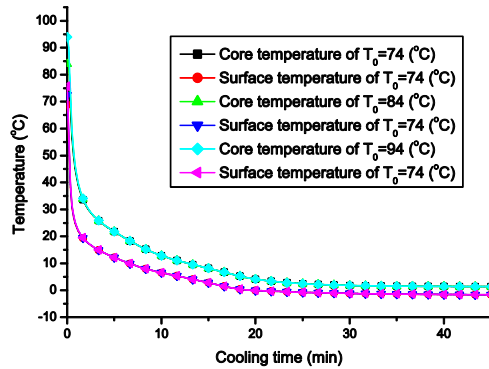
Fig.4. The initial temperature efffect on the vacuum cooling process of porous food material.

Fig.6. illustrates the effect of vacuum chamber temperature on the vacuum cooling process. The chamber temperature T_{vc} is 35, 25 and 15 ℃, respectively. The effect of vacuum chamber temperature could be shown by Eq.(9). But in fact the chamber temperature does not affect the vacuum cooling process. It is controlled by $\lambda \cdot \dot{m}_s$ in Eq.(9), evaporating rate and evaporating latent heat.

Fig.7. shows the effect of relative humidity on the vacuum cooling process. The relative humidity *RH* is 0.75, 0.65 and 0.55, respectively. The inner temperature is not affected by the relative humidity *RH* that agreeswith Eq.(13). But the surface temperature is affected by therelative humidity *RH* that agrees with Eq.(14).
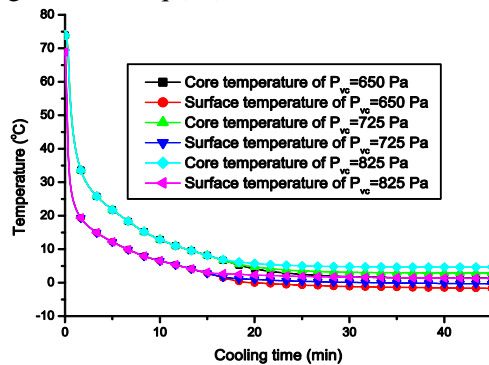
Fig.5. The vacuum chamber pressure effect on the vacuum cooling process of porous food material.
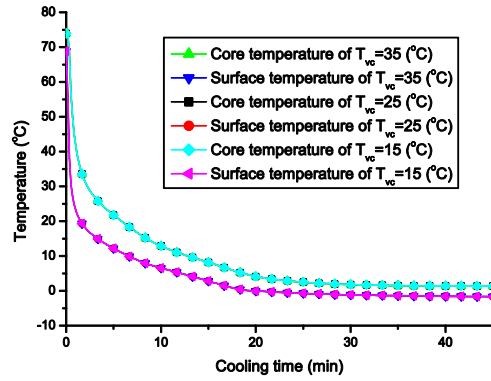
Fig.6. The vacuum chamber temperature effect on the vacuum cooling process of porous food material.
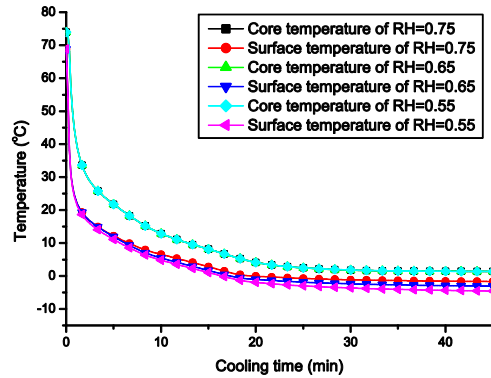
Fig.7. The relative humidity effect on the vacuum cooling process of porous food material

CONCLUSION

A coupled model of porous food material vacuum cooling based on the theory of heat and mass transfer was implemented in this paper. The effects ofinitialtemperature, vacuum chamber pressure, chamber temperature and relative humidity on the vacuum cooling process were examined. The temperature characteristics of the porous food material core and surface wereobtained. The results show that initial temperature and chamber temperature have little effect on the vacuum cooling process, but the chamber pressure affected the core and surface temperature of the porous food material. The relative humidity affected the surface temperature. The results showed that the vacuum cooling process of the porous medium is an outside controlled process. The results are meaningful for vacuum cooling of porous food material.

NOMENCLATURE

a_w - liquid H_2O activity

c - specific heat (J kg^{-1} K^{-1})

d - -diameter of pores (m)

h_m - evaporation rate (kg Pa^{-1} m^{-1} s^{-1})

h_r - heat transfer coefficient (W m^{-2} K^{-1})

i - liquid H_2O phase rate (kg s^{-1}m^{-3})

k - thermal conductivity (W m^{-1} K^{-1})

k_v - permeability (m^2)

m_v - vapor molecular mass (g mol^{-1})

m_s - mass transfer coefficient (kg m^{-2} Pa^{-1} s^{-1})

n - outer unit normal to the product

$\bar{P}$ - pressure (Pa)

P_{sat} - vaporisation pressure (Pa)

$P_{sat,0}$ - initial vapor saturation pressure (Pa)

R - universalgas constant (J kmol^{-1}K^{-1})

RH - relative humidity

t - time (s)

$\bar{T}$ - food materialtemperature (K)

T_0 - initial temperature (K)

T_{vc} - vacuum chamber temperature (K)

T_s - surface temperature of food material (K)

$\bar{V}_v$ - vapor velocity (m s^{-1})

φ - porosity (%)

μ_v - viscosity (kg m^{-1} s^{-1})

λ - latent heat of evaporation (J kg^{-1})

$\bar{\rho}_m$ - food materialdensity (kg m^{-3})

$\bar{\rho}_v$ - vapor density(kg m^{-3})

REFERENCES

1. C. H. Feng, L. Drummond, Z. H. Zhang, D. W. Sun, Q. J. Wang, *Critical Reviews in Food material Science and Nutrition*, **52**, 1024 (2012).

2. D. W. Sun and L. Y. Zheng, *Journal of Food material Engineering,* **77**, 203 (2006).

3. L. Y. Zheng, D. W. Sun, *Trends in Food materialScience & Technology*, **15**, 555 (2004).

4. K. McDonald and D. W. Sun, *Journal of Food material Engineering.* **45**, 55 (2000).

5. C. Cogne, P. U. Nguyen, J. L. Lanoiselle, E. Van Hecke, .D. Clausse, *International Journal of Refrigeration,***36**, 1319 (2013).

6. T. X. Jin, G. L. Li, Y. Gong, Y. L. Lu, Y. Shi, *Intelligent Automation and Soft Computing*, **16**, 1119 (2010).

7. T. X. Jin, L. Xu, *Journal of Food material Engineering,* **75**, 333 (2006).

8. T. Jin, L. Xu, *Energy Conversion and Management*, **47**, 1830 (2006).

9. D. W. Sun, L. J. Wang, *Journal of Food material Engineering*, **77**, 379 (2006).

10. L. J. Wang, D. W. Sun, *Transactions of the Asae*, **46,** 107 (2003).

11. D. W. Sun, Z. H. Hu, *International Journal of Refrigeration,***26**, 19 (2003).

12. Z. H. Hu and D. W. Sun, *Computers and Electronics in Agriculture,***39**, 255 (2003).

13. L. J. Wang, D. W. Sun, *International Journal ofRefrigeration*, **25**, 862 (2002).

14. L. J. Wang and D. W. Sun, *International Journal of Refrigeration,***25**, 854 (2002).

15. M. Dostal, K. Petera, *Journal of Food material Engineering,***61**, 533 (2004).

16. S. Y. He, Y. F. Li, *Applied Thermal Engineering,***23**, 1489 (2003).

17. X. Y. Song, B. L. Liu, *Food material Science and Technology Research,***20**, 43 (2014).

18. F. C. Schmidt, J. B. Laurindo, *Journal of Food material Engineering,***128**, 10 (2014).

19. F. C. Schmidt, G. M. F. Aragao, J. B. Laurindo, Journal of Food material Engineering 100, 219 (2010).

20. Z. H. Zhang, L. Drummond, D. W. Sun, *Journal of Food material Engineering,***116**, 581 (2013).

21. L. Drummond, D. W. Sun, *Innovative Food material Science & Emerging Technologies,***16**, 205 (2012).

22. L. Drummond, D. W. Sun, C. T. Vila, A. G. M. Scannell, *Lwt-Food material Science and Technology,***42,** 332 (2009).

23. L. Drummond, D. W. Sun, *Meat Science,***80**, 885 (2008).

24. L. G. G. Rodrigues, D. Cavalheiro, F. C. Schmidt, J. B. Laurindo, *Journal of Food material Processing and Preservation,***37**, 846 (2013).

25. S. Y. He, G. C. Zhang, Y. Q. Yu, R. G. Li, Q. R. Yang, *International Journal of Refrigeration,***36**, 2387 (2013).

26. C. H. Feng, L. Drummond, Z. H. Zhang, D. W. Sun, *Meat Science*, **95**, 425 (2013).

27. X. G. Dong, H. Chen, Y. Liu, R. T. Dai, X. M. Li, *Meat Science,***90**, 199 (2012).

28. D. Cavalheiro, F. C. Schmidt, L. G. G. Rodrigues, C. Siga, F. Leitempergher, J. B. Laurindo, *Journal of Food material Process Engineering,***36,** 192 (2013).

29. L. G. G. Rodrigues, D. Cavalheiro, F. C. Schmidt, J. B. Laurindo, *Ciencia E Tecnologia De Alimentos,***32**, 187 (2012).

30. X. Y. Song, W. S. Wang, C. Zhang, Q. Ma, Y. F. Li, *Philippine Agricultural Scientist,***94**, 368 (2011).

31. H. M. Ozturk, H. K. Ozturk, *International Journal of Refrigeration,***32**, 395 (2009).

32. S. Y. He, Y. F. Li, *Energy Conversion and Management*, **49**, 2720 (2008).

МОДЕЛИРАНЕ НА ТОПЛО - И МАСОПРЕНАСЯНЕТО ПРИ ВАКУУМНО ОХЛАЖДАНЕ НА ПОРЬОЗНИ МАТЕРИАЛИ

Ж. Жанг[1*], Дж. Гао[1], Ш. Жанг[1], Ю. Ксие[1], Л. Жао[2]

[1]*Училище по механично инженерство и автоматизация, Североизточен университет, Шенянг, Китай*
[2]*Училище по механично инженерство, Университет на Шенянг, Шенянг 110044, Китай*

(Резюме)

Вакуумното охлаждане е най-бързия метод за охлаждане на хранителни материали и при процесите в химическата промишленост. Множество математични методи на моделиране и симулиране са използвани за изучаване на топло и масообменните процеси. В настоящата работа на основание теорията на топло и масопренасянето е създаден модел, описващ вакуумното охлаждане на порьозни хранителни материали. Моделът е приложени решаван със софтуер COMSOL. Изследвани савлиянията на началната температура на материала, налягането, температурите на вакуумната камера, на камерата на сушилнята и на относителната влажност. Резултатите показват, че началната температура на материала и температурата на сушилната камера имат слаб ефект върху процеса на вакуумно охлаждане. Налягането в камерата влияе значително върху температурата във вътрешността и по повърхността на порьозния материал. Относителната влажност влияе на повърхностната температура. Вакуумното охлаждане на порьозни среди се контролира от процесите извън материала.

Chemical analysis of metals and essential nutrients in wetland dew

Y. Xu[1, 2*], B. Yan[3], J. Tang[2], Y. Lin[1]

[1] *Key Laboratory of Songliao Aquatic Environment, Ministry of Education, Jilin Jianzhu University, Xincheng St., Dist 5088, 130118 Changchun, China*

[2] *College of Resources and Environment, Jilin University, Qianjin St., Dist 2699, 130021 Changchun, China*

[3] *Key Laboratory of Wetland Ecology and Environment, Northeast Institute of Geography and Agroecology, Chinese Academy of Sciences, Shengbei St., Dist 4888, 130102 Changchun, China*

In order to discuss the ecological efficiency of dew and reveal the air status of surface layer, pH and the concentrations of 25 metals including K, Na, Ca, Mg and essential nutrients (ammonium nitrogen (NH_4^+-N), nitrogen (NO_3^--N) and phosphate (P)) in dew samples from the wetland of the Sanjiang Plain were monitored. *Carex lasiocarpa* dew was collected from mid July to mid September from 2008 to 2012. The results showed that the mean pH of *Carex lasiocarpa* dew was 6.41 and the acid dew did not occur in the research area during the monitoring period, therefore dew cannot damage protective surfaces on leaves. *Carex lasiocarpa* dew contained various types of metals, which can provide nutrient and trace elements to the plant. Dry deposition was the main source of elements in dew. The contents of main metals (K, Ca, Na, Mg, Mn, Fe, Zn) in *Carex lasiocarpa* dew were higher than those in rain ($P<0.05$). The trace amounts of Pb, Ba, Se, As, Co, Cr, Cu in *Carex lasiocarpa* dew implied that there was no significant contamination by automobile exhaust, coal combustion or industrial pollution in this area. The deposition amounts of NH_4^+-N, NO_3^--N and PO_4^{3-}-P from July to October in wetland dew were 0.065, 0.14 and 0.007 kg/ha, respectively. In addition, dew condenses on both sides of the leaf and can be taken up by rice more effectively. Therefore, nitrogen (N) and phosphorus (P) in wetland dew are another nutrition source. Dew is an important pathway for the nutrient transfer within a wetland. In consequence, dew can reveal the air pollution status and it is significant to monitor the chemical character of dew. Analyzing the metal content of dew is a simple and useful method to reveal the status of the surface layer. This method can provide foundation and reference of the air pollution and quality assessment.

Key words: wetland dew, metals, dry deposition, wetland surface water, dew chemical character.

INTRODUCTION

Particles and gases can be removed from the atmosphere by wet deposition (rain, fog and dew) and by dry deposition. The wet deposition process is a major pathway for the transport of acidic pollutants from the atmosphere to the biosphere [1]. Dew, which is an important part of wet deposition, occurs when the air temperature reaches to the dew point temperature, further it can indicate the quality of the near-surface atmosphere. Sanjiang Plain was the largest concentrated area of freshwater wetlands in China in the 1960s, and marsh vegetation here was distributed densely. Dew plays a crucial role in the water balance of a wetland ecosystem. As a form of wet deposition, dew is a major pathway for the transport of acidic pollutants from the atmosphere to the biosphere [2], furthermore, the acidity or alkalinity of dew can also influence plant growth [3]. Formation of acidic dew is critical to assess corrosion process. For example, acidic dew is potentially more effective than acid rain in causing damage to surface structures. Acidic dew damages the protective surfaces of leaves, interferes with guard cells, and poisons plant cells [4]. Moreover, some metals from dry deposition on leaves can dissolve in dew. Some metals in dew are helpful to plants, such as K, Mg, Ca, Zn, Na, Fe which can be assimilated by leaves [5]. However, other metals (As, Pb, Cr) are harmful to the plants [6, 7]. Therefore, identifying the relative character of dew is necessary to determine the significance of dew to the plants in the wetland. On the other hand, dew formation is a local phenomenon, significantly influenced by microclimatic ambiance, land profile, and favorable meteorological conditions. Analyzing the chemistry of dew can also provide information of the quality of air. The dew amount has attracted great interest and has been extensively studied, but few studies have focused on the chemical characterization of dew [8, 9]. Consequently, the objectives of the present study are to (a) determine the pH, and the concentrations of some elements in dew; (b) identify the source of the nutrients; (c) compare the dew with the drinking water.

MATERIALS AND METHODS

The experiment was organized at the Sanjiang Wetland Experimental Station (47°35'N, 133°31'E), Chinese Academy of Sciences, in Tongjiang, Heilongjiang Province, Northeast China. The elevation is about 56 m above sea level. An average annual temperature of 1.9°C can be expected. The annual precipitation which is in the range of 550 to 600 mm accounts for over 65% precipitation from June to September [10]. The annual dewfall in the wetland is about 10 mm [11]. *Carex lasiocarpa* is the dominant plant, and it was selected as the typical experiment plot.

The method of monitoring dewfall was validated. The woodstick as the collector on monitoring dewfall was weighed daily at sunset and sunrise with an electronic balance (accuracy is within 0.001 g). The collectors were kept in the experimental plot until the next sunrise. These collectors were gathered half an hour before sunrise and weighed again. Dew intensity and dewfall was calculated with the following formula:

$$I = 10 \times (W_r - W_s)/S \qquad (1)$$

Where, I is the dew intensity (mm); W_r is the weight of woodstick before sunrise (g); W_s is the weight of woodstick after sunset (g); S is the surface area of woodstick (cm^2)

$$DF = \sum_{i=1}^{n} DF_i \qquad (2)$$

$$DF_i = 2 \times LAI_i \times \overline{I}_i \times D_i \qquad (3)$$

Where, DF is the total dewfall (mm); DF_i is the dewfall in a particular period (mm); LAI_i is the LAI in a particular period (cm^2/cm^2); $\overline{I}_i$ is the average I in a particular period (mm); D_i is the D in a particular period (days); 2 is the coefficient of a leaf side; n is the time of measuring LAI.

It is convenient to collect dew samples in July and August since the dewfall is high [11]. The leaf dew samples were collected 30 min before sunrise in the heavy-dew days. A total of 47 leaf dew samples were collected during the growth season from 2008 to 2012 in the current study. After washing with distilled water and drying, a polyethylene basin was used to collect dew water. All samples were then placed into polyethylene bottles (50 mL) [12]. To avoid contamination during the collection process, dew water was collected *in situ*. The collector was placed close to the root of the *Carex lasiocarpa*, and the *Carex lasiocarpa* stem was slightly shaken until the dew dropped into the collector. The dew was then poured from the collector into the polyethylene bottle. The steps were repeated until the polyethylene bottle was full. The *Carex lasiocarpa* were distributed in the four corners of a 20 m × 20 m

field. Surface water was collected using a polyethylene bottle (100 mL) when the leaf dew was collected. Rainwater was collected from the same site using polyethylene containers during the experimental period. Surface water and rain were collected in three parallel samples each time. In total, 141 surface water and 63 rain samples were collected.

The analyses were carried out in a laboratory at the Sanjiang Experimental Station, Northeast Institute of Geography and Agroecology, Chinese Academy of Sciences. The pH was immediately determined after collecting the samples. The samples were filtered through a 0.45 μm pore membrane. The concentrations of K, Zn, Ca, Mn, Na, Fe, Mg in each sample were immediately measured using ICP-MS (Agilent 7500a, USA). The samples were filtered through a 0.45 μm pore size membrane. Then NH_4^+-N, NO_3^--N and PO_4^{3-}-P were measured by a Discrete Auto Analyzer (Smartchem 200, Italy).

The statistical analyses were carried out by SPSS software version 16.0. To test the normal distribution of metal concentrations, *Q-Q* probability plots were employed. The data of metal concentrations in the rain, surface water, and dew were all with normal distribution. The ANOVA of metal concentrations was performed using one-way ANOVA, and the significance limit was set to $P<0.05$. The Least Significant Difference or Tamhane's T2 procedure was used to determine the significant differences between each group of concentrations. The mean separation of pH among rain, surface water, and leaf dew was performed according to the t-test at α=0.05 level. The data of dew, rain and surface water are the mean of three replicates.

RESULTS AND DISCUSSION

pH of dew

The pH is an important aspect of the assessment of ecological effects of dew in wetland. As displayed in Table 1 and Fig. 1, dew pH varied between 5.84 and 6.95, with an average of 6.41, whereas pH of rain was higher compared with dew and surface water. Even though the dew pH was below 7, the dew cannot endanger leaves in the wetland (the pH of acid rain is around 3.0 [13]). Data for acidic dew were reported in different references, e.g., the average dew pH in the farmland in the Sanjiang Plain was 6.3 [14]. In Zadar, Croatia, the dew pH was between 5.5 and 7.8, with a mean value of 6.7 [8]. In Bordeaux, France, the average dew pH was 6.3 [15]. The pH of dew in Indianapolis was between 6.0 and 7.2 [15], whereas in north-central India, it varied between 6.0 and 7.7, with an average of 6.8 [3]. The dews in these areas are acidic. Dew acidity is derived

from the CO_2 absorption and the acidic aerosol dissolution during droplet growth. However, the rain pH in these areas is lower than dew pH because of the various quantities of acidic species (SO_2, NO_x) influenced by human activities, such as fluctuating pollutant production and wind dispersion, or preceding rain events that clear out the aerosols in these areas. In the Sanjiang Plain, no automobile exhaust, coal combustion, or industrial pollution was detected; thus, its rain pH is higher than in other areas. It can be explained that dew can absorb CO_2 and the acidic aerosol dissolution during droplet growth [8].

Table 1. The pH of dew, rain, and surface water by type during the experimental period from 2008 to 2012 in the Sanjiang Plain

	Mean±SD	Max	Min	N
Dew	6.41±0.24	6.95	5.84	47
Rain	7.26±0.14	7.52	7.06	21
Surface water	6.56±0.21	6.95	6.09	47
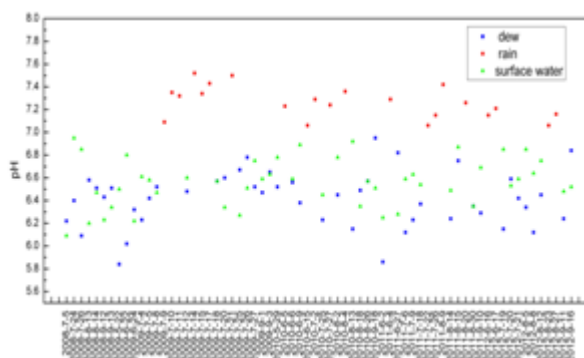
Fig. 1. Seasonal variability of pH in dew, rain, and surface water from 2008 to 2012 in the Sanjiang Plain.

Metal of dew

As the results showed, the mean concentrations of Cd, Be, Co, Se, Mo, Th, U and Tl were below 1.0 µg/L. The mean concentrations of Pb, As, Ni, Cr, V, Ag, Cu and Zn were between 1.0 µg/L and 100 µg/L. The mean concentrations of Na, Al, Fe and Ba were between 100 µg/L and 1000 µg/L. The mean concentrations of K, Mg, Ca and Mn were higher than 1000 µg/L (Table 2).

Some nutrient elements (K, Mg, Ca), trace elements (Mn, Cu, Cr, Zn, Na, Mo, V, As, Fe, Ni) [16] and heavy metals which are harmful to the plants (Cd, Pb, Al) [17] were detected in the dew. The results indicate that dew can provide various elements to the plants in the wetland ecosystem. But the process of plant assimilation is ambiguous, for instance, some elements such as As with a low concentration can stimulate plants growth, but constrain it when it is in high concentration.

The trace amounts of Pb, Ba, Se, As, Co, Cr, Cu in wetland dew implied that there is no automobile exhaust, coal combustion or industrial pollution in this area [18, 19]. Therefore, dew can reveal the air pollution status and it is significant to monitor the chemical character of dew.

Table 2. Concentrations of different metals in wetland dew from 2008 to 2012.

	Mean±SD (µg/L)	Max (µg/L)	Min (µg/L)
Cu	11.72±5.34	26.42	2.28
Pb	8.56±1.38	14.09	5.08
Zn	90.56±35.71	252.00	4.00
Cd	0.17±0.03	0.19	0.09
As	2.57±0.75	4.41	1.35
Be	0.03±0.01	0.05	0.01
K	32521±15646	149200	1089
Na	955±470	2591	52
Ca	12082±9458	55400	287
Mg	4876±2456	27360	578
Al	181.57±148.71	255.56	24.10
Mn	1956.48±1075.73	6507.00	572.00
Fe	276.04±196.35	1148.00	22.00
Co	0.81±0.09	1.520	0.35
Ni	3.53±0.87	4.29	1.36
Cr	4.74±1.82	8.25	2.31
Se	0.87±0.33	1.61	0.23
V	2.62±1.01	4.24	1.12
Mo	0.95±0.215	1.86	0.31
Ag	0.01±0.01	0.01	0.00
Sb	2.13±0.47	4.38	1.18
Ba	195.75±59.50	398.00	65.16
Th	0.03±0.02	0.07	0.01
U	0.02±0.01	0.03	0.01
Tl	0.02±0.01	0.04	0.01

NH_4^+-N, NO_3^--N and P in dew

The diffusion of NH_3 from surface water contributes some N to the wetland dew. In this N cycle process, the first step is NH_3 conversion to NH_4^+. Dew condenses under aerobic conditions. NH_4^+-N is prone to convert to NO_3^--N by the following steps:

$$NH_4^+ + 1.5O_2 \rightarrow NO_2^- + 2H^+ + H_2O, (4)$$
$$NO_2^- + 0.5O_2 \rightarrow NO_3^- (5)$$
$$NH_3 + 1.32NO_2^- + H^+ \rightarrow 1.02N_2 + 0.26NO_3^- + 2H_2O, (6)$$
$$NH_3 + 0.85O_2 \rightarrow 0.11NO_3^- + 0.44N_2 + 0.14H^+ + 1.43H_2O, (7)$$
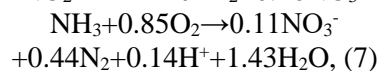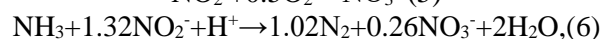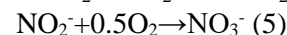
Therefore, NO_3^--N concentration is greater than NH_4^+-N. Meanwhile, H^+ is produced in this process. This phenomenon leads to the pH of dew being lower than that of surface water and rain. Maria noticed that the concentration of nitrite strongly correlates with the pH of dew [20]. NH_4^+-N and NO_3^--N concentrations may have a relationship with pH. In order to assess the nutrient concentrations in dew and to compare them with rain, the NH_4^+-N, NO_3^--N and P concentrations were analyzed (Fig. 2). It was found that the NO_3^--N concentration is significantly

higher than that of NH_4^+-N and P ($P<0.05$) in dew. The trend of NH_4^+-N, NO_3^--N and P concentrations in dew and rain is fluctuating and irregular.

Ammonia is oxidized to nitrite by ammonia-oxidizing bacteria, and nitrite is further oxidized to nitrate by nitrite-oxidizing bacteria. The concentration of nitrite is strongly correlated with the pH of dew. NH_4^+-N and NO_3^--N concentrations may have a relationship with pH. Dew samples contained many suspended solids because of the method of collecting dew. The absorbability of P is weaker under the acidic condition. This fact will lead to increased P concentrations when the pH is less than 7.0. Moreover, under alkaline conditions, NH_4^+ is prone to convert to NH_3, and the NH_4^+-N concentration declined with NH_3 diffusion. Therefore, NH_4^+-N condensation was higher under acidic conditions. Although through statistical analysis, P and NH_4^+-N condensations did not correlate with pH ($P>0.05$), as presented in Fig. 3, P and NH_4^+-N condensations increased markedly on 25 July and 8 August with a lower pH. The pH can affect P and NH_4^+-N condensations to some extent.
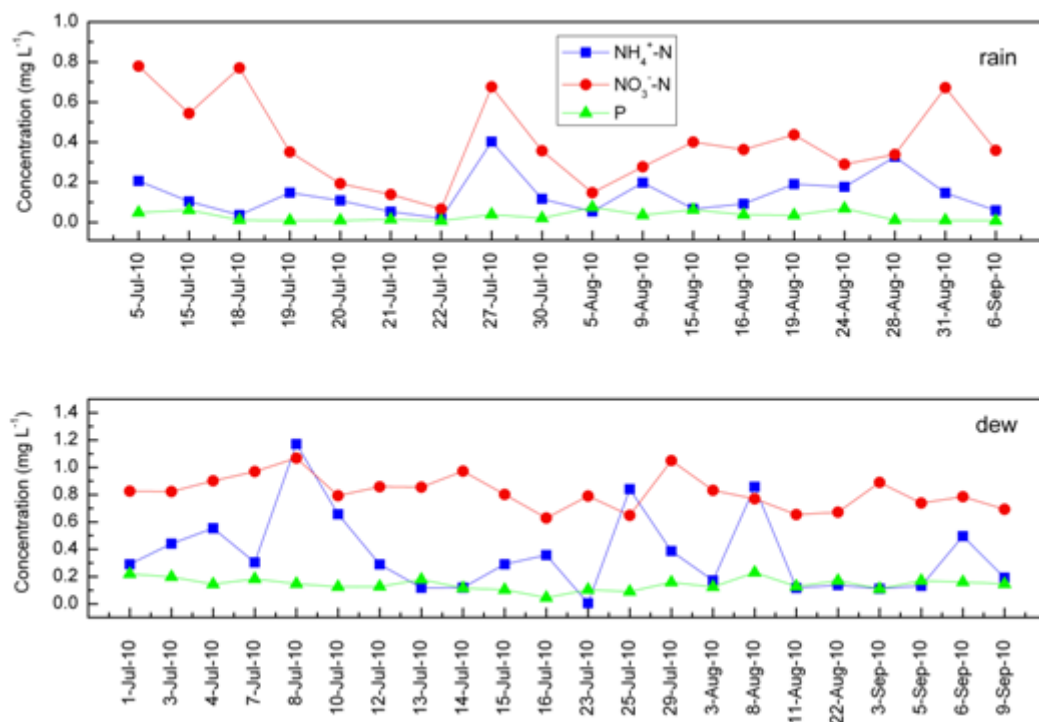
Fig. 2. Monthly variation of NH_4^+-N, NO_3^--N and P concentrations in dew and rain in 2010 in the Sanjiang Plain.
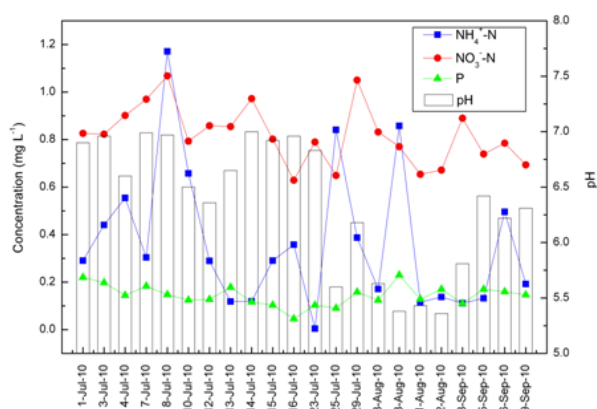
Fig. 3. Variation of pH and NH_4^+-N, NO_3^--N and P concentrations of wetland dew in 2010 in the Sanjiang Plain.
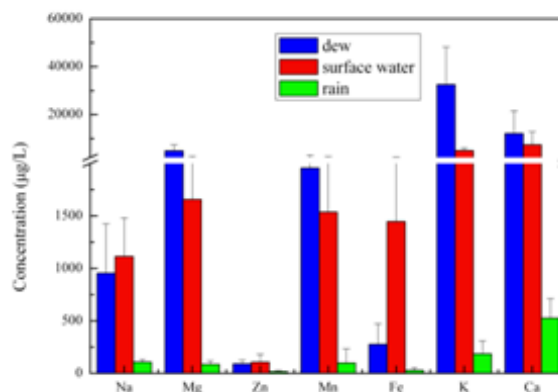
Fig. 4. Average concentrations (in ppb) of major metals in dew, rain, and surface water from 2008 to 2012 in the Sanjiang Plain.
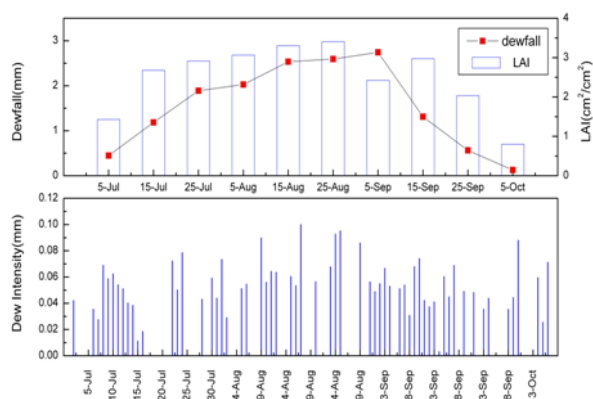
Fig.5 Variation of dewfall, *LAI* and dew intensity of wetland.

Dew and rain

As shown in Fig. 2, K, Ca, Na, Mg, Mn, Fe and Zn concentrations in dew and surface water are significantly higher than those in rain ($P<0.05$). Therefore, leaf dew can offer more nutrients to plant than rain. Similar results have been reported in south-western Morocco [22], Santiago City, Chile [20], and Amman, Jordan [23], where the concentrations of chemical species in dew were much higher than in rainwater. For instance, the concentrations of K^+, Ca^{2+}, Mg^{2+}, Na^+, Cl^-, NO_3^-, and SO_4^{2-} in dew were 6-9 times as much as in the rain in north-central India [3]. The high values in dew may be due to the dry deposition on a wet surface [22] and the variations in the composition of high altitude (cloud level) and low altitude (ground level) aerosols and gases, to which dew and rain are exposed [24].

Deposition amount

Fig. 5 presents the daily dew intensity and the monthly dewfall. The concentration and the deposition of NH_4^+-N, NO_3^--N and PO_4^{3-}-P in dew are displayed in Table 3. Because part of N in dew was from NH_3 diffusion, the concentration of N was dependent on the amount in surface water. However, it was hard to collect the dew during wetland plant shoot. Therefore, the deposition of NH_4^+-N and NO_3^--N of dew which was calculated, was below the real value. Table 3 sketches the deposition amount of NH_4^+-N, NO_3^--N and PO_4^{3-}-P from July to October 2010 in wetland dew as 0.065, 0.14 and 0.007 kg/ha, respectively.

Table 3. Concentration and deposition of NH_4^+-N, NO_3^--N and P of wetland dew

Concentration(mg/L)			Deposition(kg/ha)		
NH_4^+-N	NO_3^--N	P	NH_4^+-N	NO_3^--N	P
0.37	0.82	0.14	0.065	0.14	0.007

Timing of applying foliar fertilizer

The foliar fertilizer should be applied from 15:00 to 17:00 in a fine afternoon. From 5:00 to 8:00, the dewdrops are still clinging on the wetland and the foliar fertilizer would drop down easily. From 8:00 to 14:00, the sunshine is intense. The nutrients in the foliar fertilizer decrease because of NH_3 diffusion if this part of N does not return to the farmland ecosystem with rain, but as an input to river. This phenomenon accelerates the environment pollution. If the foliar fertilizer is applied from 15:00 to 17:00, the diffuse NH_3 would return to the leave with the condensed vapour in the night. Therefore, foliar fertilizer spayed in this period can cling on the leave more tightly. Besides, the efficiency of the fertilizer will improve and avoid polluting environment.

Advantage of dew

The research revealed that grain yield can improve when foliar fertilizer is used over time. The NH_4^+-N, NO_3^--N and PO_4^{3-}-P in the fertilizer cannot be ignored. Compared to foliar fertilizer, on one hand, dew does not cost money or manpower. On the other hand, the foliar fertilizer should be sprayed on both sides of the leaves, because the effect will be more obvious when fertilizer is sprayed on the underside of leaves. The foliar fertilizer was not sprayed on the back side of leaves, in fact. Dew naturally condenses on both sides of the leaves and is more efficient. If the foliar fertilizer concentration is high, it will not be taken up by the plant and could even burn or damage the leaves. The low concentration of nutrients in the dew can be taken up by the plant more efficiently. In a word, dew is a natural and potential fertilizer, and it is safe, efficient and convenient.

CONCLUISIONS

The mean pH of *Carex lasiocarpa* dew was 6.41 and no acid dew occurred in the research area. The metals in *Carex lasiocarpa* dew were abundant. NO_3^--N concentration in the dew was significantly higheer than that of NH_4^+-N and P. Nutrient elements and trace elements were detected in the dew. The metals in the dry bulk deposition were the main sources of metals in dew. The contents of K, Ca, Na, Mg, Mn, Fe, Zn in *Carex lasiocarpa* dew were obviously higher than those in rain ($P<0.05$) which demonstrated that dew can offer more nutrient elements than rain. The trace amounts of Pb, Ba, Se, As, Co, Cr, Cu in *Carex lasiocarpa* dew implied that there is no significant pollution by automobile exhaust, coal combustion or industry in this area. The deposition of NH_4^+-N, NO_3^--N and PO_4^{3-}-P of dew was 0.065, 0.14 and 0.007 kg/ha from July to October, respectively. Dew is a crucial input for nutrient cycling of farmland ecosystems. With dew

acting as a sort of surfactant adhering nutrients to the leaves, recognition of dew as a factor in nutrient uptake is important. The quantity of nutrients evaporating with the dew each morning seems to be an interesting question to be dealt with in further research.

REFERENCES

1. F. D. Eckardt, K. Soderberg, L. J. Coop, A. A. Muller, K. J. Vickery, R. D. Grandin, C. Jack, T. S. Kapalanga, J. Henschel. *J. Arid Environ.*, **93**, 7 (2013).
2. Y. F. Zhang, X. P. Wang, Y. X. Pan, R. Hu, *Internat. J. Biometeorol.*, **57**, 67 (2013).
3. S. P. Singh, P. Khare, K. K. Maharaj, and S. S. Srivastava, *Atmos. Res.*, **80**, 239 (2006).
4. M. Chiwa, N. Oshiro, T. Miyake, N. Nakatani, N. Kimura, T. Yuhara, N. Hashimoto, H. Sakugawa, *Atmos. Environ.*, **37**, 327 (2003).
5. R. Moratiel, D. Spano, P. Nicolosi, R. L. Snyder, *Irrig. Sci.*, **31**, 423 (2013).
6. A. Claeson, E. Lide´n, M. Nordin, S. Nordin, *Int. Arch. Occup. Envir. Health*, **86**, 367 (2013).
7. P. Kumar, S. Yadav, *Environ. Monit. Assess.*, **185**, 2795 (2013).
8. I. Lekouch, M. Mileta, M. Muselli, M. I Milimouk, V. Šojat, B. Kabbachi, D. Beysens, *Atmos. Res.*, **95**, 224 (2010).
9. Y. X. Pan, X. P. Wang, J. Arid Land, **6**, 389 (2014)
10. Z. Q. Luan, Z. X. Wang, D. D. Yan, G. H. Liu, Y. Y. Xu, *The Sci. World J.*, **2013**, 1 (2013).
11. Y. Y. Xu, B. X. Yan, Z. Q. Luan, H. Zhu, *Wetlands*, **32**, 783 (2012).
12. N. Takenaka, H. Soda, K. Sato, H. Terada, T. Suzue, H. Bandow, Y. Maeda, *Environ. Earth Sci.*, **147**, 51 (2003).
13. K. Böhmera, K. H. Schildb, B. A. Schmitt, *J.Comput. Appl. Math.* **254**, 99 (2013).
14. Y. Y. Xu, B. X. Yan, H. Zhu, Acta Agr. Scand., Sect. B-Soil Pl., **63**, 97 (2013).
15. D. Beysens, C. Ohayon, M. Muselli, O. Clus, *Atmos. Environ.*, **40**, 3710 (2006).
16. J. R. Foster, R. A. Pribush, B. H. Carter, *Atmos. Environ.*, **24**, 2229 (1990).
17. H. J. Xiao, R. Meissnerb, J. Seegerb, H. Ruppb, H. Borgc, Y. Q. Zhang , *Sci. Total Envir.*, **452-453**, 384 (2013).
18. J. M. Escalona, S. Fuentes, M. Tomás, S. Martorell, J. Flexas, H. Medrano, *Agricultur. Water Manage.*, **118**, 50 (2013).
19. M. D. Baquerizo, F. T. Maestreb, J. G. P. Rodrígueza, A. Gallardo, *Soil Biol. Biochem.*, **62**, 22 (2013).
20. M. A. Rubio, E. Lissi, G. Villena, *Atmos. Environ.*, **42**, 7651 (2008).
21. E. Mashonjowa, F. Ronsse, M. Mubvuma, J. R. Milford, J. G. Pieters, *Comput. Electron. Agric.*, **95**, 70 (2013).
22. I. Lekouch, M. Muselli, B. Kabbachi, J. Ouazzani, M. I. Milimouk, D. Beysens, *Energy*, **36**, 2257 (2011).
23. A. Jiries, *Atmos. Res.*, **57**, 261 (2001).
24. S. Yadav, P. Kumar, *Air Qual., Atmos. Health.*, **7**, 559 (2014).

ХИМИЧЕН АНАЛИЗ НА МЕТАЛИ И НЕОБХОДИМИ НУТРИЕНТИ ПРИ РОСА ВЪВ ВЛАЖНИ ЗОНИ

Й. Ксу[1,2*], Б. Ян[3], Дж. Танг[2], Й. Лин[1]

[1] *Ключова лаборатория по екология на водната среда в Сонгляо, Уиверситет Джилин, Министерство на образованието, Чангчун, Китай*

[2] *Колеж по ресурси и околна среда, Университет Джилин, Чангчун, Китай*

[3] *Ключова лаборатория по екология на влажните зони и околната среда, Североизточен институт по география и агроекология, Китайска академия на науките, Чангчун, Китай*

(Резюме)

Изследвани са екологичната ефективност на росата и състоянието на въздуха при повърхностния слой над влажната зона в равнината Санджиянг. Изследвани са pH, концентрациите на 25 метала(вкл.K, Na, Ca, Mg и др.) и необходими нутриенти – амониев азот (NH_4^+-N), нитратен азот (NO_3^--N) и фосфати (P) в росата. Събирана е росата върху*Carexlasiocarpa*от средата на м. юли до средата на м. септември от 2008 до 2012 г.Резултатите показват, че средната стойност на pH за росата на *Carexlasiocarpa* е била 6.41, като роса с кисела реакция не е била наблюдавана през изследвания период. Поради това росата не може да навреди на листата на растението.Росата върху *Carexlasiocarpa*съдържа йони на различни метали, които предоставят хранителни съставки за растението. Елементите в сухите отлагания са от същия произход, както и в росата. Съдържанието на основните метали (K, Ca, Na, Mg, Mn, Fe, Zn)в росата на*Carexlasiocarpa*е по-шисоко, отколкото в дъждовните капки (*P*<0.05).Следите от*Pb, Ba, Se, As, Co, Cr, Cu* в росата на*Carexlasiocarpa*показват, че няма значимо замърсяване от автомобилни газове, изгаряне на въглища или от промишлени източници.Отлаганите количества от NH_4^+-N, NO_3^--N и PO_4^{3-}-P от юли до октомври в росата са били съответно 0.065, 0.14и 0.007 kg/ha.Освен това росата кондензира и по двете повърхности на листата и мове да се асимилира ефективно. Затова азотът (N) и фосфорът (P) в росата на влажните зони са друг хранителен източник за растенията.Росата е важен способ за пренасянето на хранителни вещества във влавните зони. Освен това росата може да разкрива степента на замърсяване на въздуха, поради което важно да се следи химическия й състав.

Анализът на съдържанието на метални йони в росата е прост и полезен метод за определяне на състоянието на повърхността. Това дава основа за преценка за замърсяването и качеството на въздуха.

QSAR study of aromatic compounds toxicity to *Chlorella vulgaris*

N. Li[1, 2], F. Chen[1, 2], D. Yang[1, 2*], Y. B. Zhou[1, 2]

[1] Key Laboratory of Marine Bio-resources Restoration and Habitat Reparation in Liaoning Province, Dalian Ocean University, 116023 Dalian, China;
[2]Key Laboratory of North Mariculture, Ministry of Agriculture, Dalian Ocean University, 16023Dalian,China

As demands for energy have increased worldwide, oil has become the main pollutant of the ocean. The impact of aromatic compounds, which are primary pollutants in oil, on various marine ecosystems has become a growing concern. Establishing a quantitative structure–activity relationship (QSAR) model to predict the toxicity of unknown aromatic compounds may thus serve as an important pollution-preventive measure. In this study, 21 aromatic compounds, 15 of which served as a training set and 6 as a test set, were selected. The structural parameters of the compounds were obtained by multiple linear regression, and a 2-descriptor prediction model was established. The test set was used to determine the predictive ability of the model. The model built using the proposed method showed satisfactory statistical results ($R^2 = 0.974$ vs. the test set $R^2 = 0.804$). These data show that the model provides good predictability and stability and can thus be used to predict the inhibitory effect of aromatic compounds on *Chlorella vulgaris*.

Key words:Aromatic compounds,*Chlorella vulgaris*, QSAR.

INTRODUCTION

Asdemands for energy have increased worldwide, exploration and production of offshore oil and gas have steadily expanded [1]. Oil transport via marine vessels and oil pipelines in the ocean frequently resultsin oil spills. Thus, oil has become the main pollutantcausing serious damage to the marine ecosystem [2]. While aromatic compounds are widely used in the industry, most of them are toxic;in fact, aromatic compounds are the main pollutantsin oil.Bioaccumulation of aromatic compounds can destroy human hematopoietic functions and even cause cancer. The effect of aromatic compounds in marine ecosystems has elicited great concern from environmental scientists[3].

Algae are important primary producersand the bases of marine food chain. Theseorganisms maintain thefunctions of various marine ecosystems. Previous findings show that algae are more sensitive to pollution than fish or crustaceans. *Chlorella*is an algal species with a wide ecological distribution and short growthperiod.It is easy toisolateandculture. Symptoms of *Chlorella* poisoning can be directly observed at the cellular level; thus, the species is an ideal test organism in toxicity experiments [4]. As such, using algae to evaluate the effect of toxicaromatic compounds on marine ecosystems is ecologically significant.

Quantitative structure–activity relationships (QSARs) establish links between the activity of organic matter and its structure. QSAR is based on theoretical calculations of parameters and does not rely on experimental parameters; thus, the method is both convenient and timesaving. It can predict, filter, and preliminarily evaluate the activity of organic matterby establishing a mathematical model that can predict its biological activity[5,6]. QSARis widely used in predictions of biological toxicity[7]and has become a rapid, economical, and effective method to generate basic toxicity data for risk evaluation and management of compounds. QSAR employs a variety of methods, such as multiplelinearregression(MLR)[8],partialleast-squaresregression (PLS) [9], and nonlinear regression,among others, to establish a mathematical model.

The effects of aromatic compounds on algae have recently been studied using QSAR.Sacan et al.[10] built a QSAR model describing the toxicity of substituted benzene to oblique *Scenedesmus* and found that the toxicity of the aromatic hydrocarbons is associated with their molecular size, hydrophobicity, and highest occupied molecular orbital energy(EHOMO). Modelliet al. [11} usedrelevant data on ionization energy, electron affinity, and relationship between EHOMO and lowest occupied molecular orbital energy(ELUMO) to predict the ionization energy, electron affinity, and bio-toxicity of polycyclic aromatic hydrocarbons (PAH).

* To whom all correspondence should be sent:
E-mail:dzyang1979@163.com

Table 1. Aromatic compounds descriptions and toxicities to *Chlorella vulgaris*

NO.	Name	SMILES*	TpiPC	MATS3v	pEC50		
					Exp.	Pre.	Dif.
1	Phenol	Oc1ccccc1	5.119	−0.233	−2.339	−2.083	−0.256
2	*o*-chloroaniline	c1(c(cccc1)Cl)N	5.384	−0.192	−2.242	−1.858	−0.384
3	*m*-chloroaniline	c1c(cccc1Cl)N	5.376	−0.316	−2.202	−2.165	−0.037
4	*p*-nitroaniline	c1([N+](=O)[O−])ccc(N)cc1	5.889	−0.300	−1.894	−1.880	−0.014
5	nitroaniline	c1(c(cccc1)N)[N+](=O)[O−]	5.924	−0.219	−1.815	−1.672	−0.143
6	*m*-nitroaniline	c1(cc(ccc1)N)[N+](=O)[O−]	5.905	−0.300	−1.782	−1.877	0.095
7	nitrobenzene	c1(ccccc1)[N+](=O)[O−]	5.690	−0.115	−1.665	−1.529	−0.136
8	nitrophenol	Oc1cc(ccc1)[N+]([O−])=O	5.905	−0.246	−1.627	−1.745	0.118
9	2,4-dinitrotoluene	Cc1ccc(cc1[N+]([O-])=O)[N+]([O−])=O	6.534	−0.289	−1.605	−1.557	−0.048
10	*p*-nitrophenol	c1(cc(ccc1c)[N+](=O)[O−])[N+](=O)[O−]	6.534	−0.289	−1.570	−1.557	−0.013
11	2-chlorotoluene	c1(c(cccc1)Cl)c	5.384	−0.188	−1.478	−1.849	0.371
12	3-nitrochlorobenzene	c1(cc(ccc1)Cl)[N+](=O)[O−]	5.905	−0.204	−1.202	−1.644	0.442
13	2,4-nitrochlorobenzene	c1(cc(ccc1Cl)[N+](=O)[O−])[N+](=O)[O−]	6.534	−0.182	−1.503	−1.297	0.244
14	*o*-dinitrobenzene	c1(c(cccc1)[N+](=O)[O-])[N+](=O)(O-)	6.416	−0.071	−0.940	−1.082	0.142
15	2,4-dichloronitrobenzene	c1(c(cc(Cl)cc1)Cl)[N+](=O)[O−]	6.109	−0.239	−0.681	−1.633	0.952
16	naphthalene	c12ccccc1cccc2	7.454	−0.076	−0.663	−0.608	−0.055
17	acenaphthene	c12c3CCc1cccc2ccc3	8.252	−0.063	−0.233	−0.202	−0.031
18	fluorine	c12c3c(ccc3)Cc1cccc2	7.694	−0.197	−0.193	−0.791	0.598
19	benzo(a)anthracene	c12c3c(ccc1cc1ccccc1c2)cccc3	9.918	−0.039	0.658	0.635	0.023
20	pyrene	c12c3c4ccc1cccc2ccc3ccc4	9.965	0.005	0.783	0.766	0.017
21	benzo(a)pyrene	c1ccc2c(c1)cc3ccc4cccc5c4c3c2cc5	10.604	0.021	1.046	1.102	−0.056

*SMILES: Simplified molecular input line entry specification.

In the present study, PaDEL-Descriptor [12] software was used to calculate the 2D descriptors of 21 aromatic hydrocarbons, andSPSS 19.0 software was employed to perform MLR and select two optimal descriptors. Regression equations considering the *Chlorella* toxicity data and these optimal descriptors were obtained by the stepwise regression method.

DATA COLLECTION AND METHODS

Data

Data of the 21 aromatic compounds, including phenol and benzo(a)pyrene, and their toxicity to *Chlorella* within 96 h of exposure were obtained from the literature [13]. These data were used to establish a QSAR model through the linear regression method with SPSS 19.0. During model building, 15 molecules (5/7) were randomly assigned to the training set, and the remaining 6 molecules were assigned to the test set, as shown in Table 1 (Note: molecules in boldface constitute the test set). The pEC_{50}($-$LogEC_{50}) values of these compounds represent their inhibitory activities toward *Chlorella*.

PaDEL-Descriptor software was used to calculate the molecular structural descriptors of each of the 21 aromatic compounds; parameters with zero values were then deleted to obtain 36 groups of structure parameters. Finally, QSAR analysis was performed using MLR.

Calculation Methods

This study used the MLR method to build a QSAR model. MLR analysis is based on calculation of regression equations through analysis of the relationships between variables; this method is often used for QSAR modeling [14–15]. The mathematical model of the multivariate linear regression equation is:

$$Y = \beta_0 + \beta_1 x_1 + \beta_2 x_2 + \cdots + \beta_n x_n$$

where Y is the bio-activity of the aromatic compound, namely,pEC_{50}; x_1, x_2, x_3, …, x_n are the molecular structural descriptors of the compounds; β_1, β_2, β_3,…, β_n are the regression coefficients; $\beta_i$is an average change of dependent variable Y caused by one unit of change of independent variable x_i,when the other independent variables remain unchanged, i = 1, 2, …, k; and β_0 is a constant.

RESULTS

The simplified group of 36 molecular structural parameters wastreated as a group of independent variables, and the values of theinhibitory activity were considered as dependent variables. The stepwise selection method was used to analyze, predict, and build an ideal mathematical model containing two descriptors. The model equation is as follows:

$$pEC_{50} = -3.911 + 0.468 \text{TpiPC} + 2.434 \text{MATS3v}$$

(1)

The correlation coefficients obtained are as follows: $R^2=0.974$, F=226.452, SE=0.188, and n=15; these values indicate statistically sound results. Equation (1) reveals thatTpiPC and MATS3vinfluence the activity of the aromatic compounds. Equation (1) was then defined as Model I, andthe test value of each independent variableis shown in Table 2.

Table 2. Descriptions of the parameters and their test values

Variable	Descriptions	B	T	Sig.	VIF
TpiPC	autocorrelation	0.468	10.464	0	2.541
MATS3v	path count	20434	3.477	0.005	2.541

Table 2 shows thatall values of theindependent variable (VIF) <10, which illustratesthelack of multiple linear relationships between the independent variables; Sig<0.01 indicates the significant influence of the two structural parameters considered on the activity of the compounds andtherelative stabilityof the model. When Model I was applied to the test set, the correlation coefficients $R^2 = 0.809$ and SE = 0.448 were obtained. These results confirm the reliability and predictive ability of Model I.

The inhibitory activity of the 21 aromatic compounds toward *Chlorella* was predicted by using Model I, and the results are shown in Table 1. Correlations between the experimental and the predicted values are shown in Fig. 1, and residual errors between the experimental and predicted values are shown in Fig. 2. Fig. 1 demonstrates that the experimental and predicted values of the training and test sets are consistent; any variations observed were similar and good correlations were found.
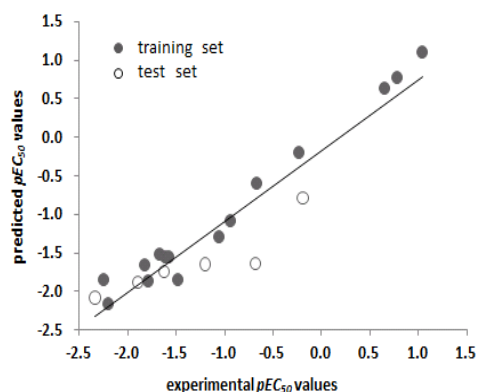
Fig. 1. Comparison between actual values and predicted values.
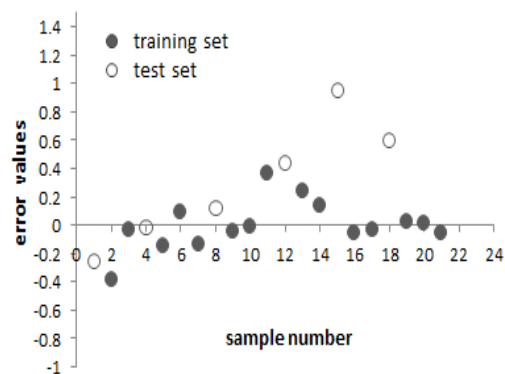
Fig. 2. Error of samples.

The values that are indicated in Fig. 2 fluctuate around the zero point, which indicates that the model achieves reliable prediction and can thus be used to predict the inhibitory toxicity pEC_{50} of aromatic compounds to *Chlorella.*

DISCUSSION

This study used PaDEL-Descriptor software to calculate the descriptors of 21 aromatic compounds; a 2DQSAR model considering the inhibitory activities of the compounds and theircompound descriptors was then built. The keyof QSAR studies is to determine how to produce structural descriptors that express the structural characteristics of various molecules [16]. Existing parameters can be divided into four categories: (1) the substituent parameter, or the linear free-energy relationship parameter, is the earliest and most commonly used structural description. It accumulates a large amount of available data and features a considerable number of successful examples. (2) With the rapid development of theoretical chemistry and computer technologies, scientistshave found that quantum chemistry, orbit energy, and geometrical features are well associated with bioactivity[17]. (3) Interaction parameters and three-dimensional molecular structure descriptors (3D descriptors). (4) Various topological parameters deduced from the 2D topology [18]. The 3DQSAR method generally well predicts relationships between the structure and properties of compounds. In case a 3D descriptor cannot be obtained for a compound, this compound should be excluded from the sample. 2D descriptors can easily beobtained as long as the molecular structure is known, and theycan serve as excellentmodels for 3D descriptors. This research used the SMILES format of the 21 aromatic compounds as input in PaDEL-Descriptor todetermine their structures. The parameters of the model in this study are ideal. We thus conclude that the 2Dmodel is stable and exhibits good ability for predicting the inhibitory effectof toxic aromatic compounds on*Chlorella.*

The 21 bioactive aromatic compounds used in this study are toxic moleculeswith different substituents and various numbers of benzene rings. The two descriptors in the model are TpiPC, and MATS3v,otherwise known as autocorrelation and path count, respectively. The topology autocorrelation descriptor reveals the distribution of atomic properties in the molecular topology, whereas the path count reflects the number of carbon atoms and branching conditions in the molecule. Bothdescriptors are molecular topology parameters. H. Wiener[19] is the first chemist to introducethe topological index. Studies have shown that the Wiener index demonstrates good correlationsbetweenthe properties of hydrocarbon molecules, such as critical constant, viscosity, surface tension, and chromatographic retention time[20]. Our model demonstrates that molecular autocorrelation and path count are also significantly correlated with the toxicity of aromatic compounds.

Several studies onQSAR between aromatic compounds and algae have been conducted.Netzeva et al.[21] built a QSAR model that showed the inhibitory effect of 65 toxic aromatic compounds to *Chlorella*; these researchers usedMLR to build a QSAR model with two descriptors and achieve the equation Log (1/EC50) = 0.73LogKow −0.59Elumo−1.91; R^2=0.84 and SE=0.43. While the statistical results of this model are satisfactory,the regression coefficients are lower compared with that (R^2=0.974) of the model presented in this paper. Thus,TpiPC and MATS3v may be more suitable for predictthe inhibitory effect of toxicaromatic compounds on*Chlorella* than other descriptors.

CONCLUSIONS

In this paper, PaDEL-Descriptor software was used to determine the molecular structure of 21 aromatic compounds. Calculations were based on 15 randomly selected molecules constituting a training set and 6 molecules constituting a test set. An ideal model with two descriptors was built by using the stepwise regression method. The model showed good correlation and strong stability after determination of its R^2, Sig, VIF, and $R^2$by using the test set. This model can predict the inhibitory effect of toxic aromatic compounds on*C. vulgaris.*

REFERENCES

1. V. Parikshit, S. R. Wate, S. Devotta, *Environ Monit Assess,***146**, 191 (2008).
2. J. Papadimitrakis, M. Psaltaki, M. Christolis, N. C. Markatos, *Environ Modell Softw*, **21**, 170 (2006).
3. E. Kriek, Aromatic amines and related compounds as carcinogenic hazards to man. In: Environmental carcinogenesis: Occurrence, risk, evalulation, mechanisms, Elsevier/North Holland Biomedical Press, Amsterdam New York Oxford, 1979.
4. J. L. Liu, P. Z. Lang, *Environmental Science*, **16,** 7 (1995).
5. P. R. Duchowicz, A. G. Mercader, F. M. Fernández, E. A. Castro, *ChemometrIntell Lab*, **90**, 97 (2008).
6. B. B. Xia, K. P. Liu, Z. G. Gong, et al., *EcotoxEnviton Safe*, **72**, 787 (2009).
7. O. Isayev, B. Rasulev, *Mol Divers*, 10, 233 (2006).
8. K. Mansouri, V. Consonni, M. K. Durjava, B. Kolar, T. Öberg, R. Todeschini, *Chemosphere*, **89**, 433 (2012).
9. E. B. de Melo*, Ecotox Environ Safe*, **75**, 213 (2012).
10. M. T. Saçan, M. Özkul, S. S. Erdem, *Chemosphere,***68**, 695 (2007).
11. A. Modelli, L. Mussoni, D. Fabbri, *J Phys Chem A,***110**, 6428 (2006).
12. C.W. Yap, ComputChem, **32**, 1466 (2011).
13. C. H. Wang, S. L. Yang, Y. Wu, *Computers and Applied Chemistry*, **29**, 297 (2012).
14. G. Moreau, P. Broto, *Nouv J Chim.,* **4**, 359 (1980).
15. Y. L. Gu, Y. M. Guo, B. Z. Li, *J Mol Sci-Int.,***19**, 155 (2003).
16. Y. J. Tseng, A. J. Hopfinger, E. X. Esposito, *J Comput Aid Mol Des*., **26**, 39 (2012).
17. A. R. Katritzky, D. C. Fara, R. O. Petrukhin, *Curr Top Med Chem*., **2**, 1333 (2002).
18. M. Karelson, V. S. Lobanov, A. R. Katritzky, *Chem Rev.*, **96**, 1027 (1996).
19. H. Wiener, *J Am Chem Soc.,***69**, 17 (1947).
20. Z. Mihalić, N. Trinajstić, *J ChemEduc,***69**, 701 (1992).
21. T. I. Netzeva, J. C. Dearden, R. Edwards, A. D. Worgan, M. T. Cronin, *Journal of chemical information and computer sciences*, **44**, 258 (2004).

QSAR-ИЗСЛЕДВАНЕ НА ТОКСИЧНОСТТА НА АРОМАТНИ СЪЕДИНЕНИЯ СПРЯМО
Chlorella vulgaris

Н. Ли[1, 2], Ф. Чен[1, 2], Д. Янг [1, 2*], Й. Жоу[1, 2]

[1] Ключова лаборатория по възстановяване на морските биоресурси и хабитатив провинция Ляонинг,Университет в Далиан, Китай
[2]Ключова лаборатория по северни морски култури, Министерство на земеделието, Университет по океанология в Далиан, Китай

(Резюме)

С увеличаването на търсенето на енергия по светапетролът е станал главния замърсител на океаните. Ароматните съединения, които са компонент на петрола са станали основна нарастваща заплаха за морските екосистеми. Съставянето на модел на количествена връзка структура-активност (QSAR) за предсказване на токсичността на неизвестни ароматни съединения може да послужи за предпазване от замърсяване. В настоящата работа са подбрани 21 ароматни съединения, от които петнадесет са за упражнение, а шест - за тестуване.Структурните параметри на съединенията са получени чрез множествена линейна регресия и е съставен 2-дескрипторен предсказващ модел. Тестовите съединения са използвани за определяне предсказващата способност на модела. Този модел, използващ предложения метод показва задоволителни статистически резултати (R^2 = 0.974 срещу тестовата стойност R^2 = 0.804).Тези данни показват, че моделът има добра предсказваща способност и затова може да се използва за предсказването на ефекта на инхибиране на ароматни съединения спрямо *Chlorella vulgaris*.

Highly sensitive fluorescence detection of mercury ion based on Lys VI stabilized gold nanoclusters

N. Zhou[1], P. Zhang[1], X. X. Zhang[1], G. Z. Shen[1], R. H. Fu[1], L. He[1], Z. M. Chen[1], H. W. Ji[1], W. M. Su[2], C. Y. Li[1,2,3]*

[1]College of Food Science and Technology, Guangdong Ocean University, Zhanjiang 524088, China

[2]Guangdong Provincial Key Laboratory of Aquatic Product Processing and Safety, Guangdong Ocean University, Zhanjiang 524088, China

[3]Key Laboratory of Advanced Processing of Aquatic Products of Guangdong Higher Education Institution, Guangdong Ocean University, Zhanjiang 524088, China

Au nanoclusters are presented as novel probes for sensitive detection of mercury ions. Au nanoclusters were synthesized by using Lys VI as a template via a convenient chemical reduction process. The as-prepared water-soluble AuNCs with average diameters of 1.6~1.8 nm exhibit unique fluorescence excitation at 400 nm, maximum emission at 625 nm, and can be quenched in the presence of mercury ions. Excellent linear relationships exist between the fluorescence intensity of the Au nanoclusters and Hg^{2+} concentrations in the range of 0.1 nM to 1 nM, 0.1 μm to 1 μM, or 2 μM to 8 μm, respectively. The detection limit for Hg^{2+} is 0.1 nM. The present nanosensor for Hg^{2+} detection possesses excellent biocompatibility, high selectivity, and good stability, which suggest its potential for diagnostic purposes.

Key words: Au nanoclusters; Lys VI; Mercury ions; High selectivity.

INTRODUCTION

It is known that Hg^{2+} is a highly toxic contaminant that exists in water, soil, and food. Mercury can accumulate in organisms and interact with the thiol groups in proteins to cause serious damage to brain, kidneys, central nervous system, immune system, endocrine system and constitute a serious threat to human health and natural environment [1-3]. Detecting Hg^{2+} is undoubtedly a significant step in environment and health monitoring. Although many methods for Hg^{2+} analysis have been well developed, existing methods require complex equipments and sophisticated operations. A variety of sensor platforms for Hg^{2+} detection have been developed using polymers, nanoparticles, grapheme oxide, carbon nanotubes, etc. [4-10]. However, the synthesis or surface modification of these materials is relatively complicated or time-consuming. Therefore, it is still very important to develop new materials, which require simple synthetic procedures for protein discrimination. Fluorescent metal nanoclusters have gained much attention, because of their burgeoning photophysical properties and potential applications in biosensing and bioimaging. Recently, Au metal clusters (Au NCs) have been employed as probes to detect Hg^{2+} based on the quenching of their fluorescence. Xie and his co-workers used native bovine serum albumin (BSA) to synthesize Au nanoclusters via one-pot chemical reduction and further used them as fluorescent probes for sensitive and selective Hg^{2+} and Cu^{2+} ions sensing [11, 12]. The limit of detection (LOD) was measured to be 10 nM and a remarkable selectivity toward Hg^{2+} could be obtained when conducting the assay in the presence of a chelating ligand, 2, 6-pyridinedicarboxylic acid (PDCA)[13]. Although the above-mentioned methods proved to be efficient, there still remains a challenge for facile one-step synthesis of fluorescent AuNCs, which could be used to detect trace Hg^{2+} below 1 nM with excellent linear relationship. Here we demonstrate the synthesis of Lys VI stabilized AuNCs with unique fluorescence in the red region of the visible spectrum and further use these clusters as sensitive and selective probes for label-free Hg^{2+}.

EXPERIMENTAL

Chemicals and Materials

Lysozyme (chicken eggwhite) was purchased from Sigma-Aldrich. $HAuCl_4$, NaOH, $CaCl_2$, $MnCl_2$, $FeCl_3$, $CrCl_3$, $NiCl_2$, $CoCl_2$, $CuCl_2$, $HgCl_2$, were obtained from Guangzhou Qiyun

---

Biotechnology Co. LTD. Milli-Q ultrapure water (Milli-pore, Hamburg, Germany) was used in all experiments.

Synthesis of Lys VI-AuNCs

The AuNCs were synthesized by chemical reduction of $HAuCl_4$ with Lys VI. A solution of Lys VI (5 mL, 25 mg/mL) was added to an equal volume of 10 mM $HAuCl_4$. The mixture was vigorously stirred for 2 min, the reaction pH was adjusted to 12.0 with NaOH. The resulting solution was incubated overnight at 37 °C.

Characterization of Lys VI-AuNCs

TEM and high resolution TEM (HRTEM) measurements were carried out by using a FEI Tecnai G20 instrument with 200 kV accelerating voltage. The absorption and fluorescence spectra of the AuNCs were obtained using a double-beam UV-visible spectrophotometer (UV-2550, Shimadzu, Japan) and a Hitachi F-7000 fluorometer (Hitachi, Japan), respectively.

Hg^{2+} Detection Using Lys VI-AuNCs

Hg^{2+} (1×10^{-10} to 1×10^{-2} M) and other metal ions (10^{-4} M) were separately added to an equal volume of the Lys VI-AuNCs. After 30 min, the mixed solutions were transferred separately into a 1 mL quartz cuvette. Their fluorescence spectra were recorded by operating the fluorescence spectrophotometer at an excitation wavelength of 400 nm.

RESULTS AND DISCUSSION

Figure 1 displays the HRTEM images of the as-prepared, well monodispersed Lys VI-AuNCs. The close-up in the top inset shows lattice planes separated by 0.235 nm, corresponding to the (111) lattice spacing of the face-centered cubic Au (0.23 nm) [14]. The average diameter of the AuNCs is 1.6~1.8 nm. The mean diameter of Lys VI-AuNCs was determined as 1.6~1.8 nm, as judged from over 100 individual particles.
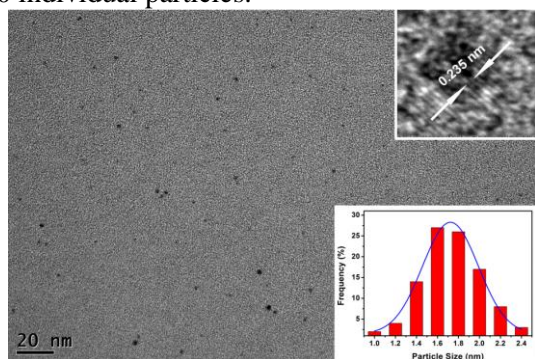
Fig. 1. Typical TEM image of the as-prepared Lys VI-AuNCs. The insets show the HRTEM image (top) and the size distribution histogram (bottom).

The as-prepared Lys VI-AuNCs showed a broad absorption band and absence of localized surface plasmon resonance bands, suggesting the formation of the Au NCs (Figure 2). In addition, the fluorescence emission (the excitation wavelength is 400 nm and the emission peak is 625 nm) was also investigated to confirm the formation of Au NCs.
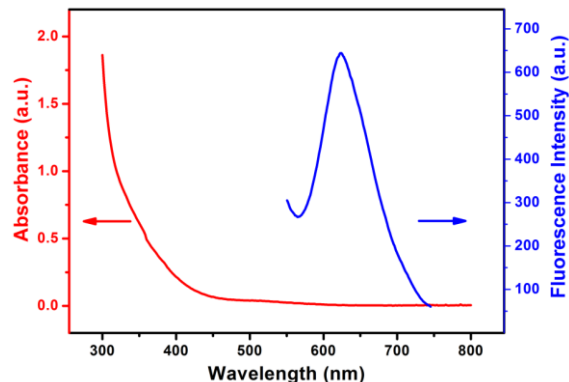
Fig. 2. UV-vis absorption spectrum and fluorescence emission spectrum of the as-prepared Lys VI-AuNCs.

Before applying the Lys VI-AuNCs for detection of mercury ions, the effect of reaction time between AuNCs and Hg^{2+} on the fluorescent AuNCs was investigated. As shown in Figure 3, the fluorescence intensity of the Lys VI-AuNCs decreases rapidly at the beginning (0~20min) after the addition of Hg^{2+}, and further maintains the same value. Thus, 30 min was selected as the reaction time. In our experiments, fluorescence detection was carried out 30 min after Hg^{2+} addition.
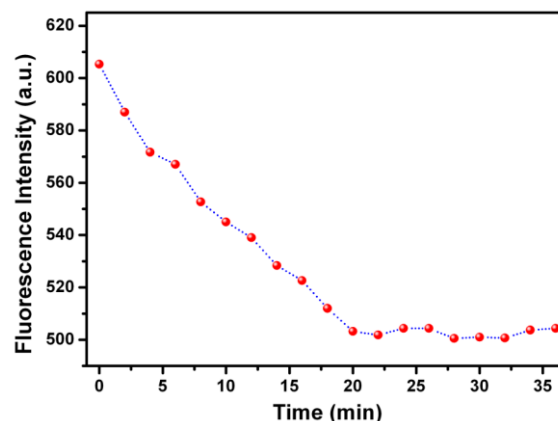
Fig. 3. The relation between fluorescence intensity and reaction time.

As shown in Figure 4, the relation between fluorescence intensity and Hg^{2+} concentration is complicated. It can be divided into four sections. In the first section, the fluorescence intensity of the Lys VI-AuNCs displayed a gradual decrease at 625 nm with increasing Hg^{2+} concentration. The fluorescence quenching of AuNCs in the presence of Hg^{2+} is presented in Figure 4 (a), which exhibits a good linear relationship in the range of 0.1 nM to

1 nM.
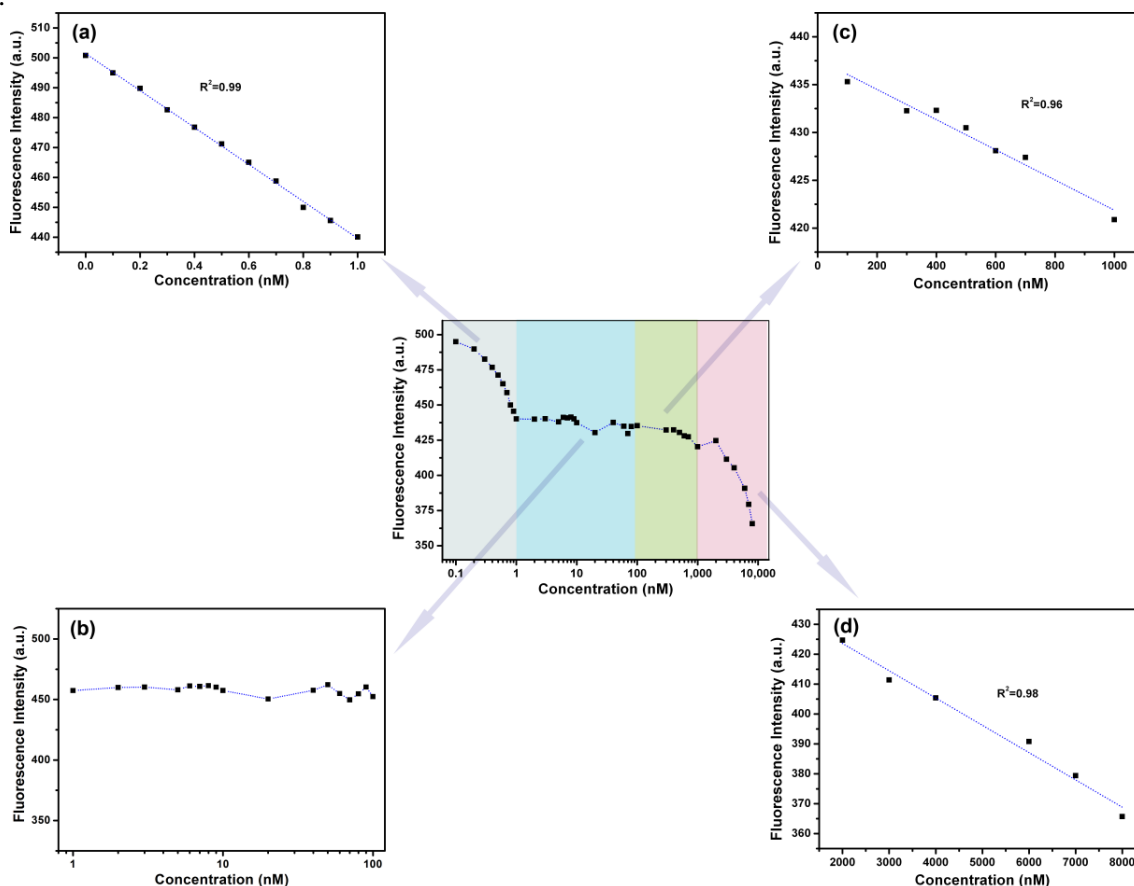
Fig. 4. Fluorescence changes of the Ag NCs in the presence of different concentrations of Hg^{2+}.

When Hg^{2+} concentrations increased to 1~100 nM, a strange phenomenon was observed. The change of fluorescence intensity is not obvious and the related reason is not found (Figure 4 (b)). However, when Hg^{2+} concentrations increased to 100~1000 nM, the fluorescence intensity versus Hg^{2+} concentrations was linear again (Figure 4 (c)). In addition, the fluorescence intensity decreased as Hg^{2+} concentrations continually increased (Figure 4 (d)). The Hg^{2+}-induced fluorescence quenching of the Lys VI-AuNCs is probably related to the formation of metallophilic bonding between $Hg^{2+}(4f^{14}5d^{10})$ and $Au^+ (4f^{14}5d^{10})$.

To further investigate the detection selectivity for mercury ions of Lys VI-AuNCs, the changes in fluorescence of the Lys VI-AuNCs that were induced with 50 μM of the following metal ions (Ca^{2+}, Mn^{2+}, Fe^{3+}, Cr^{3+}, Ni^{2+}, Co^{2+} and Cu^{2+}) were detected. As shown in Figure 5, all of the other ions including Cu^{2+} did not quench the fluorescence of Au clusters, while only Hg^{2+} could effectively quench the fluorescence. These results indicate that the Lys VI-AuNCs display excellent selectivity toward mercury ions.
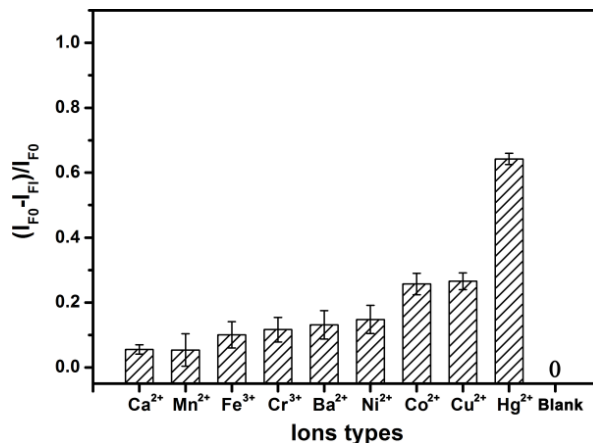
Fig. 5. Fluorescence changes of Lys VI-AuNCs in the presence of different metal ions. IF_0 and IF_I correspond to the fluorescence intensity of Lys VI-AuNCs in the absence and in the presence of metal ions.

CONCLUSIONS

In summary, we describe here a Lys VI-directed, facile one-pot method for the synthesis of water-soluble fluorescent AuNCs. The approach is simple and more environmentally friendly than previously reported etching-based or organic phase-based strategies. The as-prepared water-soluble AuNCs with average diameters of

1.6~1.8 nm exhibit a unique fluorescence excitation at 400 nm, a maximum emission at 625 nm, and can be quenched in the presence of Hg^{2+}. Excellent linear relationships exist between the fluorescence intensity of the Au nanoclusters and the concentrations of Hg^{2+} in the range of 0.1 nM to 1 nM, 0.1 μM to 1 μM, or 2 μM to 8 μM, respectively. The detection limit for Hg^{2+} is 0.1 nM. The present nanosensor for Hg^{2+} detection possesses excellent biocompatibility, high selectivity, and good stability, which suggest its potential for diagnostic purposes.

REFERENCES

1. F. Xu, T.Lou, Z. Chen, M. Lin; W. Feng, L. Chen, *ACS Appl.Mater. Interfaces*, **4**, 1080 (2012).
2. C. Guo, J. Irudayaraj, *Anal. Chem.*, **83**, 2883 (2011).
3. R. Uauy, M. Olivares, M. Gonzalez, *Am. J. Clin. Nutr.,* **67**, 952S (1998).
4. Y. Q. Chen, H. Bai, W. J. Hong, G. Q. Shi, *Analyst*, **134**, 2081(2009).
5. D. Li, A. Wieckowska, I. Willner, *Angew. Chem., Int. Ed.*, **47**, 3927 (2008).
6. M. V. Yigit, A. Mishra, R. Tong, J. J. Cheng, G. C. L. Lu, Y. Wong, *Chem. Biol.,* **16**, 937 (2009).
7. C. C. Huang, Z. Yang, K. H. Lee, H. T. Chang, *Angew. Chem., Int. Ed.,* **46**, 6824 (2007).
8. Z. D. Wang, J. H. Lee, Y. Lu, *Chem. Commun.*, 6005 (2008).
9. P. Chen, C. A. He, *J. Am. Chem. Soc.*, **126**, 728 (2004).
10. S. Yoon, E. W. Miller, Q. He, P. H. Do, C. J. Chang, *Angew. Chem., Int. Ed.,* **46**, 6658 (2007).
11. J. P. Xie, Y. G. Zheng, J. Y. Ying, *J. Am. Chem. Soc.*, **131**, 888 (2009).
12. J. P. Xie, Y. G. Zheng, J. Y. Ying, *Chem. Commun.*, **46**, 961 (2010).
13. C. Guo, J. Irudayaraj, *Anal. Chem.*, **83**, 2883(2011).
14. L. Shang, R. M. Dorlich, S. Brandholt, R. Schneider, V. Trouillet, M. Bruns, D. Gerthsen, G. U. Nienhaus, *Nanoscale.*, **3**, 2009 (2011).

ВИСОКО-ЧУВСТВИТЕЛНО ОТКРИВАНЕ НА ЖИВАЧНИ ЙОНИ НА БАЗАТА НА Lys VI – СТАБИЛИЗИРАНИ ЗЛАТНИ НАНО-КЛЪСТЕРИ

Н. Жоу, П. Жанг[1], Кс. Кс. Жанг[1], Г. З. Шен[1], Р. Х. Фу[1], Л. Хе[1], Ж. М. Чен[1], Х. У. Джи[1], У. М. Су[2], Ч. Й. Ли[1,2,3]∗

[1]Колеж похранителни науки и технологии, Океаноложки университет Гуангдонг, Жанджианг,Китай

[2]Провинциална ключова лаборатория преработка и сигурност на аквапродукти,Гуангдонг, Океаноложки университет Гуангдонг, Жанджианг,Китай

[3]Провинциална ключова лаборатория преработка и сигурност на аквапродукти,Гуангдонг, Висш образователен институт, Океаноложки университет Гуангдонг, Жанджианг,Китай

(Резюме)

Представени са златни нано-клъстери(AuNCs) като нови датчици за чувствително откриване на живачни йони. Те се синтезират с използването на Lys VI като основа чрез удобна химична редукция.   as a template via a convenient chemical reduction process. Така приготвените водо-разтворими златни нано-клъстерисъс среден диаметър 1.6~1.8 nm показватуникално флуоресцентно възбуждане при 400 nm с максимална емисия при 625 nm и могат да бъдат закалени в присъствие на живачни йони. Съществува отлична линейна зависимост между интензивността на флуоресценцията на AuNCsи концентрацията на Hg^{2+}ш интервала от 0.1 nMдо 1 nM и съответно от0.1 μMдо 1 μM, или от 2 μMдо 8 μm. Границата на откриване за Hg^{2+}е 0.1 nM. Представеният наносензор за откриване на Hg^{2+}притежава от;ична биологична съвместимост, висока селективност и добра стабилност, което внушава неговия потенциал за диагностични цели.

Accumulation of heavy metals in soil and vegetables and absorption by field weeds with phytoremediation potential in fine chemical industrial park

G. H. Yu[1,2*], X. Q. Zhang[1,2], J. W. Zhu[1,2], Y. Zhang[1], Z. G. Li[1], S. W. Li[1]

[1]The school of architecture & urban planning, Hunan university of science and technology, Xiangtan Hunan 411201, China
[2]Key Laboratory of the heavy metal ecological remediation and safe use of contaminated soil, college of Hunan Province, Xiangtan Hunan 411201, China

The Zhubugang area was a fine chemical industrial park area in Xiangtan city of China. Waste gas, water and slag discharges have caused serious heavy metals pollution to environment in this region. This study collected 10 soil samples, 5 varieties of seasonal vegetables (*Lactuca sativa*，*Lactuca sativa L. var. asparagine, Bailey, Radix Osterici Grosseserrati, Solanum tuberosum* and *Brassica rapachinensis*) and 3 varieties of field weeds (*Alopecurus aequalis Sobol, Alternanthera philoxeroides (Mart.) Griseb, Paspalum paspaloides (Michx.) Scribn.*). The concentrations of Zn, Cu, Pb and Mn were determined by hydride generation atomic fluorescence spectrometry after acid digestion. Then the environmental safety of heavy metals in soil and vegetables was evaluated and the absorption characteristics of field weeds to heavy metals were investigated. The results showed that the comprehensive pollution indices of heavy metals in the soils and vegetables were 0.79-3.43 and 1.54-4.13, respectively. Soil and vegetables were severely contaminated with heavy metals. The absorption capacity of different field weeds to heavy metals strongly differed. *Alternanthera philoxeroides (Mart.) Griseb* had the highest absorption capability to Cu of the 3 field weeds. The concentrations of Zn, Pb and Mn in *Alopecurus aequalis Sobol* were higher than in other weeds.

Key words: Zhubugang area; soil; vegetables; field weeds; heavy metals.

INTODUCTION

The heavy metal pollution of soil becomes more and more serious in China in recent years. The heavy metal pollution has directly affected the health risk of residents. Chen Xing, Yang Gang, Zhang Xiaomin, Chen Hong and Wang Lixia et al. found that some lands in China such as arable land, mines, industrial area, city soil and river sediment were seriously contaminated with heavy metals [1-5]. According to the survey of the Ministry of agriculture, the soil of sewage irrigation was about $1.40 \times 10^6 m^2$, which means that almost 2/3 of the land area suffered from heavy metal pollution in China. The area ratio of slight pollution, middle pollution, serious pollution was 467:97:84 [6-8]. The agricultural land area contaminated with heavy metals was about $2.5 \times 10^7 m^2$. The food was contaminated with heavy metals at least 1.2×10^{10}kg/y. Released in 2014, "the national survey of Soil Pollution Bulletin" showed that the rate of soils with concentrations of pollution exceeding the standard was 16.1% of all soils of China. The soil pollution with industrial and mining waste was particularly prominent and the heavy metal pollution was the main pollution. The most

serious pollution in soil was cadmium of all heavy metal in China [9].

Heavy metals were extremely easy to be enriched in the soil. If not artificially processed, it may trigger social effects of pollution and serious harm to human, animals and plant life. Once the soil has suffered from heavy metal pollution, governance was difficult [10-14].

Zhubugang fine chemical zone area was located in Xiangtan City of Xiangjiang River Basin of China and was founded in 1960s. Xiangjiang River was the first river reported to be contaminated with heavy metals. The total area was $1.74 \times 10^6 m^2$. Heavy metal pollution was very serious in this area and Zhubugang area was the key heavy metal treatment area of Xiangjiang River Basin. The enterprises of this industrial zone mainly include chemical, smelting, electroplating and pharmaceutical enterprises. The volume of wastewater discharged was 2.64×10^5kg and contained 1.2×10^6 kg of chemical oxygen, 218 kg of heavy metals, 6×10^3 kg of sulfur dioxide and 3×15 kg of industrial waste residue in 2013 by 26 enterprises in this area. Although pollution load significantly decreased in recent years through the implementation of government regulations, the land was still has not been able to grow because of the contamination with heavy metals [15].

---

* To whom all correspondence should be sent:
E-mail: guang_hui_yu@163.com

This study collected soil, vegetables and field weeds, analyzed Zn, Cu, Pb and Mn concentrations and evaluated the environmental safety of heavy metals in soil and vegetables, then investigated the absorption characteristics of field weeds to heavy metals. The conclusion of the study provided the scientific basis for the heavy metal treatment of soils in Zhubugang area.

MATERIALS AND METHODS

Collected samples

On April 20, 2014, we collected surface soil (0~20 cm) by the mixed sampling method where three samples were mixed into one sample in each point [16]. We collected plant samples in the soil sample point. The sampling location was shown in table 1.

Sample treatment

Plant sample

The edible parts of vegetables and the ground parts of field weeds were collected with a stainless steel knife. The dirt was first washed with tap water and rinsed 1 to 2 times with pure water, then washed 2-3 times with high purity water. Fixation was performed (105°C, 0.5 h) with a coarse filter paper wrap in the oven. Then the samples were dried to constant weight (80°C, about 12 – 24 h). The dried plant samples were milled in a mortar and finally put in a plastic bag for standby [16].

Soil sample

The sand and plant debris of soil were removed before natural air-drying. The soil was milled in a glass rod mill in a clean porcelain dish. Finally, the soil was filtered through 60 and 100 mesh nylon screens.

Sample analysis

At first, samples were placed in a polyethylene digestion tank and 6 ml 65% nitric acid and 2 ml 30% hydrofluoric acid were added. Then the lid was tightened and the vessel was placed in the microwave digestion instrument (USA CEM MARS 6) until the digestion tank wall dried after a period of time.

The concentrations of heavy metals in the samples were determined by flame atomic absorption spectrophotometry (Hitachi TAS 990F atomic absorption spectrophotometer) and graphite furnace atomic absorption spectrophotometry (Hitachi Z-2000 atomic absorption spectro-photometer) [16,17].

RESULTS AND ANALYSIS

Concentrations of heavy metals in soils and plants
Concentrations of heavy metals in soils

The concentrations of heavy metals in the soils were shown in table 1. Different Cu concentrations were found in the different soils, being higher in soils No.6 and No.2 and lower in soils No.9 and No.10. The concentrations of Cu in the soil didn't exceed the standard of soil environment quality. The concentrations of Mn in the soil differed significantly and the soil No.2 was of the highest Mn concentration. The concentrations of Pb exceeded the standard of soil environment quality in soils No.2, No.4 and No.6. The concentrations of Zn displayed the highest differences in all soils and the range of concentrations was 43 mg/kg-364 mg/kg. The No.2 soil was of the highest concentration of Zn.

Table.1. Sampling locations.

Soil sample	Latitude	Longitude	Distance to factory	Soil	Plant
No.1 soil	N27$^.$ 54'30"	E112$^.$ 58'17"	1m	Sludge of outfall	—
No.2 soil	N27$^.$ 54'32"	E112$^.$ 58'16"	5m	Sludge of outfall	—
No.3 soil	N27$^.$ 54'34"	E112$^.$ 58'15"	15m	Garden soil	*Lactuca sativa L. var.asparagina Bailey* *Lactuca sativa*
No.4 soil	N27$^.$ 54'23"	E112$^.$ 58'08"	25m	Paddy soil	—
No.5 soil	N27$^.$ 54'34"	E112$^.$ 58'16"	50m	Paddy soil	—
No.6 soil	N27$^.$ 54'46"	E112$^.$ 58'11"	200m	Garden soil	*Lactuca sativa L. var. asparagine Bailey* *Radix Osterici Grosseserrati*
No.7 soil	N27$^.$ 54'36"	E112$^.$ 58'18"	250m	Paddy soil	—
No.8 soil	N27$^.$ 54'38"	E112$^.$ 58'20"	400m	Paddy soil	*Alopecurus aequalis Sobol Alternant heraphiloxeroides（Mart.）Griseb Paspalum paspaloides (Michx.) Scribn.*
No.9 soil	N27$^.$ 55'08"	E112$^.$ 58'20"	1500m	Garden soil	*Solanum tuberosum*
No.10 soil	N27$^.$ 55'15"	E112$^.$ 58'23"	1800m	Garden soil	*Brassica rapachinensis*

There was no evaluation of the concentration of Mn in the soil environment quality of China. The background value of national soil was 583.0 mg/kg. The concentrations of Mn in soils No.1, No.2, No.3 and No.4 were higher than the background value of national soil.

The concentrations of heavy metals in vegetables were shown in table 3. As can be seen, the concentrations of heavy metals in the different vegetables were different. The vegetable with the highest concentrations of Cu and Mn was *Brassica rapachinensis*. The vegetable with the highest concentrations of Pb and Zn was *Lactuca sativa*. The concentrations of Pb in 3 vegetables were higher than the limit standard of this heavy meal of vegetable.

Table 2. The concentrations of heavy metals in soils (mg/kg).

Soil sample	Cu	Mn	Pb	Zn
No.1 soil	12.1b	604.4b	19.0b	74.3b
No.2 soil	56.4a	1060.2a	89.4a	360.5a
No.3 soil	44.3a	927.1a	76.3a	45.2b
No.4 soil	48.2a	768.1ab	88.7a	364.2a
No.5 soil	36.8ab	506.7b	58.5ab	324.4a
No.6 soil	62.4a	575.8b	74.4a	43.7b
No.7 soil	32.2ab	354.3c	73.2a	308.9a
No.8 soil	28.7 ab	248.5c	59.9ab	202.5a
No.9 soil	20.5b	322.9c	25.6b	49.3b
No.10 soil	20.0b	365.4c	27.5b	49.1b
Soil environment quality [18]	100	—	50/80	250
Background value of national soil [19]	22	583.0	26	74.2

There was a limit standard of Cu and Zn in vegetables in GB/T 5009.13－2003[21], GB/T 5009.14—2003[22], but the limit standard of Cu and Zn in vegetable was canceled in the new standard GB 2762－2012[19]. The main reason was the consideration that the concentrations of Cu and Zn in vegetables would not lead to problems of food safety in China. But the researchers believed that there was still risk in heavy metal polluted places. The related standard of the concentration of Mn in vegetables was not always made in China. But there was the general concentration of Mn in vegetables in "China food composition table (second volume)" [23] and the general concentrations were different in the various vegetables. We would use the data about Cu, Zn and Mn of GB/T 5009.13—2003, GB/T 5009.14—2003, and "China food composition table (second volume)" to evaluate the safety of vegetables. It was necessary to comprehensively

evaluate the food safety of every heavy metal in the vegetables because the amounts of eaten vegetables by the residents were grown locally.

Environmental safety of heavy metals in soils and vegetables
The pollution evolution method of heavy metals

The pollution evaluation method of heavy metals adopted in this study was the N. L. Nemerow index method. The latter was a comprehensive pollution evolution method. The method was presented with formula 1.

$$P = \sqrt{\frac{(Ci/Si)^2_{max} + (Ci/Si)^2_{ave}}{2}} \quad (1)$$

Ci was the heavy metal concentration of sample; *Si* was the standard value of heavy metal; *Ci/Si* was the single pollution index No.i heavy metal; *max* was the maximum single pollution index; *ave* was the average single pollution index [24].The five soil pollution grades according to the N. L. Nemerow index method [23] were: safe (P≤0.7), warning (0.7＜P≤1), slight (1＜P≤2), middle (2＜P≤3) and serious (P＞3).

The pollution evolution of soils

The pollution evolution results of soil were shown in table 4. Through comprehensive evaluation of Zhubugang soil, the soil heavy metal pollution was estimated as very serious in this region and the most serious pollution was that of Zn (comprehensive pollution index of 3.03). The Zn pollution of soils No.4, No.2, No.5, No.7 and No.8 was relatively serious in 10 soil samples, where the range of the single factor pollution index was 2.13 - 3.84. The comprehensive pollution index of Pb (2.54) was the second one among the 4 heavy metals. The pollution grade of Pb was middle. The concentrations of Pb in 7 soil samples exceeded the standard value according to the single pollution index. The pollution grade of Mn and Cu was slight, but 6 soils exceeded the standard values for Mn and 7 soils – that for Cu. The comprehensive pollution indexes of Mn and Cu were 1.86 and 1.68 respectively.

A comprehensive analysis of 10 soil samples, table 4, showed that the No.2 soil sample had the highest comprehensive pollution index of 3.43. Second was the No. 4 soil sample with comprehensive pollution index of 3.37, followed by No. 8 and No. 9 soils, which, having comprehensive pollution indices of 2.8554 and 2.76, were in the middle pollution grade. In the middle pollution grade were also the No.3 and No. 6 soils with comprehensive pollution indices of

2.17 and 2.02. No. 1 and No. 8 soils with comprehensive pollution indices between 1 and 2, were in the slight pollution grade. The control soils No.9 and No. 10 had comprehensive pollution indices of 0.77 and 0.83, thus being in the warning pollution grade.

Comprehensive tables 1 and 4 showed that the soil located in the sewage outfall of the same production factory waste, No. 1 soil was more seriously polluted than No. 2, and the difference in the comprehensive pollution index was about 3 times. Based on the sampling situation, No. 2 soil in a partial underground sewage ditch, and its surrounding still did not stop factory production, the wastewater might still be discharged into the soil around the factory. The No. 1 soil was located in an open sewage outfall, and the soil had dried after a long time of natural precipitation, low pollution soil around of the sewage outfall mixed with No. 1 soil, thereby reducing the heavy metal pollution.

We found the comprehensive pollution index of

No. 4 paddy soil (1.2) higher than that of No. 3 garden soil. At the same time, the comprehensive pollution index of No.7 paddy soil (0.7) was higher than that of No. 6 garden soil. Therefore, the heavy metal pollution of the paddy soil was more serious compared to the garden soil at the same distance to the factory in Zhubugang area. The main reason might be related to sewage irrigation in the farmland over a long period, because the wastewater of the factory in Zhubugang area was directly discharged into the nearby ditch used for farmland irrigation. We can see from table 3 that the degree of pollution of paddy soil and garden soil continuously decreased with the increase of the distance from the factory. The No.9 and No.10 garden soils had the smallest comprehensive pollution index among all soils, but their pollution grade was warning. This showed that there was a serious threat to the soil 1500 m from the factory. Measures must be taken to prevent the further spread of pollution.

Table 3. The concentrations of heavy metals in vegetables (mg/kg fresh weight).

Vegetable sample	Cu	Mn	Pb	Zn
Lactuca sativa L. var. asparagine Bailey Ⅰ	0.40b	0.80c	0.20c	1.00b
Lactuca sativa	0.53ab	0.40c	1.06a	2.11a
Lactuca sativa L.var. asparagine Bailey Ⅱ	0.60a	0.80c	0.20c	0.20c
Radix Osterici Grosseserrati	0.55ab	0.55c	0.37bc	2.03a
Solanum tuberosum	0.36b	1.98b	0.18c	0.18c
Brassica rapachinensis	0.62a	3.74a	0.62b	0.21c
The limit standard of heavy metal in vegetable [20]	—	—	0.3	—

Table 4. The pollution evolution results of soils.

Soil	Single pollution index				Comprehensive pollution index	Pollution grade
	Cu	Mn	Pb	Zn		
No.1 soil	0.44	1.32	0.64	0.78	1.13	Slight
No.2 soil	2.05	2.31	3.00	3.80	3.43	Serious
No.3 soil	1.61	2.02	2.56	0.48	2.17	Middle
No.4 soil	1.76	1.67	2.96	3.84	3.37	Serious
No.5 soil	1.32	1.10	1.95	3.41	2.86	Middle
No.6 soil	2.27	1.25	2.49	0.45	2.02	Middle
No.7 soil	1.17	0.77	2.46	3.25	2.76	Middle
No.8 soil	1.03	0.54	1.99	2.13	1.86	Slight
No.9 soil	0.73	0.70	0.84	0.52	0.77	Warning
No.10 soil	0.73	0.80	0.91	0.52	0.83	Warning
Comprehensive pollution index	1.85	1.68	2.54	3.03		
Pollution grade	Slight	Slight	Middle	Serious		

Table 5. The pollution evolution results of vegetables.

Vegetable	Single pollution index				Comprehen-sive pollution index	Pollution grade
	Cu	Mn	Pb	Zn		
Lactuca sativa L. var. asparagine Bailey Ⅰ	0.40	2.67	0.67	2.50	2.18	Middle
Lactuca sativa	0.53	0.67	3.53	5.28	4.13	Serious
Lactuca sativa L. var. asparagine Bailey Ⅱ	0.60	2.67	0.67	0.50	2.04	Middle
Apium graveolens	0.55	1.38	1.23	5.08	3.87	Serious
Solanum tuberosum	0.36	1.98	0.90	0.45	1.54	Slight
Brassica rapachinensis	0.62	2.49	2.07	0.53	2.03	Middle
Comprehensive pollution index	0.68	2.35	2.50	3.73		
Pollution grade	Safe	Middle	Middle	Serious		

Table 6. The concentrations of heavy metals in field weeds (mg/kg dry weight).

Field weeds	Cu	Mn	Pb	Zn
Alopecurus aequalis Sobol.	8.0	952.3	53.4	106.7
Alternant heraphiloxeroides（*Mart.*）*Griseb.*	12.2	359.4	16.3	21.6
Paspalum paspaloides (Michx.) Scribn.	8.5	260.9	8.1	12.4

Table 7. The enrichment coefficients of 3 field weeds.

Field weeds	Cu	Mn	Pb	Zn
Alopecurus aequalis Sobol.	0.29	3.84	0.90	0.52
Alternant heraphiloxeroides（*Mart.*）*Griseb.*	0.43	1.45	0.27	0.11
Paspalum paspaloides (Michx.) Scribn.	0.29	1.05	0.14	0.06

The pollution evolution of vegetables

The pollution evolution results of vegetables were shown in table 5. The highest pollution was for *Lactuca sativa* in all vegetables and the comprehensive pollution index was 4.13. The *Lactuca sativa* samples were contaminated with Zn and single pollution factor was up to 5.28. *Lactuca sativa L. var. asparagine Bailey* of No.3 soil was mainly contaminated with Mn and Zn, the single pollution indices were 2.67 and 2.50 respectively, and the comprehensive index was 2.18, belonging to the middle pollution grade. *Lactuca sativa L. var. asparagine Bailey* of No.6 soil was mainly contaminated with Mn, the single pollution indices were 2.67, and the comprehensive index was 2.08, belonging to the middle pollution grade. *Apium graveolens* of No.6 soil was mainly contaminated with Zn, the comprehensive index was 3.87, belonging to the serious pollution grade. The pollution grades of *Lactuca sativa* and *Apium graveolens* were serious. The comprehensive pollution index of Zn was the highest among the heavy metals and that of Cu was the lowest. The concentration of Cu was safe in all vegetables and that of Zn was serious.

In summary, the vegetable samples were polluted with heavy metals, and the pollution level of vegetables continuously decreased with the increase of the distance from the factory. The same kind of vegetable of different regions had different pollution grades; the different kinds of vegetables of the same region had different pollution grades with heavy metals. The main reason of the serious pollution was exhaust emission, sewage discharge and sewage irrigation by the factory in Zhubugang area.

The heavy metals in field weed
Concentrations of heavy metals in field weeds

The paddy field around the factory in Zhubugang area didn＇t cultivate crops for 10 years, but there were many field weeds grown. *Alopecurus aequalis Sobol., Alternant heraphiloxeroides (Mart.) Griseb.* and *Paspalumpaspaloides (Michx.) Scribn.* were better grown than the other wild plants.

The concentrations of heavy metals in field weeds were shown in table 6. It can be seen that *Alopecurus aequalis Sobol.* had the highest concentrations of Mn, Pb and Zn, *Alternant heraphiloxeroides (Mart.) Griseb.* had the highest concentrations of Cu and *Paspalum paspaloides (Michx.) Scribn.* had the lowest concentrations of the 4 heavy metals in the 3 field weeds.

Absorption ability to heavy metal off-field weeds

A plant was considered hyperaccumulator if the concentrations of heavy metal (Pb, Zn, Cu and Mn) in the plant were more than 1×10^3mg/kg, 1×10^4mg/kg, 1×10^3mg/kg and 1×10^4mg/kg, respectively; or the concentration of heavy metal was 10 times higher than in the normal plant; or the enrichment coefficient and the transfer coefficient were greater than 1 [25]. The calculation formula of the enrichment coefficient of plant was as follows:

1115

$$An = Cn / Ci \ _{[26]}(2)$$

An was the enrichment coefficient of plant; *Cn* was the concentration of heavy metal of plant; *Ci* was the concentration of heavy metal of the soil where plant grows. The enrichment coefficients of 3 field weeds in No.10 soil were shown in table 7.

According to table 7 three kinds of weeds in paddy field were in accordance with Mn hyperaccumulator characteristics, but also showed different absorption ability to the same heavy metals in different plant species [27]. The absorption ability to Cu of *Alternant heraphiloxeroides（Mart.）Griseb.* was the strongest in 3 field weeds, and the absorption abilities to Mn, Pb and Zn of *Alopecurus aequalis Sobol.* were higher than those of *Alopecurus aequalis Sobol.* and *Paspalumpaspaloides (Michx.) Scribn. For* the same plant, the order of absorption ability of *Alopecurus aequalis Sobol.* was Mn>Pb>Zn>Cu; that of *Alternant heraphiloxeroides （Mart.） Griseb.* was Mn>Cu> Pb>Zn; and that of *Paspalum paspaloides (Michx.) Scribn.* was Mn>Cu>Pb>Zn.

The concentrations of Mn in the 3 field weeds were 10 times higher than those in normal plants such as the vegetables in this study under the same conditions. So we thought of the 3 field weeds as hyperaccumulators to Mn. The concentration of Zn in *Alopecurus aequalis Sobol.* was significantly higher than in the normal plant, but the field weeds weren't significant accumulators of other heavy metals. The related research found that *Alternant heraphiloxeroides (Mart.) Griseb.* and *Paspalum paspaloides (Michx.) Scribn.* were hyperaccumulators of Cu, Pb and Zn [28,29]. But in our study, we couldn't confirm these results. Combined contamination by heavy metals could influence the absorption of heavy metals by plants.

CONCLUSIONS

(1) In the survey area, the soil was seriously contaminated with heavy metals. Through the investigation of local grown vegetables, it was found the soil was not suitable for growing vegetables, the boundary being 1800 m from the industrial zone. Heavy metal pollution was very serious in Zhubugang area. Local residents should be transferred outside the scope of heavy metal pollution as soon as possible.

(2) The absorption ability to Mn of 3 field weeds met the characteristics of a hyper-accumulating plant. Therefore, 3 field weeds could be important plants for repairing heavy metal pollution damages in local soil.

REFERENCES

1. X. Chen, J. H. Ma, X. N. Li, D. X. Liu, Y. M. LI. *Environ. Sci.*, **35**(3), 1068 (2014).
2. G. Yang, Y. Li, L. Wu, L. P. Xie, J Wu. *Environ. Chem.*, **33**(2), 269 (2014).
3. X. M. Zhang, X. Y. Zhang, T. Y. Zhong, H Jiang. *Environ. Sci.* **35**(2), 692 (2014).
4. H. Chen, L. J. Te. S. E. Na, J. H. Yang. *J. Soil and Watar. Conserv.*, **27**(3), 100 (2013).
5. L. X. Wang, Z. H. Guo, X. Y. Xiao, M. Lei, L. M. Zhai, X. Y. Liao, Y. Q. Liu. *J. Geogr. Sci.*, **18**, 353 (2008).
6. D.J. Cui, Y. L. Zhang, *Chin. J. Soil Sci.,* **35**(3), 366 (2004).
7. N. Zheng, Q. C. Wang, D. M. Zheng, *Sci. Total. Environ.*, **383**, 81 (2007).
8. Z. L. Chen, R. L. Qiu, J. S. Zhang, R. B. Wan. *Environ. Prot.*, 21 (2002).
9. Ministry of Environmental Protection of the People's Republic of China, Ministry of land and resources of the People's Republic of China. National Soil Pollution Survey Bulletin, 2014,.2.
10. X. E. Yang, X. F. Jin, Y. Feng, Y. Islam，Ejazul. *J. Integr. Plant. Biol.*, **47**(9), 1025 (2005).
11. J. Nouri, N. Khorasani, B. Lorestani1, M. Karami, A. H. Hassani, N. Youselfi. *Environ. Earth Sci.*, **59**(2), 315 (2009).
12. Y. Song, L. Wei, H. J. Wang. *Environ. Prot.,* **9**, 32 (2014).
13. S. Petr, P. Šarka, V. Radomíra, J. Song，T. Vaněk, *Chemosphere*, **104**(7), 15 (2014).
14. H. Z. Hao, T. B. Chen, M. G. Jin, M. Lei, C. W. Liu, W. P. Zu, L. M. Huang. *Chin. J. Appl. Ecol.,* **22**(3), 816 (2011).
15. http://www.ytxww.com/Info.aspx?ModelId=1&Id=5 6951.
16. S. D. Pao. Soil and agricultural chemistry analysis, China Agriculture Press, 2000, p.12.
17. *HJ/T 166* (2004).
18. *GB/15618* (2008).
19. China National Environmental Monitoring Center. The background concentrations of soil elements in China. Beijing, China Environmental Science Press, 1990.
20. *GB276* (2012).
21. *GB/T 5009.13* (2003).
22. *GB/T 5009.14* (2003).
23. Y. X. Yang, China Food Composition, Book 2, Beijing: Beijing medical university press, 2004, p.84.
24. Y. S. Lu, Environmental Assessment, Shanghai, Tongji University Press, 1999.
25. Y. H. Pan, H. B. Wang, Z. P. Gu, G. H. Xiong, F. Yi. *Act. Ecol. Sin.*, **30**(23), 6430 (2010).

26. S. Cui, Q. X. Zhou, L. Chao, *Chin. J. appl. ecol.*, **17**(3), 512 (2006).
27. P. D. Alexander, B. J. Alloway, A. M. Dourado, *Environ. Poll.*, **144**(3), 736 (2007).
28. G. L. Wang, L. L.Wang, Z. L. Li, J. H. Ding, D. Y.

Liu.*Chin. J. Ecol.,* **24**(6), 639 (2005).

S. L. Guo, C. B. Huang, Y. Bian, G. P. Lin. *J. Shanghai Jiaotong Univ. (Agric. Sci.).* **20**(1), 22 (2002).

НАТРУПВАНЕ НА ТЕЖКИ МЕТАЛИ В ПОЧВАТА И ЗЕЛЕНЧУЦИТЕ И АБСОРБЦИЯТА ИМ С ПОЛСКИ ПЛЕВЕЛИ С ФИТО-РЕМЕДИАЦИОНЕН ПОТЕНЦИАЛ

Г. Х. Ю, [1,2], Кс. Н. Жанг [1,2], Дж. У. Жу[1,2], Й. Ванг[1], Ж. Г. Ли[1], Ш. У. Ли[1]

[1].*Училище за архитектура и градско планиране, Научно-технологичен университет в Хунан, КсиангтанХунан, Китай*

[2].*Ключова лаборатория по екологично ремедиация от тежки метали и безопасно използване на замърсени почви, Колеж на провинция Хунан, КсиангтанХунан, Китай*

Постъпила на 5 април, 2015 г.

(Резюме)

Районът Жубуганг е бил индустриален парк за фина химическа промишленост в гр. Ксиангтан в Китай. Изхвърляните отпадъчни газове, води и шлаки са предизвикали сериозно замърсяване на околната среда с тежки метали. Това изследване се основава на 10 почвени проби, 5 различни сезонни зеленчуци (*Lactuca sativa, Lactuca sativa L.var. asparagine, Bailey, Radix Osterici Grosseserrati, Solanum tuberosum* and *Brassica rapachinensis*) и три вида полски плевели – *Alopecurus aequalis Sobol,(Alternanthera philoxeroides (Mart.) Griseb, Paspalum paspaloides (Michx.) Scribn.* Концентрациите на Zn, Cu, PbиMnв тях са определяни чрез атомна флуоресцент на спектрометрия след киселинно разтваряне и образуване на хидриди. Така са определени екологичната безопасност на тежките метали в почвата и абсорбционната способност на плевелите спрямо металите. Резултатите показват, че пълните индекси на замърсяване на почвата с тежки метали са съответно 0.79-3.43 и 1.54-4.13. Почвата и отглежданите зеленчуци са сериозно замърсени с тежки метали. Изследваните плевел има различна абсорбционна способност. Растението *Alternanthera philoxeroides (Mart.) Griseb* има най-висок абсорбционен капацитет спрямо медта от трите изследвани вида. Концентрациите на Zn, Pb и Mn в *Alopecurusaequalis Sobol* са най-високи спрямо останалите видове.

Upgrading ilmenite by an oxidation-magnetic separation-pressure leaching process

S. Liu[1,2,3,*], K. Zhu[1], J. Xiang[1,3], P. Huang[1,3]

[1]*Resources and Environmental Engineering College of Panzhihua University, Panzhihua of SiChuan Province, 617000, China.*
[2]*Kunming Metallurgy Research Institute, Kunming of Yunnan Province, 650031, China.*
[3]*Materials Science and Engineering College of Xihua University, Chengdu of SiChuan Province, 610039, China.*

An oxidation-magnetic separation-pressure leaching process has been found to be much more effective for upgrading Yunnan ilmenite ores to synthetic rutile. The effects of oxidation, magnetic separation and pressure leaching were examined to optimize the experimental conditions. The optimum conditions were found to be: oxidation: 900°C, 30 min; magnetic separation: excitation intensity 5.0 A, charging current 1.1 A, feeding speed 100 g/min; pressure leaching: 220 g/l HCl solution, 6 h at 135℃, S/L ratios of 1:4 and 0.12 MPa pressure. Under these conditions, synthetic rutile was obtained with 93.7% TiO_2, 2.31% Fe. The particles are mostly sized above 105 μm and can be used as a feed for chlorination processes.

Key words: Oxidation, Leaching, Ilmenite, Synthetic rutile, Hydrochloric acid.

INTRODUCTION

Nowadays, the methods for commercial production of TiO_2 pigment are the sulfate and chlorination processes. The sulfate process can utilise relatively low grade feedstocks but sulfuric acid consumption and production of large volumes of ferrous sulfate waste are major economic and environmental problems. The chlorination process is of short duration, large capacity, low cost, high grade of products, small environmental pollution and other significant characteristics (Lasheen, 2008; Sun, 2001; Dong, 2012). The chlorination process is superior to the sulfate process as regards economics and generation of less waste materials. However, the chlorination process needs high-grade raw materials. At present, the technology and equipment for production of high quality titania materials are relatively backward, production scale is small, which cannot satisfy the demand for raw materials for the chlorination process. Therefore, in order to develop the chlorination process, it is important to research large-scale production technology of titania materials using abundant low-grade titanium iron ores as raw material in China.

Titania-rich material generally refers to the electric furnace smelting titania slag or synthetic rutile which has not less than 85 mass percent TiO_2. At present, the methods of manufacturing titania-rich materials include electric furnace smelting (Natziger and Elger, 1987), reducing corrosion (Becher, 1963; Farrow and Ritchie, 1987), acid leaching (Walpole, 1997) and so on. Because of the simple production process, easy large-scaling of equipment, less "three wastes" and easy recycling, the electric furnace smelting becomes a dominant method, but has a low ability to remove calcium and magnesium. Reducing corrosion method is suitable for high grade titanium iron ore of weathering, which requires high temperature reduction related to technical difficulties. Due to the large amount of "three wastes" and process complexity, the use of the sulphuric acid leaching method has been limited. Owing to the economic and environmental aspects of the hydrochloric acid leaching method meeting the requirements of industrial production, it has been widely used.

Titanium mineral resources of Yunnan province in Cchina are relatively abundant, there are mainly primary titanium magnetite, titanium iron ores and vanadium titanium magnetite. The TiO_2 grade of primary titanium magnetite is low, it is of no development and utilization value; the reserves of vanadium titanium magnetite are small, dominant development in Yunnan is inferior to Panzhihua of China; titanium iron ores with higher grade TiO_2, easy to exploit and utilize, lower impurity content of CaO and MgO have been proven to be ideal raw materials for smelting high grade titania slag and preparation of synthetic rutile.

Investigations (Mahmoud et al., 2004; Mackey et al., 1974; Lasheen, 2005) have indicated that ilmenite can be upgraded by a combined

---

pyrometallurgical – hydrometallurgical process to a product with 90-95 mass percent TiO_2. Other investigations (Gireesh, 2013; Olanipekun, 1999; Vásquez, 2012) have studied in details the kinetics mechanism of ilmenite by hydrochloric acid leaching.

In this work, a oxidation-magnetic separation-pressure leaching process was investigated to produce synthetic rutile from Yunnan ilmenite with high Mg content. The experimental parameters affecting the grade or size of titanium dioxide and the oxidation process were investigated and optimized.

EXPERIMENTAL

Materials

Ilmenite ore utilized in this investigation was acquired from Yunnan province in China. Phase identification of ilmenite ore, oxidized ore and beneficiated ore were carried out using X-ray diffraction (XRD). The main phase in ilmenite ore is ilmenite ($FeTiO_3$) and hematite (Fe_2O_3). The chemical analyses of the sample and the dominant impurity phases are given in table 1. The particle size distribution of the samples is measured with sieve analyses. All particles passed 630 μm of a Retsch sieve shaker.

Table 1. Chemical composition of ilmenite ore.

Constituent	TiO_2	FeO	Fe_2O_3	CaO	MgO	SiO_2
Content (wt.%)	46.10	31.18	15.38	0.58	2.64	3.90

Oxidation procedures

The oxidation tests were performed in a laboratory muffle furnace. The furnace was heated to a predetermined temperature before the samples were introduced. An alumina crucible was used in the experiment. The oxidation roasting was conducted in the crucible open to air. The oxidation temperature was varied from 650℃ to 950℃. The oxidation time was 10-50 min. Titrimetric analysis was used to determined the percentage of ferric dioxide, ferrous dioxide and titanium dioxide.

Magnetic separation procedures

The oxidized ores were magnetically separated by a laboratory magnetic separator. Excitation intensity, charging current and feeding speed were controlled to meet 2 mass percent tailings, 1.5 mass percent SiO_2 of the magnetic concentrate.

Pressure-leaching and calcining procedures

The leaching process was performed in a 2L zirconium high-pressure reaction kettle. A mechanical stirrer with teflon coating was used to mix the acid and ilmenite ore. A water condenser was used to reduce the losses of water and hydrochloric acid vapour. The reaction kettle was heated by an electrothermal furnace. In all cases, 150 g of ilmenite ore was introduced into the reaction kettle, and mixed with 10-30 wt% hydrochloric acid solution. Then the solution was heated from room temperature to the boiling temperature (about100-145℃) in 20-50 minutes. The leaching process was carried out at 0.05-0.3MPa pressure, 100-500 rpm rotating speed and 4-9 h leaching time. When leaching was finished, the mother liquor and solid materials were discharged, the residues through settling separation filter were washed until no iron ions and hydrochloric acid were detected. The synthetic rutile is obtained by calcining of the separated material. The contents of titanium dioxide, ferric dioxide and ferrous dioxide were analyzed by titrimetric analysis. The particle size distribution of the samples was measured with sieve analyses. The synthetic rutile products are divided into rude rutile (> 0.074 mm) and fine rutile (< 0.074 mm), finesse rate was calculated by Eq.(1).

$$Finesse\ rate(\%) = \frac{Weight\ of\ fine\ rutile}{Weight\ of\ total\ rutile} \times 100\%,$$

$$(1)$$

RESULTS AND DISCUSSION

Effect of oxidation

The effects of oxidation temperature, oxidation time on the TiO_2 grade and recovery of titania-rich material were studied. When the ilmenite ore was oxidized for 30 min at 900℃, Fe_2TiO_5 and TiO_2 (rutile) were formed, but a little amount of $FeTiO_3$ phase remained. The effect of FeO in the oxidized ilmenite-ore on the TiO_2 grade and finesse rate is shown in table 2. Under the experimental conditions, the higher FeO in the oxidation ore, the lower was Fe in the product and the higher was the TiO_2 grade in the product. With the increase of FeO content in the oxidized ore, the finesse rate also increased. "The leaching rate of ferric iron was obviously lower than that of ferrous iron" and "the ferric iron leaching rate is within 40% ~ 50%, and that of ferrous iron can be as high as 99% " (Wang et al., 2011). Therefore, the lower ferric iron oxide in the ore, the better is the leaching rate. But to reduce the finesse rate and to control the degree of oxidation, FeO content in the oxidized ore between 25% - 28% was more appropriate. Fig.1. shows the effect of oxidation temperature on FeO content in the oxidized ore. From the results it could be concluded that at oxidation temperature of 900℃,

and residence time of 30 min, it ensured FeO content in the oxidized ore by 25%.

The oxidation also influenced the reduction of the fine materials. The oxidation reaction of ilmenite ore is written as Eq.(2).

$$2FeTiO_3 + \frac{1}{2}O_2 = 2TiO_2 + Fe_2O_3, \qquad (2)$$
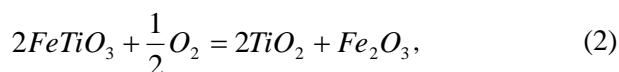
When leaching with hydrochloric acid, both iron and titanium in the ilmenite ore will be dissolved in both untreated and oxidized ilmenite. However, the rutile in oxidized ilmenite is less soluble in hydrochloric acid. The dissolved titanium will hydrate on the surface of the ilmenite and in the solution. Nevertheless, the formation of rutile in oxidized ilmenite can decrease the free energy of hydrate on the surface of the ilmenite. As crystal nucleus, rutile microcrystalline is better than ilmenite. That is to say, the hydrate occurs on the surface of oxidized ilmenite easier than on untreated ilmenite. Moreover, it will lower down the amount of homogeneous nucleation in the solution and the titanium dioxide hydrate finesse under 74 μm.
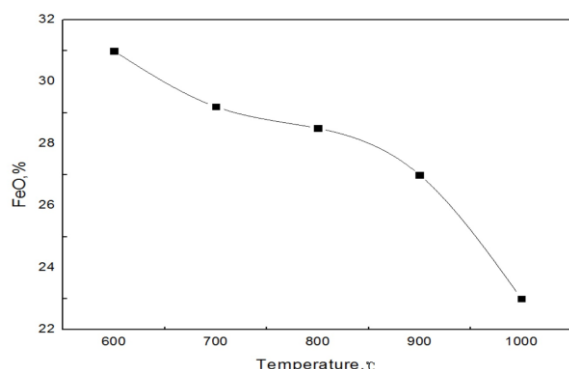
Fig. 1. The effect of oxidation temperature on FeO content in the oxidized ore.

Figs. 2 and 3 show the effect of oxidation on the finesse of rutile. Obviously, the finesse rate of oxidized products is smaller than that of un-oxidized products.

Effect of magnetic separation

Several magnetic separation experiments were performed with excitation intensity 3.0-9.0A, charging current 0.7-1.5A and feeding speed 50-300 g/min. From the results plotted in table 3, it is evident that the TiO_2 content of the concentrate increased through magnetic separation but the SiO_2 content decreased. The magnetic separation test achieved the purpose of silicon-reduction and titanium-increase. The optimum conditions of magnetic separation were excitation intensity 5.0A, charging current 1.1A and feeding speed 100g/min.
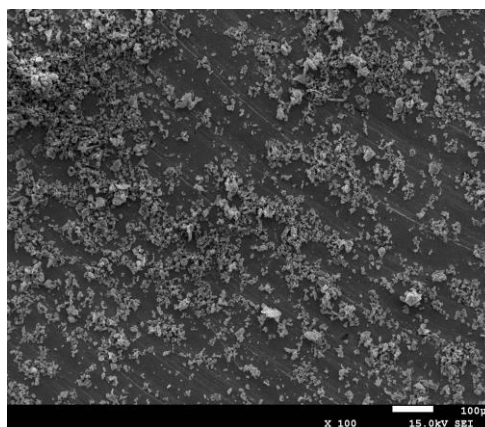
Fig. 2. SEM of rutile (unoxidized).
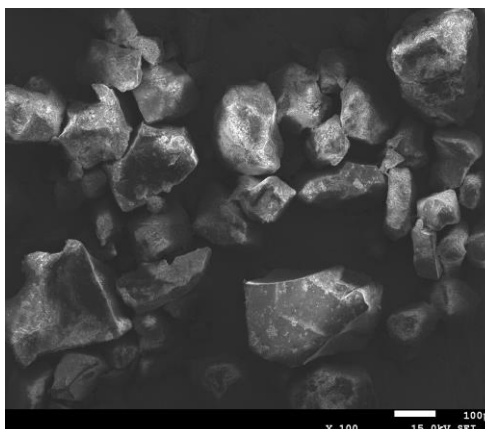
Fig. 3. SEM of rutile (oxidized).

Effect of hydrochloric acid concentration

The effect of hydrochloric acid concentration was studied in the range from 200 to 240 g/l at 6 h leaching time, S/L ratios of 1:4, 0.12 MPa pressure and 135°C. The results shown in Fig.4 indicate that with the increase in hydrochloric acid concentration, the grade of the products increases. For getting a grade of 92% or more of artificial rutile product, the concentration of hydrochloric acid should be 220 g/l or higher.
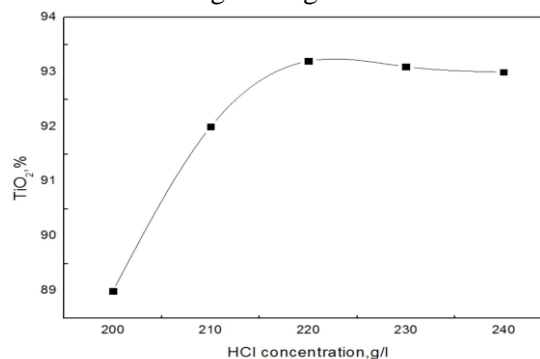
Fig. 4. The effect of HCl concentration on TiO_2 content in the rutile product.

Table 2. The effect of FeO in oxidized ilmenite ore on leaching.

Frequence /time	FeO of oxidized ore /%	Finesse rate /%	Fe of product/%	TiO$_2$ of product /%
10	23.10~23.90 23.30	10.06~12.87 11.90	3.62~3.93 3.81	87.52~89.13 88.58
10	25.20~25.93 25.61	12.94~15.06 13.37	2.52~2.86 2.72	89.21~91.27 90.87
10	28.01~28.95 28.47	16.36~19.13 17.38	2.25~2.77 2.53	90.91~92.33 91.12

Notes : $\dfrac{\text{Min} \sim \text{Max}}{\text{Mean}}$

Table 3. Results of the magnetic separation test.

Oxidized ore		Concentrate		Tail	
TiO$_2$/%	SiO$_2$/%	TiO$_2$/%	SiO$_2$/%	TiO$_2$/%	SiO$_2$/%
47.13~48.25 47.92	2.05~2.69 2.17	47.47~49.36 48.71	1.35~1.83 1.46	35.20~39.21 37.56	14.06~16.52 15.65

Notes : $\dfrac{\text{Min} \sim \text{Max}}{\text{Mean}}$

Effect of leaching temperature and pressure

Oxidized ore was leached at 105, 115, 125, 135 and 145 °C in a solution consisting of 220 g/l HCl, for 6 h at a S/L ratio of 1:4 and 0.12MPa pressure to determine the effect of temperature on Ti and Fe leaching. The results in Fig.5 reveal that by increasing leaching temperature, Fe and other impurities are dissolved and the TiO$_2$ content in the residue increases but the recovery decreases due to high titanium losses in the solution. Before the ferrous leaching rate of 90%, the leaching speed is controlled by the chemical reaction, at this stage the pressurized way and higher reaction temperature are favorable, which can significantly improve the response speed. When the temperature is elevated from 110℃ to 140℃ at 0.15 MPa pressure, the reaction rate increases 3.6 times. Therefore, the higher the temperature and pressure, the better is the leaching efficiency. But the higher temperature and the higher pressure in the ball increase the impact on the equipment. Therefore, leaching temperature and pressure were controlled at 135℃ and 0.12MPa pressure in the current study.

Effect of leaching time

The effect of leaching time on the leaching efficiency of oxidized ore was examined between 4 and 8 h using 220 g/l HCl, temperature of 135℃, S/L ratios of 1:4 and 0.12MPa pressure. The results presented in Fig.6 indicate that the residue obtained within 6 h has a maximum TiO$_2$ content (93.7%). This is due to the higher solubility of iron in hydrochloric acid. At this time about 95% of Fe$_2$O$_3$ is brought into solution. By increasing the iron dissolution efficiency, the recovery of TiO$_2$ in the residue as titanium dioxide concentrate decreases from 93.7% to 90.5% by increasing the leaching time from 7 to 8 h and the finesse rate increases. After leaching for more than 6 h, because the soluble impurities content in the titanium concentrate grain is already low, further extending the leaching time, reduces the degree of synthetic rutile. Therefore, considering factors such as product quality and efficiency of industrial production, leaching time of 6 h is advisable.
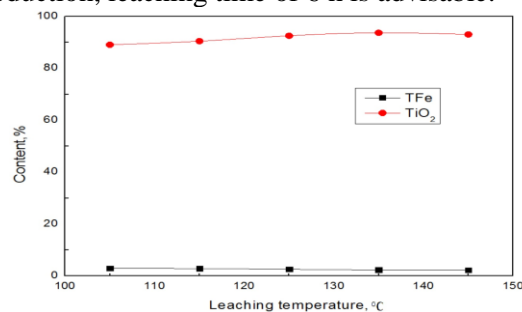
Fig. 5. Effect of HCl concentration on TiO$_2$ content in the rutile product.
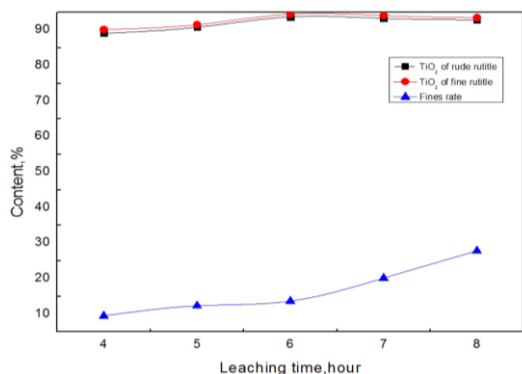
Fig. 6. Effect of leaching time on TiO$_2$ content in the rutile product.

Effect of solid/liquid (S/L) ratio

Several leaching experiments were performed using hydrochloric acid of concentration 220 g/l HCl with S/L ratios of 1:1, 1:2, 1:4, 1:6 and 1:8. In these experiments, leaching was performed at 135℃ for 6 h, with S/L ratio of 1:4 and 0.12MPa pressure. From the results plotted in Fig. 7 it is evident that with increasing S/L ratio, the total iron leaching efficiency increases, but after S/L=1:4 it decelerates. By decreasing the S/L ratio or increasing acid consumption the titanium dissolution also increases. Therefore for decreasing acid consumption and titanium dissolution S/L=1:4 is selected as optimum amount for the experiments.
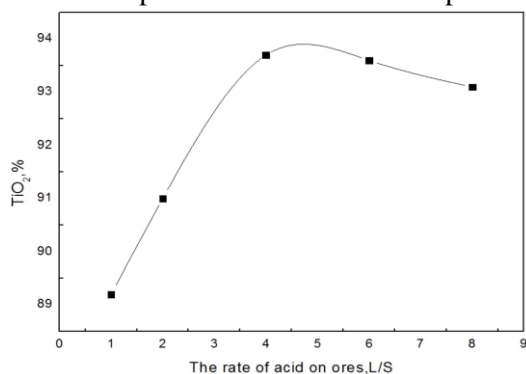
Fig. 7. Effect of acid/ore (L/S) on TiO_2 content in the rutile product.

Characterization of titanium dioxide concentrate

The produced titanium dioxide concentrate at the optimum conditions was washed and calcined at 900℃. Comparing with the raw materials shown in Fig. 8, rutile in this concentrate (Fig. 9) is the dominant phase but Ti_2O_3, anatase and iron oxide phases are also found. The chemical analysis of the calcined product obtained under optimum conditions is presented in Table 4.

Table 4. Chemical composition of the rutile product

Constituent	TiO_2	TFe	Al_2O_3	CaO	MgO	SiO_2
Content (wt.%)	93.70	2.31	1.27	0.10	0.6	1.35

The product of HCl leaching contains about 93.7% TiO_2 and only 2.31% Fe. The SEM images of the raw materials and rutile products by hydrochloric acid leaching are compared in Figs.10 and 11. These images indicate that the texture and morphology of the product obtained by HCl leaching and raw materials are very different. The morphology of titanium dioxide produced by HCl leaching is more granular than that of the raw materials. In the product of HCl leaching, the grains are mostly circular with a clear and sharp boundary while the product of the raw materials is more

elongated. Size distribution of titanium dioxide particles produced by HCl leaching was also determined by the cumulative percentage of particles analysis method shown in Fig.12. The results indicate that the particles obtained from HCl leaching are mostly sized above 105 μm which can meet the particle size requirements of the raw materials for chlorination processes.
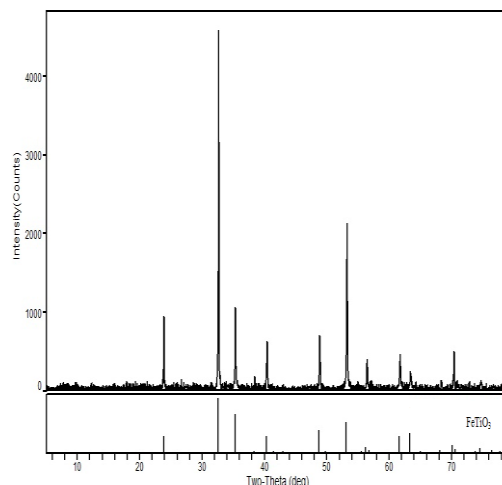
Fig. 8. XRD of the raw materials.
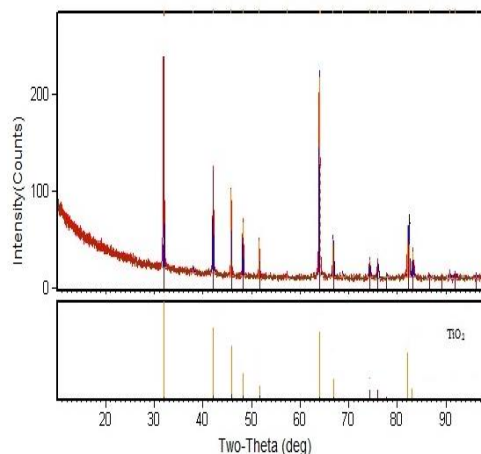
Fig. 9. XRD of the rutile product.
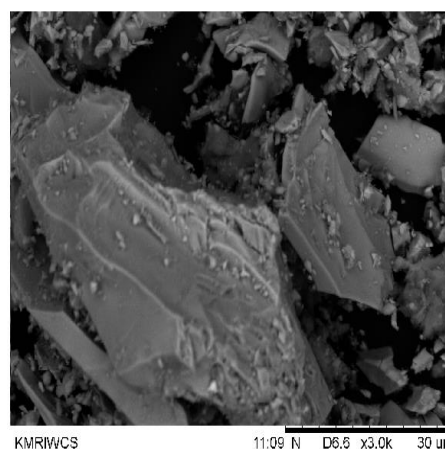
Fig. 10. SEM of the raw materials.
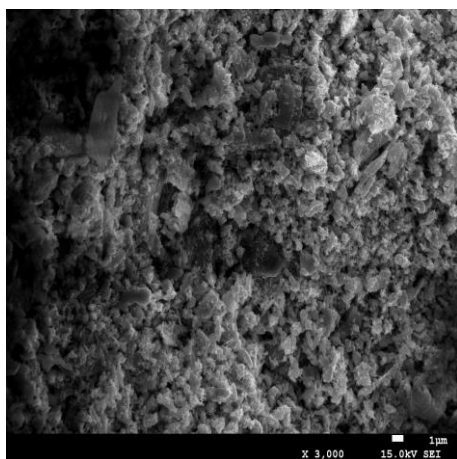
Fig. 11. SEM of the rutile product.
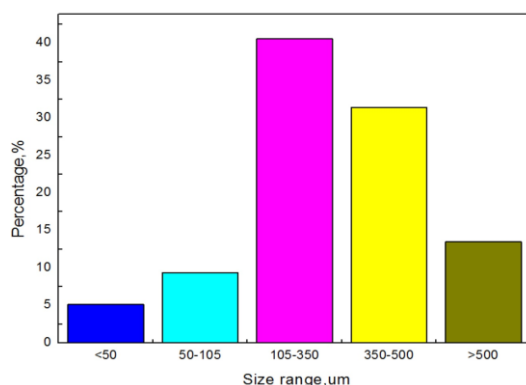
Fig. 12. Size distribution of the rutile product.

CONCLUSIONS

The pressure leaching of Yunnan ilmenite ores with HCl was found to be much more effective in the presence of oxidation-magnetic separation. Oxidation temperature and time were 900ºC, and 30 min, respectively. Magnetic separation conditions were: excitation intensity 5.0A, charging current 1.1A and feeding speed 100 g/min. The optimum leaching conditions used in this study were 220 g/l HCl at 135℃ for 6 h, at S/L ratio of 1:4 and 0.12MPa pressure. Under these conditions, the rutile products were obtained with 93.7% TiO_2 and 2.31% Fe and most particles were sized above 105 μm which can meet the particle size and quality requirements for chlorination processes.

REFERENCES

1. T. A. Lasheen, *Hydrometallurgy*, **93**, 124 (2008).
2. K. Sun, Physical and chemistry of extracting metallurgy of titanium, Metallurgy industry press, Beijing, 2001.
3. D. Haigang, *Hydrometallurgy*, **113**, 119 (2012).
4. R. H. Natziger, G. W. Elger, US Bureau of Mines, Report Invest No. 9065 (1987).
5. R. G. Becher, Australian Patent 247, 110 (1963).
6. J. B. Farrow, I. M. Ritchie, *Hydrometallurgy*, **18**, 21 (1987).
7. E. A. Walpole, Heavy Minerals, SAIMM, Johannesburg, 1997, p.169.
8. M. H. H. Mahmoud, A. A. I. Afifi, I. A. Ibrahim, *Hydrometallurgy*, **73**(1), 99 (2004).
9. T. S. Mackey, *Industrial & Engineering Chemistry Product Research and Development*, **13**(1), 9 (1974).
10. T. A. I. Lasheen, *Hydrometallurgy*, **76**(1), 123 (2005).
11. V. S. Gireesh, V. P. Vinod, S. K. Nair, G. Ninan, *Journal of Academia and Industrial Research (JAIR)*, **2**(7), 402 (2013).
12. E. Olanipekun, *Hydrometallurgy*, **53**(1), 1 (1999).
13. R. Vásquez, A. Molina, *Minerals Engineering*, **39**, 99 (2012).
14. D. S. Chen, B. Song, L. N. Wang, T. Qi, Y. Wang, W. J. Wang, Minerals Engineering, **24**, 864 (2011).

ОБОГАТЯВАНЕ НА ИЛМЕНИТ ЧРЕЗ ОКИСЛЯВАНЕ И МАГНИТНА СЕПАРАЦИЯ ПОД НАЛЯГАНЕ

С. Лю[1,2,3,*], К. Жу[1], Ж. Ксианг[1,3], П. Хуанг[1,3]

[1]Колеж по ресурси и екологично инженерство, Университет в Панжихуа, Провинция Сичуан, Китай
[2]Изследователски институт по металугия в Кунминг, Провинция Юнан, Китай.
[3]Колеж по материалознание и инженерство, Университет Ксихуа, Ченгду, Провинция Сичуан, Китай

(Резюме)

Установено е, че процесът на излугване на илменитова руда от Юнан с помощта на окисление, съчетано с магнитна сепарация под налягане е много ефективен. Получава се синтетичен рутил. Изследвани са ефектите на тези три операции за оптимизирането на опитните условия. Оптималните условия за магнитна сепарация са следните: температура 900ºC; 30 минути за окисление; интензитет на възбуждане 5.0A; токна зареждане1.1A; скорост на подаване 100g/min. Концентрацията на солна киселина е 220 g/lпри135℃ и налягане 0.12MPa в продължение на 6 часа за излугване, отношението твърда/течна фаза е 1:4. При тези условия синтетичните рутили съдържат 93.7% TiO_2, 2.31% TiFe, а размерът на частиците е над105 μm.

Geochemical characteristics and origins of the oil in Tazhong, Tarim Basin

D. R. Yu [1,2]*, B. S. Yu [1,2], F. F. Jiao [3]

[1]*The State Key Laboratory of Geological Process and Mineral Resources，China University of Geosciences，Beijing 100083*
[2]*School of Earth Sciences and Resources, China University of Geosciences, Beijing 100083*
[3]*China Petroleum and Chemical Corporation, Chengdu, 610036*

In Tazhong, the nature and distribution of oil and gas is very complex, the reservoirs are of various types,and the source of oil and gas has been a very difficult problem. According to the whole oil $\delta^{13}C$ and monomer hydrocarbon $\delta^{13}C$ characteristics the oil in Tazhong area originates from the same source, mainly from the Cambrian – Ordovician. The comparison with molecular weight hydrocarbon $C_9 \sim C_{18}$ fingerprints, once again proved that tower area oil is from a uniform oil source. The conventional biomarker compounds are used to distinguish between typical Cambrian - Ordovician oil sources, and the aromatization class misogamy alkalies detection prove that all the oil and gas have condensed from anaerobic, strong reducing environment, deposited under the action of photosynthetic green sulfur bacteria in Cambrian-Ordovician source rocks.

Key words: Carbon Tazhong, Carbon isotope, Geochemical characteristics, Oil source correlation

INTRODUCTION

The oil and gas resources in Tazhong area are very rich [1, 2, 3].This area is one of the key strata for oil and gas exploration.Currently, a series of breakthroughs were achieved in the Tazhong 4zone, Tazhong I belt, Tazhong 10.Found from the reservoir [4, 5], not only the nature and distribution of oil and gas are very complex, but the oil and gas source problem has always been very hard to avoid. The main reason is that hydrocarbon source rocks involve carbonate rocks, which have always been a major problem of geochemical research field both at home and abroad [1,6,9], and hydrocarbon source rocks are very old, they involve upper Paleozoic hydrocarbon source rocks, maturity difference is big, complex tectonic evolution history and thermal evolution history had experienced several phases of oil and gas gathering and destruction, all of which increase the difficulty of the study of oil source correlation. In this paper, we study the ethnic division and oil source identification in Tazhong area through the geochemical characteristics of Ordovician crude oil.

SAMPLE COLLECTION AND EXPERIMENTAL METHODS

The samples were stored in 5ml glass bottles to prevent oil pollution, using bottle pads with tin foil. Samples were placed in a $-6℃$ freezer after collection. Light hydrocarbons (C_4-C_8) and saturated hydrocarbons were analyzed by gas chromatography using ms fine quartz wool column equipped with DB-1MS (60 m×0.20 mm×0.25μm) Agilent 6890GC chromatographic instrument

injected directly with the helium carrier gas. In order to detect lighter hydrocarbon compounds, the initial temperature was set to $35℃$ for 5 min.The heating rate was $2℃$/minup to $135℃$.

Later C^{13}following ingredients were washed at a heating rate of 6 $℃$/min up to 300 $℃$.

AND DISCUSSION

Carbon isotope characteristics of crude oil

The results of carbon isotope analysis in Tazhong area of crude oil and condensate (Table1) show that the carbon isotopes are very light, generally less than32‰ (Fig.1), carbon isotopes in the Cambrian and lower Ordovician source of oil in Lunnan area are mainly distributed in the31.1～32.6‰, carbon isotopes of oil in the areas are relatively light and located in the south and north sides of Man JiaEr sag, which should have the same source.
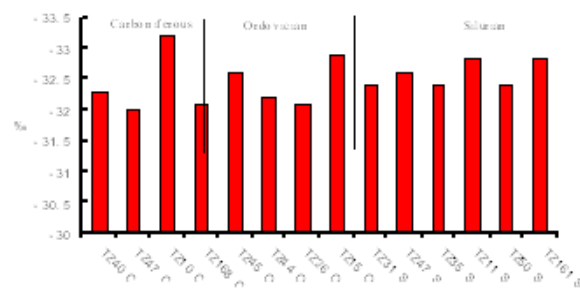
Fig.1. Carbon isotope of oil distribution in Tazhong area

In Tazhong area, consequently, the oil and various group carbon isotopic compositions are consistent with the Lunnan area.

* To whom all correspondence should be sent:
E-mail: yudingru@qq.com

Geochemical characteristics of light hydrocarbon in crude oil

Light hydrocarbons are an important part of condensate and crude oil, which are from about 1/4 to 1/3 of the total amount of crude oil [5, 6], the biomarker compounds content in the crude oil were accounted for only 1% or less, in the overall characteristics of the crude oil the light hydrocarbon compounds are more representative than the biomarkers. In fact, the former were in higher amounts and the composition of light hydrocarbons was related to the characteristics of kerogen type and maturity.

Group Composition of C₄- C₇

Humic type organic matter derived from higher plants, compared with the sapropel type organic matter, were rich in benzene, toluene, methyl cyclopean and cyclopean compounds, while the latter was relatively rich in naphthenes [5]. Studies of light hydrocarbon group composition of $C_4 \sim C_7$ in the area showed that chain alkanes content was mainly 52 ~79%,the content of aromatics was 3~ 11%.It is relatively rich in alkenes and lean aromatics, which is characteristic of oil and saprogenic source rocks of the typical source(Fig.2)

C7 group

Research showed that the heptane mainly came from algae and bacteria while methyl cyclohexane mainly transformed from higher plants, lignin and cellulose [7, 8],which are good examples of parameters for terrigenous parent material type; the lipid compound2-methyl cyclopentane mainly came from aquatic organisms,therefore,using the three kinds of composition as a triangular diagram of n-heptane,methyl cyclohexane and 2-methyl cyclopentane,the condensate can be distinguished between different sources of oil and crude oil. Wang Tingdong studied the light hydrocarbon compounds of the C_7 group from some condensate oils and crude oils in Sichuan and the Tarim Basin. They confirmed that these parameters can be well distinguished from different genetic types of condensate oil and crude oil. The n-heptane content is 47-65% and the methyl cyclohexane content is 23~39% in the composition of condensate and crude oil C_7 of light hydrocarbons. The analysis results are shown in the group composition diagram (Fig.3) which falls in type parent material area, therefore, we can judge that it was a sapropelic type rock source.
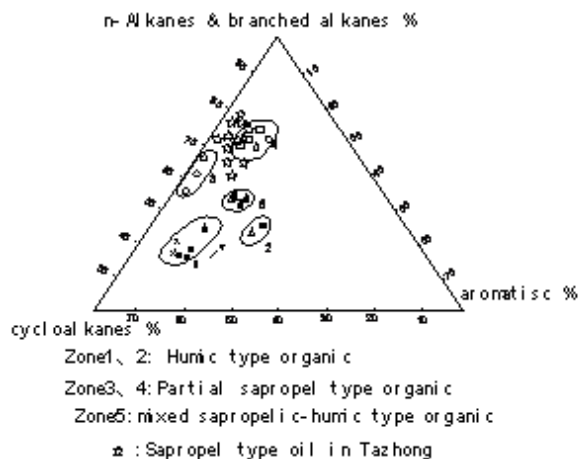
Fig.2. Triangle composed of light hydrocarbon of condensate oil and crude oil C₄-C₇ in Tazhong
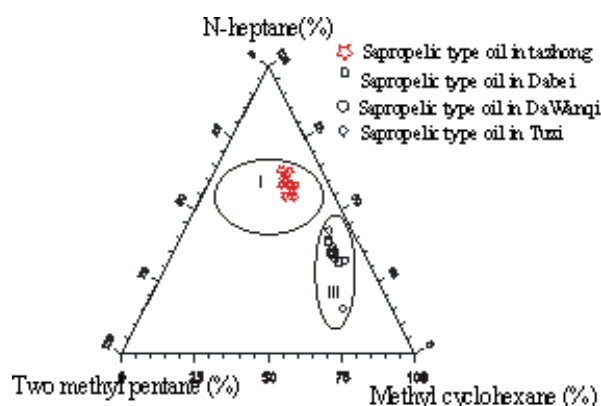
Fig. 3. Triangle composed of light hydrocarbon of condensate oil and crude oil C₇ in Tazhong.

The ratio of light hydrocarbon compounds Erdman identification

The method of light hydrocarbon fingerprint determination, proposed by Erdman in 1974, had obtained widespread application in the oil-oil correlation study [8, 9]. The analysis of Erdman data from the Tazhong area according to the parameter mapping showed good similarity in the crude oil area (Fig. 4),which indicated that they should belong to the same source. However, these crude oils differed poorly in comparison with Tazhong low uplift of the middle upper Ordovician argillaceous limestone and the further evidence showed that only the Cambrian and lower Ordovician source rocks provided the main contribution to the oil and gas currently found in theTazhong area.

Table 1. Carbon isotope composition of crude oil in Tazhong Area.

Well No.	Well depth, m	Hori-zon	Samples	Totality oil $\delta^{13}C/‰$	Saturated hydrocarbon $\delta^{13}C/‰$	Aromatic hydrocarbon $\delta^{13}C/‰$	Non hydro-carbon $\delta^{13}C/‰$	Asphal-tene $\delta^{13}C/‰$
tz40	4307.35-4343	C		-32.3	-32.5	-32.2		
tz47	4216.4-4335.3	C_{I-II}	oil	-32	-32.7	-32.3	-32.4	-31.7
tz10	4139-4150	C_{II}	oil	-33.22				
tz168	3799-3850	C_{III}	oil	-32.1	-33.5	-32.3		
tz45	6020-6150	O	oil	-32.6	-30.5			
tz44	4854-4877	O	oil	-32.2	-32	-32		
tz26	4300-4360	O	oil	-32.1	-31.7	-31.9		
tz15	5238-5247	O	oil	-31.7	-31.3	-31.6		
tz15	4656-4673	O	oil	-32.9	-33.1	-32.7		
tz31	4946-4951	S	oil	-32.4	-32	-32.3		
tz47	4978.5-4986	S	oil	-32.6	-32.9	-32.9	-32.4	-32.6
tz35	4946-4951	S	oil	-32.4	-32	-32.3		
tz11	4294-4434	S	oil	-32.8				
Tz50	4378-4385	S	oil	-32.4	-32.3	-32.1		
Tz161	4178-4181	S	oil	-32.8	-33	-33.8		

Table 2. Comparison of biomarker parameters from source rock of Cambrian and Ordovician.

Hydrocarbon source rock / Biomarker parameters	Source rocks of lower middle Cambrian-Lower Ordovician	Source rocks of middle upper Ordovician
Gammacerane/C_{31}hopane	High	Low
C_{28} Sterane	High	Low
C_{27}、C_{28}、C_{29} Sterane distribution	$C_{27}<C_{28}<C_{29}$ or $C_{27}>C_{28}<C_{29}$	$C_{27}>C_{28}<C_{29}$
Tricyclic terpanes/hopane	High	Low
Diasterane/regular steranes	Low	High
Long chain tricyclic terpaneC_{28}、C_{29}	High	Low
HopaneC_{31}/C_{30}	Low	High
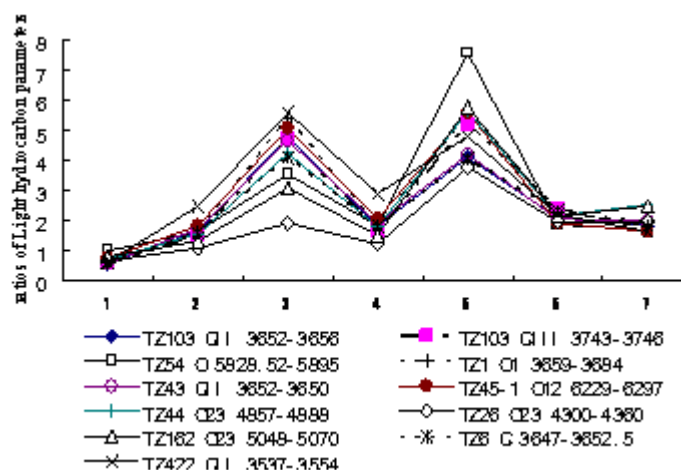
Fig. 4. Comparison chart on hydrocarbon parameters by Erdman of Crude oil and condensate light.
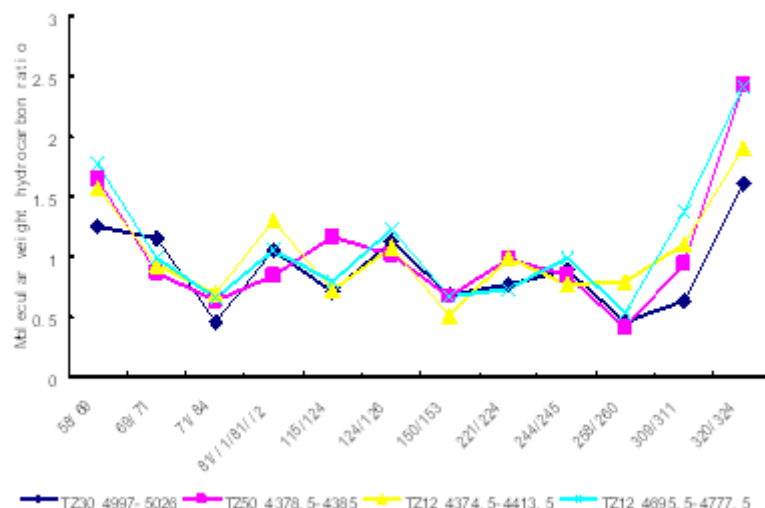
Fig. 5. Comparison of molecular weight hydrocarbon in crude oil.
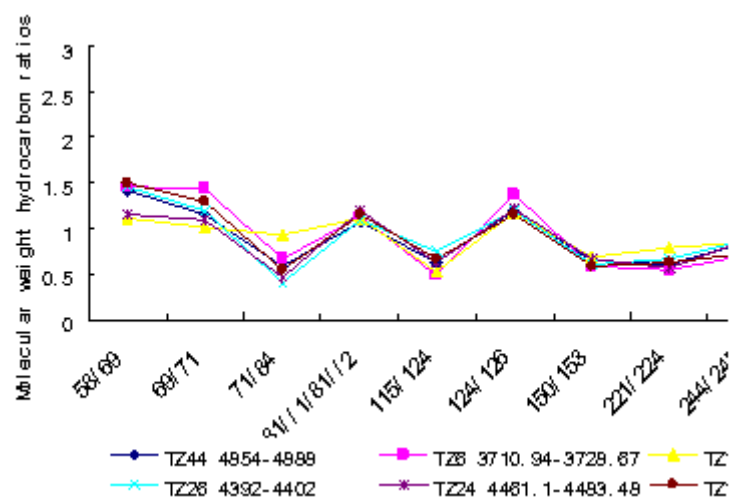
Fig. 6. Comparison of molecular weight hydrocarbon in Condensate oil.

Middle molecule weight hydrocarbon

Comparison of hydrocarbon molecular weight is mainly performed using compounds of molecular weight similar to ($C_9\sim C_{18}$) for isomeric alkane carbon number, some of the same general alkanes, chain alkanes with a methyl substituent and isoprenoid alkanes.The comparison results of the fingerprints of crude oil, condensate oil molecular weight hydrocarbons in Tazhong area shows that there was resemblance between the samples (Figs.5, 6), suggesting that these oils have the same source. From the results of molecular weight hydrocarbons we couldn't decide whether the crude oil was derived from the middle upper Ordovician source rocks, or from the Cambrian source rocks, but it gave us a very clear message that the oil or condensate found in Tazhong had only one main source

Biomarker characteristics of Sterane and terpane

According to the identification of the conventional biomarkers sterane and terpane, the oil and condensate oil in Tazhong Ordovician originated from the Cambrian and lower Ordovician source rocks, including TZ45,TZ44,TZ24 and TZ26 in upper Ordovician, the carboniferous oil of TZ24 also originated from the Cambrian and lower Ordovician source rocks.(Table2). In addition, carboniferous condensate of TZ1and TZ1- 6 wells in the east of Tazhong Low Uplift, part of the oil in Tazhong 16 wells area and portion of the oil or oil sands oil from TZ10, TZ11 were all derived from Cambrian. These oils were of consistent biomarkers of TC1 Cambrian oil and typical Cambrian hydrocarbon source rocks, which have the characteristics of high gammacerane and high C_{28} sterane (Fig.7).
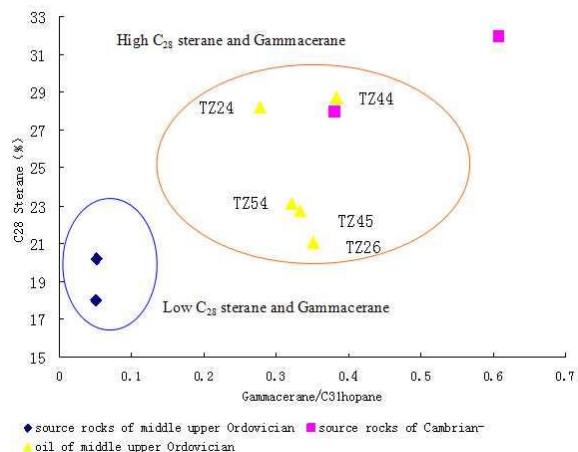
Fig. 7. Oil source contrastion of crude oil and condensate.

In addition, in a large number of reservoir bitumens characteristics of the typical Cambrian source of oil were detected (Table 2) and these reservoir bitumens have the characteristics of high content of gamma cerane and C_{28}sterane.

Isoprenoid hydrocarbon aromatization

Aromatization of isoprenoid hydrocarbons takes place in anaerobic, strong reducing environment by photosynthetic green sulfur bacteria, which is a sign of strong reductive water environment [10, 11, 12, 13]. In Tazhong area, whether the conventional biomarkers were determined to be source of Cambrian oil or were judged as similar oil source rocks from middle upper Ordovician, (Figs.8,9,10)we detected the aromatization isoprenoids to prove that these oils were formed from the hydrocarbon source rocks which deposited in the anaerobic and strong reducing environment.
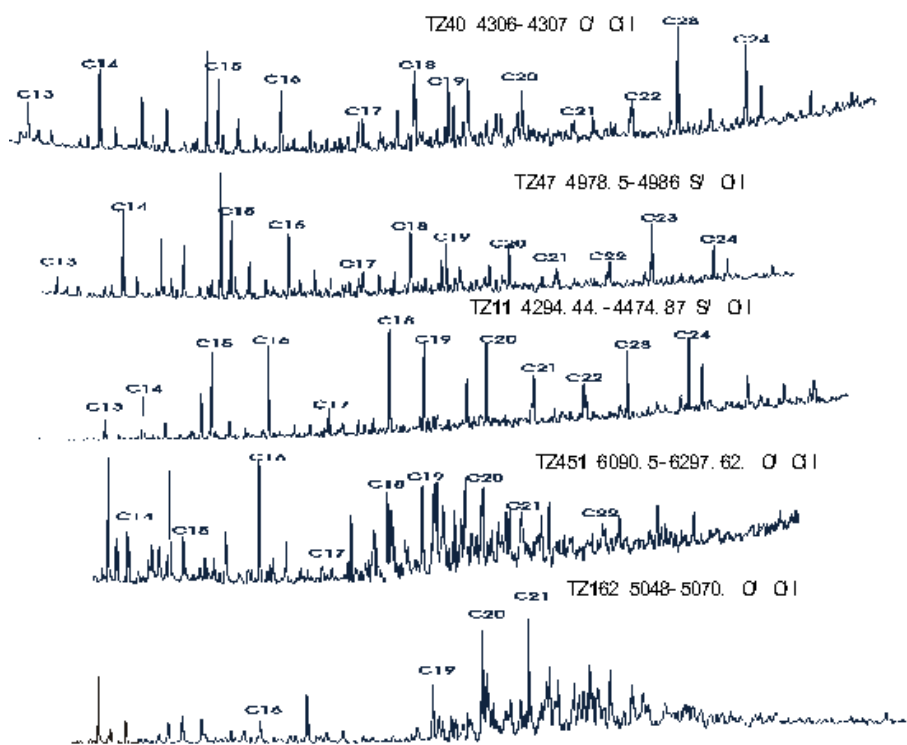
Fig. 8. The isoprenoid hydrocarbon mass chromatogram of TZ40, TZ47, TZ11, TZ451 and TZ162.
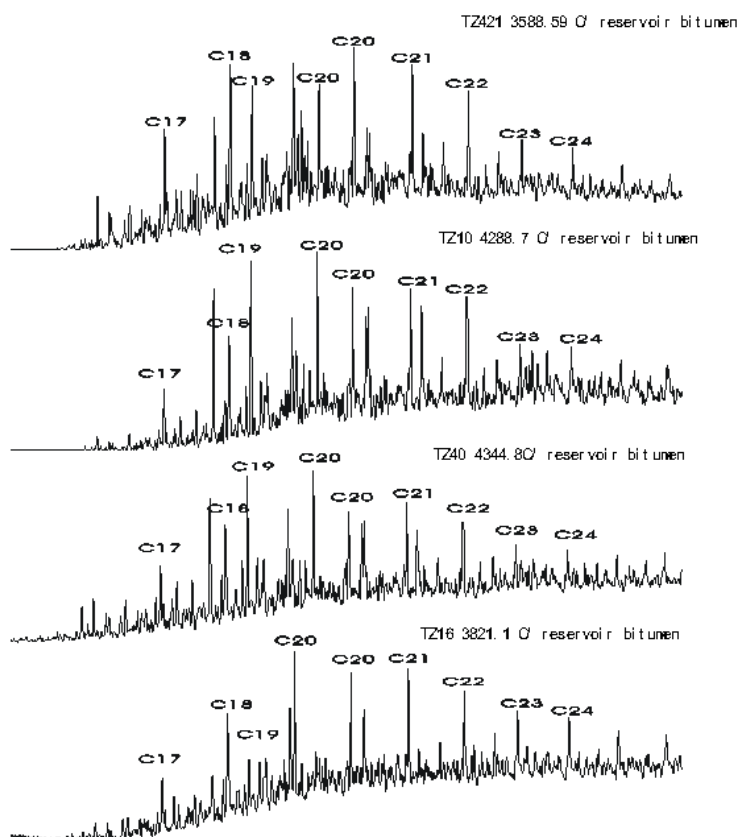
Fig. 9. The isoprenoid hydrocarbon mass chromatogram of TZ421, TZ10, TZ40 and TZ16.
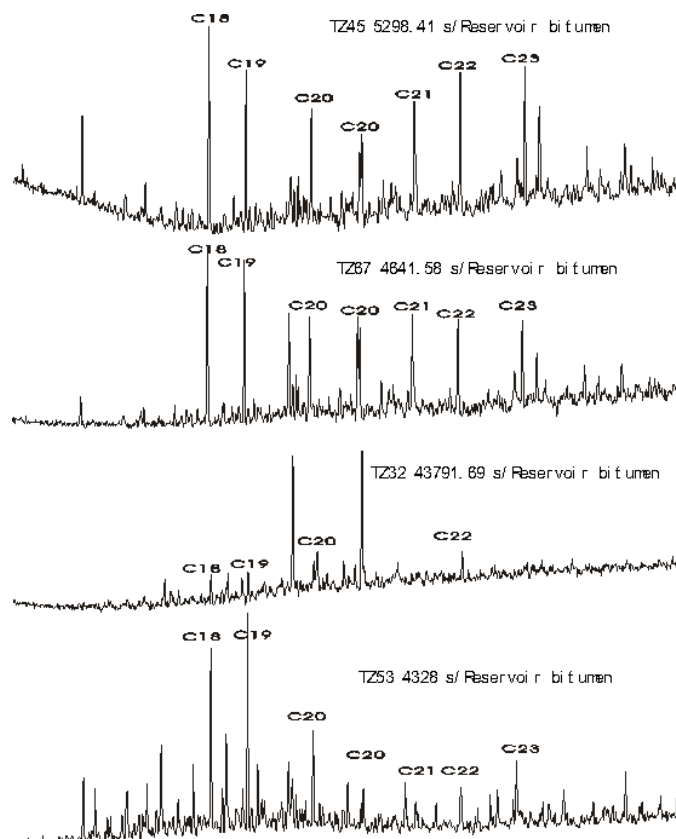
Fig. 10. The isoprenoid hydrocarbon mass chromatogram of TZ45, TZ67, TZ32 and TZ53.

CONCLUSION

The main sources of crude oil and condensate oil in Tazhong area are the Cambrian and lower Ordovician source rocks, with a small contribution of oil generated from middle and upper Ordovician source rocks. Carbon isotopes of crude oil and condensate, monomer hydrocarbon carbon isotopes and molecular weight hydrocarbon fingerprint distribution showed that they had the same source; light hydrocarbons proved that oil and condensate were not derived from middle upper Ordovician source rocks. Conventional biomarkers over theTazhong area proved that most of oil and condensate oil came from the Cambrian and lower Ordovician source rocks. Aromatization class isoamyl two olefin certify that oil and condensate were derived in anaerobic and strong reducing environment, a photosynthetic green sulfur bacteria playing a role in the deposition of Cambrian and Lower Ordovician source rocks.

REFERENCE

1. Q. X. Liu, M. Zhang, U. H. Huang, *Natural Gas Geoscience*, **17,** 319 (2006).
2. D. G. Liang, T. L. Guo, J. P. Chen, *Marine oil and gas geology*，**14**, 1 (2009).
3. X. X. Lv, H. J. Yang, X. Wang, *Oil and Gas Geology*,**31**,838 (2010).
4. S. M. Li, Z. Y. Xiao, X. X. Lv, *Petroleum Geology*, **32**, 272 (2011).
5. S. C. Zhang, D. G. Liang, M. W. Li, *Chinese Science Bulletin*, **16**-23 (2009).
6. F. D. Mango, *Geoch. Cosmoch. Acta*, **58**, 895 （1994).
7. D. R. Yu, C. L. Liu *Journal of Chongqing University of Science and Technology: Natural Science Edition*, **13**, 16 (2011).
8. X. Q. Wu, X. W. Tao, J. D. Liu, *Natural Gas Geoscience*, **25**, 53 (2014).
9. X. W. Tao, M. Li, J. H. Jia, *Natural Gas Geoscience*, **25**, 70 (2014).
10. J. X. Dai, C. Yu, S. P. Huang, *Petroleum exploration and development*, **41**, 1 (2014).
11. Q. Wang, P. G. Peng, J. Zeng, Y. R. Zou, C. L Yu, B. Zhang, Z. Y. Xiao, *Geochimica*, **5**, 5(2014).
12. K. T. Singh, G. N. Nayak, L. L. Fernandes, *Palaeogeography, Palaeoclimatology, Palaeoecology*, **397**, 61 (2014).
13. N. P. Connor, S. Sarraino, D. E. Frantz, *Applied Geochemistry*, **47**, 209 (2014).

ГЕОХИМИЧНИ ХАРАКТЕРИСТИКИ И ПРОИЗХОД НА ПЕТРОЛА В ТАЖОНГ, БАСЕЙН ТАРИМ

Д. Р. Ю [1, 2, *], Б. С. Ю [1, 2], Ф. Ф. Джяо [3]

[1] *Училище по науки за земята и земните ресурси, Китайски университет по геологични науки, Бейджин, Китай*

[2] *Държавна ключова лаборатория по геология и минерални ресурси，Китайскиуниверситетпогеонауки, Бейджин, Китай*

[3] *Китайска корпорация за петрол и химия, Ченгду, Китай*

(Резюме)

В Тажонг е трудно да се определят природата и разположението на петрол-съдържащите естествени резервоари. С помощта на белязан въглерод $\delta^{13}C$ и белязани мономери на въглеводороди с $\delta^{13}C$ е установено, че петролът в района Тажонг е от източник от периода Камбрий-Ордовисиан. Чрез сравнение на молекулните тегла на въглеводороди с формула C_9 - C_{18} е доказано още веднъж, че петролът в Тажонг е от един източник. Конвенционалните биомаркерни съединения, с които се установява източника Камбрий-Ордовисиан и наличието на ароматизирани изотерпенови въглеводороди доказват, че целият нефт и газ се получават от анаеробна, силно редукционна среда и отлагане под действието на фотосинтезиращи зелени тиобактерии в скалите от периода Камбрий-Ордовисиан.

Fiberboard made of miscellaneous wood fibers oxidized by laccase mediator system

X. Guan[1,2,*], M. Guo[2], J. Lin[1], J. Li[1], X. Liu[1]

[1]*College of Material Engineering, Fujian Agriculture and Forestry University, Fuzhou 350002, Fujian Province, P.R.China.*
[2]*Key Lab. of Bio-Based Material Science and Technology of Ministry of Education, Northeast Forestry University, Harbin 150040,Heilongjiang Province, P.R.China*

Laccase was applied to wood processing due to its special significance in the ecological environment security. According to the synergic effect of nature mediator and artificial mediator, miscellaneous wood fibers were modified by the laccase mediator system (LMS) to press medium density fiberboard. Based on response surface methods, the best technological parameters were 60 U/ml of laccase activity, 0.28 mmol/L of ABTS concentration, 1.66 mmol/L of vanillin concentration and 55 min of treatment time. The study of the mechanism showed that increasing covalent bonds and hydrogen bonds between the fibers were the root cause for the mechanical properties. Moreover, the reaction of lignin and laccase with the mediator was competing. Excessive mediators restrained the oxidation reaction of lignin, and the amount of mediators was related to the amount of lignin. There is good industrialization prospect to press medium density fiberboard by LMS without adhesive.

Key words: laccase mediator system, miscellaneous fiber, medium density fiberboard.

INTRODUCTION

Laccase was applied to wood treatment authentically in the mid-1990s. After that, many countries carried out research on activation processes, adhesive, decoloration, bioremediation, etc. The binding force was mainly due to covalent bond between fibers and polymerization of lignin (Felby, 2002; Zhu, 2004; Felby, 2004). The movement of free radicals would hinder the generation of lignin (Barsberg,1999). The bonding strength was related with the quantity of cellulose and lignin (Duan, 2007). On account of non-phenolic lignin, low molecular weight compound was introduced as redox mediator (Srebotnik, 2000; Xu, 2000; Camarero, 2007; Camarero, 2005). Therefore, we have undertaken investigations into the performance and bonding mechanism in medium density fiberboards (MDF) made from LMS treated and untreated miscellaneous wood fibers.

MATERIALS AND METHODS

Test materials

Miscellaneous wood fibers were supplied by Heilongjiang Nancha Fiberboards Co. Ltd. Enzyme activity was 4060 U/g. Artificial mediator is ABTS supplied by Sigma-Aldrich Co. Vanillin is nature mediator supplied by Adamas Reagent Co. All other chemicals were with the highest purity of analytical grade from commercial vendors.

Medium density fiberboard (MDF) preparation

First of all, fibers were pretreated by UV light to modify functional groups. The distance between fibers and UV light was 50 cm. The intensity of UV light was 150 W/m^2. Irradiation time was 24 h. Then, fibers were treated by laccase mediator system (LMS), Table 1 shows the technological parameters. The control wood fibers were treated for 60 min without laccase and mediators at 4% consistency as a suspension in demineralized water. After that, the moisture content of the fibers reached 20±3%, and then fiberboards of dimensions 150 mm×150 mm×3.2 mm were made by hot pressing. Target density for the boards was 800 kg/m^3. The hot pressing was divided into drying process and plasticizing process. Drying process was a cycling drying method with two steps. The first step was at 12 MPa for 60 s and 4 MPa for 40 s, and the second step was at 12 MPa for 40 s and 4 MPa for 60 s. Plasticizing process was performed at 12 MPa for 200 s. The temperature during the whole process was 180°C

Fiberboard properties

For each treatment, the fiberboards were tested for moisture content, density, modulus of rupture (MOR), internal bond strength (IB) and water absorption (WA) following a 24 h cold water (20±2°C) soak. All testing was done according to

RG7-20A, except that the fiberboard samples were equilibrated at 65% RH and 21 ^{o}C prior to testing.

FTIR analysis

The fibers in the interior of MDF were removed using a razor blade and analyzed by direct transmission (KBr pellet technique) (Pandey and Pitman, 2002). All spectra were measured at a resolution of 4 cm^{-1} and 30 scans were recorded per sample. Peak heights of IR bands were measured using OMNIC software according to previously published methods.

XPS analysis

X-ray photoelectron spectra were obtained with a physical electronics (England) ESCALAB MK instrument equipped with a monochromatic Mg K$_{\alpha}$ X-ray source. A Gaussian curve fitting program was used to deconvolute C1 carbon (C-C, C-H and C=C functional groups) signal at 285 eV as an internal standard. The chemical shifts relative to C1 used in the deconvolution were 1.7 ± 0.2 eV for C2 (C-O), 3.1 ± 0.2 eV for C3 (C=O or O-C-O), and 4.3 ± 0.2 eV for C4 (O-C=O groups).

Mechanical properties of MDF

Regression models of MOR, IB and WA were analyzed by the method of descent. Response surface is shown in Fig.1. MOR, IB and WA achieved the ideal value since the laccase activity was between 59.08 U/ml and 70U/ml, mediator concentration was between 1.94 mmol/L and 2.33 mmol/L, and time was controlled between 54.98 min and 90 min. Lignin was the catalytic object of LMS, but overmuch laccase possibly hindered the reaction due to steric hindrance. Mediators could promote oxidation reaction of non-phenolic lignin, but excess mediator could restrain oxidation reaction of non-phenolic lignin. Reaction time was important factor to guarantee complete reaction, but longer time could reduce mechanical properties due to the hydrolysis of lignin. The best technological parameters were 60 U/ml of laccase activity, 0.28 mmol/L of ABTS concentration, 1.66 mmol/L of vanillin concentration and 55 min of treatment time.

Table 1. Technological parameters of LMS treated fiber.

ABTS(mmol/L)	Vanillin(mmol/L)	Laccase(U/ml)	Time(min)	Temperature(˚C)	pH value
0.25	1.5	50	30		
0.3	1.8	60	60	50	5
0.35	2.1	70	90		
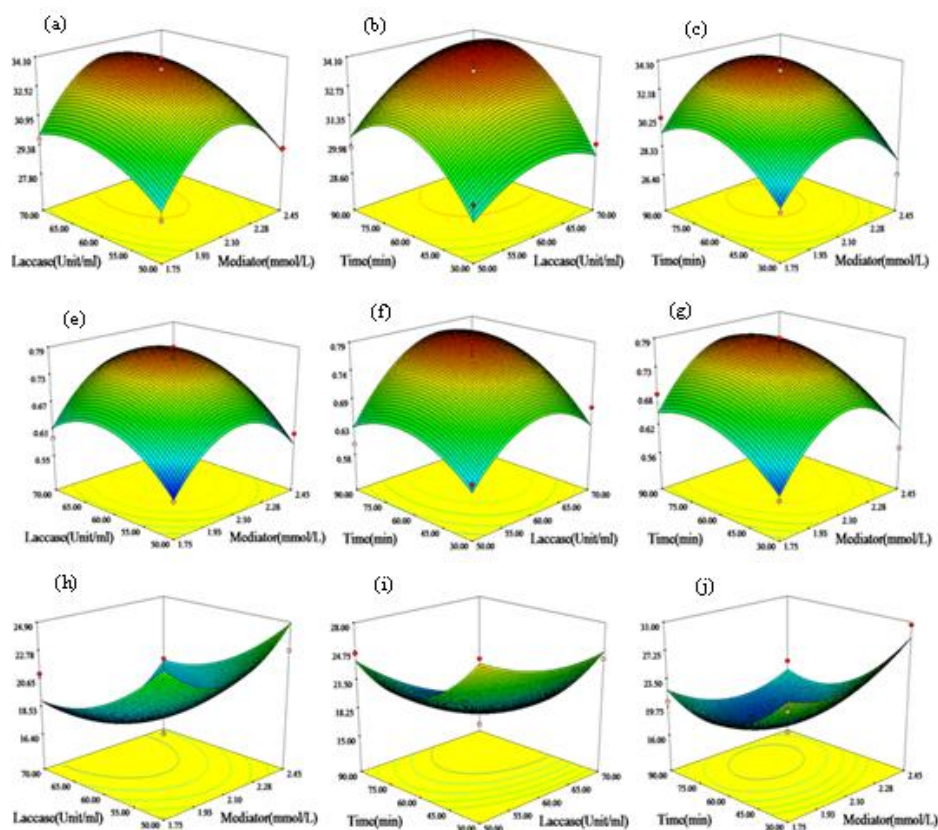
Fig. 1. Response surfaces of MOR, IB and WA interacted by laccase, mediator and time
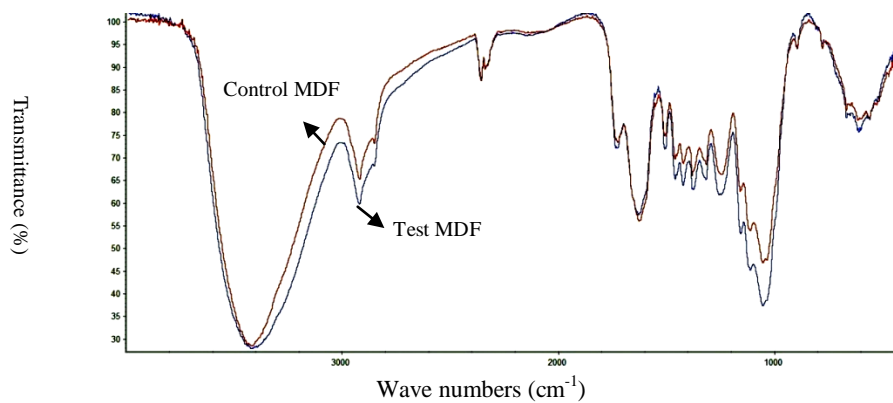
Fig. 2. FTIR spectrum of control sample and test sample.
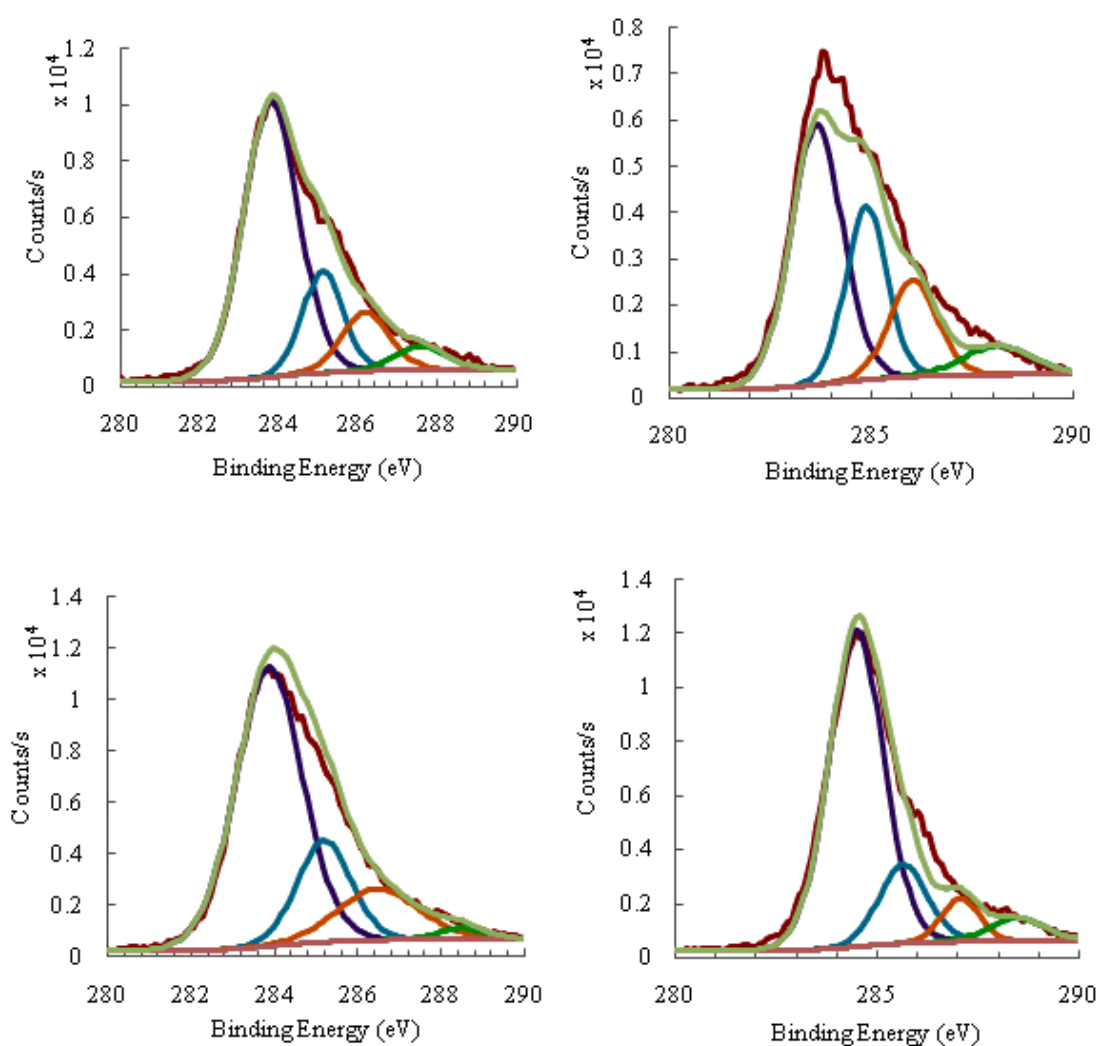
Fig. 3. XPS of control sample and test sample on the surface and in the interior: .a) XPS of control sample in the interior; b) XPS of test sample in the interior; c) XPS of control sample on the surface: d) XPS of test sample on the surface.

Evidence for Cross-linking of MDF

FTIR analysis

FTIR of control samples and test samples is shown in Fig.2. An increase at 3426 cm^{-1} and 2927 cm^{-1} showed that phenolic hydroxyl groups increased, which was due to the substitution reaction of aromatic nucleus prompted by LMS. The decrease in the characteristic absorption peak of aromatic ring in pos. 2 (781 cm^{-1}) further prove it. Moreover, the increases at 1729 cm^{-1}, 1159 cm^{-1}, 1112 cm^{-1}, 1058 cm^{-1} and 1037 cm^{-1} showed that new ether bond and carbonyl were generated in pos. 3 of aromatic ring. Accordingly, skeletal vibration of aromatic ring weakened (1625 cm^{-1}). It showed that LMS could induce the etherification and aldolization in pos. 3 of the aromatic ring. All issues considered, the increase of ether bond, carbonyl group and hydrogen bond was the dominant reason for achieving higher mechanical properties.

XPS analysis

The distribution in terms of carbon classes shows a marked increase in C2, C3, C4 and a decrease in C1 for the interior of the test sample (Fig.3 (a) and (b)). Hydroxyl group in lignin was oxidized to aldehyde or ketone under the effect of LMS, so the chances of lignin to combine with cellulose decreased. Oppositely, the chances of hydrogen generation in/among cellulose increased. So the component of C2 increased. The increase of C3 was due to the new carbonyl group, which was dominant from non-phenolic lignin oxidized by LMS. The increase of glucosidic bond generated from degraded lignin and cellulose also increased C3. The possible explanation for increased C4 was the further oxidation of aldehyde under the effect of LMS. The C1 component could give information similar to the O/C ratio and directly affect the amount of lignin. The degradation of lignin was the reason of decreased C1 component. Simultaneously, it had an increase in C1, C4 and a decrease in C2, C3 for the surface of test sample (Fig.3 (c) and (d)). There was obvious difference in compound concentration between fiberboard surface and interior. The degradation of lignin made more pores among fibers so that the lignin could easily reach fiberboard surface. More lignin lead to increased C1. The grafting reaction between cellulose and

vanillin covered the hydroxyl in cellulose, so the C2 component decreased. Semicellulose pyrolyzed under high temperature, so C3 decreased, but the product increased C4.

CONCLUSIONS

The mechanical properties of MDF corresponded to China MDF standard. The increase of covalent bond and hydrogen bond was the dominant reason for high mechanical intensity. The reaction of lignin and laccase with the mediator was competing. Excessive mediators restrained the oxidation reaction of lignin, and the amount of mediators was related to the content of lignin.

REFERENCES

1. S. Barsberg, L.G. Thygesen, Biochimica et Biophysica Acta - General Subjects, **1472**, 625 (1999).
2. S. Camarero, D. Ibarra, M.J. Martínez, A.T. Martínez, *Enzyme Microb Technol.*, **71**, 1775 (2005).
3. S. Camarero, D. Ibarra, Á.T. Martínez, J. Romero, A. Gutiérrez, J.C. del Rio. *Enzyme Microb Technol.*, **40**, 1264 (2007).
4. Xinfang D, Yuanlin C, Yongjian C, Guanwu Z, Yongsheng C, Jiaqi Z, Baolu, Z, *Scientia Silvae Sinicae.*, **43**, 134 (2007).
5. C. Felby, J. Hassingboe, M. Lund, *Enzyme and Microbial Technology.*, **31**, 736 (2002).
6. C. Felby, L. G. Thygesen, A. Sanadi, S. Barsberg, Industrial Crops and Product., 20, 181 (2004).
7. K. .K. Pandey, A. J. Pitman, *J Appl Polym Sci.,* **85**, 622 (2002).
8. E. Srebotnik, K. E. Hammel, J Biotechnol., **81**, 179 (2000).
9. F. Xu, J.J. Kulys, K. Duke, K. Li, K. Krikstopaitis, H.-J. W. Deussen, E. Abbate, V. Galinyte, P. Schneider, *Appl Environ Microbiol.*, **66**, 2052 (2000).
10. J. Q. Zhu, G. X. Shi, *Scientia Silvae Sinicae.*, **4**, 153 (2004).

ФИБРОКАРТОН ОТ ДЪРВЕСНИ ВЛАКНА ОКИСЛЕНИ В СИСТЕМА С ЛАКАЗА КАТО МЕДИАТОР

Кс. Гуан[1,2,*], М. Гуо[2], Дж. Лин[1], Дж. Ли[1], Кс. Лю[1]

[a] Колеж по материалознание, Аграрен и горски университет във Фуджиян, Фуджоу, Провинция Фуджиян, Китай
[b]Ключова научно-технологична лаборатория по материали на биологична основа, Министерство на образованието, Североизточен горски университет, Харбин, Провинция, Хейлонгджиян, Китай

(Резюме)

Използвана е лаказа при екологичното третиране на дървесинат. Използва се синергичният ефект на естествените и изкуствените медиатори, при което лаказната медиаторна система (LMS) позволява да се получи като продукт фиброкартон със средна плътност. Най-добри технологични параметри са получени при лаказа с активност 60 U/ml, концентрация на ABTS от 0.28 mmol/L, 1.66 mmol/L ванилини, време за третиране 55 минути. Анализът показва увеличаване на ковалентните връзки и водородни връзки между влакната, които са коренната причина за механичните свойства на картона. Освен това реакцията между лигнина при медиаторлаказа е конкурираща. Излишъкът на медиатори ограничава окислението на лигнина. Въобще, налице добра промишлена перспектива за получаването на фиброкартон със средна плътност без адхезив.

Research on adsorption of phenols in wastewater with cyclodextrin

G. Shi [1], G. Zhang [2*], Y. Liu [1], Ch. Yan [1], W. Lai [3]

[1]Xuzhou College of Industrial Technology, Jiangsu Xuzhou China 221140

[2]XuzhouCentralHospital,Jiangsu Xuzhou China 221009

[3]Tajen University, Pingtung, Taiwan 90741

Study of optimal process conditions of cyclodextrins (CDs) for treating wastewater containing phenol. adsorption time is 240 min, the pH value is 5 – 7, CDS dosage is 4 g/L, initial phenol concentration of 100 mg/L, adsorption temperature of 40˚C, the highest absorption efficiency can attainment 42,5 %. In the condition of 30˚C, adsorption phenol of wastewater by CDs process accords with the Freundliehadsorption model.

Key words: cyclodextrins (CDs), phenol of wastewater, adsorption.

INTRODUCTION

Typical cyclodextrins(CDs)[1-5],constituted by 6-8 glucopyranoside units, can be topologically represented as toroids with the large and the small openings of the toroid exposed to the solvent secondary and primary hydroxyl groups, respectively. Because of this arrangement, the interior characteristic of the toroid was changed from hydrophobic to less hydrophobic, as a result being able to host other hydrophobic molecules. In contrast, the exterior is sufficiently hydrophilic to impart CDs (or their complexes) into water.

The formation of inclusion compounds greatly modifies the physical and chemical properties of the guest molecule, mostly in terms of water solubility. This is the reason why CDs have attracted much interest in many fields, especially in pharmaceutical applications: since inclusion compounds of CDs with hydrophobic molecules are able to penetrate body tissues, these can be used to release biologically active compounds under specific conditions.

Phenolic compounds are highly toxic substances; they are a kind of industrial pollutants, mainly from oil refining, coal gas scrubbing, paper-making, ammonia and other chemicals production. Tap water containing microgram amounts of chlorophenols has significantly different smell; when taken by humans the chlorophenols accumulate and can cause poisoning symptoms; long-term consumption of phenol- polluted water can cause dizziness, itching, anemia and various neurological symptoms. At present, 6 kinds of phenolic compounds are involved in the national quality standards of water, the Environmental Protection Bureau of America involves 14 kinds of phenolic compounds, and our priority control involves 12 kinds of phenolic compounds in the pollutants: phenol and chlorophenols, cresol and nitro phenols. The phenol molecule diameter is around 0.59 nm, thus the phenol molecules can enter CDs of slightly larger diameter, so CDs have the ability of removing phenol pollutants from water. This paper studied the treatment of phenol wastewater by CDs in order to find out the best process conditions of wastewater treatment.

MATERIALS AND METHODS

Agents and apparatus

Phenol and CDs of analytical grade were used by Sinopharm Chemical Reagent Co. Ltd. Prior to usage; they were pretreated by vacuum drying. Three flasks, mechanical agitator, vacuum dryer, UV spectrophotometer were used in the study. More description should be listed like size, operational conditions etc.

Experimental apparatus

The experimental apparatus shown in Fig.1, included heater, mechanical agitator, temperature controller, and water bath.
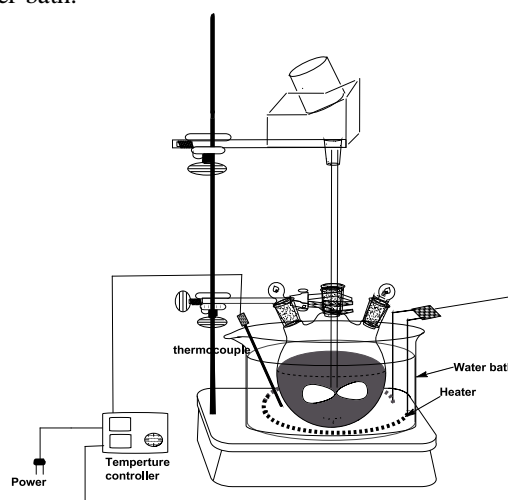
Fig. 1. Experimental apparatus of phenol in waste water by CDs.

* To whom all correspondence should be sent:
E-mail: ZhangGang_XZ@163.com

Adsorption efficiency

CDs were added to the phenol solution under mechanical stirring at a speed of 150 rpm for 30 min. After the adsorption equilibrium was reached, the solution and CDs were separated by a centrifugal separator. The supernatant was poured into the cell and analyzed at a wave length of 270nm using a spectrophotometer. The calibration curve of phenol solution was prepared with a series of phenol concentrations. The phenol solution adsorption efficiency was expressed by the following equation[6-8]:

$$\eta = \frac{c_o - c_e}{c_o} \times 100\%$$

η - adsorption efficiency, % ;

c_o - initial phenol concentration, mg/L;

c_e- phenol concentration in the supernatant at equilibrium, mg/L.

RESULTS AND DISCUSSION

Effect of different adsorption times on phenols removal by CDs[9,10].

An amount of 0.4 g of CDs, added to 100 mL of phenol solution of initial concentration of 100 mg/L, was operated at varied times at a temperature of 40^oCat a stirring speed of 150rpm. The effect of reaction time on phenol removal by CDs is plotted in Fig. 2.As can be seen from Fig.2, the removal efficiency of phenol by CDs adsorption increased with time. At a time of 160 min, the adsorption rate reached 34.5% and gradually increased till 300 min with phenol removal of 42.5%.Phenol removal on CDs was attributed to the cylindrical structure of CDs with cone. The cavity diameter of CDs was slightly larger than that of the phenol molecule, providing Van der Waals interaction between phenol and the hydrophobic groups of C-4, C-5 located in CDs. It is assumed in the literature that the removal of phenol by CDs is mainly due to the structure of CDs having inclusion ability for phenol. According to the current results, the optimal time of phenol removal by CDs is close to 240 min.
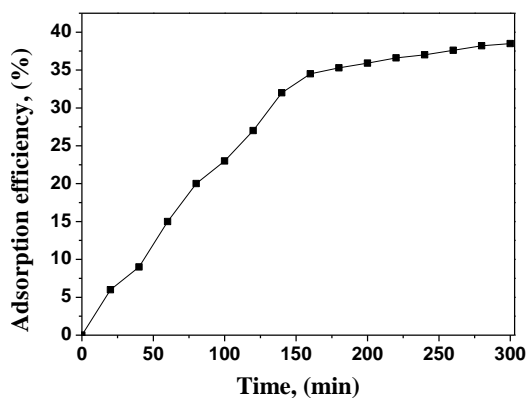
Fig. 2. Effect of different adsorption times on phenol removal by CDs.
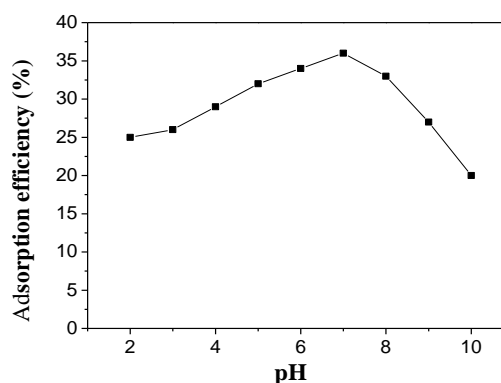
Fig. 3. Effect of pH on phenol removal by CDs.

Effect of pH on phenol removal by CDs

The reaction of 0.4 g of CDs, added to 100 mL of 100 mg/L phenol solutions with different pH, was performed at a temperature of 40°Cfor 60 min at a stirring speed of 150 rpm for 240 min. The results are plotted in Fig.3.

Fig.3 reveals that the pH value can affect phenol removal efficiency by CDs. Alkaline conditions are more unfavorable for phenol removal than acidic conditions. The phenol removal is 37.2% at pH=7, and decreases to 20.3% at pH=10. This is related to the hydrogen bond formation between phenol hydroxyl and hydroxyl group in CDs. With the increase of pH from neutral to alkaline, the formed sodium phenolate has a larger diameter than phenol, so that the sodium phenolate can not enter into the cavity of CDs, resulting in phenol desorption.

Effect of the initial concentration of CDson phenol removal[11,12]

Different amounts of CDS, such as 0.2 g, 0.3 g, 0.4 g and 0.5 g CDs were added to 100mL of the phenol solution with initial concentration of 100 mg/L at a temperature of 40℃, pH=6, stirring time 60 min, stirring speed of 150rpm, and adsorption time of 240 min. It follows from the results shown in Fig.4 that the increasing amount of CDs leads to improved removal of phenol. Larger amounts of CDs possess more active sites, resulting in higher adsorption. However, the larger amount of CDs consumed is related with ascending cost of water treatment, indicating that this process is not feasible for industrial application. With CDs concentration of 40 g/L, the solution becomes cloudy which interferes with the spectrophotometric analysis. As optimal concentration of CDs 4 g/L is considered.

Effect of phenol concentration on the adsorption efficiency of CDs

Amounts of 0.4 g CDs were added to 100 mL of aqueous phenol solutions with initial phenol concentration of 100 mg/L, 150 mg/L, 200 mg/L and 250 mg/L ata temperature of 40℃, pH=6, stirring time of 60 min, stirring speed of 150 rpm and adsorption time of 240 min, as shown in Fig.5.
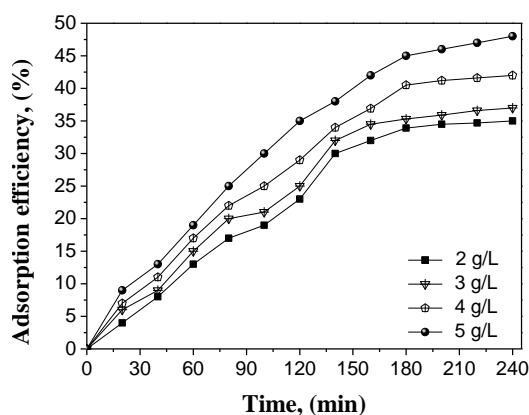
Fig. 4. Effect of initial CDs concentration on phenol removal.
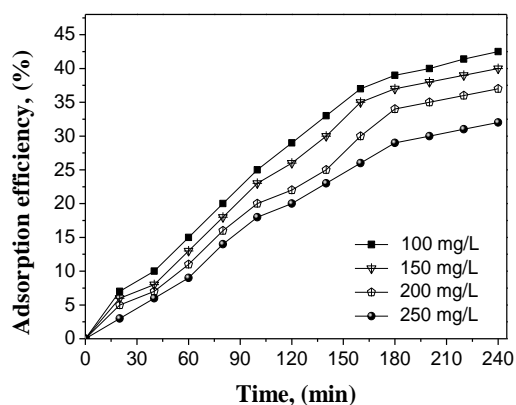
Fig. 5. Effect of initial concentration of phenol on its removal by CDs.

Fig.5 reveals that the adsorption efficiency of phenol byCDs decreases with increasing phenol concentration, the highest phenol removal efficiency was 42.5%.From the analysis of the figure, the adsorption rate in less than 160 min of time reached 30%, and at an adsorption time of 180 min, the adsorption rate slowly increased, the adsorption reaching equilibrium after 3h. This may be due to the dynamic adsorption equilibrium between adsorption and desorption as two reversible processes. With the increase of initial phenol concentration, the adsorption rate decreased, probably because of the steric effect between the concentration of phenol molecules, resulting in greater rate, and lower adsorption of phenol.

Effect of temperature on adsorption efficiency of CDs

0.4 g of CDs was added to100 mL ofa100 mg/L phenol solution at pH=6, stirring time of 60 min, stirring speed of 150 rpm, and adsorption time of 240 min. The effect of different temperatures on the rate of phenol removal and the adsorption is shown in Fig.6.

As you can see from Fig. 6, the removal rate of phenol on CDs with the increase of temperature first increased and then decreased, the removal effect at 40 to 60℃ was relatively high, respectively: 42.5%, 45.1% and 43.2%;at temperatures above 60℃ the removal rate significantly decreased because the process of adsorption is exothermic, while desorption is endothermic. The adsorption process is also influenced by other factors such as the impact of the formation of hydrogen bonds

1138

and van der Waals force forming and disappearing process. With the temperature increase, the removal of phenol first increased and then decreased. Considering a future industrial popularization and application, the adsorption experiments were performed at 40℃ with an adsorption efficiency of 42.5%.

CONCLUSIONS

CDs treatment of phenol wastewater, with the extension of time, the content of CDs phenol adsorption on the increase, to 300 after min adsorption, adsorption ratio reached 42.5%; the pH value has influence on the adsorption efficiency, with the increase of alkaline solution, CDs on phenol adsorption efficiency decreased, removal rate of pH is the highest at 7 37.2%, in the process of adsorption of phenol wastewater by pH can be adjusted to between 5 and 7; with the increase of amount of CDs, phenol adsorption rate increases, determine the quantity of CDs of 4 g/L; the adsorption efficiency of CDs decreased with the increase of initial concentration of phenol; CDs on phenol removal rate with temperature rise first increased and then decreased, the temperature above 60˚C after the removal rate decreased significantly, considering the promotion and application of industrialization, adsorption temperature can be set as 40˚C.
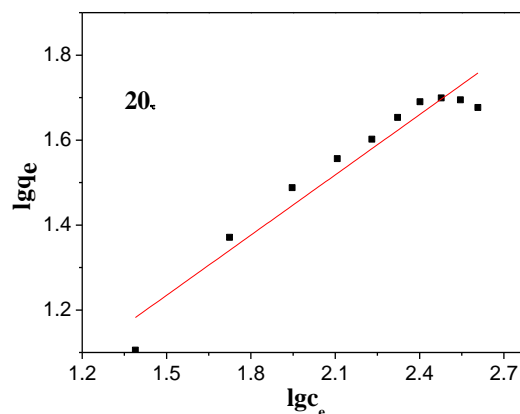
Fig. 7. Effect of temperature on the adsorption efficiency of CDs.

REFERENCES

1. K. Uekama, *Yakugaku Zasshi*, **132**, 85 (2012).
2. T. Osa, I. Suzuki. Journal of Japan Oil Chemists Society, **43**, 857 (1994).
3. W. Saenger, *AngewChemIntEd.*, **19**, 344 (1980).
4. M. A. Elwahedi, A.M. Eldeeb. Pharmatutor, **2**, 40 (2014).
5. D. K. Roy, D. Nipamanjari, G. Bankim Chandra, Asok K. Mukherjee, *SpectrochimicaActa Part A: Molecular and Biomolecular Spectroscopy*, **73**, 201 (2009).
6. K. Uekama, *Chemical & Pharmaceutical Bulletin,*

52, 900 (2004).

7. K. Harata, K. Kawano, *Carbohydrate Research*, **337**, 537 (2002).

8. S. Jozsef, *Chem. Rev.,* **98**, 1743 (1998).

9. H. Yamasaki, M. Hand, Fukunaga K. *Jpn Environ Conser Eng.*, **36** (2007).

10. R. Villalonga, R. Cao, A. Fragoso, *ChemRev.,* **107,** 3088 (2007).

11. S. Li, W. C. Purdy, *Chem Rev.,* **92**, 1457 (1992).

12. M. S. Chiou, H. Y. Li, *J Hazard Mater.* B, **93**, 248 (2002).

ИЗСЛЕДВАНЕ НА АДСОРБЦИЯТА НА ФЕНОЛИ ОТ ОТПАДЪЧНИ ВОДИ ЧРЕЗ ЦИКЛОДЕКСТРИНИ

Г. Ши [1], Г. Жанг [2*], Ю. Лю [1], Ч. Ян [1], У. Лай

[1]Колеж по индустриални технологии Ксужоу, Джиангсу Ксужоу, Китай
[2]Централна болница в Ксужоу, Джиангсу Ксужоу, Китай
3Университет Таджен, Пингтунг, Тайван 90741

(Резюме)

Изследвани са оптималните условия за третиране на фенол-съдържащи отпадъчни води с циклодекстрини (CDs). Времето за адсорбция е 240 мин., pH-стойностите са между 5 и 7, концентрацията на CD е 4 g/L. Опитите са проведени при начална концентрация на фенол от 100 mg/L при 40℃. Максималната ефективност на адсорбция е 42.5%. При 30℃ адсорбцията на фенола с CDs се описва от изотермата на Freundlich.

Comprehensive evaluation of the geochemical characteristics of the hydrocarbon source rocks in Zhenjing block

L. Wang [1, 2, 3], Y. Wang [1, 2, *], D. Yu [4], Q. An [5]

[1] *School of Geophysics and Information Technology, China University of Geosciences, Beijing 100083, China*
[2] *Key laboratory of Geo-detection (China University of Geosciences (Beijing)), Ministry of Education, Beijing 100083, China*
[3] *Software Engineering Center Chinese Academy of Sciences, Beijing, 100190, China*
[4] *School of Earth Sciences and Resources, China University of Geosciences, Beijing 100083*
[5] *School of Humanities and Economic Management, China University of Geosciences, Beijing 100083, China*

Hydrocarbon source rocks are developed in the Zhenjing block of Ordos basin. In order to better study the maturity of the hydrocarbon source, 99 samples were analyzed, and organic carbon was mainly classified in two intervals, one being less than 1% (25.5%), and the other ranging from 1% to 4% (55.56%). The ratio of hydrogen to oxygen was generally less than 0.86, and that of oxygen to carbon was less than 0.08. From the zones of Chang 9 to Chang 7, the type of organic matter gradually improves, being typically of mixed type. Up to the Chang 7 zone, source rocks and environmental conditions are getting worse, so is the organic matter type, dominantly controlled by humic kerogen. Through the study of the maturity of organic matter under the conditions of a maximum temperature of 443.5°C, we found that the minimum Ro was 0.57%, the maximum was 0.98%, and the average OEP was 1.28. TT and Ro showed that low mature stage of hydrocarbon source was characteristic of Yanan 2 zone, and the mature stage of hydrocarbon source was characteristic of Yanan 2 and 3 zones. The thermal evolution analysis indicates that the main hydrocarbon source was affected by tectonic thermal events and reached a hydrocarbon generation peak at the end of Cretaceous period.

Key words: Hydrocarbon source rocks, Geochemical characteristics, Kerogen, Thermal evolution.

INTRODUCTION

Ordos basin is a large continental sedimentary basin in the eastern part of China, and the Triassic Yanchang formation is a potential oil & gas reservoir in the area. Triassic Yanchang formation is characterized by hydrocarbon source rocks, integration of resource, reservoir and cap rocks, and potential reservoirs with wide area (Huang et al., 2009, Zhang et al., 2006). The Mesozoic oil and gas exploration in Zhenjing block began in the 1990s, and only a small oil-bearing area in the Chang 6 zone was found (Li X, Zhu Z, Feng C, et al., 2009). There has not been great breakthrough until 2006. Since then, with the discovery of ZJ5 well, the exploration upsurge in Chang 8 zone began. Successively there were many wells with high production, but the exploration rate was very low, because the geologists, who were restricted in the understanding of the geological background of this area (Sun Y, Liu C, Lin M, et al., 2009), could not distinctly assign the geological conditions and the law of the Mesozoic reservoirs and slowed down

the procedure of exploration (Yang H, Fu J, Wei X, et al., 2008). So, the study of the geochemical characteristics of hydrocarbon source rocks in Zhenjing block should explain the relationships between reservoir and hydrocarbon source rocks, and provide theoretical basis for further research.

ABUNDANCE OF ORGANIC MATTER

There are 93 core samples of hydrocarbon source rocks, among them one sample from a ding zone and two samples from Zhi luo zone. Statistical results show that the organic carbon of core samples is generally less than 1.2% (accounting for 88.57%), and the majority of it is less than 1%, (accounting for 68.57%). However, the organic carbon of debris samples is generally greater than 1% and for most of them it is greater than 2%.

The organic carbon of the source rock is low (less than 0.5%) or high (greater than 10%) to generate and expulse hydrocarbon. The hydrocarbon content and the conversion ratio should be chosen as the primary indexes to evaluate organic matter and set up the standard suitable for this area. Inferred by tables 1 and 2: (1) organic matter in this area is mainly classified in two intervals, one being less than 1% (accounting for

* To whom all correspondence should be sent:
E-mail: wangyanchun_bj@163.com

25.5%), and the other ranging from 1% to 4% (accounting for 55.56%). The minority of organic carbon ranges from 4% to 8% (accounting for 10%). A few scattered points are greater than 10% (accounting for 8.89%). Considering the characteristics of high carbon in this area, we plan to make the organic carbon of the conventional shale expand to 8%, although the organic carbon ranges from 8% to 10%. (In fact the cutoff of organic carbon in this area is 6%). (2) The properties of non-organic matter in this area are characterized by organic carbon less than 0.6% and hydrocarbon content less than 100 ppm and its conversion rate is less than 1. Therefore, we define the organic carbon of 0.6% as the cutoff of organic matter. (3) The shale with high carbon has strong absorbability, which is distributed in poor hydrocarbon source rock and non-hydrocarbon source rock, so generally there exists a positive relationship between hydrocarbon content and organic carbon, but its corresponding conversion rate is low. However, the conversion rate in different strata probably varies due to the difference of source and environmental conditions. Generally its conversion rate in Chang 7 zone is higher, and it can reach the poor or moderate class of hydrocarbon source rock. (4) The conversion rate in the area is generally lower than the common conversion rate. Therefore, organic carbon of 1% to 4% and hydrocarbon content of 800 ppm corresponds to a conversion rate ranging from 1% to 4%. Accordingly, hydrocarbon content higher than 1000 ppm corresponds to a conversion rate from 2% to 6%.

Through the above analysis we found that the abundance of organic matter of T_3y^2 section in Zhenjing block is better than of T_3y^3, and best in Chang 7 zone of T_3y^2 section, and worst of the Jurassic Yanan section (J_1y^2).

<center>ORGANIC MATTER TYPE</center>

Organic matter type is a quality evaluation indicator of hydrocarbon source rock. Generally the source rock conditions and sedimentary background determine the kerogen quality of hydrocarbon source rock (Durand, Bernard, 1980, Song D, He D, Wang S, 2013, Lu S, Chen F, Li J, et al., 2012)

Identification of micro-components of kerogen

Organic mineral mirror (transmission, reflection) is a statistical method for qualitative and semi-quantitative analysis. It is a simple, rapid method for evaluation of the type of organic matter, and is not affected by the thermal evolution of organic matter (Jansa et al., 1990, Xiuqin et al.,

2008). The identification results show that under the microscope (Fig.1) Yanchang Formation mudstone kerogen and coal amorphous content are low and occasionally display dark fluorescence. The liptinite in each layer has a certain distribution, the content is relatively low, with large differences. Various macerals, such as sporinite, cutinite, dendrimer, etc. are yellow green, bright yellow, dark yellow fluorescent; vitrinite came from the xylem. Mudstone kerogen vitrinite did not fluoresce, coal rock desmocollinite shows dark brown fluorescence. Inertinite from higher plant xylem strongly carbonized or based on xylem gelation further on the carbonization. From the mudstone kerogen maceral triangle (Fig.1) it can be seen on the top and bottom that Yanchang formation was mainly mudstone kerogen in vitrinite and inertinite two components, in a few samples of liptinite and the amorphous content was higher, the type of organic matter was of basically humic type. The content of mudstone kerogen amorphous particles and liptinite was higher in Ch 4 to Ch 8 of Yanchang, organic matter types are mixed type partial sapropel, of which most Ch 7 samples showed sapropelic type or near sapropelic type.
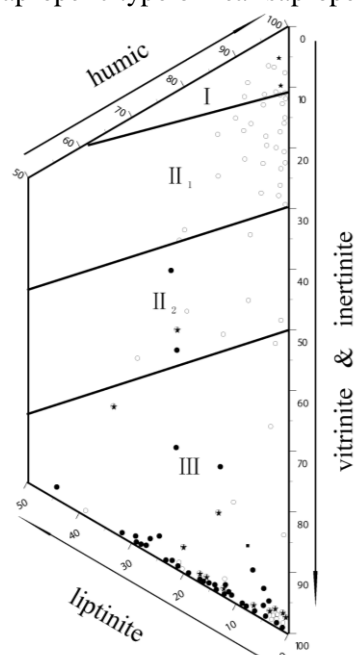
Fig. 1. Triangle of kerogen fractions in mudstone of Erdos basin.

Microscopically, identification of micro-components is an effective means of classifying kerogen types. The overall statistics of 28 microscopy samples is classified into three types, II_1 accounting for 39.29%, II_2 accounting for 50%, II_1 accounting for 10.71% (table 3).

Table 1. Statistics of hydrocarbon content from hydrocarbon source in Zhenjing area.

Horizon		Total number of Samples	Good hydrocarbon source rock (>1000ppm)		Moderate hydrocarbon source rock (200-1000ppm)		Inferior Hydrocarbon source rock (100-200ppm)		Non hydrocarbon source rock(<100ppm)		Proportion of Moderate to good hydrocarbon source rock (%)	Evaluation of hydrocarbon source rock
		Number	Number	Percentage (%)	Number	Percentage (%)	Number	Percentage (%)	Number	Percentage (%)		
J_1y^2	y9+10	11			4	36.36	6	54.55	1	9.09	36.36	Inferior
T_3y^3	ch5	10			7	70	1	10	2	20	63.64	Moderate
	ch6	30	1	3.33	7	23.33	10	33.38	12	40	25.81	Inferior
T_3y^2	ch7	18	5	27.78	6	33.33	5	27.78	2	11.11	61.11	Good
	ch8	11			6	54.55	4	36.36	1	9.09	50	Moderate
	ch9	5			4	80			1	20	80	Moderate
T_3y^1	ch10	2			1	50	1	50			poor representation	Inferior
Total		87	6	6.9	35	40.23	27	31.03	19	21.84		

Table 2. Organic matter conversion rate of hydrocarbon source rock in Zhenjing area.

Horizon		Total number of samples	Good hydrocarbon source rock HC/C (>4%)		Moderate hydrocarbon source rock HC/C (2-4%)		Inferior Hydrocarbon source rock HC/C (1-2%)		Non hydrocarbon source HC/C (<1%)		Proportion of Moderate to good hydrocarbon source rock (%)	Evaluation of hydrocarbon source rock
		Number	Number	Percentage (%)	Number	Percentage (%)	Number	Percentage (%)	Number	Percentage (%)		
J_1y^2	y9+10	11					7	63.64	4	36.36	0	Inferior
T_3y^3	ch5	10					2	20	8	80	0	Inferior
	ch6	30	2	6.67	1	3.33	11	36.67	16	53.33	10	Inferior
T_3y^2	ch7	18	3	16.67	8	44.44	5	27.78	2	11.11	61.11	Good
	ch8	11			1	9.09	7	63.64	3	27.27	9.09	Inferior
	ch9	5			1	20	4	80			20	Moderate
T_3y^1	ch10	2			1	50			1	50	poor representation	Inferior
Total		87	5	5.75	12	13.79	36	41.38	34	39.08		

Table 3. Statistics of organic matter type of Mesozoic source rock in Zhenjing area.

Horizon / Hydrocarbon source rock	Humic (%)	Liptinite (%)	Vitrinite (%)	Inertinite (%)	TI	Organic matter type
Ch7	28.2-72.1	4.26-44.39	3.85-50.84	0.19-18.09	-24.67-15.05	II_2
Ch8	32.85-63.35	9.95-19.19	26.7-47.09	0.87	6.25-48.3	II_2, II_1
Ch9	10.33-36.29	12.27-17.0	50.57-72.04	0.61-8.86	-35.8-3.66	II_2-III

Table 4. Elemental analysis of Kerogen of Mesozoic in Zhenjing area.

Horizon / Ratios	H/C (KTI on Average)	O/C (KTI on Average)	KTI (KTI on Average)	Organic matter type
Ch6	0.560-0.984(0.755)	0.04-0.139(0.067)	22.98-58.2(39.21)	III_1 main type II secondary
Ch7	0.589-1.190(0.859)	0.038-0.100(0.059)	24.6-70.77(44.85)	II main type III_1 secondary
Ch8	0.600-0.790(0.726)	0.07-0.120(0.093)	23.73-40.9(34.16)	II-III_1
Ch9	0.674-0.875(0.771)	0.06-0.091(0.072)	35.22-49.53(42.98)	II_1-II

Kerogen elemental analysis

Extension of coal group and analysis results of mudstone kerogen elements in Yanan group of Mesozoic in the Basin are displayed in Fig.2. Terrestrial plant debris being the main organic matter of Jurassic mudstone kerogen and coal elemental composition being very close, 29 mudstone kerogen samples and two coal samples were of humic type; the top of Yanchang Formation Ch 1 - 3 and the bottom of Ch 10 shale kerogen, in addition to Fu 2 well Ch 3 and low 2 well Ch10 two samples at the bottom of the distribution, unable to determine the original source material type, while the other 8 samples were of humic type; analysis of 31 samples in Yanchang Formation Ch 9 – Ch 4+5, the Ch 7 of 14 samples, 6 samples in a type II kerogen intervals, in the initial section II type track for the Jiefang 674 wells and two Tong chuan low mature kerogen samples (Ro = 0.65%, 0.54%), Mixed type of parent material reflects the western basin and the southern edge of the source rock for the partial sapropelic. It was also proved that the central basin is rich in algae and other aquatic organisms – semi-deep lake faces mudstone kerogen. In addition, the 17 Ch 7 samples were outside, 5 samples are distributed in type II kerogen interval, 12 samples are distributed in type III kerogen interval.

For the 67 samples collected in this study, the results of kerogen elemental analysis showed that the atomic ratio of hydrogen to carbon is commonly less than 0.86 and the atomic ratio of oxygen to carbon is less than 0.08. The samples data fall between II and III area of the plot (Fig 3). From tables 3 and 4 we knew that organic matter type is gradually getting better from Chang 9 zone to Chang 7 zone, and is dominated by mixed type. Up Chang 7 zone, since the source and environmental conditions are getting worse, organic matter type is getting poor, mainly characteristic of humic kerogen type.

THE ORGANIC MATTER MATURITY

Organic matter maturity is an important aspect of hydrocarbon source rock evaluation (Zhang T, Ellis G S, Ruppel S C, et al., 2012, Sun X, Zhang T, Milliken K L, 2014, Marynowski L, Salamon M, Narkiewicz M, 2012). According to the theory of kerogen pyrolysis oil, it is generally believed that temperature and burial time restrain the evolution of organic matter when the vitrinite reflectance of hydrocarbon source rock is equal to or higher than 0.5%. In this case, the odd-even predominance value of n-paraffin is gradually dropping down to 1. When the maximum pyrolysis temperature is higher than 435°C, then the mature stage is to form.
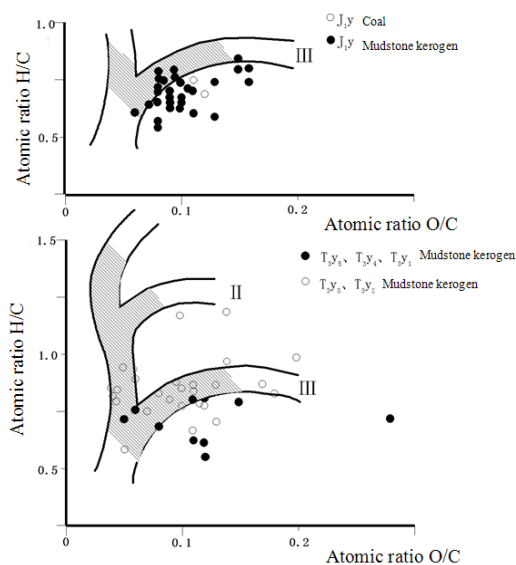
Fig. 2. Elemental map coordinates of mudstone kerogen in the basin.
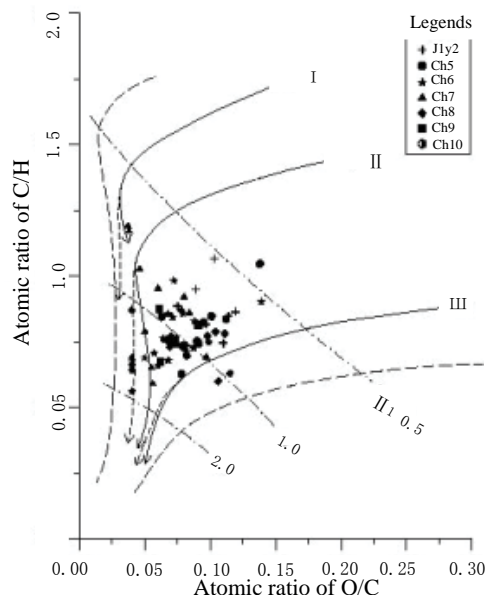
Fig. 3. Mesozoic kerogen type in Zhenjing area.

Vitrinite reflectance

Among the Ro values of 31 samples, the minimum is 0.57%, and the maximum is 0.98%. The Ro in Zheng block is consistent with the Ro in Jing block. The Ro value of hydrocarbon source rock in the J_1y^2 section is commonly from 0.57% to 0.67%, and the average value of 0.62% is less than 0.7%, so the mature source rock is a low one.

The Ro value of hydrocarbon source rock in the T_3y^3 section ranges from 0.60% to 0.98%, averagely 0.75%. The values are less than 0.7% accounting for 40%. All properties indicate that the hydrocarbon source rock in T_3y^3 section belongs to the low mature and mature one.

1143

The Ro value of hydrocarbon source rock in the T_3y^2 section is greater than 0.7%, ranging from 0.7% to 0.89%, averagely 0.78%. Therefore these parameters show that the hydrocarbon source rock in T_3y^2 section belongs to mature one.

According to the Ro and coal rank analysis, the degree of the evolution of the hydrocarbon source rocks in Yan and Chang zones is reducing from Qingyang east to its surroundings. The Zheng-Jing blocks are located in the west basin of the thermal evolution band. In the south of Qingyang - Fuxian and North of Zhengning - Yijun, the Ro value in T_3y^{2+3} sections generally ranges from 0.7% to 1.0%. For example, in Tong Chuan county, the Ro value of An 1 well in T_3y^2 section, is 0.7%, and 1.0% of Xiang 1 well and 0.8% of Qing 36 well. Determined from coal field data, the metamorphic center of Wayaobao coal series in T_3y^5 sections exists in Huanglingdian area, in which a lot of coal abundant with gas and with a large degree of metamorphism was explored. From Huangshen 1 well to Tongchuan area, the Ro value of 0.918% gradually decreases to 0.695%.

As above said, hydrocarbon source rocks of Yan- Chang zones buried or exposed to surface have entered the mature stage. By contrast, the evolution degree of Chang zones is higher and reaches the mature stage. However, the mature stage of Yanan zones is low, belonging to low mature source rock.

Maximum peak temperature of rock pyrolysis

The pyrolysis peak temperature of hydrocarbon source rock in Yanan No.2 section is from 430°C to 439°C, with an average of 433.7°C, and it reflects non-mature and low mature characteristics. The pyrolysis peak temperature in Yanan No.3 section is 439°C - 459°C, individually reaching 473°C, averagely 449°C. In Yanan No.2 section the lowest peak pyrolysis temperature is 437°C, and the highest is 455°C, commonly between 440 - 450°C, with an average of 443.5°C. According to the standard pyrolysis peak temperature, all in Yanan No.2 and No.3 belong to mature hydrocarbon source rock.

Odd-even predominance value of n-paraffin

The distribution of OEP value is not obvious in different characteristics strata, but it clearly reflects the maturity in the different strata (Guo J, Fang J, Cao J, 2012). Generally in the Yanan zone of Jurassic, OEP value is approximately from 1.15 to 1.44, much more than 1.30, the average of 1.28, and the characteristics show low maturity. In Yanchang No.3 section of Triassic, the minimum of OEP is 0.97, and the maximum is 1.60, much less than 1.30, with an average of 1.193. In Yanchang No.2 section of Triassic, the OEP value is from 1.03 to 1.28, with an average of 1.107. According to the OEP classification standard, the Triassic hydrocarbon source rock has met a mature stage.

Time - temperature index (TTI)

Based on the burial history and TTI value of Zhentan 2 well and Jingtan 2 well, it is inferred that the Yanan bottom of Jurassic in Zhenjing block could be at the maximum depth of 1700 m in Cretaceous era, along with the paleo temperature of 67.5°C. The current TTI value is from 8.1641 to 8.5168, equivalently the converted Ro value is 0.58%. By a similar method, the buried depth of the Yanchang No.2 section of Triassic could be at 2300 m in the early Cretaceous, along with the paleo temperature of 82°C - 86°C. The current TTI value is 23.8333 in Jingchuan block and 32.5677 in Zhengyuan block. Equivalently the converted Ro value is from 0.73 to 0.73.

Thermal evolution shows that the hydrocarbon source rock of Yanan No.2 section belongs to the low mature stage of thermal evolution. The hydrocarbon source rock of Yanchang No.2 and 3 has reached its mature stage of thermal evolution. Overall evolution degree is consistent with the Ro values.

THERMAL EVOLUTION ANALYSIS OF HYDROCARBON SOURCE ROCK

To facilitate the thermal evolution analysis of hydrocarbon source rock, we made the burial evolution chart of Zhengtan 2, Jingtan 2 and Qing 36 wells according to the drilling data and adjacent borehole formation data. On the basis of the above formation temperature data, the paleo temperature and its gradient of each structural layer were calculated using the compensation coefficient method. Subsequently the TTI value of the thermal evolution process was obtained. By comparing TTI with Ro we consider the results as basically reliable.

According to the burial history (Fig 4) and TTI value, the oil threshold time of hydrocarbon source rock in Yanchang No.2 and 3 sections roughly matches the evolution degree time. For example, comparing the oil and gas evolution with its corresponding zones of Zhengtan 2 well, burial history shows that the oil threshold time of the main hydrocarbon source rock in Yanchang No.2 section is earlier than in Yanchang No.3 section, and namely late Jurassic and early Cretaceous (approximate 142Ma) or early Cretaceous

(approximate 131Ma). The main hydrocarbon source rock influenced by tectonic thermal events has entered the hydrocarbon generation peak at the end of early Cretaceous, other part of the rock probably later.
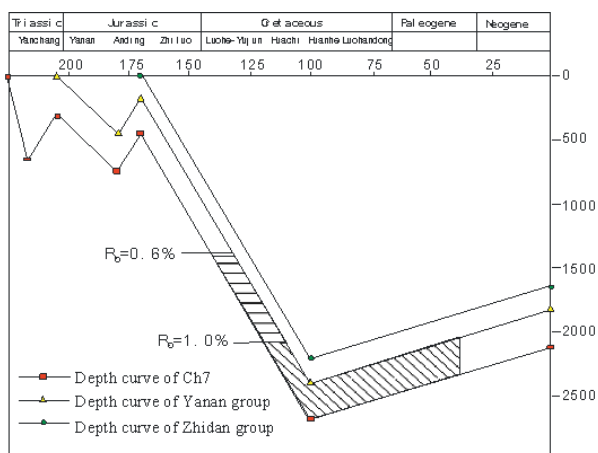
Fig. 4. The burial history of well HongHe 1

COMPREHENSIVE EVALUATIONS ON THE HYDROCARBON SOURCE ROCK

According to the characteristic analysis of the hydrocarbon source rock above, it is inferred that hydrocarbon source rock mainly exists in Chang 7 section. According to the shale thickness distribution in Chang 7 section, we knew that the thicker shale expands to the north and north-east, the thickness ranging from 20 m to 100 m, and the center of hydrocarbon generation and hydrocarbon supply is located in north-east in the studied area.

In Zhenjing block, the hydrocarbon source rock of T_3y^3 is relatively good, the best in Chang 7 zone, better in T_3y^2, the worst in J_2y^2. The oil threshold time of hydrocarbon source rock in Yanchang No.2 and 3 sections roughly matches the evolution degree time. The oil threshold time of the main hydrocarbon source rock in Yanchang No.2 section began in the late Jurassic and early Cretaceous (approximate 142Ma). And the oil threshold time in Yanchang No.3 section was in the early Cretaceous (approximate 131Ma). The hydrocarbon generation of the main hydrocarbon source rock in this area reaches the peak in Paleozoic (33Ma - 43Ma), in south-west probably later. It explains the peak period in this area up to now. Obviously it is later than the main oil region of Ordos basin in early Cretaceous.

CONCLUSION

(1) The hydrocarbon source rock of J_2y^2 is low mature. The hydrocarbon source rock in T_3y^3 is low and mature. The hydrocarbon source rock in T_3y^2 is mature.

(2) The hydrocarbon source rock of Yan-Chang zones buried or exposed to surface has entered the mature stage. By contrast, the evolution degree of Chang zones is higher and has reached the mature stage. However, the mature stage of Yanan zones is low, belonging to low mature source rock.

(3) The hydrocarbon generation of the main hydrocarbon source rock in this area reached the peak in Paleozoic (33Ma - 43Ma), in south-west probably later. It explains the peak period in this area up to now. Obviously it is later than the main oil region of Ordos basin in early Cretaceous.

REFERENCE

1. Z. L. Huang, Q. C. Jiang, S. l. Xi, C. L. Zhang, J. H. Zhong, *Journal of Xi'an Shiyou University: Natural Science Edition*, **24**(1), 21 (2009).
2. W. Z. Zhang, H. Yang, J. F. Li, J. M, *Shiyou Kantan Yu Kaifa (Petroleum Exploration and Development)*, **33**(3), 289 (2006).
3. X. M. Li, Z. D. Zhu, C. M. Feng, Z. G. Hu, *Journal of Jianghan Petroleum Institute*, **26**(2), 18 (2004).
4. Y. Sun, C. Liu, M. Lin, Y. Li, P. Qin, *Energy, Exploration & Exploitation*, **27**(1), 1 (2009).
5. H. Yang, J. H. Fu, X. S. Wei, X. S. Liu, *Marine and Petroleum Geology*, **25**(4), 387 (2008).
6. Ｂ. Durand, Kerogen: Insoluble organic matter from sedimentary rocks. Editions Technip, Paris, France, 1980.
7. D. Song, D. He, S. Wang, *Journal of Earth Science*, **24**, 355 (2013).
8. S. F. Lu, F. W. Chen, J. J. Li, W. M. Wang, H. G. Li, R. C. Cao, Y. L. Ma, *Petroleum Science*, **9**(1), 10 (2012).
9. L. F. Jansa, V. H. N. Urrea, *AAPG Bulletin*, **74**(10), 1640 (1990).
10. X. Q. Deng, F. X. Lin, X. Y. Liu, J. L. Pang, J. W. Lv, S. X. Li, X. Liu, *Journal of Palaeogeography*, **10**(2), 159 (2008).
11. T. W. Zhang, G. S. Ellis, S. C. Ruppel, K. Milliken, R. S. Yang, *Organic Geochemistry*, **47**, 120 (2012).
12. X. Sun, T. Zhang, K. L. Milliken, AAPG Annual Convention and Exhibition, Houston, Texas, USA, 2014.
13. L. Marynowski, M. Salamon, M. Narkiewicz, *Geological Quarterly*, **46**(1), 25 (2012).
14. J. Guo, J. Fang, J. Cao, *Chemistry Central Journal*, **6**(1), 1 (2012).

ПОДРОБНА ОЦЕНКА НА ГЕОХИМИЧНИТЕ ХАРАКТЕРИСТИКИ НА НЕФТОНОСНИ СКАЛИ В БЛОКА ЖЕНДЖИНГ

Л. Уанг [1, 2, 3], Я. Уанг [1, 2, *], Д. Ю [4], К. Ан [5]

[1]*Училище по геофизика и информационни технологии,Китайски университет по геонауки, Бейджин, Китай*
[2]*Ключовалабораторияпогео-детекция, Китайски университет по геонауки, Министерство на образованието, Бейджин, Китай*
[3]*Центърпософтуерноинженерство, Китайскаакадемиянанауките, Бейджин, Китай*
[4]*Училище по геология и георесурси, Китайски университет по геонауки, Бейджин, Китай*
[5]*Училище по по икономика и управление на човешките ресурсиКитайски университет по геонауки, Бейджин, Китай*

(Резюме)

Известни са нефтоносни скали в блока Женджинг в басейна Ордос. Анализирани са 99 проби от тях. Установено е, че органичният въглерод е разпределен главно в два интервала – единия под 1% (25.5%), а другия - от 1% to до 4% (55.56%). Отношението на водорода към кислорода е главно под 0.86, а на кислорода към въглерода е под 0.08. Видът на органичната материя постепенно се подобрява от зоната Chang 9 до Chang 7с характеристики от среден тип. В зоните под Chang 7 нефтоносните скали и природните условия се влошават, така че органичната материя е главно от хуминовкероген. Внимателното изследване на възрастта на органичната материя при максимална температура443.5°C показва, че Ro е 0.57%, а максималнатастойност е 0.98%. Средната OEP е 1.28. Времево-температурният индекс TT и Ro показват, че въглеводородните компоненти отговарят на характеристиките в зоната Янан 2, а степента на зрялост на въглеводородния източник отговаря на зоните Янан 2 и 3. Термичният еволюционен анализ показва, че главният въглеводороден източник е повлиян от тектонични термични процеси и достига връх в образуването на въглеводороди в края на периода Креда.

A photometric method for organophosphorus pesticide detection based on microfluidic chip

N. Yang[1,2], H. Mao[2*], J. Sun[1], C. Xiang[1], P. Xu[1]

[1] *School of Electrical and Information Engineering, Jiangsu University, Zhenjiang, PR China*
[2] *Insitute of Argricultural Engineering, Jiangsu University, Zhenjiang, PR China*

Water pesticide pollution is one of the important environmental issues which need to be urgently solved, but organophosphorus pesticide detection in water environment often relies on traditional laboratory techniques which have poor timeliness and low degree of automation. The paper proposes a photometric detection based on microfluidic chip. We designed a special microfluidic chip according to the characteristics of water pollution pesticide detection and created an automation system platform including sample introducing, mixing, reacting and detecting on the basis of organic phosphorus pesticide hydrolysis reaction. The working parameters of the detection system were optimized under microscale conditions. Experimental results showed that the designed system parallels traditional chromatography in detecting the organic phosphorus pesticide content in seawater, with a correlation coefficient of 0.963. At the same time, reagent dosage of the designed system is one-thousandth of that in traditional chromatography, and the degree of automation is greatly improved.

Key words: Microfluidic chip; water pesticide contamination; photometric detection; detection limit.

INTRODUCTION

Pesticides are indispensable capital goods in modern agricultural production, they can greatly increase crop yield. But they also have some disadvantages such as posing a threat to the ecological environment and human lives. When we use pesticides in daily lives, only about 1% of them are applied to the target organisms. The rest remains in the soil or enters into the sea areas, eventually flowing into the ocean by means of rainfall, river and air transport [1]. These pesticides inhibit photosynthesis of algae, and moreover, cause a large-scale drop in the production of fish and shellfish. These pesticides can also do great harm to human through the food chain. Therefore, rapid detection of pesticides in seawater is necessary to prevent and control water pollution [2, 3].

Currently, the main pesticides detection technologies include chromatography [4], spectroscopy [5], chromatography-mass spectrometry and other instrumental analysis methods [6~8]. These methods provide a basis for determining pesticides pollution. However, the traditional methods of instrumental analysis have some shortcomings such as expensive instruments, long and tedious pre-processing. Moreover, each step of the routine detection process such as pesticides extraction, purification, preconcentration and detection, are affected by hardware facilities, personals, laboratory's technical proficiency, level of management and other aspects. These factors also lead to inaccurate measurement results [9]. Because enzyme immunoassay has many advantages: high detection speed, high specificity, high sensitivity, large analytical capacity, low cost analysis, safety and reliability, it has become the first choice for on-line detection based on antigen antibody specificity recognition and association reaction [10, 11]. Currently, enzyme immunoassay mainly relies on test strips or test cards. The method has three shortcomings: (1) a large amount of reagents is consumed; (2) the accurate detection readout is hard to acquire by the naked eye; (3) the automation level of this method is low.

As a new detection technology, a microfluidic chip was developed in recent years [12]. It integrates samples' reaction, separation, detection and other processes concerning chemistry, biology and other fields into a single chip. Because the technology of the microfluidic chip has features of miniaturization and automation, therefore it has been considered as one of the seven technologies that will change our world. In 2006, the Nature journal published the technology of the microfluidic chip in a special issue [13]. The scale of microfluidic chip channel is usually tens to hundreds of microns. Meanwhile, a detection process only requires nanoliters or picoliters of samples. Undoubtedly, it is particularly suitable for

meeting the needs of reducing pesticides consumption for detection. Therefore, the present paper proposes a photometric detection system to water pesticides pollution based on the microfluidic chip. As an example, microfluidic chip based organophosphorus pesticides detection to the study of water pesticides pollution is taken. The working parameters of the detection system under microscale conditions were optimized. The research provided theoretical bases for developing a rapid detection system for the assessment of water pesticides pollution.

PHOTOMETRIC DETECTION SYSTEM OF MICROFLUIDIC CHIP

The basic principle

Methyl parathion is a common organophosphorus pesticide. Therefore, the paper takes methyl parathion as the research subject. From methyl parathion, p-nitrophenol can be obtained under the action of hydrolytic enzyme, the solution of p-nitrophenol being of yellowish color. The reaction process is shown in **Fig. 1.**

When exposed to the sun, the molecule of p-nitrophenol can undergo polarization, a forced oscillation appears with the frequency of incident light. On the basis of the Helmholtz equation, we obtain the following expression:

$$2n^2\kappa = \frac{Nze^2}{\varepsilon_0 m} \frac{\gamma\omega}{\left(\omega_0^2 - \omega^2\right)^2 + \gamma^2\omega^2} \tag{1}$$

In the equation, n is the planar optical refractive index，κ is attenuation coefficient, m is electronic mass, γ is damping constant, e is electron charge, E is electric field intensity of incident light, ω is the frequency of the incident light, N is the molecule number of p-nitrophenol per unit volume, z is the number of electrons in an atom，ω_0 is the natural electron frequency.

At the same time, p-nitrophenol has the ability to absorb light, the absorption index is:

$$\alpha = \frac{4\pi}{\lambda} n\kappa = \frac{4\pi\omega}{V_0} n\kappa \tag{2}$$

In this equation, λ is wavelength of light in vacuum. V_0 represents the speed of light. By substituting equation (2) in equation (1), the following equation is obtained:

$$\alpha = \frac{2\pi Nze^2}{nV_0\varepsilon_0 m} \frac{\gamma\omega^2}{\left(\omega_0^2 - \omega^2\right)^2 + \gamma^2\omega^2} \tag{3}$$

It may be concluded that when the absorption coefficient α reaches a maximum, then resonance and absorption occur as ω goes to ω_0. In other words, the substance will absorb light when the frequency of light approaches the electron natural frequency. Furthermore, N is the number of molecules of p-nitrophenol per unit volume and reflects the concentration of methyl parathion, the concentration value is C, while the other parameters are inherent parameters. Therefore, absorption index can be conveyed as:

$$\alpha = kC \tag{4}$$

In this equation, k is proportionality coefficient of methyl parathion, which integrates several parameters of methyl parathion. The value of k is associated with the molecular character of the absorbing material and the frequency of detection light; k is irrelevant to the concentration of the solution. According to Lambert's law, we know that:

$$I = I_0 \cdot 10^{-\alpha g l} \tag{5}$$

In this equation, I is the light output intensity, I_0 is the incident light intensity. Substituting equation (4) in equation (5)，we obtain:

$$I = I_0 \cdot 10^{-kCl} \tag{6}$$

To describe sample's absorbance by the intensity of light this paper introduces the concept of absorbance with the following equation:

$$A = -\log_{10} \frac{I}{I_0} \tag{7}$$

Substituting equation (6) in equation (7), we obtain the mathematical expression of the absorbance A:

$$A = kCl \tag{8}$$
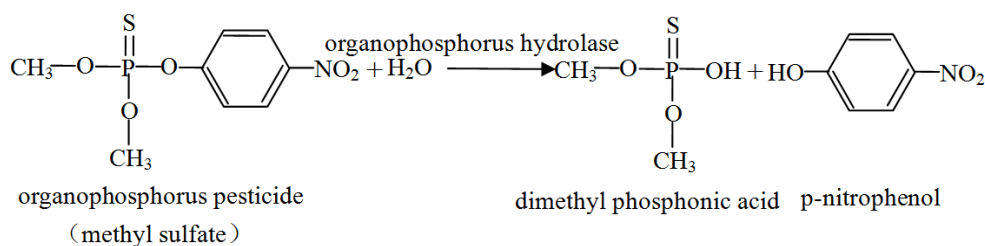
Fig. 1. Free sketch of the hydrolysis of organophosphorus pesticide.

In this equation, l is the optical length. Thus, absorbance is closely associated with the coeffcient of proportionality k, the concentration of methyl parathion C and the optical length l. If we can ascertain the numerical values of k and l, so absorbance A is proportional to the concentration of the material C and we can determine the concentration by measuring the absorbance.

Design of the microfluidic chip

The designed microfluidic chip consists of four parts, which are shown in figure 2. A is the area of sample introduction, B is the area of mixing, C is the area of reaction and D is the area of detection. The chip is made of polydimethylsiloxane (PDMS).
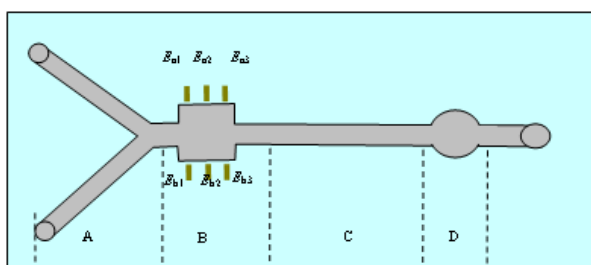
Fig. 2. Structure model graph of the design of microfluidic chip.

The area of sample introduction A is used to introduce the sample of organophosphorus pesticide (methyl sulfate) and the solution of hydrolytic enzyme. The area of mixing B is designed into chaotic mixing structure driven by the electrical field. In the picture, E_{a1}, E_{a2}, E_{a3} and E_{b1}, E_{b2}, E_{b3} are microelectrodes, which are used to produce chaotic reaction. The microelectrode material is ITO conducting glass. The area of mixing B is mainly used for mixing the organophosphorus pesticide and the solution of hydrolytic enzyme in order to trigger a complete organophosphate hydrolysis reaction. Because the progress of organophosphate hydrolysis reaction needs some time, the reaction area C can provide the space for mixing organophosphorus pesticide and organophosphorus hydrolase. There will be photometric detection after hydrolysis reaction has happened between the two fluids. The structure of the photometric detection zone D is shown in figure 3 which is the front view of the microfluidic chip model structure. From the picture we can conclude that the photometric detection zone penetrates the whole microfluidic chip, thus it can bring 5 mm detection optical path for absorbent detection. The cover is used to prevent overflowing of liquid from the detection zone. The cover is also made of PDMS. Figure 4 is a photograph of the microfluidic chip. The mixed zone extracts microelectrode. The material of the microelectrode is ITO conducting glass. The latter

is welded with dupont line by silver paste so as to connect to the outside.
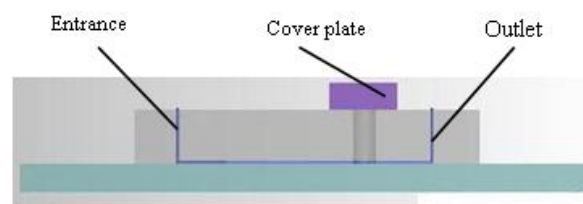
Fig. 3. Model structure front view of microfluidic chip.
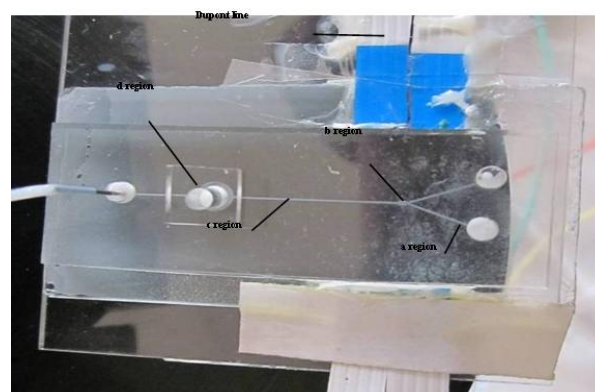
Fig. 4. Photograph of the microfluidic chip.

Experimental platform of the detecting system

Figure 5 is a photograph of the photometric detection system based on a microfluidic chip. The photometric check system is equipped with two channel squirt sampling pumps (0.098 µm/step, flow inaccuracy of CVs less than 1%) and two trace microinjectors (Terumo®, Terumo Corporation, Tokyo, Japan) (capacity of 1 mL), used to introduce seawater containing organophosphorus pesticide and organophosphorus hydrolase. The microfluidic chip is placed in the bracket of transmittance measurement, there is an optical fiber probe on the bracket and the optical fiber probe clings to the detection port of the microfluidic chip. There is detection fiber under the bracket. The detection fiber clings to the lower surface of the chip. The launching fiber is also connected with the optic precision light source (HL-2000-HP-FHSA). The optical fiber probe is connected with the USB2000 fiber optic probe spectrometer, and the light-emitting optical fiber probe is connected with a precise light source. The host computer, DSP system board and power drive plate form chaotic electric field controller. The chaotic electric field controller connects with the microfluidic chip electrode which can exert chaotic electric field to enable intensive mixing between organophosphorus pesticide and organophosphorus hydrolase.
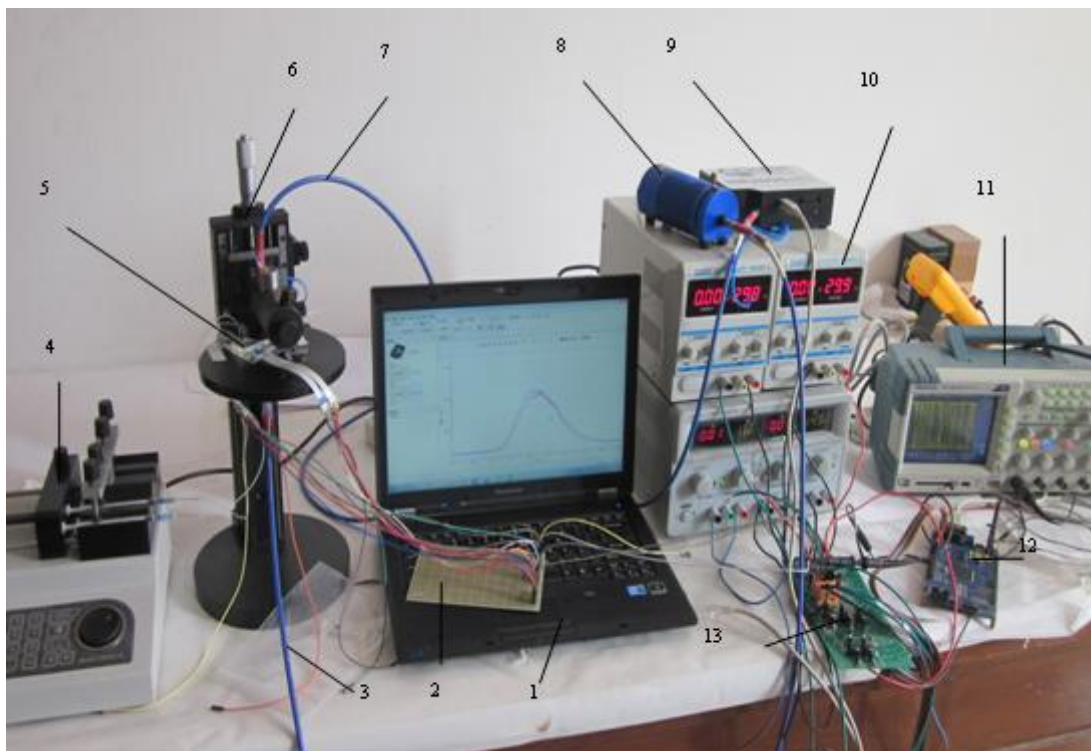
Fig. 5. Photograph of the detection system. 1-Host computer, 2-Expansion board, 3-Launching fiber, 4-Injection pump, 5-Microfluidic chip, 6-Transmission detector bracket; 7-Absorbance detection fiber, 8-UV-visible light, 9-Spectrometer, 10-Adjustable power supply, 11-Oscilloscope, 12-DSP system board, 13-Power driver board

Systematic approach to determine the optimal parameters

There are two main working parameters for rapid organophosphorus pesticide detection in microfluidic systems including optimum chaotic electric field parameter and optimal detection wavelength. The working parameters of the chaotic electric field are determined by simulating the mixing process between organophosphorus pesticide and organophosphorus hydrolase. As we know, different wavelengths have different sensitivity to the absorption of the hydrolyzate, so it is necessary to detect the absorbance of seawater samples on the basis of different concentrations of the pesticides. We can choose the most sensitive absorption wavelength as detection wavelength.

WORKING PARAMETERS OPTIMIZATION FOR THE DESIGNED SYSTEM

Optimizing the parameters of the chaotic electric field

Lorenz model is a typical kinetic model to study chaos in fluid turbulence. The Reynolds number of the fluid in microfluidic systems is usually very small, therefore we use the chaotic electric field to enable the intensive mixing of the laminar flow. This paper chooses the chaotic Lorenz model as a driving source in the micro-mixing chamber. We selected Lorenz chaotic driving electric field which is coupled by three different variables x, y, z. Formulas 9, 10 and 11 are the initial electric field expressions:

$$\frac{dx}{dt} = -c(x - y) \tag{9}$$

$$\frac{dy}{dt} = ax - y - xz \tag{10}$$

$$\frac{dz}{dt} = xy - bz \tag{11}$$

x, y, z are the three control signals which are used to drive the electrode of the micro-mixing chamber. b and c are dimensionless parameters, a is the working parameter of chaotic electrical field. The paper sets an initial value as: $x(0) = y(0) = z(0) = 1$. x is the electrode control signal of E_{a1} and E_{b2}, φE is equal to βx. y is the drive signal, y is negated for $-y$ which is referred as a signal to control the electrode. The electrode includes E_{b1} and E_{a2} in figure 2, while φE is equal to $-\beta y$. The driving signal z develops into z-a as the driving signal to the electrode includes E_{a3} and E_{b3}. In figure 2, φE is equal to $\beta(z$-$a)$, β is the amplification factor. The dimensionless parameter b is equal to 8/3, c is equal to 10 and a is equal to 28. Figure 6 is Lorenz chaotic orbit diagram under the control of

the placed signals.
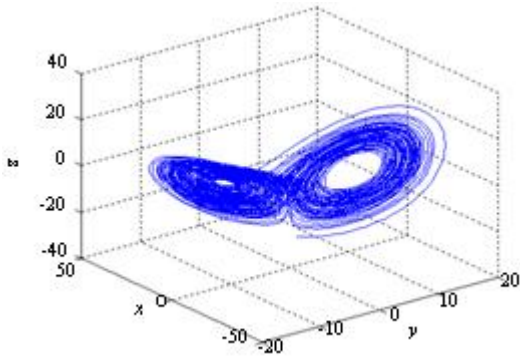
Fig. 6. Track diagram of chaotic state of the control electrodes.

Figure 7 is the microfluidic flow chart under the conditions of electric field controlled by Lorenz chaotic signal at 400 ms. According to section 3.2.1, the Lorenz chaotic signal x connects with E_{a1} and E_{b2}, while the Lorenz chaotic signal y connects with E_{a2} and E_{b1}. At the same time, E_{a3} and E_{b3} are connected with the signal of z. The connection type and the electric chaotic anti-control algorithm induce dynamic electroosmotic 7 vortices, wherein, the first two are large vortices and the others are small vortices. The stirring vortices promote the mixing process. Figure 8 is the scatter diagram of microfluidic concentration field under the conditions of electric field which is controlled by Lorenz chaotic signal control at 400 ms. From the picture, under the combined action of the double electrical layer electrodes on the wall surface of the microfluidic chip, an electric driving force which compels the fluid to move in, is produced. Under the configuration of electric field, the liquid near the wall of the mixing chamber moves from the high potential to low potential. Since the phase relationship between E_a and E_b is orthogonal, the wall driving force emerges under the action of the mixing chamber and forms synergy driven relationship. The relationship induces the formation of a significant convergence between the vortex circulation flow and swirl flow divergence. The marked circulation in the middle part of the micro-mixing chamber stretches and disperses the fluid. Then, a small vortex behind the micro-mixing chamber will have a secondary further dispersion after the fluid is dispersed, so as to promote the process of mixing.
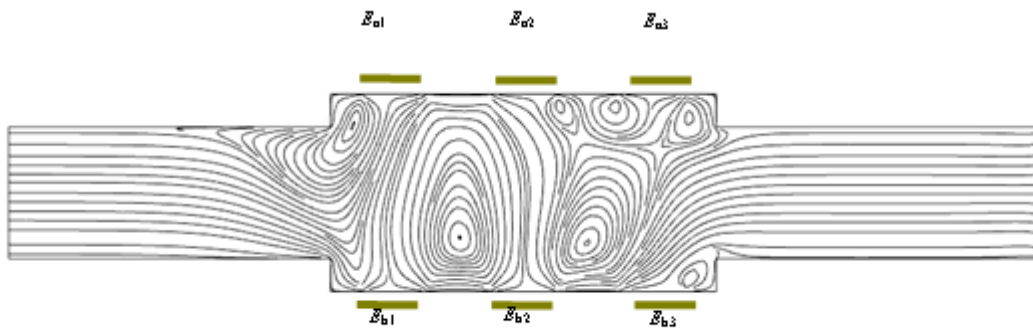
Fig. 7. Flow picture of microfluid under the conditions of electric field controlled by Lorenz chaotic signal.
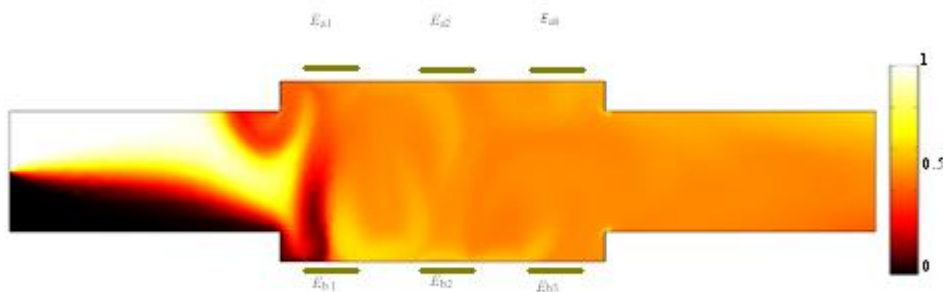
Fig. 8. Microfluidic concentration field distribution picture under the Lorenz chaotic signal control electric field conditions.

As can be seen from the figure, when the liquid flow is on the outlet of the mixing chamber, the concentration of fluid has become uniform. It is easy to conclude from the figure that the condition of laminar flow is broken and irregular movement appears when liquid enters the micro-mixing chamber.

The evaluation criteria of the mixing effect should include the uniformity coefficient of the sample solution, the concentration of tracer liquid, and the mass fraction of the tracer liquid. Therefore, we adopt the state of the concentration field to represent the variance in the gray image. The concentration distribution picture which is shown in figure 8 is converted to a gray-scale picture. The two gray-scale entrance boundaries are defined as 0 and 1, 0 representing the lowest concentration, and 1 representing the highest concentration. Other chromas are normalized as:

$$C_i = \frac{x_i - y}{z - y} \tag{12}$$

In the equation, C_i is the value of chromaticity after normalization. x_i is the value of chromaticity that will be calculated. y is the entrance of low concentration, while the low concentration can be expressed to 0 "gray-scale". z is a high concentration entrance, while the high concentration can be expressed to 1 "gray-scale". The target of mixing effect can be expressed as:

$$\sigma = \sqrt{\frac{1}{N} \sum_{i=1}^{N} (C_i - \sigma_0)^2} \tag{13}$$

In the equation, N is sample size, σ_0 is the average chromatic value after the liquid is completely mixed, while the liquid is the mixture of organophosphorus pesticide and the solution of hydrolytic enzyme, so $\sigma_0 = 0.5$. In terms of the numerical simulation object, the value of σ varies from 0 to 0.5, 0 indicates intensive mixing, 0.5 shows incomplete mixing. Figure 9 is the distribution graph of the mixing effect evaluation at the outlet of the micro-mixing chamber. The working parameter a is chosen from 2, 35, 120 and 240.

From the figure, when the working parameter a is equal to 2, the mixing evaluation index σ little changes over the time and the working parameter is in a large state (about 0.4) at the outlet. This phenomenon indicates that the electric field is not clearly an effective way to control over hybrid drive. When the working parameter $a=35$ or 120, in other words, fluid particles are under the conditions of chaotic motion, the mixing index σ changes largely over time and stops at the point of a small value (0.04) at the outlet, which indicates that the

1152

chaotic system has control over the mixing drive at the moment.
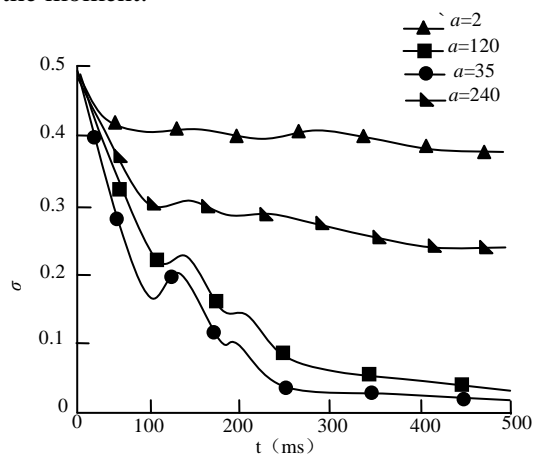
Fig. 9. Mix effect changes in different working parameters at the export.

When the working parameter a is equal to 240, in other words, fluid particles are in a non-chaotic motion, the mixing evaluation index σ has small change over time at the outlet and eventually stops at the larger state of about 0.28, which indicates that the system of Lorenz has poor control over the mixing results. Therefore, the paper selects 35 for the working parameter a of the chaotic electric field.

Determination of the optimal detection wavelength

Only when the hydrolysis product of organophosphate pesticide has resonance with the frequency of light wave, the proportional relation between the concentration and the absorptivity of light can be truly reflected. Therefore, experimental methods are needed to select the optimal detection wavelength. In the experiment, the adopted concentrations of organophosphorus pesticide are 2×10^{-5} mol/mL, 4×10^{-5} mol/mL, 6×10^{-5} mol/mL, 8×10^{-5} mol/mL, and 1×10^{-4} mol/mL, respectively. Organophosphorus pesticide will react with the hydrolytic enzyme, the absorption spectrum is shown in the figure. Different concentrations of organophosphorus solution will be obtained by diluting with sodium tetraborate. From the figure, we can also conclude that when increasing the concentration of organophosphorus pesticide, the absorption spectrum curve also increases.

The wavelength should be within the range of 200 nm~800 nm. It is necessary to screen characteristic absorption wavelength. The principle of screening is to select the wavelength which has the largest variance ratio as the characteristic wavelength. After calculating, we have found that the change rate reaches a maximum when the absorbance is at 405 nm, the maximum is at 0.08 Abs/($\times 10^{-5}$ mol/mL).
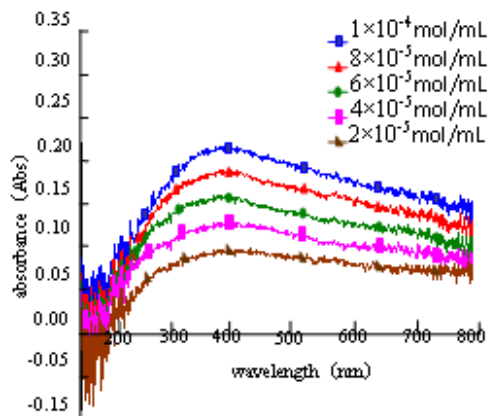
Fig. 10. Absorption spectra of different concentrations of organophosphorus pesticide hydrolyzate

ANALYSIS OF THE DETECTION SYSTEM

According to the optimal system parameters obtained in section 3, the analysis results were compared with those of the traditional chromatographic detection method.

Calibration curve

Different concentrations of organophosphorus pesticide reagent and the solution of hydrolytic enzyme were added into the syringe pump system. The measurement result is regarded as one part of the calibration curve which is shown in figure 11. A good linearity is seen between organophosphorus pesticide and absorbance, the linear equation is $y=2.995\times10^3x-9.74\times10^{-3}$, the correlation coefficient (R) is 0.9934.
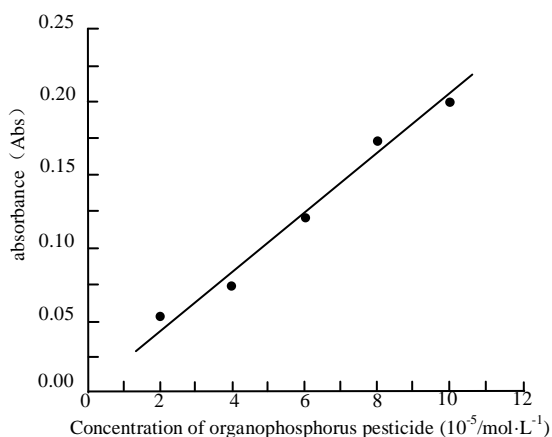
Fig. 11. Absorbance changes with the concentration of organophosphorus pesticide.

Comparative analysis of samples detection accuracy

In order to analyze the detection accuracy of the designed microfluidic chip system, nine samples were selected whose concentrations change with

the step of 1×10^{-5} mol/mL in the absorbance detection experiment. The concentrations of pesticide samples in seawater were from 2×10^{-5} mol/mL to 10×10^{-5} mol/mL. Finally, a relation analysis between detection result and the result of chromatographic detection was performed. Figure 12 is the scattergram obtained by adopting two methods to detect organophosphorus pesticide. The correlation coefficient obtained by the regression analysis method was 0.963. Compared to the traditional chromatography, these data indicate that water pesticide pollution detection method based on microfluidic chip has no obvious deviations in terms of the accuracy of detection.

For the present water pesticide pollution detection method, the consumption of reagent is only 1/1000 compared to the traditional method and the level of automation of the designed system is improved.
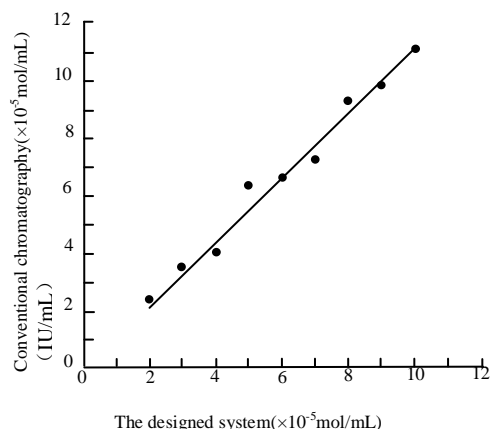
Fig. 12. Regression analysis between designed system and chromatography.

CONCLUSIONS

This paper presents a water pesticide contamination detection system based on a microfluidic chip. The organophosphorus pesticide pollution detection is taken as an example and the working parameters of the system are optimized. The experimental results show that the accuracy of the system detection is basically the same as in conventional chromatography, using only nanoliter quantities of the reagent. For the designed system, the liquid consumption is only 1/1000 of that in chromatography. Therefore, the paper can provide a theoretical basis for a portable and on-line water pesticide contamination monitoring system.

REFERENCES

1. S. Zhou, H. Yang, A. Zhang, Y.F Li, W Liu. Chemosphere, 114, 26 (2014).
2. T. Tomiyasu, S. Takenaka, Y. Noguchi, H. Kodamatani, A. Matsuyamab, K. Oki, Y. Kono, R. Kanzaki, H. Akagi. Marine Chemistry, 159,19 (2014).
3. M. Sarkhosh, A. Mehdinia, A. Jabbari, Y. Yamini. Journal of the Brazilian Chemical Society, 25(11), 2048 (2014).
4. P. Wang, Y. Xiao, W. Liu, J. Wang, Y. Yang. Food chemistry, 172, 385 (2015).
5. Y. Sultanbawa, D. Cozzolino, S. Fuller, A. Cusack, M. Currie, H. Smyth. Food chemistry, 172, 207 (2015).
6. B.H. Zainudin, S. Salleh, R. Mohamed, K. C. Yap, H. Muhamad. Food chemistry, 172, 585 (2015).
7. Z. He, L. Wang, Y. Peng, M. Luo, W. Wang, X. Liu. Food chemistry, 169, 372 (2015).
8. S. Qu, Z. Du, Y. Zhang. Food chemistry, 170, 46 (2015).
9. S. Walorczyk, D. Drożdżyński. Journal of AOAC international, 94(5), 1625 (2011).
10. Z. Xu, L. Zheng, Y. Yin, J. Wang, P. Wang, L. Ren, S. Eremin, X. He, M. Meng, R. Xi. Food Control, 47, 472 (2015).
11. B. Chowdhury, I. H. Cho, N. Hahn, J. Irudayaraj. Analytica Chimica Acta, 852, 212 (2014).
12. R. M. Guijt, J. P. Armstrong, E. Candish, V. Lefleura, W. Percey, S. Shabala, P.C. Hauserc, M.C. Breadmore. Sensors and Actuators B: Chemical, 159(1), 307 (2011).
13. N. Yang, R. Zhang, P. Xu, Z. X. Xiang. Electronics world, 119(1926), 40 (2013).

МЕТОД ЗА ФОТОМЕТРИЧНО ОТКРИВАНЕ НА ОРГАНО-ФОСФОРНИ ЕСТИЦИДИ, ОСНОВАН НА МИКРОФЛУИДЕН ЧИП

Н. Янг[1,2], Х. Мао[2*], Дж. Сун[1], Ч. Ксианг[1], П. Ксу[1]

[1]*Училище по електро- и информационно инженерство, Университет Джиангсу, Женгджиан, Китай*
[2] *Институт по аграрно инженерство, Университет Джиангсу, Женгджиан, Китай*

(Резюме)

Замъряването на водите с пестициди е един от най-важните проблеми, които спешно трябва да се решат от човечеството, но откриването на органо-фосфорните пестициди във водна среда често зависи от традиционните лабораторни условия при дълго време и ниска степен на автоматизация. Настоящата работа предлага фотометрично откриване с микрофлуиден чип. За целта бяха създадени специален микрофлуиден чип и автоматизирана система, включваща въвеждане на пробата, смесване, реакция и откриване, основано на хидролиза на пестицидите. В работата също се оптимизират работните параметри на детекторната система в микромащаби. Експерименталните резултати показват, че създадената система е паралелна на традиционната хроматография за откриването на органо-фосфорни пестициди в морски води, като корелационният коефициент достига 0.963. В също време анализираното количество е една хилядна от това в традиционната хроматография, а степента на автоматизация е много по-висока.

Catalytic polymerization of lignin model compounds using laccase and mediators

X. Guan[1*,2], M. Guo[2], J. Lin[1], J. Li[1], X. Liu[1]

[1]*College of Material Engineering, Fujian Agriculture and Forestry University,*
Fuzhou 350002, Fujian Province, P.R.China
[2]*Key Lab. of Bio-Based Material Science and Technology of Ministry of Education, Northeast Forestry University,*
Harbin 150040

Biotechnology and environmental effects concept make laccase important to biological characteristics during the processing of wood-based panels. Reactions performed by laccase are complex. The products generated in different phases affect the properties of wooden materials in different ways. The similarity and otherness between laccase system, laccase artificial mediator system and laccase natural mediator system in the same reaction conditions were researched in this paper. Lignin model compound was taken as a research object which was set in processing of wood-based panels. The results show that products polymerize by ether bonds in the laccase system and overlong reaction time causes benzene degradation following unsaturated olefins. However, products polymerize by hydrogen bonds and/or unsaturated bonds in the laccase mediator system and overlong reaction time causes benzene degradation following unsaturated carboxylic acids. Different bonding modes and products affect the physical and mechanical properties of wood-based panels. Moreover, natural mediator relative to artificial mediator has low cost, low toxicity and low catalytic efficiency.

Key words: laccase, mediator, guaiacol, ABTS, vanillin.

INTRODUCTION

Laccase was discovered in the 19th century in nature. Laccase plays multiple roles in synthesis and degradation (Yoshida 1883; Mayer and Staples 2002). Under the sponsorship of environmental friendly biotechnology, the biological properties of laccase have attracted more attention in chitosan, lignin and so on (Sharma and Kuhad 2008; Tetsch et al. 2006). Moreover, biotechnology and environmental effects concept make laccase important to biological characteristics during the processing of wood-based panels. In nature, the most abundant organic matter is cellulose, followed by lignin. Lignin is an aromatic high-molecular compound in the xylary tissues, and plays a role in sticking fibers (Li Jian and Luan Shujie 1993). Volatile organic compounds (VOC) in wood-based panels could be reduced through aromatic alcohol and phenol catalyzed by laccase (Thurston 1994; Reshma et al 2007). The oxidation-reduction potential of laccase is lower. Laccase can partly oxidize phenolic lignin, but not non-phenolic lignin. In order to get away from the restriction, the natural growth process of lignin was simulated and the results showed that some small molecules could effectively strengthen the catalysis of laccase to non-phenolic lignin. The system which contained small molecules and laccase was called laccase mediator system (LMS) (Kawai et al. 1987; Bruce and Palfreyman 1998). For now, there are artificial mediators (ABTS, HBT, NHA, etc.) and natural mediators (vanillin, syringaldehyde, sinapic acid, acetosyringone, etc.). Their catalytic mechanisms and catalyzing efficiencies are various (Moldeset al.2008; Tukayi et al. 2010; Kumarasamy et al. 2010; Atika et al. 2007). Lignin is a kind of complex phenolic polymer which consists of p-coumaric alcohol, coniferyl alcohol, 5-hydroxyl coniferyl alcohol and sinapic acid. Lignin model compound was selected as a research object for qualitative and quantitative analysis. The main structure units of lignin are guaiacyl (G) units, syringe (S) units and hydroxyphenyl (H) units. G units are widespread in hardwood, softwood and herb. The model compounds of G units have guaiacol, 4-methyl guaiacol, 4-vinyl guaiacol, 4-ethyl guaiacol, eugenol, etc. Catalytic mechanisms and catalyzing efficiencies of LMS to non-phenolic lignin have been researched by some scholars, but catalytic mechanisms and catalyzing efficiencies of LMS to phenolic lignin, especially for natural mediators had not been researched (Bourbonnais et al. 1998; Fabbrini et al. 2002; Baiocco et al. 2003). In this paper, guaiacol, ABTS and vanillin were taken as lignin model compound, artificial mediator and natural mediator, respectively, and were set in processing of

* To whom all correspondence should be sent:
E-mail: xinguan_fafu@163.com

wood-based panels. The reactions of guaiacol and products during the different phases were analyzed. Moreover, the effects of products in the different phases on the properties of wood-based panels were analyzed based on binding mechanism.

EXPERIMENTAL PROCEDURES

Chemicals

Laccase was kindly supplied by Wuhan Yuancheng Technology Development Co., Ltd. (China). The laccase (4000 units/g) was stored at -10°C for further use. Guaiacol (2-metoxyphenol) was purchased from Sinophurm Chemical Reagent Co., Ltd. ABTS (2, 2'-azino-bis-(3-ethylbenzothiazoline-6-sulfonate)) was supplied by Sigma-Aldrich Co. Vanillin (3-methoxy-4-hydroxybenzaldehyde) was supplied by Adamas Reagent Co. All other chemicals were of highest purity of analytical grade from commercial vendors.

LMS treatment of guaiacol

The guaiacol was dissolved in 0.1M acetate buffer (pH 4.5) with final concentration of 10 mmol/L as a target substrate. ABTS and vanillin were dissolved in the target substrate at 5% consistency (by mass of guaiacol). The solution was magnetically stirred at 45°C in O_2 atmosphere (continuous bubbling) to ensure a sufficient supply of oxygen for the enzyme reaction. The enzymatic treatment was performed using 20 U/ml of laccase relative to the liquid volume for 60 min, 240 min, 600 min and 720 min. At pre-determined intervals, the reaction vials were removed and the reaction was stopped immediately by preserving at -10 °C and avoiding introducing impurities. As control, solutions were treated under the same conditions but without mediators.

UV analysis

To identify the products and reaction rate of guaiacol transformation, especially the effects of mediators, the reaction mixture was assayed by UV-Visible spectrophotometry (unit type: TU-1900 PC). Due to the overlap of characteristic absorption wavelength between guaiacol, ABTS and vanillin, the multi-composition measurement was performed according to additivity of absorbance and Lambert-Beer Law. To measure molar absorption coefficients, standard solutions of guaiacol, ABTS and vanillin were prepared as described in 2.2. Test samples were diluted at 1:50 (v/v), and detection wavelength was from 200 nm to 600 nm. Regulations were analyzed on the basis of absorbancy and Lambert-Beer Law.

FTIR analysis

The changes of molecular structures were qualitatively characterized by using infrared spectroscopy (unit type: MAGNA-IR560 E.S.P). The liquid sample was pre-processed by liquid membrane. All spectra were measured at a resolution of $4 cm^{-1}$, and 40 scans per sample were recorded. Sampling gain was 1.0. The spectra were baseline corrected and peak heights of the IR bands were measured using OMNIC software.
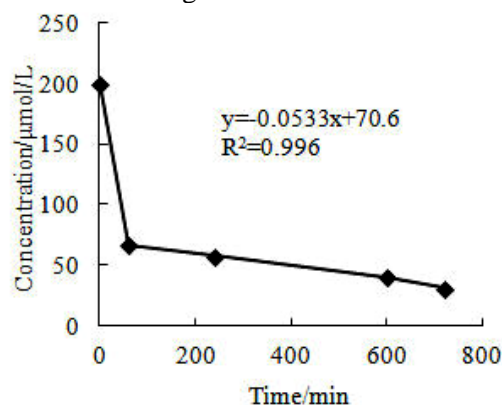
Fig. 1. Concentration of guaiacol treated by laccase with time.
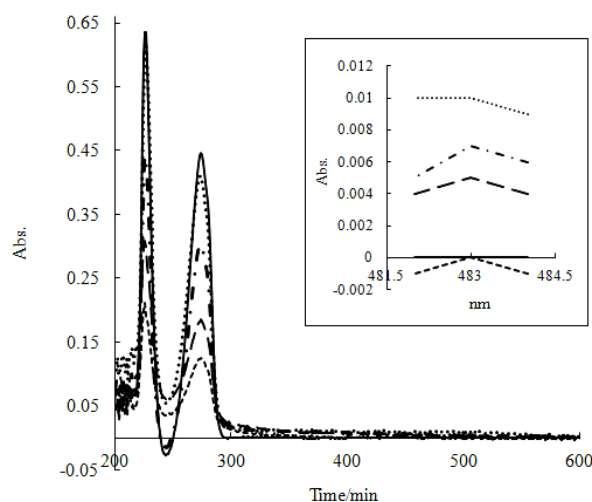
Fig. 2. UV spectra of guaiacol treated by laccase with time.

RESULTS AND ANALYSIS

Laccase treatment of guaiacol

The experiment was conducted as described in 2.2 without mediators. The color of the solution was from purple to colorless. The changes of guaiacol concentration are shown in Figure 1 on the basis of Lambert-Beer Law. The guaiacol concentration was sharp down within 60 min, followed by linear decrease. In Figure 2, the absorbancy of B belt and E belt decreased with the extension of reaction time.

.
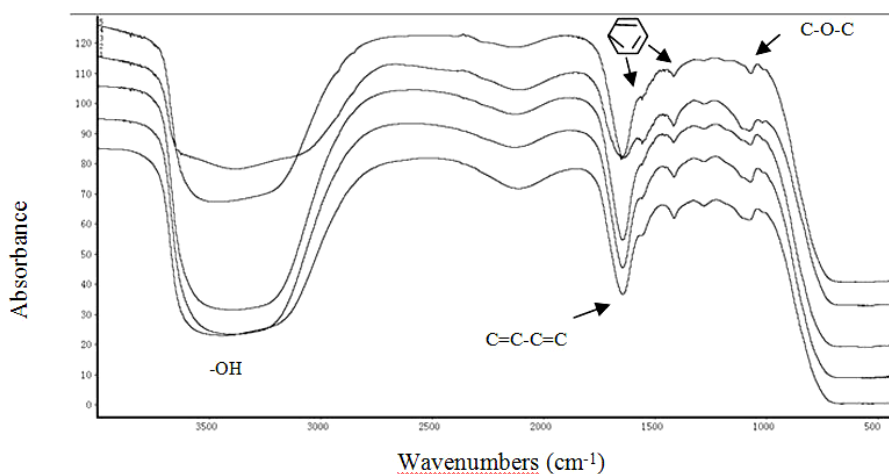
Fig. 3. FTIR spectra of guaiacol treated by laccase with time.
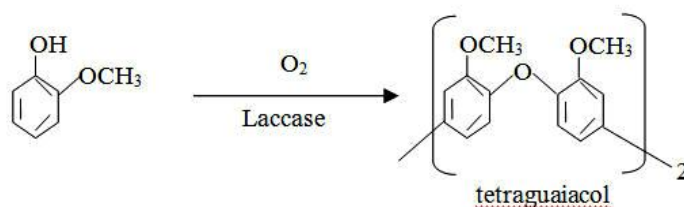
Fig. 4. Reaction process of guaiacol treated by guaiacol.

The main product was tetraguaiacol (Figure 4). The reaction mechanism included generation of phenoxy radicals by the action of laccase and oxygen, and creation of tetraguaiacol by cross-linking reaction. The characteristic absorption wavelength of tetraguaiacol was 484 nm which would degrade with time. Figure 2 also shows that the concentration of the product was max in 60 min, and gradually decreased to 0 in 720 min. However, there was no absorbency of the degradation product which declared that product was a saturated hydrocarbon or a conjugated alkene. Figure 3 shows that the peak intensity of hydroxyl significantly decreased, and peak intensity of ether strengthened in 60 min. This proved that guaiacol was catalyzed into phenoxy radical, and then cross-bonding took place between phenoxy radicals. With time, the peak intensity of ether decreased and the peak intensity of C=C increased. This further specified that the benzene ring was cracked and generated conjugated alkenes.

Laccase-ABTS system treatment of guaiacol

The color of the solution was aubergine in the initial stage, and gradually disappeared with time. UV absorption wavelengths of ABTS were 228 nm and 340 nm. UV absorption wavelengths of guaiacol were 226 nm and 274 nm. The concentration of guaiacol decreased gradually with the reaction time (Figures 5 and 6). The degradation rate of guaiacol was slower than that without mediator in the first 60 min. Then the degradation rate linearly diminished, but quicker than without mediator. Moreover, there were new absorption peaks at 303 nm and 488 nm which declared that new compounds were generated. On the basis of mechanism analysis and experienced wavelength calculation, 303 nm was the featured wavelength of 2-methoxy-para-benzoquinone, and 488 nm was the featured wavelength of 3,3'-dimethoxy-4,4'-biphenoquinone (Figure 8). There were exceptional values at 720 min in Figure 6 which showed that a new compound was created and its absorption band overlapped with E belts of ABTS and guaiacol. This is due to cracking of 2-methoxy-para-benzoquinone into 2-methoxy-butene diacid (Figure 8), verified by the IR spectrum (Figure 7). In the first 60 min, the peak intensity of hydroxyl decreased, meaning that guaiacol was catalyzed into phenoxy radical. The peak intensity of benzene ring decreased, meaning that benzene ring was degraded. The peak intensity of ABTS decreased, meaning that ABTS reacted with laccase and oxygen. The characteristic absorption peaks at 1645 cm^{-1} and 1663 cm^{-1} were C=O of 3,3'-dimethoxy-4,4'-biphenoquinone and

1157

2-methoxy-para-benzoquinone, respectively. With time, the peak intensity of ABTS gradually increased. In 240 min, guaiacol was transformed into 2-methoxy-benzenediol and 3,3'-dimethoxy-4,4'-dioxydiphenyl which strengthened the peak intensity of hydroxyl. Furthermore, 2-methoxy-benzenediol and 3,3'-dimethoxy-4,4'-dioxydiphenyl generated during prior period were transformed into 3,3'-dimethoxy-4,4'-biphenoquinone and 2-methoxy-para-benzoquinone, so the peak intensity of 1645 cm^{-1} and 1663 cm^{-1} increased and the peak intensity of benzene ring continually decreased. In 600 min, the formation reactions of 3,3'-dimethoxy-4,4'-biphenoquinone and 2-methoxy-para-benzoquinone were dominant with the decrease of hydroxyl and benzene ring. Some 2-methoxy-para-benzoquinone was cracked into 2-methoxy-butene diacid in 720 min. During the whole reaction, the peak intensity (1104 cm^{-1}) of the intermediate product was constant after 60 min which illustrated that reaction speed was constant.
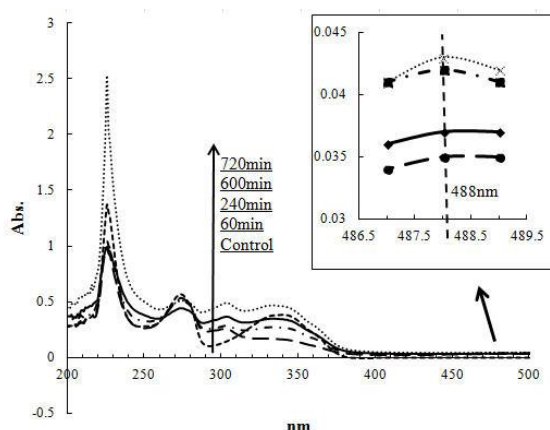
Fig. 5. Absorption of guaiacol treated by laccase-ABTS system with time.
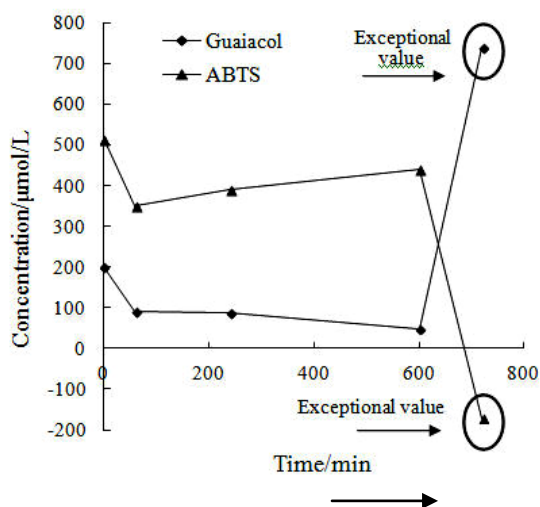
Fig. 6. Concentration of guaiacol and ABTS with time.

Laccase-vanillin system treatment of guaiacol

The color of the solution was aubergine in the initial stage, and gradually disappeared with time. UV absorption wavelengths of vanillin were 226 nm, 279 nm and 309 nm. UV absorption wavelengths of guaiacol were 226 nm and 274 nm. Due to the overlap of substrate and products and the unknown product concentration, only qualitative analysis was performed. It is shown in Figure 9 that vanillin was transformed into intermediate under the effect of laccase and oxygen on the basis of transfer reaction of hydrogen atom. Then, guaiacol was transformed into phenoxy radical by intermediate, and intermediate was reverted to vanillin by absorbing a hydrogen atom. After that, the phenoxy radical was transformed into 2-methoxy-benzenediol and 3,3'-dimethoxy-4,4'-dioxydiphenyl. Then 2-methoxy-benzenediol and 3,3'-dimethoxy-4,4'-dioxydiphenyl were transformed into 2-methoxy-para-benzoquinone and 3,3'-dimethoxy-4,4'-biphenoquinone, respectively. UV absorption wavelengths of 2-methoxy-benzenediol were 267 nm and 306 nm. UV absorption wavelength of 2-methoxy-para-benzoquinone was 303 nm. UV absorption wavelength of 3,3'-dimethoxy-4,4'-biphenoquinone was 488 nm. With time, 2-methoxy-para-benzoquinone was cracked into 2-methoxy-butene diacid. UV absorption wavelength of 2-methoxy-butene diacid was 223 nm. Before 60 min, the reaction of vanillin and laccase was dominant. With time, vanillin reverted, followed by strong absorption of products, verified by the infrared spectrum. There existed a competitive relation between the reaction of -OH and the reaction of C=O all the while. The peak intensity did not change from 60 min to 600 min which showed that the reactions of –OH and C=O were in equilibrium. However, the peak intensities of –OH and benzene ring increased at 1645 cm^{-1} in 720 min. This means that the formation reactions of 2-methoxy-benzenediol and 3,3'-dimethoxy-4,4'-dioxydiphenyl were dominant. After 720 min, the enhancement at 1104 cm^{-1} revealed that 2-methoxy-benzenediol and 3,3'-dimethoxy-4,4'-dioxydiphenyl were generated during this phase. During the whole reaction, the quantities of 2-methoxy-para-benzoquinone and 3,3'-dimethoxy-4,4'-biphenoquinone were small.
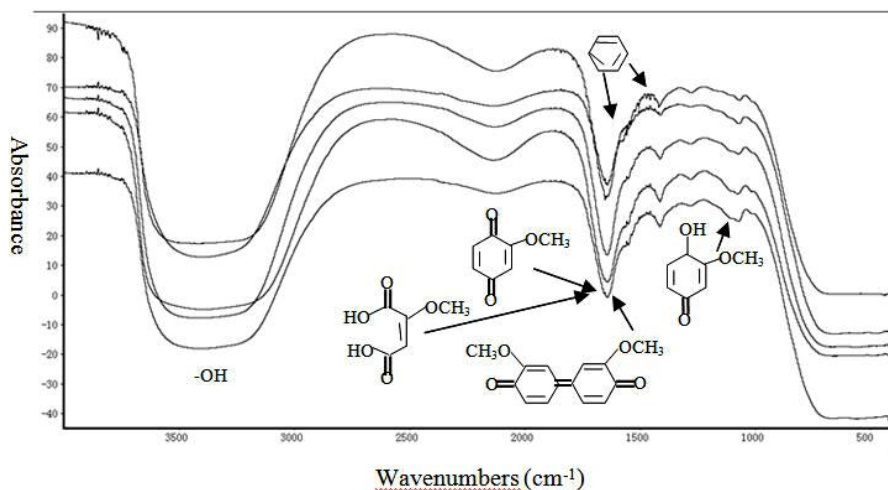
Fig. 7. FTIR spectrum of guaiacol treated by laccase-ABTS system with time.
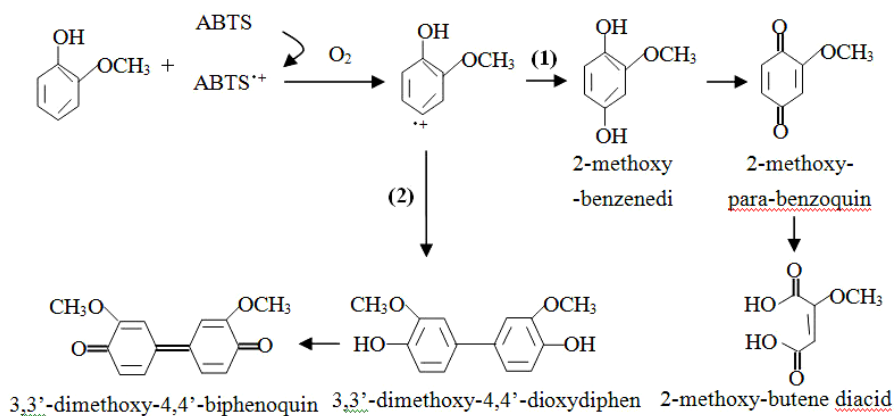
Fig. 8. Reaction process of guaiacol treated by laccase-ABTS system.
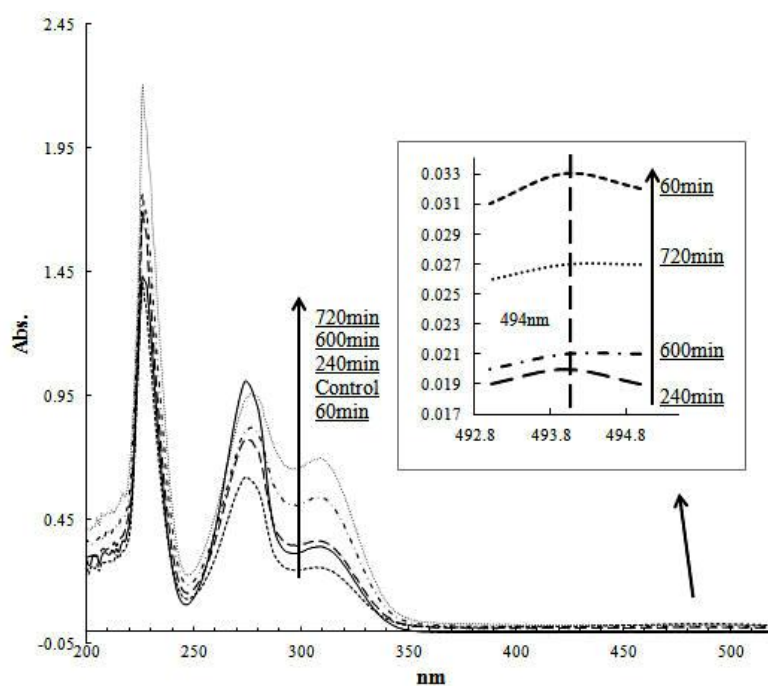
Fig. 9. Absorption of guaiacol treated by laccase-vanillin system with time.
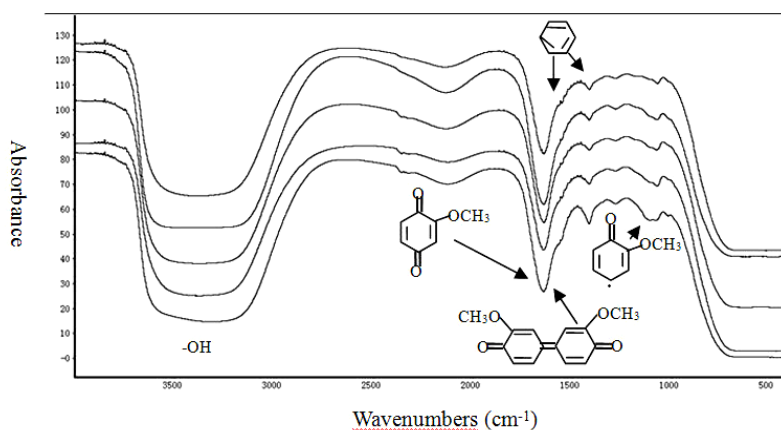
Fig. 10. FTIR spectrum of guaiacol treated by laccase-vanillin system with time
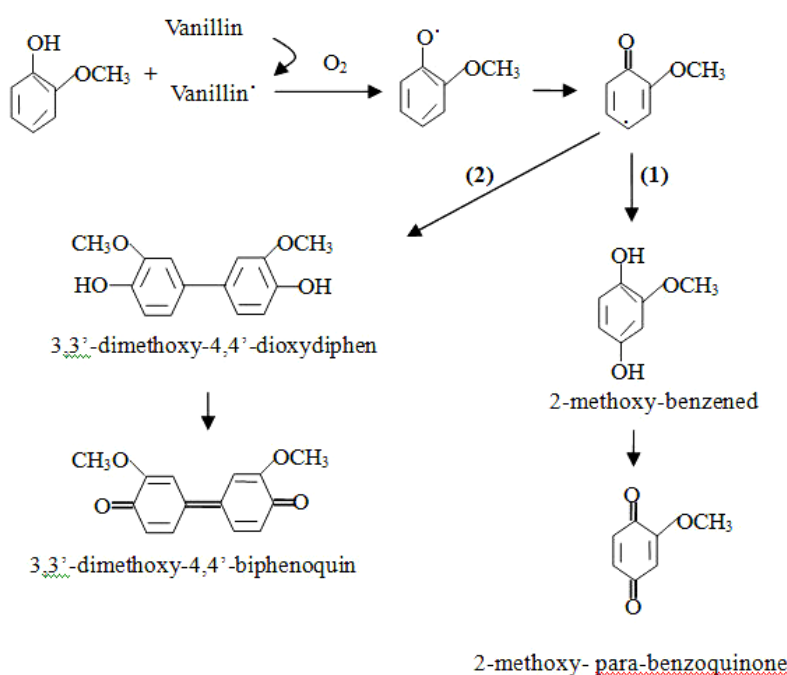
Fig. 11. Reaction process of guaiacol treated by laccase-vanillin system.

Comparative analysis of the different systems

In the laccase system, guaiacol was directly transformed into phenoxy radical, followed by polymerization with ether bond. The product was cracked into unsaturated alkene with time because of the unstability of ether bonds. In the laccase-ABTS system, ABTS reacted preferentially under the action of laccase and oxygen. Then, guaiacol was transformed into 2-methoxy-benzenediol, 2-methoxy-para-benzo-quinone, 3,3'-dimethoxy-4,4'-dioxydiphenyl, 3,3'-dimethoxy-4,4'-biphenoquinone and 2-methoxy-butene diacid by transfer of electron. The main product and the ratio of products were different during the different phases. In the

laccase-vanillin system, vanillin reacted preferentially under the action of laccase and oxygen. Then, guaiacol was transformed into 2-methoxy-benzenediol, 2-methoxy-para-benzo-quinone, 3,3'-dimethoxy-4,4'-dioxydiphenyl, 3,3'-dimethoxy-4,4'-biphenoquinone and 2-methoxy-butene diacid by transfer of hydrogen atom. The main product and the ratio of products were different during the different phases. This showed that the reaction mechanisms of laccase-ABTS system and laccase-vanillin system were different with the same products. Furthermore, the reaction rate of the laccase-vanillin system was slower than that of the laccase-ABTS system.

Comparing the laccase system with th laccase

1160

mediator system, the products were different. The main reaction proceeded by ether bond in the laccase system. However, guaiacol was transformed into quinine, acid and so on in the laccase mediator system. The color of the solution changed from purple to aubergine due to quinine which was the main factor to cause the yellow color.

CONCLUSIONS

To ensure the quality of wood-based panels treated by a laccase system, three conditions must be observed: (1) the surface density of lignin must be sufficient in the raw materials; (2) the process time must be kept within 600 min to prevent lignin degradation; (3) a proper amount of water-resistance agents should be added to overcome the instability of the ether bond.

For the laccase-ABTS system applied in processing of wood-based panels, the quality of wood-based panels was discrepant depending on quinone, phenol, acid and ketone. In the first 60 min, phenoxy radicals were the main product which had no observable effect on the quality of wood-based panels. During the phase from 60 min to 240 min, phenol was the main product which could enhance the dry strength by hydrogen bonds, but had no effect on the wet strength. During the phase from 240 min to 600 min, quinone and ketone were the main products which could enhance both dry strength and wet strength by unsaturated bonds. However, elastic modulus of wood-based panels decreased because of lignin degradation from 600 min to 720 min.

The products of laccase-vanillin system and laccase-ABTS system were similar, but the production rates were different. From 0 min to 600 min, formation and transformation of intermediates was slow. During the phase from 600 min to 720 min, phenol was the main product with small amounts of quinone and ketone. If the reaction continued, a mass of quinone and acid would be generated. This showed that catalytic efficiency of vanillin was significantly lower than that of ABTS at the same concentration. However, vanillin had advantages as regards economic cost and toxic

properties.

REFERENCES

1. O. Atika, M. Erika, S. Rogério, Q, João, J. Emma, *J Anal Appl Pyrolysis*, **78**, 233 (2007).
2. P. Baiocco, A. M. Barreca, M. Fabbrini, C. Galli, P. Gentili, *Org. Biomol. Chem.*, **1**, 191 (2003).
3. R. Bourbonnais, D. Leech, M. G. Paice, *BBA Gen. Subjects*, 1379, 381 (1998).
4. A. Bruce, J. W. Palfreyman, Forest products biotechnology, Taylor and Francis Ltd, London, 1998.
5. S. Kawai, T. Umezawa, M. Shimada, T. Higuchi, K. Koide, T. Nishida, N. Morohoshi, T. Haraguchi, *Mokuzai Gakkaishi*, **33**, 792 (1987).
6. M. Fabbrini, C. Galli, P. Gentili, *J Mol Cat B Enzym*, **16**, 231 (2002).
7. T. Kudanga, G. S. Nyanhongo, G. S. Guebitz, S. Burton, *Enzyme and Microbial Technology*, **48**. 195, 2011.
8. J. Li, S. J. Luan, Biological wood science, Northeast Forestry University Press, Harbin, 1993.
9. A. M. Mayer, R. C. Staples, *Phytochemistry,* **60**, 551 (2002).
10. D. Moldes, M. Díaz, T. Tzanov, T. Vidal, *Bioresource Technology,* **99**, 7959 (2008).
11. K. Murugesan, Y. Y. Chang, Y. M. Kim, J. R. Jeon, E. J. Kim, Y. S. Chang, *Water Research*, **44,** 298 (2010).
12. L. K. Reshma, V. S. G. Thanga, R. P. Murugan *Research Journal of Biotechnology,* **2**, 21 (2007).
13. K. K. Sharma, R. C. Kuhad, *Indian J Microbiol,* **48**, 309 (2008).
14. L. Tetsch, J. Bend, U. Holker, A. Van Leeuwenhoek, *International Journal of General and Molecular Microbiology*, **90**, 183 (2006).
15. C. F. Thurston, *Microbiology*, **140**, 19 (1994).
16. H. Yoshida, *J. Chem. Soc*, **43**, 472 (1983).

КАТАЛИТИЧНА ПОЛИМЕРИЗАЦИЯ НА ЛИГНИНОВИ МОДЕЛНИ СЪЕДИНЕНИЯ С ИЗПОЛЗВАНЕ НА ЛАКАЗА И МЕДИАТОРИ

Кс. Гуан[1*,2], М. Гуо[2], Дж. Лин[1], Дж. Ли[1], Кс. Лю[1]

[1]*Колеж по материалознание, Аграрен и горски университет във Фуджиян, Фуджоу, Провинция Фуджиян, Китай*

[2]*Ключованаучно-технологичналабораторияпоматериалинабиологичнаоснова, Министерство на образованието, Североизточен горски университет, Харбин, Провинция Хейлонгджиян, Китай*

(Резюме)

Концепцията на биотехнологиите и опазването на околната среда дава възможност за пълно използване на лаказата за биологично изработване на панели на дървесна снова. Продуктите, генерирани в различни фази от процеситевлияят различно на свойствата на дървесните материали. Разгледани са подобието и разликите в изкуствените и естествените медиаторни системи с лаказапри еднакви реакционни условия. Като обект на изследване за получаването на панели на дървена основа са взети моделни лигнинови съединения. Резултатите показват, че продуктите полимеризират чрез етерни връзки и при продължителна реакция се стига до разлагане на бензен с образуване на олефини. От друга страна продуктите на полимеризацията чрез водородни връзки и/или ненаситени връзки в медиаторната система на лаказата води до ненаситеникарбоксилни киселини. Различните типове химични връзки и продукти влияят различно на физичните и механичните свойства на панелите. В сравнение с изкуствените медиатори, естествените имат ниска цена, ниска токсичност и ниска каталитична активност.

Simultaneous determination of nonylphenol and short-chain nonylphenolpolyethoxylates by DLLME-HPLC

Y. Xie[1,*], A. Wei[2], Y. Pan[3], Z. He[4], Q. Li[5], Y. Xu[5], T. Zhu[1]

[1]*School of Mechanical Engineering and Automation, Northeastern University, Shenyang 110004, China*
[2]*Shenshuiwan Wastewater Treatment Plant, Guodian Northeast Environment Industry Group Co. Ltd, Shenyang 110141, China*
[3]*Sinosteel Anshan Research Institute of Thermo Energy Co., Ltd, Anshan 114004, China*
[4]*Liaoning Academy for Environmental Planning Co., Ltd, Shenyang 110031, China*
[5]*College of Sciences, Northeastern University, Shenyang 110004, China*

A method for the simultaneous determination of nonylphenol (NP) and short-chain nonylphenolpolyethoxylates (SCNPEOs) in water samples by dispersive liquid-liquid microextraction - high performance liquid chromatography (DLLME-HPLC) was developed. The six components of NP and SCNPEOs (n=1, 2, 3, 4, 5) were simultaneously extracted and enriched under the optimized microextraction conditions with enrichment factors of 86, 106, 93, 84, 76, and 62, respectively. The six components were simultaneously determined within 18 min under the optimized chromatographic conditions. The working curves of the six components are characterized with a linear concentration range of up to 3 orders of magnitude, correlation coefficients from 0.9991 to 0.9999 and detection limits ranging from 0.09 to 2.1 ng/mL. The spike recoveries and relative standard deviations (RSD) of this method were 88.9%~117% and 1.9%~4.3%, respectively.

Key words: dispersive liquid-liquid microextraction, high performance liquid chromatography, nonylphenol, short-chain nonylphenolpolyethoxylates, simultaneous determination.

INTRODUCTION

Recently, it was discovered that only a very small dosage of environmental endocrine disruptors could interact with the endocrine system of the receiver by seriously threatening humans' health [1]. Therefore, the monitoring of hormone-like substances in the environment attracted increasing attention.

Nonylphenol (NP) and short-chain nonyl-phenolpolyethoxylates (SCNPEOs, n=1, 2) are typical environmental hormones [2]. Most of them present in the environment are biodegradation products of nonylphenolethoxylates (NPEOs, n=1~20). NPEOs are stable, hard to hydrolyze, easy to dissolve in organic solvents, and gradually degrade++-+ to NP and SCNPEOs [3-8]. Studies [9-11] showed that NP and SCNPEOs had an estrogen-like property that could disrupt the endocrine and neuroendocrine systems of organisms, and therefore could affect reproductive development, reduce immunity and increase cancer risk. The harm of NP and SCNPEOs to organism, especially to human, obviously increased. Thereby, the detection and monitoring of NP and SCNPEOs in the environment had become a public focus.

Currently gas chromatography-mass spectro-metry (GC-MS) and high performance liquid chromatography (HPLC) are the main methods for NP and NPEOs detection [12,13]. GC-MS is suitable for the analysis of low-molecular compounds such as NP and NPEOs (n <4). But the high cost of GC-MS hinders its extensive application. Due to the presence of NP5EO in the water samples, HPLC was selected to detect the NP and SCNPEOs in this study.

NPEOs are usually in trace amounts in water samples and enrichment must be performed before instrumental analysis. Solid phase extraction has poor reproducibility; ordinary liquid-liquid extraction has a low enrichment factor. To solve this problems, dispersive liquid-liquid micro-extraction (DLLME) was adopted as pretreatment to enrich the samples. DLLME has good reproducibility and high enrichment factor. It could improve the detection sensitivity and lower the detection limit and was therefore suitable for the enrichment of NP and SCNPEOs in water samples.

In this study, the DLLME technology was used as a pretreatment method to enrich the NP and SCNPEOs before HPLC measurement. The new combined DLLME - HPLC method was developed to simultaneously determine NP and SCNPEOs in water samples.

---

* To whom all correspondence should be sent:
E-mail: islandxyh@yeah.net

EXPERIMENTAL SECTION

Instruments and reagents

The pH meter was PHSJ-3F type from Shanghai Leici, China. Refrigerating centrifuge was SIGMA-3k15 type from Sigma, Germany. HPLC was Waters 2695 type from Waters, USA, combined with 2487 UV detector and Hypersil APS-2 amino chromatographic column (250*4.6 mm, 5 μm, Thermo Electron, USA).

N-hexane (C_6H_{14}), isopropanol (C_3H_8O), methylene chloride (CH_2Cl_2), methanol (CH_3OH) and acetonitrile (C_2H_3N) were chromatographically pure chemicals from Tianjin Concord, China. Acetone (C_3H_6O), carbon tetrachloride (CCl_4) and chloroform ($CHCl_3$) were analytically pure chemicals from Tianjin Damao, China. Standard NP and SCNPEOs (average n≈2) reagents were from TCI (Shanghai), China.

Experimental methods

The water sample was centrifuged for 5 min at 6000 r/min. The supernatant was filtered through a 0.45 μm organic membrane. 0.5 g sodium chloride (NaCl) was added into 8 mL permeate. After complete dissolution, a mixture of 80 μL carbon tetrachloride and 0.6 mL methanol were quickly added to the permeate. The mixed permeate was treated by ultrasound for 3 min and was then centrifuged for 5 min at 4500 r/min. After centrifugation, the lower organic phase was moved into a glass cannula using a microsyringe. The glass cannula was put into the lidded sample bottle which was then put at the designated position of the sample tray for measurement.

RESULTS AND DISCUSSION

Determination of DLLME parameters

DLLME is equivalent to miniaturized liquid-liquid extraction. It is characterized by simple operation, low cost, high enrichment factor and small dosage of organic solvent. As a kind of environmentally friendly liquid phase microextraction technique, DLLME is increasingly used for sample preparation in chromatography measurements. In DLLME process, extractant type and dosage, dispersant type and dosage, salt dosage, pH and ultrasound-assisted extraction time needed to be optimized. The volume of the water sample used in this study was 8 mL.

Extractant and its dosage

In DLLME process, the type of extractant is one of the most important parameters that affects the enrichment factor. Methylene chloride, chloroform and carbon tetrachloride were used as extractants in this study. The results in Fig. 1 show that all three extractants had good extraction properties. Carbon tetrachloride presented a little higher effect on the six target objects and had no influence on component separation and HPLC measurement. So carbon tetrachloride was selected as the extractant.
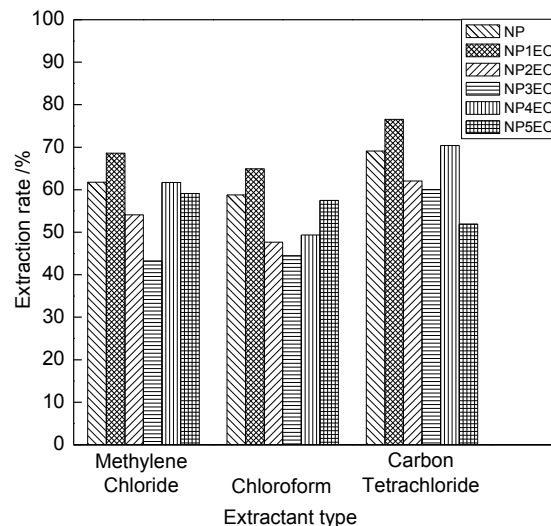
Fig. 1. The influence of extractant type on the extraction rate.

Furthermore, the extractant dosage also affects the enrichment factor of the target objects. Smaller extractant dosage means higher sensitivity. But too small extractant dosage can lead to incomplete extraction and troubles with organic phase separation. Different volumes (80, 100, 150, 200 μL) of carbon tetrachloride were added to the water samples (8 mL) to investigate its effect on extraction efficiency and enrichment factor (Fig. 2).
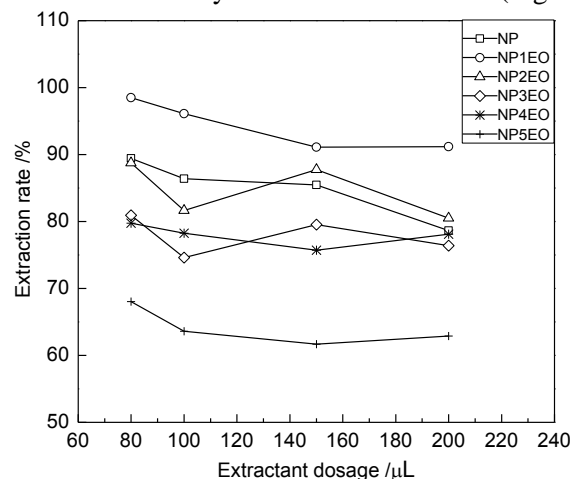
Fig. 2. The influence of extractant dosage on extraction rate.

The extraction efficiencies of NP, NP2EO and NP5EO obviously decreased on increasing extractant dosage. With carbon tetrachloride volume of 80 μL, the best extraction efficiencies of

all components were achieved. So the extractant dosage was eventually determined as 80 μL.

Dispersant and its dosage

In DLLME process, the dispersant should not only have a good solubility in the extractant but also be miscible with water, and thus play a bridging role in the system. An appropriate dosage of dispersant contributes to the formation of a homogeneous water/dispersant/extractant system. An appropriate dispersant with appropriate dosage can significantly increase the extraction efficiency of the components. Isopropanol, acetonitrile, acetone, and methanol were used as dispersants to investigate the extraction efficiency of the components. The results showed that acetone seriously interferes with the analysis. Therefore the extraction efficiency with acetone was not further investigated.

The results in Fig. 3 show that the three dispersants have similar extraction effects. Methanol presented the best effect of more than 60% on the six target objects. So methanol was selected as the dispersant. Different volumes (0.2, 0.4, 0.6, 0.8, 1 mL) of methanol were added to the water samples (8 mL) to investigate its effect on extraction efficiencies (in Fig. 4). The extraction efficiencies increased on increasing dispersant dosage in the range of 0.2~0.6 mL. But in the range of 0.6~1 mL, the extraction efficiencies showed slight variations and even downward trends for some components. So the dispersant dosage was eventually determined as 0.6 mL.
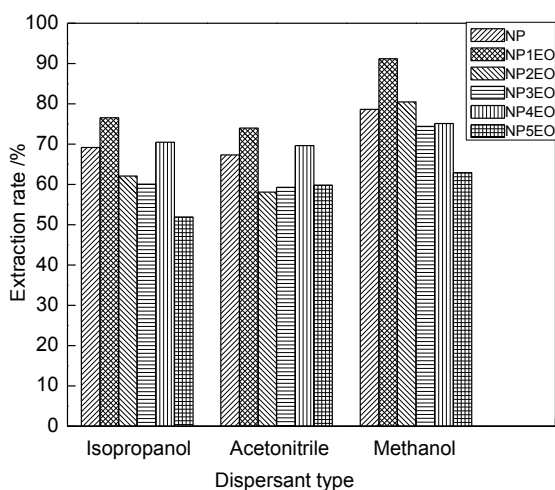
Fig. 3. The influence of dispersant type on extraction rate.

Salt dosage

The addition of an appropriate amount of sodium chloride (NaCl) during extraction can reduce the solubility of components and extractant in the liquid phase, increase the ionic strength of the sample, decrease emulsification, and thus increase the extraction efficiency. The effect of different amounts of salt on the extraction efficiency of the components was investigated. Different amounts (0.1, 0.2, 0.3, 0.4, 0.5 g) of salt were added to the extraction system. The results in Fig. 5 show that the salt dosage didn't notably affect the extraction efficiency. But with increasing salt dosage, emulsification significantly decreased. So, the salt dosage was determined to 0.5 g in the study.
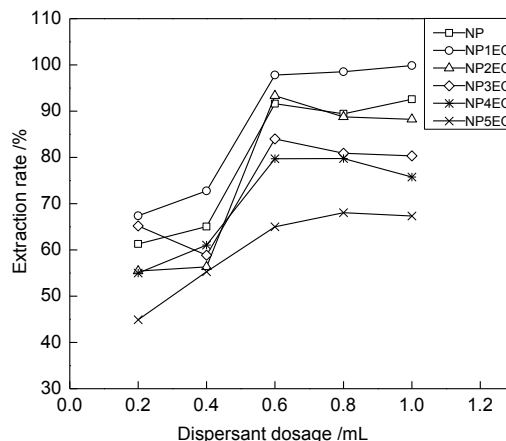
Fig. 4. The influence of dispersant dosage on extraction rate.
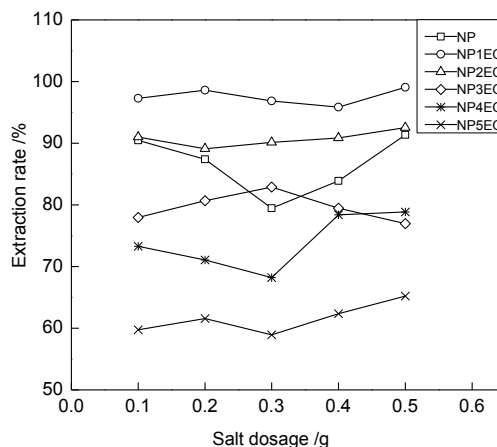
Fig. 5. The influence of salt dosage on extraction rate.

Determination of sample pH

The pH value of the sample system can affect the existence form of the test substance. An appropriate pH value can benefit the process of extraction and improve the extraction efficiency. The extraction efficiency of each component was measured at pH values of 5.0, 6.0, 7.0, 8.0, and 9.0. The results in Fig. 6 show that the extraction efficiency of the components is relatively higher in the pH range from 6 to 8. In this study, the pH values of the samples were 6.5~7.8 and no pH adjustment was needed.
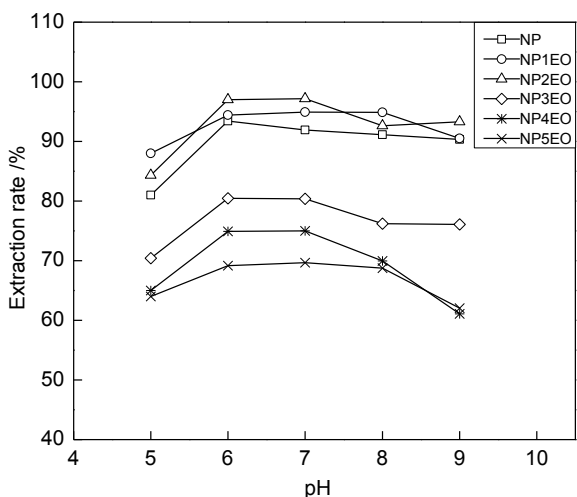
Fig. 6. The influence of pH on the extraction rate.

Ultrasound-assisted extraction time

Ultrasound can promote the contact and mixing of extractant and sample solution, and thus improve the extraction efficiency. But overlong ultrasonication time may increase the volatilization of reagents and cause emulsification, and thus affect the extraction efficiency. The effect of ultrasound-assisted extraction time on the extraction efficiency of the components was investigated (Fig. 7). The results indicated that on increasing the ultrasonication time, the extraction efficiency of each component showed a rising trend. Except for NP4EO, the other five components reached the highest extraction rate with 3 min of ultrasonication. The extraction rate began to decrease when the ultrasonication time was 4 min. The optimal ultrasonic time was 3 min in this study.
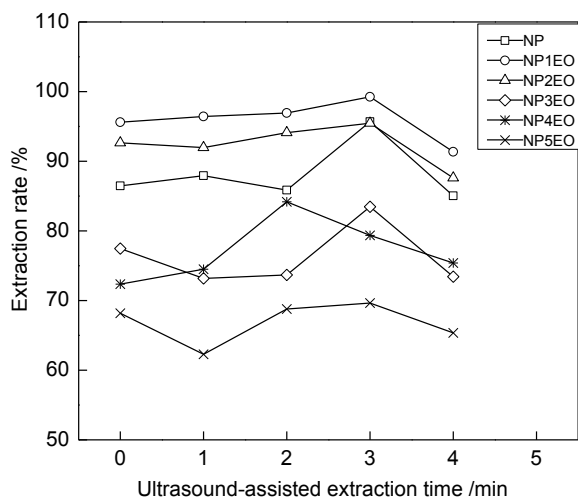
Fig. 7. The influence of ultrasound-assisted extraction time on extraction rate.

Under the above optimal DLLME pretreatment parameters (water sample volume of 8 mL, carbon tetrachloride extractant of 80 μL, methanol dispersant of 0.6 mL, ultrasound-assisted extraction time of 3 min, salt dosage of 0.5 g), the effective enrichment factors of NP, NP1EO, NP2EO, NP3EO, NP4EO and NP5EO were 86, 106, 93, 84, 76 and 62, respectively.

HPLC measurement

HPLC operational parameters

In this study, mobile phase mixture ratio and change rate, UV detection wavelength, flow velocity, injection volume and column temperature were optimized as follows: mobile phase of isopropyl (A)-n-hexane (B)-methylene chloride (C), gradient elution procedure (Table 1), UV detection wavelength of 277 nm, flow velocity of 1.0 mL/min, injection volume of 10 μL and column temperature of 35 °C.

Table 1. Gradient elution program

Time (min)	A%	B%	C%
0	7	92	1
5	7	92	1
8	75	24	1
11	75	24	1
13	7	92	1
18	7	92	1

The chromatogram of NP and SCNPEOs standard solution under the optimal operation parameters is shown in Fig. 8. The results show that each component is clearly separated. The peak shapes meet the experimental requirement.

Working curve and detection limit

Different amounts of the standard solution were added to blank water samples. After DLLME enrichment and HPLC measurement, the working curves of NP, NP1EO, NP2EO, NP3EO, NP4EO and NP5EO were obtained. The detection limits of the six components were simultaneously determined. The detailed results are shown in Table 2. It follows from the results that the linear concentration range of each component was up to 3 orders of magnitude. The correlation coefficients were from 0.9991 to 0.9999 and the detection limits ranged from 0.09 to 2.1 ng/mL. This means that the method is stable, accurate, and can be used for the analysis of real samples.
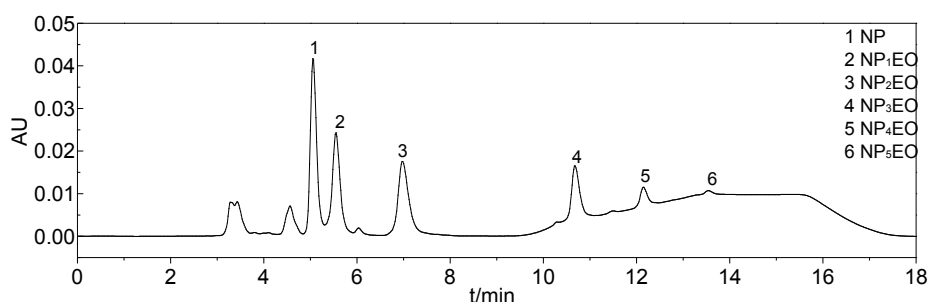
Fig. 8. Chromatogram of NP and SCNPEOs standard solution

Table 2. Regression equation, correlation coefficient, linear range and detection limit of 6 components.

Component	Linear equation	Correlation coefficient	Linear range (µg/mL)	Detection limit (ng/mL)
NP	Y=387588x+28346	0.9991	0.005~10	1.5
NP1EO	Y=302278x+36103	0.9992	0.007~6.5	2.1
NP2EO	Y=255272x+13869	0.9996	0.004~7.7	1.2
NP3EO	Y=240353x-705.36	0.9992	0.005~2.3	1.5
NP4EO	Y=217875x+1030.5	0.9998	0.001~1.3	0.3
NP5EO	Y=200798x+945.47	0.9999	0.0003~0.3	0.09

Table 3. Spike recoveries of water sample.

Component	Original (µg/mL)	Added (µg/mL)	Recovered (µg/mL)	Recovery (%)	RSD (%)
NP	1.05	0.500, 1.00, 1.50	1.58, 1.99, 2.61	106, 94.0, 104	1.9, 2.2, 3.2
NP$_1$EO	1.49	1.31, 1.96, 3.27	2.74, 3.50, 4.78	95.4, 103, 101	3.5, 4.1, 4.3
NP$_2$EO	2.65	1.53, 2.30, 3.84	4.17, 4.90, 6.51	99.3, 97.8, 101	4.2, 3.3, 2.8
NP$_3$EO	1.89	0.93, 1.39, 2.32	2.85, 3.30, 4.25	103, 101, 102	3.1, 3.4, 2.8
NP$_4$EO	0.48	0.26, 0.38, 0.64	0.73, 0.89, 1.14	96.2, 108, 103	2.7, 1.9, 2.5
NP$_5$EO	0.09	0.06, 0.09, 0.15	0.16, 0.17, 0.25	117, 88.9, 107	4.2, 4.3, 3.8

Spike recoveries

High, medium and low concentrations of the standard solution were added to the water samples to study spike recoveries, the results are showed in Table 3. The spike recoveries were from 88.9% to 117% and the relative standard deviations (RSD) were less than 5%, showing that the method was accurate, reliable, and appropriate for common analytical testing.

CONCLUSIONS

A method for the simultaneous determination of NP and SCNPEOs in water samples by DLLME-HPLC was developed. The DLLME pretreatment parameters were determined as water sample volume of 8 mL, carbon tetrachloride extractant of 80 µL, methanol dispersant of 0.6 mL, ultrasound-assisted extraction time of 3 min and salt dosage of 0.5 g. The HPLC operation parameters offering wide linear concentration range, low detection limits, good correlation coefficients, high spike recovery and low RSD were also determined. This method can be applied to the separation and determination of NP and SCNPEOs from microbial and bacterial degradation water. The combined method is sensitive, accurate, and friendly to the environment.

REFERENCES

1. A. Miodovnik, *Mount Sinai Journal of Medicine*, **78**, 58 (2011).
2. Y. J. Zhou, X. Huang, H. D. Zhou, *Water Sci. Technol.*, **64**, 2096 (2011).
3. Z. J. Yue, W. Y. Li, *Heilongjiang Environmental*

Journal, **36**, 35 (2012). (In Chinese)

4. E. Calvo, R. Bravo, A. Amigo, *J.Gracial-Fadrique,Fluid Phase Equilibria*, **282**, 14 (2009).
5. P. Navarro, J. Bustamante, A. Vallejo, A. Prieto, A.Usobiaga, S.Arrasate, E.Anakabe, E. Puy-Azurmendi, O. Zuloaga, *Journal of Chromatography A*, **1217**, 5890 (2010).
6. M. J. Lopez-Espinosa, C. Freire, J. P. Arrebola, N. Navea, J. Taoufiki, M. F. Fernandez, O. Ballesteros, R. Prada, N. Olea, *Chemosphere,* **76**, 847 (2009).
7. A. K. Venkatesan, R. U. Halden, *Environmental Pollution*, **174**, 189 (2013).
8. R. A. Rudel, L. J. Perovich, *Atmospheric Environment*, **43**, 170(2009).
9. Q. T. Gao, Y. S. Wong, N. F. Y. Tam, *Marine Pollution Bulletin*, **63**, 445 (2011).
10. L. L. Chang, W. S. Alfred Wun, P. Wang, *Chemico-Biological Interactions*, **195**, 11 (2012).
11. Y. H. Xie, X. J. Li, C. S. Xu, L. T. Lv, Y. N. Zhu, J. Han, M. Y. You, T. Zhu, J. *Chem. Pharm. Res.*, **5**, 424 (2013).
12. M. E. G. C. Silva, A. L. Guimarães, A. P. Oliveira, C. S. Araújo, J. A. S. Filho, A. P. Fontana, P. K. F. Damasceno, C. R. C.Branco, A. Branco, J. R. G. S Almeida1, *J. Chem. Pharm. Res.*, **4**, 1160 (2012).
13. U. S. Baghel, M.Singhal, M. M.Gupt, H. P. Singh, S. Dave, M. Sahu, *J. Chem. Pharm. Res.*, **1**, 271 (2009).

ЕДНОВРЕМЕННО ОПРЕДЕЛЯНЕ ЧРЕЗ DLLME-HPLC НА НОНИЛ-ФЕНОЛ И НОНИЛ-ФЕНОЛ-ПОЛИЕТОКСИЛАТИ С КЪСА ВЕРИГА

Ю. Ксие[1,*], А. Уей[2], Я. Пан[3], Ж. Хе[4], К. Ли[5], Й. Ксу[5], Т. Жу[1]

[1]*Училище за машинно инженерство и автоматизация, Североизточен университет, Шенянг, Китай*
[2]*Станция за пречистване на отпадъчни води в Шеншуйван, Североизточна екологично-промишлена група в Гуодиан, Шенянг, Китай*
[3]*Изследователски институт по термоенергия „Синостийл“ ООД, Аншан, Китай*
[4]*Академия за екологично планиране Ляонинг ООД, Шенянг, Китай*
[5]*Колеж за наука, Североизточен университет, Шенянг, Китай*

(Резюме)

Създаден е метод за едновременно определяне на нонил-фенол (NP) и нонил-фенол-полиетоксилати с къса верига (SCNPEOs) във водни проби чрез дисперсивна течно-течна микроекстракцияивисоко-ефективна течна хроматография (DLLME-HPLC).Шестте компонентиот NP и SCNPEOs (n=1, 2, 3, 4, 5) са екстрахирани едновременно и обогатени чрез оптимизирана микро-екстракция. Факторите на обогатяване са съответно 86, 106, 93, 84, 76и 62. Шестте компонента са определени едновременно в продължение на 18 минути при оптимизирани хроматографски условия. При тези условия калибрационните линии са прави в рамките на три порядъка от концентрации с корелационни коефициенти от 0.9991 до 0.9999 и предели на откриване от 0.09 до 2.1 ng/mL. Добивите при инжектиранеи относителното стандартно отклонение достигат съответно 88.9%~117% и 1.9%~4.3%.

IL-assisted synthesis of mesoporous AgCl/MCM-41 microspheres and their photodegradation properties

H. Q. Zhang[1*], Q. Wu[1], J. F. Gao[1], H. L. Chen[1], Z. K. Xuan[1]

[1]*Department of Chemistry, Hebei Normal University for Nationalities, 067000, Chengde, P.R.China*

Hybrid mesoporous MCM-41 microspheres were prepared using N-(trimethoxysilanepropyl) imidazole hydrochloride ionic liquid, then AgCl materials were *in-situ* deposited on the surface of the mesoporous MCM-41 by inducing Cl⁻ in the ionic liquid. AgCl on the mesoporous MCM-41 microspheres was of high dispersion, and the composite displayed an especial pore size distribution with two maximum values centered at 4.0 nm and 7.9 nm. The final loaded amount of AgCl in MCM-41 may be changed by using different amounts of N-(trimethoxysilanepropyl) imidazole hydrochloride. The AgCl materials on MCM-41 possess higher catalytic performance than AgCl bulk materials in the photogradation of dyes such as methyl orange, isatin, methylene blue and congo red.

Key words: mesoporous silica, AgCl, photogradation, ionic liquid.

INTRODUCTION

AgCl materials are used as photosensitive materials in photographic films. It has been found that AgCl supported under UV/Vis illumination can photocatalyze O_2 production from water [1-3]. Recently, AgCl particles with silver NPs were testified as an active and stable photocatalyst under visible light [4]. Further investigations have shown that the morphology of Ag@AgCl nanoparticles has a great influence on their photocatalytic properties, and different morphologies directly determine the photocatalytic activity because of different surface areas [5]. With the exception of the direct preparation of high-surface AgCl materials, the loading method is another efficient way to obtain AgCl nanoparticles with high surface. It has been reported that AgBr dispersed on an Al-MCM-41 support is an effective visible-light photocatalyst for the decomposition of acetaldehyde [6].

Room temperature ionic liquids (RTILs) as special solvents or reactants have been successfully applied in the synthesis of nano- and microstructured inorganic materials [7]. Grafted ionic liquids on solid materials were attracting more attention owing to their special application in catalysis, electrochemistry and adsorption [8-10]. Moreover, the desirable materials can also be introduced by exchanging the anion in the grafted ionic liquid, and the resultant active materials often displayed high dispersion and density. Recently, Pt precursors with negative charge were enriched on the surface of supporting materials by this method, which resulted in the formation of high-density Pt nanoparticles [11-12]. Wang and coauthors have also developed a facile procedure to synthesize carbon nanotubes/ILs/Pt hybrids using amine-terminated imidazolium ionic liquid as a linker [13].

In the present work, we attempted to obtain AgCl materials in high dispersion on mesoporous MCM-41 by using the N-(trimethoxysilanepropyl) imidazole hydrochloride ionic liquid as an induced reactant. The investigation results confirmed that the hybrid mesoporous MCM-41 synthesized by the direct method showed microspheric morphology after the addition of N-(trimethoxysilanepropyl) imidazole hydrochloride ionic liquid and AgCl nanoparticles in high dispersion were *in-situ* prepared through the reaction of Ag^+ with Cl^- in the ionic liquid. The catalytic performance of AgCl materials on mesoporous MCM-41 under UV/Vis illumination exceeded that of AgCl bulk materials in the photogradation of dyes.

EXPERIMENTAL SECTION

Synthesis of 3(N-imidazolyl)propyltrimethoxysilane hydrochloride ionic liquid

3 (N-imidazolyl) propyltrimethoxysilane hydrochloride was prepared as follows [14]: a 6.8 g sample of imidazole was added into a 250 ml three-necked flask containing 100 ml of dried toluene, and then the mixture was heated to 383K in N_2 atmosphere. After that, 18.4 ml of (3-chloropropyl) trimethoxysilane liquid was added, and the resultant solution was further heated at the circumfluent temperature for 12 h. The

bottom layer liquid was separated, washed with hot toluene, and the final 3(N-imidazolyl) propyltrimethoxysilane hydrochloride product was obtained by removing the toluene.
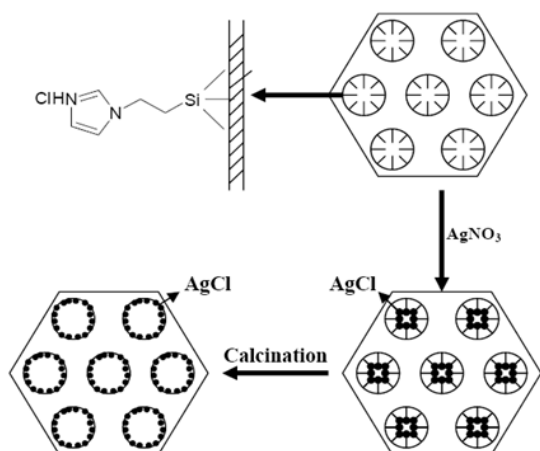
Scheme 1. The synthesis of Ag@AgCl/MCM-41 photo catalyst.

Synthesis of modified mesoporous MCM-41 microspheres and AgCl /MCM-41 materials

In a typical synthesis for mesoporous hybrid MCM-41, 0.87 g of cetylmethylammonium bromide (CTAB) was added to a solution containing 41 g of deionized water and 10.5 g of 25 wt% $NH_3 \cdot H_2O$ under vigorous stirring. Then 0.53 g of as-prepared 3 (N-imidazolyl) propyltrimethoxysilane hydrochloride ionic liquid and 3.7 g of tetraethylorthosilicate (TEOS) were added to the above mixture. The ionic liquid:TEOS molar ratio is 0.1:0.9 in this synthesis. The resulting solution was stirred at 353K for two days. The product was filtered, washed with water, and dried overnight at room temperature. The CTAB template was removed by solvent extraction and the resultant sample was referred to as 10wt%-MCM-41. 5wt%-MCM-41 and 20wt%-MCM-41 mesoporous hybrid MCM-41 samples were also prepared using a similar preparation process with a different ionic liquid:TEOS molar ratio (0.05:0.95 and 0.2:0.8).

For the synthesis of the AgCl/MCM-41 material, 1 g of hybrid mesoporous MCM-41 sample was added into 150 ml of alcohol-water (1:1 vol.) solution of 0.075M $AgNO_3$ and stirred for 1 h in dark. The AgCl/MCM-41 product was obtained by further calcination at 623K for 4 h, with a heating rate of 1K/min.

Photodegradation properties of AgCl /MCM-41 materials

Photodegradation experiments were carried out in a cylindrical Pyrex glass cell, and were performed at 298 K under constant stirring. In a typical photodegradation experiment, a 0.1 g AgCl/MCM-41 sample was placed in a 150 ml aqueous solution containing dyes (10 mg/L methyl orange, 20 mg/L isatin, 10 mg/L congo red, 5 mg/L methyl blue and 5 mg/L rhodamine B). Before irradiation, the reaction system was equilibrated for 30 min to allow absorption of the dye molecules. The suspended solution was irradiated with a 250W middle-pressure mercury lamp (wavelength >290 nm) surrounded by cooling water circulation, while magnetically stirred. The absorbance of the solution during the photodegradation experiment was determined by visible spectrophotometry. The degradation ratio of dyes was represented as:

$$C_t = 1-C/C_0 = 1-A/A_0$$

(t is the irradiation /photodegradation time; A_0 is the absorbance value after the adsorption equilibrium, A is the absorbance value after the photodegradation of dyes).

Characterizations

The X-ray diffraction patterns of all samples were collected in θ–2θ mode using a Rigaku Corporation D/MAX 2200PC diffractometer (Cu Kα radiation; λ= 0.154 nm). The porous textures of the mesoporous materials were evaluated from nitrogen adsorption–desorption isotherms at 77 K using a Micromeritics ASAP 2000 system. Surface areas were determined according to the BET method, while the pore size distributions were calculated from the desorption isotherm using the BJH model. Transmission electron microscopy (TEM) was performed with JEM-2010 electron microscope operated at 200 kV. Infrared spectra (FT-IR) were recorded on a Nexus-870 Fourier-transform spectrophotometer from KBr pellets in the range 400–4000 cm^{-1}. The amount of Ag in the synthesized samples was determined by ICP-AES analysis on a Thermo Elemental PERKIN ELMER PLASMA-2000 spectrometer. UV–VIS diffuse reflectance spectra were measured with a JASCO UV550 UV–VIS absorption spectrometer.

RESULTS AND DISCUSSION

X-ray diffraction

The powder X-ray diffraction pattern of the hybrid mesoporous silica from 1◦ to 10◦ (2θ) exhibited similar reflections to siliceous MCM-41 with hexagonal structure (Figure 1 a), and the low-angle XRD patterns of AgCl modified 10wt%-MCM-41 sample did not reveal remarkable changes (Figure 1 b and c). The diffraction peaks assigned to AgCl were also observed in the high-angle patterns of as-prepared

AgCl/10wt%-MCM-41. These peaks had slightly increasing intensity after heat treatment in air owing to the growing-up of AgCl crystals. However, there are no diffraction peaks ascribed to Ag metal in the high-angle XRD, while a darkening color was observed for the AgCl modified sample which indicates trace amounts of Ag metal in the sample.
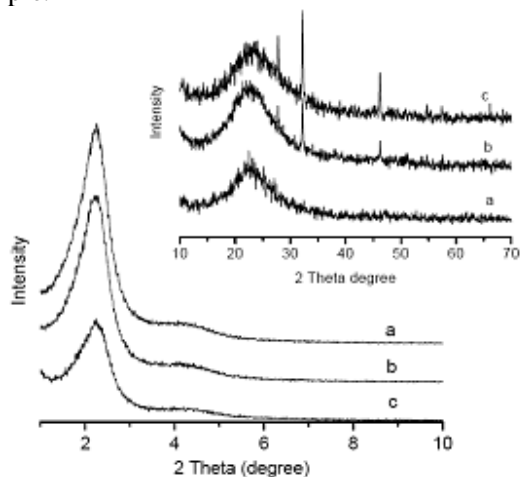
Fig. 1. Low-angle and high-angle (inset) XRD patterns of 10wt%-MCM-41(a), as-prepared AgCl/10wt%-MCM-41(b) and calcined AgCl/10wt%-MCM-41(c)

The X-ray diffraction patterns of AgCl modified 5wt%-MCM-41 and 20wt%-MCM-41 were also recorded (Fig. 2).
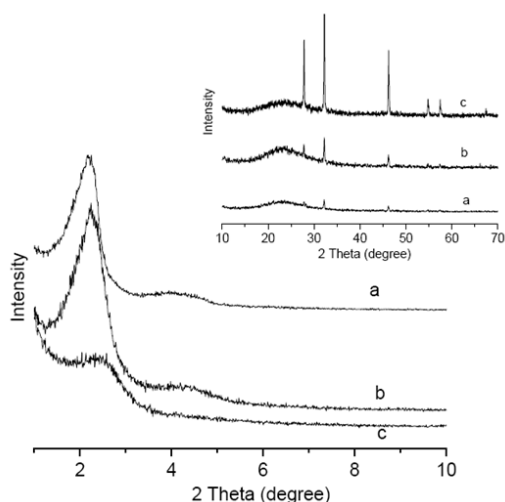
Fig. 2. Low-angle and high-angle (inset) XRD patterns of the calcined AgCl/5wt%-MCM-41(a), AgCl/10wt%-MCM-41(b) and AgCl/20wt%-MCM-41(c).

The calcined AgCl/5wt%-MCM-41 has the same low-angle diffraction pattern as that of AgCl/10wt%-MCM-41, and high angle peaks assigned to AgCl showed lower intensity. Moreover, the low-angle XRD (100) peak of AgCl/20wt%-MCM-41 testified a shift to larger

degrees and the peaks at 4-6° disappeared, suggesting a decreasing order in the mesostructure of AgCl/20wt%-MCM-41 because of the increasing use of 3(N-imidazolyl) propyltrimethoxysilane hydrochloride ionic liquid. The increasing amount and particle size of AgCl in the AgCl/20wt%-MCM-41 samples resulted in a stronger XRD reflection of AgCl in the intensity.

UV-vis DRS and the loaded amount

The UV/Vis diffuse-reflectance spectra of the prepared AgCl loaded mesoporous MCM-41 are shown in Figure 3.
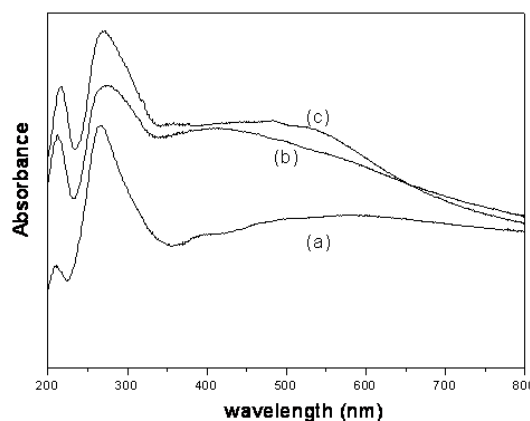
Fig. 3. UV-vis DRS of the calcined AgCl/5wt%-MCM-41(a), AgCl/10wt%-MCM-41(b), AgCl/20wt%-MCM-41(c).

As pure MCM-41 mesoporous silica material is almost transparent in the range of 200–800 nm, the absorption at 290 nm in the UV spectrum of as-prepared AgCl/10wt%-MCM-41 may mainly comes from AgCl. On calcination, the ionic liquid molecule grafted on the MCM-41 surface is eventually removed, and well-dispersed AgCl on MCM-41 is obtained. The Ag^0 could be formed during carbonization and removal of ionic liquid molecule since a reducing environment could be present in the pores under these conditions. A strong absorption in the visible region was observed in the calcined AgCl/10wt%-MCM-41 sample, which was attributed to the plasmon resonance of silver nanoparticles deposited on AgCl particles [4]. Furthermore, the absorption intensity in the UV and visible region increased with increasing of the added amount of ionic liquid. The loaded amount of elemental Ag in the AgCl modified silica materials is 1.27wt% (for 5wt%-MCM-41), 4.69%(for 10wt%-MCM-41) and 12.02wt% (for 20wt%-MCM-41), according to the ICP-AES analysis.

TEM images

TEM images of AgCl/10wt%-MCM-41 and

AgCl/20wt%-MCM-41 (Figure 4) reveal the typical hexagonal mesostructure of MCM-41 over a large area, in agreement with the low-angle XRD of these samples.
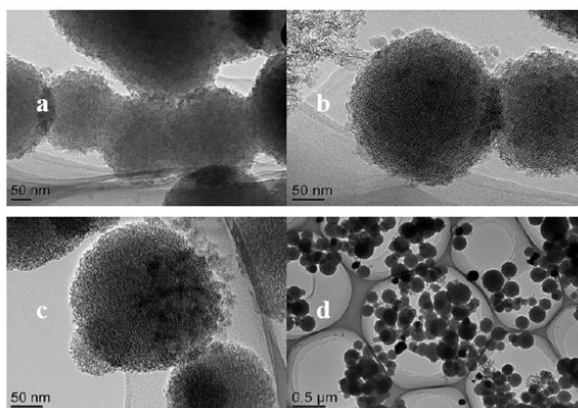
Fig. 4. TEM images of AgCl/10wt%-MCM-41 (a and b) and AgCl/20wt%-MCM-41(c and d).

These AgCl loaded MCM-41 samples show a special microsphere morphology with a diameter about 200 nm. The self-assembling behavior of inorganic and organic specie in the formation of MCM-41 may be affected by the addition of 3(N-imidazolyl) propyltrimethoxysilane hydrochloride ionic liquid. Moreover, the filling phenomenon of AgCl can be observed in all these images because of their more dark contrast grade in the silica particles. Few AgCl particles on the external surface of mesoporous silica can be found in the observed TEM images of AgCl loaded 10wt%-MCM-41, suggesting that most of AgCl species are well-dispersed on the internal surface of MCM-41 materials. However, few AgCl particles are observed in the samples of AgCl/20wt%-MCM-41, which is in good agreement with the sharper diffraction peaks of AgCl/ 20wt%-MCM-41.

N_2 adsorption–desorption analysis

Fig. 5 shows the N_2 adsorption–desorption isotherms and the corresponding pore size distribution curves for AgCl/10wt%-MCM-41. The mesoporous materials exhibit type-IV isotherms with a clear hysteresis loop. In particular, there seem to be two H_1 hysteresis loops in the relative pressure region between 0.4-0.9, and the corresponding pore size distribution curve testified two maximum values at 4.0 nm and 7.9 nm. The former is assigned to the mesopore size. The latter may be due to the intergranular pores between the 10wt%-MCM-41 particles or another mesopores resulting from the addition of 3(N-imidazolyl) propyltrimethoxysilane hydrochloride. The AgCl/ 10wt%-MCM-41 sample shows a 438m^2/g BET surface area and a 0.51 cc/g pore volume.

1172
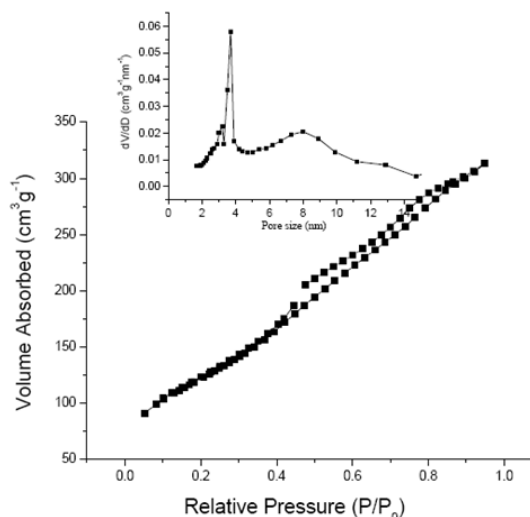
Fig. 5. N_2 adsorption–desorption isotherms and the corresponding pore size distribution curves for AgCl loaded 10wt%-MCM-41.

Photocatalytic performance of AgCl /10wt%-MCM-41

The photocatalytic degradation of dyes in solution was accomplished by visible light irradiation with only slight ultraviolet contribution. From the full wavelength spectra of the used light source (Fig. 6 a), it is seen that its irradiation is mainly concentrated in the visible range with little ultraviolet. The degradation experiment results of different dyes under irradiation are shown in Fig. 6 b-c. There is weak degradation of the dyes within the test time without irradiation or without the photocatalyst. Methyl orange is hardly detected after irradiating the solution over AgCl/10-wt%-MCM-41 for 30 min. For comparison, blank experiment of methyl orange decomposition over AgCl was also carried out under the same conditions, and about 80wt% of methyl orange was found to be degraded during irradiation for 50 min. Furthermore, the decomposition of 20 mg/L isatin over AgCl/10-wt%-MCM-41 materials was completed in 15 min. For methylene blue and congo red, decomposition was completed for about 50 min. Bulk AgCl revealed a decomposition property under irradiation which is obviously lower than that of AgCl/10-wt%-MCM-41. These results exhibit that the AgCl supported on MCM-41 has an enhanced photocatalytic performance probably resulting from the better dispersion of AgCl materials and the different size and morfology of the loaded particles.
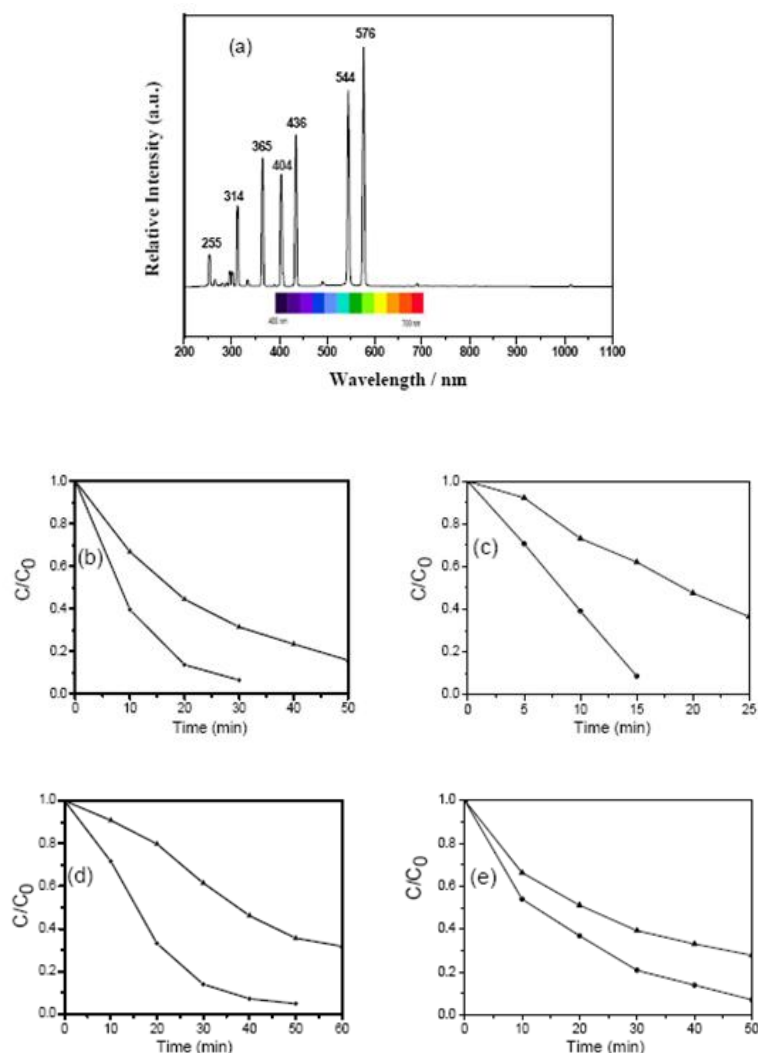
Fig. 6. The full wavelength spectra of the used light sources (a); The photodegradation performance of AgCl, AgCl/10wt%-MCM-41 for dyes: (b) 10mg/L methyl orange, (c) 20mg/L isatin, (d) 10mg/L methylene blue, (e) 5mg/L Congo red

CONCLUSIONS

We have synthesized a novel hybrid mesoporous microspheric AgCl/MCM-41 using N-(trimethoxysilanepropyl) imidazole hydrochloride ionic liquid. The AgCl/MCM-41 material reveals higher catalytic performance than AgCl bulk material in the photodegradation of dyes such as methyl orange, isatin, methylene blue and congo red.

REFERENCES

1. M. Lanz, D. Schürch, G. Calzaferri, *J. Photochem. Photobiol.A:Chem*, **120**, 105 (1999).
2. M. Ashokkumar, J. L. Marignier, *International journal of hydrogen energy,* **24**, 17 (1999).
3. V. R. Reddy, A. Currao, G. Calzaferri, *J. Mater. Chem.,* **17**, 3603 (2007).
4. A. S. Arico, P. Bruce, B. Scrosati, J. M. Tarascon, W. Van Schalkwijk, *Nat. Mater.,* **4**, 366 (2005)
5. P. Wang, B. Huang, X. Qin, X.Zhang, Y. Dai, J. Wei,, M.-H. Whangbo, *Angew. Chem. Int. Ed.*, **47**, 7931 (2008).
6. P. Wang, B. Huang, Z. Lou, X. Zhang, X. Qin, Y. Dai, Z. Zheng, X. Wang, *Chem. Eur. J.* **16,** 538 (2010).
7. S. Rodrigues, S. Uma, N. Igor, K. J. Martyanov, *Klabunde Journal of Catalysis,* **233,** 405 (2005).
8. M. Antonietti, D. Kuang, B. Smarsly, Y. Zhou, *Angew. Chem. Int. Ed.,* **43**, 4988 (2004)

9. C. P. Mehnert, R. A. Cook, N. C. Dispenziere, M. Afeworki, *J. Am. Chem. Soc.,* **124**, 12932 (2002).

10. Y. F. Shen, Y. J. Zhang, Q. X. Zhang, L. Niu, T. Y. You, A. Ivaska, *Chem.Commun.,* 4193 (2005).

11. S. Udayakumar, S. W. Park, D. W. Park, B. S. Choi, *Catalysis Communications*, **9**,1563 (2008).

12. Z. J. Wang, Q. X. Zhang, D. Kuehner, A. Ivaska, L.

Niu, *Green Chem.*, **10**, 907 (2008).

13. B. Wu, D. Hu, Y. Kuang, B. Liu, X. Zhang, J. Chen, *Angew. Chem. Int. Ed.*, **48**, 4751 (2009).

14. S. Guo, S. Dong, E. Wang, *Adv. Mater.*, **22**, 1269 (2010).

15. A. M. Lazarin, Y. Gushikem, S. C. Castro, J. *Mater. Chem.,* **10**, 2526 (2000)..

СИНТЕЗА НА МЕЗОПОРЕСТИ МИКРОСФЕРИ ОТ AgCl/MCM-41 С ПОМОЩТА НА ЙОННИ ТЕЧНОСТИ И ФОТО-ДЕГРАДАЦИОННИТЕ ИМ СВОЙСТВА

Х. К. Жанг[1*], К. У[1], Ж. Ф. Гао[1], Х. Л. Чен[1], Ж. К. Ксюан[1]

[1]Департамент по химия, Многонационален университет в Хебей, Ченгде, Китай

(Резюме)

Приготвени са мезопорестимикросфери MCM-41 с помощта на N-(триметоксисиланпропил) имидазолхидрохлорид като йонна течност, след което върху тях се отлага AgCl чрез индуциране на Cl⁻в йонннната течност. Частиците от AgCl върху мезопорестимикросфери MCM-41 са с голям дисперзитет, а разпространението на порите е би-модално с максимуму при 4.0 nm и 7.9 nm. Количеството на вложения AgCl може да бъде променено използвайки различни количества от йонната течност при приготвянето на MCM-41. Така приготвените микросфери със AgCl върху MCM-41 показват по-висока каталитична активност от обемен материал от AgCl за фото-деградацията на багрила като метил оранж, изатин, метиленово синьо и конго червено.

The nitrogen and phosphorus release in the sediment by the *Perinereis aibuhitensis* bioturbation effect

D. Yang [1,2,3], C. Cao[2,3], F. Chen[2,3], Y. Zhou[2,3], Z. Xiu[1*]

[1]*College of Life science and Technology, Dalian University of Technology, 116021,Dalian, China;*

[2]*Key Laboratory of Marine Bio-resources Restoration and Habitat Reparation in Liaoning Province, Dalian Ocean University, 116023,Dalian,China*

[3]*Key Laboratory of North Mariculture, Ministry of Agriculture, Dalian Ocean University, 16023,Dalian,China*

Eutrophication in sediment is harmful to the marine ecology system. Polychaetes are important marine benthic animal populations; their bioturbation can promote the release of nutrients to the upper water. In the current study, using a simple, self-made test device, we studied the influence of *P. aibuhitensis* on the regular release of nitrogen and phosphorus from the sediments. The experiment was designed in three groups: low concentration (354 ind/m^2, 293.81 g/m^2), high density (708 ind/m^2, 587.61 g/m^2) and control group. The results of a test in a 10-day experimental period showed that released concentrations of NH_4^+-N, NO_3^--N, and PO_4^{3-}-P in worms' sediment were significantly higher than those in the control group. Among them, the change of NH_4^+-N and PO_4^{3-}-P was the most significant. The NH_4^+-N concentration reached the highest value at the sixth day in the high density group (708 ind/m^2) and its value was 11.4365 mg/L. The released concentration of PO_4^{3-}-P reached a peak at the third day with a value of 0.1574 mg/L. The experimental results proved that *P. aibuhitensis* could improve the sediment quality.

Key words: Bioturbation, nitrogen, phosphorus, *Perinereis aibuhitensis*.

INTRODUCTION

Eutrophication-induced changes to an ecosystem can cause reduced water quality, shifts in species composition, and a bottom dead-zone. Eutrophication in aquatic systems is caused by the input of excess nitrogen, phosphorus, and other nutrients, and therefore, the fate of these nutrients in aquatic systems has attracted wide attention. For example, while nitrogen and phosphorus are two essential nutrient elements in the ecosystem, excess input of nitrogen and phosphorus in aquatic systems can lead to eutrophication, which may destroy the balance of an ecosystem [1-4]. As an example, the release of nitrogen from the sediments, as one of the essential limiting nutrients, facilitates the growth of plankton in the water column. However, excessive deposition of nitrogen can cause sediment pollution, especially under anaerobic conditions, with the generation of toxic ammonia through de-nitrification resulting in a bottom dead-zone. Therefore, the cycle of nitrogen, especially regarding the release of nitrogen from sediment to the water column, plays an important role in the health of the sediment environment [5]. Phosphorus has no direct toxic action, but it is also an important facilitator of phytoplankton growth. Therefore, the release of phosphorus from the sediment is a major limiting factor on the growth of phytoplankton. Dynamic nutrient equilibrium exists between the sediment and the water column [6]. Nitrogen and phosphorus in the sediments will gradually diffuse into the water column down a concentration gradient, which can cause secondary pollution [7, 8]. Therefore, it is very important to understand the mechanisms behind sediment nutrient release.

Bioturbation refers to the sedimentary structure change caused by organisms, mainly through the turnover of deposited particles by crawling, feeding, burrowing, and habitat construction. Different forms of bioturbation exist, such as cave-making, irrigation, diffusive and advective mixing, and other dynamic processes, which redistribute the sediments [9]. The direct effect of bioturbation is the vertical transport and mixing of sediments, or "turnover." Turnover of sediments can accelerate the material exchange between interstitial water and the overlying water column, thereby facilitating the decomposition, mineralization, and metabolism of organic matter [10]. Studying the mechanisms behind biological disturbance may allow an understanding of the load release from the sediments to the water column, thereby assisting the prediction of algal blooms and incidents of red tide. Furthermore, this knowledge provides the basic parameters and conceptual understanding for ecological modeling and water

treatment [11].

Polychaetes are a dominant benthic fauna in the marine environment and as such, they play a key role in energy flow and material recycling in the marine ecosystem. Some polychaetes are of economic importance, such as the adults and larvae of the family *Nereidae*, reported to be food for many economically important fishes, and also used as bait for recreational fishing. Due to their wide distribution and sensitivity to pollution, *polychaetes* play an important role in biomonitoring of the marine environment for effects of toxic materials and pollution. *Polychaetes* also facilitate bioremediation of eutrophic, toxic and heavy metal polluted sediment [12]. The application of aquaponic systems using *nereis-paralichthys* and *nereis*-shrimp are good examples of using bioremediation to improve eutrophication, through improving the exchange between sediment-water interfaces, purifying water quality, and generally improving the environment. Furthermore, *polychaetes* can reduce the pollution from aquaculture wastewater, thereby reducing the effect on the ocean and the cost of breeding, and therefore, promote sustainable aquaculture [13]. However, few studies have reported the role of *nereis* in nutrient cycling and the release of nitrogen and phosphorus from the sediments. The current study reports on a laboratory study using *Perinereis aibuhitensis*, a widely distributed and economically important *polychaete* in coastal China [14], to determine the effect of its bioturbation on the release of nitrogen and phosphorus from sediments.

MATERIALS AND METHODS

Animal collection and experimental installation

Perinereis aibuhitensis individuals were collected from a coastal area in Dalian City, China. The collected specimens had an average body length and weight of 10.55 ± 2.86 cm and 0.83 ± 0.29 mg/ind, respectively. After collection, the experimental animals were immediately brought to the laboratory and placed into a temporary culture for 72 hours, then, individuals of similar size and seemingly good health were selected as the experimental animals.

Sediment samples were collected from the Dalian Heishijiao coastal area. Sediment was separated from the surface mud, placed into a closed tank, and shipped to the laboratory, where it was frozen for future use. The experimental system used was a 1,000 ml glass beaker. A total of 300 g of sediment sample, creating a bottom layer of approximately 7.5 cm thickness, was placed into each beaker. Sand filtered seawater was then added

to the 1,000 ml scale line of the beaker. The seawater was filtered by a 0.45 μm fiberglass microfiltration membrane. A plastic hose was used to input air into the system when adding water without stirring the sediment. Water samples were collected through the siphon method using another plastic hose. The equipment used in the experimental system is shown in Fig. 1.
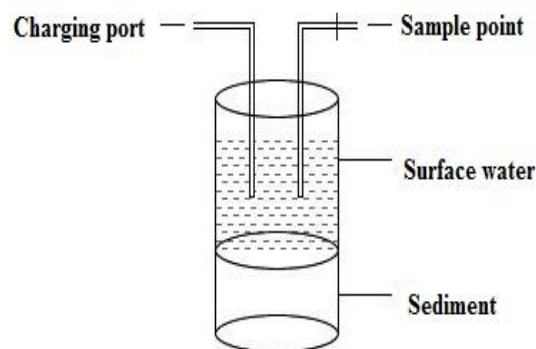
Fig. 1. Equipment used in the sediment release experiment.

Experimental methods

The experimental system was divided into three different groups by worm density: 1) control group; 2) high density group; and 3) low density group. Three repeated experiments were set for each group. The control group did not contain any worms. The low density group contained four worms with a density of 354 ind/m^2 and a total worm mass of 293.81 g/m^2. The high density group contained eight worms in each beaker with a density of 708 ind/m^2 and a worm mass of 587.61g/m^2.

The experimental period was 10 days; sampling for phosphorus occurred twice a day at 8:00 am and 8:00 pm. Ammonia nitrogen (NH_4^+-N), nitrite (NO_2^--N), and nitrate (NO_3^--N) were sampled once a day at 8:00 am. The environmental variables measured in each beaker during the experimental period are shown in Table 1.

Table 1. The environmental variables of each system during the experiment.

	Control	Low	High
Density (/m^2)	0	354	708
Biomass (g/m^2)	0	293.81	587.61
Temperature (°C)	17 ± 1	17 ± 1	17 ± 1
Dissolved oxygen (mg/L)	7.87-9.67	8.03-9.67	7.44-9.67
pH	7.78-8.06	7.76-7.98	7.76-7.91

Method for determination of nitrogen and phosphorus

Ammonia nitrogen (NH_4^+-N) was determined by a colorimetric method using Nessler's reagent;

nitrite (NO$_2^-$-N) was measured by the naphthyl ethylenediamine dihydrochloride spectrophotometric method, nitrate (NO$_3^-$-N) was measured using a cadmium reduction column, and soluble phosphate (PO$_4^{3-}$-P) was determined by the molybdenum blue photometric method. Dissolved oxygen (DO) was determined by the iodometric method. Ammonia nitrogen, nitrite, nitrate, and phosphate were measured using a 721 spectrophotometer [15].

RESULTS

Variation in ammonium (NH$_4^+$-N) concentration between the different groups

The variation in ammonium concentration between the groups is shown in Fig. 2. The control group, high density group, and low density group all showed a similar general trend: the concentration of ammonium rapidly increased at the start of the experiment, reached a peak value, after which the concentration stabilized. The change of ammonium concentration in the high density group was 0.4724 mg/L at the start, reaching a peak of 11.4185 mg/L on the sixth day, achieving a steady state for about 2 days, following which the concentration began to decline. The concentration of the low density group changed from 0.3228 mg/L up to 8.9540 mg/L, reaching a peak on the eighth day, after which the concentration of NH$_4^+$-N showed minor fluctuations. In the control, the scale of concentration variation of ammonium was 0.4409-5.5529 mg/L.
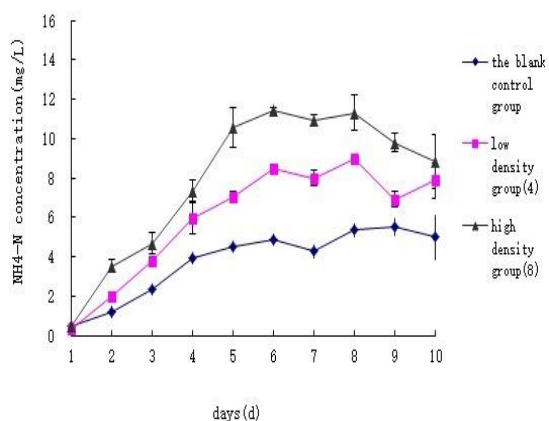
Fig. 2. The changes in NH$_4^+$-N concentration over time in the different worm density groups.

Fig.3 shows the ammonium concentration regressed against time for the first 6 days for the different groups, representing the period when the ammonium concentration showed a linear increasing trend (see Fig. 2). According to the data, the trend line was calculated in the different density

groups. The concentration/time (days) curve in the first 6 days was linear. The highest to lowest slopes of the regression lines referred to the high density group, the low density group, and the control group. Analysis of one-way variance indicated that the effect of worm density in the sediment on the amount of ammonium released was very significant (P < 0.001). The worms' action played a significant role in promoting ammonium release.
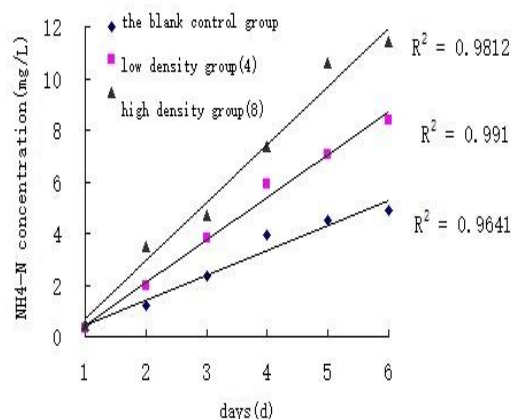
Fig. 3. The NH$_4^+$-N changes in the different groups over the first six days of the experiment.

The variation in nitrite (NO$_2^-$-N) concentration among the different groups

As shown in Fig. 4, the fluctuation in nitrite concentration between the different density groups was very small. The nitrite concentrations in all groups showed a declining trend until the sixth or seventh day, after which the concentrations began slowly to rise. The ranges of nitrite concentrations were 0.6244-1.8880 mg/L, 0.4814-1.7423 mg/L, and 0.4763-1.6762 mg/L in the high density group, low density group, and control group, respectively. Statistical analysis showed that there was no significant difference in the concentration of NO$_2^-$-N between the different density groups (P > 0.005).
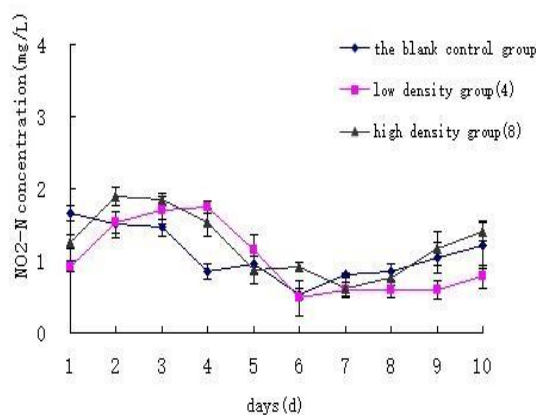
Fig. 4. The changes in NO$_2^-$-N concentrations between the different density groups.

The variation in nitrate (NO_3^--N) between the different groups

The changes in nitrate (NO_3^--N) concentration over time for the different groups can be seen in Fig. 5. A slow rising trend during the entire experimental period is evident for all groups. The nitrate concentrations in the groups ordered from highest to lowest were the high density group, the low density group, and the control group. The range of concentration changes was 0.6643-1.2356 mg/L, 0.6577-1.12184 mg/L, and 0.6217-0.9214 mg/L in the high density, low density, and control group, respectively. Statistical analysis showed that nitrate concentrations in the different groups were significantly different (P < 0.005).
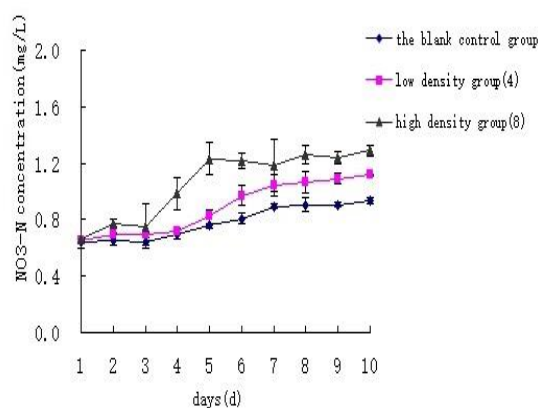
Fig. 5. The changes in NO_3^--N concentration between the different groups over time.

Variation in phosphate (PO_4^{3-}-P) between the different groups

The concentrations of soluble phosphate PO_4^{3-}-P showed a similar trend in the high density and low density groups (Fig. 6): the concentrations rapidly increased from low starting values to the peak values within 3 days, after which a gradual decrease was observed. A final steady state was reached after 6 days.
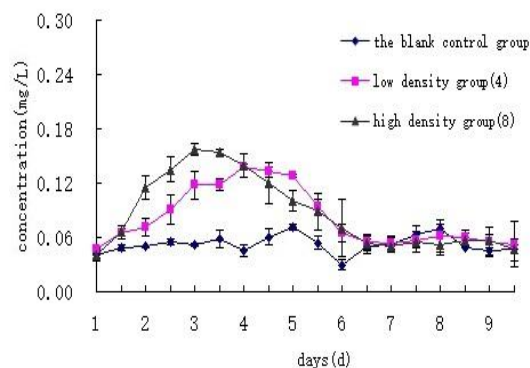
Fig. 6. The changes in PO_4^{3-}-P between the different groups over time.

1178

The concentration in the high density group was higher than that in the low density and control groups. The day when peak values were obtained was different for the two density groups: peak values of 0.1574 mg/L and 0.1378 mg/L occurred at day 3rd and day 4th for the high density and low density group, respectively. The range of fluctuation of soluble phosphate concentration during the experimental period was 0.0463-0.0703 mg/L, 0.0521-0.0645 mg/L, and 0.0295-0.0717 mg/L in the high density group, the low density group, and the control group, respectively.

Using the same method as for ammonium, we made a concentration/time (days) figure using data of the first 3 days (Fig. 7). It displayed the effect of worm density on the release speed of soluble phosphate. In the first 3 days, the relationship of time and concentration was linear for the high and low density groups, with an R^2 of 0.9770 and 0.9603, respectively. An R^2 of 0.7384 was obtained for the blank group. The slope of the regression line from highest to lowest was as follows: high density group, low density, and control group. Using analysis of variance, the concentrations of soluble phosphate in the different density groups showed very significant differences (P < 0.001).
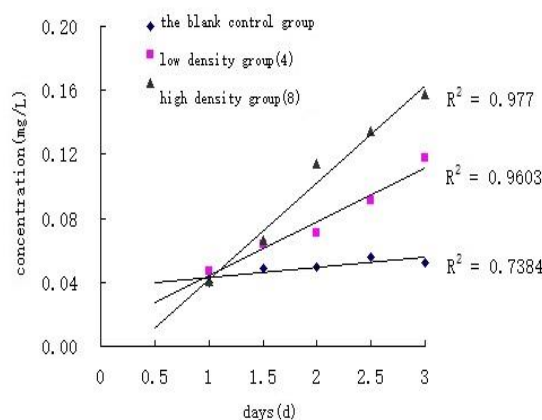
Fig. 7. The PO_4^{3-}-P changes of each group for the first 3 days of the experiment.

CONCLUSIONS

In aquatic ecosystems, different forms of nitrogen are involved in a variety of reactions and processes. Important forms of nitrogen are ammonium (NH_4^+), ammonia (NH_3), nitrate (NO_3^-), nitrite (NO_2^-), and nitrogen gas (N_2). Ammonium, nitrate, and nitrite constitute the soluble inorganic nitrogen (DIN). The chemical species of nitrogen are consumed by the phytoplankton and are used by bacteria as electron acceptors. Organic forms of nitrogen consist of organic detritus, which tends to settle as dead organic matter to the sediment.

Organic nitrogen in the sediment can be converted to inorganic nitrogen by anaerobic bacteria. The sediments can not only recycle nutrients and other chemical compounds back to the water column, but also act as a sink for nutrients. This is the reason why sediments play a major role in controlling eutrophication [16]. If the release of inorganic nitrogen back to the water column occurs slowly, major eutrophication of the sediment could take place while the primary productivity of the surface water would be low. Therefore, the release of nitrogen from the sediment is very important [17]. In the current study, the release of DIN in the control group also showed an increasing trend from the start of the experiment. Because the concentrations of DIN in the water and the sediment were different, diffusion from the high to the low concentration gradient could occur. The concentration of nitrate and ammonium in the overlying water was obviously higher in the groups containing worms than in the control group. The average concentrations of NH_4^+-N and NO_3^--N in surface water were 5.9252 mg/L and 0.8869 mg/L, respectively, in the low density group; 7.8902 mg/L and 1.0608 mg/L, respectively, in the high density group; 3.7451 mg/L and 0.7832 mg/L, respectively, in the control group. The reason for these differences was mainly due to the effect of the worms on bioturbation, thereby facilitating the mixing of sediments, interstitial water, and surface water, allowing inorganic nitrogen to quickly spread to the overlying water [18].

The release of NH_4^+-N and NO_3^--N which was obvious higher in the groups containing worms than in the control group, occurred mainly during the initial days of the experiment. The concentrations in the high density group reached a peak value at day 6th and were stable for 2 days, after which the concentrations began to decrease. The concentration of NH_4^+-N increased during the initial experimental days, but later decreased, mainly because of two possible reasons: 1) building of caves occurs when the worms arrive at a new environment, following which, stable concentrations are obtained; and 2) bioturbation by the increased intensity of the worms can produce a larger amount of nitrogen in an aerobic environment, strengthening nitrification, while decreasing denitrification. The degradation of organic matter in an oxygen environment will consume a large amount of $NH4^+$-N, which is partially converted into NO_3^--N [19]. The low density and high density groups showed a similar trend with only a time delay (approximately two days). It also follows from the results that the release rate of ammonia nitrogen strongly correlates with worm density. The concentration change of NO_2^--N was similar in each group because NO_2^--N is an intermediate chemical species of nitrogen between NH_4^+-N and NO_3^--N, so it is very unstable under oxidizing conditions, and is soon converted to NO_3^--N. The concentration of NO_3^--N always maintained an upward trend during the experimental process. This may be because the surface water was always in aerobic conditions, and therefore, the nitrification process exceeded the denitrification one. During nitrification, a proportion of NH_4^+-N and NO_2^--N was oxidized into NO_3^--N, causing a continuous accumulation of NO_3^--N [20,21].

Under natural conditions, phosphorus in sediments is subjected to simultaneous adsorption and desorption. The rate of phosphate release, which is accelerated by wind and biological disturbance, can exceed the adsorption rate of phosphate in sediment [22]. The apparent release rate of phosphate in the sediments in the current study was therefore different from the amount of released and adsorbed phosphate. It is evident from Fig. 7 that worm bioturbation promotes the release of soluble phosphate from the sediments in the initial period (3 days). The bioturbation action of the high density group was higher than that of the low density group, and therefore, the day of phosphorus peak appearance of the high density group was slightly ahead of that of the low density group (about 1 day). After reaching a peak, soluble phosphate in the high and low density groups began to decline. This is because the *nereis* continued to effect bioturbation beyond the phosphate peak, but the release rate of phosphorus had little effect, or the content of phosphorus in the sediment declined. This demonstrates that during the experiment, the effect of bioturbation on the released phosphorus was only a short-term and therefore, limited effect. Phosphorus in sediments undergoing *nereis* bioturbation may become depleted over time [23, 24]. At this point, adsorption and release of phosphorus to and from the sediments achieves a dynamic equilibrium. Therefore, while the phosphorus concentration in the overlying water may decrease, the release of phosphorus from the sediments continues.

Nereis bioturbation is a physical process that affects dissolved phosphate concentrations by resuspension of particular phosphorus and accelerating the diffusion of phosphorus from the sediments through the sediment-water interface, causing a sharp rise in soluble phosphate concentration. Therefore, the more intense the

physical disturbance, the more obvious is the phosphorus release. The experiments showed that the quantity of phosphorus released and the density of *P. aibuhitensis* have a very significant correlation.

In this decade, bioturbation has been studied widely for different species and environments. In the ocean, various animal groups cause bioturbation effects, such as sea cucumber [25], shrimp [26], crabs [27], clams [28], shellfish [29], and polychaete [30]. In 2012, Kristensen defined bioturbation in aquatic environments to include all transport processes carried out by animals that directly or indirectly affect sediment matrices. These processes include both particle reworking and burrow ventilation [31]. Particle reworking occurs through burrow construction and maintenance, as well as ingestion and defecation, and causes biomixing of the substratum. Organic matter and microorganisms are thus vertically and laterally displaced within the sediment matrix. Burrow ventilation occurs when animals flush their open- or blind-ended burrows with overlying water for respiratory and feeding purposes, causing advective or diffusive bio-irrigation exchange of solutes between the sediment pore water and the overlying water body. Many bioturbating species simultaneously perform reworking and ventilation.

From the results of the current study, it is evident that *P.aibuhitensis* can significantly promote the release of nitrogen and phosphorus in sediments through churning the sediments and accelerating the migration processes of nitrogen and phosphorus in the sediments from the subsurface and finally to the water. Meanwhile, its eating, caving, excreting, and other metabolic and ecological habits may affect the process of water management. This biological disturbance will bring changes to the physical and chemical properties of sediments, and affect the structure and various dynamic processes of the sediment-water interface through simultaneous reworking and ventilation of the sediments [32]. Theoretically speaking, the bioturbation of Nereis can increase the dissolved oxygen of the sediment-overlying water interface, which should not promote the release of nitrogen and phosphorus from the sediments, but bioturbation can promote the mixing and exchange between sediment and the water interface, and the effects of mixing and exchange is more obvious than the impact of simple dissolved oxygen on nitrogen and phosphorus release in the sediment [21]. Indeed, polychaetes bioturbation has been widely used in sediment environment bioremediation or multiculture. Zhou found that Nereis can remediate the sediments

through its feeding and living behavior. A Nereis biomass of 200 g/m^2 can process sediments of up to 762.6 g/m^2/d, which is equivalent to the amount of 558.9 cm^3 of sediment [33]. This means, in three months, Nereis can remediate the entire sediment surface of 5 cm in a shrimp pond. A study on the benthic animals of Tamar estuaries in the UK showed that in regions with *Neanthes diversicolar* densities of 4,000 ind/m^2, the flux of soluble ammonia from sediment to water is 1,565 μmol/m^2/d; while the flux is -134 μmol/m^2/d in polychaetes sparse regions [34]. It is therefore obvious that bioturbarion can greatly improve the efficiency of material circulation and transformation and therefore, polychaete bioturbation can improve the quality of sediment and the state of the marine environment [35].

REFERENCES

1. A. A. Ansari, S. S. Gill, F. A. Khan, in Eutrophication: causes, consequences and control, Springer Netherlands, 2011, p. 143.
2. F. A. Khan, F. Naushin, F. Rehman, A. Masoodi, M. Irfan, F. Hashmi, A. A. Ansari, in Eutrophication: causes, consequences and control, Springer Netherlands, 2014, p. 17.
3. S. R. Carpenter, *PNAS*, **102**, 10002 (2005).
4. D. J. Conley, H. W. Paer, R. W. Howarth, D. F. Boesch, S. P. Seitzinger, K. E. Havens, C. Lancelot, G. E. Likens, *Science*, **323**, 1014 (2009).
5. J. N. Galloway, F. J. Dentener, D. G. Capone, E. W. Boyer, R. W. Howarth, S. P. Seitzinger, G. P. Asner, C. C. Cleveland, P. A. Green, E. A. Holland, D. M. Karl, A. F. Michaels, J. H. Porter, A. R. Townsend, C.J. Vorosmarty, *Biogeochemistry,* **70**, 153 (2004).
6. A. P. Davis, M. Shokouhian, H. Sharma, C. Minami, *Water Environ. Res.*, **78**, 284 (2006).
7. E. S. Bernhardt, L. E. Band, C. J. Walsh, P. E. Berke, *Ann. N.Y. Acad. Sci*., **1134**, 61 (2008).
8. W. C. Lucas, M. Greenway, *J. Irrig. Drain. Eng.*, **134**, 613 (2008).
9. J. Y. Yingst, D. C. Rhoads, The role of bioturbation in the enhancement of bacterial growth rates in marine sediments. Marine benthic dynamics, University of South Carolina Press, Columbia, 1980, p.407.
10. L. R. Gardner, P. Sharma, W. S. Moore, *J. Environ. Radioactiv.,* **5**, 25 (1987).
11. K. Hansen, E. Kristensen, *Estuar. Coast. Shelf.S ,* **45**, 613 (1997).
12. H. K. Dean. *Rev. Biol. Trop,* **56**, 11 (2008).

13. A. K. Amirkolaie, *Rev. Aquacult,* **3,** 19 (2011).
14. D. Yang, Y. Zhou, H. Zhao, X. Zhou, N. Sun, B. Wang, X. Yuan, *Environ. Toxicol. Phar*, **34**, 841 (2012).
15. National Standard of People's Republic of China. Specification for marine monitoring GB17378 (1998).
16. M. A. Altabet, R. Francois, *Global. Biogeochem. Cy*., **8**, 103 (1994).
17. R. C. Dugdale, J. J. Goering , *Limnol. Oceanogr,* **12**, 196 (1967).
18. S. P. Pelegri, T. H. Blackburn, *Ophelia*, **42**, 289 (1995).
19. C. O. Quintana, M. Tang, E. Kristensen. *J. Exp. Mar. Biol. Ecol.*, **352**, 392 (2007).
20. K. Henriksen, M. B. Rasmussen, A. Jensen, *Ecological Bulletins*, 35, 193 (1983).
21. S. P. Pelegri, T. H. Blackburn. *Ophelia*, **42**, 289 (1995).
22. K. B. Föllmi, *Earth-Sci. Rev.*, **40**, 55 (1996).
23. E. Kristensen, *J. Exp. Mar. Biol. Ecol*, **75**, 171 (1984).
24. R. C. Aller, *Chem. Geol.*, **114**, 331 (1994).
25. Yuan, X., Yang, H., Wang, L., Zhou, Y., & Gabr, H. R., *J. Therm. Bio.,* **34**, 315 (2014).
26. S. Widdicombe, M. C. Austen. *Vie et milieu*, **53**, 163 (2003).
27. X. Qin, H. Sun, C. Wang, Y. Yu, T. Sun, *Environ. Toxicol. Chem.*, **29**, 1248 (2010).
28. L. Sgro, M. Mistri, J. Widdows, *Hydrobiologia*, **550**, 175 (2005).
29. S. Schmidt, J. L. Gonzalez, P. Lecroart, J. Tronczyński, I. Billy, J. M. Jouanneau, *Aquat. Living. Resour.*, **20**, 163 (2007).
30. X. Yuan, A. Chen, Y. Zhou, H. Liu, D. Yang, *Chin. J. Oceanol. Limn.,* **28**, 849 (2010).
31. E. Kristensen, G. Penha-Lopes, M. Delefosse, T. Valdemarsen, C. O. Quintana, G. T. Banta, *Mar. Ecol. Prog. Ser.,* **446**, 285 (2011).
32. C. O. Quintana, M. Tang, E. Kristensen, *J. Exp. Mar. Biol. Ecol.*, **352**, 392 (2007).
33. Y. Zhou, X. Z.Hun, *Journal of Fisheries of China*, **2**, 140 (1995).
34. J. T. Davey, P. G. Watson, *Ophelia*, **41**, 57 (1995).
35. J. E. Hewitt, M. J. Anderson, S. F. Thrush, *Ecol. Appl.*, **15**, 942 (2005).

ОТДЕЛЯНЕ НА АЗОТ И ФОСФОР ОТ СЕДИМЕНТИТЕ ОТ *PERINEREIS AIBUHITENSIS* ЧРЕЗ БИОТУРБАЦИОНЕН ЕФЕКТ

Д. Янг [1,2,3], Ч. Цао[2,3], Ф. Чен[2,3], Й. Жу[2,3], Ж. Ксю[1*]

[1]*Колеж за науки за живота и технологии, Университет в Далиан, Китай*
[2]*Ключова лабораторияпо възстановяване на морски биоресурси и подобряване на жилищната среда в провинция Ляонинг, Океаноложки университет в Далиан, Китай*
[3]*Ключова лабораторияпо северни морски култури, Министерство на земеделието, Океаноложки университет в Далиан, Китай*

(Резюме)

Еутрофикацията на седиментите е вредна за здравето на морските екологични системи. Polychaetesса важни за животинските популации в бентоса. Техните биотурбации могат да предизвикат отделяне на нутриенти в горните водни слоеве. В настоящата работа използвахме прост, собствен тест за изследване на *P. aibuhitensis*и ролята му за редовното изхвърляне на азот и фосфор от седиментите. Изследването е остроено на три групи: при ниски концентрации (354 ind/m^2, 293.81 g/m^2), висока плътност (708 ind/m^2, 587.61 g/m^2) и контролна група. Съгласно тестовете, проведени в продължение на 10 дни отделяните концентрации на NH_4^+-N, NO_3^--N и PO_4^{3-}-P в седименти от червеи за значително по-високи, отколкото в контролната група. Сред тях изменениетона NH_4^+-N и PO_4^{3-}-P е най-значимо.Концентрациите на NH_4^+-N достигат най-високи стойности при групата с висока плътност (708 ind/m^2) и неговата стойност беше   11.4365mg/L. Концентрацията на отделения фосфор стига до максимум на третия ден   със стойност   0.1574 mg/L. Опитните резултати доказват, че *P. aibuhitensis*може да подобри качеството на седимента.

Geographical origin identification and quantitative calibration analysis of *Polygonum perfoliatum* L. by near infrared spectroscopy

Y. P. Zhang[1], Z. X. Jin[1*], Y. C. Yuan[2], X. S. Wang[3]

[1] *Research Center on Life Sciences and Environmental Sciences, Harbin University of Commerce, Harbin 150076, China*
[2] *Chemical and Pharmaceutical Department, Henan University of Science and Technology, Luoyang 471023, China*
[3] *Forecasting and Analysis Center, Liming Chemical Research Institute, Luoyang 471001, China*

Rapid near infrared (NIR) spectroscopic analysis models were developed to distinguish the geographical origin and determine the content of *Polygonum perfoliatum* L. The spectra of 94 samples of differing origin were recorded using two NIR instruments (Antaris II and Nicolet 6700). The spectral pretreatment methods used were the first-derivative (FD) and the standard normal variate correction (SNV). Distance match (DM) pattern was applied to classify the geographical origins of the samples, which had better predictive ability (>81%). For the quantitative calibration, the polyphenol and flavone models were established with a partial least squares (PLS) algorithm. The established models were evaluated with root mean square error of prediction (RMSEP) and correlation coefficients. The correlation coefficients of both calibration models were above 0.910, indicating satisfactory predictive abilities. This study demonstrated that NIR diffuse reflection spectroscopy can be used for rapid discrimination of geographical origin and content determination of *P. perfoliatum* L., and   is a beneficial quality control method for this raw material.

Key words: Near infrared spectroscopy, Polygonum perfoliatum L., distance match, partial least squares, polyphenols, flavones.

INTRODUCTION

Polygonum perfoliatum L. (PPL) is a traditional herb used to treat upper respiratory tract infections, bronchitis, whooping cough, acute tonsillitis, enteritis, dysentery, nephritis edema, as well as for the topical treatment of herpes zoster, eczema, acute folliculitis, snake bite [1]. Owing to its curative effects, it was recorded in the 2010 edition of the Chinese pharmacopoeia (ChP) as a new variety [2]. The plant is widely distributed in China. Accordingly, the quality of the herbal raw materials fluctuates, owing to varying ecological environment. Thus, a control method to distinguish and quantify samples is necessary. Currently, traditional Chinese medicines (TCMs) are identified by microscopic and physicochemical evaluations, which can depend on personal experience to make a judgment. Therefore, most quality control methods for TCMs involve the use of HPLC for the identification of one or two main compounds. However, it is difficult to comprehensively evaluate TCMs using this method [3, 5].

The main compounds in PPL are polyphenols and flavones [6-9]. According to the ChP, PPL quality is evaluated by microscopic identification, determination of caffeic acid by TLC, and detection of sophorin by HPLC [2]. However, these methods require tedious sample preparation, take much time, and require large solvent amounts, making them unsuitable for fast analysis during industrial production. Furthermore, sophorin and caffeic acid are poor indicators of product quality. Therefore, it is necessary to develop a low-cost, rapid, multi-component, and controlled method to address this issue.

Fourier transform near-infrared spectroscopy (FT-NIR) is a high-speed, non-destructive technique that has been widely applied for low-cost, reliable qualitative and quantitative analyses in the food, chemical, agrochemical, and petrochemical industries [10-14]. This method has been used for raw material testing [15, 16], product quality control, and process monitoring [17-19], and is being extended to TCM research [20-25].

In this study, two NIR models were established. One is a qualitative model, which can distinguish PPL obtained from different geographical origins, whereas the other is a quantitative calibration model for the rapid determination of polyphenols and flavones in PPL.

---

* To whom all correspondence should be sent:
E-mail: Jin_ai_pu@163.com

MATERIALS AND METHODS

Sample preparation

PPL samples (n = 94) were collected from 12 provinces and 22 locations in China. All samples were identified by Dr. ZhexiongJin (Commercial University of Harbin), and are listed in Table 1.

Table 1. **S**ummary of the tested samples

Ser. no.	Origin	Sam. no.	Ser. no.	Origin	Sam. no.
1	Meizhou Guangdong	6	12	Guizhou	2
2	Jieyang Guangdong	6	13	Sanming, Fujian	2
3	Qingyuan Guangdong	6	14	Nanyang, Henan	3
4	Fuzhou Fujian	6	15	Changsha Hunan	2
5	Wuyishan Fujian	6	16	Nanjing Jiangsu	2
6	Hechi Guangxi	6	17	Fuzhou Jiangxi	1
7	Yizhou Guangxi	8	18	Yingtan Jiangxi	2
8	Yongjia Zhejiang	6	19	Yunnan	2
9	Wenzhou Zhejiang	6	20	Taizhou, Zhejiang	2
10	Luoyang Henan	10	21	Chong qing	2

The samples were milled into powder with a grinder. The final powder samples were obtained by passing the ground powder through a 50-mesh sieve. To ensure that moisture was not an interfering factor, all samples were dried in an oven at 40°C for 12 h. In order to reduce operating error, each sample was scanned three times.

NIR spectra collection

The NIR diffuse reflection spectra were recorded from 10000 to 4000 cm^{-1} at 4 cm^{-1} intervals using the Integrating Sphere module of the Antaris II FT-NIR analyzer (Thermo Scientific, Madison, WI, USA) with an InGaAs detector. Each sample was scanned 64 times, and the resolution was 16 cm^{-1}. The environmental temperature was held at 20-22°C and the relative humidity was 25-30%. Result workflow-based software (Thermo Scientific) was used to obtain the NIR spectra, and the spectra were recorded as the logarithm of the reciprocal reflectance, log (1/R). In order to reduce operating error, each sample was scanned three times.

To explore the application of the established quantitative calibration models on NIR instruments from different facilities, a second NIR analyzer (Nicolet 6700, Thermo Scientific) was used for NIR spectra collection, under the working conditions mentioned above. The NIR spectra

collected by the two types of instruments are shown in Fig. 1.
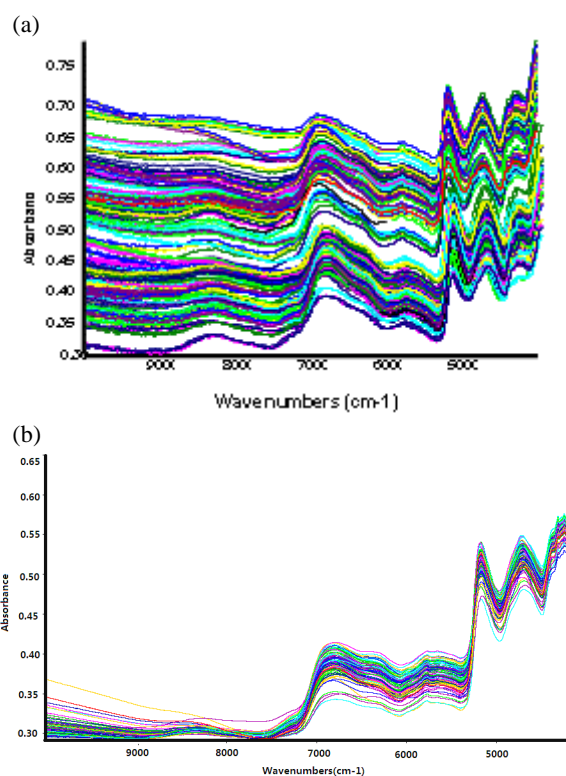
Fig. 1. Spectra of samples collected from Antaris II (A) and Nicolet 6700 (B) FT-NIR.

Reference analysis method

A UV spectrophotometer was used to detect total polyphenols and flavones. Samples (2 g) were reflux-extracted in a water bath with 50 mL of mixed solvent (70:30 [v/v] methanol and water) for 0.5 h. After filtration, samples were placed in 250 mL brown volumetric flasks and diluted with water to the mark. Folin-Ciocalteu colorimetry was used to determine total polyphenols at 760 nm by using gallic acid as a reference substance. $AlCl_3$ colorimetry was used to determine total flavones at 413 nm by using rutin as a reference substance.

Chemometric methods

For determining the geographical origin, distance match (DM) patterns were applied. For the quantitation of components, the partial least squares (PLS) method was adopted. Spectral pretreatment and chemometric analyses were implemented using the TQ Analyst (V8.0, Thermo Scientific) and Matlab (V7.0, Math Works, Natick, MA, USA).

RESULTS AND DISCUSSION

Content analysis

Polyphenols and flavones are the main active constituents of PPL, and are widely occurring

Table 2. Methodology parameters and calibration curves of the reference UV method.

Compound	Linearity range (mg/ml)	Calibration curve	R	Repeatability (RSD %, n=6)	Recovery (%,n=6)
Polyphenol	0.001-0.006	C=0.009A-0.001	0.999	1.532	97.65
Flavone	0.007-0.025	C=0.0302A-0.001	0.998	1.083	98.05

secondary metabolites. Using the UV method described in Section 2.3, all 94 samples were analyzed three times, using the main parameters listed in Table 2. The average content of samples from different provinces is listed in Table 3. We found that samples from different provinces have obvious differences. For example, samples from Jiangxi and Henan provinces had higher polyphenol and flavone content.

Table 3. Average contents of samples from different provinces.

Ser. no.	Province	Content of polyphenol (mg/g ± s)	Content of flavone (mg/g ± s)
1	Guangxi	34.91±11.25	15.68±7.01
2	Guangdong	37.95±14.76	16.36±6.22
3	Fujian	35.48±18.98	16.28±5.11
4	Chongqing	31.42±7.98	13.89±5.14
5	Guizhou	21.01±5.68	10.98±2.12
6	Yunnan	23.9±6.21	13.94±1.38
7	Hunan	30.19±11.75	17.69±4.42
8	Jiangxi	40.14±14.12	23.45±7.06
9	Zhejiang	32.82±12.44	17.68±2.65
10	Henan	44.12±11.94	23.56±5.23
11	Hubei	26.51±6.94	17.30±5.48
12	Jiangsu	27.69±0.99	15.92±2.95

NIR spectral characteristics

FT-NIR can reveal the transitions of corresponding chemical constituents, including O-H, N-H, and C-H. Fig. 1 shows the NIR spectra collected with two NIR instruments. Importantly, the Nicolet 6700 and Antaris II NIR analyzers have different interferometers. The former is equipped with a no wear electromagnetic interferometer, whereas the latter - with a Michelson interferometer. Compared with the Nicolet 6700 NIR analyzer, the spectral absorption intensity obtained using the Antaris II NIR analyzer was higher, and the between-sample intensity variation ranges were wider. However, the shapes of the fundamental spectra were analogous in appearance. For the further research we used the Antaris II NIR analyzer.

Origin identification model

PPL samples from twelve geographical origins with sample numbers above six were used to construct models. In this study, DM was carried out by the traditional authenticity recognition method on the basis of NIR spectral data.

Spectral pre-processing

Spectral pre-processing is used to reduce the effects of systematic noise, base line variation, light scattering, and path length differences. There are several different types of pre-processing available, including first-derivative (FD), second-derivative (SD), multiplicative scatter correction (MSC), standard normal variate correction (SNV), Savitzky-Golay (SG), and Norris derivative (ND). Through multiple optimization calculation, we selected FD, SNV, and 7500-4119 cm^{-1} to set up the models.

Results of the DM method

When establishing the origin identification analysis model, the threshold value is particularly important. The threshold values of the samples are shown in Table 4.

Table 4. Threshold values and identification accuracy rate

Ser. no.	Origin	Threshold	Accuracy rate (%)
1	Meizhou, Guangdong	0.3	90.9
2	Jieyang Guangdong	0.69	100
3	Qingyuan Guangdong	0.23	90.9
4	Fuzhou, Fujian	0.46	81.8
5	Wuyishan, Fujian	0.92	100
6	Hechi, Guangxi	0.1	100
7	Yizhou, Guangxi	0.46	90.9
8	Yongjia, Zhejiang	0.23	100
9	Wenzhou, Zhejiang	0.23	100
10	Luoyang, Henan	0.92	100
11	Suizhou, Hubei	0.92	0.909

These twelve models were added to the workflow in the form of measurements, selecting composite measurements in the classification. We used the rest of the samples for validation, obtaining a distance value of the sample spectrum after the software analysis. The identification accuracy rates are listed in Table 4. Six models

reached 100%, Fuzhou was 81.8%, and the other models were above 90%. From these values we found that DM can be used as an origin identification method, and that NIR can identify PPL samples from different geographical origins.

PLS QUANTITATIVE CALIBRATION MODEL

Division of calibration and validation sets

The 94 samples were randomly divided into calibration and validation sets, which were designed to examine the extrapolation performance. The polyphenol and flavone content in the calibration and validation sets must cover a wide range, which is helpful to develop robust models. The statistical values for the calibration and validation sets are listed in Table 5.

Table 5. Statistical values of the active ingredient contents in calibration and validation sets.

Active ingredients	Average value (X±s,%)	Calibration sets (%)	Validation sets (%)
Polyphenol	32.11±14.69	5.6-84.92	15.3-54.67
Flavone	18.24±6.76	4.7-32.15	7.12-23.94

Selection of the most suitable conditions for building the calibration model

There are many methods of qualitative analysis, including simple Beer's law, classical least squares (CLS), stepwise multiple linear regression (SMLR), partial least squares (PLS), and principal component regression (PCR). For the natural products used in TCM, which have a complex composition, PLS is typically used.
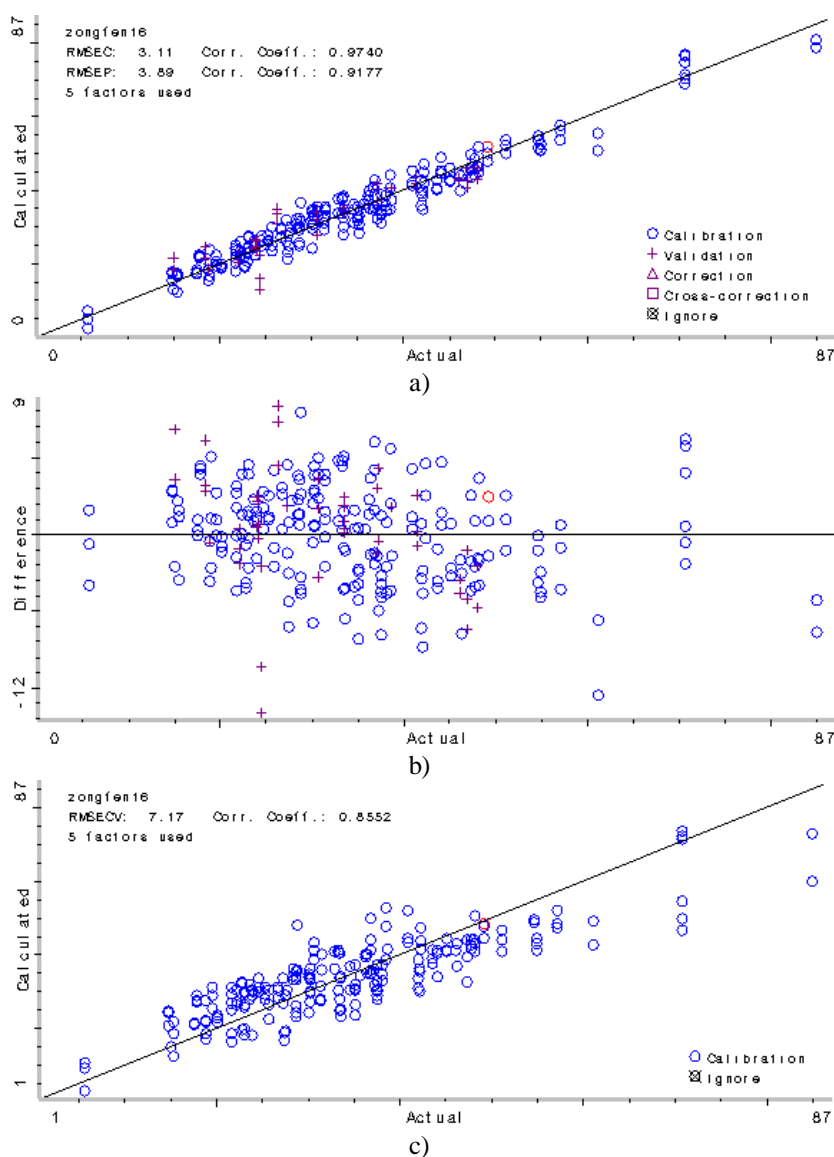
Fig. 2. Calculated model, difference and cross-validated chart of polyphenol.

1185

Table 6. Performance parameters of the established models.

Component	Pretreatment method	PC no.s	Calibration		Cross-validation		External validation	
			RMSEC	R	RMSECV	R	RMSEP	R
Flavone	SNV+1-d	4	2.19	0.9463	3.96	0.8127	2.16	0.9139
Polyphenol	SNV+1-d	5	3.11	0.9740	7.17	0.8552	3.89	0.9177

A good NIR calibration model should have a low root mean square error of calibration (RMSEC) and root mean square error of prediction (RMSEP) value, high correlation coefficient (R), and small differences between root mean square error of cross-validation (RMSECV) and RMSEP. In the spectral pre-processing, FD, SD, MSC, SNV, SG, and ND were compared to optimize the models. These parameters are listed in Table 6. Fig. 2 is a chart of the calculated model (A), difference (B), and cross-validation (C) of polyphenols. The RMSEC and RMSEP correlation coefficients are above 0.91, indicating that these two models possess acceptable fitting results and predictive ability, and can be used for the rapid analysis of polyphenol and flavone content in PPL.

Accuracy and precision of the established NIR method

In order to validate the accuracy of the established NIR method, the sample content in the prediction set was determined with the NIR and UV method, and evaluated with the paired two sample *t*-test. In the 95% confidence interval, the polyphenols and flavones had statistical *t* values of -0.3268 and -0.7167, respectively, with absolute values less than the two-tail critical value, t = 2.179, 2.262. The two-tail p-values were greater than 0.05, indicating that there was no significant difference between the NIR and UV method.

CONCLUSIONS

In the present study, a set of qualitative and quantitative NIR spectroscopic models were developed for PPL quality control. Based on these models, we showed that no sample pretreatment was necessary. Furthermore, data on the content of polyphenols, flavonoids, and the sample origin could be obtained in 1 min. Compared with traditional methods, this method affords rapid and low-cost detection; it can distinguish geographical origin and detect multiple components in one analysis. The overall results show the feasibility of NIR spectroscopy for quality control of TCM pharmaceuticals.

REFERENCES

1. J. S. Guo. Recognition and application of Chinese herbal medicine. People's Medical Publishing House, Beijing, 2009.
2. Ministry of Public Health of the People's Republic of China, Pharmacopoeia of the People's Republic of China, China Pharmaceutical Technology Press, Beijing, 2010.
3. X. Y. Song, Y. D. Li, Y. P. Shi, L. Jin, J. Chen, *Chin. J. Nat. Med.*, **11**, 596 (2013).
4. S. P. Li, J. Zhao, B. Yang, *J. Pharm. Biomed, Anal.*, **55**, 802 (2011).
5. Y. Jiang, David B, P. Tu, Y. Barbin, *Anal. Chim. Acta.*, **657**, 9 (2010).
6. J. Lei, N. Yao, K. Wang, *Biochem. Syst. Ecol.*, **48**, 186 (2013).
7. K. W. Wang, J.R. Zhu, L. Q. Shen, *Nat. Prod. Res.*, **27**, 568 (2013).
8. G. H. Zhu, D. Y. Wang, G. J. Men, *Indian. J. Heterocycl. Ch.*, **10**, 41 (2000).
9. C. Zhao, H. G. Chen, X. J. Gong, *Chin. Herb. Med.*, **41**, 365 (2010).
10. X. M. Chen, X. Z. Yu, Y. G. Wang, Y. D. Yang, J. Y. Zhang, *J. Oleo Sci.*, **64**, 255 (2015).
11. G. Valentina, B. Roberto, G. Riccardo, *J. Food Eng.*, **142**, 80 (2014).
12. M. Romera-Fernandez, L. A. Berrueta, S. Garmon-Lobato, B. Gallo, F. Vicente, J. M.Moreda, *Talanta*, **88**, 303 (2012).
13. C. W. Huck, *J. Pharmaceut. Biomed. Anal.*,**87**, (2014).
14. Y. Yoshihisa, S. Toyofumi, M. Mika, O. Michiteru, H. Shuichi, F. Toshiro, T. Kazuo, *Chem. Pharm. Bull.*, **60**, 624 (2012).
15. B. Jamshidia, S.Minaeia, *Comput. Electron. Agr.*, **85**, 64 (2012).
16. J. R. Lucio-Gutiérrez, J. Coello, S. Maspoch, *Food Res. Int.,* **44**, 557 (2011).
17. M. Snežana, P, Ksenija, K. Janez, H. Matej, *Eur. J. Pharm. Biopharm.*, **88**, 847 (2014).
18. H. Xiong, X. Gong, H. Qu, *J. Pharm. Biomed. Anal.*, **70**, 178 (2012).
19. H. Huang, H. Qu,*Anal. Chim. Acta.*, **707**, 47 (2011).
20. C. Zhang, J. Su, *Acta. Pharm. Sinica B*, **4**, 182 (2014).
21. W. Li, Y. Wang, H.Qua, *Vib. Spectrosc.*, **62**, 159 (2012).
22. Q. Shao, A. Zhang, W.Ye, H. Guo, R. Hu, *Spectrochim. Acta. A*, **120**, 499 (2014).
23. Y. Lai, Y. Ni, S. Kokot, *Vib. Spectrosc.*, **56**, 154 (2011).
24. W. Li, L. Xing, Y. Cai, H., *Vib. Spectrosc.,* **55**, 58 (2011).
25. A. Rohman, A. Nugroho, E. Lukitaningsih, ?. Sudjadi, *Appl. Spectrosc. Rev.*, **49**, 603 (2014).

ИДЕНТИФИКАЦИЯ НА ГЕОГРАФСКИ ПРОИЗХОД И КОЛИЧЕСТВЕН АНАЛИЗ НА *Polygonum perfoliatum* L. ЧРЕЗ БЛИЗКА ИНФРАЧЕРВЕНА СПЕКТРОСКОПИЯ

И. П. Жанг[1], З. Кс. Джин[1*], И. Ц. Юан[2], Кс. С. Уанг[3]

[1] *Изследоеателски център за науки за живота и околната среда, Търговски университет в Харбин, Китай*
[2] *Департамент по фармация, Научно-технологичен университет Хенан, Луоянг, Китай*
[3] *Център за прогнози и анализи, Химически изследователски институт Лиминг, Луоянг, Китай*

(Резюме)

Разработен е модел за анализ, основан на бързата близка инфрачервена спектроскопия (NIR) за разпознаване на географския произход и определяне на съдържанието на *Polygonum perfoliatumL.* Определени са спектрите на 94 проби от различен произход с помощта на два NIR-уреда (Antaris II and Nicolet 6700). Приложени са специални методи за предварителна подготовка – на първата производна (FD) и стандартната корекция на нормалната дисперсия (SNV). Приложен е методът на дистанционното съпоставяне (DM) за класифицирането на географския произход на пробите с с по-добра предсказувмост (>81%). Количествената калибровка е направена с помощта на полифеноли и флавони по алгоритъма на най-малките квадрати (PLS). Корелационните коефициенти на двата калибрационни моделаса над 0.910, указвайки за добра предсказуемост. Тази статия демонстрира факта, че NIR-дифузионната отражателна спектроскопия може да се използва за бързо разграничаване на географския произход и количеественото определяне на *P. perfoliatum* L. и е удобен метод за качествен контрол на тази суровина.

The potential impact of PBDEs contamination on human health via oral media in E-waste dismantling area

Y. Yang[1], X. Li[1], R. Xu[1], M. Li[2*], Y. Yu[3*]

[1] School of Environment & Safety Engineering, Changzhou University, Dist. 10, 213164 Changzhou, China
[2] Chinese Research Academy of Environmental Sciences, Dist. 10, 100012 Beijing, China
[3] South China Institute of Environmental Sciences, Ministry of Environmental Protection, Dist. 10, 50655 Guangzhou, China

PBDEs are a class of brominated persistent organic pollutants, which can be transferred via the food chain and finally cause damage to human health. The study on BDEs contamination via oral media, such as drinking water, soil and foods (dried sweet potato, rice, chicken, pork), was conducted in the E-waste dismantling area in Taizhou, Zhejiang province. The study included: BDEs concentration, distribution features and degree of exposure to human body. According to the calculation method for exposure dose developed by U.S. National Academy of Sciences (NAS), the exposure parameters were optimized and the daily average human exposure via oral media in the studied area was calculated. The analysis of the correlation between the exposure to drinking water and the serum concentrations of PBDEs showed a positive result. However, the serum concentrations of PBDEs did not correlate to other oral media. Therefore, the preliminary conclusion was that the amount of human exposure to drinking water in the studied area affected PBDEs concentrations in the blood. The study showed a significant correlation between the years of residence and the concentrations of PBDEs in the blood. The longer the residents lived in the locality, the higher was the blood concentrations of PBDEs in their bodies.

Key words: PBDEs, Oral media, Population, Health.

INTRODUCTION

Polybrominated diphenyl ethers (PBDEs) are a class of brominated persistent organic pollutants (POPs), commonly used as flame retardants, which include 209 monomers. Because of their excellent flame resistance, they are widely used in textiles, furniture, building materials, circuit boards, and plastic polymers for electrical appliances (such as television sets, computers, etc.)[1]. PBDEs tend to be stable in the environment, as they are hydrophobic, persistent, non-degradable, environmentally stable and bio-accumulated. They can be transferred via the food chain, poison the organisms existing in highly trophic environment and eventually damage human health [2,3]. It was reported throughout the study that PBDEs were detected in fish, human adipose tissue, blood and breast milk [4-6]. The relevant studies on the toxicity mechanism of PBDEs showed that they are toxic to the nerves, thyroid, reproductive organs, embryo, etc., and can disturb endocrine function, change the instinct behavior of animals, thus being potentially toxic to human beings [7-9].

Taizhou is situated in the southeast coastline of China. It is China's typical electronic waste dismantling area. In the late 1970s, some people in the area started to be engaged in dismantling work. Simple manual dismantling and direct combustion were the main treatment methods applied, e-wastes were not appropriately recycled, waste residues were directly thrown away. These dismantling activities caused serious PBDEs contamination in the area [10-13]. This study analyzed the content of PBDEs transferred via oral media in the area. The exposure calculation method recommended by EPA was adopted to analyze the correlation between PBDEs exposure and blood concentration. The preliminary study was conducted on the potential impact of PBDEs contamination on human health.

RESEARCH METHODS

Experiment
Reagents

The standard solutions of PBDEs were purchased from Accustandard (USA), recovery indicators including 13C-PCB141, PCB209 and internal standard 13C-PCB208 were purchased from Cambridge Isotope Laboratories (USA). BF-2000M-type Termovap Sample Concentrator was purchased from Beijing Dafang Century Technology Co. Ltd. Hexane, acetone and

* To whom all correspondence should be sent:
E-mail: limin@craes.org.cn,yuyunjiang@scies.org

methylene chloride were pesticide residues purchased from the Tedia Company (USA).

Sample collection and questionnaire

Altogether 60 samples of 0-20 cm-thick surface soil clods were collected in the electronic waste dismantling area in Wenqiao Town, Wenling city of Taizhou. The sampling instruments were inserted directly into the drinking water well collecting 34 water samples from the top, middle and bottom of the well for every 8 households. Corresponding to the location of soil samples, crops grown on each clod - 12 samples of dried sweet potato and 36 samples of rice, altogether 50 pieces, were collected. Pork samples from 4 pigs were purchased from the local farmers, 500 g fresh meat from the back and legs, respectively; chicken meat samples were collected from 4 chickens out of 4 households from different villages, back and legs of each chicken were cut off for backup.

For human blood samples, a cotton swab was damped with 75% ethanol, skin was wiped with 0.44 mol/L HNO_3, about 8 ml of venous blood was drawn with a vacuum tube, altogether 437 blood samples were collected from the studied area. After the samples were put aside for 15 min, they were centrifuged for 10 min at 3000 r/min (centrifuge radius=6 cm). Supernatant was put in a polyethylene centrifuge tube and immediately freezed at a temperature of -70 ˚C. Repeated freezing and storage were avoided.

The questionnaire was self designed based on the status in the studied area, concentrated discussions were held and consultation was conducted with experts in the area of epidemiology, environmental sanitation, etc., the information related to the questionnaire was verified and identified, which covered general and basic conditions, lifestyle, diet habits, etc.

Sample pretreatment was performed according to reference literature for pretreatment methods for water samples [14]. Water samples were filtered with glass fiber filter (Whatman, GF/F, 142 cm in diameter, 0.7 μm in aperture). Filtrates were loaded to a XAD2/XAD4 resin column (mass ratio 1:1), the organic compounds were enriched, recovery indicators 13C-PCB141 and PCB-209 were added, the resin column was washed with 50 mL of methanol and methylene chloride. The washed mixed resin was extracted three times with 50 mL of a mixture of dichloroethane and methanol (1:1 volume ratio) using a ultrasonic device; then 50 mL of saturated sodium chloride solution was added, and extracted four times with 50 mL of dichloromethane solution. Water was removed from

the organic layer with anhydrous sodium sulfate column, rotated, evaporated and replaced with hexane, volume was set to 1 mL, and then transferred to a multi-grade composite silica gel/alumina chromatographic column for separation and purification.

The composite column was wet-loaded from bottom up as follows: 6 cm alumina, 2 cm neutral silica gel, 5 cm alkaline silica gel, 2 cm neutral silica gel, 6 cm acidic silica gel. Eluted with 50 mL hexane-dichloromethane solution (1:1 volume ratio), concentrated to 1 mL, then the volume was set to 0.1 mL using Termovap Sample Concentrator. The internal standard (13C-PCB208, 10mL×200ng/ mL) was applied for instrumental analysis.

Membranes were freeze-dried and weighed, and recovery indicators were added, a mixture of 400 mL of dichloromethane-acetone (1:1 volume ratio) was extracted with soxhlet for 71 h, activated copper was added to the extract to remove sulfur. The extracts were rotated, evaporated, condensed and then transferred to a multi-grade composite silica/alumina chromatographic column, the final volume was set to 1 mL.

The collected soil samples were taken to the laboratory in brown glass jars, placed in clean beakers (500 mL) baked at a temperature of 400ºC, and let to dry naturally in the darkroom. Sands, particles and other admixtures were removed from the samples, placed in a mortar for grinding, passed through a 0.85 mm aperture sieve, placed in a brown bottle and put in a refrigerator at a temperature of -4 ºC.

Filled silica gel column: the bottom of a glass column with diameter of 1.5 cm and length of 30 cm was covered with a small amount of glass wool, and then filled with 2 g of neutral silica gel, 5 g of alkaline silica gel, 2 g of neutral silica gel, 8 g of acidic silica gel, 2 g of neutral silica gel and 5 g of anhydrous sodium sulfate.

Before loading the samples, the silica gel column was activated with 50 mL of hexane, pre-rinsed with 20 mL of hexane, and then eluted with 100 mL of hexane-dichloromethane (1:1 volume ratio), the eluate was concentrated to 1~2 mL, transferred to the quantitative tube, 100 mL of nonane was added, the volume was reduced to 10 mL using Termovap Sample Concentrator, then the internal standard 13C-PCB208 was added for the measurement.

The chicken and pork samples were dissected to remove the internal organs which were then minced with tweezers and scissors, packed in bags, and sealed for refrigeration. The samples were ground

to powder in a mortar after which they were refrigerated and dried. About 5 g of dried muscles were weighed separately; recovery indicators 13C-PCB141 and PCB209 were added. About 15~25 mL of hexane-acetone (1:1 volume ratio) was used as the extracting agent for ultrasonic extraction for 10 min and the upper extract was removed. The residue was then extracted twice with 10 mL of ultrasonic extraction agent; the three extracts were combined and concentrated to 2~3 mL volume with nitrogen. About 1 mL of sample was taken and measured gravimetrically to determine the fat content, the rest was passed to a glass chromatographic column.

The components in the glass chromatographic column from bottom up were: cotton, 5 g of anhydrous sodium sulfate, 10 g of silica gel, 10 g of acidic silica gel and 10 g of anhydrous sodium sulfate. The concentrated extract was transferred to a glass chromatographic column which was eluted with 10 mL of hexane, then the washer-extractor with 30 mL of hexane-CH_2Cl_2 (1:1 volume ratio) was used for elution. After the liquid nitrogen was condensed and dried, hexane was used to dissolve the extract in the test bottle, 100 mL PCB208 (IS) standard solution was added and the volume was set to 50 mL using Termovap Sample Concentrator for instrumental analysis.

The collected dried sweet potato and rice samples were washed and mixed with a blender, freezed, dried and weighed, ground into powder, passed through a 0.18 mm sieve. 5 g of dried samples were taken separately, recovery indicators 13C-PCB141 and PCB209 were added, 250 mL of n-hexane-acetone (1:1 volume ratio) soxhlet were used to extract for 72 h. Extracts were concentrated to 1 mL using silica gel-alumina column chromatography for purification.

The components in the chromatographic column from bottom up were: cotton, 6 cm alumina, 2 cm deactivated silica gel, 5 cm alkaline silica gel, 2 cm deactivated silica gel, 6 cm acid silica gel and 2 cm anhydrous sodium sulfate. Eluted with 50 mL hexane - dichloromethane (1:1 volume ratio) mixture, internal standard $^{13}C-PCB208$ was added to the components, condensed and transferred to 2 mL sample bottle, volume was set to 100 mL using Termovap Sample Concentrator and the sample was stored in a refrigerator at a temperature of -4 °C for analysis.

A 5 mL exact amount of human serum was drawn and inserted into a separatory funnel of polyvinyl chloride, recovery indicators (13C-PCB141and PCB209) and 2 mL 6 M hydrochloric acid solution were added, then 12 mL

of isopropyl alcohol were added after shaking quickly and vigorously; 10 mL of the prepared mixed solution of hexane and methyl tert-butyl ether (1:1 volume ratio) were added, shaken, let stay still for phase separation, and the organic phase was separated. Then 10 mL and 5 mL of the above-mentioned mixture were used, respectively, for two-fold extraction, the three extracts were combined, washed with 5 mL dichloromethane solution (1%) and the latter was discarded. The organic phase was dehydrated with anhydrous sodium sulfate and dried, concentrated in a rotary evaporator to about 0.5 mL, transferred to the bottle for micro-cell, and dried with Termovap Sample Concentrator, the scale was weighed and the fat weight was obtained.

About 5 mL of hexane was used to dissolve fat and transfer it to a centrifuge tube, 2 mL of concentrated sulfuric acid was added, shaken, centrifuged, the upper part of the organic solution was transferred to another centrifuge tube, and hexane was used to extract the concentrated sulfuric acid. The organic phases were combined, rotated, evaporated and condensed to 1 mL, passed through acidic silica gel column dry-loaded as follows: 2 g acidic silica gel, 5 g neutral silica gel, 2 g acidic silica gel, 2 g diatomite, 2 g acidic silica gel, 5 g neutral silica gel, 2 g acidic silica. Then the organic phase was leached with a mixture of hexane and methyl tert-butyl ether (1:1 volume ratio). Again it was passed through silica gel loaded with: 5 g neutral silica gel, 3 g acidic silica gel, 3 g diatomite, leached with a mixture of hexane and methyl tert-butyl ether (1:2 volume ratio), rotated and evaporated to 0.5 mL, dried with Termovap Sample Concentrator, internal standard 13C-PCB208 was added, volume was set to 20 uL, sealed in a micro-cell bottle for analysis.

Instrumental analysis

The PBDEs samples were analyzed with Agilent 7890N gas chromatograph of high resolution (Wilmington, USA) coupled with an Autospec Ultima mass spectrometer of high resolution (Waters Micromass, UK). The ionization of the mass spectrometer was electron impact (EI). The electron emission energy was set to 35 eV. The data acquisition mode was SIR mode, with source temperature of 270ºC, carrier gas（He）flow velocity of 1.2 mL/min, R≥10000. Chromatographic column of DB-5MS（0.25 mm ID×0.25 μm) film. The temperature in the chromatographic column rose as follows：100ºC (2 min), ~230 ºC (15 ºC/min)，230~270ºC (5ºC /min)，270~330 ºC (8 min，10 ºC/min). Exactly 1 μL of sample solution was

injected with a CTC PAL auto sampler in splitless mode i.

Quality assurance and quality control

Quantitative analysis was performed using the internal calibration method and five-point calibration curves. The correlation coefficient of each calibration curve was greater than 0.99. The limit of detection (LOD), defined as a signal/noise ratio (S/N) = 3, was based on a 50 L water sample. The test limit of the method was: 2.2－108 pg/g. For each set of 10 field samples, a blank test was conducted. The results showed that all monomers of PBDEs were below the detection limit. The average recovery rates of the recovery indicators 13C-PCB141 and PCB209 were 83%~112% and 86%~120% respectively, both meeting the requirements for US EPA1614.

RESULTS AND DISCUSSIONS

Exposure Concentration to PBDEs via Oral Media

The PBDEs concentrations in drinking water, soil and foods (dried sweet potato, rice, chicken, pork) were tested and the results are shown in Table 1. Among the 6 media, low-brominated BDEs and high-bromo-PBDEs were detected, and the concentrations of the former were 35 to 495 times higher than of the latter ones. The low bromide ΣBDEs in soil were 1178.47 ng/g, and were the highest among all tested media.

Table 1. PBDEs levels in serum (ng/g fat).

	Mean	Std. deviation
BDE209	7.08	12.34
BDE077	4.03	15.75
BDE085	1.97	20.95
BDE126	6.68	18.42
BDE205	9.36	15.28
BDE203	4.34	13.49
BDE100	1.97	3.76
BDE119	9.94	10.75
BDE99	1.81	4.68
BDE118	4.40	11.94
BDE116	4.31	17.03
BDE85	2.28	3.59

The low bromide concentration contributed 48.9% to the soil contamination, among which BDE-47 had the highest concentration of 523.55 ng/g. The result shown in Fig.1 was similar to that found in Guangdong, China [15], Chicago, USA [16] and Kyoto, Japan [17]. The cause was analyzed and it was concluded that high-brominated BDEs, BDE-209 could be degraded in soil to low-brominated BDEs monomer (BDE-47) [18].

In the study on ground drinking water, BDE-1 and BDE-47 were found to be the monomers with higher concentrations, with concentration values of 1.81 ng/g and 0.79 ng/g, respectively. In comparison, the contribution of low brominated BDEs was higher. Chinese scientists found that BDE-47 was the main pollutant in the sea water of Pearl River Delta and the water for cultivation in Jiaozhou Bay [19], which was consistent with the findings of this study [20]. BDE-1, BDE-7 contents were found to be the highest in the four oral media: chicken, pork, rice and dried sweet potato. Researchers in China have found out that the highest detection rate and concentrations of BDE-47 and BDE-99 were in chicken in the e-waste dismantling area of Guangzhou [21]. BDE-47 and BDE-99 were also dominant in the fish samples in Yueqing Bay waters [22], in some foods from Dalian [23] and in carrots, spinach, etc. from Shanghai area [24]. The above-mentioned research findings on oral media are inconsistent with the findings of this study, probably because these four groups of studied organisms had different absorption and metabolism to BDE-47 [21].
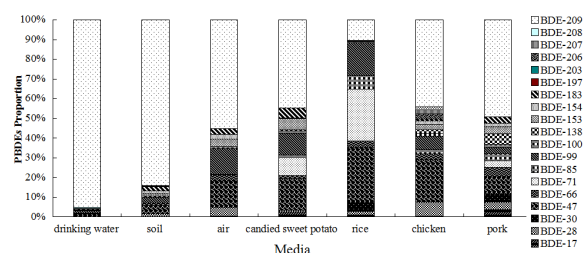
Fig. 1. PBDEs proportion in media.

Analysis on PBDEs concentrations in human blood

PBDEs enter the human body via oral media, air and other media when people are exposed to them in the environment [25]. The content and distribution model can be assessed by detecting the PBDEs levels in the blood. The highest BDE-47 content was found in the blood samples of Spanish infants studied by Meneses et al. [26] and in the blood samples of Belgian infants and mothers studied by Covaci et al. [27]. BDE-47 concentration among the homologous series of PBDEs was found to be the highest in the blood samples based on the following studies: blood tests of PBDEs affected population in North America conducted by Hites [28]，blood tests of Norwegian men aged between 40~50 conducted by Thomsen [29], tests on samples of umbilical cords of Swedish infants and mothers' vein samples for PBDEs conducted by Sjudin [30]. Researchers from Indiana University [31] and Stockholm University [32] found from the analysis of blood samples of children in an e-waste

dismantling area that the content of low-brominated BDEs, such as BDE-47 and BDE-99, etc., was high and they could accumulate in the blood. The highest BDE-209 content was found in placenta tests of Danish women conducted by Frederiksen [33]. In addition, BDEs monomers were also found in samples of umbilical cords of Spanish infants and serum samples of their parents conducted by Gomarab [34]. Different levels of PBDEs were found in the blood samples of infants and their mothers in the test conducted in a city in the southern part of China by Qu [35]. The content of BDE-209 was found to be as high as 64.99 ng/g when testing PBDE in the serum of the workers in the e-waste dismantling area in Guiyu, Guangdong province, and those were metabolized and accumulated in the human body according to the study conducted by Ren [36] Gas chromatography/mass spectrometry approaches were adopted to detect PBDEs content in the blood of newborns in the e-waste dismantling region in

Guangdong, and the distribution of PBDEs was discussed by Wu [37] The distribution of PBDEs in human blood was studied and the content was analyzed by Qu [38].

In this study, 12 kinds of PBDEs congeners were detected from 437 blood samples in the studied area, see Table 2 for the monomer concentration. The content of ΣPBDEs was 58.17 ng/g (fat) in the analyzed samples. BDE-119 contribution was the highest, up to 17.1% in total, followed by BDE-205 and BDE-209. BDE-47 was found to be with the highest content in the domestic and international studies on PBDEs accumulation in human body [28,39]. The contribution of each monomer to PBDEs in blood samples in the studied area was slightly different from the reported findings. The cause was explored and it was believed that some monomers could be converted into BDE-47 through body metabolism. PBDEs metabolites were found in rat

Table 2. Risk assessment of exposure parameters

	CS	mg/kg	*
	IR	mg/day	50
	CF	kg/mg	10-6
Formula for daily soil exposure dose：	BW	kg	62.5
	ED	a	30
$ADD(mg/kg \bullet day) \dfrac{CS \times IR \times FI \times EF \times ED}{BW \times AT}$	FI	%	1.0
	EF	days/year	365
	AT	days	Carcinogenic：70×365
			Non-carcinogenic：ED×365
	CW	mg/L	*
Drinking water：	IR	L/day	2.0
	BW	kg	62.5
$Intake(mg/kg \bullet day) = \dfrac{CW \times IR \times EF \times ED}{BW \times AT}$	ED	a	30
	EF	days/year	365
	AT	days	Carcinogenic：70×365
			Non-carcinogenic：ED×365
	CF	mg/kg	*
	IR	kg/meal	0.104
Diet：	EF	meals/year	365×3
	FI	%	1.0
$ADD(mg/kg \bullet day) = \dfrac{CF \times IR \times FI \times EF \times ED}{BW \times AT}$	ED	a	30
	BW	kg	62.5
	AT	days	Carcinogenic：70×365
			Non-carcinogenic：ED×365

Note: "*" is the actual value, others are reference values of US EPA.

Table 3. Daily exposure dose to PBDEs via environmental media in e-waste dismantling area (mg/kg·day).

Environmental media	Daily average exposure dose
Drinking water	0.0902
Soil	8.26×10^{-4}
Dried sweet potato	0.1926
Rice	0.3921
Chicken	2.0282
Pork	0.0136
Total daily dose of exposure	2.7175

feces by Maish [40]; BDE-209 was found to be metabolized and converted to BDE-47 and other monomers in rats experiment by Qiu [31,41]. Therefore, it could be preliminarily concluded that BDE-209, etc. in the samples tested by domestic and international scientists might have been metabolized to BDE-47, while BDE-209, etc. in the samples of this study have not been metabolized *in vivo*, but the rule of metabolism in other homologues needs further study. BDE-119, BDE-205 belong to the 5-brominated flame retardants which showed high contents in this study. The extensive use of such flame retardants in the studied area might be the cause for the difference between the obtained results and the findings by domestic and international scientists. The variance of domestic and international research findings may relate to race, lifestyle, genetics and polluting factors.

Daily average exposure amount via oral media

Studies have shown that PBDEs were accumulated in large amounts inside the organisms after they were absorbed via the food chain, while the human being as the terminal of food chain, took in huge amount of PBDEs from foods [36]. The daily average exposure amount by the population in the studied area via oral media was calculated for this study by adopting the exposure dosage calculation method of the four-step approach proposed by U.S. National Academy of Sciences (NAS), based on questionnaires and optimized exposure parameters actually measured, see Tables 2, 3. It is obvious that the daily average exposure amount of 2.71 mg/kg/day to ∑PBDEs by the population in the studied area is much greater than the risk dose of 0.01 mg/kg/day issued by EPA.

Both domestic and international studies have shown that the amount of PBDEs intake via oral exposure pathways should not be ignored [42]. It was found that poultry and meat products accounted for 60% to 70% of the Americans total intake of PBDEs via foods. Canadians took in 44 ng/g of PBDEs per day from foods [43,44]. The highest concentration of PBDEs was found in poultry, fatty foods and in animal liver. In Sweden

[45] Finland [46], local residents took in 47% and 55%, respectively, of the PBDEs via eating high-fat food. 50% of Swedish intake of PBDEs was from high-fat food. The average concentration of PBDEs in the body of those people who didn't eat fish was 0.4 ng/g (fat), while the PBDEs level was 2.2 g/g (fat) [47] in those people who ate fish 10 to 20 times per month. Lind [48] pointed out that high-fat food was the main source of PBDEs intake accounting for two-thirds of the total intake. Otha [49] found that vegetables and grain could absorb PBDEs from the air and PBDEs entered the body via food chain resulting in accumulation.

Potential impact of PBDEs contamination on human health via mouth media in e-waste dismantling area

Domestic and international reports have found that smoking and drinking status, amount of fruit intake, water intake, all had great impact on human metabolism and absorption capacity. Correlation analysis was conducted on PBDEs content in the blood of the studied group with its relevance with gender, age, smoking, drinking, fruit and food intake, water intake and other factors. The results showed that the blood levels of PBDEs did not correlate with gender. The correlation analysis, conducted on different age groups for PBDEs in human blood found that PBDEs concentration in the blood of people aged between 30 to 45 years correlated with age (P=0.031). According to the actual survey and the epidemiological statistics, this age group probably lived in the studied area when e-waste dismantling industry was most prosperous. The accumulation of PBDEs in the blood correlated with alcohol (P = 0.047) and did not correlate with other confounding factors [50].

The data collected from the questionnaire regarding the studied subjects were: years of residence, lifestyle, diet habit etc.; the daily average exposure to PBDEs via oral media was calculated, and its correlation with PBDEs accumulation in the blood was analyzed (Table 4). The findings showed that years of residence obviously correlated with PBDEs concentration in blood:

Table 4. Correlation between years of residence and blood concentration exposure dose via oral media.

Correlation	Residence	Exposure dose via oral media					
		Drinking water	Soil	Dried sweet potato	Rice	Chicken	Pork
Correlation coefficient	0.963	0.879	0.434	0.561	0.465	0.519	0.442
P	0.005**	0.045*	0.489	0.285	0.456	0.311	0.483

*P<0.05 closely related **P<0.01 closely related.

The longer they lived in the locality, the higher was the PBDEs accumulation in the blood. Only the oral exposure pathway in the studied area was considered for this study, no occupational exposure was studied. The correlation analysis on the oral exposure dose with serum accumulation of PBDEs showed that it obviously correlated with the exposure to drinking water, and did not correlate with any other media. Therefore it can be preliminarily concluded that the exposure dose to drinking water by the people in the studied area affected the accumulation in the blood. Whether it is due to the human function of metabolizing drinking water was not reported at home or abroad, and it requires the support by the results of toxicology tests on animals.At present the toxicology study on PBDEs mainly relies on animal experiments. Eriksson [51] exposed rats and mice to BDE-209 with purity of 94% to 97%, the results showed that the incidence of liver tumors in rats and mice significantly increased. The exposure via oral media to male rats, mice, female rats, mice was 2240 mg/kg·day, 1120 mg/kg·day 2550 mg/kg·day, and 1200 mg/kg·day, respectively. The animal tests conducted by U.S. NTP [52] found that after rats and mice were exposed to BDE-209 at a dose of 0.25 mg/kg and 50 mg/kg, respectively, for 103 weeks, those with high dose had significantly higher incidence of liver cancer and pancreatic cancer, and slightly higher incidence of thyroid follicular cells adenocarcinoma and cancer. Vberg [53] found that administering BDE-209 with different single dosage to rats during their rapid growth period (postnatal 3rd day, 7th day, 10th day) for interventions could affect neurotransmitter secretion, resulting in neurobehavioral changes in rats with neurodevelopmental toxicity. Hites [54] tracked male mice after they were exposed to BDE-47 (10.5 mg/kg) once on the 10th day of birth and found that BDE-47 was toxic to the nervous system, and the effects increased with age and became more pronounced. Many domestic and international experiments on animals showed that PBDEs caused harm to the nervous system which was genetic [55]. Birmbanm [56] found out from the study on the toxic effects on male rats that the concentration of thyroxine decreased while thyroid-stimulating hormone concentration increased, the enzyme activity of EROD, PROD and UDPG inside rats increased when the concentration was 30.60 mg/kg. Stoker [57] studied male and female mice, and found out that the serum thyroxine of male mice significantly increased when exposed to PBDEs with a dose of 30.60 mg/kg on the 21th day of birth, same with female rats when exposed to doses of 3.30 and 60 mg/kg on the 31th day of birth.

CONCLUSION

It is quite obvious that PBDEs contamination has been accumulated in the blood of the residents in the studied area, and the results correlated with the oral route of exposure to certain extent. Many domestic and international experiments on animals have shown that the toxicity of PBDEs is diversified. Although there are reports available regarding the amount of PBDEs accumulation in the human body and the risk values of daily exposure to PBDEs proposed by EPA, the damaging effects of PBDEs contamination on human health and their accumulation are rarely known and will be further studied.

REFERENCES

1. R. Renner, *Environ. Sci. Technol.*, **34**, 222 (2000).
2. C. A. Wit, *Chemosphere*, **46**, 583 (2002).
3. T. A. McDonald, *Chemosphere*, **46**, 745 (2002).
4. K. Noren, D. Meironyte, *Chemosphere*, **40**, 1111 (2000).
5. D. R. Oros, D. Hoover, F. Rodigari, D. Crane, J. Sericano, *Environ. Sci. Technol.*, **39**, 33 (2005).
6. W. L. Song, J. C. Ford, A. Li, N. C. Sturchio, K. J. Rockne, D. R. Buckley, W. J. Mills, *Environ. Sci. Technol.*, **38**, 3286 (2004).
7. O. I. Kalantzi, F. L. Martin, G. O. Thomas, R. E. Alcock, H. R. Tang, S. C. Drury, P. L. Carmichael, J. K. Nicholson, K. C. Jones, *Environ. Health Perspect.*, **112**, 1085 (2004).
8. A. Mazdai, N. G. Dodder, M. P. Abernathy, R. A. Hites, R. M. Bigsby, *Environ. Health Perspect.*, **111**, 1249 (2003).
9. M. Alae, *Environ. Monit. Assess.*, **88**, 327(2003).
10. S. G. Chu, X. B. Xu, *Acta Scien. Circum.*, **15**, 423 (1995).
11. Y. M. Li, G. B. Jiang, Y. W. Wang, P. Wang, Q. H. Zhang, *Chinese Sci. Bull.*, **53**, 165 (2008).
12. T. Chen, C. Zhou, Y. J. Mou, B. B. Yu, *J. Ecol. Rural Environ.*, **27**, 20 (2011).
13. Y. Yang, D. L. Li, H. M. Wang, *Modern Preventive Medicine*, **37**, 1834 (2010).

14. X. Luo, B. Mai, Q. Yang, J. Fu, G. Sheng, Z. Wang, *Mar. Pollut. Bull.*, **48**, 1102 (2004).
15. L. G. Chen, B. X. Mai, Z. C. Xu, J. L. Han, X. C. Peng, G. Y. Sheng, *Acta Scien. Circum.,* **28**, 150 (2008).
16. H. Eunha, A. H. Ronald, *Environ. Sci. Technol.*, **39**, 7749 (2005).
17. K. Hayakawa, H. Takatsuki, I. Watanabe, S. I. Sakai, *Chemosphere*, **57**, 343 (2004).
18. J. Jin, Y. Wang, W. Z. Liu, X. T, Tang. *Acta   Scien. Circum.,* **28**, 1463 (2008).
19. S. Chen, B. Mai, Y. P. Zeng, X. Luo, M. Yu, G. Sheng, J. Fu, *Acta Scien. Circum.,* **25**, 1265(2005).
20. Y. F. Guan, X. Y. Tu, M. H. Wu, *Ecol. Environ. Scien.,* **20**, 474(2011).
21. M. Y. Zhou, H. Z. Zhang, B. Xia, Y. Cui, X. Y. Qiao, B. J. Chen, K. L. Leng, *Mar.   Environ. Sci.*, **24**, 293 (2009).
22. L. G. Lin, L. L. Zhang, R. N. Sun, X. M. Zhou, S. N. Peng, W. J. Jiang, *J. Analyt. Sci.*, **24**, 512(2008).
23. S. K. Chen, X. F. Shen, J. H. Jiang, *J. Anhui. Agric. Sci.*, **37**(23), 11040 (2009).
24. Z. F. Liu, Y. H. Lang, Z. M. Cao, *Chinese Journal of Science*, **38**, 1227 (2007).
25. X. Z. Meng, Y. Z. Zeng, L. P. Yu, Y. Guo, B. X. Mai, *Environ. Sci. Technol.*, **41**, 4882 (2007).
26. A. Covaci, J. D. Boer, J. J. Ryan, S. Voorspoels, P. Schepens, *Environ Res.*, **88**, 210 (2002).
27. M. Meneses, H. Wingfors, M. Schumacher, J. L. Domingo, G. Lindström, B. V. Bavel, *Chemosphere*, **39**, 2271 (1999).
28. R. A. Hites. *Environ. Sci. Technol.*, **38**, 945(2004).
29. C. Thomsen, E. Lundanes, G. Becher, *Environ. Sci. Technol.*, **36**, 1414 (2002).
30. A. Sjödin, L. Hagmar, E. Klasson-Wehler, K. Kronholm-Diab, E. Jakobsson, A. Bergman, *Environ. Health Perspect.*, **107**, 643 (1999).
31. X. Qiu, R. M. Bigsby, R. A. Hites, *Environ. Health Perspect.*, **117**, 93 (2009).
32. D. M. Athanasia, S. N. Cuadra, G. Marsh, *Environ. Health Perspect.*, 2008; **116**, 400 (2008).
33. M. Frederiksen, M. Thomsen, K. Vorkampk, L. E. Knudsen, *Chemosphere*, **76**, 1464 (2009).
34. B. Gomara, L. Herrerd, J. J. Ramos, J. R. Mateo, M. A. Ferandez, J. F. Garcia, M. J. Gonzalez, *Environ. Sci. Technol.*, **41**, 6961 (2007).
35. W. Y. Qu, D. C. Wang, G. Y. Sheng, *China Environ. Sci.*, **27**, 269 (2007).
36. G. F. Ren, Z. Q. Yu, Y. F. Sun, *J. Shanghai University*, **16**, 441 (2010).
37. K. S. Wu, Y. Y. Guo, J. X. Liu, *J. Shantou University medical College.*, **23**, 65 (2009).
38. W. Y. Qu, X. H. Bi, G. Y. Sheng, S. Y. Lu, J. M. Fu, *Chinese J. Analyt. Chem.*, **35**, 1015 (2007).
39. A. Sjödin, L. Hagmar, E. Klasson-Wehler, K. Kronholm-Diab, E. Jakobsson, A. Bergman, *Environ. Health Perspect.*, **107**, 643 (1999).
40. G. Marsh, M. Athanasiadou, I. Athanssandis, A. Sandholm, *Chemosphere*, **63**, 690 (2006).
41. X. H. Qiu, M. Mercado-Feliciano, R. M. Bigsby, R. A. Hites, *Environ. Health Perspect.*, **115**, 1052 (2007).
42. A. Schecter, O. Papke, T. R. Harris, K. C. Tung, A. Musumba, J. Olson, L. Bimbaum. *Environ. Health Perspect.*, **114**, 1515 (2006).
43. J. J. Rayan, B. Rarty, *BFR Part 4*, **51**, 226(2001).
44. M. Frederiksen, K. Vokkanp, M. Thomsen, L. E. Knudsen, *International Journal of Hygiene and Environmental Health*, **212**, 109 (2009).
45. P. O. Darnerud, S. Atuma, M. Aune, R. Bbjerselius, A. Glynn, K. P. Grawe, W.Becker, *Food Chem. Toxicol.*, **44**, 1597 (2006).
46. Kiviranta H, M. L. Ovaskainen, T.Vartiaine, *Environ. Int.*, **30**, 923 (2004).
47. A. Sjödin, L. Hagmar, E. Klasson-Wehler, J. Bjork, A. Bergman, *Environ. Health Perspect.*, **108**, 1035 (2000).
48. Y. Lind, M. Aune, S. Atuma, *Organohalogen Compd.*, **58**, 181 (2002).
49. S. Ohta, D. Ishizuka, H. Nishimuk, T. Nakao, O. Aozasa, Y. Shimidzu, F. Ochioi, T. Kida, M. Nishi, H. Miyata, *Chemosphere*, **46**, 689(2002).
50. Y. J. Yu, *Beijing: Environ Sci Press.*, 2011: 91. (In Chinese).
51. P. Eriksson, Jakobsson E, Fredriksson A, *Organohalogen Compd.*, **35**, 375 (1998).
52. NTP. Toxicology and Carcinogenesis Studies of Decabromodiphenyl Oxide (CAS No 1163-19-5) in R334/N rats and B6C3F1 mice (feed studies). NTP Technical Report Series No 309. Research Triangle Park，NC: National Toxicology Program, 2011.
53. H. V. Berg, A. Fredriksson, P. Eriksson, *Toxicol Sci.*, **81**, 344 (2004).
54. R. A. Hitea, J. A. Foran, S. J. Schurager, B. A. Knuth, M. C. Hamilton, D. O. Caepenter, *Environ. Sci. Technol.*, **38**, 4945 (2004).
55. T. A. McDonald, *Chemosphere*, **46**, 745 (2002).
56. L. S. Birnbaum,D. F. Staskal, *Environ. Health Perspect.*, **112**, 9 (2004).
57. T. E. Stoker , S. C. Lavrs, K. M. Crofton, *Toxicol. Sci.*, **78**, 144 (2004).

ПОТЕНЦИАЛНО ВЪЗДЕЙСТВИЕ НА ЗАМЪРСЯВАНИЯ ОТ ПОЛИБРОМИРАНИ ДИФЕНИЛОВИ ЕТЕРИВЪРХУ ЧОВЕШКОТО ЗДРАВЕ В ПЛОЩАДКИ ЗА ОБЕЗВРЕЖДАНЕ НА ЕЛЕКТРОННИ ОТПАДЪЦИ

Я. Янг[1], Кс. Ли[1], Р. Ксу[1], М. Ли[2*], Ю. Ю[3*]

[1]Училище по екологично инженерство и сигурност, Университет в Чангжоу, Китай
[2]Китайска изследователска акадмия по екологични науки, Бейджин, Китай
[3]Южнокитайски институт по екологични науки, Министерство по опазване на околната среда, Гуангжоу, Китай

(Резюме)

Полибромираните дифенилови етери (PBDE) са клас от устойчивите бромирани органични замърсители, които се пренасят чрез хранителната верига и могат да причинят увреждания на човешкото здраве. Изследването на заразявания с BDE чрез устата, например с питейна вода, почва или храна(сушени сладки картофи, ориз, пилешко, свинско месо) е проведено в района Таижоу (провинция Жейианг) в район за разкомплектоване на електронни отпадъци. Изследвани са концентрациите на BDE, тяхното разпределение и степента на експозиция за човешкото тяло. Параметрите на експозиция и дневните дози, приети орално в изследвания район са определени съгласно изчислителната методика за дозата на експозиция, разработена от U.S. National Academy of Sciences (NAS). Анализът на корелацията между експозицията на питейна вода и концентрацията на PBDE в кръвен серум показва положителен резултат. Обаче серумната концентрация на PBDE при други орални заразяванияне се корелира. Затова предварителното заключение е че количеството приета питейна вода влияе върху съдържанието на PBDE в кръвта. Изследването показва значителна корелация между годините престой и концентрацията на PBDE в кръвта, като последната се повишава с увеличаването на живота в засегнатия район.

QSAR study of halogenated benzene bioaccumulation factors in fish

F. Chen[1,2], N. Li[1,2], D. Yang [1,2,3], Y. Zhou[1,2*]

[1]Key Laboratory of Marine Bio-resources Restoration and Habitat Reparation in Liaoning Province, Dalian Ocean University, 116023, Dalian, China
[2]Key Laboratory of North Mariculture, Ministry of Agriculture, Dalian Ocean University, 16023, Dalian, China
[3]College of Life science and Technology, Dalian University of Technology, 116021, Dalian, China

Certain elements or compounds, that are difficult to decompose, accumulate in organisms. The phenomenon of higher compound concentrations in organisms than in the environment is called bio-concentration. This research studies 21 bio-concentration factors (B_{CF}) of halogenated benzene in fish. Here, 14 halogenated benzene molecule parameters are randomly selected as a training set and the remaining parameters are considered as a testing set to calculate halogenated benzene molecule descriptors. A prediction model of the quantitative structure–activity relationship between bio-concentration and molecular descriptors is built using the multiple linear regression method. The independent variable with serious collinearity is eliminated to obtain an optimal prediction model (R^2=0.919). The prediction data of linear regression are also obtained using the molecular parameters of the test set. A support vector machine (SVM) is used to predict the result of the test set using the training set as study samples. The best method for predicting the bio-concentration factor of halogenobenzene in fish is determined by comparing the prediction accuracy of the two methods. The final results indicate that the model officially built by stepwise regression can effectively predict B_{CF}. SVM is more accurate in predicting B_{CF}. SVM possesses better predictive capability in issues with a small amount of samples.
Key words: Bio-concentration factor, halogenobenzene, linear regression, quantitative structure-activity relationship, prediction model, support vector machine.

INTRODUCTION

Halogenated benzenes are compounds that feature replacement of one or more hydrogen atoms in benzene by halogen atoms; these compounds are widely distributed in the air, soil, groundwater, surface water, and the sea [1]. Halogenated benzenes are widely used in chemical, electronic, and pharmaceutical industries as chemical raw materials. They have become the focus of many researchers because of their strong carcinogenic, teratogenic, and mutagenic effects, toxicity, persistence, and bio-concentration [2]. The concentration of halogenated benzenes in the environment stepwise increases through the food chain. The more high-end creatures in the food chain, the more harmful are the side effects. This phenomenon is called bio-concentration.

The bio-concentration factor is the ratio between the balance concentration of a compound in an organism and its balance concentration in water. B_{CF} is generally used to express bio-concentration. Bio-concentration is associated with the food chain, where different creatures are closely linked by eating and being eaten. While the concentrations of some chemicals may be harmless to some creatures in the environment, they can become harmful to human health through biological enrichment and biomagnifications in the food chain [3,4]. Therefore, studying the bio-concentration factor of toxic halogenated benzenes is significant. Studying the physical and chemical properties of halogenated benzenes may also provide a means of predicting bio-concentration.

The quantitative structure–activity relationship (QSAR) between the molecular structures of halogenated benzenes and their bio-concentration is the primary subject of this study. The essence of the QSAR model is to obtain information from the structure-bio concentration factor model through a sufficient amount of data and establish the molecular structure of halogenated benzenes and their enrichment factor using multiple linear regression (MLR) [5,6]. The law of large numbers of classical statistical mathematics states that the statistical law will be accurately known and the results of the fitting model can fully reflect the real law only when the known sample number approaches infinity. In actual problems such as chemicals, drug design, and environment protection, obtaining the known sample number is often difficult. Vapnik proposed statistical learning theory by studying mathematical theory for over 30 years and developed the support vector machine on the basis of statistical learning theory [7, 8]. SVM, which includes SV classification and SV

regression, has been successfully applied in language recognition, facial recognition, text recognition, and drug design [9, 10, 11]. SVM is not only effective at simplifying structures but also presents outstanding capability for all technology types, especially in the field of generalization, as confirmed by many previous experiments [12, 13]. Therefore, we used SVM to verify small sample descriptors that have been screened out in the present work. A liable mathematical prediction model is further established using SVM to provide a theoretical basis for analyzing the biological toxicity of halogenated benzene compounds.

MATERIALS AND METHODS

Data set

This study employed experimental data of 21 halogenated benzene bio-concentration factors described in ref. [14]. The SMILES format of halogenated benzene was searched to obtain descriptor information and construct the MLR model. PaDEL-Descriptor software was used to obtain the molecular descriptors of halogenated benzene [15]. The 3D descriptors of halogenated benzene were calculated to select the most suitable descriptor parameter by MLR. The QSAR model between the descriptor and B_{CF} was finally built. The logarithm $\lg B_{CF}$ was used to express the bio-concentration in a more scientific manner because the different B_{CF} values of halogenated benzene largely vary. The higher the value of $\lg B_{CF}$, the higher is the bio-concentration capability of the compound. Here, 14 molecular parameters were randomly selected as a training set for modeling, and the remaining 7 parameters were classified as a testing set. The optimal prediction model was determined by MLR of the parameters.

Method

MLR

MLR provision is the classic QSAR modeling method that establishes the forecast method by analyzing two or more independent variables and a dependent variable correlation analysis [16]. A linear relationship for the calculation of the correlation between the independent and dependent variables cannot determine which descriptors exactly predict and establish the mathematical model using the selection of the 3D descriptor parameters. Therefore, this study uses stepwise regression method to establish the halogenated benzene bio-concentration factor B_{CF} covariant relationship with molecular descriptors. The mathematical function expression of the MLR equation is as follows:

$$Y = \alpha_0 + \alpha_1 x_1 + \alpha_2 x_2 + \cdots + \alpha_n x_n, \quad (1)$$

In eq. (1) Y is the concentration fact; α_0 is a constant; $x_1 \dots x_n$ are molecular descriptors; and $\alpha_1 \dots \alpha_n$ are regression coefficients.

SVM

SVM was used to validate the results and compare them with MLR forecasting to verify the accuracy of MLR in reducing errors and make more accurate predictions. SVM may be completely described by the training set and kernel function [13]. Finding the optimal hyper plane, which is the plane that separates all samples with the maximum margin, is an essential principle of SVM [17, 18]. This plane helps to improve the predictive ability of the model and lowers the error that may occasionally occur during classification.

Fig. 1 illustrates the optimal hyper plane; here, "red" indicates the samples of type 1 and "blue" represents the samples of type 1.
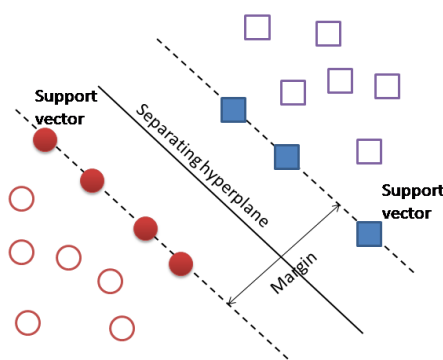
Fig. 1.Support vectors determining the position of the optimal hyper plane.

The SVM method can be applied to the function fitting problem. SVM was applied in this study to obtain the regression formula as follows:

$$Y = f(x) = \sum_{i=1}^{n}(T_i^* - T_i)(i_i \times i) + b, \quad (2)$$

The nonlinear problem must be transformed into a linear problem using the kernel function method to project the original data to a high-dimensional feature space. The following formula is then obtained:

$$Y = f(x) = \sum_{i=1}^{n}(T_i^* - T_i)K(i_i \times i) + b, \quad (3)$$

RESULTS

QSAR model of the stepwise regression method

The 3D molecular descriptors of halogenated benzene compounds are studied through 3D

autocorrelation. We describe the bio-concentration factor by using the descriptors as charged partial surface area, length over breadth, and weighed holistic invariant molecule [19,20,21]. Vv and LOBMAX are filtered from the existing molecular descriptors by the stepwise regression method. Vv is used to describe the weighed holistic invariant molecula [19], and LOBMAX is used to describe the length over breadth. The QSAR model between B_{CF} and the molecular structure descriptors is established according to the minimal relative standard deviation and the maximum principle of correlation coefficient as:

$$Y = 2.132 + 0.245 \times Vv - 1.029 \times LOBMAX, \quad (4)$$

First, the sample size of the regression model is four times larger than the independent variable based on data with statistical regularity. Second, the correlation coefficient of the regression equation established in Table 1 is $R^2=0.919$, which indicates that the model provides good correlation. The model test value of F is 74.294, and the significance level is less than 0.05.

Table 1. Statistical universe of the regression equation.

R	R^2	R^2_{adj}	F	Sig.
0.965	0.931	0.919	74.294	0.000

The equations of each variable test value are listed in Table 2. The results of the *t* test show that the coefficients of the statistic equation are 2.675, 7.535, and -2.557. The probability of the *t* test is 0, which means that the regression equation matches the standard. The VIF values are 1.69 and 1.69 when the VIF value is larger than 10. This result indicates that the independent variables have strong collinearity. The independent variables at this point are consistent with the collinearity inspection, so it can be considered as linear fitting.

Table 2. Determination of the regression equation.

	Beta	t	Sig.	VIF
Constant	2.132	2.675	0.022	
Vv	0.245	7.535	0.000	1.690
LOBMAX	-1.029	-2.557	0.027	1.690

Tables 3 and 4 show the SMILES of the halogenated benzene compounds, descriptor parameters, experimental values, calculated values, and residual errors. Fourteen of the halogenated benzene lgB_{CF} were selected as the training set, and 7 were selected as the test set. The absolute value of the minimum residual error is 0.01, while the absolute value of the maximum residual error is 2.06. The ratios of the experimental values are

0.54% and 67.8%, respectively.

Fig. 2 shows the solid dots indicating the training set and the hollow dots indicating the test set. The experimental and predicted values of the training and testing set molecules are similar to some extent.
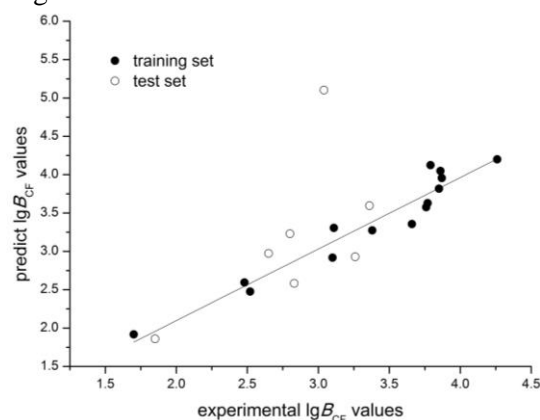
Fig.2. Comparison of the experimental and predicted values

SVM prediction of the test set results

The selected compound structure description parameters should have significant structural characteristics in the SVM application to build a matching model and help predict the compound properties. We obtained Vv and LOBMAX in this study using the stepwise regression method of molecular descriptors with 14 descriptors taken as training samples for SVM learning. The lgB_{CF} predicted by the SVM is obtained by inputting the descriptor parameters of the test set into SVM.

Seven of the halogenated benzene lgB_{CF} were selected as the test set. The absolute value of the minimum residual error is 0.15, whereas the absolute value of the maximum residual error is 1.22. The ratios of the experimental values are 8% and 40%, respectively.

MLR and SVM results

The appropriate horizontal ordinate range is selected and the prediction scatter plot of the MLR test set is described as follows:

Fig. 3 shows precise matching results, and the predicted and experimental values are close. Figs. 3b and 3c reveal the residual, experimental, and predicted relationships. The residual values are relatively low.

The SVM test results are highly similar to those of MLR. SVM can generate a fairly analogical and precise result compared with the MLR test results. In summary, both MLR and SVM can be suitably applied for determining halogenated benzene bioaccumulation factors in fish.

Table 3. MLR prediction of the training set parameters of the bio-concentration factor of halogenated benzene compounds in fish.

Name	Vv	LOBMAX	SMILES	lgB$_{CF}$		
				experimental	predicted	residual
1,2,3,4-tetrachlorobenzene	11.04	1.17	c1(c(c(ccc1Cl)Cl)Cl)Cl	3.77	3.63	0.14
1,2,3-trichlorobenzene	9.63	1.15	c1(c(cccc1Cl)Cl)Cl	3.11	3.31	-0.20
1,2,4,5-tetrachlorobenzene	10.81	1.17	c1(c(cc(c(c1)Cl)Cl)Cl)Cl	3.76	3.58	0.18
1,2-dichlorobenzene	7.90	1.43	c1(c(cccc1)Cl)Cl	2.48	2.59	-0.11
1,3,5-trichlorobenzene	9.94	1.26	c1(cc(cc(c1)Cl)Cl)Cl	3.38	3.27	0.11
1,4-dichlorobenzene	7.38	1.42	c1(ccc(Cl)cc1)Cl	2.52	2.47	0.05
hexachlorobenzene	14.12	1.35	c1(c(c(c(Cl)c(c1Cl)Cl)Cl)Cl)Cl	4.26	4.20	0.06
2,4,5-Trichlorotoluene	12.51	1.21	c1(c(cc(Cl)c(c1)Cl)Cl)C	3.87	3.96	-0.09
1,2,3,4,5-Pentachlorobenzene	12.63	1.15	c1(c(c(cc(c1Cl)Cl)Cl)Cl)Cl	3.86	4.05	-0.19
1,2,4,5-Tetrabromobenzene	13.17	1.20	c1(c(cc(Br)c(c1)Br)Br)Br	3.79	4.12	-0.33
1,2,4-Tribromobenzene	11.06	1.44	c1(c(ccc(c1)Br)Br)Br	3.66	3.36	0.30
1,3,5-Tribromobenzene	12.15	1.25	c1(cc(cc(c1)Br)Br)Br	3.85	3.82	0.03
Bromobenzene	6.73	1.81	c1(ccccc1)Br	1.7	1.92	-0.22
1,2-dibromobenzene	9.17	1.42	c1(c(cccc1)Br)Br	3.1	2.92	0.18

Table 4. MLR prediction of the test set parameters of the bio-concentration factor of halogenated benzene compounds in fish.

Name	Vv	LOBMAX	SMILES	lgB_{CF}		
				experimental	predicted	residual
1,2,3,5-tetrachlorobenzene	11.26	1.26	c1(c(cc(Cl)cc1Cl)Cl)Cl	3.36	3.60	-0.24
1,2,4-trichlorobenzene	9.29	1.44	c1(c(ccc(c1)Cl)Cl)Cl	3.26	2.93	0.33
1,3-dichlorobenzene	7.96	1.08	c1c(cccc1Cl)Cl	2.65	2.97	-0.32
Chlorobenzene	6.16	1.73	c1(ccccc1)Cl	1.85	1.86	-0.01
1,3-dibromobenzene	9.28	1.14	c1c(cccc1Br)Br	2.8	3.23	-0.43
Hexabromobenzene	17.76	1.34	c1(c(c(c(Br)c(c1Br)Br)Br)Br)Br	3.04	5.10	-2.06
1,4-dibromobenzene	8.30	1.54	c1(ccc(Br)cc1)Br	2.83	2.58	0.25

Table 5. SVM prediction of the test set parameters of the bio-concentration factor of halogenated benzene compounds in fish.

Compound	Experimental	Predicted	Residual
1,2,3,5-tetrachlorobenzene	3.36	3.77	-0.41
1,2,4-trichlorobenzene	3.26	3.1	0.16
1,3-dichlorobenzene	2.65	2.48	0.17
Chlorobenzene	1.85	1.7	0.15
1,3-dibromobenzene	2.8	3.1	-0.3
Hexabromobenzene	3.04	4.26	-1.22
1,4-dibromobenzene	2.83	2.48	0.35

a)

b)

c)

a)

b)

c)
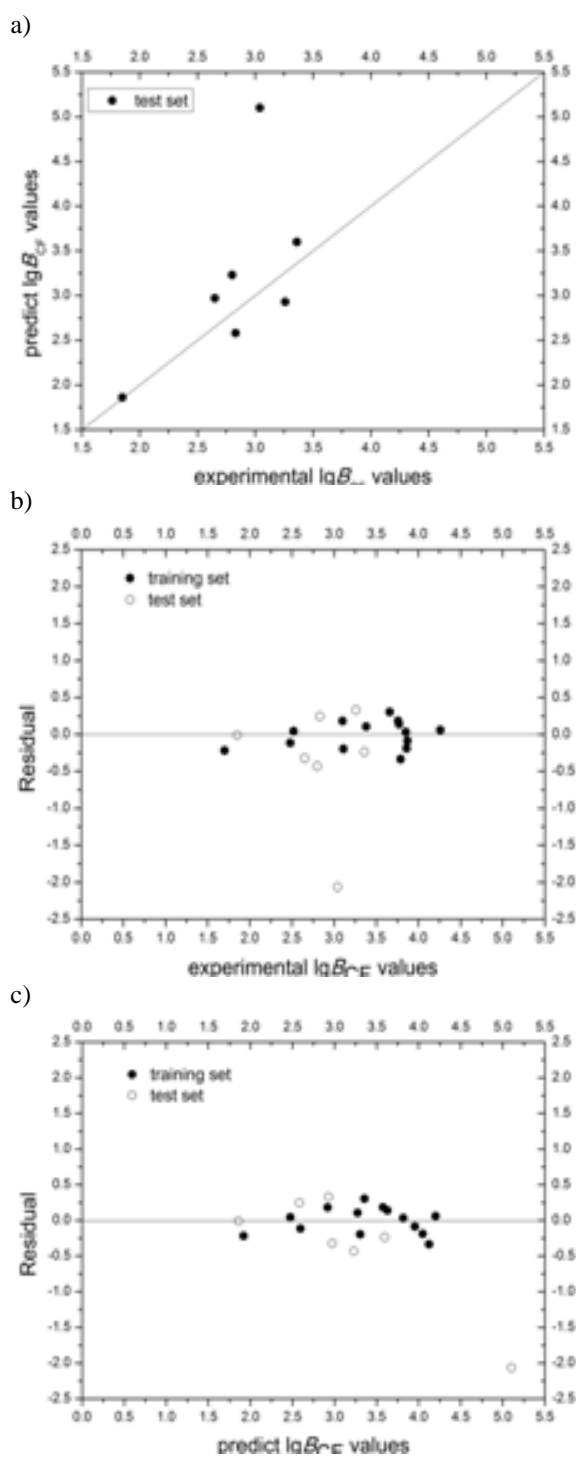
Fig. 3. Test results of the MLR model. a) experimental *vs* predicted values; b) experimental *vs* residual values; and c) predicted *vs* residual values.
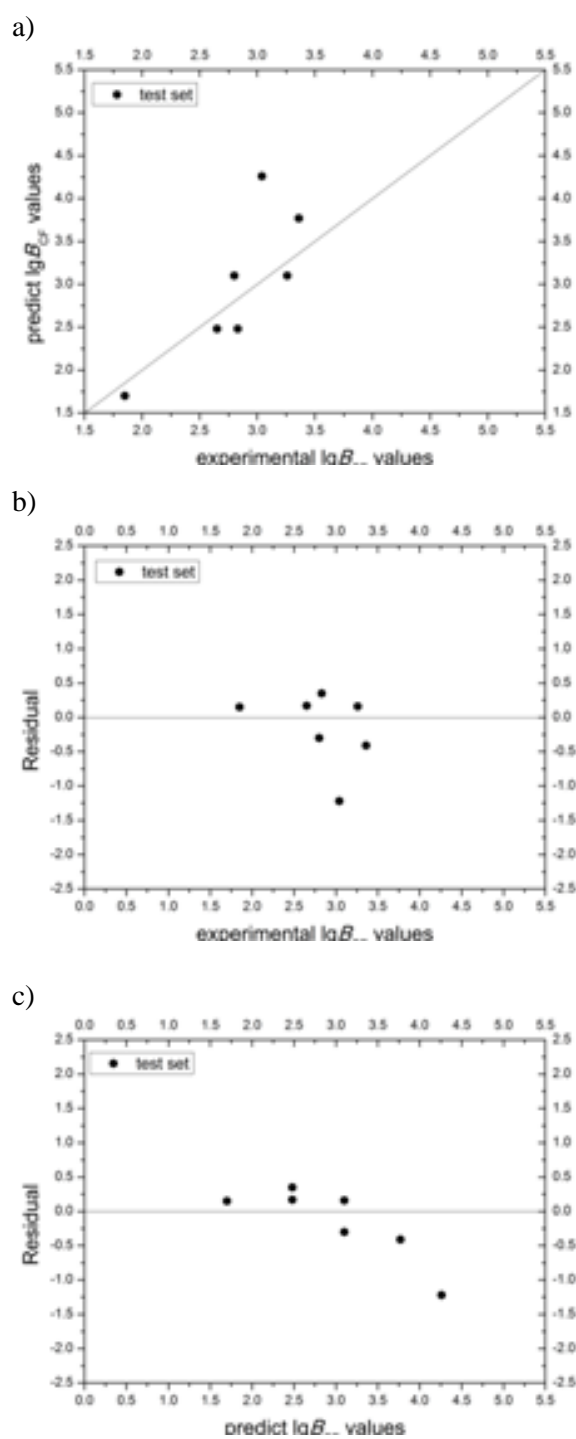
Fig. 4. Test results of the SVM model. a) experimental *vs* predicted values; b) experimental *vs* residual values; and c) predicted *vs* residual values.

1201

CONCLUSIONS

In this work, we used the SVM and MLR stepwise analysis methods. The principle of the MLR stepwise analysis method considers the size of the contribution of each variable to the dependent variable by introducing the variables one at a time and simultaneously inspecting the previously introduced variable. The capability of discriminating a previously introduced variable becomes non-significant as a new variable is introduced. This new variable is removed when a discriminant variable is remarkable, and stepwise regression ends when no important variable for the rest of the variables can be introduced to the discriminant [22]. The equation must conform to the test, the parameters of the obtained descriptors must be remarkable, and the training set correlation coefficient must be $R^2=0.919$ to eliminate collinearity independent variables in the model and ensure that the model has strong predictive ability. The test set molecules are substituted into the equation to obtain the predicted values. The residual distributions of the training and test sets are even. This model has two independent variables, thereby highlighting the influence of Vv and LOBMAX on the B_{CF} of the halogenated benzenes.

Given that SVM has the advantage of solving the problems of small samples, this study also uses SVM to validate the results of MLR. The Vv and LOBMAX descriptors of the 14 groups of training set data are used as learning samples, and the remaining 7 groups of test data are substituted into SVM to obtain the predicted values. The residual value of the prediction obtained from SVM is more stable than that obtained from MLR. The root mean square error (RMSE) of the SVM prediction is 0.42, whereas that of the MLR prediction is 0.94. These values illustrate that the SVM model prediction error is smaller and the model obtained through this method is more stable. The residual value of the MLR prediction of hexabromobenzene is 67.8%, whereas that predicted by SVM is 40.1%. These values show that hexabromobenzene cannot fit the QSAR model; however, in this study, we still retained the full information of hexabromobenzene to authenticate results.

In conclusion, the statistical results of the stepwise method are suitable (training set $R^2=0.919$), and the prediction ability of the model is outstanding. We can obtain more precise prediction values by using SV Minstead of MLR. The model can better specify the descriptors of LOB and WHIM. Thus, we can accurately predict the ultimate bio-concentration factor. The model obtained provides guidance for future research on halogenated benzene concentration factors. The method proposed in this work may be an important means of halogenated benzene compounds concentration research in the fields of chemistry, drug design, and environment protection.

REFERENCES

1. L. H. Hall, E. L. Maynard, L. B. Kier, *Environ. Toxicol. Chem*., **5**, 333 (1986).
2. H. Bahadar, S. Mostafalou, M. Abdollahi, *Toxicol. Appl. Pharmacol.*, **276**, 83 (2014).
3. S. M. Choi, S. Y. Kwan, C. M. Wong, *Microbial*, **53**, 54 (1996).
4. P. G. Hatcher, P. A Mcgillivary, *Environ. Sci. Technol.,* **13**, 1225 (1979).
5. G. Piir, S. Sild, U. Maran, SAR. *QSAR. Environ. Res.*, **24,** 175 (2013).
6. E. Papa, J. C. Dearden, P. Gramatica, *Chemosphere,* **67**, 351 (2007).
7. C. Cortes, V. Vapnik, *Mach. Learn*., **20**, 273 (1995).
8. V. Vapnik, Statistical Learning Theory, New York: Wiley, 1998.
9. R. Burbidge, M. Trotter, B. Buxton, S. Holden, *Comput. Chem.,* **26,** 5 (2001).
10. E. Byvatov, U. Fechner, J. Sadowski , G. Schneider, *J. Chem. Inf. Comput. Sci.,* **43**, 1882 (2003).
11. V. Wan, W. M. Campbell, *Proceedings of the 2000(SiPS) IEEE.*, **2**, (2014).
12. P. Bartlett, J. Shawe-Taylor, Generalization performance of support vector machines and other pattern classifiers, Advances in Kernel Methods - Support Vector Learning, MIT Press, 1999.
13. B. Sholkopf, K. Sung, C. J. C Burges, F. Girosi, P. Niyogi, T. Poggio, V. Vapnik, *IEEE. Trans. Signal. Process.*, **45,** 2758 (1997).
14. C. J. Feng, X. H. Du, *Journal of Shenzhen University Science and Engineering*, **31,** 96 (2014).
15. C. W. Yap, *J. Comput. Chem.*, **32**, 1466 (2011).
16. R. M. Rose, M. St. J. Warne, R. P. Lim, *Environ. Contam. Toxicol.,* **34**, 248 (1998).
17. X. Zhong, J. Li, H. Dou, S. J. Deng, G. F. Wang, Y. Jiang, Y. Wang, Z. Zhou, L. Wang, F. Yan, *PLoS ONE*, **8**, p. e69434 (2013).
18. Y, Shen, Z, He, Q. Wang, Y. Wang, in IEEE International Instrumentation and Measurement Technology Conference (I2MTC), Graz, AUSTRIA 2012, p. 1977.
19. R. Todeschini, P. Gramatica, 3D QSAR in Drug Design, Springer, Netherlands, 1998, p. 355.
20. R. Todeschini, V. Consonni, Molecular Descriptors for Chemoinformatics John Wiley & Sons., New York, 2009.

21. D. T. Stanton , P. C. Jurs, *Anal. Chem*., **62**, 2323 (1990).

22. A. Ciampi, J. Thiffault, *Comput. Stat. Data Anal*, **4**, 185 (1986).

QSAR-ИЗСЛЕДВАНЕ НА БИО-КОНЦЕНТРИРАНЕТО НА ХАЛОГЕНИРАН БЕНЗЕН В РИБИ

Ф. Чен[1,2], Н. Ли[1,2], Д. Жан[1,2,3], Й. Жоу[1,2*]

[1]*Ключова лаборатория по възстановяване на морски биоресурси и подобряване на жилищната среда в провинция Ляонинг, Океаноложки университет в Далиан, Китай*

[2]*Ключова лаборатория по северни морски култури, Министерство на земеделието, Океаноложки университет в Далиан, Китай*

[3]*Колеж за науки за живота и технологии, Университет в Далиан, Китай*

(Резюме)

Някои натрупани съединения се разграждат трудно в организмите. Явлението на повишена концентрация в организмите спрямо в околната среда се нарича био-концентриране. В тази работа са изследвани 21 фактори на био-концентриране (B_{CF}) на халогениран бензен в риби. Четиринадесет молекулни параметри на халогенираните бензени са произволно избрани като базова мрежа, а останалите се смятат като зависими променливи за изчисляван на молекулни дескриптори. Създаден е модел за предсказване на отношението количествена структура-активност между био-концентрирането и молекулните дескриптори чрез множествена линейна регресия. Елиминирани са независимите променливи със значима взаимна линейна връзка за постигането на оптимални предвиждания с коефициент на корелация R^2=0.919. Предсказаните данни от линейната регресия са получени и чрез молекулните параметри от зависимите променливи. Използван е поддържащ вектор (SVM) за предсказване на зависимите променливи от базовите данни като проби. Най-добрият метод за предсказване на фактора на био-концентриране на халогено-бензени в риби се определя чрез сравняване на точността на предвиждане на двата метода. Крайният резултат показва, че моделът, построен чрез степенна регресия може ефективно да предскаже B_{CF}. Прилагането на SVM може да е по-точно в предвиждането на B_{CF}, особено при малък брой проби.

Soft-sensing modeling of crucial parameters for penicillinfed-batch fermentation process

B. Wang[1*], X. F. Ji[1], Y. K. Sun[2]

[1]*School of Electrical and Information Engineering, Jiangsu University, 212003Zhenjiang, China*
[2]*Nanjing Institute of Technology, 211167Nanjing, China*

A modeling approach for soft-sensing based on PSO-LSSVM inversion was presented to solve the problem of penicillin fed-batch fermentation being a non-linear, large time-delay and multivariable dynamic coupling process in which crucial bioprocess parameters are difficult to be measured online in real-time. First, a non-linear dynamic model of the system was developed based on the material balance relation of the penicillin fed-batch fermentation process, and the existence of an inverse system was checked. Second, an initial inverse model was off-line developed by using the fitting capacity of a least square support vector machine, online corrected by using the particle swarm optimization algorithm. Last, a combined pseudo-linear system was formed by a corrected inverse model being cascaded behind the original fermentation process; thereby non-direct measurable crucial bioprocess parameters could be online predicted. A penicillin fed-batch fermentation process was investigated as an example. The modeled soft-sensing method was demonstrated to be effective and practicable.

Key words:Penicillin fed-batch fermentation,material balance relations, inverse model, soft-sensing.

INTRODUCTION

As the first kind of antibiotic that was purified and clinically used on a large scale, penicillin has initiated a new era of antibiotic therapy and is still the most commonly used antibiotic. Penicillin fermentation is a highly non-linear and tight coupling dynamic process with characteristics of a non-linear system such as time variance, relevance and uncertainty. Moreover, in the fermentation process, some crucial bioprocess parameters cannot be measured online in real-time and there is no accurate mechanism model to be used. Now crucial bioprocess parameters are obtained through offline analysis and laboratory tests; there exist a big time-delay in data measurement, and thus it is difficult to meet real-time control requirements for the penicillin fermentation process. Therefore, the research on how to obtain crucial status information of fermentation processes in time is significant for optimizing penicillin fermentation process and thus improving penicillin yield and quality [1-5].

In recent years, the inverse system approach has offered an effective way for soft-sensing of non-direct measurable parameters of a non-linear system. There exist two application restrictions in traditional inverse-system approaches when used for practical engineering: 1) the mathematical models of relevant objects and the specific system parameters should be known; 2) the analytic expression of the inverse model can be accurately determined. With respect to the limitations of the inverse system approaches, an ANN dynamic soft-sensing method was presented by employing artificial neural network to identify the inverse model and an excellent application result was obtained [6]. But in this paper, the system model used in inverse system analysis is a simplified model based on Monod equation which ignores many nonlinear components and does not cover the actual fermentation process. Thus, it is not applicable to an original nonlinear coupled system.Moreover, the identification approach of a neural network is based on the asymptotic theory when a sample approximates to infinite. Practical samples, however, are always limited, especially in tight coupling and large time-delay of non-linear systems such as biological fermentation processes, in which it is very difficult to obtain accurate sample data. There still exist some other difficulties such as the selection of model structures, the convergence of arithmetic and the uniqueness of solution. Compared with neural network, the support vector machine theory based on the statistical theory presents an excellent performance when used in the study of small samples. It provides good generalization ability and non-linear identification ability, and is thus suitable for the identification of non-linear, tight coupling and large time-delay systems [7-13].

In this work, by applying a mechanism modeling approach, a dynamic model of a fed-batch penicillin

---

fermentation system was developed based on the material balance relation in fermentation processes. With respect to the multi-variable non-linear model,the existence of its inverse system and constructing a method of an inverse model were analyzed. The inverse model was obtained through offline identification by a least square support vector machine (LSSVM) and online optimization applying the particle swarm optimization algorithm (PSO). The inverse model was cascaded behind the original fermentation process as soft-sensing model, so that the online prediction of crucial bioprocess parameters which are non-direct measurable can be realized. The theoretical analysis and simulation results demonstrated that the approach provides higher prediction accuracy than common modeling approaches such as PSO-LSSVM.

FERMENTATIONPROCESSMODELING

The concentrations of mycelia and metabolite in various fed-batch liquids were assumed to be 0. According to the material balance relation eq. (1) of various substances (mycelia, substrate, metabolite, oxygen, H⁺ and so on) in the fed-batch fermentation process, a system dynamic model was developed [2]:

$$\frac{dx}{dt} = \mu(X, S, P, C_L, pH)X - \frac{x}{V}\frac{dV}{dt} \quad (1)$$

where $x \in \{X, S, P, C_L, pH\}$, X, S, P, C_L, pH, V are the concentrations ofmycelia, substrate, product, dissolved oxygen, pH value and volume of the fermentation liquor, respectively; is the specific rate of the various substances.

In the fed-match fermentation process of penicillin, various substrates were flowingly fed as per specific concentrations to provide the necessary carbon source, nitrogen source, inorganic salt and precursor substances, as well as to adjust and control the pH value of the fermentation liquor to be maintained in an optimal range. Fermentation volume V and pHwere varied by the addition of various substrates. Their balance equations are expressed as:

$$\frac{dV}{dt} = f_1 + f_2 + f_3 + f_4 + f_5 \quad (2)$$

$$\frac{dpH}{dt} = \gamma(X, S, P, C_L, pH)X - \frac{X}{V}\frac{dV}{dt}$$
$$+ \frac{S_2 f_2 - S_1 f_1 - S_4 f_4 - S_5 f_5}{V} \quad (3)$$

where f_1, f_2, f_3, f_4 and f_5 are the feeding rates of glucose, aqueous ammonia, monopotassiumphosphate (KDP) and phenylacetic acid (PAA), respectively; S_1, S_2, S_4, S_5 are the flow liquidconcentrations of glucose, aqueous ammonia, KDP and PAA, respectively; and γ is the specific

consumption rate of H⁺.

As the only restrictive substrate of penicillin fermentation, the carbon source was required in a large quantity and would be consumed at a comparatively fast speed. Considering the influence of carbon source (glucose) addition on the fermentation process, the balance equation of substrates is expressed as:

$$\frac{dS}{dt} = -v(X, S, P, C_L, pH)X + \frac{s_1}{V}f_1 - \frac{S}{V}\frac{dV}{dt} \quad (4)$$

where v is the specific consumption rate of the various substrates.

In the stage of penicillin synthesis, the hydrolysis reactions of precursor substance (PAA) and penicillin would remarkably affect the penicillin yield. The influence of PAA addition and hydrolysis rate K on the fermentation process is considered in the following balance equation of product concentration:

$$\frac{dP}{dt} = \rho(X, S, P, C_L, pH)X - KP + \frac{K_1}{V}f_5 - \frac{P}{V}\frac{dV}{dt} \quad (5)$$

where K_1 is inhibition constant and ρ is specific production rate of the product.

With respect to the aerobiotic characteristic of penicillin fermentation and considering the influence of reactor size on the dissolved oxygen level of the fermentation liquor, the volume oxygen-transferring system (K_2) was introduced into the dissolved oxygen balance equation:

$$\frac{dC_L}{dt} = -\eta(X, S, P, C_L, pH)X + K_2(C_L^* - C_L) - \frac{C_L}{V}\frac{dV}{dt} \quad (6)$$

where C_L^* is the oxygen saturated concentration and η is the specific consumption rate of oxygen.

The concentrationsof mycelia, substrate and product $\hat{x} = [X, S, P]^T$ were selected as non-direct measurable parameters; the dissolved oxygen concentration, the pH value and the fermentation liquor volume $z = [z_1, z_2, z_3] = [C_L, pH, V]^T$ were selected as direct measurable parameters; and the feeding rates of the various substrates $u = [f_c, f_{nh}, f_s, f_p, f_{paa}]^T$ were selected as input. The state equations are given by (7)where $x = [x_1, x_2, x_3, x_4, x_5, x_6]^T = [X, S, P, C_L, pH, V]^T$ is a state vector, $u = [u_1, u_2, u_3, u_4, u_5]^T = [f_1, f_2, f_3, f_4, f_5]^T$ is an input vector, $\mu, v, \rho, \eta, \gamma$ are smooth functions of various state variables, and $s_i(i = 1, \cdots, 8)$ are all non-zero constants.

$$\begin{cases} \dot{x}_1 = \mu(x_1,x_2,x_3,x_4,x_5)x_1 - \dfrac{x_1}{x_6}\sum_{i=1}^{5}u_i \\[2mm] \dot{x}_2 = -\nu(x_1,x_2,x_3,x_4,x_5)x_1 + \dfrac{s_1u_1}{x_6} - \dfrac{x_2}{x_6}\sum_{i=1}^{5}u_i \\[2mm] \dot{x}_3 = \rho(x_1,x_2,x_3,x_4,x_5)x_1 - s_2x_3 - \dfrac{x_3}{x_6}\sum_{i=1}^{5}u_i + \dfrac{s_3u_5}{x_6} \\[2mm] \dot{x}_4 = -\eta(x_1,x_2,x_3,x_4,x_5)x_1 - s_4x_4 - \dfrac{x_4}{x_6}\sum_{i=1}^{5}u_i + s_5 \quad (7) \\[2mm] \dot{x}_5 = \gamma(x_1,x_2,x_3,x_4,x_5)x_1 - \dfrac{x_5}{x_6}\sum_{i=1}^{5}u_i \\[2mm] \qquad + \dfrac{s_6u_2 - s_1u_1 - s_7u_4 - s_8u_5}{x_6} \\[2mm] \dot{x}_6 = \sum_{i=1}^{5}u_i = u_1 + u_2 + u_3 + u_4 + u_5 \end{cases}$$

SYSTEM REVERSIBILITYANALYSIS

In view of the system dynamic model of penicillin fermentation, the soft-sensing model of nonlinear multivariable system was established based on the inverse system method. The inverse system method has a good effect in soft-sensing modeling of nonlinear systems, which is a kind of feedback linearization method of nonlinear systems.Under the condition that the original system is invertible, the inverse system, with the function of dynamic compensator, is cascaded with the original system to transform the input-output relationship of the compound system to be a decoupled identity mapping relation. This realizes the mirror of some crucial bioprocess variables. The reversibility analysis and the corresponding inverse model are given as follows.

Lemma 1: System Σ is invertible in a certain (x_0, u_0) neighborhood, only if the relative order of this system equals $rank\left(\partial \mathbf{Z}_m^{\mathrm{T}}/\partial \hat{\mathbf{x}}^{\mathrm{T}}\right) = r_m = l$ [6],where l is the number of variables impossible to be directly measured.

By using the Interactoralgorithm[6], the reversibility analysis of penicillin fermentation dynamic model is given as follows:

The derivative of direct measurable parameters to time should be calculated primarily until the useful information for structuring the inverse model could be obtained. Eq. (7) leads to:

$$\begin{cases} \dot{x}_4 = -\eta(x_1,x_2,x_3,x_4,x_5)x_1 - s_4x_4 \\[2mm] \qquad + s_5 - \dfrac{x_4}{x_6}\sum_{i=1}^{5}u_i \\[2mm] \ddot{x}_4 = g_1(\mathbf{x},\mathbf{u}) + g_2(x_4,x_5,x_6,\mathbf{u},\dot{\mathbf{u}}) \qquad (8) \\[2mm] \dot{x}_5 = \gamma(x_1,x_2,x_4,x_5)x_1 - \dfrac{x_5}{x_6}\sum_{i=1}^{5}u_i \\[2mm] \qquad + \dfrac{s_6u_2 - s_1u_1 - s_7u_4 - s_8u_5}{x_6} \end{cases}$$

where $g_1(\mathbf{x},\mathbf{u}) = s_7 \dfrac{\partial \eta}{\partial x_5}\dfrac{x_1}{x_6}u_4 - s_6\dfrac{\partial \eta}{\partial x_5}\dfrac{x_1}{x_6}u_2 - \dfrac{\partial \eta}{\partial x_3}\dfrac{x_1}{x_6}u_5$

$\qquad + \left(\dfrac{\partial \eta}{\partial x_1}x_1 + \dfrac{\partial \eta}{\partial x_2}x_2\right)\dfrac{x_1}{x_6}\sum_{i=1}^{5}u_i + \dfrac{x_1}{x_6}\sum_{i=1}^{5}u_i$

$\qquad + \left(\dfrac{\partial \eta}{\partial x_3}x_3 + \dfrac{\partial \eta}{\partial x_4}x_4 + \dfrac{\partial \eta}{\partial x_5}x_5\right)\dfrac{x_1}{x_6}\sum_{i=1}^{5}u_i$

$\qquad + \left(\dfrac{\partial \eta}{\partial x_1}\mu - \dfrac{\partial \eta}{\partial x_2}\nu + \dfrac{\partial \eta}{\partial x_3}\rho\right)x_1^2 - \dfrac{\partial \eta}{\partial x_4}s_5x_1$

$\qquad - s_1(\dfrac{\partial \eta}{\partial x_2} - \dfrac{\partial \eta}{\partial x_5})\dfrac{x_1}{x_6}u_1 - \eta\mu x_1 - \dfrac{\partial \eta}{\partial x_5}\gamma x_1^2$

$\qquad + \dfrac{\partial \eta}{\partial x_3}x_3 + \dfrac{\partial \eta}{\partial x_4}s_4x_1x_4 + s_4\eta x_1 - \dfrac{\partial \eta}{\partial x_4}\eta x_1^2$

$g_2(x_4,x_6,\mathbf{u},\dot{\mathbf{u}}) = \dfrac{2s_4x_4}{x_6}\sum_{i=1}^{5}u_i - \dfrac{s_5}{x_6}\sum_{i=1}^{5}u_i - \dfrac{x_4}{x_6}\sum_{i=1}^{5}\dot{u}_i$

$\qquad + \dfrac{2x_4}{x_6^2}(\sum_{i=1}^{5}u_i)^2 - s_4s_5 + s_4^2x_4$

Let matrix $\mathbf{J} = \partial \mathbf{Z}_m^{\mathrm{T}}/\partial \hat{\mathbf{x}}^{\mathrm{T}}$, then

$$\mathbf{J} = \begin{bmatrix} \dfrac{\partial g_1(\mathbf{x},\mathbf{u})}{\partial x_1} & \dfrac{\partial g_1(\mathbf{x},\mathbf{u})}{\partial x_2} & \dfrac{\partial g_1(\mathbf{x},\mathbf{u})}{\partial x_3} \\[3mm] -\dfrac{\partial \eta}{\partial x_1}x_1 - \eta & -\dfrac{\partial \eta}{\partial x_2}x_1 & -\dfrac{\partial \eta}{\partial x_3}x_1 \\[3mm] \dfrac{\partial \nu}{\partial x_1}x_1 + \nu & \dfrac{\partial \nu}{\partial x_2}x_1 & \dfrac{\partial \nu}{\partial x_3}x_1 \end{bmatrix} (9)$$

Through elementary transformation of $\mathbf{J}$, we obtain:

$$\tilde{\mathbf{J}} = \begin{bmatrix} g_5(\mathbf{x},\mathbf{u}) - \dfrac{g_6(\mathbf{x},\mathbf{u})}{g_4(\mathbf{x},\mathbf{u})}g_3(\mathbf{x},\mathbf{u}) & 0 & 0 \\[3mm] g_3(\mathbf{x},\mathbf{u}) & g_4(\mathbf{x},\mathbf{u}) & 0 \\[3mm] \dfrac{\partial \nu}{\partial x_1}x_1 + \nu & \dfrac{\partial \nu}{\partial x_2}x_1 & \dfrac{\partial \nu}{\partial x_3}x_1 \end{bmatrix} (10)$$

where $g_3(\mathbf{x},\mathbf{u}) = \left[(x_1\dfrac{\partial \nu}{\partial x_1} + \nu)\dfrac{\partial \eta}{\partial x_3}\right] \Big/ \dfrac{\partial \nu}{\partial x_3} - \dfrac{\partial \eta}{\partial x_1}x_1 - \eta$;

$g_4(\mathbf{x},\mathbf{u}) = \left(x_1\dfrac{\partial \nu}{\partial x_2}\dfrac{\partial \eta}{\partial x_3}\right) \Big/ \dfrac{\partial \nu}{\partial x_3} - \dfrac{\partial \eta}{\partial x_2}x_1$; $g_5(\mathbf{x},\mathbf{u}) = \dfrac{\partial g_1(\mathbf{x},\mathbf{u})}{\partial x_1}$

$\qquad - \left[(\dfrac{\partial \nu}{\partial x_1} + \dfrac{\nu}{x_1})\dfrac{\partial g_1(\mathbf{x},\mathbf{u})}{\partial x_3}\right] \Big/ \dfrac{\partial \nu}{\partial x_3}$; $g_6(\mathbf{x},\mathbf{u}) = \dfrac{\partial g_1(\mathbf{x},\mathbf{u})}{\partial x_2}$

$$-\left(\frac{\partial v}{\partial x_2}\frac{\partial g_1(\boldsymbol{x},\boldsymbol{u})}{\partial x_3}\right)\Big/\frac{\partial v}{\partial x_3}.$$

If $\det(\boldsymbol{J})$ is not zero in the real vector space, this system is globally invertible by using Lemma 1. However, it is very difficult to give such a condition under which this variable is not zero anywhere. Note that the practical working state of penicillin fermentation process is only in a small sub-region of the real vector space. With this consideration, we can first assume this system to be invertible in the working area and then construct the inverse-based soft measurement model for some crucial biochemical process variables in the penicillin fermentation model. The experimental result is finally used to verify the rationality and reliability of this assumption.

We were working on the assumption that the system model satisfies the reversible conditions in the work area of the penicillin fermentation process. From the inverse-function existence theorem and eqs. (7-8), the inverse model expression of penicillin fermentation process may be developed as:

$$\hat{\boldsymbol{x}}=\begin{pmatrix}\varphi_1\left(x_4,x_5,x_6,\dot{x}_4,\ddot{x}_4,\dot{x}_5,\boldsymbol{u},\dot{\boldsymbol{u}}\right)\\\varphi_2\left(x_4,x_5,x_6,\dot{x}_4,\ddot{x}_4,\dot{x}_5,\boldsymbol{u},\dot{\boldsymbol{u}}\right)\\\varphi_3\left(x_4,x_5,x_6,\dot{x}_4,\ddot{x}_4,\dot{x}_5,\boldsymbol{u},\dot{\boldsymbol{u}}\right)\end{pmatrix} \quad (11)$$

It is difficult to determine the analytic expression of the inverse model.However, the support vector machine algorithm[11,12] based on the statistical theory provides a new perspective of machine learning from the risk minimization principle, it provides good generalization ability and non-linear identification ability, and is thus suitable for the identification of non-linear systems, From that point, three non-linear functions $\varphi_1,\varphi_2,\varphi_3$ of eq. (12) were identified using least square support vector machine(LSSVM).

As for LSSVM system identification, the selection of kernel function σ and penalty parameter C exerts an important effect on the developing of the inverse model. Most of traditional parameter selection approaches, however, are based on experience and trial-error method so that the regression precision and computation speed cannot be guaranteed. In order to obtain an inverse model with a better prediction effect, this work applies particle swarm optimization algorithm to the online optimization and adjustment of LSSVM parameters[14-17].

SOFT-SENSING MODELING

The inverse model of a fermentation process was identified applying PSO-LSSVM, following the three steps:

(1) Samples obtaining

In order to stimulate the non-linear characteristic within the penicillin fed-batch fermentation, we selected the random signals in the field of practical work as input to real-time measurement of the response of the fermentation process. From eq. (11) we can see the training sample set of the inverse model in penicillin fermentation process as $\{\bar{x}_1,\bar{x}_2,\bar{x}_3\}$ and $\{x_4,\dot{x}_4,\ddot{x}_4,x_5,\dot{x}_5,x_6\,\boldsymbol{u},\dot{\boldsymbol{u}}\}$. The former is the output of the inverse model, i.e. desired output; and the latter is the input, where the direct measurable parameters $\{x_4,x_5,x_6\}$ and input parameters $\boldsymbol{u}=\{u_1,u_2,u_3,u_4,u_5\}$ could be obtained by direct sampling; and the various-order derivative information of the direct measurable parameters $\{\dot{x}_4,\ddot{x}_4,\dot{x}_5,\dot{\boldsymbol{u}}\}$ was offline determined by using high-precision five-point numerical algorithm. The non-direct measurable parameters $\{\bar{x}_1,\bar{x}_2,\bar{x}_3\}$ were determined by offline analysis and chemical test. The obtained data were differentially fitted using the least square method to obtain the training sample corresponding to the input.

(2)Offline modeling

The three SVM were offline studied applying the least square method based on input/output training sample data, to obtain corresponding a_k and b, and develop the initial inverse model of a fermentation process.

(3) Online correcting

There exist unmodeled dynamic and static errors in an initial inverse model. In order to improve the identification accuracy of the inverse model so that its soft-sensing model can fit the variation of the object based on the deviation information between the input of the fermentation process and the output of the inverse model, LSSVM performance parameters were online optimized applying the particle swarm optimization algorithm and the initial inverse model was online corrected.

The series connection of corrected PSO-LSSVM inverse model following the original fermentation process constituted a pseudo-linear combined system. This made the input and the output of the combined system display a decoupled identical mapping relation; therefore we could realize the online prediction of crucial parameters. The three non-linear functions $\varphi_1,\varphi_2,\varphi_3$ were offline identified by 3 static LSSVM and online optimized by PSO.
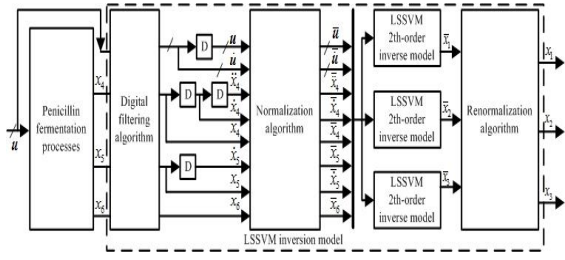
Fig. 1. Combined pseudo linear system structure

Fig.1 is a combined pseudo-linear system chart, in which the PSO-LSSVM inverse model serves as soft-sensing model and digital filtering pre-processing approach.

SIMULATION AND ANALYSIS

The experimental research was undertaken to the penicillin fed-batch fermentation process in the laboratory fermentation tank. The experimental process was designed to be close to practical productive processas follows:

(1)Penicillin fed-batch fermentation period of each batch was 200h and the sampling period T was 30min. C_L, pH, V, u were collected by sensors, X, S, P were sampled each 4h and offline analyzed. X was measured by high-performance liquid chromatography (HPLC), S was measured by SBA-40C type multi-functional biosensor and P was measured using enzyme linked immunosorbent assay (ELISA).

(2)Only 10 batches of medium were considered to examine the modeling ability of PSO-LSSVM inversion with respect to small samples. The initial conditions of the various batches were set to be different, the fed-batch strategies of the various substrates varying correspondingly to enlarge batch differences. The pressure of the fermentation tank was controlled between 0～0.07 MPa and the pH of the fermentation liquor between 6.8 ～ 7.2, the temperature in the early period and the medium period was set at about 26℃ and in the late period was set at about 24℃, the stirring speed was 150~250rpm, and the concentration of the precursor PAA <1kg/m³.

The fermentation data of the first 6 batches were selected as a training sampling set, and were offline trained to obtain the initial inverse model of the fermentation process, then the data of the 7th and 8th batch were used to online correct the initial inverse model;and the data of the 9th and 10th batch were used to examine the identification precision of the inverse model.

PSO-LSSVM inverse algorithm was compiled using MATLAB language. In order to verify the performance of the method, we compared it with

1208

purely data-driven algorithm LSSVM and computed the relative error of soft-sensing results. The three initial performance parameters of LSSVM were selected as empirical values: $C = [12, 12, 12]$ and $\sigma^2 = [1.0, 1.0, 1.0]$. The three performance parameters of LSSVM corrected by PSO were $C = [11.6, 7.3, 9.8]$ and $\sigma^2 = [0.67, 1.33, 0.59]$.

Fig.2 shows the comparison of result predictions based on PSO-LSSVM inversion and the soft-sensing model of LSSVM. Fig.3 shows the relative errors of the soft sensing values to the corresponding offline analysis values. Table 1 lists the maximum relative errors of the soft-sensing results using the two approaches.

(a) Biomass concentration

(b) Substrate concentration

(c) Product concentration
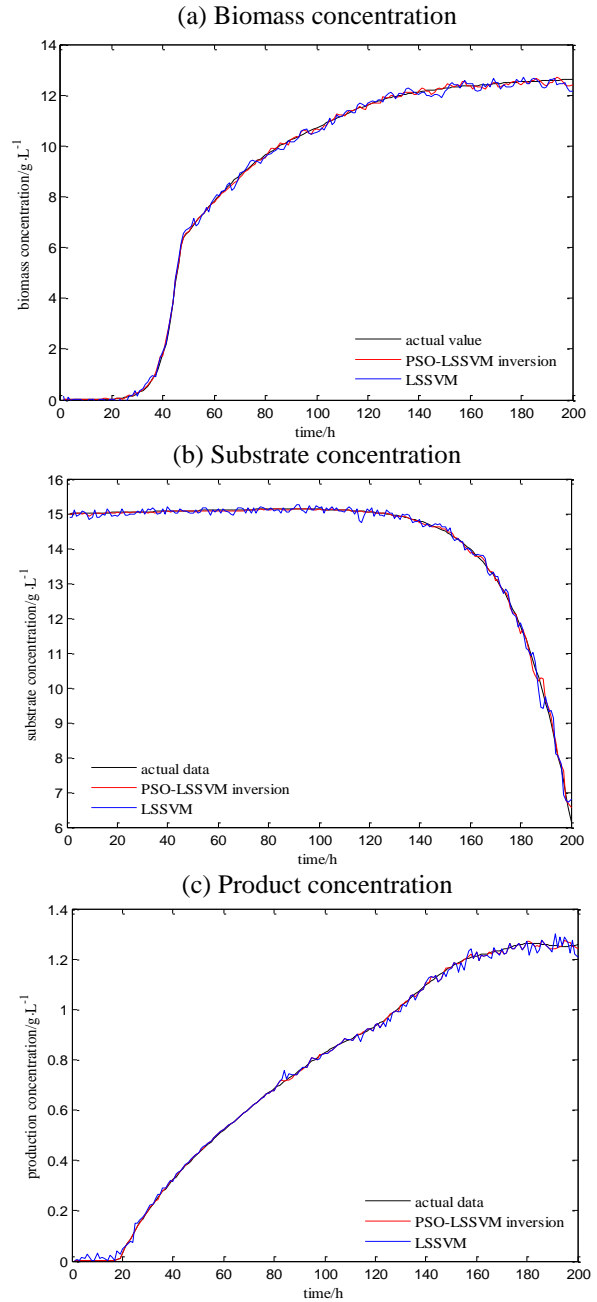
Fig. 2. Comparison of prediction results.

From Figs.2 and3 we can see that compared with the soft-sensing result applying LSSVM approach, the soft-sensing values applying PSO-LSSVM inversionapproach are more approximate to the practical offline laboratoryvalues, especially the effect of substrate concentration being notable, thus, the hypothesis that $\det\left(\mathcal{J}_0\right)$ is not zero constantly inthe work area is entirely reasonable. In the main stage of penicillin fermentation (50h-180h), by applying LSSVM soft-sensing approach, the RMSE average values of soft-sensing of mycelia concentration, substrate concentration, and product concentration are 0.0292, 0.0189 and 0.0472, respectively; while with PSO-LSSVM inversion they are 0.0133, 0.0125 and 0.0178 respectively.

(a) Biomass concentration

(b) Substrate concentration

(c) Product concentration
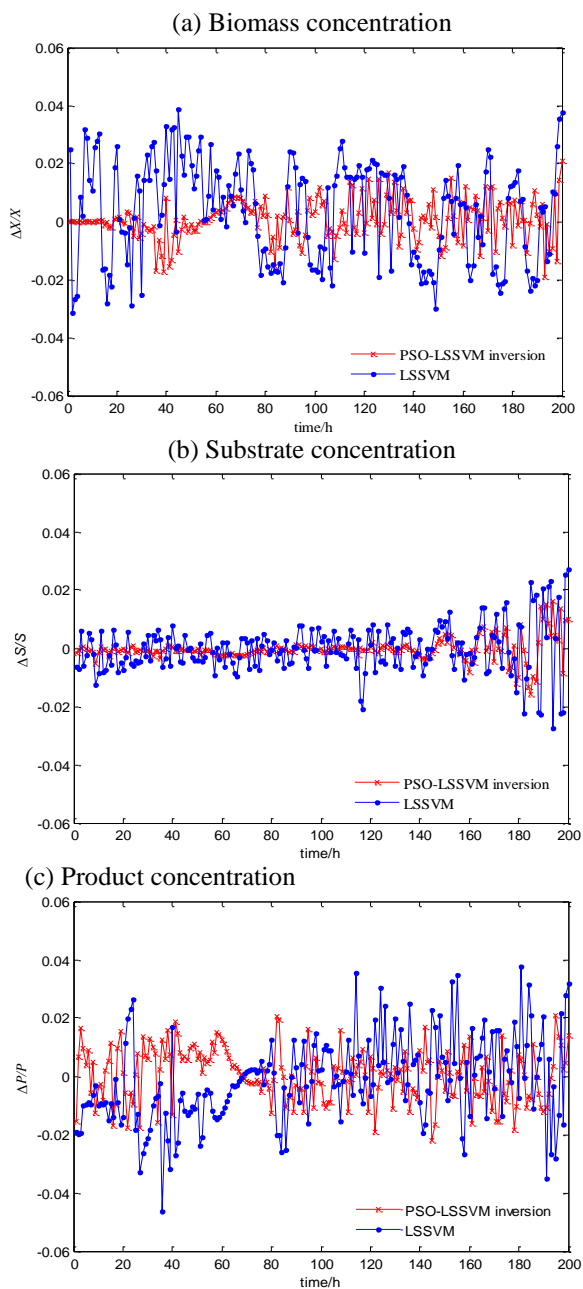
Fig. 3. Comparison of relative errors.

This meansthat the PSO-LSSVM inversion soft-sensing approach is effective and reliable with an ability to improve the soft-sensing precision of mycelia, substrate and product concentrations. We have achieved the anticipated objective, solved the problem of the low precision of online soft-sensing of crucial biomass parameters in penicillin fermentation process, and thus laid a solid foundation for applying optimization control of fermentation processes.

CONCLUSIONS

In this work, by applying PSO-LSSVM inverse model identification and soft-sensing principle, the soft-sensing was undertaken with respect to crucial biomass parameters in a penicillin fed-batch fermentation process. The simulation experiment indicates that:

(1)LSSVM can successfully perform inverse model identification regarding the penicillin fermentation process, as well as online correcting the inverse model based on PSO algorithm. This eliminated the non-linear modeling errors, making the inverse model fit with the variations in the fermentation process.

(2)The inverse model is no longer corresponding to the structure form of direct analysis of the inverse system. It not only retains all advantages of LSSVM inverse model that apply the fundamental structure, but also remarkably enhances the function of LSSVM inverse model, and therefore gives a play to the advantage of the inverse soft-sensing approach and makes the LSSVM inverse soft-sensing more suitable to practical engineering application.

(3) This approach needs no*a priori* knowledge about penicillin fermentation process; it only needs the relative order and a few input/output sample sets in the fermentation process, to obtain ideal identification effect. That broke through the two limitations of traditional approaches.

The above results can be developed to fit complex non-linear process modeling and high precision prediction such as biochemical reactions. PSO-LSSVM inversion system approach is also suitable to the modeling and soft-sensing of common non-linear reversible systems, and thus provides a new way for the soft-sensing of multi-variable non-linear systems.

REFERENCES

1. M.Pcolka, S.Celikovsky, *Bioprocess Biosyst. Eng.*, **37**(1), 71 (2013).
2. Z. P. Shi, F. Pan, Fermentation Process analysis, control and detection technology, **126**, Beijing: Chemical Industry Press, 2010.
3. J. D. Chen, F. Pan, *Chinese Journal of Chemical Engineering(CIESC.)*,**61**(8), 2092 (2010).
4. Y. H. Liu, J. X. Bi, A. P. Zeng, *Bioprocess and Biosystems Engineering (Bioprocess Biosyst. Eng.)*, **30**(10), 1464 (2008).
5. P. V. D. Kerkhof, G. Gins, J. Vanlaner, *Computers and Chemical Engineering(ComputChem Eng.),* **40**(3), 12 (2012).
6. X. Z. Dai, W. C. Wang, Y. H. Ding, *Computers and Chemical Engineering (ComputChem Eng.)*, **30**(8), 1203 (2006).
7. W. J. Chen, Y. H. Shao,*Journal of Control and Decision*, **28**(12), 1817 (2013).
8. X. J. Chen, Y. H. Shao, *Control and Decision,***28** (12), 1817 (2013).
9. X. F. Wang, J. D. Chen, C. B. Liu, F. Pan, *Chemical Engineering Research and Design (CEHM ENG RES DES.),***88**(4), 415 (2010).
10. W. Liu, C. H. Liu, L. Zheng, *Transactions of the Chinese Society of Agricultural Engineering (Transactions of the CSAE.)*, **30**(10), 145 (2014).
11. X. D. Wang, C. J. Zhang, *Chines Journal of Scientific Instrument*, **27**(7), 730 (2006).
12. K. Desai, Y. Badhe, B. D. Kulkarni, *Biochemical Engineering Journal (BIOCHEM ENG J.),***27**(3), 225 (2006).
13. G. H. Liu, D. W. Zhou, X. H. Xu, C. L. Mei, *Expert Systems with Applications (EXPERT SYST APPL.)*, **37**(4), 2708(2010).
14. Q. L. Ye, C. X. Zhao, *Pattern Recognition Letters*, **31**(13), 2006 (2010).
15. X. M. Yang, W. Q. Liu, J. Yang, *Chinese Journal of Chemical Engineering (CIESC.)*, **46**(9), 3262 (2013).
16. W. H. Chih, J. L. Chih, *IEEE Transactions on Neural Networks (IEEE T NEURAL NETWOR.)*, **13**(2), 415 (2002).
17. X. G. Zhang, *ActaAutomaticaSinica,***26**(1), 32(2000).
17. W. Li, H. Y. Su, R. L. Liu, *Chinese Journal of Chemical Engineering (CIESC.)*, **61**(8), 1927 (2010).
.

SOFT-SENSING МОДЕЛИРАНЕ НА КЛЮЧОВИ ПАРАМЕТРИ ПРИ ПОЛУ-НЕПРЕКЪСНАТА ФЕРМЕНТАЦИЯ НА ПЕНИЦИЛИН

Б. Уанг[1*], Кс. Ф. Джи[1], И. К. Сун[2]

[1]*Училище по електро-инженерство и електронна информация, Университет Джиянгсу, Женджиянг, Китай*

[2]*Технологичен институт в Нанджинг, Нанджинг, Китай*

(Резюме)

Подходът на soft-sensing моделиране, основан на PSO-LSSVM инверсия е използван за решаване на нелинейната многомерна задача за полу-непрекъснатата ферментация с продукт пеницилин. Процесът е с времево закъснение и ключови биопроцесни параметри се измерват трудно online и в реално време. Най-напред е съставен нелинеен модел на базата на материалния баланс за този ферментационен процес, а който инверсия е известна, но не е анализирана. След това началният инверсионен модел е разработен за off-line изпълнение с помощта на метода на най-малките квадрати, както и чрез online-корекция чрез оптимизационен алгоритъм. Накрая е образувана псевдо-линейнасистема, почиваща на коректен инверсионен модел с каскадно представяне на ферментационния процес. По този начин става възможно online-предсказването на не-пряко определяните ключови параметри на ферментацията.Като работен пример е дадено получаването на пеницилин по полу-непрекъснат начин. Показано е, че soft-sensing-моделирането е ефикасно и практично за експерименталната практика и анализ на опитните данни.

Synthesis and antibacterial activity of 1β-methyl-2-[5-(pyrrolidine or piperidine-2-N-substituted carbamoyl) pyrrolidin-3-ylthio]carbapenem derivatives

X. Jiang [1, 2], Z. Yuan [2*], X. Yu [2], W. Zhou [2]

[1] *School of Medicine, Guangxi University of Science and Technology, 545006 Liuzhou, China;*
[2] *State Key Lab of New Drug and Pharmaceutical Process, Shanghai Institute of Pharmaceutical Industry, 200437 Shanghai, China*

A series of new 1β-methylcarbapenems having a substituted pyrrolidine or piperidine-2-N-substituted carbamoyl pyrrolidine moiety were synthesized. Their *in vitro* antibacterial activities against both Gram-positive and Gram-negative bacteria were tested and the effect of substituent on the carbamoyl pyrrolidine was investigated. Of these new carbapenems, **7e** and **7f** showed the most potent antibacterial activity and are worth further studying.

Key words: synthesis; antibacterial activity; 1β-Methylcarbapenem.

INTRODUCTION

Carbapenem antibiotics, which were developed in the late 1970s, are some of the most potent types of antibacterial agents and are among those used as last resort against infections in the clinical field, due to their broad antibacterial spectra and potent bactericidal effects [1]. They play an important role in the treatment of severe infections in hospitals. In particular, carbapenems bearing a 1β-methyl substituent, exemplified by meropenem [2], biapenem [3], ertapenem [4], doripenem [5], tebipenem [6] have excellent antibacterial activities and good resistance to renal dehydropeptidase I (DHP-I). However, they are limited in their use, as their activity against resistant Gram-positive bacteria such as methicillin-resistant *Staphylococcus aureus* (MRSA) and Gram-negative pathogens is relatively weak [7]. There is an urgent need to find new antibiotics with stable properties, long $t_{1/2}$, less side effects and more potent activities.

During the past decade, a large number of carbapenem derivatives have been synthesized and investigated. These include a (3S)-pyrrolidin-3-ylthio group introduced as the C-2 side chain of the carbapenem nucleus. As a result, some carbapenem derivatives with potent *in vitro* antibacterial activity have been identified [8-12].

Previously, we reported that 1β-methyl carbapenem compounds containing 5′-pyrrolidine or piperidine derivatives substituted pyrrolidin-3′-ylthio group as C-2 side chain have improved antibacterial activity [13].

In this study, we describe the synthesis and antibacterial activity of new lβ-methyl-carbapenems having 5′-(pyrrolidine or piperidine-2-N-substituted carbamoyl) pyrrolidin -3-ylthio as C-2 side chain and discuss our approach to improve the antibacterial activity of the carbapenems.

INVESTIGATIONS AND RESULTS

The general synthetic route leading to new carbapenems involved the preparation of appropriately protected thiols group at the 3-position containing substituted pyrrolidine ring as a side chain. The intermediates thus prepared were then coupled with carbapenem diphenylphosphates, followed by deprotection of the protected carbapenems in a usual manner.

Synthesis of the intermediates (**4a-f**) was conducted as shown in Scheme 1. The starting material (2S, 4R)-4-acetylthio-1- (allyloxy carbonyl) pyrrolidine-2-carboxylic acid (**1**) was prepared according to ref. [14]. The compounds (**2a-f**) were prepared according to ref. [15]. The preparation of compounds (**4a-f**) was achieved as follows: compound (**1**) was activated with ethyl chloroformate followed by reaction with compounds (**2a-f**) to afford compounds (**3a-f**). Then the compounds (**3a-f**) were readily hydrolyzed with an aqueous/methanolic solution of 4N NaOH to give mercaptan compounds (**4a-f**), which were used in the subsequent reaction without purification.

Finally, the reaction of 1β-methyl-carbapenem nucleus allyl (1R, 5S, 6S)-2- (diphenyl-phosphoryloxy)-6-[(R)-1-hydroxyethyl]-1-methylcarbapen-2-em-3-carb-oxylate (**5**) was prepared according to ref. [16] and mercaptan compounds

(**4a-f**) in the presence of diisopropylethylamine gave the corresponding protected carbapenem esters (**6a-f**). Deprotection of these compounds by treating with 1,3-dimethyl-barbituric acid (NDMBA), tetrakis-(triphenylphosphine)-palladium(0) (Pd(PPh$_3$)$_4$) and triphenylphosphine (Ph$_3$P) gave the corresponding carbapenems (**7a-f**) [17], as shown in Scheme 2.

Measurement of *in vitro* antibacterial activity:

The MIC of a compound was defined as the lowest concentration that visibly inhibited growth. The MIC was determined by the standard agar dilution method using test agar. The *in vitro* antibacterial activities of the new carbapenems (**7a-f**) against Gram-positive and Gram-negative bacteria are listed in Table 1. For comparison, the MIC value of meropenem as positive control is also listed.
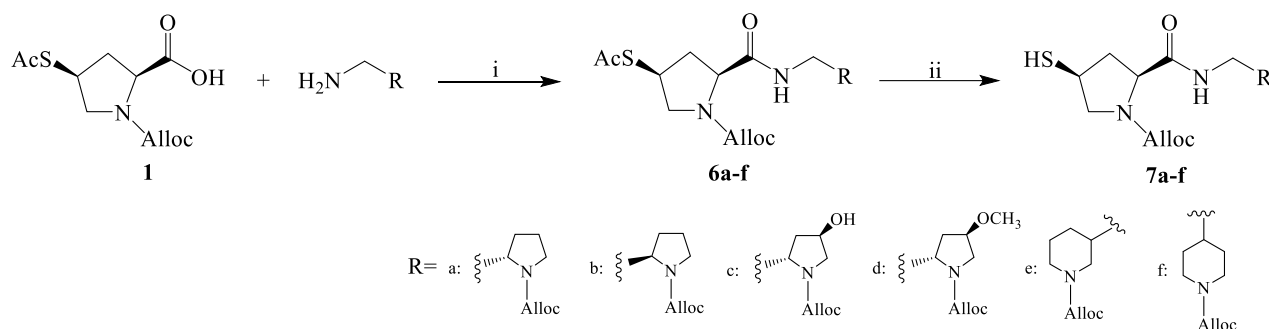
Scheme 1. Scheme of synthesis of intermediate compounds **4a-f** (i) ethyl chloroformate/Et$_3$N/THF/-5℃/5h; (ii) 4N NaOH/MeOH/0-5℃/3h.
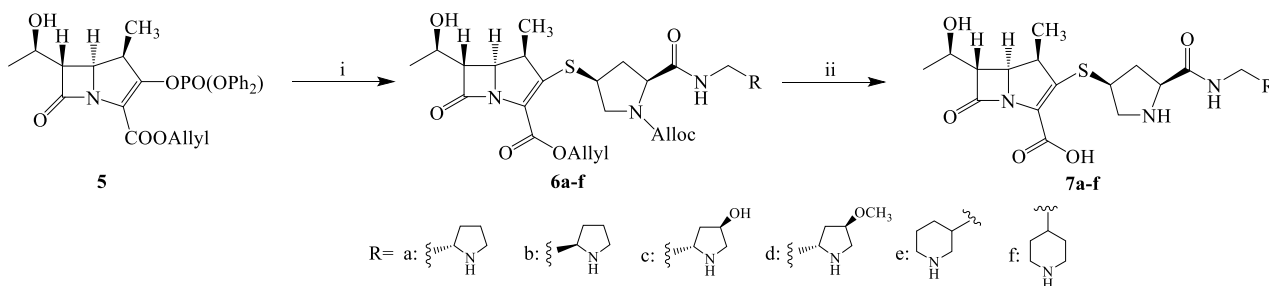
Scheme 2. Scheme of synthesis of 1β-methylcarbapenem compounds **7a-f** (i) **4a-f**, DIPEA/DCM/-5℃/5h; (ii) NDMBA/Ph$_3$P/Pd(PPh$_3$)$_4$/THF/-5-0℃/6h.

Table 1. *In vitro* antibacterial activity (MIC, μg/ml) of the carbapenem derivatives

	7a	7b	7c	7d	7e	7f	MPM
Staphylococcus aureus 26003	0.39	0.39	0.78	0.39	0.098	0.195	0.39
Pneumococcal pneumonia 31002	0.195	0.195	0.098	0.098	0.098	0.098	0.098
Staphylococcus albus 26101	0.39	0.39	0.78	0.39	0.098	0.78	0.39
Enterococcus 32220	0.39	0.39	0.78	0.39	0.098	0.195	6.25
Gamma streptococcus 32206	6.25	6.25	6.25	6.25	12.5	12.5	6.25
Staphylococcus epidermidis 26069	0.39	0.39	0.78	0.39	0.098	0.39	0.195
Shigella boydii 51313	0.195	0.195	1.56	0.78	0.098	0.098	<0.049
Proteus mirabilis 49005	0.78	0.39	1.56	1.56	0.098	0.39	<0.049
Proteus vulgaris 49085	0.78	0.39	1.56	0.78	0.098	0.195	<0.049
Morgan proteus 49086	0.195	0.195	1.56	0.195	0.098	0.195	<0.049
Pseudomonas aeruginosa 10124	12.5	12.5	>25	>25	>25	>25	0.78
Pneumobacillus 46101	0.78	0.78	3.13	1.56	3.13	0.78	<0.049
Salmonella enteritidis 50041	0.39	0.39	1.56	0.39	0.098	0.195	<0.049
Salmonella typhi 50097	0.39	0.39	0.78	0.195	0.098	0.098	<0.049
Citrobacter 48017	0.39	0.195	3.13	1.56	3.13	0.195	<0.049
Aerobacter aerogenes 45102	0.39	0.39	3.13	0.78	3.13	0.39	<0.049
Serratia marcescens 41002	0.78	0.39	3.13	0.78	3.13	0.39	<0.049
Shigella sonnei 51081	0.195	0.39	1.56	1.56	0.098	0.098	<0.049
Shigella flexneri 51573	0.195	0.195	0.78	0.39	0.098	0.098	<0.049
Escherichia Coli 44102	0.39	0.39	1.56	0.098	0.098	0.195	<0.049

The compounds exhibited excellent antibacterial activity. Among these compounds, **7e** and **7f** showed superior or similar antibacterial activity against Gram-positive bacteria compared to MPM except *Gamma streptococcus*. Slightly lower activity was displayed on Gram-negative by **7a-f**, especially against *Pseudomonas aeruginosa* compared to MPM. It was also shown that the larger the size of the 5-substituents, the more difficult was to penetrate the cell membrane of Gram-negative bacteria and the lower was the activity against Gram-negative bacteria. The effects of substituent on the carbamoyl pyrrolidine were investigated. Results showed that the compounds of substituted pyrrolidine displayed slightly lower activity than piperidine against Gram-positive bacteria except *Gamma streptococcus*.

EXPERIMENTAL

All solvents and chemicals used were of analytical grade, purchased from Sinopharm Chemical Reagent Co., Ltd (SCRC) (China) and Aladdin Reagent, were used without further purification. The ^{1}H-NMR spectra (400 MHz) were measured on a DRX-400 spectrometer using DMSO-*d6* or CDCl$_3$ or D$_2$O as solvent and TMS as an internal standard. Chemical shifts were expressed in ppm units. Multiplicities were recorded as s (singlet), brs (broad singlet), d (doublet), t (triplet), q (quartet), m (multiplet). Mass spectra were obtained on a LC-MSD 1100 spectrometer with ESI.

Spectral data of compounds **7a-f**: these are new compounds and their structures were fully confirmed by ^{1}H-NMR and ESI-MS. **7a**: Yield: 28.6%; ^{1}H-NMR (400Hz, D$_2$O): δ1.06 (d, 3H, *J*=7.2Hz, β-CH$_3$), 1.12 (d, 3H, *J*=6.0Hz, CH$_3$CHOH), 1.82~2.01 (m, 4H), 2.45~2.58 (m, 3H), 3.02~3.13 (m, 3H), 3.62~3.69 (m, 3H), 3.87~3.96 (m, 2H), 4.02~4.07 (bs, 1H), 4.12 (bs, 1H) 4.52~4.56 (m, 2H); ESI-MS: *m/z* = 439.23 [M+H]$^+$. **7b**: Yield: 30.3%; ^{1}H-NMR (400Hz, D$_2$O): δ1.05 (d, 3H, *J*=7.2Hz, β-CH$_3$), 1.13 (d, 3H, *J*=6.4Hz, CH$_3$CHOH), 1.76~1.98 (m, 4H), 2.43~2.55 (m, 3H), 3.00~3.11 (m, 3H), 3.61~3.70 (m, 3H), 3.86~3.98 (m, 2H), 4.05 (bs, 1H), 4.13 (bs, 1H), 4.50~4.54 (m, 2H); ESI-MS: *m/z* = 439.23 [M+H]$^+$. **7c**: Yield: 30.7%; ^{1}H-NMR (400Hz, D$_2$O): δ1.02 (d, 3H, *J*=7.2Hz, β-CH$_3$), 1.13 (d, 3H, *J*=6.0Hz, CH$_3$CHOH), 1.53~1.64 (m, 2H), 2.55~2.70 (m, 3H), 3.07~3.19 (m, 3H), 3.49~3.59 (m, 4H), 3.95~4.00 (m, 3H), 4.13 (bs, 1H), 4.51~4.55 (m, 2H); ESI-MS: *m/z* = 455.25 [M+H]$^+$. **7d**: Yield: 32.4%; ^{1}H-NMR (400Hz, D$_2$O): δ1.01 (d, 3H, *J*=7.2Hz, β-CH$_3$), 1.14 (d, 3H, *J*=6.0Hz,

CH$_3$CHOH), 1.51~1.63 (m, 2H), 2.51~2.65 (m, 3H), 2.79 (s, 3H), 3.03~3.16 (m, 3H), 3.53~3.66 (m, 4H), 3.94~3.98 (m, 3H), 4.14 (bs, 1H), 4.50~4.54 (m, 2H); ESI-MS: *m/z* = 469.20 [M+H]$^+$. **7e**: Yield: 32.7%; ^{1}H-NMR (400Hz, D$_2$O): δ1.05 (d, 3H, *J*=7.2Hz, β-CH$_3$), 1.15 (d, 3H, *J*=6.0Hz, CH$_3$CHOH), 1.50~1.63 (m, 4H), 2.50~2.62 (m, 1H), 2.76~2.87 (m, 3H), 2.97~3.05 (m, 3H), 3.50~3.55 (m, 2H), 3.61~3.65 (m, 2H), 3.95~4.06 (m, 3H), 4.11~4.15 (m, 1H), 4.50~4.54 (m, 2H); ESI-MS: *m/z*=453.21 [M+H]$^+$. **7f**: Yield: 31.2%; ^{1}H-NMR (400Hz, D$_2$O): δ1.03 (d, 3H, *J*=7.2Hz, β-CH$_3$), 1.11 (d, 3H, *J*=6.0Hz, CH$_3$CHOH), 1.60~1.67 (m, 4H), 2.65~2.75 (m, 4H), 2.96~3.09 (m, 3H), 3.56~3.66 (m, 2H), 3.61~3.65 (m, 2H), 3.94~3.98 (m, 3H), 4.02~4.11 (m, 1H), 4.50~4.54 (m, 2H); ESI-MS: *m/z* =453.26 [M+H]$^+$.

CONCLUSIONS

We have designed and synthesized a novel series of new 1β-methyl-2-[5-(pyrrolidine or piperidine-2-N-substituted carbamoyl) pyrrolidin-3-ylthio] carbapenem derivatives. These compounds were prepared from **1** in the reaction with the pyrrolidine or piperidine group containing derivatives (**2a-f**). The antibacterial activity of the obtained carbapenem derivatives was determined by the standard agar dilution method. Then the MIC values were calculated and compared with positive control (MPM). We have found that **7e** and **7f** showed superior or similar antibacterial activity against Gram-positive bacteria compared to MPM except *Gamma streptococcus*, and were worth further studying. Due to the increased size of the 5-substituents, their penetration into the cell membrane of Gram-negative bacteria is hampered and the derivatives display slightly lower antibacterial activity than MPM in most cases.

REFERENCES

1. I. Kawamoto, *Drugs Future*, **2**, 181 (1998).
2. Y. Fukasawa, T. Okuda, *J. Antibiot.,* **3**, 314 (1990).
3. Y. Nagao, Y. Nagase, T. Kumagai, et al., *J. Org. Chem*., **15**, 4243 (1992).
4. P.M. Shah, R.D. Isaacs, *J. Antimicrob. Chemother.,* **4**, 538 (2003).
5. Y. G. Ge, M. A. Wikler, D.F. Sahm, R. S. Blosser-Middleton, and, J. A Karlowsky, *Antimicrob. Agents Chemother.,* **4**, 1384 (2004).

6. R. Kobayashi, M. Konomi, K. Hasegawa, M. Morozumi, K. Sunakawa, K. Ubukata, *Antimicrob. Agents Chemother.,* **3**, 889 (2005).

7. C. Okereke, *Current Therapeutic Research*, **61**, 289 (2000).

8. S. H. Ahn, H. Jeon, J. H. Choi, D. Baek, S. H. Seo, J. H. Cho, C. H. Oh, *Arch. Pharm*., **339**, 67 (2006).

9. Oh C., Lee S., Cho J., *Eur. J. Med. Chem.*, **38**, 751 (2003).

10. J. H. Lee, K. S. Lee, Y. K. Kang, K. H. Yoo, K. J. Shin, D. C. Kim, D. J. Kim, *Bioorg. Med. Chem. Lett*., **13**, 4399 (2003).

11. K. S. Lee, J. H. Lim, Y. K. Kang, K. H. Yoo, D. C. Kim, K. J. Shin, D. J. Kim, *Eur. J. Med. Chem*., **41**,

1347 (2006).

12. H. C. K. J. W. Jeon, J.H. Hong, *Eur. J. Med. Chem*., **41**, 1201 (2006).

13. X. D. Jiang, Z. D. Yuan, X. Yu, W. Zhou, *Bulg. Chem. Commun.*, **4**, 852 (2014).

14. X. D. Jiang, L. Liao, *Guangdong Chem. Ind*., **252**, 207 (2013).

15. X. D. Jiang, *Shanghai institute of pharma- ceutical industry (SIPI)*, 39 (2010).

16. X. D. Jiang., X. F. Cao., Z. D. Yuan, X. Yu, W.C. Zhou, *Chin. J. Antibiot*., **36**, 132 (2011).

17. I. Kawamoto, Y. Shimoji, O. Kanno K. Kojima, K. Ishikawa; E. Matsuyama; Y. Ashida; T. Shibayama; T. Fukuoka; S. Ohya, *J. Antibiot*., **56**, 565 (2003).

СИНТЕЗА И АНТИБАКТЕРИАЛНА АКТИВНОСТ НА ПРОИЗВОДНИ НА 1β-МЕТИЛ-2-[5-(ПИРОЛИДИН ИЛИ ПИПЕРИДИН-2-N-ЗАМЕСТЕНИ КАРБАМОИЛ) ПИРОЛИДИН-3-ИЛТИО] КАРБАПЕНЕМ

Кс. Джиянг[1, 2], Ж. Юан[2*], Кс. Ю[2], У. Жу[2]

[1] *Училище по медицина, Научно-технологичен университет Гуанкси, Люжоу, Китай*
[2] *Държавна ключова лаборатория за нови лекарства и фармацевтични процеси, Институт по фармацевтична индустрич в Шанхай, Китай*

(Резюме)

Синтезирана е серия от нови производни на 1β-метил-2-[5-(пиролидин или пиперидин-2-n-заместени карбамоил) пиролидин-3-илтио]карбапенем. Изпитана е *in vitro*тяхната антибактериална активност спрямо Грам-положителни и Грам-отрицателни бактерии, като е изследван ефекта на заместителите на карбаноил-пиролидина. Най-висока антибактериална активност проявяват 7е и 7f – производните на карбапенема и заслужават следващи изследвания.

Quantum dots sensitized solar cells

Wenbo Jiang [1,2*]

[1]*School of Electrical Engineering and Electronic Information, Xihua University, 610039 Chengdu, China*
[2]*Key Laboratory of Signal and Information Processing (Sichuan Province), Xihua University, 610039 Chengdu, China*

To improve the conversion efficiency of solar cells, quantum dots (QDs) have been widely used for the design of third generation solar cells for their interesting properties, such as multiple exciton generation, high absorption coefficient, tunable band gap, hot electron transfer, etc. Quantum dots sensitized solar cells (QDSSCs) as some of the third generation solar cells are under intense investigation. Immense efforts have been devoted to improve the photovoltaic performance of QDSSCs in the past few years. The conversion efficiency of QDSSCs was greatly improved and the best record of 7.04% has been achieved in a recent report. In this paper, the QDSSCs were reviewed from the aspects of working principle, performance, current research progress and developing trends of key parts (QDs sensitized photo-anode, counter electrodes, and electrolyte). Finally, some potential solutions for QDSSCs are proposed for further development.

Key words: Quantum dots (QDs), quantum dots sensitized solar cells (QDSSCs), conversion efficiency, counter electrodes, electrolyte.

INTRODUCTION

Due to excessive use of fossil energy, many problems have been caused, such as energy shortage, global warming, ecological deterioration, environmental pollution, etc. [1-3]. In recent years, these problems are becoming more and more serious. To figure out these problems, several renewable energy sources are being investigated to evaluate their potential to address large-scale demand. These sources include wind power [4], tidal power [5], solar energy [6-8], etc. Compared with other renewable energies, solar energy has these advantages: clean, widespread, inexhaustible, safe and reliable. So, many countries have invested a lot of research funding on the exploitation and utilization of the solar energy, and action plans have been formulated by the governments of these countries. The most direct way to utilize the solar energy is the use of photovoltaic (PV) cells, and the PV market has shown exponential growth over the last few years. Worldwide PV systems with a total peak power of about 6GW were installed in 2008. Nevertheless, PV electric power cannot compete with the price of electricity from the grid and is therefore supported by national subsidy programs with the aim of reducing the cost of PV systems by increasing the production volume. So, more research should be done in the future to increase the conversion efficiency and reduce the costs of PV systems.

So far, the PV cells have gone through two generations, which depends on the underlying technologies. The first generation device is single or multi-crystalline p-n junction silicon solar cells, which are the most common PV systems with a market share of about 85%. The second generation device is semiconductor thin film solar cells, which have currently a market share of about 15% and are mostly based on CdTe, $CuInS_2$, $CuInGaSe_2$, etc. The former has reached conversion efficiency of over 20% [9]. However, many problems have not been solved out, such as high material costs, high fabrication temperature, negative influence for environmental protection, etc. The latter has lower cost but low conversion efficiency. The highest conversion efficiency is only about 14%.

According to the limit theory of S-Qmodel [10], which was proposed by Schockley and Queisser, the limit conversion efficiency of 1st and 2nd generation PV systems is about 32.9% [11]. How to balance the costs and the conversion efficiency is becoming more and more important, this being the bottleneck in developing solar cells.

To figure out this bottleneck, several potential PV technologies were proposed, such as dye sensitized solar cells (DSSCs) [12], quantum dots sensitized solar cells (QDSSCs) [13], and organic solar cells (OSCs) [14]. Although these technologies are still at the exploratory stage, they are becoming the hottest topic in the field of solar cells, considered as third generation PV devices.

DSSCs were firstly fabricated by Grätzel and O'Regan in 1991 [15]. Since then, extensive efforts

* To whom all correspondence should be sent:
E-mail: caswenbojiang@gmail.com

have been exerted to increase the conversion efficiency of DSSCs. However, the development of DSSCs has not contributed to more than 12% of the highest recorded conversion efficiency over the last 20 years [12, 16]. There are several problems that should be further studied and solved out, such as complicated fabrication process, weak absorption in the near infrared wavelength range, poor steadiness, short life of excited state. The performance of the sensitizer is the key factor for improving the conversion efficiency of DSSCs. Therefore, some new sensitizers or semiconductors are required, which can replace the organic dye.

Over the last few years, quantum dots (QDs) have attracted widespread attention due to their outstanding opto-electronic properties. QDs are nano-crystals made of quasi-zero-dimension semiconductor materials. The size of QDs is usually about 1-10 nm, which is small enough to exhibit quantum mechanical properties. Specifically, their excitons are confined in all three spatial dimensions, which are smaller than or comparable to their deBroglie wavelength or to the Bohr radius of the excitons in the semiconductor bulk. The frequency range of emitted light is inversely related to its size. Since the size of QDs can be set during their production, their conductive properties may be carefully controlled. This allows the excitation and emission of QDs to be highly tunable. Moreover, they show quantum confinement effect (QC) and multiple excitons generation effect (MEG) [17-19]. QD-based solar cells devices were proposed to realize 3rd PV systems and to achieve conversion efficiency beyond the S-Q limit, where the QDSSCs are one of these architectures.

The QDSSCs were evolved from DSCs, and they have similar structures. The big difference between them is that QDs were used in QDSSCs to replace the organic dye in DSCs to excite more electrons. Compared with DSCs, QDSSCs have many advantages, such as broad absorption spectrum range, good chemical stability, high extinction coefficient, multiple excitons generation effect, etc.

However, the results of recent research have shown that the conversion efficiency of QDSCCs is lower than that of DSCs. The main reason is that there is serious electron loss because of charge recombination at the electrolyte-electrode or electrolyte-counter electrode interfaces [20-21]. In order to overcome this problem, many studies have been done, and some important results have been achieved. It is beneficial for the researchers to do some further study after the current research results

are reviewed.

Here, I will review the QDSSCs from the aspects of working principle, performance, current status and developing trend. Finally, some potential solutions for QDSSCs are proposed to reduce the costs and improve the conversion efficiency.

WORKING PRINCIPLE OF QDSSCs

Fig.1 shows the working principle of typical QDSSCs, where Fig.1 (b) is the amplified picture of the dotted line rectangle of Fig.1 (a).

In general, QDSSCs consist of quantum dots sensitized photo-anode, a counter electrode, and an electrolyte. The photo-anode is composed of an oxide semiconductor material, mostly TiO_2, which can be prepared and sintered easily as the TiO_2 colloidal solution is coated on transparent conductive oxide (TCO) substrate. The QDs are used to create electron-hole pairs as they transit from the lower state to the excited state. Electrons from the conductive band (CB) of QDs are injected into that of TiO_2. The counter electrons are Pt- and carbon-based materials coated on the TCO substrate. The electrolyte I^-/I_3^- is frequently used to transfer electrons between TiO_2 and the counter electrodes [23-24].

(a)

(b)
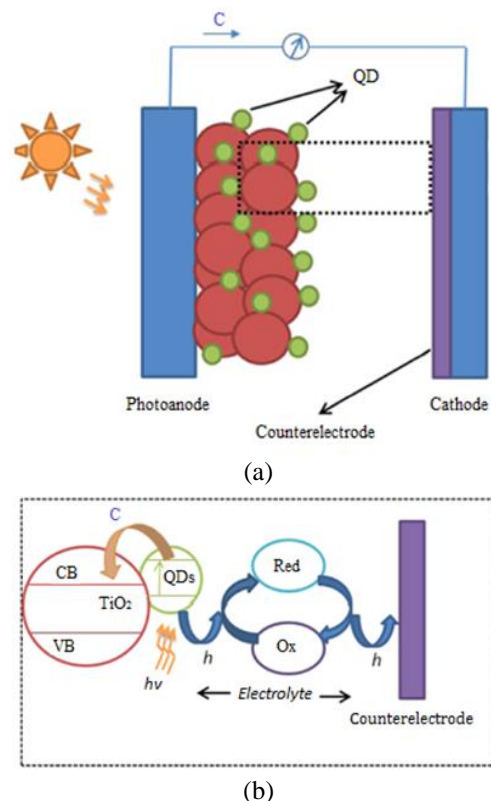
Fig.1. Working principle of typical QDSSCs [22].

As shown in Fig.1, the ground state of QDs is regenerated through electron donation from the electrolyte, which is commonly a redox system,

such as polysulfide (S^{2-}/S_x^{2-}) redox couples. Another oxidation occurs in the photo-anode electrolyte interface in the electrolyte [25-27].

$$S^{2-} + 2h^+ \rightarrow S \qquad (1)$$
$$S + S_{x-1}^{2-} \rightarrow S_x^{2-}(x = 2 - 5) \qquad (2)$$
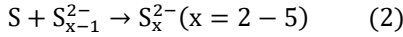
On the counter electrode, the oxidized groups $S_x^{2-}$are re-reduced toS^{2-}. So, electrons migrate via the external load to complete the circuit [26].

$$S_x^{2-} + 2e^- \rightarrow S_{x-1}^{2-} + S^{2-} \qquad (3)$$
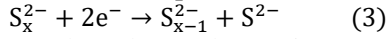
Subsequently, the voltage is generated by variation in Fermi levels between the electron in the photo-electrode and the redox potential of I^-/I_3^- in the electrolyte.

QDSSCs PERFORMANCE

To evaluate the performance of QDSSCs, the conversion efficiency (ŋ) and the incident photon-to-electron conversion efficiency (IPCE) will be introduced in this section. They are two important parameters.

The conversion efficiency (ŋ) can be expressed by [28]:

$$\eta = \frac{P_0(max)}{P_{in}} = \frac{I_{sc} \times V_{oc} \times FF}{P_{in}} \quad (4)$$

Where, $P_0(max)$ is the maximum of the output power; P_{in} is the input power; I_{sc} is the short current; V_{oc} is the open circuit voltage; FF is the fill factor.

The ideal value of FF is equal to 1, but the actual value is always below the ideal value.

The incident photon-to-electron conversion efficiency (IPCE) can be expressed by [29]:

$$IPCE(\lambda) = LHE(\lambda) \times \varphi_{inj} \times \varphi_{coll} \quad (5)$$

Where, $LHE(\lambda)$ is the light harvesting efficiency at a certain wavelength; φ_{inj} is the quantum yield of electron injection; φ_{coll} is the efficiency of collecting injected electrons at the back contact.

In order to compare the performances of different QDSSCs, the above data should be measured under uniform conditions. A standard solar spectrum of AM (air mass), 1.5G (global) is used. This spectrum is derived from the path length the light needs to travel through the atmosphere and reach the surface [29].

CURRENT RESEARCH OF QDSSCs

Many theoretical and experimental results of the QDSSCs proved that the conversion efficiency of QDSSCs is related to the QDs sensitized photo-anode, the counter electrode, the electrolyte, etc.

In this section, some current research results about the above three factors will be proposed.

QDs sensitized photo-anode

The major advantage of using QDs as sensitizers in QDSSCs is the size-dependent band gap, which is a characteristic of the optical properties of QDs. By varying the size of QDs, the light harvesting energy in the solar spectrum can be controlled [30].

The QDs employed in QDSSCs as sensitizers include CuInS$_2$ [31], PbS [32], CdS [33], CdSe [34], CdTe [35], ZnS [36], etc. Some research results have shown that CdS and CdSe QDs have been considered as an adequate sensitizer of QDSSCs.

Besides using different materials, changing the size of QDs, and improving the fabrication process are also important for improving the conversion efficiency of QDSSCs.

Chen et al.[37] reported that higher conversion efficiency was obtained when two different sizes of QDs were used in QDSSCs. Jung et al.[20] used a passivation layer (ZnS) in their research to improve the performance of QDSSCs located between TiO$_2$ and the electrolyte in CdS QDs. Hu et al.[38] fabricated multi-layer QDs using the chemical bath deposition (CBD) method to improve the conversion efficiency from 0.34% to 1.47%. Yu et al.[39] found the influence rules between the annealing temperature and the QDSSCs performance. A remarkable efficiency of 4.21% was obtained based on a TiO$_2$-CdSe/CdS-ZnS photo-anode (400°C, 300s calcination), polysulfide electrolyte and Cu$_2$S counter electrode achieving a power conversion efficiency of 4.21% under AM 1.5 G one-sun illumination. Fig. 2 shows the structure of QDSSCs.
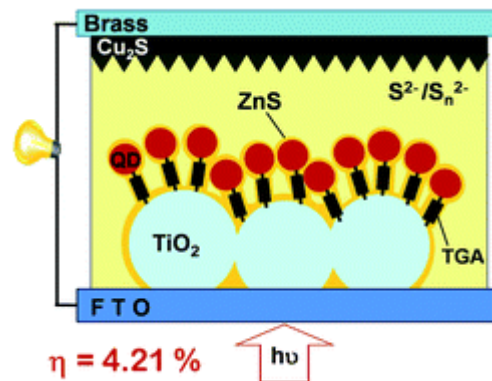
Fig.2. Structure of QDSSCs (ŋ=4.21%, under AM 1.5 G one-sun illumination) [39].

These results show that higher conversion efficiency will be obtained using multi-layered QDs incorporated with a passivation layer.

Counter electrodes

Platinum (Pt) was commonly used as counter

electrode in QDSCs and initial QDSSCs systems. It has been confirmed that Pt counter electrodes have low resistance and superior electro-catalytic activity for the iodide/triiodide redox couple in DSSCs [40]. Nevertheless, Pt counter electrodes have short lifetime and are expensive when iodide/triiodide is used as the electrolyte in QDSSCs. It was also reported that Pt counter electrodes have problems when a polysulfide redox couple is used as the electrolyte in QDSSCs. The conductivity and surface activity of the Pt electrodes decreased and their lifetime was short [33].

To figure out this problem, various non-Pt materials such as PbS, CuS and other materials have been investigated [41-44]. Kim et al.[41] have proved that doping of a PbS counter electrode with Mn ions in a QDSSC greatly improves the electro-catalytic activity compared with Pt and PbS counter electrodes, achieving an efficiency of 3.61%. Chandu et al.[44] used Mn-doped CuS as counter electrodes, which were in situ grown on FTO glass substrate by a facile CBD method and then tested for use in the QDSSCs system as counter electrodes catalyst without any post-treatment. Their research results proved that Mn-doped CuS counter electrodes showed better catalytic activity for polysulfide reduction than bare-CuS and Pt counter electrodes. Thus, the obtained Mn-doped CuS counter electrode delivered an efficiency of 5.46%, which was comparable to that of the bare-CuS electrode (4.29%) and Pt electrode (1.37%) tested under similar conditions.

Many research results also show that higher performances will be obtained using as counter electrodes compound materials containing metal sulfides and carbon.

Fig.3 shows the current density-voltage (J-V) characteristics of QDSSCs based on CuS, Mn-CuS and Pt counter electrodes.
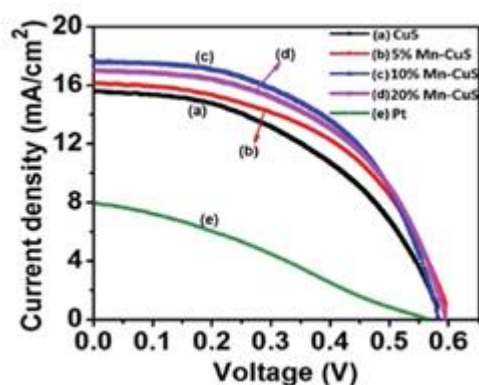
Fig.3. J-V characteristics of QDSSCs based on CuS, Mn-CuS and Pt counter electrodes [44].

Electrolyte

For QDSCs, Na_2S and S aqueous solution was commonly used as electrolyte, which has high surface tension. So it is difficult to permeate to the mesopores of TiO_2 film, which means that the photo-anode and electrolyte cannot be in close contact, and the performance of QDSCs is poor. To solve out this problem, alcohol was used to replace part of the aqueous solution, but its electrolytic dissociation is worse than that of the aqueous solution. Considering the permeability and the dissociation, Lee et al.[26] proposed an aqueous solution mixed with methanol (7:3). Sixto et al.[45], reported that electrolytes with a low concentration of S can inhibit the reaction between the QDs and the electrolyte, and the concentration was set as 1 mol/L. Li et al.[46] achieved a 3.2% conversion efficiency and 0.89 fill factor (FF) using methyl ammonium sulfide electrolyte, which was synthetized by themselves. Their research provided a novel method for electrolyte preparation.

Fig.4 shows the J-V characteristics of the TiO_2/TGA/CdS-3-based cell measured under one-sun illumination (AM 1.5G, 100 mW cm^{-2})
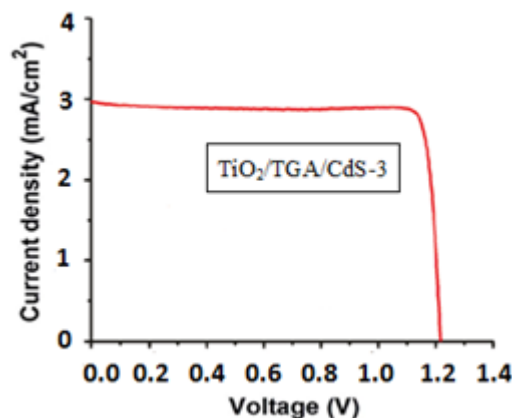
Fig.4. J-V characteristics of TiO_2/TGA/CdS-3-based cell measured under one-sun illumination (AM 1.5G, 100 mW cm^{-2}) [46]

Besides the above single electrolyte material used in QDSSCs, Karageorgopoulos et al.[47] employed two different electrolytes, namely, a quasi-solid electrolyte that contains a polysulfide (S^{2-}/S_x^{2-}) and a hybrid organic-inorganic (ICS-PPG230) material in ZnO/CdS/CdSe QDSSCs. The conversion efficiency of solar cells was enhanced from 1.2% to 4.5%. Their results showed that the quasi-solid electrolyte was more appropriate than the aqueous electrolyte.

ANALYSIS AND OUTLOOK

As a representative of the third generation solar cells, the QDSSCs are under intense investigation. Immense efforts have been devoted to improve the

photovoltaic performance in the past few years. The conversion efficiency of QDSSCs was greatly enhanced and the best record of 7.04% has been recently reported [48].

However, the conversion efficiency of QDSSCs is still much lower than that of DSSCs (about 12%). And most of these current results are obtained only in the lab, and are not suitable for industrial production. In order to obtain higher conversion efficiency of QDSSCs, the future work should be focused on these following aspects:

1)develop a new material of semiconductor QDs with a large wavelength range of optical absorption, and improve the QDs loading onto TiO_2 to increase the light harvesting efficiency of QDs;

2)develop a new material and optimize the fabrication process of counter electrodes for improving the catalytic activity;

3)develop a novel organic polysulfide electrolyte and a solid-state hole conductor as electrolyte;

4)improve the long-term stability of the counter electrode for polysulfide electrolyte;

5)reduce the fabrication costs of QDSSCs.

CONCLUSIONS

In this paper, QDSSCs are reviewed from the aspects of working principle, performance, current research progress and developing trends. Immense efforts have been devoted to improve the photovoltaic performance of QDSSCs in the past few years, and some theoretical and experimental results of the QDSSCs have been achieved, but most of them were obtained only in the lab, and are not suitable for industrial production. Studies of many key issues for practical applications are currently under way. The conversion efficiency of QDSSCs is still much lower than that of 1st and 2nd generation PV systems, but they offer a potential novel developing direction of solar cells.

With the development of the material science, nanotechnology and the fabrication process, the conversion efficiency of QDSSCs will be highly improved in the near future. It is a promising 3rd generation PV systems.

REFERENCES

1. N. Lior, *Energy*, **33**, 842 (2008).
2. M. Aydin, K. R. Verhulst, E. S. Saltzman, M. O. Battle, S. A. Montzka, D. R. Blake, Q. Tang, M. J. Prather, *Nature*,**476**, 198 (2011).
3. R. York, *Nat. Clim. Change*,**70**, 441(2012).
4. M. Z. Jacobson, C. L. Archer, *Proc. Natl. Acad. Sci. USA*,**109**,15679 (2012).
5. C. Frost, C. E. Morris, A. M. Jones, D. M. O'Doherty, T. O'Doherty, *Renew. Energy*,**78**,609 (2015).
6. J. J. Sarralde, D. J. Quinn, D. Wiesmann, K. Steemers, *Renew. Energy*,**73**, 10 (2013).
7. H. A. Atwater, A. Polman, *Nat. Mater*,**9**, 205 (2010).
8. Z. Liu, T. W. Zhou, L. L. Li, Y. H. Zuo, C. He, C. B. Li, C. L. Xue, B. W. Cheng, Q. M. Wang, *Appl. Phys. Lett*,**103**, 082101 (2013).
9. T. Saga, *NPG. Asia. Mater*, **2**, 96 (2010).
10. A. S. Brown, M. A. Green, *Phys. E*, **14**, 96 (2002).
11. W. Shockley, H. J. Queisser, *J. Appl. Phys*, **32**, 510 (1961).
12. A. Yella, H. W. Lee, H. N. Tsao, C. Y. Yi, A. K. Chandiran, M. K. Nazeeruddin, E. W. G. Diav, C. Y. Yeh, S. M. Zakeeruddin, M. Grätzel, *Science*, **334**, 629 (2011).
13. S. Rühle, M. Shalom, A. Zaban, *Chem. Phys. Chem*, **11**, 2290 (2010).
14. H. Hoppe, N. S. Sariciftci, *J. Mater. Res*, **19**, 1924 (2004).
15. O. Regan, M. Gratzel, *Nature*, **353**, 737 (1991).
16. M. Grätzel, *J. Photochem. C: Photochem*, **4**, 145 (2013).
17. R. D. Schaller, V. I. Klimov, *Phys. Rev. Lett*, **92**, 18660 (2004).
18. M. C. Beard, K. P. Kuusten, P. R. Yu, J. M. Luther, Q. Song, W. K. Metzger, R. J. Ellingson, *Nano. Lett*,**7**, 2506(2007).
19. S. K. Stubbs, S. J. O. Hardman, D. M. Graham, B. F. Spencer, W. R. Flavell, P. Glarvey, O. Masala, N. L. Pickett, D. J. Binks, *Phys. Rev. B*,**81**, 081303 (2010).
20. S. W. Jung, J. H. Kim, H. S. Kim, C. J. Choi, and K. S. Ahn, *J. Curr. Appl. Phys,* **12**, 1459 (2012).
21. J. M. Kim, H. S. Choi, C. W. Nahm, C. H. Kim, S. H. Nam, S. J. Kang, D. R. Jung, J. I. Kim, J. Y. Kang, B. W. Park, *J. Power. Sources*, **220**, 108 (2012).
22. M. Kouhnavard, S. Ikeda, N. A. Ludin, N. B. A. Khairudin, B. V. Ghaffari, M. A. M. Terdi, M. A. Ibrahim, S. Sepeai, K.Sopian, *Renew. Sust. Energy. Rev*, **37**, 397 (2014).
23. H. Kohjiro, M. Shogo, Dye-sensitized solar cell, **2nd edition**, 642 (2005).
24. J. W. Gong, J. Liang, K. Sumathy, *Renew. Sustain. Energy. Rev*, **16**, 5848 (2012).
25. L. Lee, Y. S. Lo, *J. Adv. Funct. Mater*, **19**, 604 (2009).
26. Y. L. Lee, C. H. Chang, *J. Power. Sources*, **185**, 584 (2008).
27. Z. Yang, C. Y. Chen, P. Roy, H. T. Chang, *Chem. Commun*, **47**, 9561 (2011).
28. M. K. Nazeetuddin, M. Grätzel, *J. Am. Chem. Soc*,**115**, 6383 (1993).
29. Fuke, L. B. Hoch, A. Y. Koposov, V. M. Manner, D. J. Werder, A. Fukui, N. Koide, H. Katayama, M.

Sykora, *ACS. Nano*, **4**, 6377 (2010)

30. R. Vogel, P. Hoyer, H. Weller, *J. Phys. Chem.*, **98**, 3183 (1994).
31. Z. J. Zhou, S. J. Yuan, J. Q. Fan, Z. L. Hou, W. H. Zhou, Z. L. Du, S. X. Wu, *J. Nanoscale. Res. Lett*, **7**, 652 (2012).
32. J. Jiao, Z. J. Zhou, W. H. Zhou, S. X. Wu, *Mater. Sci. Semicond. Process*, **16**, 435 (2013).
33. Q. X. Zhang, Y. D. Zhang, S. Q. Huang, X. M. Huang, Y. H. Luo, Q. B. Meng, D. M. Li, *Electrochem. Commun*, **12**, 327 (2010).
34. G. P. Victoria, X. Q. Xu, M. S. Ivan, B. Juan, *ACS. Nano*, **4**, 5783 (2010).
35. Z. S. Yang, H. T. Chang, *Sol. Energy. Mater. Sol. Cells*, **94**, 2046 (2010).
36. B. Nikolaos, D. Vassilions, B. Kyriakos, L. Panagiotis, *Electrochim. Acta*, **91**, 246 (2013).
37. J. Chen, W. Lei, W. Q. Deng, *Nanoscale*, **2**, 674(2011).
38. X. Hu, Q. X. Zhang, X. M. Huang, D. M. Li, Y. H. Luo, Q. B. Meng, *J. Mater. Chem*, **21**, 15903 (2011).
39. X. Y. Yu, B. X. Kuang, D. B. Su, C. Y. Su, *J. Mater. Chem,* **22**, 12058 (2012).
40. K. Imoto, K. Takahashi, T. Yamaguchi, T. Komura, J. I. Nakamura, K. Murata, *Energy. Mater. Sol. Cells,* **79**, 459 (2003).
41. B. M. Kim, M. K. Son, S. K. Kim, N. Y. Hong, S. Park, M. S. Jeong, H. Seo, K. Prabakar, H. J. Kim, *Electrochim. Acta,***117**, 92 (2004).
42. L. L. Li, P. N. Zhu, S. J. Peng, M. Srinivasan, Q. Y. Yan, A. S. Nair, B. Liu, S. Samakrishna, *J. Phys. Chem. C,***118**, 16526 (2014).
43. C. J. Raj, K. Prabakar, A. D. Savariraj, H. J. Kim, *Electrochim. Acta*, **103**, 231 (2013).
44. V. V. M. G. Chandu, M. V. Haritha, S. K. Kim, S. S. Rao, D. Punnoose, H. J.Kim, *RSC. Adv,***5**, 2963 (2015).
45. G. Sixto, M. S. Ivan, M. Lorena, G. Nestor, L. V. Teresa, G. Roberto, J. D. Lina, S. Qing, T. Taro, B. Juan, *Nanotechnology,***20**, 295204 (2009).
46. L. Li, X. C. Yang, J. J. Gao, H. N. Tian, J. Z. Zhao, A. Hagfeldt, L. C. Su, *J. Am. Chem. Soc*, **133**, 8458 (2011).
47. D. Karageorgopoulos, E. Stathatos, E. Vitoratos, *J. Power. Sources*, **219**, 9 (2012).
48. Z. X. Pan, I. M. Sero, Q. Shen, H. Zhang, Y. Li, K.Zhao, J. Wang, X. H. Zhong, J. Bisquert, *J. Am. Chem. Soc,* **136**, 9203 (2014).

СОЛАРНИ КЛЕТКИ, СЕНСИБИЛИЗИРАНИ С КВАНТОВИ ТОЧКИ

Уенбо Джиянг[1, 2] *

[1]*Училище по електро-инженерство и електронна информация, Университет Ксихуа, Ченгду, Китай*
[2] *Държавна ключова лаборатория за обработка на сигнали и информация,Университет Ксихуа, Ченгду, Китай*

(Резюме)

Квантовите точки (QDs) се използват широко за подобряването на ефективността на превръщане при соларните клетки и за проектирането на трето поколение соларни клетки (QDSSC). Това се дължи на интересните им свойства (генерирането на множествени екситони, висок абсорбционен коефициент,подходяща забранена зона и горещ електронен пренос).Огромни усилия са положени през последните години за подобряването на фотоволтаичните характеристики на QDSSCs.Ефективността на конверсия на QDSSC е била значително подобрена, като по последни сведения най-добрия резултат е 7.04%. В настоящата работа тези соларни клетки са разгледани от гледна точка на работния принцип, работата им, съвременния напредък и тенденциите на развитие (QD-сенсибилизарни фото-аноди, противо-електродите и електролитите). Накрая са предложени някои решения за бъдеще развитие на QDSSC.

Molecular simulation of protein transport controlled by pressure-driven flow in silica nanofluidic channels

K. Liu[1*], S. L. Chen[1], S. W. Xiao[2], X. L. Zhang[3], D. C. Ba[1*], D. Y. Wang[1], G. Y. Du[1], Y. S. Ba[1]

[1]*School of Mechanical Engineering and Automation, Northeastern University, Shenyang, 110089, China;*
[2]*Institute of High Energy Physics Chinese Academy of Sciences, 100049 Beijing, China;*
[3]*Capital Aerospace Machinery Company, Beijing, 100076, China*

A series of NEMD (non-equilibrium molecular dynamics) simulations were performed to study the biomolecular migration process driven by pressure in nanoscale channels. Several parameters, including channel height, driving pressure, system temperature and wall charge, were used to investigate the density and transport velocity of molecules and ions. The results show that the channel height has a significant influence on the distribution of density and velocity depended on the size of biomolecules. The wall charge density also greatly influences the velocity and ion concentration of proteins nearby the channel wall while the temperature only has a slight influence. The conclusions are useful to the design and manipulation of nanofluidic devices.

Key words: Molecular simulation, nanofluidic channel, protein molecules, transport process, NEMD, pressure-driven, nanoscale silica channels.

INTRODUCTION

Among the simulation techniques, EMD (equilibrium molecular dynamics) has been extensively applied to study the equilibrium fluid flow [11]. Meanwhile, for atomic systems far from equilibrium, NEMD (non-equilibrium molecular dynamics) offers an alternative method, especially in solving the nanofluidic problems [11-15]. In the nanofluidic field, electroosmosis and electrophoresis have been widely used to manipulate the fluid and biomolecules in simulations [16-24] and experiments [2, 25-28]. However, the flow can be driven by pressure in one direction unlike electricity-driven flow. There are some reports on modeling and numerical simulation of pressure-driven flow in the nanochannels [11-13, 15, 29-42]. While a single fluid is usually considered, biomolecule flows generated by pressure received less attention [43]. Some researchers have studied how the physical and geometric factors affected the biomolecular flux through the nanopores [43]. However, the interfacial interactions in the nanochannel have not been deeply explored. Besides, the factors affecting the transport of molecules and ions have not been completely understood yet.

The research purpose is to investigate the pressure-driven biomolecular flow in the nanochannel. This issue tries to analyze how the flow characteristics are influenced by the channel

parameters. Before the simulations are started, β-cristobalite SiO_2 is selected as the channel wall while hen egg albumen lysozyme is selected as the biomolecule.

MODEL AND SIMULATION DETAILS

The simulation model is schematically presented in Fig.1, where the simulation region is regarded as a *3-D* box.

As shown in Fig.1, two silica walls are on the top and bottom, water molecules are hidden, three biomolecules are located in the central channel, blue and red spheres represent Na^+ and Cl^- ions respectively. The length L_x is 26.918 nm, the width L_z is 9.420 nm and the height L_y has five different values, namely, 8.438 nm, 9.438 nm, 10.438 nm, 11.438 nm and 12.438 nm for each system.
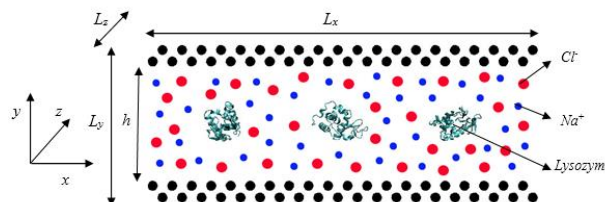
Fig.1. Cross-section of the simulation model for the pressure-driven flow

Table 1 lists the parameters including channel height h, driving acceleration α, temperature T and wall charge density ρ_{wall}. According to Table 1, a series of simulations have been performed. Periodic boundary conditions are imposed along x and z directions.

---

* To whom all correspondence should be sent:
E-mail: kliu@mail.neu.edu.cn (K. Liu),
dchba@mail.neu.edu.cn (D. C. Ba)

Table 1. Parameters of the simulation model.

No.	a (nm/ps^2)	ρ_{wall} (C/m^2)	h (nm)	T (K)
1	5.0	0.3	8.478	300
2	5.0	0.5	8.478	300
3	5.0	0.1	8.478	300
4	5.0	-0.1	8.478	300
5	5.0	-0.3	8.478	300
6	5.0	-0.5	8.478	300
7	5.0	0.3	6.478	300
8	5.0	0.3	7.478	300
9	5.0	0.3	9.478	300
10	5.0	0.3	10.478	300
11	2.0	0.3	8.478	300
12	8.0	0.3	8.478	300
13	5.0	0.3	8.478	320
14	5.0	0.3	8.478	340

Two silica substrates with identical surfaces are placed with the channel height along *y* direction. To simulate the real physical silica wall, the (111) crystallographic face of *β-cristobalite SiO₂* is used as the silica wall [44]. To obtain a chemically realistic surface, all non-bridging oxygen atoms on the top of the *β-cristobalite* crystal are hydroxylated [45]. The *Si-O* bond is changed to the *Si-OH* bond in order that surface hydroxyl group density is 13.5 *OH*/nm².

The hydrogen atoms are positioned at 0.1 nm perpendicular to the surface. The wall atoms are kept around their original *fcc* lattice positions due to an elastic spring potential as following

$$u_{wall}\left(\left|r(t)-r_{eq}\right|\right)=\frac{1}{2}K\left(\left|r(t)-r_{eq}\right|\right)^2 \quad (1)$$

Where, *r(t)* is the position of an atom at time *t*, r_{eq} is its initial lattice position and *K* is the spring constant [11, 46]. This initial allows the wall molecules to vibrate, which could achieve the momentum transfer between fluid molecules and wall molecules. Here, *K* is set at 1000. The wall charge density ρ_{wall} is simulated with six cases: -0.5, -0.3, -0.1, 0.1, 0.3 and 0.5C/m².

Three hen egg albumen *lysozymes*, labeled as protein 1, protein 2 and protein 3, from left to right, are added in the center of the nanochannel with spacing of 9 nm and phase difference of 90 degrees. The *lysozyme* is positively charged with 8e. The water molecules are treated with *SPC/E* mode. The concentration of *NaCl* aqueous solution was as constant as 0.83 M throughout the whole simulation.

Because of the relatively large pressure drop in the nanochannels, an external large acceleration α (2, 5 and 8 nm/ps² for each case) is applied along the *x* direction to every fluid atom in order to simulate the real pressure-driven flow in the nanochannels. Flow energy caused by the pressure is converted into thermal energy absorbed by the wall atoms, resulting

in an increase in system temperature [32]. Thus a velocity rescaling thermostat at the thermal walls is applied to keep the system temperature constant, described by:

$$dK=(K_0\text{-}K)\frac{dt}{\Gamma T}+2\sqrt{\frac{KK_0}{N_f}}\frac{dW}{\sqrt{\Gamma T}} \quad (2)$$

Where, *K* is the kinetic energy, N_f is the number of freedom degrees and *dW* is a *Wiener* process [47]. The system temperature *T* is kept constant at three values 300 K, 320 K and 340 K. The force field used here is the *charmm27* inside *Gromacs 4.5*. The *van der Waals* interactions are treated according to the 12-6 *Lennard-Jones* potential

$$V_{LJ}\left(r_{ij}\right)=\frac{C_{ij}^{(12)}}{r_{ij}^{12}}-\frac{C_{ij}^{(6)}}{r_{ij}^{6}} \quad (3)$$

The electrostatic forces are described by a coulombic potential with a cutoff set to 1.0 nm. Long-range interactions are calculated by the *PME* (particle mesh *Ewald*) method.

The simulation step time for the system is 2.0 fs. First of all, energy minimization is carried out. Then the system would reach equilibrium with a relaxation step at 1×10^5. Last, the *NEMD* simulation is performed with duration of 2×10^5 steps with an additional acceleration applied on each molecule.

RESULTS AND DISCUSSION

In order to solve the density and velocity distribution, the channel is divided into *n* bins along *z* direction. Then density and mean velocity are computed at each bin for all time steps and averaged upon 14 groups of parameters, as listed in Table 1.

Density and velocity distribution of water molecules

Fig.2 shows the water molecule density distribution along the height direction. Due to the strong solid–liquid interactions, the water molecules are distributed orderly near the solid interface. The distance between the first peaks and walls is about 0.3 nm, which is about the size of molecule diameter.

As shown in Fig.2(a), two peaks of water density are observed near the solid interface at the channel height of 9.478 nm and 10.478 nm. With decreasing channel height, the number of peak increases to three and the newly appeared peak becomes more obvious and closer to the wall. The oscillatory characteristics of water molecular density near the walls change drastically with the decreasing of channel height *h* under 8.478 nm. On the contrary, the layered water molecular density near the walls becomes stable above 8.478 nm.

(a)

(b)

(c)

(d)
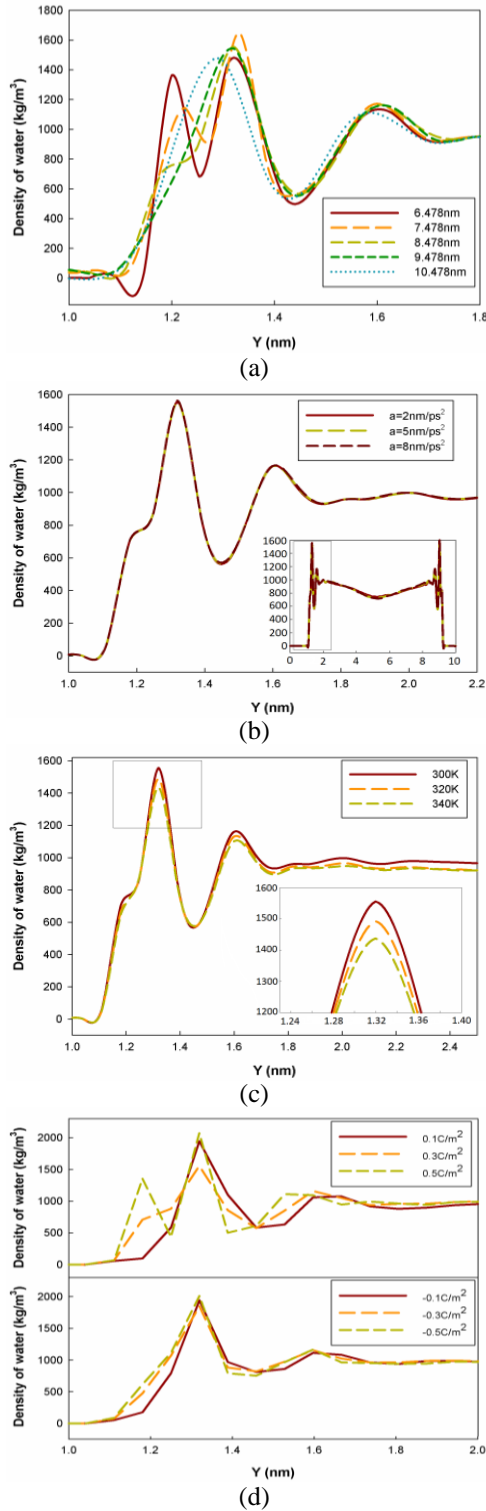
Fig. 2. Density distribution of water molecules at h=8.478 nm, $\bar{a}$ =5 nm/ps^2, T=300K and ρ_{wall}=0.3C/m^2 (unless otherwise stated), (a) at h=6.478, 7.478, 8.478, 9.478 nm and 10.478 nm, (b) at $\bar{a}$ =2, 5 and 8 nm/ps^2, (c) at T=300, 320 and 340K, (d) at ρ_{wall}=-0.5, -0.3, -0.1, 0.1, 0.3 and 0.5 C/m^2.

In Fig.2(b) we examine the pressure influence on water molecular density by exerting acceleration on all molecules. The central water molecular density only decreases marginally with the acceleration

while the density near the wall seldom changes. The similar situation is observed in Fig.2(c), which is used to examine the influence of temperature (from 300 to 340K) on water molecular density profile. The central water molecular density is marginally increasing with the temperature. Besides, the two distinct peaks are very close to the wall interface, which decrease with the temperature.

Fig.2(d) summaries the influences of wall surface charge on density. When the wall is positively charged, the water density near the wall reaches the peaks twice when ρ_{wall} equals 0.1C/m^2, while it reaches three times when ρ_{wall} equals 0.5C/m^2. In fact, the additional peak is closer to the wall. However, the situation is quite different when the wall is negatively charged. Both the peak number and the value change little with the charges. The different mass of the hydrogen and oxygen atoms could be considered as the cause. The oxygen ions are adsorbed to the wall when the wall is positively charged while the hydrogen ions are adsorbed when the wall is negatively charged. However, the mass of the oxygen atoms is 16 times that of the hydrogen, so a new peak will appear near the positively charged wall.

The water velocity distribution along the height direction was calculated and shown in Fig.3, which is similar to *Poiseuille* distribution. The center is high due to the small resistance here. Furthermore, the closer the water molecules are to the wall, the stronger are the solid-fluid interactions while the smaller is the water velocity.

The influence of channel height on water molecular velocity is shown in Fig.3(a): when h equals 6.478 nm, the velocity in the channel center is the highest, and the velocity difference between layers close to walls is also the largest. Although the velocity and the differences decrease with h, they become negligible when h increases to 9.478. This states that the channel height has a great influence on the velocity of water molecules under 8.478 nm. Increased velocity was also observed when the pressure increases, as shown in Fig.3(b). The kinetic energy of water molecules increases with the exerted acceleration, so does the velocity.

The influences of temperature on water molecular velocity are also examined, as shown in Fig.3(c). It shows that the influences are so complicated that no rules can explain the changes. However, these results could be understood when considering the thermal motion of water molecules under different temperatures. Due to the disorder of thermal motion, the profile of the temperature influencing the water velocity is irregular. The similar situation happens as shown in Fig.3(d) which examines the influence of wall charge density on

water molecular density.

(a)

(b)

(c)

(d)
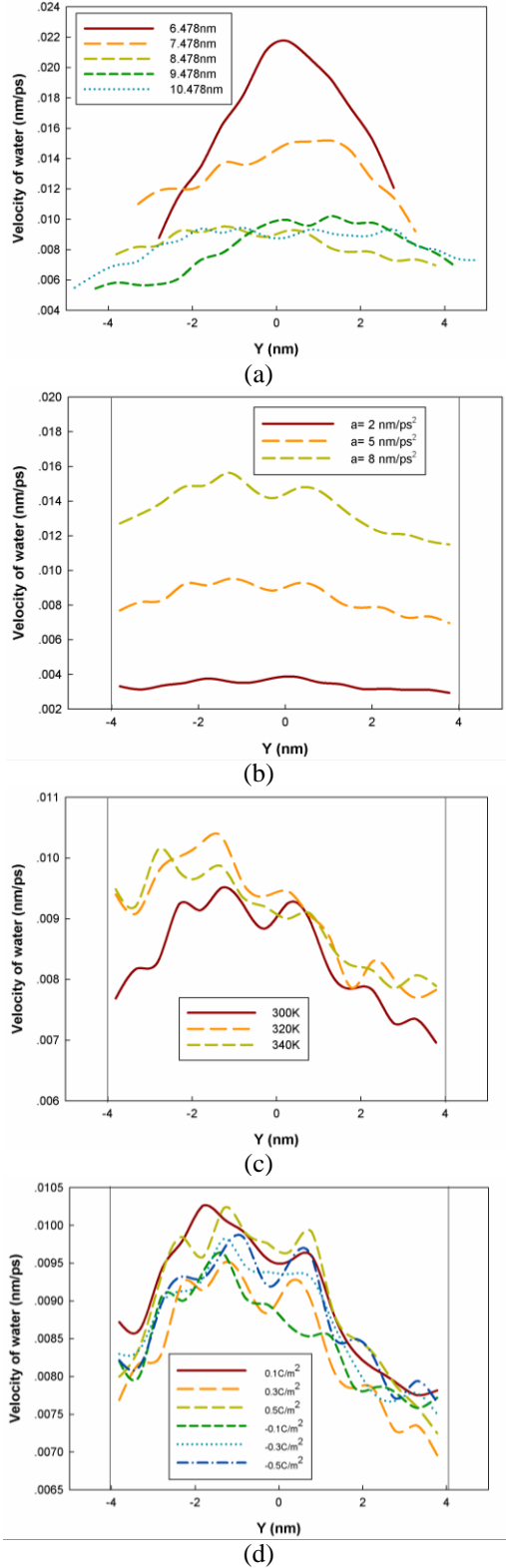
Fig. 3. Velocity distributions of water at h=8.478 nm, $\vec{a}$ =5 nm/ps^2, T=300K and ρ_{wall}=0.3C/m^2 (unless otherwise stated), (a) at h=6.478, 7.478, 8.478, 9.478 nm and 10.478 nm, (b) at $\vec{a}$ =2, 5 and 8 nm/ps^2, (c) at T=300, 320 and 340K, (d) at ρ_{wall}=-0.5, -0.3, -0.1, 0.1, 0.3and 0.5C/m^2.

Ion concentration distribution

Fig.4 shows the ion concentration distribution along the channel height direction. Due to the strong electrostatic interactions, the co-ions are mainly located in the central channel while the counter-ions are mainly adsorbed to the channel wall.

In Fig.4(a)～(b), we examine the influence of channel height on ion concentration. The ions distribution is uneven with a distinct peak when *h* equals 6.478 nm. On the contrary, the distribution becomes uniform when *h* increases to 7.478 nm. However, two unobvious peaks appear in both sides of the center with the increasing of *h*. This is mainly because three positively charged *lysozyme* molecules in the center will stay away from the Na^+ ions. As shown in Fig.4(b), two distinct peaks appear near the wall when *h* equals 6.478 nm. However, the peak number decreases to one with *h*. The peaks of Cl^- ion concentration decrease with *h*, but they hardly change above 8.478 nm.

As shown in Fig.4(c)～(d), the influence of pressure on ion concentration is negligible. The similar situation happens in Fig.4(e)～(f) showing the temperature's influence on ion concentration. Moreover, increasing of Cl^- ion concentration with temperature is shown in Fig.4(f).

The wall charge density's influence on ion concentration is shown in Fig.4 (g)～(j). With the increase in absolute wall charge density, more co-ions are repelled to the center. When the ion concentration in the center increases, ion concentration distribution becomes more uneven. As shown in Fig.4(h), there is only one peak of Cl^- ion concentration close to the wall due to the wall electrostatic interactions. Meanwhile, the distance between the peak and wall decreases with the positive wall charge density. However, the peak increases. On the other hand, when the wall is negatively charged, the situation becomes complicated. The Na^+ ion concentration reaches the peak when ρ_{wall} equals -0.1C/m^2. It has three peaks at -0.3C/m^2 and two peaks at -0.5C/m^2. Moreover, the similar phenomena happen in Fig.4(j), the distance between the peak of Na^+ ion concentration and the wall decreases with the negative wall charge density. However, the peak increases.

Biomolecular density and velocity distribution

Due to the complexity and high surface activity of the biomolecules, the effect of the parameters (*h*, $\vec{a}$,*T*, ρ_{wall}) on the biomolecular movements becomes very complicated. Fig.5 shows the biomolecular density distribution along the height direction. As shown in Fig.5, the lysozyme biomolecules are mainly located in the center.
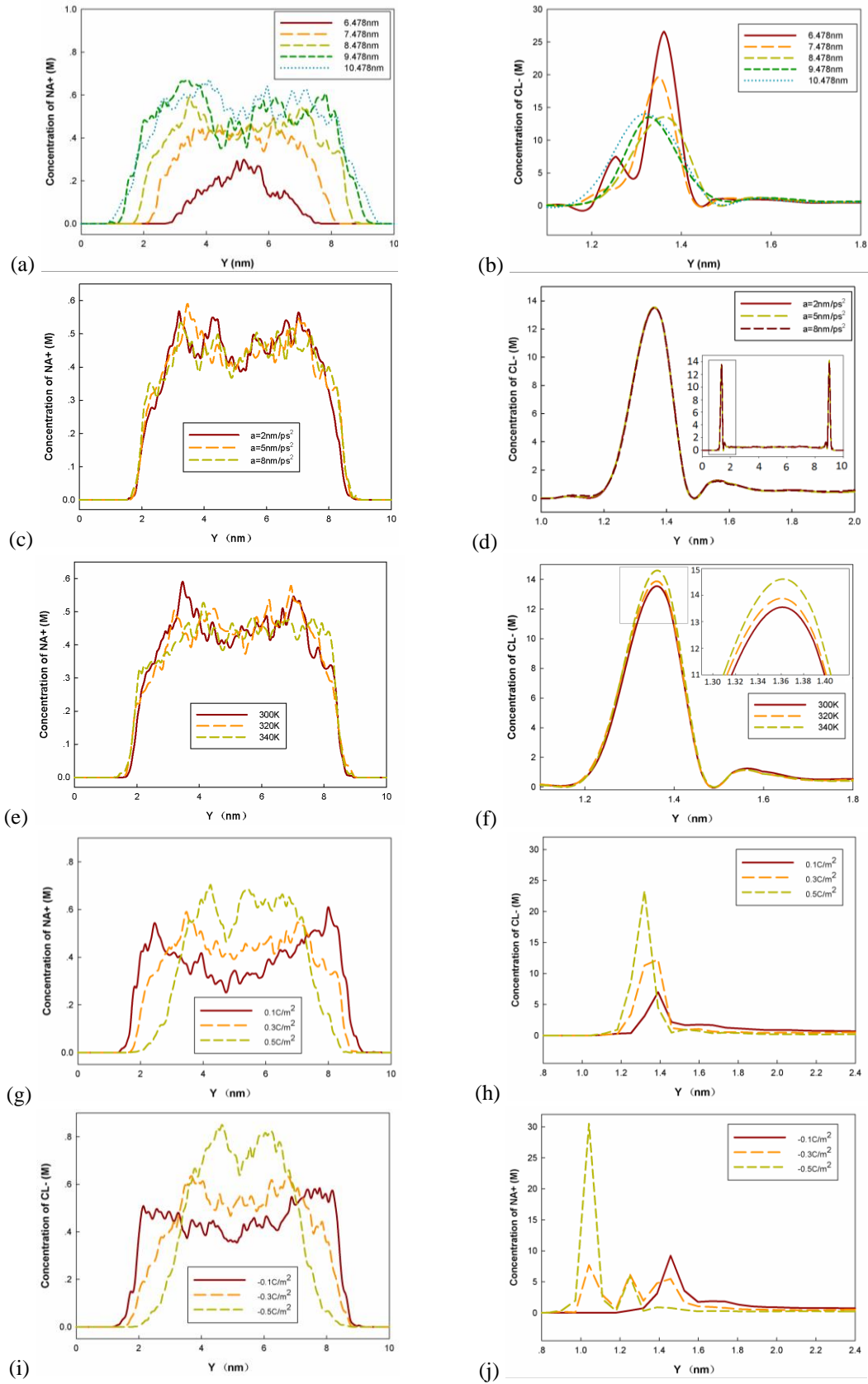
Fig. 4. Concentration distributions of ions at h=8.478 nm, $\vec{a}$ =5 nm/ps^2, T=300K and ρ_{wall}=0.3 C/m^2 (unless otherwise stated), (a) (b) at h=6.478, 7.478, 8.478, 9.478 nm and 10.478 nm, (c) (d) at $\vec{a}$ =2, 5 and 8 nm/ps^2, (e) (f) at T=300, 320 and 340K, (g) (h) at ρ_{wall}= 0.1, 0.3 and 0.5C/m^2, (i) (j) at ρ_{wall}= -0.1, -0.3, and -0.5 C/m^2.

1225

(a)

(b)

(c)

(d)
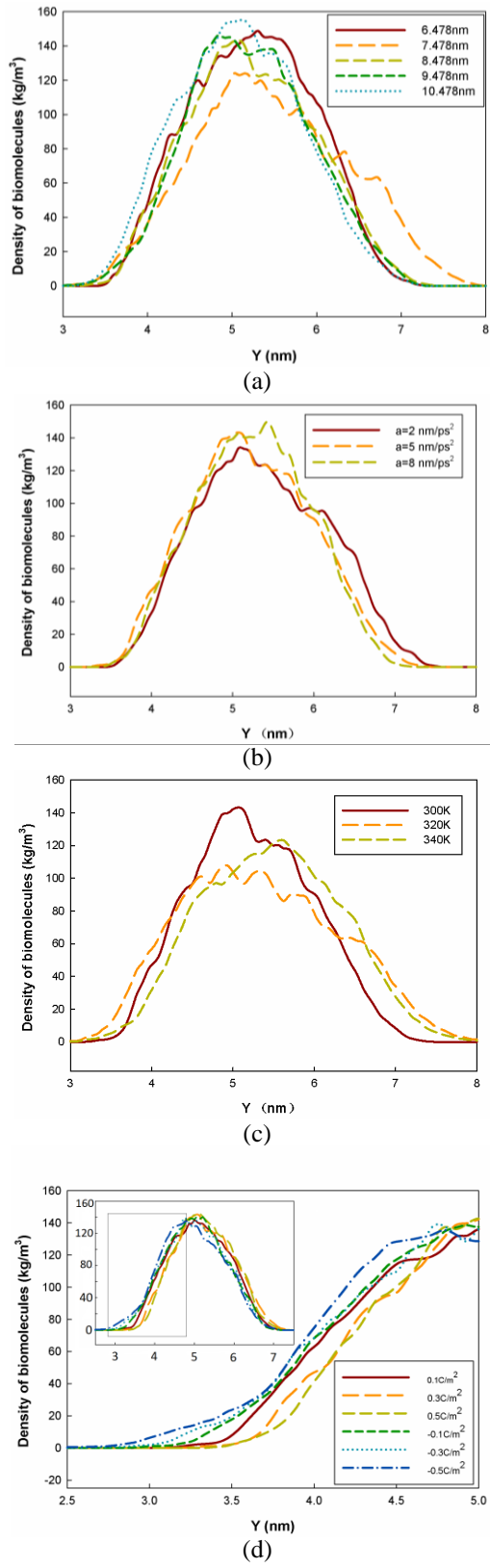
Fig. 5. Biomolecular density distribution at h=8.478 nm, $\vec{a}$ =5 nm/ps², T=300K and ρ_{wall}=0.3 C/m² (unless otherwise stated), (a) at h=6.478, 7.478, 8.478, 9.478 nm and 10.478 nm, (b) at $\vec{a}$ =2, 5 and 8 nm/ps², (c) at T=300, 320 and 340K, (d) at ρ_{wall}=-0.5, -0.3, -0.1, 0.1, 0.3 and 0.5

C/m².

As shown in Fig.5(a), the channel height's influence on biomolecular density is unpredictable. The similar situation happens in Fig.5(c), which shows the temperature's influence on biomolecular density. The pressure effect on biomolecular density is summarized in Fig.5(b), which shows that it increases with the acceleration peaking at 8 nm/ps². Because greater pressure exerted on the biomolecules brings greater speeds and resistance, the biomolecules have to shrink their shape, which leads to high biomolecular density in the middle.

Fig. 5(d) shows the influence of wall charge density on biomolecular density. The distance between the wall and biomolecules increases with the wall charge density from -0.5 to 0.5 C/m². As a result, the positively charged biomolecules are attracted by the negatively charged wall or excluded by the positively charged wall. However, either the attractive force or repulsive force increases with the wall charge density.

Fig. 6 shows the average velocity of three lysozyme biomolecules in the channel numbered with *p1*, *p2* and *p3*. Among them, *p1* has the lowest velocity and *p2* has the highest velocity.

Fig. 6(a) shows the channel height's influence on biomolecular velocity. It shows that the biomolecular velocity decreases with *h* and reaches the peak point at 6.478 nm. As the water molecular velocity decreases with channel height, the biomolecular velocity also decreases with channel height. Moreover, the velocity increments of biomolecules become smaller with the increase in channel height above 8.478 nm, so the height's influence on biomolecular velocity becomes less important with the increase. Fig. 6(b) shows the pressure's influence on biomolecular velocity. As the water molecular velocity increases with acceleration, the biomolecular velocity increases linearly.

Fig. 6(c) shows the temperature's influence on biomolecular velocity. As the disorder of thermal motion increases with temperature, biomolecular velocity slightly decreases except for *p2* at 340K.

Fig. 6(d) shows the influence of wall charge density on biomolecular velocity. It shows that the biomolecular velocity increases marginally with the absolute wall charge density. As a fact, the central water molecules face the smallest resistance, so this velocity is greater than that nearby the wall. Due to the attractive or compulsive force induced by the charged wall, more biomolecules are limited in the central channel with the increase in the wall charge

density. Thus the greater the absolute wall charge density, the higher is the biomolecular velocity. However, this influence is much smaller than the pressure's, which results in a slight increase of the biomolecular velocity.

(a)

(b)

(c)

(d)
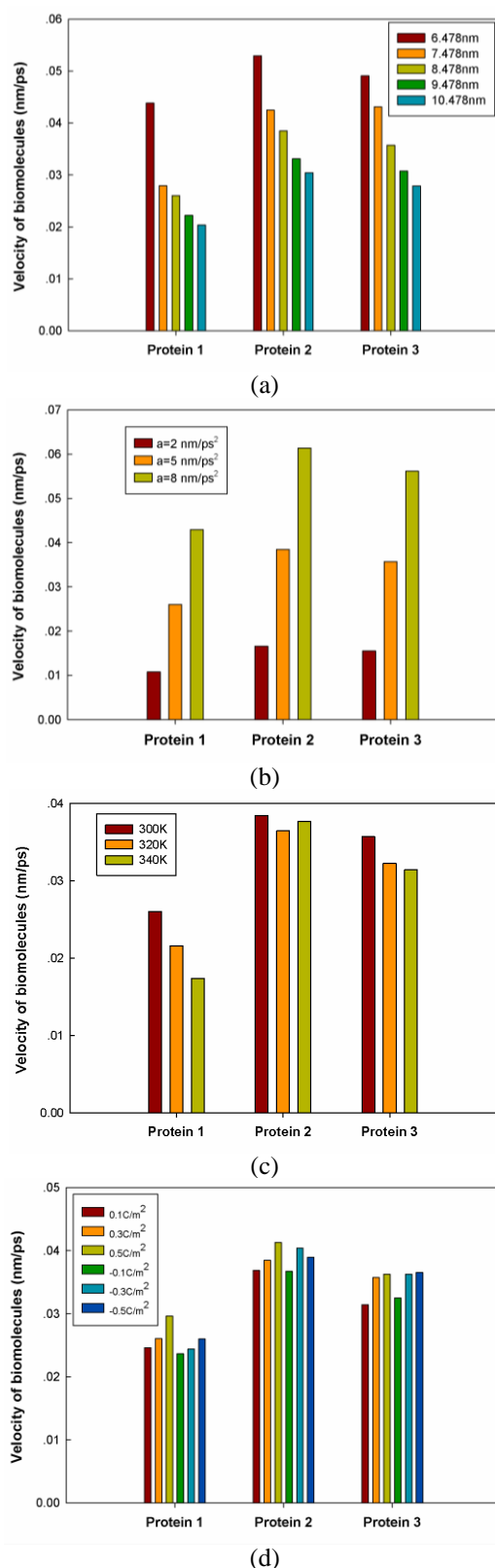
Fig. 6. Velocity distribution of biomolecules at h=8.478 nm, $\bar{a}$ =5 nm/ps^2, T=300K and ρ_{wall}=0.3 C/m^2

(unless otherwise stated), (a) at h=6.478, 7.478, 8.478, 9.478 nm and 10.478 nm, (b) at $\bar{a}$ =2, 5 and 8 nm/ps^2, (c) at T=300, 320 and 340K, (d) at ρ_{wall}=-0.5, -0.3, -0.1, 0.1, 0.3 and 0.5 C/m^2.

CONCLUSIONS

The *NEMD* simulation of biomolecular flows in a *SiO$_2$* nanochannel driven by pressure is presented. The results show that the interfacial interactions play an important role in determining the transport characteristics of ions, water molecules and biomolecules in the nanochannel. The following conclusions can be drawn from the present simulation. First, the change in water molecular density and ion concentration close to the wall becomes sharper with the decrease in channel height under 8.478 nm while the molecular velocity decreases with the channel height. Second, the velocity of water molecules and biomolecules linearly increases with the exerted acceleration. Third, the characteristics near the walls are slightly influenced by the temperature. Last, the wall charge density greatly affects the ion concentration distribution, but not the water molecular velocity.

As the channel height and wall charge density are decisive to the density distribution, they should be carefully chosen in designing nanofluidic devices. Besides, the system temperature should also be considered.

REFERENCES

1. R. Karnik, K. Castelino, R. Fan, P. D. Yang, A. Majumdar, *NanoLett.*, **5**, 1638 (2005).
2. R. Karnik, R. Fan, M. Yue, D. Y. Li, P. D. Yang, A. Majumdar, NanoLett. **5**, 943 (2005).
3. R. Karnik, K. Castelino, *Appl. Phys. Lett.*, **88**, 123114 (2006).
4. E. Tamaki, A. Hibara, H. B. Kim, M. Tokeshi, T. Kitamori, *J. Chromatogr. A*, **1137**, 256 (2006).
5. J. Fu, R. B. Schoch, A. L. Stevens, S. R. Tannenbaum, J. Han, *Nature Nanotech.*, **2**, 121 (2007).
6. N. Douville, D. Huh, S. Takayama, Anal Bioanal Chem., **391**, 2395 (2008).
7. T. Tsukahara, K. Mawatari, A. Hibara, T. Kitamori, *Anal Bioanal Chem.,* **391**, 2745 (2008).
8. M. A. G. Zevenbergen, B. L. Wolfrum, E. D. Goluch, P. S. Singh, S. G. Lemay, *J. AM. CHEM. SOC.*, **131**, 11471 (2009).
9. M. Ben Ishai, F. Patolsky, *J. AM. CHEM. SOC.*, **131**, 3679 (2009).

10. D. Frenkel, B. Smit, Understanding Molecular Simulation: from Algorithms to Applications, Academic Press, San Diego, 1996.
11. F. Sofos, T. Karakasidis, A. Liakopoulos, *Int. J. Heat Mass Transfer*, **52**, 735 (2009).
12. F. Sofos, T. E. Karakasidis, A. Liakopoulos, *Contemporary Engineering Sciences*, **2**, 283 (2009).
13. G. González, J. C. Tejas, J. P. A. Vallejo, J. F. J. Alvarado, O. Manero, *Rheol. Acta*, **48**, 1017 (2009).
14. F. Sofos, T. E. Karakasidis, A. Liakopoulos, *Int. J. Heat Mass Transfer,* **53**, 3839 (2010).
15. D. T. Semiromi, A. R. Azimian, *Heat Mass Transfer*, **46**, 791 (2010).
16. J. W. Kanga, K. R. Byuna, J. Y. Lee, S. C. Kong, Y. W. Choi, H. J. Hwang, *Physica E*, **24**, 349 (2004).
17. R. Qiao, N. R. Aluru, *Colloids and Surfaces A: Physicochem. Eng. Aspects*, **267**, 103 (2005).
18. R. Qiao, *Langmuir*, **22**, 7096 (2006).
19. R. Qiao, *MicrofluidNanofluid*, **3**, 33 (2007).
20. S. M. Cory, Y. Liu, M. I. Glavinović, *Biochim. Biophys. Acta*, **1768**, 2319 (2007).
21. D. Duong-Hong, J. S. Wang, G. R. Liu, Y. Z. Chen, J. Han, N. G. Hadjiconstantinou, *MicrofluidNanofluid*, **4**, 219 (2008).
22. C. D. Lorenz, P. S. Crozier, J. A. Anderson, A. Travesset, *J. Phys. Chem. C*, **112**, 10222 (2008).
23. Y. S. Choi, S. J. Kim, *J. Colloid Interface Sci.*, **333**, 672 (2009).
24. E. C. Yusko, R. An, M. Mayer, *ACS Nano*, **4**, 477 (2010).
25. A. Plecis, R. B. Schoch, P. Renaud, *Nano Lett.*, **5**, 1147 (2005).
26. Y. Liu, K. Oh, J. G. Bai, C. Chang, W. Yeo, J. Chung, K. Lee, W. K. Liu, *Comput. Methods Appl. Mech. Engrg.*, **197**, 2156 (2008).
27. Y. J. Oh, A. L. Garcia, D. N. Petsev, G. P. Lopez, S. R. J. Brueck, C. F. Ivoryc, S. M. Han, *Lab Chip.*, **9**, 1601 (2009).
28. U. Vermesh, J. W. Choi, O. Vermesh, R. Fan, J. Nagarah, J. R. Heath, *Nano Lett.*, **4**, 1315 (2009).
29. D. T. W. Lin, C. K. Chen, *Acta Mech.*, *173*, 181 (2004).
30. S. Das, T. Das , S. Chakraborty, *Sens. Actuators B*, **114**, 957 (2006).
31. D. T. W. Lin, *Int. J. Biol. Macromol.*, 41, 260 (2007).
32. A. Ghosh, R. Paredes, S. Luding, Poiseuille flow in a nanochannel–use of different thermostats, (PARTEC 2007–International Congress on Particle Technology).
33. F. H. J. van der Heyden, D. J. Bonthuis, D. Stein, C. Meyer, C. Dekker, *Nano Lett.*, 7, 1022 (2007).
34. X. J. Gong, J. Y. Li, H. Zhang, R. Z. Wan, H. J. Lu, S. Wang, H. P. Fang, *Phys. Rev. Lett.*, **101**, 257801 (2008).
35. M. Cieplak, *Eur. Phys. J. Spec. Top.*, **161**, 35 (2008).
36. Y. H. Wu, B. Wiwatanapataphee, M. B. Hu, *Physica A*, **387**, 5979 (2008).
37. S. Joseph, N. R. Aluru, *NanoLett.*, **8**, 452 (2008).
38. J. Goldsmith, C. C. Martens, *J. Phys. Chem. Lett.*, **1**, 528 (2010).
39. A. Szymczyk, H. Zhu, B. Balannec, *Langmuir*, **26**, 1214 (2010).
40. J. A. Thomas, A. J. H. McGaughey, O. Kuter-Arnebeck, Int. J. Therm. Sci., 49, 281 (2010).
41. H. Hoang, S. Kang, Y. K. Suh, *J. Mech. SCI. Technol.,* **24**, 1401 (2010).
42. Y. X. Li, J. L. Xu, D. Q. Li, *MicrofluidNanofluid*, **9**, 1011 (2010).
43. G. De Luca, M. I. Glavinović, *Glutamate, Biochim. Biophys. Acta*, **1768**, 264 (2007).
44. W. W. Schmahl, I. P. Swainson, M. T. Dove, A. G-Barber, Z. *Kristallogr.*, **201**, 125 (1992).
45. D. Argyris, D. R. Cole, A. Striolo, *ACS Nano*, **4**, 2035 (2010).
46. R. Kamali, A. Kharazmi, *Int. J. Therm. Sci.*, **50**, 226 (2011).
47. G. Bussi, D. Donadio, M. Parrinello, *J. Chem. Phys.*, **126**, 014101 (2007).

МОЛЕКУЛНО СИМУЛИРАНЕ НА ТРАНСПОРТА НА ПРОТЕИНИ, КОНТРОЛИРАН ЧРЕЗ ПОТОК, ЗАДВИЖВАН ЧРЕЗ НАЛЯГАНЕ В НАНО-КАНАЛИ ОТ СИЛИЦИЕВ ДИОКСИД

К. Лю[1,*], Ш. Л. Чен[1], Ш. У. Ксиао[2], С. Л. Жанг[3], Д. Ч. Ба[1, *], Д. Я. Ванг[1], Г. Ю. Ду[1], Я. Ш. Ба[1],

[1]*Училище по машинно инженерство и автоматика, Североизточен университет, Шенгянг, Китай*
[2]*Институт по физика на високите енергии, Китайска академия на науките, Бейджин, Китай*
[3]*Столична компания за космическо машиностроене, Бейджин, Китай*

Постъпила на 4 април, 2015 г.

(Резюме)

В серия от симулации с неравновесна молекулна динамика (NEMD) са изследвани процесите на би-молекулна миграция, предизвикана от налягане в канали с нано-размери. Използвани са различни параметри, включително височина на каналите, налягане, температура и заряд на стените за изследването на плътността и скоростта на транспорт на молекули и йони. Резултатите показват, че височината на каналите има значително въздействие върху плътността и скоростта в зависимост от размера на био-молекулите. Плътността на заряда също влияе силно на скоростта и йонната концентрация в близост до стените на канала, докато температурата има слабо влияние. Направените зводи са полезни при конструирането на уреди с нано-флуиди.

AUTHOR INDEX

АВТОРСКИ УКАЗАТЕЛ

SUBJECT INDEX

ПРЕДМЕТЕН УКАЗАТЕЛ

BULGARIAN CHEMICAL COMMUNICATIONS

Instructions about Preparation of Manuscripts

General remarks: Manuscripts are submitted in English by e-mail or by mail (in duplicate). The text must be typed double-spaced, on A4 format paper using Times New Roman font size 12, normal character spacing. The manuscript should not exceed 15 pages (about 3500 words), including photographs, tables, drawings, formulae, etc. Authors are requested to use margins of 3 cm on all sides. For mail submission hard copies, made by a clearly legible duplication process, are requested. Manuscripts should be subdivided into labelled sections, e.g. **Introduction, Experimental, Results and Discussion**, *etc*.

The title page comprises headline, author's names and affiliations, abstract and key words.

Attention is drawn to the following:

a) **The title** of the manuscript should reflect concisely the purpose and findings of the work. Abbreviations, symbols, chemical formulas, references and footnotes should be avoided. If indispensable, abbreviations and formulas should be given in parentheses immediately after the respective full form.

b) **The author**'s first and middle name initials, and family name in full should be given, followed by the address (or addresses) of the contributing laboratory (laboratories). **The affiliation** of the author(s) should be listed in detail (no abbreviations!). The author to whom correspondence and/or inquiries should be sent should be indicated by asterisk (*).

The abstract should be self-explanatory and intelligible without any references to the text and containing not more than 250 words. It should be followed by key words (not more than six).

References should be numbered sequentially in the order, in which they are cited in the text. The numbers in the text should be enclosed in brackets [2], [5, 6], [9–12], etc., set on the text line. References, typed with double spacing, are to be listed in numerical order on a separate sheet. All references are to be given in Latin letters. The names of the authors are given without inversion. Titles of journals must be abbreviated according to Chemical Abstracts and given in italics, the volume is typed in bold, the initial page is given and the year in parentheses. Attention is drawn to the following conventions:

a) The names of all authors of a certain publications should be given. The use of "*et al.*" in the list of references is not acceptable.

b) Only the initials of the first and middle names should be given.

In the manuscripts, the reference to author(s) of cited works should be made without giving initials, e.g. "Bush and Smith [7] pioneered...". If the reference carries the names of three or more authors it should be quoted as "Bush *et al*. [7]", if Bush is the first author, or as "Bush and co-workers [7]", if Bush is the senior author.

Footnotes should be reduced to a minimum. Each footnote should be typed double-spaced at the bottom of the page, on which its subject is first mentioned.

Tables are numbered with Arabic numerals on the left-hand top. Each table should be referred to in the text. Column headings should be as short as possible but they must define units unambiguously. The units are to be separated from the preceding symbols by a comma or brackets.

Note: The following format should be used when figures, equations, *etc*. are referred to the text (followed by the respective numbers): Fig., Eqns., Table, Scheme.

Schemes and figures. Each manuscript (hard copy) should contain or be accompanied by the respective illustrative material as well as by the respective figure captions in a separate file (sheet). As far as presentation of units is concerned, SI units are to be used. However, some non-SI units are also acceptable, such as °C, ml, l, etc.

The author(s) name(s), the title of the manuscript, the number of drawings, photographs, diagrams, etc., should be written in black pencil on the back of the illustrative material (hard copies) in accordance with the list enclosed. Avoid using more than 6 (12 for reviews, respectively) figures in the manuscript. Since most of the illustrative materials are to be presented as 8-cm wide pictures, attention should be paid that all axis titles, numerals, legend(s) and texts are legible.

The authors are asked to submit **the final text** (after the manuscript has been accepted for publication) in electronic form either by e-mail or mail on a 3.5'' diskette (CD) using a PC Word-processor. The main text, list of references, tables and figure captions should be saved in separate files (as *.rtf or *.doc) with clearly identifiable file names. It is essential that the name and version of

the word-processing program and the format of the text files is clearly indicated. It is recommended that the pictures are presented in *.tif, *.jpg, *.cdr or *.bmp format, the equations are written using "Equation Editor" and chemical reaction schemes are written using ISIS Draw or ChemDraw programme.

The authors are required to submit the final text with a list of three individuals and their e-mail addresses that can be considered by the Editors as potential reviewers. Please, note that the reviewers should be outside the authors' own institution or organization. The Editorial Board of the journal is not obliged to accept these proposals.

EXAMPLES FOR PRESENTATION OF REFERENCES

REFERENCES

1. D. S. Newsome, *Catal. Rev.–Sci. Eng.*, **21**, 275 (1980).
2. C.-H. Lin, C.-Y. Hsu, *J. Chem. Soc. Chem. Commun.*, 1479 (1992).
3. R. G. Parr, W. Yang, Density Functional Theory of Atoms and Molecules, Oxford Univ. Press, New York, 1989.
4. V. Ponec, G. C. Bond, Catalysis by Metals and Alloys (Stud. Surf. Sci. Catal., vol. 95), Elsevier, Amsterdam, 1995.
5. G. Kadinov, S. Todorova, A. Palazov, in: New Frontiers in Catalysis (Proc. 10th Int. Congr. Catal., Budapest, 1992), L. Guczi, F. Solymosi, P. Tetenyi (eds.), Akademiai Kiado, Budapest, 1993, Part C, p. 2817.
6. G. L. C. Maire, F. Garin, in: Catalysis. Science and Technology, J. R. Anderson, M. Boudart (eds), vol. 6, Springer-Verlag, Berlin, 1984, p. 161.
7. D. Pocknell, *GB Patent* 2 207 355 (1949).
8. G. Angelov, PhD Thesis, UCTM, Sofia, 2001.
9. JCPDS International Center for Diffraction Data, Power Diffraction File, Swarthmore, PA, 1991.
10. CA **127**, 184 762q (1998).
11. P. Hou, H. Wise, *J. Catal.*, in press.
12. M. Sinev, private communication.
13. http://www.chemweb.com/alchem/articles/1051611477211.html.

CONTENTS

СЪДЪРЖАНИЕ